Daniel Ogochukwu Okanigbe *Editor*
Abimbola Patricia Popoola *Co-editor*

Resource Recovery and Recycling from Waste Metal Dust

Springer

Resource Recovery and Recycling from Waste Metal Dust

Daniel Ogochukwu Okanigbe
Abimbola Patricia Popoola
Editors

Resource Recovery and Recycling from Waste Metal Dust

Springer

Editors
Daniel Ogochukwu Okanigbe
Department of Chemical, Metallurgical and Materials Engineering
Faculty of Engineering and the Built Environment
Tshwane University of Technology
Pretoria, South Africa

Abimbola Patricia Popoola
Department of Chemical, Metallurgical and Materials Engineering
Faculty of Engineering and the Built Environment
Tshwane University of Technology
Pretoria, South Africa

Pantheon Virtual Engineering Solutions
Nigel, South Africa

ISBN 978-3-031-22491-1 ISBN 978-3-031-22492-8 (eBook)
https://doi.org/10.1007/978-3-031-22492-8

This Springer imprint is published by the registered company Springer Nature Switzerland AG
The registered company address is: Gewerbestrasse 11, 6330 Cham, Switzerland

Preface

Efficiency in managing minerals and the byproducts produced when extracting them from ore bodies is becoming increasingly important. Some examples of these byproducts include concentrated wastes, diluted streams and effluent, used catalysts, plating solutions, process water, and waste metal dust.

The nature of many metallurgical processes leads to the inevitable generation of these byproducts that have no direct use for the main metal sector. Many of them, which are frequently regarded as "waste," end up in landfills or tailings ponds. Such waste products have also accumulated in enormous amounts, necessitating immediate action for resource recovery and recycling. Resource recovery and recycling from waste metal dust is also stressed because it may stop usable materials from being burned or dumped, which lowers waste disposal costs and eliminates the need for landfills and tailing ponds. Resource recovery and recycling is one of the best strategies to reduce the amount of energy needed in the metal business. The energy required for ore mining is cut down since metal recovery and recycling is done by processing the metal or engineering the ore.

That is why the reduction of waste, or ideally its elimination, is a highly desired goal. In addition, recent technical developments have sparked fresh progress in this direction thanks to scientific understanding of the processes that take place. However, it must be acknowledged that resource recovery and recycling has been and will continue to be a key job in the metallurgical industry. Because metals are a limited resource, their virgin natural ores are steadily running out in industrialized nations. It goes without saying that resource recovery and recycling from waste metal dust is essential to ensuring that metals are available in the appropriate quantities.

The need to recover resources from such "waste" or transform them into usable byproducts is expanding. To fulfill the objective of sustainable development, continuous industrial expansion for healthy living standards, which demands a clean environment and continuous resource availability, they will be more and more in demand.

Hence, this book strives to offer more comprehensive treatment of all aspects of resource recovery and recycling from waste metal dust, explaining the goals and objectives of this theme. This book is organized into six parts, each of which has two chapters.

Tshwane University of Technology
Pretoria, South Africa
Pantheon Virtual Engineering Solutions
Nigel, South Africa

Daniel Ogochukwu Okanigbe

Contents

Part I
Resource Recovery and Recycling from Waste Metal Dust

Chapter 1
Resource Recovery and Recycling from Waste Metal Dust (I): Waste Iron Dust and Waste Aluminum Dust

Daniel Ogochukwu Okanigbe

1.1 Waste Metal Dusts

Extractive metallurgy uses smelting to create a metal from its ore [1]. Heat and a chemical reduction agent are used in smelting to break down the ore, removing other components as gases or slag and only leaving the metal behind [2, 3] while purifying an impure metal is the purpose of refining in the field of metallurgy [4–6]. In contrast to smelting, which results in a chemical change to the raw material, refining typically results in a purer finished product that is typically chemically same to the original [7].

However, in order to convert metal ores like copper glance [8, 9], pisolitic ironstone [10], bauxite [11], and galena [12] into pure copper, iron, aluminum, and lead, respectively, these two metallurgical processes need to reach extremely high temperatures. As a result, throughout the smelting process, it is crucial to know these metals' melting points, for instance, copper melts at 1085 °C [13, 14], iron melts at 1536 °C [15, 16], aluminum melts at 660 °C [17], lead melts at 328 °C [18] and so on. Many other metals and metal compounds also melt or volatilize at these temperatures; for instance, lead has a melting point of 328 °C [18], and mercury, cadmium, zinc, and arsenic all have boiling points of 357 °C [19], 765 °C [20], 906 °C [21], and 613 °C [22], respectively.

Wastes are produced during the metal smelting and refining processes, including dusts among others [23]. Metals including copper, iron, aluminum, lead, zinc, nickel, cadmium, chromium, mercury, selenium, arsenic, cobalt, etc., are frequently found in these wastes.

D. O. Okanigbe (✉)
Department of Chemical, Metallurgical and Materials Engineering, Faculty of Engineering and the Built Environment, Tshwane University of Technology, Pretoria, South Africa

Pantheon Virtual Engineering Solutions, Nigel, South Africa
e-mail: okanigbedo@tut.ac.za; okanigbeogochukwu@gmail.com

D. O. Okanigbe, A. P. Popoola (eds.), *Resource Recovery and Recycling from Waste Metal Dust*, https://doi.org/10.1007/978-3-031-22492-8_1

To create metal alloys, these elements may be present in the ores utilized or they may be introduced as mixed metals to the melting [24].

In this chapter, the dusts created during metal smelting and refining are referred to as waste metal dust (WMD) because they frequently contain considerable amounts of valuable metal oxides. Due to the high metal concentrations, WMD created in the smelting furnace is categorized as both a lucrative by-product and a dangerous pollution [25]. In order to manage this type of metallurgical waste, this has inspired various researchers in the past and even now to study further acceptable ways on resource recovery and recycling from WMD.

Because of this, this chapter provides a summary of resource recovery and recycling from WMD, concentrating on the generation of WMD, their description, their recirculation or disposal, as well as modern methods for resource recovery and recycling from WMD.

1.2 Types of Waste Metal Dusts

1.2.1 Waste Iron Dust

1.2.1.1 Generation

For the most part, low-carbon stainless steels are refined using the argon oxygen decarburization (AOD) and vacuum oxygen decarburization (VOD) procedures. During the refining process, waste iron dust (WID) [26, 27] is generated. It has a significant amount of precious metal oxides of Fe, Cr, and Ni, and its production rises together with that of stainless steel [28, 29].

Several reports have been shared on its treatment, because of these valuable metals, WID often contains [30–34]. WID is metal and slag mixes that primarily found their way into the equipment used for collecting. Additionally, some WID was released from the flue gas pipelines as a result of the ferociously violent stirring of molten steel during the operations for producing stainless steel.

1.2.1.2 Description of WID

Particle Size Distribution of WID

WID is very fine material, according to all reported analyses [30, 31, 35]. Particles with a diameter of less than 5 μm made up roughly 70–90% (by weight) of the dusts, and even more of them had a diameter of less than 1 m. In WID, there are still a few sizable solid agglomerates that make about 10–30% of the total weight and may have had a diameter of more than 150 μm.

Chemical Composition of Typical WID

According to Sofilić et al. [29], the chemical species in WID depend on the quality of the steel scrap treated, the type of steel being produced, technological and operating circumstances, and the degree of dust returned into the process.

According to this assertion, Table 1.1 illustrates the several chemical species that make up the predominant composition of these WID. Since iron ore is

Table 1.1 Chemical Species in WID from Various Processing Facilities across the World

Species	Content						
	WID 1	WID 2	WID 3	WID 4	WID 5	WID 6	WID 7
CaO	14.00	6.59	9.02	9.14	12.90	9.14	2.31
SiO_2	5.60	5.76	5.14	5.45	4.81	5.45	6.42
Al_2O_3	0.70	0.74	0.64	0.66	0.40	0.66	6.67
MgO	2.60	4.25	3.63	3.48	5.44	3.48	2.35
Cr_2O_3/CrO	14.30[Cr_2O_3]	–	16.30[Cr_2O_3]	15.10[Cr_2O_3]	14.60[Cr_2O_3]	13.51[CrO]	9.09[Cr_2O_3]
MnO/MnO_2	3.30[MnO]	5.88[MnO]	4.41[MnO_2]	4.67[MnO_2]	5.08[MnO]	4.67[MnO_2]	2.64[MnO]
Fe_2O_3	45.20	39.56	51.30	48.00	43.40	56.00	≈ 46.28
CuO	–	–	–	–	–	–	0.43
WO_3	–	–	–	–	–	–	0.91
BiO	–	–	–	–	–	–	≈ 0.07
SnO_2	–	–	–	–	–	–	≈ 0.05
TiO_2	–	0.16	0.08	0.12	0.08	–	≈ 0.07
NiO	4.30	–	6.25	6.70	2.79	6.70	2.42
ZnO	5.80	–	0.96	0.93	4.49	0.93	7.41
Na_2O	4.20	1.01	0.60	0.53	0.60	–	
K_2O	–	0.48	0.72	1.47	0.97	–	
P_2O_3	–	0.04	0.30	0.62	0.04	–	
V_2O_5	–	–	–	–	0.09	–	0.13
PbO	–	–	0.29	0.16	0.39	0.16	0.45
CdO	–	–	0.01	0.01	–	–	≈ 0.01
MoO_3	–	–	–	–	1.35	–	
CoO		–	–	–	–	–	≈ 0.04
ZrO_2	–	–	–	–	–	–	0.02
Nb_2O_5	–	–	–	–	–	–	≈ 0.07
SO_3	–	–	–	–	0.47	–	–
F	–	–	–	–	–	–	–
Cl				–	0.86	–	–
S	–	–	–	–	–	–	0.13
LOI	–	3.67	–	–	0.21	–	–
Others	–	31.86	–	–	1.45	–	9.75

Key: WID 1 = Kim and Sohn [26] (wt%); WID 2 = Laforest and Duchesne [32] (mass fraction, %); WID 3 = Tang et al. [33] (mass fraction, %, bag house); WID 4 = Tang et al. [33] (mass fraction, %, stockpile); WID 5 = Ma and Garbers-Craig [34] (mass fraction, %); WID 6 = Peng et al. (2007) (mass fraction, %, stockpile); WID 7 = Takano [36] (wt%); LOI = loss on ignition

involved, Fe_2O_3 had the highest percentage in each WID (39.56–56.00%), as one might anticipate. Then comes CaO (2.31–14.00%), ZnO (0.93–7.41%), NiO (2.42–6.70%), SiO_2 (4.81–6.42%), MnO/MnO_2 (2.64–5.88%), MgO (2.35–5.44%), and Cr_2O_3/CrO (9.09–16.30%). The variety of these WID's contents and compositions places a great emphasis on the need for categorization of these WID [29]. Information like this demonstrates even more how the WID from the various sources listed in Table 1.1 differs in terms of harmful chemical species like Cr_2O_3. This has influenced how waste management strategies have been adopted [34].

Mineralogy of WID

Some researches [26, 29, 32] looked at the phase structures of the WID. Complex oxides, which frequently take the form of phases like $ZnS_2O_4Na_2S_2O_4nH_2O$ [29] and $Fe_2(SO_4)3H_2SO_42H_2O$, are abundant in the WID and predominate there. Sulfides (FeS, Fe_9S_8, Ni_7S_6 [29], and silicate SiO_2, $2FeOSiO_2$ [29]) are also present, though. Before disposal, a suitable process path has always been designed for the recovery of the valuable metals, depending on the composition of these compounds and associations.

Morphology of WID

Several researches have investigated the micro-shape of the WID constituents [29, 32, 37]. Individual particles were typically spherical [30, 37, 38] and frequently seen in aggregate forms; angular particles were uncommon [29, 39].

1.2.1.3 Stabilization/Solidification for Recirculation or Disposal of WID

WID must first be converted into briquettes using a suitable reducing agent, such as carbon, in order to be recirculated [26, 40, 41]. But because they require more binder, such as bentonite or cement, and increase the volume of slag, impurities like CaO, SiO_2, Al_2O_3, MgO, and ZnO in the recirculated WID might reduce the furnace's efficiency and use unnecessary electricity [26, 40, 42].

Recirculation to the furnace is also not an option due to the presence of harmful heavy metals, some of which are partially soluble, such as the fatal hexavalent chromium (Cr^{6+}) [26].

Should these harmful heavy metals in WID be stabilized or consolidated for ultimate disposal to class one landfill sites, like the large but expensive Vlakfontein investment in South Africa (SA) (Fig. 1.1)? Where this WID are disposed of, potential liability issues may still exist.

Fig. 1.1 Shows the enormous Vlakfontein investment in SA, which was built to address the problem of hazardous wastes. (Source: google image)

1.2.1.4 Resource Recovery and Recycling from WID

The Recovery of Metals from WID

For both economic and environmental reasons, many regions have been processing these WID during the past 20 years in order to extract the valuable metal components, such as nickel, chromium, molybdenum, and iron.

The Use of Hydrometallurgical Techniques
Four processes make up the majority of the hydrometallurgical process: roasting, leaching, purification, and electrowinning. It is a common technique for obtaining non-ferrous metals including zinc, lead, copper, and so forth. According to several commercial methods, hydrometallurgical techniques have been employed to recover Zn from WID using alkaline leaching [43–46].

The Use of Pyrometallurgical Techniques
WID mixes from several researchers have been used in laboratory size reduction smelting studies [36]. Approximately 90% of the total iron, 95% of the chromium, and practically 100% of the nickel in the WID, according to the results, may be recovered by combining molten metals at the right temperature with additives and reductants.

The Use of Physical Separation Techniques
Smaller, more polluted particles are often removed using physical separation methods. Centrifugation, sedimentation, gravity separation, magnetic separation, and other techniques are among them. According to reports, certain commercial

processes have recovered Ni and Cr from stainless-steel wastes using magnetic separation or gravity separation techniques, but the majority of research has remained in the lab [47]. When separating minerals with radically differing densities, gravity separation is an efficient technique. The recovery of ferromagnetic metals from non-ferrous metals and other non-magnetic wastes is frequently accomplished using magnetic separation.

Conversion of WSD into Value-Added Product

Ordoez and Colorado [48] used WID in their research as a complementing material in the additive manufacturing (AM) of kaolinite-based clays as an example of attempts toward the conversion of WID into value-added product. The direct ink writing method was the AM technique used. Since the residues can be immobilized and the water can be less contaminated, adding WID to the clay is good for the environment. The current study demonstrates the potential for employing WID in 3D printed components as well as an admixture with clay ceramics after sintering.

1.2.2 Waste Aluminum Dust

1.2.2.1 Generation

One of the materials that can be recycled the most easily is aluminum [49, 50]. In fact, according to one estimate, 75% of the aluminum that has ever been produced is still in use [51]. This is due to the existence of industrial procedures for the conversion of primary aluminum and scrap into secondary or second fusion aluminum, which generates a number of by-products.

Even so, enormous amounts are wasted as dusts (such as waste aluminum dust), slags, etc. [52], salt slag (more than 500 kg/MT Al), aluminum slag (less than 10,000 MT/year), and furnace filter fines (more than 35 kg/MT Al [53], herein referred to as waste aluminum dust), are the waste products produced in the secondary aluminum melting step (WAD).

1.2.2.2 Description of WAD

Particle Size Distribution of WAD

The particle size of the WAD examined in the study by Nifuku et al. [54] was primarily greater than 105 μm for samples 1 and 2 and primarily in the range of 8–20 μm for sample 3. According to Liu et al. [55], the WAD employed in their

investigation had a larger size dispersion and a mean particle size of about 80 μm. The samples examined, according to Galindo et al. [52], had a significant percentage of fine particles. According to Wang et al. [50], the particle distributions for the WAD under study are 1.34 μm, 3 μm, and 6.59 μm, respectively.

Chemical Composition of Typical WAD

The claim of WAD containing significant amounts of value metals is supported by Table 1.2, which lists the many chemical species that make up the bulk of these WAD's composition. Al_2O_3 has the largest percentage in each WAD (21.56–82.28%), as one might expect given that aluminum ore is included [52, 55]. SiO_2 (range: 0.38–6.30%), MgO (range: 2.37–4.31%), CaO (range: 1.00–2.80%), and Fe_2O_3 (range: 0.64–1.40%) follow.

The amount of salts employed in the melting process in order to achieve a higher aluminum recovery, according to the researchers, is what caused the high sodium concentration, Na_2O (range: 4.7–21.69%).

Table 1.2 Chemical Compositions of WAD Used in Different Study

	Content (wt. %)		
Composition	WAD 1	WAD 2	WAD 3
Al_2O_3	82.28	75.00	21.56
SiO_2	5.74	6.30	0.38
Na_2O	4.71	2.20	21.69
MgO	4.31	4.00	2.37
CaO	1.00	2.80	1.37
Fe_2O_3	0.72	1.40	0.64
K_2O	0.41	0.70	5.88
TiO_2	0.27	2.80	0.37
CuO	0.25	–	–
MnO_2/MnO	$0.13^{[MnO_2]}$	–	$0.05^{[MnO]}$
ZnO	0.08	–	–
V_2O_5	0.05	–	–
Cr_2O_3	0.04	–	–
NiO	0.02	–	–
P_2O_5	–	–	0.03
S	–	–	2.69
F	–	–	2.89
Cl	–	1.20	24.42
LOI	–	–	21.82
Others	–	3.30	–

Key: WAD 1 = Liu et al. [55]; WAD 2 = Galindo et al. [52]; WAD 3 = Eliche-Quesada et al. [56]

Mineralogy of WAD

Aluminum metal and aluminum oxide were found to be the primary crystal phases in the investigation by Liu et al. [55] using an XRD diffractogram of WAD. Aluminum nitride, aluminum magnesium oxide, and silicon are additional crystal phases.

Morphology of WAD

According to the morphology of the WAD particles utilized in the investigation by Liu et al. [55], they had an irregular form and a rough surface. While many small rod-like particles congregate on the surface of larger particles, some particles have a plate-like shape. On the other hand, the WAD employed in the study by Wang, Xu, and Wang [50] shows that the particles are roughly spherical and the surface is not rough.

1.2.2.3 Recirculation of WAD

A type of WMD having explosive potential [57–59], WAD produced during the production of aluminum goods is categorized as a hazardous waste in many nations [55, 60].

1.2.2.4 Resource Recovery and Recycling from WAD

Conversion of WAD into Value-Added Product As an illustration of efforts to convert WAD into a value-added product, refractory mullite was prepared using WAD from the fine polishing process used in the manufacture of aluminum parts (also known as aluminum buffing dust) [61]. Ball milling was used to combine Ranong kaolin with WAD in a ratio of 100:0 to 40:60. By dry pressing, the batch mixtures were shaped. The temperature used to fire the green specimens ranged from 1100 to 1400 °C.

In the work by Liu et al. [55], WAD was utilized to create autoclaved aerated concrete by acting as a foaming agent, while Eliche-Quesada et al. [56] produced geopolymer foams using the WAD from the secondary aluminum industry's dust filter as a foaming agent. The source of alumina and the foaming agent in this study was WAD. By using a commercial sodium silicate solution and a sodium hydroxide aqueous solution, precursors were chemically activated. The authors claim that the synthetic geopolymer foam materials are equivalent to traditional building products including gypsum boards, foamed concrete, and insulating materials in terms of

their qualities. They suggested using these synthetic geopolymer foams as materials for gas filtration or catalyst support in other applications.

1.3 Conclusions

The comparative particle size distribution, chemical composition and morphology results of WID and WAD, provide a better analysis of the possibility of their recirculation or disposal after their stabilization/solidification. Hence, the following deductions were reached:

1. All particle size distribution results show that WID was very fine, with particle size smaller than 5 μm in diameter.
2. The chemical composition of WID produced by steel producers around the world is often identical, with Fe_2O_3 having the highest content (39.56–56.00%), as followed by Cr_2O_3/CrO (9.09–16.30%), then CaO (2.31–14.00%), ZnO (0.93–7.41%), NiO (2.42–6.70%), SiO_2 (4.81–6.42%), MnO/MnO_2 (2.64–5.88%), MgO (2.35–5.44%).
3. The metals in WID were mainly present in the form of complex oxide, and also as silicates.
4. On some occasions, the particle size of WAD ranged between 80 and 105 μm. whereas WAD's PSD was reported between 1.34 and 20 m size fractions.
5. Al_2O_3 makes up the greatest percentage of each WAD (21.56–82.28%), followed by SiO_2 (0.38–6.30%), MgO (2.37–4.31%), CaO (1.00–2.80%), and Fe_2O_3 (0.64–1.40%).
6. Aluminum metal and aluminum oxide were found to be the primary crystal phases in WAD. Aluminum nitride, aluminum magnesium oxide, and silicon are additional crystal phases reportedly present in WAD.
7. The WAD particle shapes range from small rod-like particles with a roughly spherical shape to smooth surfaces.

All of these findings indicate that the WMDs mentioned contain significant amounts of precious metals and other components in addition to hazardous metals. Direct stabilization/solidification techniques for disposal or recirculation were not the most effective ways to manage WMD, though, due to the scarcity of mineral resources. Therefore, resource recovery and recycling from these WMDs is a sustainable strategy from both an economic and environmental standpoint.

Acknowledgments The author will want to appreciate the Council for scientific and industrial research, Pretoria, South Africa and Tshwane University of Technology, Pretoria, South Africa, for the financial support. The author additionally acknowledges the facilities provided by Gravity concentrator Africa (PTY), Randburg, South Africa; Vaal University of Technology, Vanderbijlpark, South Africa; and University of Pretoria, Pretoria, South Africa.

References

1. F. Habashi, *Principles of Extractive Metallurgy: Pyrometallurgy* (Routledge, Abingdon, 2017)
2. L. Lu, J. Pan, D. Zhu, Quality requirements of iron ore for iron production, in *Iron Ore*, (Woodhead Publishing, Oxford, 2015), pp. 475–504
3. L. Brückner, J. Frank, T. Elwert, Industrial recycling of lithium-ion batteries—A critical review of metallurgical process routes. Metals **10**(8), 1107 (2020)
4. J. Li, B. Ban, Y. Li, X. Bai, T. Zhang, J. Chen, Removal of impurities from metallurgical grade silicon during Ga-Si solvent refining. Silicon **9**(1), 77–83 (2017)
5. S. Esfahani, M. Barati, Purification of metallurgical silicon using iron as an impurity getter part I: Growth and separation of Si. Met. Mater. Int. **17**(5), 823–829 (2011)
6. F. Huang, Q. Lu, M. Wu, L. Zhao, Purification of metallurgical-grade silicon by Sn-Si solvent refining with different tin content. Silicon, **14**, 1–11 (2022)
7. M. Cavallini, Thermodynamics applied to iron smelting techniques. Appl. Phys. A **113**(4), 1049–1053 (2013)
8. K. Murari, R. Siddique, K.K. Jain, Use of waste copper slag, a sustainable material. J. Mater. Cycles Waste Manag. **17**(1), 13–26 (2015)
9. G.A. Flores, C. Risopatron, J. Pease, Processing of complex materials in the copper industry: Challenges and opportunities ahead. JOM **72**(10), 3447–3461 (2020)
10. E.E. Okafor, *Early Iron Smelting in Nsukka-Nigeria: Information from Slags and Residues* (Doctoral dissertation, University of Sheffield, 1992)
11. C.R. Borra, B. Blanpain, Y. Pontikes, K. Binnemans, T. Van Gerven, Recovery of rare earths and major metals from bauxite residue (red mud) by alkali roasting, smelting, and leaching. J. Sustain. Metall. **3**(2), 393–404 (2017)
12. M. Shamsuddin, H.Y. Sohn, Constitutive topics in physical chemistry of high-temperature nonferrous metallurgy—A review: Part 1. Sulfide roasting and smelting. JOM **71**(9), 3253–3265 (2019)
13. X.H. Chen, X. Tang, Z.D. Wang, X.D. Hui, M. Li, Y.W. Wang, Manufacturing process and microstructure of copper-coated aluminum wires. Int. J. Miner. Metall. Mater. **22**(2), 190–196 (2015)
14. J.P. Tavener, Development of a standard platinum resistance thermometer for use up to the copper point. Int. J. Thermophys. **36**(8), 2027–2035 (2015)
15. S.A. Oglezneva, V.Y. Bulanov, Y.V. Kontsevoi, I.E. Ignat'ev, Production of nickel and iron nanopowders by hydrogen reduction from salts. Russ. Metall. (Met.) **2012**(7), 654–658 (2012)
16. K.T. Jacob, C.B. Alcock, The oxygen potential of the systems Fe+ FeCr2O4+ Cr2O3 and Fe+ FeV2O4+ V2O3 in the temperature range 750–1600 C. Metall. Trans. B **6**(2), 215–221 (1975)
17. S. Hasani, M. Panjepour, M. Shamanian, The oxidation mechanism of pure aluminum powder particles. Oxid. Met. **78**(3), 179–195 (2012)
18. V.P. Itkin, C.B. Alcock, The Ca-Pb (calcium-lead) system. J. Phase Equilib. **13**(2), 162–169 (1992)
19. C. Guminski, The melting and boiling points of mercury (I-Ig). J. Chem. Thermodyn. **4**, 603 (1972)
20. Z. Han, Z. Guo, Y. Zhang, X. Xiao, Z. Xu, Y. Sun, Pyrolysis characteristics of biomass impregnated with cadmium, copper and lead: Influence and distribution. Waste Biomass Valoriz. **9**(7), 1223–1230 (2018)
21. C. Wang, B. Lei, P. Jiang, X. Xu, G. Mi, Numerical and experimental investigation of vacuum-assisted laser welding for DP590 galvanized steel lap joint without prescribed gap. Int. J. Adv. Manuf. Technol. **94**(9), 4177–4185 (2018)
22. P. Kumar, A. Kumar, R. Kumar, Phytoremediation and Nanoremediation, in *New Frontiers of Nanomaterials in Environmental Science*, (Springer, Singapore, 2021), pp. 281–297
23. R.H. Hanewald, W.A. Munson, D.L. Schweyer, Processing EAF dusts and other nickel-chromium waste materials pyrometallurgically at INMETCO. Min. Metall. Explor. **9**(4), 169–173 (1992)

24. J. Banhart, Manufacturing routes for metallic foams. JOM **52**(12), 22–27 (2000)
25. Z. Wang, Z. Cui, L. Liu, Q. Ma, X. Xu, Toxicological and biochemical responses of the earthworm Eisenia fetida exposed to contaminated soil: Effects of arsenic species. Chemosphere **154**, 161–170 (2016)
26. G. Kim, I. Sohn, Selective metal cation concentration during the solidification of stainless steel EAF dust and slag mixtures from high temperatures for increased Cr recovery. J. Hazard. Mater. **359**, 174–185 (2018)
27. I.F. Kurunov, The direct production of iron and alternatives to the blast furnace in iron metallurgy for the 21st century. Metallurgist **54**(5), 335–342 (2010)
28. J. Rieger, J. Schenk, Residual processing in the European steel industry: A technological overview. J. Sustain. Metall. **5**(3), 295–309 (2019)
29. T. Sofilić, A. Rastovčan-Mioč, Š. Cerjan-Stefanović, V. Novosel-Radović, M. Jenko, Characterization of steel mill electric-arc furnace dust. J. Hazard. Mater. **109**(1–3), 59–70 (2004)
30. C.L. Li, M.S. Tsai, Mechanism of spinel ferrite dust formation in electric arc furnace steelmaking. ISIJ Int. **33**(2), 284–290 (1993)
31. P.J. Nolasco-Sobrinho, D.C.R. Espinosa, J.A.S. Tenório, Characterisation of dusts and sludges generated during stainless steel production in Brazilian industries. Ironmak. Steelmak. **30**(1), 11–17 (2003)
32. G. Laforest, J. Duchesne, Characterization and leachability of electric arc furnace dust made from remelting of stainless steel. J. Hazard. Mater. **135**(1–3), 156–164 (2006)
33. M.T. Tang, J. Peng, B. Peng, D. Yu, C.B. Tang, Thermal solidification of stainless steelmaking dust. Trans. Nonferrous Metals Soc. China **18**(1), 202–206 (2008)
34. G. Ma, A.M. Garbers-Craig, Stabilisation of Cr (VI) in stainless steel plant dust through sintering using silica-rich clay. J. Hazard. Mater. **169**(1–3), 210–216 (2009)
35. L. Wu, N.J. Themelis, The flash reduction of electric arc furnace dusts. JOM **44**(1), 35–39 (1992)
36. C. Takano, F.L. Cavallante, D.M. dos Santos, M.B. Mourão, Recovery of Cr, Ni and Fe from dust generated in stainless steelmaking. Miner. Process. Extr. Metall. **114**(4), 201–206 (2005)
37. Z. Huaiwei, H. Xin, An overview for the utilization of wastes from stainless steel industries. Resour. Conserv. Recycl. **55**(8), 745–754 (2011)
38. F. Škvára, F. Kaštánek, I. Pavelková, O. Šolcová, Y. Maléterová, P. Schneider, Solidification of waste steel foundry dust with Portland cement. J. Hazard. Mater. **89**(1), 67–81 (2002)
39. P. Rocabois, E. Lectard, J.C. Huber, F. Patisson, Thermodynamic assessment of the oxide phase in the Fe–Zn–O system-application to dust formation in electric arc furnace. In Proceedings of the 10th International IUPAC Conference on High Temperature Materials Chemistry, Julich, Germany, 10–14 April 2000; pp. 1–12.
40. H. Zhang, J. Dong, H. Xiong, Z. Wang, Y. Lu, Investigation on cooperative desulfurization efficiency for bearing carbon stainless steel dust briquettes chromium and nickel recovery process. J. Alloys Compd. **699**, 408–414 (2017)
41. S. Ri, M. Chu, Separation of metal nugget from self-reduced product of coal composite stainless steel dust briquette. ISIJ Int. **55**(8), 1565–1572 (2015)
42. S.S. Jung, G.B. Kim, I. Sohn, Understanding the solidification of stainless steel slag and dust mixtures. J. Am. Ceram. Soc. **100**(8), 3771–3783 (2017)
43. A.J.B. Dutra, P.R.P. Paiva, L.M. Tavares, Alkaline leaching of zinc from electric arc furnace steel dust. Miner. Eng. **19**(5), 478–485 (2006)
44. B. Lindblom, C. Samuelsson, G. Ye, Fine-particle characterization—An important recycling tool. JOM **54**(12), 35–38 (2002)
45. N. Menad, J.N. Ayala, F. Garcia-Carcedo, E. Ruiz-Ayúcar, A. Hernandez, Study of the presence of fluorine in the recycled fractions during carbothermal treatment of EAF dust. Waste Manag. **23**(6), 483–491 (2003)
46. S. Kelebek, S. Yörük, B. Davis, Characterization of basic oxygen furnace dust and zinc removal by acid leaching. Miner. Eng. **17**(2), 285–291 (2004)
47. J. Geldenhuis, A.W. Home, in *85th Steelmaking Conference Proceedings*, Iron and Steel Society, Nashville TN, 661–668 (2002).

48. E. Ordoñez, H.A. Colorado, Additive manufacturing via the direct ink writing technique of kaolinite-based clay with electric arc furnace steel dust (EAF dust), in *Energy Technology 2020: Recycling, Carbon Dioxide Management, and Other Technologies*, (Springer, Cham, 2020), pp. 307–315
49. M.F. Gándara, Aluminium: The metal of choice. Mater. Tehnol. **47**(3), 261–265 (2013)
50. B. Wang, K. Xu, Y. Wang, Using sodium D-gluconate to suppress hydrogen production in wet aluminium waste dust collection systems. J. Hazard. Mater. **397**, 122780 (2020)
51. M. Bertram, S. Ramkumar, H. Rechberger, G. Rombach, C. Bayliss, K.J. Martchek, D.B. Müller, G. Liu, A regionally-linked, dynamic material flow modelling tool for rolled, extruded and cast aluminium products. Resour. Conserv. Recycl. **125**, 48–69 (2017)
52. R. Galindo, I. Padilla, O. Rodríguez, R. Sánchez-Hernández, S. López-Andrés, A. López-Delgado, Characterization of solid wastes from aluminum tertiary sector: The current state of spanish industry. J. Miner. Mater. Charact. Eng. **3**(2), 55–64 (2015)
53. C. Directive, 96/61/EC of 24 September 1996 concerning integrated pollution prevention and control. Off. J. L **257**(10), 10 (1996)
54. M. Nifuku, S. Koyanaka, H. Ohya, C. Barre, M. Hatori, S. Fujiwara, S. Horiguchi, I. Sochet, Ignitability characteristics of aluminium and magnesium dusts that are generated during the shredding of post-consumer wastes. J. Loss Prev. Process Ind. **20**(4–6), 322–329 (2007)
55. Y. Liu, B.S. Leong, Z.T. Hu, E.H. Yang, Autoclaved aerated concrete incorporating waste aluminum dust as foaming agent. Constr. Build. Mater. **148**, 140–147 (2017)
56. D. Eliche-Quesada, S. Ruiz-Molina, L. Pérez-Villarejo, E. Castro, P.J. Sánchez-Soto, Dust filter of secondary aluminium industry as raw material of geopolymer foams. J. Build. Eng. **32**, 101656 (2020)
57. L. Marmo, D. Cavallero, M.L. Debernardi, Aluminium dust explosion risk analysis in metal workings. J. Loss Prev. Process Ind. **17**(6), 449–465 (2004)
58. R. Malviya, R. Chaudhary, Factors affecting hazardous waste solidification/stabilization: A review. J. Hazard. Mater. **137**(1), 267–276 (2006)
59. R.B. Moussa, C. Proust, M. Guessasma, K. Saleh, J. Fortin, Physical mechanisms involved into the flame propagation process through aluminum dust-air clouds: A review. J. Loss Prev. Process Ind. **45**, 9–28 (2017)
60. E. David, J. Kopac, Aluminum recovery as a product with high added value using aluminum hazardous waste. J. Hazard. Mater. **261**, 316–324 (2013)
61. N. Kongkajun, B. Cherdhirunkorn, W. Borwornkiatkaew, P. Chakartnarodom, Utilization of aluminium buffing dust as a raw material for the production of mullite. J. Met. Mater. Miner. **29**(3), 71–75 (2019)

Chapter 2
Resource Recovery and Recycling from Waste Metal Dust (II): Waste Copper Dust

Daniel Ogochukwu Okanigbe

2.1 Introduction

The complex process [1] of extracting copper from mineral resources [2] is shown in Fig. 2.1.

These mineral deposits create mineralization zones that are commercially advantageous to the miner. As a result, several mining techniques are employed to explore and make use of them for their copper values [3]. Unit operations are performed before, during, and after the mining process [4], and they normally take place on a facility and are done directly to speed up the mining process [5]. These activities before, during, and after mining frequently produce desired items as well as undesirable by-products [6], such as waste copper dusts (WCD).

WCD produced by copper mining operations is currently inevitable [7], and if not appropriately controlled, they constitute a risk to human health and the environment [7–11].

When metal ore is chemically heated, dangerous gases are created, and WCD are frequently composed of copper and other metal values close to these gases [12, 13]. These composites are usually categorized as dangerous under South Africa (SA) legislation due to their poisonous ingredients (Fig. 2.2).

Adhering to this legislation often presents a challenge, because most copper mining businesses work on a linear economic model, which is rather straightforward because it is based on extracting mineral resources and converting them into a product that eventually becomes waste (i.e., "taking, manufacturing, and wasting")

D. O. Okanigbe (✉)
Department of Chemical, Metallurgical and Materials Engineering, Faculty of Engineering and the Built Environment, Tshwane University of Technology, Pretoria, South Africa

Pantheon Virtual Engineering Solutions, Nigel, South Africa
e-mail: okanigbedo@tut.ac.za; okanigbeogochukwu@gmail.com

D. O. Okanigbe, A. P. Popoola (eds.), *Resource Recovery and Recycling from Waste Metal Dust*, https://doi.org/10.1007/978-3-031-22492-8_2

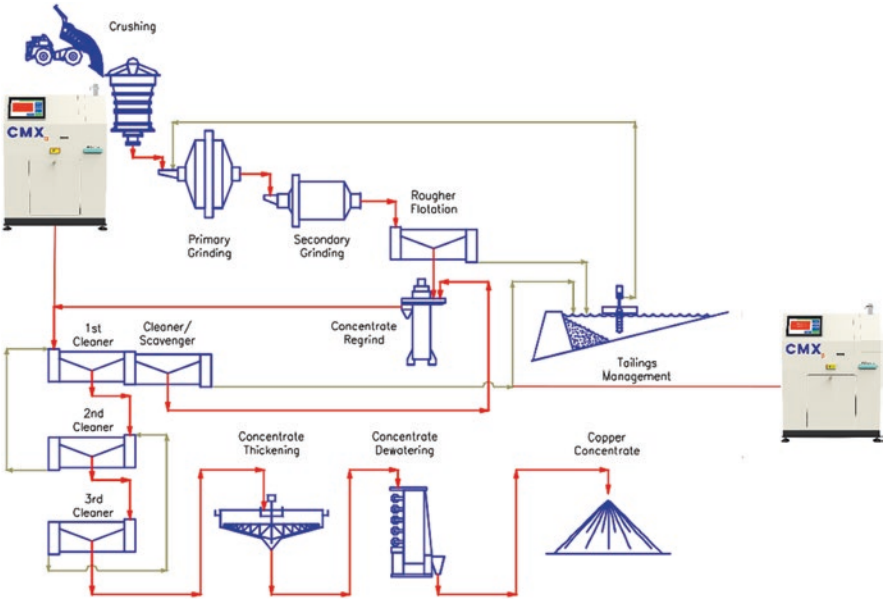

Fig. 2.1 Flowchart of the copper mining process. (Source: Google image)

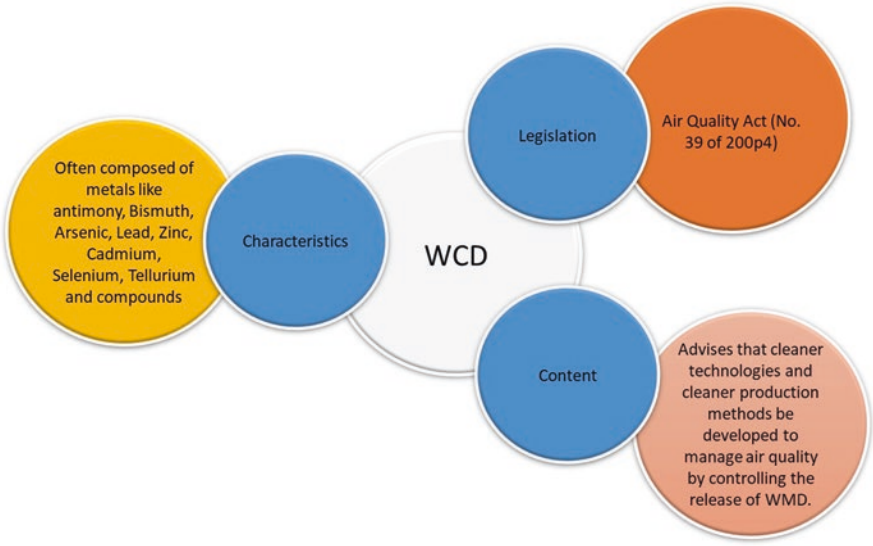

Fig. 2.2 Characterization, content, and SA legislation on WCD [14]

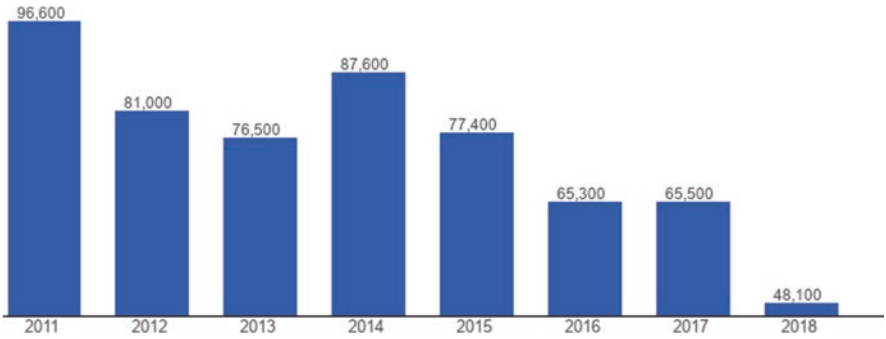

Fig. 2.3 South Africa's copper mine production in metric tons from 2011 to 2018. (Image courtesy of Google)

[15–17]. This economic model is distinct from the circularity model, which contains ideas like "resource recovery and recycling; a system that minimizes the use of resource inputs that result in waste, pollution, and carbon emissions [17, 18]."

Given the aforementioned, Evert Swanepoel, the executive chairperson of the Copper Development Association of Africa (CDAA), stated in a report from Mandarin Finance and Economics [19] that "Due to the declining and limited domestic copper production (Fig. 2.3), SA is expected to prioritize the recycling of copper resources to ensure there remains sufficient stock as the economy becomes more energy efficient and less dependent on fossil fuels" [20, 21]. Two-thirds of all copper ever produced is still in use today, the CDAA chairman continued. Nevertheless, he noted that only Palabora Mining Company was still in operation to provide domestic demand in SA, where copper was becoming increasingly rare [22]. According to the CDAA chairman, the mine was on the verge of closing down [23], while explorer and developer Orion Minerals is constructing a new copper mine in the town of Prieska in the Northern Cape [24]. Ultimately, this project will not be finished until 2023.

Furthermore, exporting a lot of copper scrap to foreign recyclers limits the amount of domestic copper available, giving local recyclers less supplies of copper scrap to work with. This leaves the nation with the options of "using recycled copper or importing copper raw material?"

Therefore, it is noteworthy at this moment to conduct research into resource recovery and recycling from waste metal dust (WCD) [25–29]. In fact, as a result of these efforts, the circularity model is given a powerful voice in the copper mining industry. This approach closes the copper loop while also helping to lessen adverse environmental consequences.

This chapter will explore the generation, description, and recirculation of WCD, as well as resource recovery and recycling from WCD, in light of this line of thinking. Following that, a list of suggested research fields for turning the South African WCD into a useful resource follows.

2.2 Waste Copper Dust

2.2.1 Generation

Impurities must be removed in copper metallurgy in order to produce copper that is of a high quality [30, 31], but they must also be removed for environmental reasons [32]. It is reasonable to anticipate an even more dire situation in the future given the continuous rise in impurities in copper ore over time [33]. Impurities must be kept below the limits permitted by national and international regulations for the copper industry [34], and the overall emission of hazardous substances must be reduced.

Oxidation, slagging, and volatilization are used to remove impurities from copper during the smelting, conversion, and refining processes [35, 36]. The Teniente Converter, Inco Flash, Outokumpu Flash, and Mitsubishi processes, among others, have all seen advancements thanks to a mix of intensive reactors that use oxygen or oxygen-enriched air as the blowing gas. The way of removing impurities, however, has remained unchanged and has instead turned into a significant constraint in the contemporary method of copper smelting and conversion [37, 38].

Gaseous emissions generated from copper processing include heavy metals, water vapor, SO_2, N_2, and O_2 in addition to other contaminants [39]. As a result of the gas cleaning procedure, WCD is produced [40]. WCD contains condensate matter and small semi-melted concentrate particles that are carried with the off-gas.

2.2.2 Description of WCD

2.2.2.1 Particle Size Distribution of WCD

The WCD is primarily made up of fine-grained particles, according to the WCD production mechanism and the results of characterizing the WCD for its particle size distribution. The following researchers: Okanigbe et al. [25], Ha et al. [41], Bakhtiari et al. [42, 43], Vakylabad et al. [44], Morales et al. [45], Balladares et al. [46], and Xu et al. [47] shared that the majority of the particles, measured quantitatively, are very small and lie within the size range of 5–50 μm below the 53-μm sieve aperture. When Okanigbe, [48], studied the South African WCD's −53 μm size fraction using the laser diffraction technique, the results showed that the bulk particle sizes in this size fraction were primarily between 24 and 30 μm, with no particles falling within the nano-small range (Table 2.1). This knowledge was helpful, especially for the actual separation of the South African WCD [27].

Table 2.1 PSD of WCD as Determined with the Laser Diffraction [48]

Size (μm)	%Change	%Passing	Size (μm)	%Change	%Passing
2000.00000	0.00	100.00	4.63000	1.21	3.88
1674.00000	0.00	100.00	3.39000	0.93	2.67
1408.00000	0.00	100.00	3.27000	0.71	1.74
1184.00000	0.00	100.00	2.75000	0.54	1.03
995.60000	0.00	100.00	2.31300	0.38	0.49
837.20000	0.00	100.00	1.94500	0.11	0.11
704.00000	0.00	100.00	1.53500	0.00	0.00
592.00000	0.00	100.00	1.37500	0.00	0.00
497.30000	0.00	100.00	1.15600	0.00	0.00
418.60000	0.00	100.00	0.97200	0.00	0.00
352.00000	0.00	100.00	0.81800	0.00	0.00
296.00000	0.34	100.00	0.68800	0.00	0.00
248.90000	0.44	99.66	0.57800	0.00	0.00
209.30000	0.57	99.22	0.48500	0.00	0.00
176.00000	0.72	98.65	0.40900	0.00	0.00
148.00000	0.90	97.93	0.34400	0.00	0.00
124.60000	1.16	97.03	0.28900	0.00	0.00
104.70000	1.53	95.37	0.24300	0.00	0.00
88.00000	2.07	94.34	0.20400	0.00	0.00
74.00000	2.87	92.27	0.17200	0.00	0.00
62.23000	3.92	89.40	0.13500	0.00	0.00
52.33000	5.12	85.43	0.12200	0.00	0.00
44.00000	6.29	80.36	0.10200	0.00	0.00
37.00000	7.30	74.07	0.08600	0.00	0.00
31.11000	8.09	66.77	0.07200	0.00	0.00
26.16000	8.57	58.63	0.06100	0.00	0.00
22.00000	8.63	50.11	0.05100	0.00	0.00
18.50000	8.28	41.43	0.04300	0.00	0.00
15.56000	7.33	33.20	0.03600	0.00	0.00
13.03000	6.14	25.37	0.03000	0.00	0.00
11.00000	4.98	19.73	0.02550	0.00	0.00
9.25000	3.96	14.75	0.02150	0.00	0.00
7.73000	3.06	10.79	0.01810	0.00	0.00
6.59000	2.26	7.73	0.01520	0.00	0.00
5.50000	1.59	5.47	0.01280	0.00	0.00

Table 2.2 Different chemical compositions of WCD

Composition	Content (wt. %)						
	WCD 1	WCD 2	WCD 3	WCD 4	WCD 5	WCD 6	WCD 7
Cu	18.02	10.8	10.90	27.00	7.53	41.70	4.00
Fe	13.36	0.8	1.60	11.00	–	29.60	
Zn	0.27	15.6	7.80	5.8	40.21	0.30	18.00
S	3.44	10.4	–	7.5	–	13.00	7.00
Bi	0.02	3.5	1.90	0.20	–	2.30	1.10
As	–	19.4	7.10	13.0	–	0.40	20.5
Ca	3.52	–	–	–	–	–	–
Mg	2.86	–	–	–	–	–	–
Ti	1.11	–	–	–	–	–	–
Si	33.06	–	–	–	–	–	–
Al	22.19	–	–	–	–	–	–
Cd	–	–	1.30	–	–	–	9.50
Pd	0.12	7.80	14.20	1.50	6.62	0.00	8.00
Sb	–	0.1	0.10	–	–	–	1.20
Others	1.95	31.6	55.10	33.80	45.64	12.4	–

Key: WCD 1 = Okanigbe et al. [25]; WCD 2 = Montenegro et al. [39]; WCD 3 = Ha et al. [41]; WCD 4 = Morales et al. [45]; WCD 5 = Qiang et al. [49]; WCD 6 = Vítková et al. [50]; WCD 7 = Font et al. [51].

2.2.2.2 Chemical Composition of Typical WSD

According to Table 2.2, the composition of this WCD varies depending on the operation. The mineralogy of the concentrates, fluxes, and circulating material (slag, WCD, etc.), as well as their corresponding proportions, determines the composition [46], while the type of reactor used in the smelting and conversion procedures mostly affects the mass of WCD produced [47].

As shown in Table 2.2, WCD typically contains the minor elements copper (Cu), iron (Fe), lead (Pb), arsenic (As), cadmium (Cd), antimony (Sb), zinc (Zn), bismuth (Bi), and selenium (Se), but the exact form of each element depends on the environmental factors and operational parameters of the smelting and converting processes [39]. The ratio of these components in the WCD aids in determining the best waste management approach (i.e., disposal, recirculation, resource recovery, and recycling) to use.

2.2.2.3 Mineralogy of WCD

Researchers Vakylabad et al. [44, 52], Morales et al. [45], Qiang et al. [49], Vtková et al. [50], Font et al. [51], Alguacil et al. [53], Ettler et al. [54], and Xu et al. [55] examined the phase structures of the WCD. The phases that are frequently found in WCD are represented in Table 2.3 and mostly consist of complex copper oxides and sulfides, although the compositions of these WCD vary greatly (Table 2.3).

Table 2.3 Mineralogy of different WCD

Composition	Phases			
	WCD 1	WCD 2	WCD 3	WCD 4
Cu	$Cu_{6.88}Fe_{17.12}O_{32.00}$ $Cu_{4.00}Fe_{4.00}S_{32.00}$	CuO	$CuSO_{4.00}.5H_{2.00}O$, $CuFeO_{2.00}$	$CuSO_{4.00}$, CuS
Fe	$Mg_{0.04}Fe_{2.96}O_{4.00}$	–	$Fe_{3.00}O_{4.00}$	–
Zn	–	ZnO	–	ZnS, $ZnSO_{4.00}$
Ca	$Ca(SO_{4.00})(H_{2.00}O)_{2.00}$			
Pb	–	PbO	–	$PbSO_{4.00}$
As	–	–	–	$As_{2.00}O_{3.00}$
Al	$Al(Al_{0.69}Si_{1.22}O_{4.85})$	$AlCl_{3.00}$	–	–
Si	$SiO_{2.00}$	–	–	–

Key: WCD 1 = Okanigbe et al. [25]; WCD 2 = Qiang et al. [49]; WCD 3 = Vítková et al. [50]; WCD 4 = Font et al. [51]

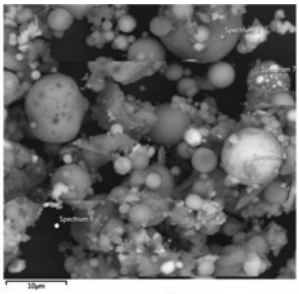

Elements	Spectrums									
	4		5		6		7		Average	
	Wt%	σ	Wt%	σ	Wt%	σ	Wt%	σ	=Wt%	=σ
Cu	31.0	0.3	4.7	0.2	30.2	2.0	37.5	0.3	25.9	0.7
Fe	39.4	0.3	14.3	0.2	7.4	1.4	13.9	0.2	18.8	0.5
O	23.3	0.3	40.7	0.3	36.2	1.8	30.4	0.2	32.7	0.7
Ca	3.2	0.1	6.7	0.1	-	-	1.3	0.1	3.7	0.1
Al	1.2	0.1	15.2	0.1	13.2	1.0	5.3	0.1	8.7	0.3
Si	1.0	0.1	15.0	0.1	12.9	1.1	4.7	0.1	8.4	0.4
S	0.4	0.0	0.7	0.0	-	-	3.3	0.1	1.5	0.0
Tb	0.4	0.4	0.0	0.3	-	-	-	-	0.2	0.4
K	-	-	1.4	0.1	-	-	1.3	0.0	1.4	0.0
Ti	-	-	1.2	0.1	-	-	1.3	0.1	1.3	0.1
Zn	-	-	-	-	-	-	1.0	0.2	1.0	0.2

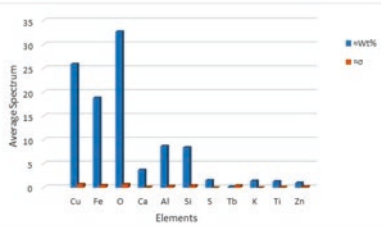

Fig. 2.4 Scanning electron micrograph and energy dispersive spectrums of WCD from South Africa

2.2.2.4 Morphology of WCD

SEM images and energy dispersive spectra of a WCD from SA are shown in Fig. 2.4. Few unevenly shaped particles can be seen in the micrographs, whereas most particles are typically spherical in shape [25, 47]. The appearance of the WCD under the electron microscope is typical of semi-molten or molten material solidified by cooling in a gas transport system [25], as agreed upon by various researchers [25, 47], as opposed to particles reacting in the solid state, which have a more angular look [46]. The diameters of the particles, which range from submicron to micron, and their adhesion to one another [25] can also be seen in Fig. 2.4.

2.2.3 Recirculation of WCD

The approach of recycling the WCD back into the furnaces, according to Bakhtiari et al. [43], decreases their efficacy and raises the amount of energy needed for smelting; additionally, due to its characteristically fine nature, 5–50 μm [25, 41, 47], it damages the refractory bricks when returned to the furnace and places a circular load on the furnaces.

To determine the impact of WCD recirculating in the smelting process on WCD generation and the behavior of certain impurities among the matte and slag phases, Montenegro et al. [39] tested this recirculation strategy at the laboratory scale. The authors claim that copper can be successfully recovered using WCD recirculation. Recirculation into the smelting process can reduce WCD generation if the carry-over of recirculated WCD is successfully reduced. However, the ultimate matte quality determines how much WCD recirculation occurs.

Additionally, the recirculation of WCD into the smelting process will be prevented by exceptionally high As concentrations and higher concentrations of other impurities including Bi, Pb, and Sb [39, 56]. This is because recirculation causes the distributions of these contaminants in matte to dramatically rise. Therefore, the way those contaminants behave may restrict how much WCD recirculation occurs during the process.

2.2.4 Resource Recovery and Recycling from WCD

2.2.4.1 The Recovery of Metals from WCD

It is common for one or more extractive metallurgy unit activities to be combined in order to recover metal values from WCD. Following is a discussion of the various extractive metallurgy and mineral processing unit activities for the recovery of these metal values:

The Use of Hydrometallurgical Techniques

The work by Li et al. [57] showed how arsenic was removed from the WCD leach solution by co-precipitation with ferric ions. Secondary products from WCD, are abundant in bismuth (Bi) and other significant metals, claim Ha et al. [41]. They provided a cost-effective hydrometallurgical method for extracting Bi from WCD in their paper. When used as leaching reagents, a solution of H_2SO_4 and NaCl can effectively remove Bi from WCD. Under ideal circumstances, a 92% leaching efficiency was attained. Guo et al. [58] created a hydrometallurgical procedure to selectively recover arsenic from WCD by leaching the WCD with NaOH-Na_2S.

The Use of Bio-Hydrometallurgy Techniques

The bioleaching of WCD from smelters in Iran's Sarcheshmeh copper complex was studied by Bakhtiari et al. [43]. Although sulfide minerals, notably pyrite, in copper concentrates undergo oxidation processes that release acid, authors reported that the WCD bio-treatment process consumes acid. A different study by Bakhtiari et al. [42] looked at the bioleaching of copper from the WCD of the Sarcheshmeh copper smelting plant. In the study, the outcomes of a series of continuous tests performed on two-stage airlift bioreactors injected with bacteria that were originally produced from acid mine drainage were described.

The Use of Pyrometallurgical–Hydrometallurgical Techniques

The recovery of precious metals and the removal of arsenic from WCD have both been extensively investigated using the pyro-hydrometallurgical method [47].

The Use of Physical Separation Techniques

The process parameterization of a centrifugal concentrator for the separation of a WCD was followed by a theoretical contribution including the creation of a system of predictive models in the work by Okanigbe et al. [27]. According to the findings, a maximum grade of approximately 35.02 wt% Cu was attained at 120G for the rotational bowl speed, 3.0 L/min for the water flow rate, 1.48 L/min for the continuous experimental flow rate, and 0.5 L/min for the liquid to solid ratio. Similar to this, under the same testing conditions, a minimum output of 14.58% SiO_2 and 10.29% Al_2O_3 was attained. This clearly shows a trend toward ideal experimental settings designed to maximize Cu output and reduce SiO_2 and Al_2O_3 levels.

Using unit operations of zinc vapor evaporation and condensation as well as super-gravity separation of copper droplets, researchers from Gao et al. [59] suggested a novel method to efficiently extract metallic copper and crown zinc from WCD.

Stabilization/Solidification

Most of WCD are considered as hazardous pollutants because they contain lots of heavy metals; consequently, several researchers have focused on the stabilization/solidification of them [45, 60–62]. Furthermore, since As_2O_3 is abundant worldwide, it is not practical from an economic standpoint to entirely recycle As-rich WCD from non-ferrous metallurgies [63]. Should WCD not meet the conditions set forth by the European Union (EU) for landfilling in hazardous waste disposal sites (Table 2.2), it must be solidified or stabilized before it can be accepted at any landfill site.

Conversion of WCD into Value-Added Product

With the shortage of mineral resources, direct disposal after stabilization/solidification processes might not be the best methods for treating WCD like the one generated in SA.

Granted the WCD from SA has the bare minimum As, Bi, Pb, and Sb contents necessary for landfilling in hazardous waste disposal facilities. The best way to manage this waste is through resource recovery and recycling by conversion into useful commodities for additional value.

Hence, the following research suggestions on transforming WCD from SA into a value-added product are listed below, these ideas have been made public in their whole forms:

1. Thermal and Mechanical Properties (I): Optimum Predictive Thermal Conduction Model Development for Epoxy Filled Copper Oxide Nanoparticles Composite Coatings on Spent Nuclear Fuel Steel Casks.
2. Thermal and Mechanical Properties (I): Spark Plasma Sintered Ti–6Al–4V Alloy Reinforced with Mullite-Rich-tailings for Production of Energy Efficient Brake Rotor.
3. Wave Energy Converter Design: Seawater Integrity and Durability of Epoxy-Resin Filled Corrosive Microorganism Surface Modified Waste Copper Dust.
4. Aircraft Engine Fan Blade Design: Impact Tolerance Prediction of Partially Filled 3D Printed Aluminum, Titanium, and PEEK Filled Waste Copper Dust.
5. Preparation and Characterization of Hydrotalcite-Derived Material from Mullite-Rich-Tailings (I): Transesterification of Used Cooking Oil to Biodiesel.
6. Preparation and Characterization of Hydrotalcite-Derived Material from Mullite-Rich-Tailings (II): CO_2 Capture from Coal-Fired Thermal Power Plants.

2.3 Conclusions

Discussions on the production, description, and recirculation of WCD, as well as resource recovery and recycling from South Africa's WCD, were given in this chapter and arrived at the following deductions:

1. As a result of the gas cleaning procedure, WCD is produced.
2. The bulk particles in the South African WCD's −53 μm size fraction were primarily made up of 24–30 μm particle sizes.
3. Because of the chemical makeup and/or mineralogy of some WCD, recirculation has been deemed unacceptable.
4. The WCD from SA contains the minimal minimum amount of As, Bi, Pb, and Sb required for landfilling at facilities for the disposal of hazardous waste.

Therefore, it was suggested that the adoption of creative ideas that aim to transform WCD into functional material rather than recirculation or disposal will help to reduce adverse environmental consequences while also closing the copper loop (Zero-waste production).

Acknowledgments The author wishes to express his gratitude to Tshwane University of Technology in Pretoria, South Africa, for allowing use of facilities.

References

1. P.R. Jadhao, S. Mishra, A. Pandey, K.K. Pant, K.D.P. Nigam, Biohydrometallurgy: A sustainable approach for urban mining of metals and metal refining, in *Catalysis for Clean Energy and Environmental Sustainability: Biomass Conversion and Green Chemistry*, vol. 1, (Springer, Cham, 2021), pp. 865–892
2. M.L. Free, Metal extraction, in *Hydrometallurgy*, (Springer, Cham, 2022), pp. 145–196
3. J.A.D. Cavalcanti, M.S. da Silva, C. Schobbenhaus, H. de Mota Lima, Geo-mining heritages of the Mariana anticline region, southeast of Quadrilátero Ferrífero-MG, Brazil: Qualitative and quantitative assessment of Chico Rei and Passagem mines. Geoheritage **13**(4), 1–29 (2021)
4. Z. Bian, X. Miao, S. Lei, S.E. Chen, W. Wang, S. Struthers, The challenges of reusing mining and mineral-processing wastes. Science **337**(6095), 702–703 (2012)
5. R. Lorenz, J. Senoner, W. Sihn, T. Netland, Using process mining to improve productivity in make-to-stock manufacturing. Int. J. Prod. Res., **59(16), 4869–4880 (2021)**
6. Y. Taha, A. Elghali, R. Hakkou, M. Benzaazoua, Towards zero solid waste in the sedimentary phosphate industry: Challenges and opportunities. Fortschr. Mineral. **11**(11), 1250 (2021)
7. B. Paluchamy, D.P. Mishra, D.C. Panigrahi, Airborne respirable dust in fully mechanised underground metalliferous mines–generation, health impacts and control measures for cleaner production. J. Clean. Prod. **296**, 126524 (2021)
8. M. Mpanza, E. Adam, R. Moolla, Dust deposition impacts at a liquidated gold mine village: Gauteng Province in South Africa. Int. J. Environ. Res. Public Health **17**(14), 4929 (2020)
9. T.L. Noble, A. Parbhakar-Fox, R.F. Berry, B. Lottermoser, Mineral dust emissions at metalliferous mine sites, in *Environmental Indicators in Metal Mining*, (Springer, Cham, 2017), pp. 281–306
10. D.H. Brouwer, D. Rees, Can the South African milestones for reducing exposure to respirable crystalline silica and silicosis be achieved and reliably monitored? Front. Public Health **8**, 107 (2020)
11. G. Nelson, *Living in the Shadow of a Dust Cloud: Occupational Respiratory Diseases in the South African Mining Industry, 1975 to 2009* (Doctoral Dissertation, 2014)
12. H. Li, J. Peng, H. Long, S. Li, L. Zhang, Cleaner process: Efficacy of chlorine in the recycling of gold from gold-containing tailings. J. Clean. Prod. **287**, 125066 (2021)
13. X. Xiao, S. Zhang, F. Sher, J. Chen, Y. Xin, Z. You, L. Wen, M. Hu, G. Qiu, A review on recycling and reutilization of blast furnace dust as a secondary resource. J. Sustain. Metall., **7(2), 340–357 (2021)**
14. E. Matinde, G.S. Simate, S. Ndlovu, Mining and metallurgical wastes: A review of recycling and re-use practices. J. South. Afr. Inst. Min. Metall. **118**(8), 825–844 (2018)
15. A. Halog, S. Anieke, A review of circular economy studies in developed countries and its potential adoption in developing countries. Circ. Econ. Sustain., **1(1), 209–230 (2021)**
16. S. Jawadand, K. Randive, A sustainable approach to transforming mining waste into value-added products, in *Innovations in Sustainable Mining*, (Springer, Cham, 2021), pp. 1–20
17. A. Upadhyay, T. Laing, V. Kumar, M. Dora, Exploring barriers and drivers to the implementation of circular economy practices in the mining industry. Resour. Policy **72**, 102037 (2021)
18. F. Pavloudakis, C. Roumpos, P.M. Spanidis, Optimization of surface mining operation based on a circular economy model, in *Circular Economy and Sustainability*, (Elsevier, Amsterdam, 2022), pp. 395–418
19. Mandarin Finance and Economics, African Copper Development Association calls on South Africa to increase the scale of waste copper recycling. (2020). https://news.metal.com/newscontent/101199398/african-copper-development-association-calls-on-south-africa-to-increase-the-scale-of-waste-copper-recycling

20. V.R. Nalule, Transitioning to a low carbon economy: Is Africa ready to bid farewell to fossil fuels? in *The Palgrave Handbook of Managing Fossil Fuels and Energy Transitions*, (Palgrave Macmillan, Cham, 2020), pp. 261–286
21. G. Mutezo, J. Mulopo, A review of Africa's transition from fossil fuels to renewable energy using circular economy principles. Renew. Sust. Energ. Rev. **137**, 110609 (2021)
22. B. Barlow, E. Fosso-Kankeu, K. Nyembwe, F. Waanders, E.N. Malenga, *Prediction of Dissolution of Copper from a Chalcopyrite Carbonatite Ore of South Africa* (EARET, 2018)
23. H. Paetzold, P. Lourens, R. Brazier, Reopening and closure of a block cave, in *MassMin 2020: Proceedings of the Eighth International Conference & Exhibition on Mass Mining*, (University of Chile, 2020 December), pp. 103–114
24. L. Hockaday, Solar thermal applications in minerals processing in South Africa, in *Proceedings of the 6th South African Solar Energy Converence*, (2019)
25. D.O. Okanigbe, A.P.I. Popoola, A.A. Adeleke, Characterization of copper smelter dust for copper recovery. Procedia Manuf. **7**, 121–126 (2017)
26. D.O. Okanigbe, A.P.I. Popoola, A.A. Adeleke, Hydrometallurgical processing of copper smelter dust for copper recovery as nano-particles: A review. Energ. Technol. **2017**, 205–226 (2017)
27. D. Okanigbe, P. Olawale, A. Popoola, A. Abraham, A. Michael, K. Andrei, Centrifugal separation experimentation and optimum predictive model development for copper recovery from waste copper smelter dust. Cogent Eng. **5**(1), 1551175 (2018)
28. D.O. Okanigbe, A.P.I. Popoola, A.A. Adeleke, I.O. Otunniyi, O.M. Popoola, Investigating the impact of pretreating a waste copper smelter dust for likely higher recovery of copper. Procedia Manuf. **35**, 430–435 (2019)
29. D.O. Okanigbe, M.K. Ayomoh, O.M. Popoola, P.A. Popoola, V.S. Aigbodion, Oxidative roasting experimentation and optimum predictive model development for copper and iron recovery from a copper smelter dust. Results Eng. **7**, 100125 (2020)
30. W.G. Davenport, M. King, M.E. Schlesinger, A.K. Biswas, *Extractive Metallurgy of Copper* (Elsevier, Amsterdam, 2002)
31. G.A. Flores, C. Risopatron, J. Pease, Processing of complex materials in the copper industry: Challenges and opportunities ahead. JOM **72**(10), 3447–3461 (2020)
32. M.E. Schlesinger, K.C. Sole, W.G. Davenport, G.R. Alvear, *Extractive Metallurgy of Copper* (Elsevier, Amsterdam, 2021)
33. B. Lucheva, P. Iliev, D. Kolev, Hydro-pyrometallurgical treatment of copper converter flue dust. J. Chem. Technol. Metall. **52**(2), 320–325 (2017)
34. S.A. Awe, J.E. Sundkvist, N.J. Bolin, Å. Sandström, Process flowsheet development for recovering antimony from Sb-bearing copper concentrates. Miner. Eng. **49**, 45–53 (2013)
35. A. Yazawa, Thermodynamic considerations of copper smelting. Can. Metall. Q. **13**(3), 443–453 (1974)
36. A. Yazawa, T. Azakami, Thermodynamics of removing impurities during copper smelting. Can. Metall. Q. **8**(3), 257–261 (1969)
37. F. Habashi, Copper metallurgy at the crossroads. J. Min. Metall. B: Metall. **43**(1), 1–19 (2007)
38. T. Utigard, G. Sanchez, J. Manriquez, A. Luraschi, C. Diaz, D. Cordero, E. Almendras, Reduction kinetics of liquid iron oxide-containing slags by carbon monoxide. Metall. Mater. Trans. B **28**(5), 821–826 (1997)
39. V. Montenegro, H. Sano, T. Fujisawa, Recirculation of Chilean copper smelting dust with high arsenic content to the smelting process. Mater. Trans. **49**(9), 2112–2118 (2008)
40. H. Zhou, G. Liu, L. Zhang, C. Zhou, Formation mechanism of arsenic-containing dust in the flue gas cleaning process of flash copper pyrometallurgy: A quantitative identification of arsenic speciation. Chem. Eng. J. **423**, 130193 (2021)
41. T.K. Ha, B.H. Kwon, K.S. Park, D. Mohapatra, Selective leaching and recovery of bismuth as Bi2O3 from copper smelter converter dust. Sep. Purif. Technol. **142**, 116–122 (2015)
42. F. Bakhtiari, H. Atashi, M. Zivdar, S.S. Bagheri, Continuous copper recovery from a smelter's dust in stirred tank reactors. Int. J. Miner. Process. **86**(1–4), 50–57 (2008)

43. F. Bakhtiari, M. Zivdar, H. Atashi, S.S. Bagheri, Bioleaching of copper from smelter dust in a series of airlift bioreactors. Hydrometallurgy **90**(1), 40–45 (2008)
44. A.B. Vakylabad, M. Schaffie, M. Ranjbar, Z. Manafi, E. Darezereshki, Bio-processing of copper from combined smelter dust and flotation concentrate: A comparative study on the stirred tank and airlift reactors. J. Hazard. Mater. **241**, 197–206 (2012)
45. A. Morales, M. Cruells, A. Roca, R. Bergo, Characterization of flue dusts from a copper smelter furnace, copper recovery and arsenic stabilization, in *The John E. Dutrizac International Symposium on Copper Hydrometallurgy, Cu 2007*, ed. by P.A. Riveros, D.G. Dixon, D.B. Dreisinger, M.J. Collins, vol. 4, (2007), pp. 177–189
46. E. Balladares, U. Kelm, S. Helle, R. Parra, E. Araneda, Chemical-mineralogical characterization of copper smelting flue dust. Dyna **81**(186), 11–18 (2014)
47. B. Xu, Y. Ma, W. Gao, J. Yang, Y. Yang, Q. Li, T. Jiang, A review of the comprehensive recovery of valuable elements from copper smelting open-circuit dust and arsenic treatment. JOM **72**(11), 3860–3875 (2020)
48. D.O. Okanigbe, *Production of Copper and Copper Oxide Nano-Particles from Leach Solution of Low Grade Copper Smelter Dust* (2019)
49. L. Qiang, I.S. Pinto, Z. Youcai, Sequential stepwise recovery of selected metals from flue dusts of secondary copper smelting. J. Clean. Prod. **84**, 663–670 (2014)
50. M. Vítková, V. Ettler, J. Hyks, T. Astrup, B. Kříbek, Leaching of metals from copper smelter flue dust (Mufulira, Zambian Copperbelt). Appl. Geochem. **26**, S263–S266 (2011)
51. O. Font, N.A.T.A.L.I.A. Moreno, G. Aixa, X.A.V.I.E.R. Querol, R.O.D.R.I.G.O. Navia, Copper smelting flue dust: A potential source of germanium. Rev. Soc. Esp. Mineral. **15**, 87–88 (2011)
52. A.B. Vakylabad, A comparison of bioleaching ability of mesophilic and moderately thermophilic culture on copper bioleaching from flotation concentrate and smelter dust. Int. J. Miner. Process. **101**(1–4), 94–99 (2011)
53. F.J. Alguacil, I. Garcia-Diaz, F. Lopez, O. Rodriguez, Recycling of copper flue dust via leaching-solvent extraction processing. Desalin. Water Treat. **56**(5), 1202–1207 (2015)
54. V. Ettler, M. Vítková, M. Mihaljevič, O. Šebek, M. Klementová, F. Veselovský, P. Vybíral, B. Kříbek, Dust from Zambian smelters: Mineralogy and contaminant bioaccessibility. Environ. Geochem. Health **36**(5), 919–933 (2014)
55. Z.F. Xu, L.I. Qiang, H.P. Nie, Pressure leaching technique of smelter dust with high-copper and high-arsenic. Trans. Nonferrous Metals Soc. China **20**, s176–s181 (2010)
56. V. Montenegro, H. Sano, T. Fujisawa, Recirculation of high arsenic content copper smelting dust to smelting and converting processes. Miner. Eng. **49**, 184–189 (2013)
57. T. Li, Y. Wang, W.J. Li, J.M. Chen, T. Wang, W.X. Wang, Concentrations and solubility of trace elements in fine particles at a mountain site, southern China: Regional sources and cloud processing. Atmos. Chem. Phys. **15**(15), 8987–9002 (2015)
58. X. Guo, J. Shi, Y. Yi, Q. Tian, D. Li, Separation and recovery of arsenic from arsenic-bearing dust. J. Environ. Chem. Eng. **3**(3), 2236–2242 (2015)
59. J. Gao, Z. Huang, Z. Wang, Z. Guo, Recovery of crown zinc and metallic copper from copper smelter dust by evaporation, condensation and super-gravity separation. Sep. Purif. Technol. **231**, 115925 (2020)
60. A. Shahnazi, S. Firoozi, D.H. Fatmehsari, Selective leaching of arsenic from copper converter flue dust by Na2S and its stabilization with Fe2 (SO4) 3. Trans. Nonferrous Metals Soc. China **30**(6), 1674–1686 (2020)
61. A. Morales, M. Cruells, A. Roca, R. Bergó, Treatment of copper flash smelter flue dusts for copper and zinc extraction and arsenic stabilization. Hydrometallurgy **105**(1–2), 148–154 (2010)
62. L.G. Twidwell, A.K. Mehta, Disposal of arsenic bearing copper smelter flue dust. Nucl. Chem. Waste Manag. **5**(4), 297–303 (1985)
63. V. Dutre, C. Vandecasteele, Immobilization mechanism of arsenic in waste solidified using cement and lime. Environ. Sci. Technol. **32**(18), 2782–2787 (1998)

Part II
Pre-treatment of Waste Copper Dust

Chapter 3
Pre-treatment of Waste Copper Dust (I): Potential of Oxidative Roasting–Density Separation–Sulphuric Acid Leaching Technology for Copper Recovery

Daniel Ogochukwu Okanigbe, Abimbola Patricia Popoola, and Abraham Adewale Adeleke

3.1 Introduction

Numerous researchers have thoroughly investigated and reported on the treatment of waste copper dust (WCD) [1–11]. These procedures, which include roasting WCD [12, 13], smelting WCD [14–16], roasting WCD followed by dissolution [17–20], and sulphuric acid leaching of WCD [21–23], have been presented or used at various levels (pilot and/or industrial levels).

In comparison with hydrochloric (HCl) and nitric acid (HNO_3), sulphuric acid (H_2SO_4) is the most effective and popular acid for leaching oxides, according to Teir et al. [24], Trans et al. [25], and Habashi [26]. In order to recover the copper value present in waste/by-products containing copper, such as WCD, sulphuric acid has been employed extensively [11, 27].

In WCD, copper is primarily present as copper oxides and, to a lesser extent, as copper sulphides [5]. Yes, it is noticeable given that 70,000–100,000 kilograms of WCD is produced annually [2, 3, 28]. Chalcopyrite forms passive layers over itself

D. O. Okanigbe (✉)
Department of Chemical Metallurgical and Materials Engineering, Faculty of Engineering and the Built Environment, Tshwane University of Technology, Pretoria, South Africa

Pantheon Virtual Engineering Solutions, Nigel, South Africa
e-mail: okanigbedo@tut.ac.za; okanigbeogochukwu@gmail.com

A. P. Popoola
Department of Chemical, Metallurgical and Materials Engineering, Faculty of Engineering and the Built Environment, Tshwane University of Technology, Pretoria, South Africa

A. A. Adeleke
Department of Materials Science and Engineering, Faculty of Technology, Obafemi Awolowo University, Ile-ife, Osun state, Nigeria

D. O. Okanigbe, A. P. Popoola (eds.), *Resource Recovery and Recycling from Waste Metal Dust*, https://doi.org/10.1007/978-3-031-22492-8_3

during sulphuric acid leaching, which slows the rate of dissolution and ultimately results in low copper recovery, therefore recovering its copper sulphides like chalcopyrite with this method will defeat the purpose of conserving mineral resources [29, 30]. However, a pre-treatment method frequently preferred in the industry for copper sulphides [17–20] involves subjecting the WCD to either low temperatures (partial roasting) [31] or high temperatures (dead roasting) [32] in the hope of producing dissolvable oxidative products (or calcines) for copper recovery.

In addition, the complex mineralogy (mineralogy that might contain gangue minerals such clays, jarosites, gypsum, quartz, and micas) and porosity structure of WCD continue to produce side reactions [33] and poor mass transfer of solution. Sulphuric acid consumption from side effects is a problem and thus reduces the effectiveness of leaching. The diffusion mechanism in the solid particles of the WCD can also have an impact on the leaching efficiency; this mechanism is dependent on the pore distribution (also known as porosity) of the WCD and can have a positive or negative impact on the leaching efficiency depending on the nature of the pore distribution in the WCD, which in turn affects the mass transfer of solution to the sites of leaching reactions.

In light of the foregoing, research into the impact of pre-treatments including oxidative roasting and density separation of WCD on mineralogy, side reactions, and mass transfer of solution is required to determine whether copper recovery may be improved. The results of these investigations will thus be presented in this chapter.

3.2 Experimental Method

3.2.1 Material

Waste Metal Dust

The WCD from South Africa was used as source of metal ore for this study.

3.2.2 Methods

3.2.2.1 Pre-Treatment Methods

Oxidative Roasting

Read Okanigbe, Popoola and Adeleke [7], Okanigbe et al. [9], and Okanigbe [34] for further information on thermal behaviour, thermodynamic modelling, experiment design, and the experimental process of oxidative roasting pre-treatment of the WCD.

Density Separation Method

The articles by Okanigbe et al. [8], Okanigbe [34], and Okanigbe et al. [35] provide more information on sample preparation, density determination, experiment design, and the experimental process of density separation pre-treatment of WCD.

3.3 Results and Discussion

3.3.1 Effect of Pre-Treatments on Mineralogy of WCD

3.3.1.1 Oxidative Roasting

Figure 3.1a, b displays the differential scanning calorimetry (DSC) and thermogravimetric analyser (TGA) results at various heating rates. The DSC curves have similar shapes, but when the heating rate rises, the peaks alter at higher temperatures (Fig. 3.1a). It was discovered that heating the WCD between 40 °C and 138 °C causes moisture to evaporate, which on the TGA curve equates to a loss of mass as well (Fig. 3.1b). Between 120 °C and 150 °C, an endothermic peak was seen in the DSC profile; this was most likely caused by the loss of water during crystallization, which occurs in species of minerals like gypsum [7]. However, pyrite began to oxidize at intervals of 173 °C–261 °C, which was shown by mass loss in the TGA curve (Fig. 3.1b) and an exothermic peak at 248 °C in the DSC profile (Fig. 3.1a).

The publication by Okanigbe, Popoola, and Adeleke [5] contains the findings of the XRD analysis of the heat treated WCD.

Thermodynamic modelling of the oxidative roasting of WCD (using FACTSage 6.8 version) was done utilizing the results of the DSC (Fig. 3.1a), TGA (Fig. 3.1b), and XRD analyses (Table 3.1).

Based on these modelled results, a special superimposed predominant area diagram (SPAD) was created for the Cu-S-O and Fe-S-O systems (also known as Cu-Fe-S-O) at temperatures of 100 °C, 680 °C, 740 °C, and 800 °C (Fig. 3.2a, b).

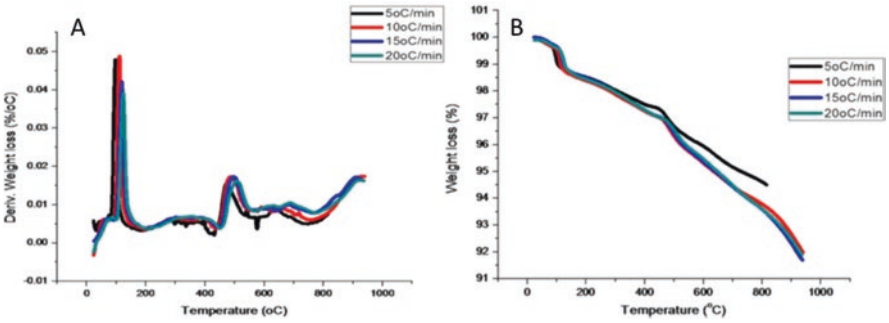

Fig. 3.1 Thermal Behaviour of CSD as derived from (**a**) DSC and (**b**) TGA Curves at 5, 10, 15, and 20 °C/Min [7]

Table 3.1 Mineralogical Composition and Specific Gravity of WCD [5, 6]

No.	Minerals	Chemical Formulae	Content (Wt %)	Specific gravity
1	Cuprospinel	$Cu_{0.98}O_{1.02}$	24.34	6.50 (Landes [36])
2	Chalcopyrite	$Cu_{6.88}Fe_{4.00}S_{8.00}$	7.95	4.20 (Landes [36])
3	Mullite	$Al(Al_{0.69}Si_{1.22}O_{4.85})$	42.97	3.16 (Tripathi et al. [37])
4	Gypsum	$Ca(SO_{4.00})(H_{2.00}O)_{2.00}$	11.69	2.33 (Landes [36])
5	Quartz	$SiO_{2.00}$	11.45	2.70 (Landes [36])
6	Magnetite	$Fe_{2.96}O_{4.00}$	1.60	4.95 (Landes [36])

The SPAD model displays the Cu-Fe-S-O system's potential phases at low temperature (680 °C), intermediate temperature (740 °C), and high temperature (800 °C) (Fig. 3.2a, b).

Copper and iron sulphides, such as chalcopyrite and bornite (Fig. 3.2a) and pyrite (Fig. 3.2b), respectively, oxidize at lower temperatures to form sulphates and oxysulphates, such as chalcocyanite and dolerophanite. These minerals transform into oxides like tenorite, hematite, and magnetite at high temperatures (800 °C). Accordingly, it will be anticipated to detect copper ferrite/Cuprospinel-$CuFe_2O_4$, which was created in the WCD at temperatures of 900 °C, which is near to the operating temperature (i.e. oxidative roasting in reverberatory furnace-1400 °C) under which it was produced (Fig. 3.2a). This modelled premise fits in nicely with a prior report on the characteristics of this specific WCD [5].

According to theory, chalcopyrite native solid-phase migration into spinel form ferrite is what creates cuprospinel [7]. $CuSO_4$, Fe_3O_4, CuO, and Fe_2O_3 are intermediary phases that allow $CuFe_2O_4$ to form inside grains. The thermodynamic model was also used to predict the theoretical equilibrium composition (TEC) of the WCD after roasting in the air (Eq. 3.1).

$$\begin{aligned}&24.34\left(Cu_2O\right)\left(Fe_2O_3\right)+7.95CuFeS_2+42.97Al_6Si_2O_{13}+11.69CaSO_4\left(H_2O\right)_2\\&+11.45SiO_2+1.60MgFe_2O_4+\left(71\%N_2,19\%O_2,10\%CO_2\right)Air\end{aligned} \tag{3.1}$$

The thermodynamic model for WCD was experimentally validated by roasting the WCD in a muffle furnace with the furnace door slightly ajar to let in fresh air. It was found that even at 800 °C, the mullite, quartz, and gypsum in the WCD as it was received persisted in the roast product unaltered (Fig. 3.3). While gypsum was observed to lose its water of crystallization at temperatures between 120 °C and 200 °C to form anhydrite (Fig. 3.3), this was not the case for iron in WCD, which oxidized into iron II (Fe^{2+}) and/or iron III (Fe^{3+}). These findings are consistent with those made from analyses of DSC and TGA results (Fig. 3.1a, b).

Because some sulphur did not completely oxidize during partial roasting, sulphur is still present in the roast products (RP) as Cu_2S and FeS. In the RP, oxygen coexists with either copper or iron. It was found that varying temperature and time were related to variations in the sulphate and oxide levels in the RP. Certain circumstances made it more likely to produce sulphates than oxides, and vice versa (Fig. 3.4).

In terms of mineralogical composition, it was found that test 8 with treatment settings of 800 °C for 2 hrs produced the closest experimental result to TEC [9].

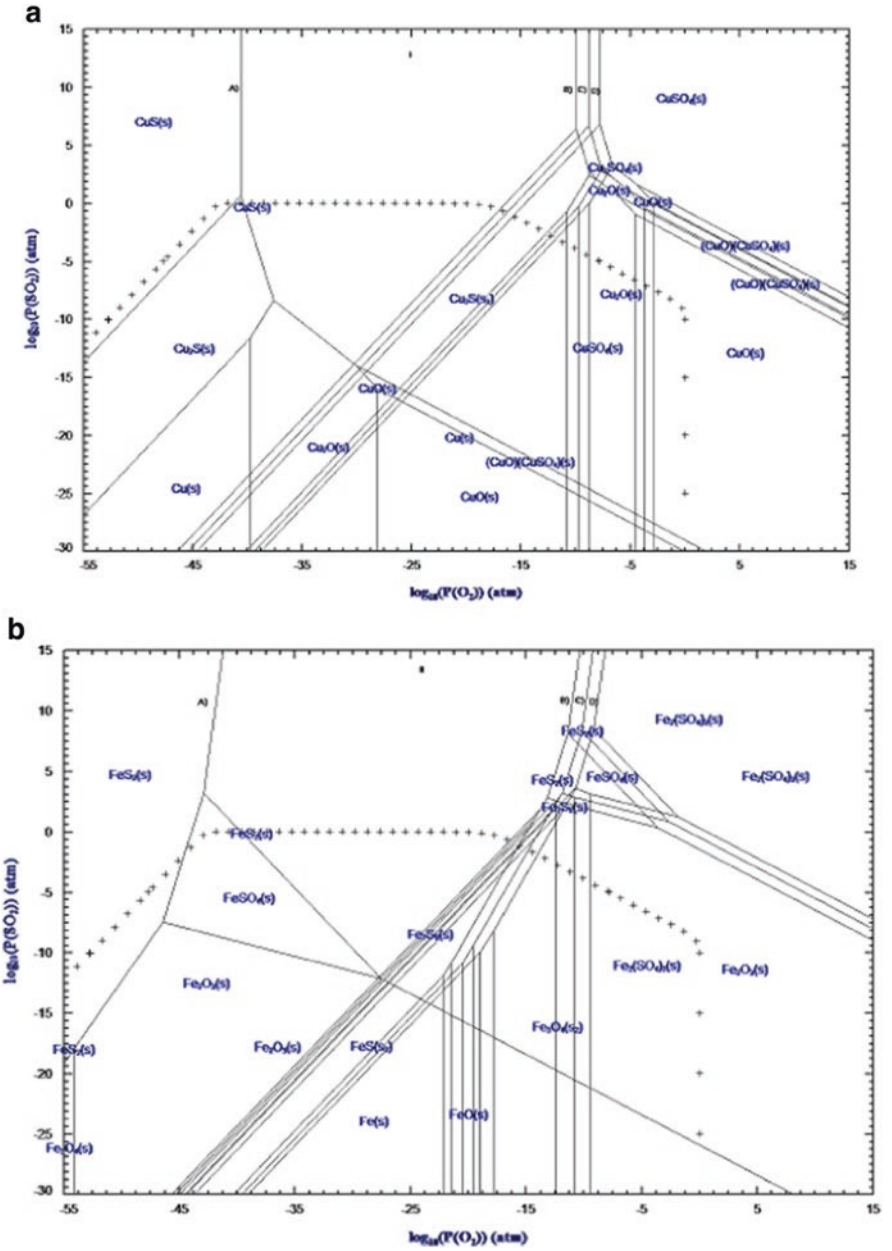

Fig. 3.2 Superimposed predominance area (**a**) Cu-S-O and (**b**) Fe-S-O system diagrams at 100 °C, 680 °C, 740 °C, and 800 °C [7]

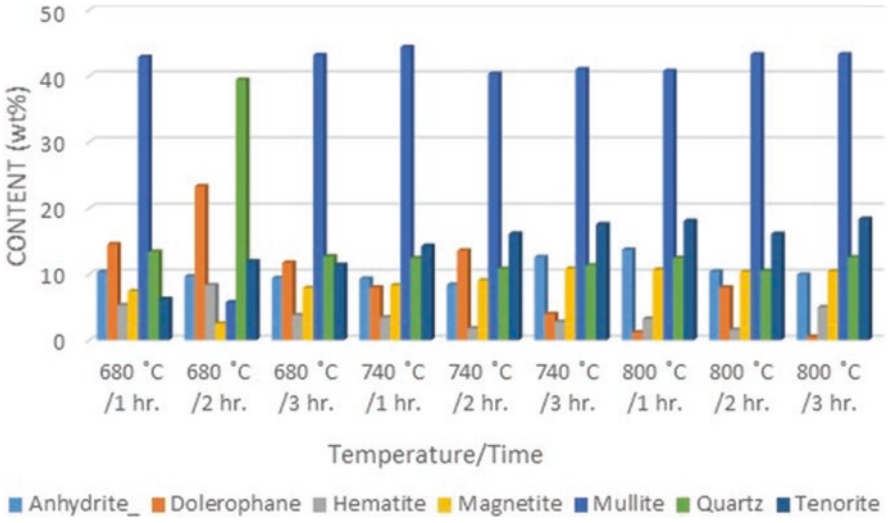

Fig. 3.3 XRD Result of the Oxidative Roasting Carried Out on WCD

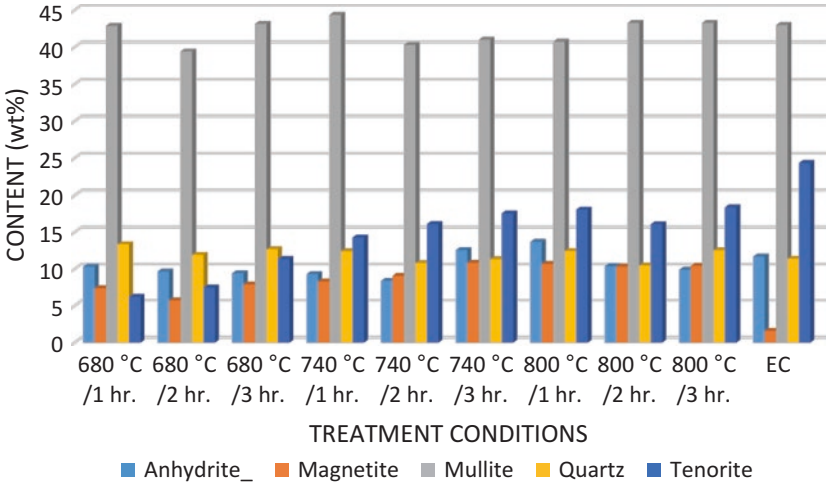

Fig. 3.4 Experimental Equilibrium Compositions at Different Test Conditions

3.3.1.2 Density Separation

In Table 3.2, you can see the mineralogical composition of copper value in tailings obtained from TC-7 of DS. According to Table 3.1 and Fig. 3.5, the composition of the copper value in this group of tailings is primarily composed of copper sulfides with a minor quantity of metallic copper, which is consistent with the theoretical deductions previously established. The copper value that reported to the tailings is primarily made up of sulfides with a very tiny proportion of metallic copper, i.e. according to the mineralogical analysis of the tailings acquired after DS (Table 3.2).

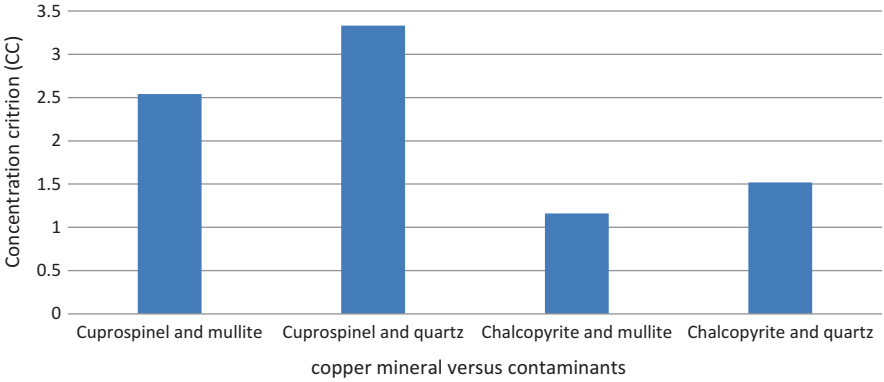

Fig. 3.5 Concentration criterion for different minerals in the WCD

Table 3.2 Mineralogical Composition of Copper Value in Tailings from TC-7 of DS

No	Minerals	Chemical formulae of minerals	CC (between CuS and SiO_2/ SiO_2-Al_2O_3)
1	Copper	$Cu_{4.00}$	≤2.5
2	Chalcopyrite	$Cu_{4.00}$ $Fe_{4.00}$ $S_{8.00}$	≤ 2.5
3	Pyrite	$Fe_{4.00}$ $S_{8.00}$	≤2.5
4	Wassonite	$Cu_{28.00}$ $S_{16.00}$	≤2.5
5	Tochilinite	$Fe_{8.00}$ $S_{10.00}$	≤2.5
6	Isocubanite	$Cu_{1.33}$ $Fe_{2.67}$ $S_{4.00}$	≤2.5

Despite being less in content than copper oxides (Table 3.1), these copper sulfides are nevertheless of significant value, especially in light of the 70,000–100,000 kilograms of WCD produced annually [2, 3, 28]. Therefore, it is advised that oxidative roasting (400–500 °C) be combined with DS in the pre-treatment protocol to change these copper sulfides into copper sulphates or oxides before physical separation.

3.3.1.3 Effect of Pre-Treatment on Classification of WCD

The transformation (i.e. phase change) of minerals (Fig. 3.3) was the major outcome of using oxidative roasting alone to pre-treat WCD. The objective of minimizing adverse effects (i.e. side reactions and poor porosity structures) while copper is being leached from the WCD persist. Since the gangue minerals (such as mullite, gypsum, and quartz), which cause the side reactions during leaching, are still tightly linked to copper value.

Copper oxide, iron oxide, calcium oxide, and magnesium oxide were much more prevalent in the concentrates than in the tailings, hereafter referred to as group A, after the physical separation of WCD with the centrifugal concentrator. However, the tailings had substantially more silicon oxide, aluminium oxide, and titanium

oxide than concentrate did (Fig. 3.6). The optimal combination of maximal copper content and minimal quartz and mullite content, which acts as a baseline for centrifugal performance, was found in Test 7, and it was also noted (Fig. 3.7).

The information acquired (Figs. 3.8, 3.9, 3.10, 3.11, 3.12, 3.13, 3.14, and 3.15) shows that the separation of copper oxide minerals from undesirable minerals

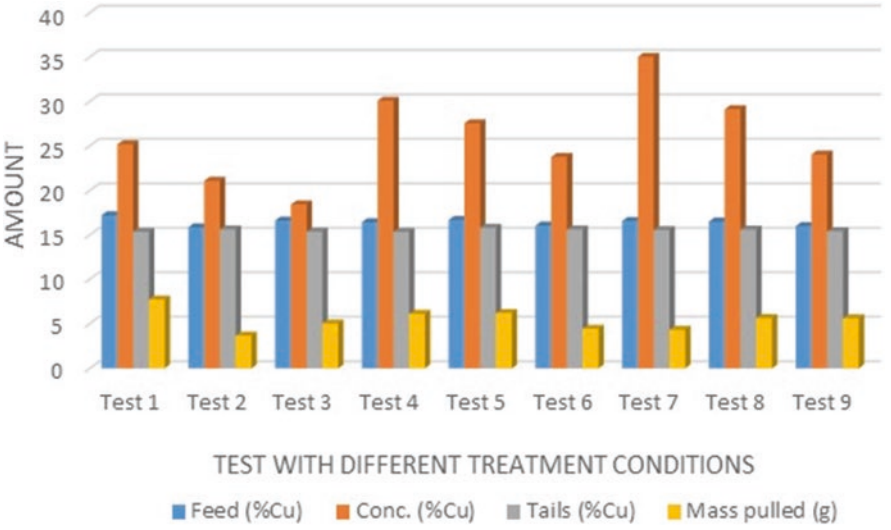

Fig. 3.6 Total Mass Pull for Tests Performed with the KGC

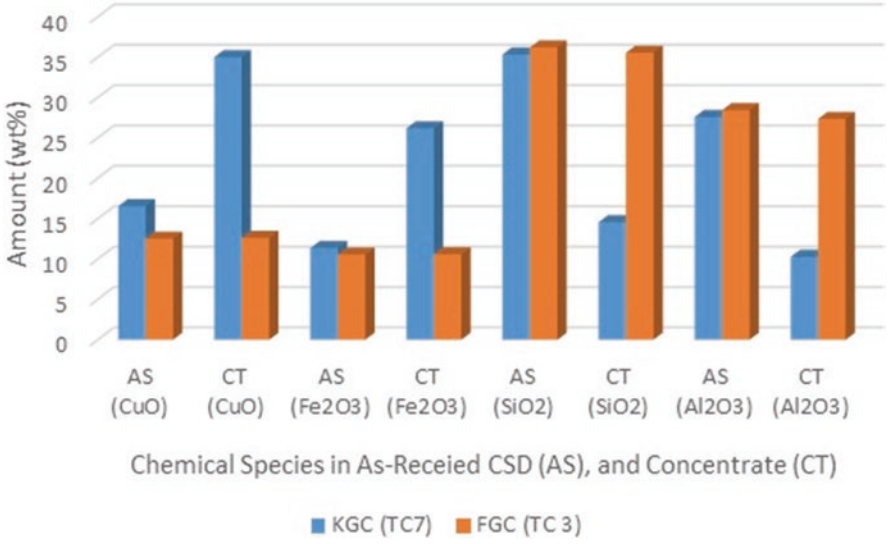

Fig. 3.7 Total Mass Pull for Tests Carried out with the KGC

(aluminium oxide and silicon oxide) was made possible by applying this pre-treatment method (i.e. DS) alone. With this outcome, side reactions during the leaching of copper from the WCD can be brought to the barest minimal (Okanigbe et al. [8]).

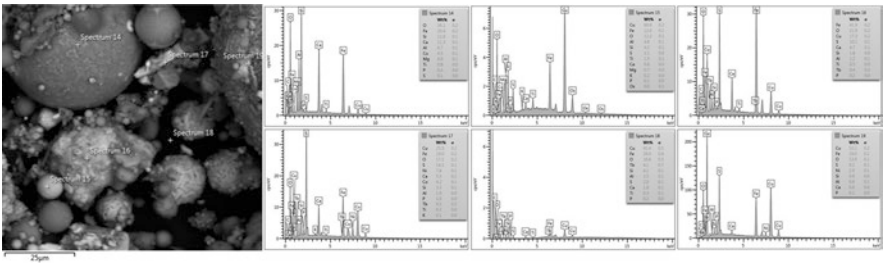

Fig. 3.8 Spectrums showing copper, aluminium, and silicon contents in concentrate from DS test 1

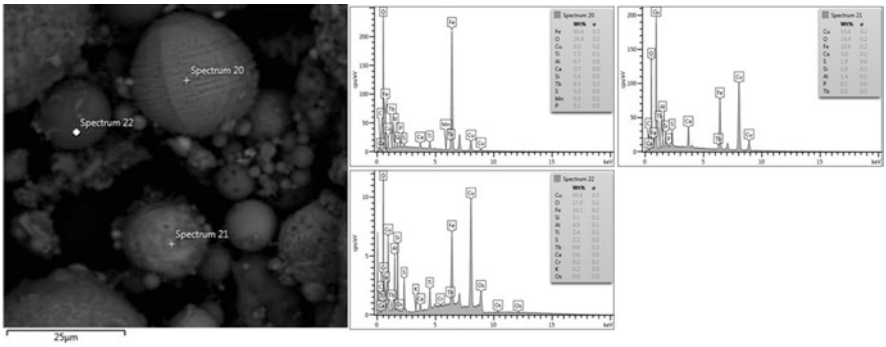

Fig. 3.9 Spectrums showing copper, aluminium, and silicon contents in concentrate from DS test 2

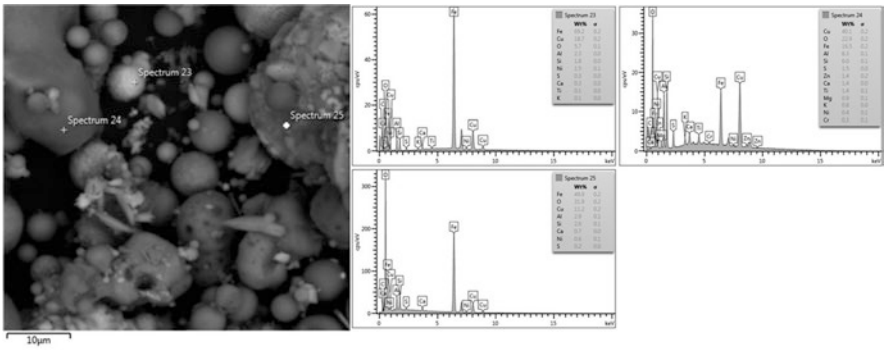

Fig. 3.10 Spectrums showing copper, aluminium, and silicon contents in concentrate from DS test 3

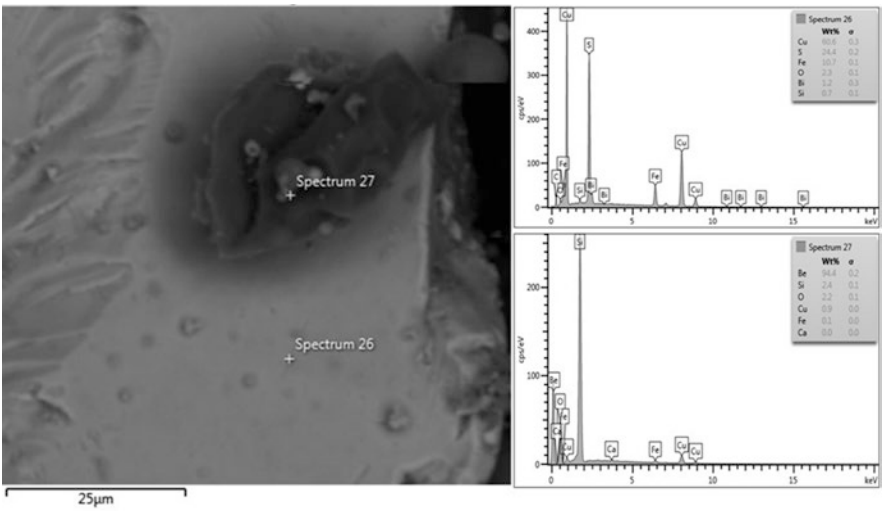

Fig. 3.11 Spectrums showing copper, aluminium, and silicon contents in concentrate from DS test 4

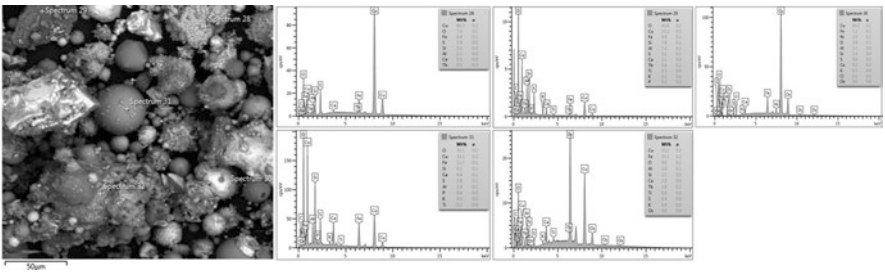

Fig. 3.12 Spectrums showing copper, aluminium, and silicon contents in concentrate from DS test 5

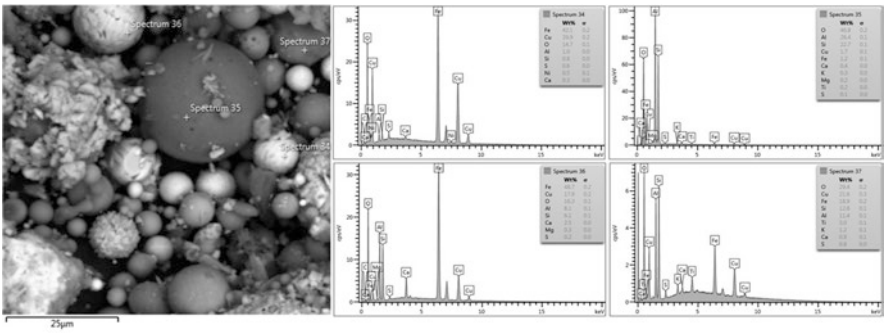

Fig. 3.13 Spectrums showing copper, aluminium, and silicon contents in concentrate from DS test 6

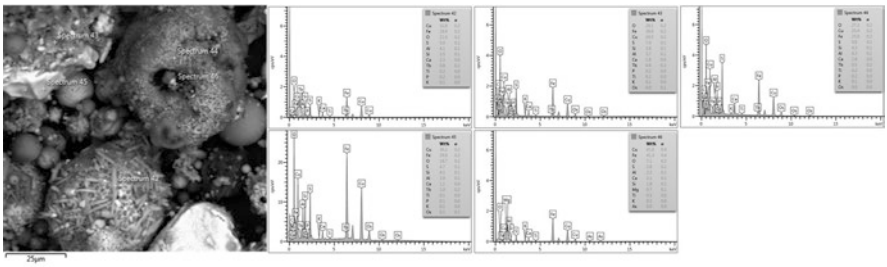

Fig. 3.14 Spectrums showing copper, aluminium, and silicon contents in concentrate from DS test 8

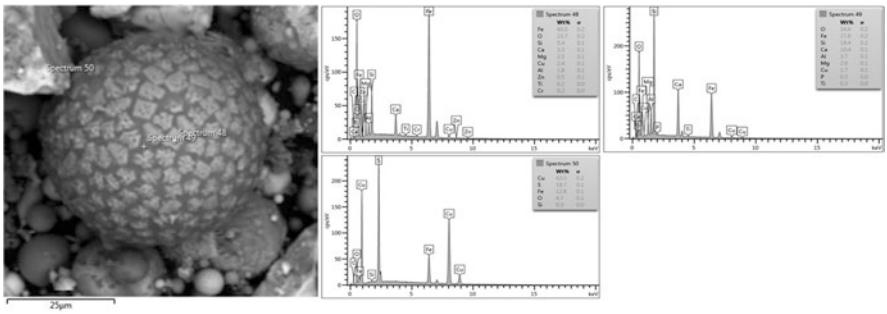

Fig. 3.15 Spectrums showing copper, aluminium, and silicon contents in concentrate from DS test 9

3.3.1.4 Effect of Pre-Treatment on Micro-Porosities

The force that attempts to pull an object in a circle toward its centre is known as centripetal force.

Centripetal force is occasionally experienced by objects, although not as frequently as gravitational force or frictional force. Only when moving in a circle can you experience centripetal force. It makes it possible for items to move along a circular path without being forced off the path by inertia. The condition in which we rotate, swing any object, or travel in orbits around a centre is an excellent example. We talk about the centripetal force in relation to the classification of the WCD in this section of Chap. 4. The force necessary for circular motion is the centripetal force, and in accordance with Herivel's [38] interpretation of Newton's second law of motion, net force equals mass times acceleration. The centripetal acceleration is the acceleration in a homogeneous circular motion. Thus, using Eq. 3.2, it is possible to calculate the centripetal force's (F) magnitude. As a result, Eq. 3.2 can be used to estimate the size of the centripetal force acting on WCD particles during classification.

$$C = MA \tag{3.2}$$

where

C = centripetal force; M = mass of solid used for test; A = acceleration due to gravity

Hence:

$$C = 83.0562\,\text{g} \times 9.8\frac{\text{m}}{\text{s}^2}$$

$$C = 813.9508\,\text{gm}/\text{s}^2$$

$$C = 813.9508\,\text{N}$$

However, it is possible to estimate the centripetal force that really affected the particles during WCD classification as follows:

For level 1 (i.e. 60 G)

$$C = 60 \times 813.9508\,\text{N}$$

$$C = 48{,}837.048\,\text{N}$$

This force (48,837.048 N) is comparable to what 86 adults of average weight would apply to a single particle (Fig. 3.16).

For level 2 (i.e. 90 G)

$$\text{C} = 90 \times 813.9508\,\text{N}$$

$$\text{C} = 73{,}255.572\,\text{N}$$

This force (73, 255.572 N) is comparable to what 129 adults of average weight would apply to a single particle (Fig. 3.17).

For level 3 (i.e. 120 G)

$$\text{C} = 120 \times 813.9508\,\text{N}$$

$$\text{C} = 97{,}674.096\,\text{N}$$

This centripetal force, which is equal to 97,674.096 N, is comparable to what 172 adults of average weight would apply to a single particle (Fig. 3.18).

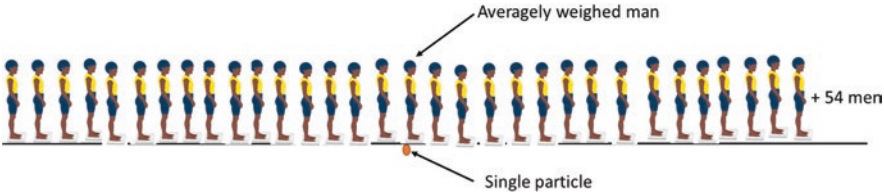

Fig. 3.16 Illustration of the force applied to a single particle by 86 averagely weighed men

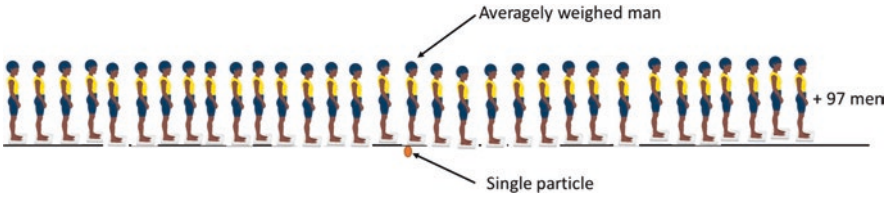

Fig. 3.17 Illustration of the force applied to a particle by 129 adults of average weight

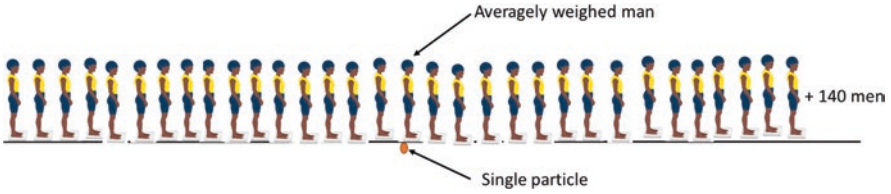

Fig. 3.18 Picture showing the force applied to a single particle by 172 adults of average weight

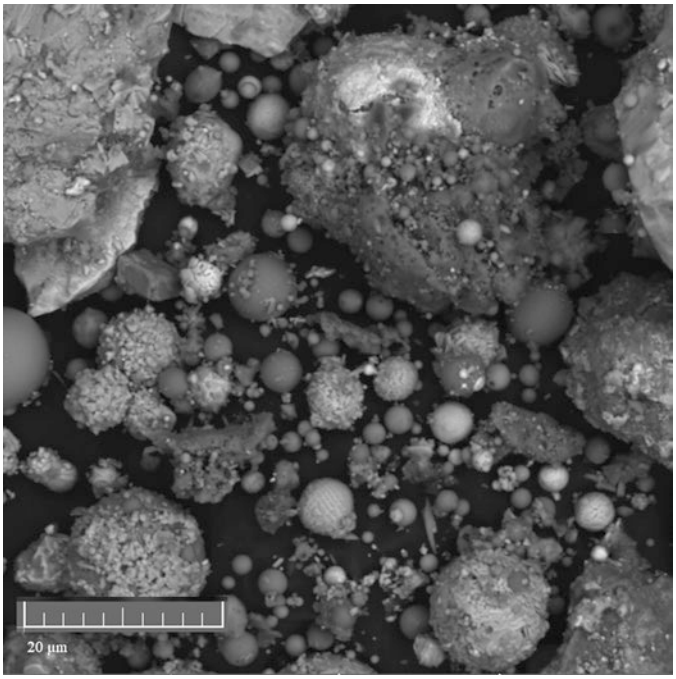

Fig. 3.19 SEM photo of Concentrate from DS Test 1

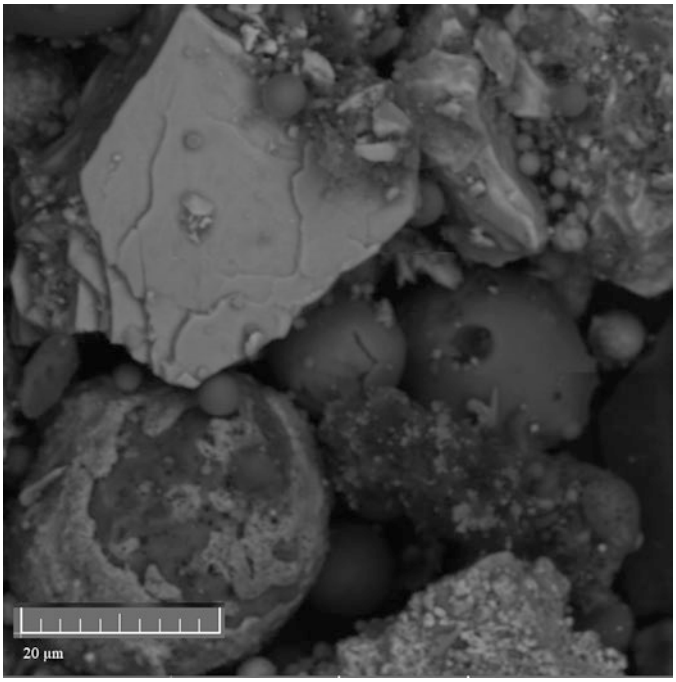

Fig. 3.20 SEM photo of Concentrate from DS Test 2

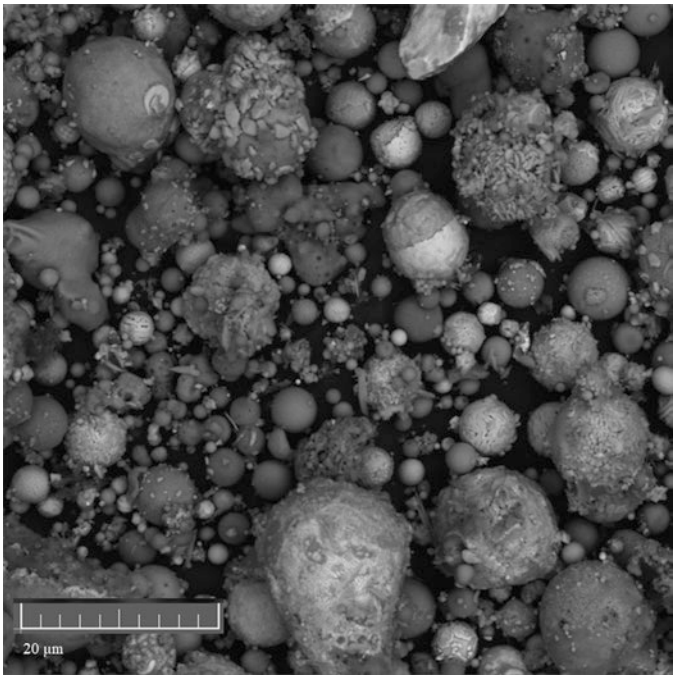

Fig. 3.21 SEM photo of Concentrate from DS Test 3

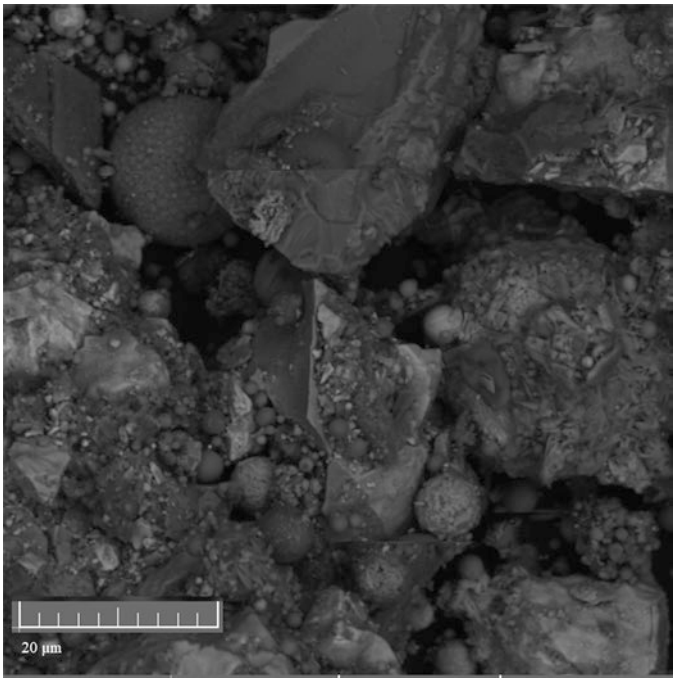

Fig. 3.22 SEM photo of Concentrate from DS Test 4

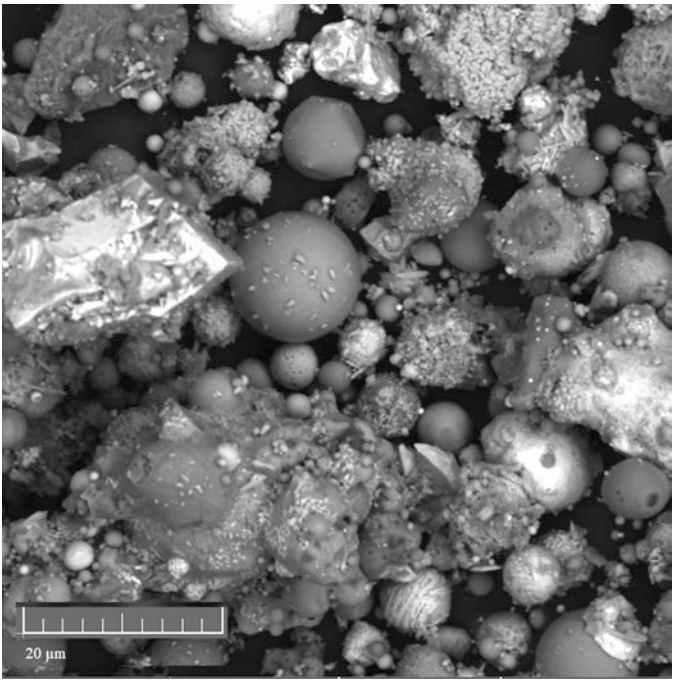

Fig. 3.23 SEM photo of Concentrate from DS Test 5

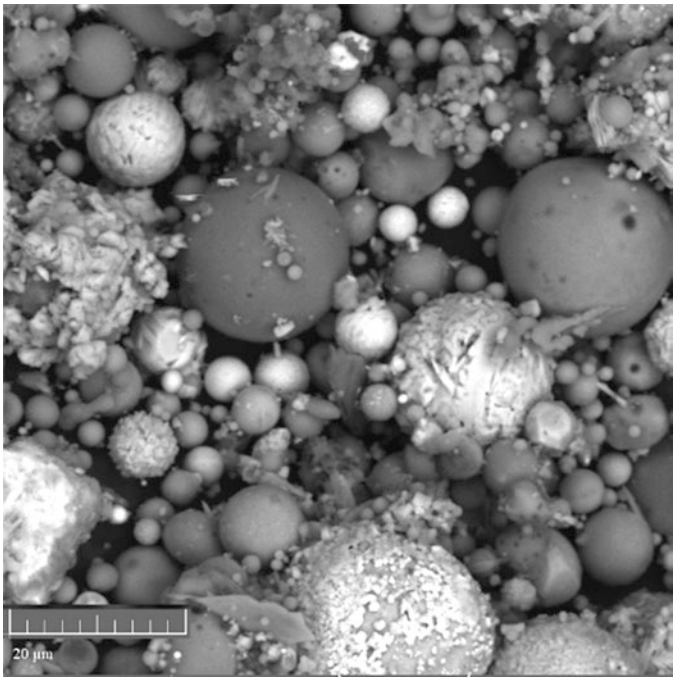

Fig. 3.24 SEM photo of Concentrate from DS Test 6

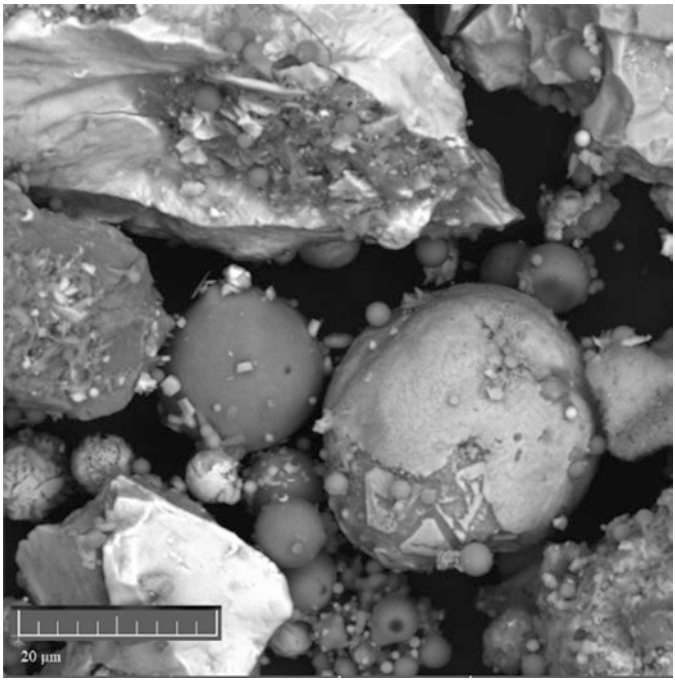

Fig. 3.25 SEM photo of Concentrate from DS Test 7

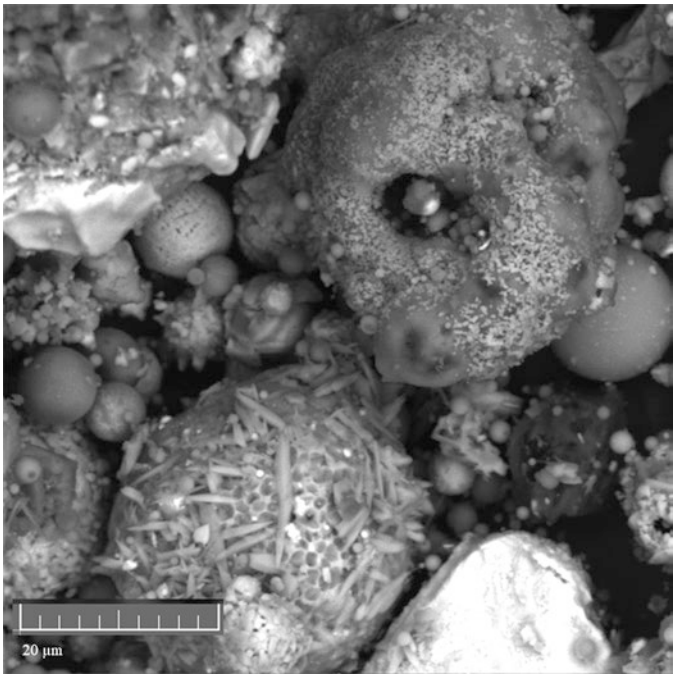

Fig. 3.26 SEM photo of Concentrate from DS Test 8

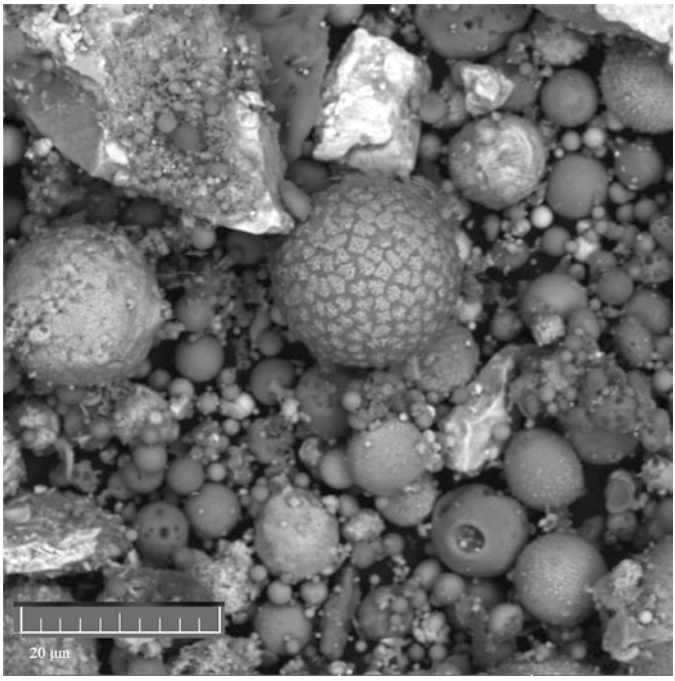

Fig. 3.27 SEM photo of Concentrate from DS Test 9

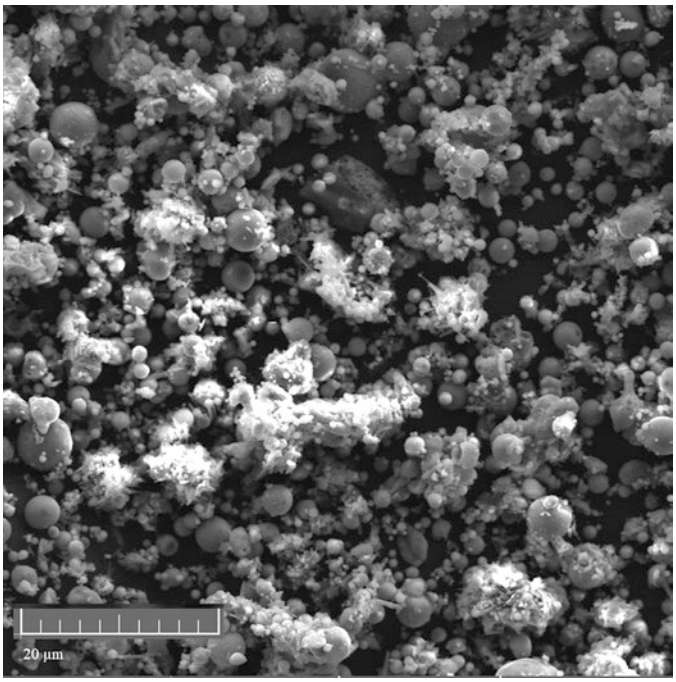

Fig. 3.28 SEM photo of As-received WCD

Consequently, the concentrates after classification exhibit micro-porosities such as cracks and peels as illustrated by SEM images in Figs. 3.19, 3.20, 3.21, 3.22, 3.23, 3.24, 3.25, 3.26, and 3.27 when compared to the as-received WCD (Fig. 3.28).

The concentrate from Test 7 yielded the greatest copper content, which was measured (Fig. 3.25). On the basis of the SEM photos that follow, it can be seen that the number of smaller particles gradually decreased until the ideal condition (test 7) was attained, which displayed the fewest number of smaller particles. This finding is consistent with the prior EDS results in this chapter (Figs. 3.8, 3.9, 3.10, 3.11, 3.12, 3.13, 3.14, and 3.15).

3.3.1.5 Effect of Pre-Treatment on Surface Area, Pore Volume, and Pore Diameter of CSD

Both the pore volume (0.0087 to 0.0027 cm^3/g) and BET surface area (4.1730 to 0.4634 m^2/g) for RP significantly decreased. Shrinkage due to moisture loss caused particle aggregation, sintering, and formation of larger-sized pores (i.e. 82.9530 Å and 233.5759 Å for AS and RP, respectively) in RP (Table 3.3). Although CT had a much bigger pore diameter (increase from 82.9530 Å in CSD to 410.8530 Å in concentrate), it had a much lower specific surface area (down from 4.1730 m^2/g in the WCD to 0.3321 m^2/g in concentrate). In this case, the change was attributed to

Table 3.3 BET Measurement of WCD [34]

BET	WCD	RP	Difference	CT	Difference
Surface area (m^2/g)	4.166100 4.179900	0.458100 0.468700	– –	0.320500 0.343700	– –
Average	4.173000	0.463400	−900%	0.332100	−1200%
Pore volume (cm^3/g)	0.008506 0.008802	0.002663 0.002749	– –	0.003139 0.003685	– –
Average	0.008654	0.002706	−320%	0.003412	−200%
Pore diameter (Å)	80.057900 85.848100	213.654300 253.497500	– –	396.514200 425.191800	– –
Average	82.953000	233.575900	+280%	410.853000	+400%

the CT having more heavier/larger particles and less lighter/smaller particles. The leaching rate of copper from this WCD is anticipated to benefit from the increased pore diameter (Table 3.3).

3.4 Conclusions

The aim of this chapter is to present the potentials of introducing DS into OR-SAL technology. This was achieved by comparing OR and DS pre-treatments. Result showed average surface area of WCD decreased by 900% and 1200% when pre-treated with OR and DS, respectively. The pore volume decreased by 320% and 200% when WCD was pre-treated using OR and DS, respectively. However, pore diameter increased by 280% and 400% when WCD was pre-treated with OR and DS, respectively. Furthermore, DS pre-treated particles revealed enhanced micro-porosities in form of peels and cracks. Significant amounts of gangue minerals (e.g. aluminium and silicon) reported to the tailings, presupposing reduced SR and enhanced PS. In conclusion, OR-DS-SAL is a technology with capacity to enhance copper recovery from WCD. Hence, recommended.

Acknowledgements The author will want to appreciate Tshwane University of Technology, Pretoria, South Africa, for facilities made available.

References

1. A.A. Adeleke, A.P.I. Popoola, O.M. Popoola, D.O. Okanigbe, Experimentation, modeling, and optimum conditions of pyro-hydrometallurgical-precipitation reaction technology for recovery of copper as oxide of nanoparticles from a copper dust, in *Energy Technology 2020: Recycling, Carbon Dioxide Management, and Other Technologies*, (Springer, Cham, 2020), pp. 189–201
2. E. Balladares, U. Kelm, S. Helle, R. Parra, E. Araneda, Chemical-mineralogical characterization of copper smelting flue dust. Dyna **81**(186), 11–18 (2014)

3. T.K. Ha, B.H. Kwon, K.S. Park, D. Mohapatra, Selective leaching and recovery of bismuth as Bi_2O_3 from copper smelter converter dust. Sep. Purif. Technol. **142**, 116–122 (2015)
4. A. Morales, M. Cruells, A. Roca, R. Bergó, Treatment of copper flash smelter flue dusts for copper and zinc extraction and arsenic stabilization. Hydrometallurgy **105**(1–2), 148–154 (2010)
5. D.O. Okanigbe, A.P.I. Popoola, A.A. Adeleke, Characterization of copper smelter dust for copper recovery. Proc. Manuf **7**, 121–126 (2017)
6. D.O. Okanigbe, A.P.I. Popoola, A.A. Adeleke, Hydrometallurgical processing of copper smelter dust for copper recovery as nano-particles: A review. Energ. Technol. **2017**, 205–226 (2017)
7. D.O. Okanigbe, A.P.I. Popoola, A.A. Adeleke, Thermal analysis and kinetics of the oxidative roasting process of a copper smelter dust. Int. J. Adv. Manuf. Technol. **94**(5), 2393–2400 (2018)
8. D. Okanigbe, P. Olawale, A. Popoola, A. Abraham, A. Michael, K. Andrei, Centrifugal separation experimentation and optimum predictive model development for copper recovery from waste copper smelter dust. Cogent Eng **5**(1), 1551175 (2018)
9. D.O. Okanigbe, M.K. Ayomoh, O.M. Popoola, P.A. Popoola, V.S. Aigbodion, Oxidative roasting experimentation and optimum predictive model development for copper and iron recovery from a copper smelter dust. Results Eng **7**, 100125 (2020)
10. M. Vítková, V. Ettler, J. Hyks, T. Astrup, B. Kříbek, Leaching of metals from copper smelter flue dust (Mufulira, Zambian Copperbelt). Appl. Geochem. **26**, S263–S266 (2011)
11. J.Y. Wu, F.C. Chang, H.P. Wang, M.J. Tsai, C.H. Ko, C.C. Chen, Selective leaching process for the recovery of copper and zinc oxide from copper-containing dust. Environ. Technol. **36**(23), 2952–2958 (2015)
12. M. Carter, E.R. Vance, L.P. Aldridge, M. Zaw, G. Khoe, Immobilization of arsenic trioxide in cementitious materials, in *Australasian Institute of Mining and Metallurgy*, (1994), pp. 275–280
13. Y. Fu, L. Jiang, D. Wang, Removal of arsenic from copper smelter flue dust by calcinations. Yelian Bufen **6**, 14–16 (2000)
14. V.I. Ermakov, Complex treatment of fine dusts of Urals copper-smelting firms. Tsvetn. Met. (12), 26–30 (1979)
15. Z. Yu, Process for bismuth recovery from the flue dust of copper smelting. Huaxue Shijie **28**(10), 465–468 (1987)
16. H. Mochida, O. Iida, Copper smelter flue dust treatment (Kokai Tokkyo Koho, Jap, 1988), p. 3
17. Sumitomo Metal Mining, Metal Recovery from Flue Dust Containing Copper. Japan Patent 57.201.577 (1982)
18. Z.B. Yin, E. Caba, L. Barron, D. Belin, W. Morris, M. Vosika, R. Bartlett, Copper extraction from smelter flue dust by lime-roast/ammoniacal heap leaching, in *Residues and Effluents: Processing and Environmental Considerations*, (1992), pp. 255–267
19. C.T. Mulale, M.D. Mwema, G.B. Mashala, Retreatment of dust waste from the copper smelter and converter, in *Global Symposium on Recycling and Clean Technology*, vol. 2, (1999), pp. 1201–1208
20. B. Gorai, R.K. Jana, Z.H. Khan, Electrorefining electrolyte from copper plant dust. Mater. Trans. **43**(3), 532–536 (2002)
21. R. Hanks et al., "Bismuth at Rokana Copper Smelter, Zambia: Its Behavior and Extraction from Flue Dusts," Trans. IMM, 88 (1979), pp. C99–C106.
22. M.P. Smirnov, V.T. Khvan, G.A. Bibenina, R.P. Kefilyan, N.I. Il'yasov, Complex treatment of lead and rhenium containing sulfate dusts from copper plants. Tsvetnye Metally **6**, 3–6 (1984)
23. Z.W. Zhang, W. Lu, F. Zheng, Separation and recovery of copper and zinc from flue dust. Huanjing Kexue **11**(6), 1012–1016 (1992)
24. S. Teir, H. Revitzer, S. Eloneva, C.J. Fogelholm, R. Zevenhoven, Dissolution of natural serpentinite in mineral and organic acids. Int. J. Miner. Process. **83**(1–2), 36–46 (2007)
25. L.H. Tran, K.K. Mueller, L. Coudert, J.F. Blais, Optimized indium solubilization from LCD panels using H2SO4 leaching. Waste Manag. **114**, 53–61 (2020)

26. F. Habashi, *Metals from Ores: An Introduction to Extractive Metallurgy* (Métallurgie Extractive Québec, Sainte Foy, 2003)
27. R.K.K. Mbaya, M.M. Ramakokovhu, C.K. Thubakgale, Atmospheric pressure leaching application for the recovery of copper and nickel from low-grade sources, in *The Southern African Institute of Mining and Metallurgy (Base Metals Conference 2013)*, (The Southern African Institute of Mining and Metallurgy, Johannesburg, 2013), pp. 255–268
28. L. Qiang, I.S. Pinto, Z. Youcai, Sequential stepwise recovery of selected metals from flue dusts of secondary copper smelting. J. Clean. Prod. **84**, 663–670 (2014)
29. F. Barriga, I. Palencia, F. Carranza, The passivation of chalcopyrite subjected to ferric sulfate leaching and its reactivation with metal sulfides. Hydrometallurgy **19**, 159–167 (1987)
30. C. Klauber, A critical review of the surface chemistry of acidic ferric sulphate dissolution of chalcopyrite with regards to hindered dissolution. Int. J. Miner. Process. **86**, 1–17 (2008)
31. S.E. Khalafalla, I.D. Shah, Oxidative roasting of covellite with minimal retardation from the $CuO \cdot CuSO_4$ film. Metallur. Trans **1**(8), 2151–2156 (1970)
32. F. Magagula, High temperature roasting of sulphide concentrate and its effect on the type of precipitate formed (Doctoral dissertation, Doctoral dissertation) (2012)
33. E. Hsu, K. Barmak, A.C. West, A.H.A. Park, Advancements in the treatment and processing of electronic waste with sustainability: A review of metal extraction and recovery technologies. Green Chem. **21**(5), 919–936 (2019)
34. D.O. Okanigbe, Production of copper and copper oxide nano-particles from leach solution of low grade copper smelter dust (2019)
35. D.O. Okanigbe, A.P.I. Popoola, A.A. Adeleke, O.M. Popoola, Upgrading the copper value in a waste copper smelter dust with the falcon gravity concentrator, in *TMS Annual Meeting & Exhibition*, (Springer, Cham, 2018), pp. 283–295
36. K.K. Landes, A mineral specific gravity chart. Am. Miner. J. Earth Planet. Mater **15**(11), 534–535 (1930)
37. H.S. Tripathi, S.K. Das, B. Mukherjee, A. Ghosh, Sintered mullite from aluminous ore for refractory application. Am. Ceram. Soc. Bull. **86**(5), 9301–9306 (2007)
38. J.W. Herivel, Newton's discovery of the Law of Centrifugal Force. Isis **51**(4), 546–553 (1960)

Chapter 4
Pre-treatment of Waste Copper Dust (II): Optimum Predictive Models and Experimental Data Error Margin

Daniel Ogochukwu Okanigbe, Micheal Kowejo Ayomoh, and Shade Rouxzeta Van Der Merwe

4.1 Introduction

Customarily, in mineral processing and pyrometallurgy, unit operations are integrated for successful resource recovery. These operations often entail rigorous and costly experimental evaluation of laboratory tests and/or pilot-scale equipment trials. These evaluations are carried out to assess the performance of the unit operations. As a result, developing a low-cost, time-saving tool with the ability to correctly predict the performance of these unit operations would be advantageous. A mathematical model can be used to achieve this purpose of predicting certain occurrences, while expressing it as a set of equations [1]. Additionally, the optimization and development of both old and new processes can be achieved via mathematical modelling in a cost-effective manner. Mathematical models have the advantage of today, because of the availability and obvious decline in the cost of hardware and software. The past few years have recorded significant achievements with the use of mathematical modelling in areas of

D. O. Okanigbe (✉)
Department of Chemical, Metallurgical and Materials Engineering, Faculty of Engineering and the Built Environment, Tshwane University of Technology, Pretoria, South Africa

Pantheon Virtual Engineering Solutions, Nigel, South Africa
e-mail: okanigbedo@tut.ac.za; okanigbeogochukwu@gmail.com

M. K. Ayomoh
Department of Industrial and Systems Engineering, Faculty of Engineering, Built Environment and Information Technology, University of Pretoria, Pretoria, South Africa

S. R. Van Der Merwe
Department of Chemical, Metallurgical and Materials Engineering, Faculty of Engineering and the Built Environment, Tshwane University of Technology, Pretoria, South Africa

Department of Mechanical and Mechatronics Engineering, Faculty of Engineering and the Built Environment, Tshwane University of Technology, Pretoria, South Africa
e-mail: vandermerweR1@tut.ac.za

D. O. Okanigbe, A. P. Popoola (eds.), *Resource Recovery and Recycling from Waste Metal Dust*, https://doi.org/10.1007/978-3-031-22492-8_4

mechanistic modelling, system modelling, and the representation of distributed parameter systems. In the past non-natural obstacle has been positioned between the scientists and engineers saddled with the responsibility of structure and properties of the finished product on one hand and on the other hand those focused on metals extraction and refining, i.e. the production of semi-finished products like slabs, rods, bars, or billets. Apart from this obstacle being non-natural and needless, it is also positively harmful. Hence, this challenge requires a holistic approach, one capable of fully integrating the "primary," "secondary," and the finishing operations, in order to come to the optimal approach. Mathematical models therefore possess the capacity in bringing about such an approach [2].

The success of mineral processing and/or pyrometallurgy pretreatment unit operations depends on the selection of suitable process variables at which the response attains its best. One of the experimental design methods used to achieve best responses is the full factorial experimental design methodology (FFEDM), which was used to design the density separation experimentation of a waste copper dust (WCD), for enhanced copper recovery [3] and oxidative roasting experimentation of WCD for copper upgrade [4]. Granted, there are other experimental design methods that can be used to screen relevant variables during mineral processing and/or pyrometallurgy of several ore materials [5–7]. Nonetheless, reports on optimum predictive model development for mineral processing and/or pyrometallurgy of secondary copper resources in order to determine behaviour of copper recovery under specified conditions are limited [3, 4] Additionally, the determination of error margin between developed optimum predictive models for mineral processing and/or pyrometallurgy of secondary copper resources like WCD has not been published in literature.

Hence, in this study, findings from determining the consistency between developed optimum predictive models and experimental data for pretreatment of copper smelter dust were presented.

4.2 Experimental Method

4.2.1 Materials

4.2.1.1 Waste Metal Dust (WMD)

The WCD from South Africa was used as the waste metal dust (WMD) for this study.

4.2.1.2 Methods

Design of Experiment (DOE)

In the present study, the FFEDM was used to determine the interaction between the response functions—$CuSO_4$, CuO, and Fe_2O_3:Fe_3O_4 (Tables 4.1 and 4.2) contents during oxidative roasting (OR) experimentation and the two operating variables

Table 4.1 Experimental inputs and outputs of CuO and $CuSO_4$ contents after oxidative roasting of WCD [4]

	Input		PC				CuO (wt%)	$CuSO_4$ (wt%)
S.N	CuO (wt%)	$CuSO_4$ (wt%)	*T* (°C)	*t* (h)	OFR	FDO (mm)	EO	EO
1	24.34	7.95	680	1.0	NC	25	6.22	14.52
A	23.97	7.82	680	1.5	NC	25	NE	NE
2	23.85	7.86	680	2.0	NC	25	7.49	23.31
B	24.34	7.62	680	2.5	NC	25	NE	NE
3	23.97	7.45	680	3.0	NC	25	11.37	11.72
4	24.84	8.43	740	1.0	NC	25	14.27	7.94
C	24.84	8.39	740	1.5	NC	25	NE	NE
5	24.77	8.35	740	2.0	NC	25	16.11	13.55
D	23.93	8.31	740	2.5	NC	25	NE	NE
6	23.93	8.29	740	3.0	NC	25	17.55	3.94
7	24.61	7.90	800	1.0	NC	25	18.06	1.16
E	24.89	8.11	800	1.5	NC	25	NE	NE
8	24.89	8.11	800	2.0	NC	25	16.07	7.95
F	23.91	8.31	800	2.5	NC	25	NE	NE
9	23.91	8.31	800	3.0	NC	25	18.37	0.52

Table 4.2 Experimental inputs and outputs of Fe_3O_4:Fe_2O_3 ratios after oxidative roasting of WCD [4]

	PC					Fe_3O_4:Fe_2O_3
S.N	Fe_3O_4:Fe_2O_3	*T* (°C)	*t* (h)	OFR	FDO (mm)	EO
1	1	680	1.0	NC	25	0.72
A	1	680	1.5	NC	25	NE
2	1	680	2.0	NC	25	0.44
B	1	680	2.5	NC	25	NE
3	1	680	3.0	NC	25	0.43
4	1	740	1.0	NC	25	0.41
C	1	740	1.5	NC	25	NE
5	1	740	2.0	NC	25	0.26
D	1	740	2.5	NC	25	NE
6	1	740	3.0	NC	25	0.20
7	1	800	1.0	NC	25	0.18
E	1	800	1.5	NC	25	NE
8	1	800	2.0	NC	25	0.15
F	1	800	2.5	NC	25	NE
9	1	800	3.0	NC	25	0.12

Key: *PC* parameters considered, *T* temperature, *t* time, *OFR* oxygen flow rate, *FDO* furnace door opening, *EO* experimental output, *PO* predictive output, *%E* percentage error, *NC* not controlled, *NE* no experiment was performed in the affected rows; hence, they were included for better predictive modelling intervals

Table 4.3 Experimental inputs and outputs of CuO, Fe_2O_3, SiO_2, and Al_2O_3 after density separated WCD [4]

	Chemical composition (feed)						Chemical composition (concentrate)			
	Experimental input						Experimental output			
S.N	CuO (wt%)	Fe_2O_3 (wt%)	SiO_2 (wt%)	Al_2O_3 (wt%)	RBS (G)	FWFR (l/min)	CuO (wt%)	Fe_2O_3 (wt%)	SiO_2 (wt%)	Al_2O_3 (wt%)
1	17.22	11.26	35.34	27.45	60	3.0	25.17	21.90	22.97	18.08
A	NE	NE	NE	NE	60	3.75	NE	NE	NE	NE
2	15.86	11.00	35.94	28.15	60	4.5	21.09	18.66	27.97	22.00
B	NE	NE	NE	NE	60	5.25	NE	NE	NE	NE
3	16.61	10.63	36.29	28.38	60	6.0	18.43	15.75	31.36	24.67
C	NE	NE	NE	NE	60	5.25	NE	NE	NE	NE
D	NE	NE	NE	NE	60	4.5	NE	NE	NE	NE
4	16.42	11.23	35.30	27.64	90	3.0	30.08	24.41	18.10	13.98
E	NE	NE	NE	NE	90	3.75	NE	NE	NE	NE
5	16.68	11.79	34.95	27.40	90	4.5	27.54	23.14	20.86	16.09
F	NE	NE	NE	NE	90	5.25	NE	NE	NE	NE
6	16.05	11.21	35.69	27.96	90	6.0	23.74	20.83	24.93	19.32
G	NE	NE	NE	NE	90	5.25	NE	NE	NE	NE
H	NE	NE	NE	NE	90	4.5	NE	NE	NE	NE
7	16.56	11.36	35.34	27.59	120	3.0	35.02	26.18	14.58	10.29
I	NE	NE	NE	NE	120	3.75	NE	NE	NE	NE
8	16.50	11.49	34.74	27.63	120	4.5	29.12	24.08	19.25	14.81
J	NE	NE	NE	NE	120	5.25	NE	NE	NE	NE
9	15.99	11.03	35.85	28.04	120	6.0	24.03	21.49	24.14	18.93

Key: *RBS* rotational bowl speed, *WFR* water flow rate, *FR* flow rate = 1.48 (l/min) (constant), *LSR* liquid-to-solid ratio = 0.5 (constant), *NE* no experiment was performed in the affected rows; hence, they were included for better predictive modelling intervals

(temperature and time), while CuO, Fe_2O_3, SiO_2 Al_2O_3 (Table 4.3) contents during density separation (DS) and the two operating variables (fluidized water flow rate (FWFR) and rotational bowl speed (RBS)) were based on principles of experimental design, mathematical equations or models, and outcomes of the factors. The FFEDM contains all likely combinations of the operating variables (factors). The effect of all factors and interaction effects on the responses are investigated methodically.

Modelling

Modelling Procedure for Output Prediction

According to Okanigbe et al. [3, 4], the modelling procedure for the output prediction will follow these steps detailed subsequently:

Step #1: Study trend of experimental samples.

Step #2: Set up constraint models to categorize and group samples into sub-classes based on #1.
Step #3: Compute absolute difference between input and output samples in same class as grouped in #2.
Step #4: Identify different experimental levels for selected classes.
Step #5: Apply interpolant model to predict output.
Step #6: End.

A generalized representation of model variables is presented in Table 4.4 [3, 4]. These variables were built into a model and used for the determination of the predictive outputs of the different mineral constituents as contained in the experimental concentrates. The modelling procedure herein is premised on constrained interpolation of outputs from any three sequenced experimental samples. Usually, two of these outputs are known via experimentation while the third unknown output is obtained via predictive modelling. In Table 4.4, the first and second columns represent the sequenced experimental trials under consideration for interpolation. The third and fourth columns, respectively, represent the (%) proportions of the inputs (p_{i_1} , p_{i_2} , and p_{i_3}) and outputs (p_{o_1} , p_{o_2} , and p_{o_3}) for the mineral constituents under investigation. Furthermore, column five represents the experimental levels while column six represents the absolute difference between the input and output values expressed in terms of Φ_1, Φ_2, and Φ_3 for each of the three experimental samples under consideration.

Presented as follow in this research are the under listed modelling notations:

$$\text{Output} = f\left(\text{speed, flow rate, input, feed rate, liquid solid ratio}\right)$$

Let: serial number for inputs: $s_i = \{1, \ldots, n-1, n\}$ and serial number for outputs $s_o = \{1, \ldots, n-1, n\}$ for $\forall n \in R$.

Where:

$\exp_{(i)i,j}$ = Experimental inputs,
$\exp_{(o)i,j}$ = Experimental outputs,

Table 4.4 Generalized representation of model variables [3, 4]

Level	Data acquisition procedure	Input value for variant factor p_{i_j}	Output value for variant factor p_{o_j}	Expt. levels	Absolute difference between p_{i_j} and p_{o_j}
1-First	Prediction	p_{i_1}	p_{o_1}	ξ	$\left\|p_{i_1} - p_{o_1}\right\| = \Phi_1$
2-Second	Experiment	p_{i_2}	p_{o_2}	μ	$\left\|p_{i_2} - p_{o_2}\right\| = \Phi_2$
3-Third	Experiment	p_{i_3}	p_{o_3}	σ	$\left\|p_{i_3} - p_{o_3}\right\| = \Phi_3$

$\text{Pre}_{(o)i,j}$ = Predictive outputs,
p_{i_j} = % input proportion of selected samples,
p_{o_j} = % output proportion of selected samples,
$\Delta p_j = \left| p_{i_j} - p_{o_j} \right|$ absolute difference between p_{i_j} and p_{o_j}

Where $j = \{1, \ldots, k-1, k\}$ represents experimental levels.

The "absolute difference" models detailed with respect to experimental levels are shown on Eq. (4.1) through to Eq. (4.3), while Eq. (4.4) through to Eq. (4.6), in the light of Table 4.1, signify the final computational models for predicting the unknown outputs.

$$\Phi_1 = \left[\frac{\Phi_3(\mu - \xi) - \Phi_2(\mu - \xi) - \Phi_2(\sigma - \mu)}{(\mu - \sigma)} \right] \tag{4.1}$$

$$\Phi_2 = \left[\frac{\Phi_3(\mu - \xi) + \Phi_1(\sigma - \mu)}{(\sigma - \mu) + (\mu - \xi)} \right] \tag{4.2}$$

$$\Phi_3 = \left[\frac{\Phi_1(\mu - \sigma) + \Phi_2(\sigma - \mu) + \Phi_2(\mu - \xi)}{(\mu - \xi)} \right] \tag{4.3}$$

$$\left| p_{i_1} - p_{o_1} \right| = \Phi_1 \tag{4.4}$$

$$\left| p_{i_2} - p_{o_2} \right| = \Phi_2 \tag{4.5}$$

$$\left| p_{i_3} - p_{o_3} \right| = \Phi_3 \tag{4.6}$$

Hence, $\Delta p_j = \Phi_j$.

Modelling Constraint for OR and DS

As presented in the report by Okanigbe et al. [3, 4], the constrained interpolant models ranging are focused on theoretical recovery of all experimental outputs OR (i.e. CuO, $CuSO_4$, Fe_2O_3:Fe_3O_4) and DS (i.e. CuO, Fe_2O_3, SiO_2 Al_2O_3) as obtained from the DOE shown in Tables 4.1, 4.2, and 4.3, respectively. Added to this capability of these constrained models is an ability to predict output proportions of mineral compositions not represented in the DOE. This robust predictive capability was made possible, by a global optimum interval of 0.5 unit deemed suitable as an upper interpolation limit, which was obtained via the rule of thumb, taking into account predictions output consistency and a minimized overall number of predictive trials as major guiding factors. The interval of 0.5 units was introduced to the time (t) column to effect the expanded DOE as presented in Tables 4.1, 4.2, and 4.3, thus resulting in additional non-experimented rows with alphabetic serial numbering. Furthermore, some generic parameters common to OR (i.e. CuO, $CuSO_4$,

Fe_2O_3:Fe_3O_4) and DS (i.e. CuO, Fe_2O_3, SiO_2 Al_2O_3) mineral include the following: LSR = 0.5 and FR = 1.48 while the following notations viz t = time; temp = temperature (for oxidative roasting); RBS = rotational bowl speed, FWFR = fluidized water flow rate (for density separation); together with i = input; and o = output are also common to the constraint equations for the mineral compositions [3, 4].

Modelling Constraint for [CuO] Prediction (OR)
Report on the modelling constraint for CuO prediction has been published by Okanigbe et al. [4].

Modelling Constraint for [$CuSO_4$] Prediction (OR)
Report on the modelling constraint for $CuSO_4$ prediction has been published by Okanigbe et al. [4].

Modelling Constraint for [Fe_2O_3:Fe_3O_4] Prediction (OR)
Report on the modelling constraint for Fe_2O_3:Fe_3O_4 prediction has been published by Okanigbe et al. [4].

Modelling Constraint for [CuO] Prediction (DS)
Report on the modelling constraint for CuO prediction has been published by Okanigbe et al. [3].

Modelling Constraint for [Fe_2O_3] Prediction (DS)
Report on the modelling constraint for Fe_2O_3 prediction has been published by Okanigbe et al. [3].

Modelling Constraint for [SiO_2] Prediction (DS)
Report on the modelling constraint for SiO_2 prediction has been published by Okanigbe et al. [3].

Modelling Constraint for [Al_2O_3] Prediction (DS)
Report on the modelling constraint for Al_2O_3 prediction has been published by Okanigbe et al. [3].

In the words of Okanigbe et al. [3, 4], "A tenth order polynomial model as presented in Eqs. (4.8) and (4.9) was adjudged the best fit for trend analysis of the experiments conducted for CuO, $CuSO_4$ and Fe_2O_3:Fe_3O_4 (OR) and CuO, Fe_2O_3, SiO_2 Al_2O_3 (DS). While Eq. (4.7) represents a generalized form of the polynomial function, Eqs. (4.8) and (4.9) are specific functions with respect to the different minerals in the mix."

$$y = P_1x^{10} + P_2x^9 + P_3x^8 + P_4x^7 + P_5x^6 + P_6x^5 + P_7x^4 + P_8x^3 + P_9x^2 + P_{10}x + P_{11} \pm e \tag{4.7}$$

$CuSO_4$

$$y = -1.2e-06x^{10} + 9.8e-05x^9 - 0.0035x^8 + 0.069x^7 - 0.82x^6 + 6x^5 - 27x^4 + 72x^3 - 1.1e+02x^2 + 82x - 12 \pm e \tag{4.8}$$

CuO

$$y = 2.8e-07x^{10} + 2e-05x^{9} - 0.00063x^{8} + 0.011x^{7} - 0.11x^{6} \\ +0.77x^{5} - 3.5x^{4} + 10x^{3} - 18x^{2} + 17x - 0.55 \pm e \quad (4.9)$$

where e = error factor.

Optimum Experimental Trend and Condition
This section presents both the optimum experimental condition and optimum experimental trend represented in a generalized mathematical expression. The optimum and most viable experimental condition is directly linked to the maximization of the reduction process during density separation of dominant SiO_2 and Al_2O_3 (silica and alumina) impurities in the resultant concentrates, while also maximizing the recovery of CuO and Fe_2O_3 (Copper oxide and Iron oxide) in the same resulting concentrates [3]. While the same optimum and most viable experimental condition is also directly linked to the maximization of the reduction process during oxidative roasting of dominant Fe_2O_3 or Fe_3O_4 impurities in the resultant concentrates, while also maximizing the recovery of CuO and $CuSO_4$ (copper oxide and copper sulphate) in the same resulting concentrates [4].

4.3 Results and Discussion

4.3.1 Model Development for Outputs from OR and DS

4.3.1.1 Different Experimental Conditions and Constraints for OR

Under this sub-section, an expanded view of the DOE which was initially presented in compact form in Tables 4.1 and 4.2 is presented in Tables 4.5 and 4.6. Furthermore, additional experimental conditions with unknown percentage output proportion are also presented in Tables 4.5 and 4.6. These new inputs are represented in alphabetic serial order while the actual experimental conditions from the DOE are represented using numeric serial order. Different experimental trends in a sequential order were identified from the same Tables 4.5 and 4.6, which was used to develop a set of constraint models as presented in the following sub-sections.

Categorizing Constraint Models for OR

According to Okanigbe et al. [3], the major governing variables used in ordering the constraint models into sub-groups are the experimental time (t) and experimental outputs. Figures 4.1, 4.2, and 4.3 are graphical representations of experimental outputs, whereas the steps taken to develop the interpolation model, prediction of output together with the discussion of observed trends, are reported in the work of Okanigbe et al. [4].

Table 4.5 Experimentation and constrained interpolant predictive outputs for CuO and $CuSO_4$ [4]

	Input		PC				Outputs for CuO (wt%)			Outputs for $CuSO_4$ (wt%)		
S.N	CuO (wt%)	$CuSO_4$ (wt%)	*T* (°C)	*t* (h)	OFR	FDO (mm)	EO	PO	*%E*	EO	PO	*%E*
1	24.34	7.95	680	1.0	NC	25	6.22	6.22	0.00	14.52	14.52	0
A	23.97	7.82	680	1.5	NC	25	NE	6.86		NE	18.83	
2	23.85	7.86	680	2.0	NC	25	7.49	7.49	0.00	23.31	23.31	0
B	24.34	7.62	680	2.5	NC	25	NE	9.86		NE	17.48	
3	23.97	7.45	680	3.0	NC	25	11.37	11.37	0.00	11.72	11.72	0
4	24.84	8.43	740	1.0	NC	25	14.27	14.27	0.00	7.94	7.94	0
C	24.84	8.39	740	1.5	NC	25	NE	15.23		NE	11.24	
5	24.77	8.35	740	2.0	NC	25	16.11	16.11	0.00	13.55	13.56	0.07
D	23.93	8.31	740	2.5	NC	25	NE	16.23		NE	13.09	
6	23.93	8.29	740	3.0	NC	25	17.55	17.19		3.94	3.94	0
7	24.61	7.90	800	1.0	NC	25	18.06	18.07	0.06	1.16	1.16	0
E	24.89	8.11	800	1.5	NC	25	NE	17.21		NE	4.66	
8	24.89	8.11	800	2.0	NC	25	16.07	16.08		7.95	7.95	0
F	23.91	8.31	800	2.5	NC	25	NE	16.73		NE	4.34	
9	23.91	8.31	800	3.0	NC	25	18.37	18.37	0.00	0.52	0.52	0

Key: *PC* parameters considered, *T* temperature, *t* time, *OFR* oxygen flow rate, *FDO* furnace door opening, *EO* experimental output, *PO* predictive output, *%E* percentage error, *NC* not controlled, *NE* no experiment was performed in the affected rows; hence, they were included for better predictive modelling intervals

Table 4.6 Experimentation and constrained interpolant predictive outputs for Fe_3O_4:Fe_2O_3 [4]

	PC					Fe_3O_4:Fe_2O_3		
S.N	Fe_3O_4:Fe_2O_3	*T* (°C)	*t* (h)	OFR	FDO (mm)	EO	PO	*%E*
1	1	680	1.0	NC	25	0.72	0.72	0.00
A	1	680	1.5	NC	25	NE	0.58	
2	1	680	2.0	NC	25	0.44	0.44	0.00
B	1	680	2.5	NC	25	NE	0.44	
3	1	680	3.0	NC	25	0.43	0.43	0.00
4	1	740	1.0	NC	25	0.41	0.39	0.00
C	1	740	1.5	NC	25	NE	0.34	
5	1	740	2.0	NC	25	0.26	0.27	0.00
D	1	740	2.5	NC	25	NE	0.23	
6	1	740	3.0	NC	25	0.20	0.20	
7	1	800	1.0	NC	25	0.18	0.19	0.06
E	1	800	1.5	NC	25	NE	0.17	
8	1	800	2.0	NC	25	0.15	0.16	
F	1	800	2.5	NC	25	NE	0.14	
9	1	800	3.0	NC	25	0.12	0.13	0.00

Key: *PC* parameters considered, *T* temperature, *t* time, *OFR* oxygen flow rate, *FDO* furnace door opening, *EO* experimental output, *PO* predictive output, *%E* percentage error, *NC* not controlled, *NE* no experiment was performed in the affected rows; hence, they were included for better predictive modelling intervals

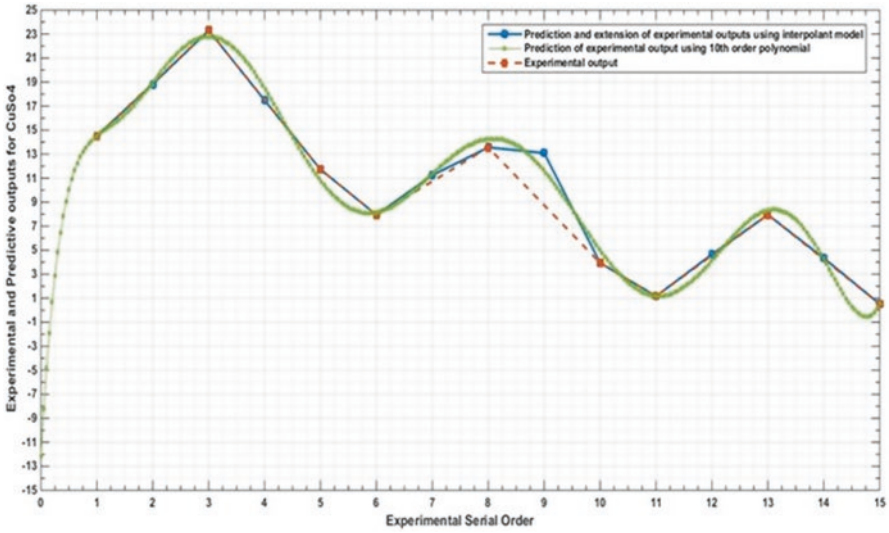

Fig. 4.1 Experimental and predictive output for $CuSO_4$ [4]

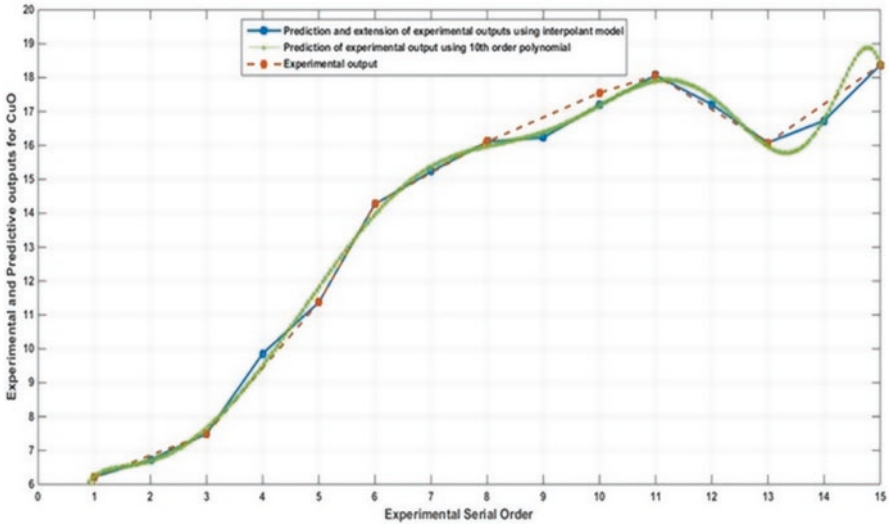

Fig. 4.2 Experimental and predictive output for CuO [4]

4.3.1.2 Different Experimental Conditions and Constraints for DS

Under this sub-section, an expanded view of the DOE which was initially presented in compact form in Table 4.3 is presented in Table 4.7. Furthermore, additional experimental conditions with unknown percentage output proportion are also presented in Table 4.7. These new inputs are represented in alphabetic serial order

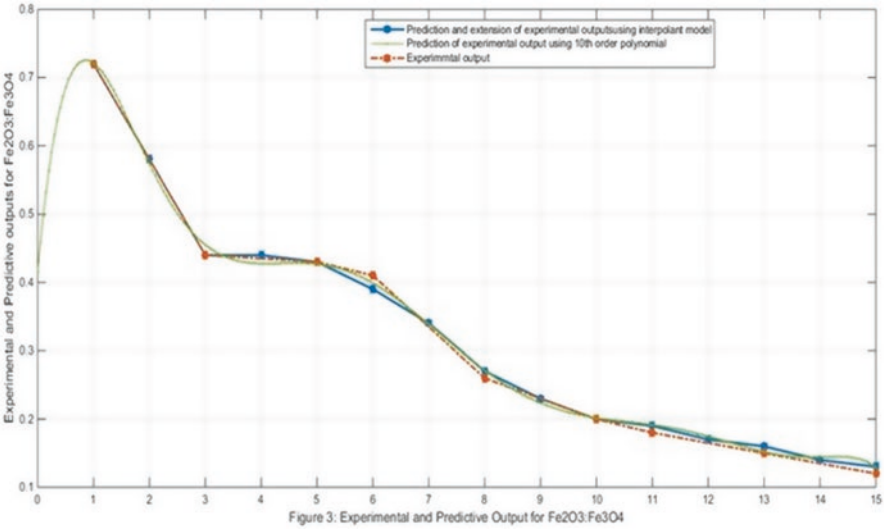

Fig. 4.3 Experimental and predictive output for Fe_2O_3:Fe_3O_4 [4]

while the actual experimental conditions from the DOE are represented using numeric serial order. Different experimental trends in a sequential order were identified from the same Table 4.7, which was used to develop a set of constraint models as presented in the following sub-section.

Categorizing Constraint Models for DS

According to Okanigbe et al. [3], the major governing variables used in ordering the constraint models into sub-groups are the rotational bowl speed (RBS), fluidized water flow rate (FWFR), and experimental outputs. Figures 4.4, 4.5, 4.6, and 4.7 are graphical representations of experimental outputs, whereas the steps taken to develop the interpolation model, prediction of output together with the discussion of observed trends, are reported in the work of [4].

4.3.1.3 Data Error Margin for OR

A root-mean-square error was computed for each point on the dataset generated from the constrained interpolant and polynomial curve fitting models. These were compared with the experimental outputs, and error computations carried out for all seven compounds investigated are the following: CuO, $CuSO_4$ and Fe_3O_4:Fe_2O_3 (OR); CuO, Fe_2O_3, SiO_2, and Al_2O_3 (DS).

Figure 4.8a, b, respectively, presents the plotted errors for the interpolant and polynomial models for CuO. Figure 4.8a presents a relatively consistent low error

Table 4.7 Experimental inputs and outputs of CuO, Fe_2O_3, SiO_2, and Al_2O_3 before and after density separated CSD [3]

	Chemical composition (feed)						Chemical composition (concentrate)							
	Experimental input						Experimental output				Predicted output			
S.N	CuO (wt%)	Fe_2O_3 (wt%)	SiO_2 (wt%)	Al_2O_3 (wt%)	RBS (G)	FWFR (l/min)	CuO (wt%)	Fe_2O_3 (wt%)	SiO_2 (wt%)	Al_2O_3 (wt%)	CuO (wt%)	Fe_2O_3 (wt%)	SiO_2 (wt%)	Al_2O_3 (wt%)
1	17.22	11.26	35.34	27.45	60	3.0	25.17	21.90	22.97	18.08	25.17	21.9	22.97	18.08
A	NE	NE	NE	NE	60	3.75	NE	NE	NE	NE	23.13	20.28	25.47	20.04
2	15.86	11.00	35.94	28.15	60	4.5	21.09	18.66	27.97	22.00	21.09	18.66	27.97	22.00
B	NE	NE	NE	NE	60	5.25	NE	NE	NE	NE	19.76	17.21	29.67	23.34
3	16.61	10.63	36.29	28.38	60	6.0	18.43	15.75	31.36	24.67	18.43	15.76	31.37	24.68
C	NE	NE	NE	NE	60	5.25	NE	NE	NE	NE	19.76	17.21	29.67	23.34
D	NE	NE	NE	NE	60	4.5	NE	NE	NE	NE	21.09	18.66	27.98	22.01
4	16.42	11.23	35.30	27.64	90	3.0	30.08	24.41	18.10	13.98	30.08	24.42	18.10	13.98
E	NE	NE	NE	NE	90	3.75	NE	NE	NE	NE	28.81	23.78	19.48	15.04
5	16.68	11.79	34.95	27.40	90	4.5	27.54	23.14	20.86	16.09	27.54	23.14	20.86	16.10
F	NE	NE	NE	NE	90	5.25	NE	NE	NE	NE	26.27	21.99	22.90	17.71
6	16.05	11.21	35.69	27.96	90	6.0	23.74	20.83	24.93	19.32	25	20.84	24.94	19.32
G	NE	NE	NE	NE	90	5.25	NE	NE	NE	NE	26.27	21.99	22.9	17.71
H	NE	NE	NE	NE	90	4.5	NE	NE	NE	NE	27.54	23.14	20.87	16.1
7	16.56	11.36	35.34	27.59	120	3.0	35.02	26.18	14.58	10.29	35.02	26.18	14.58	10.29
I	NE	NE	NE	NE	120	3.75	NE	NE	NE	NE	32.07	25.13	16.92	12.55
8	16.50	11.49	34.74	27.63	120	4.5	29.12	24.08	19.25	14.81	29.12	24.08	19.26	14.81
J	NE	NE	NE	NE	120	5.25	NE	NE	NE	NE	26.58	22.79	21.70	16.87
9	15.99	11.03	35.85	28.04	120	6.0	24.03	21.49	24.14	18.93	24.04	21.5	24.14	18.93

Key: *RBS* rotational bowl speed, *WFR* water flow rate, *FR* flow rate = 1.48 (l/min) (constant), *LSR* liquid-to-solid ratio = 0.5 (constant), *NE* no experiment was performed in the affected rows; hence, they were included for better predictive modelling intervals

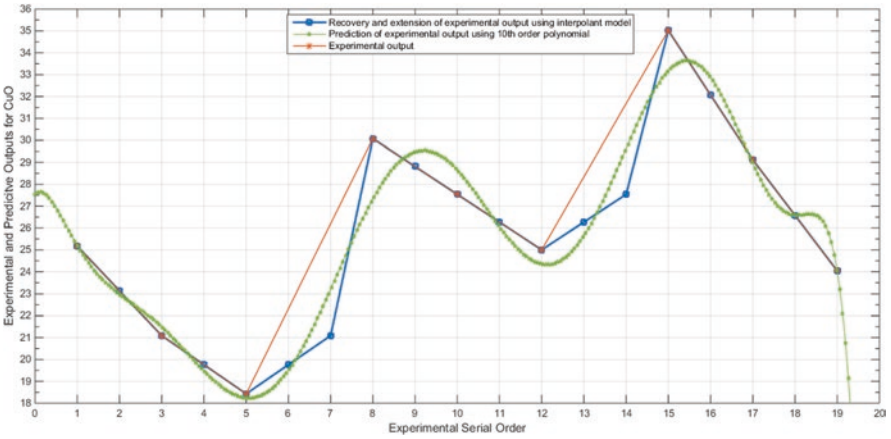

Fig. 4.4 Experimental and predictive output for CuO [3]

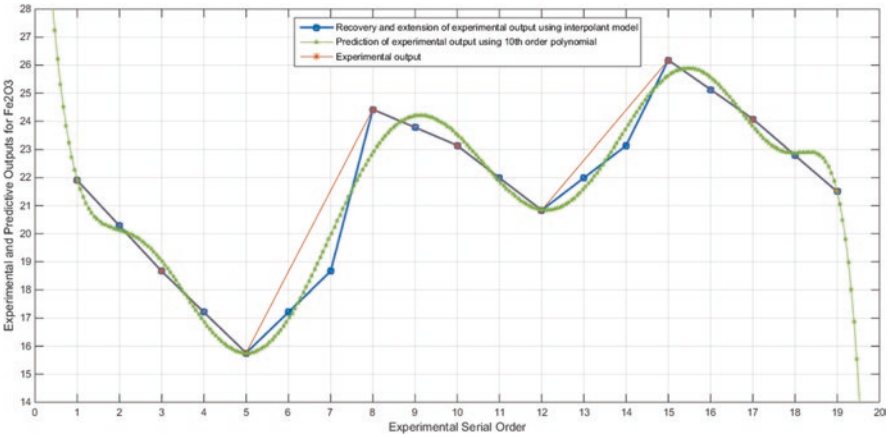

Fig. 4.5 Experimental and predictive output for Fe_2O_3 [3]

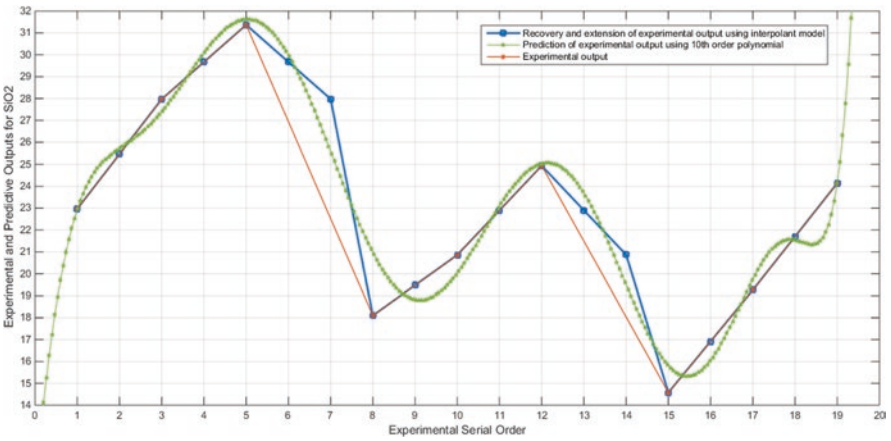

Fig. 4.6 Experimental and predictive output for SiO_2 [3]

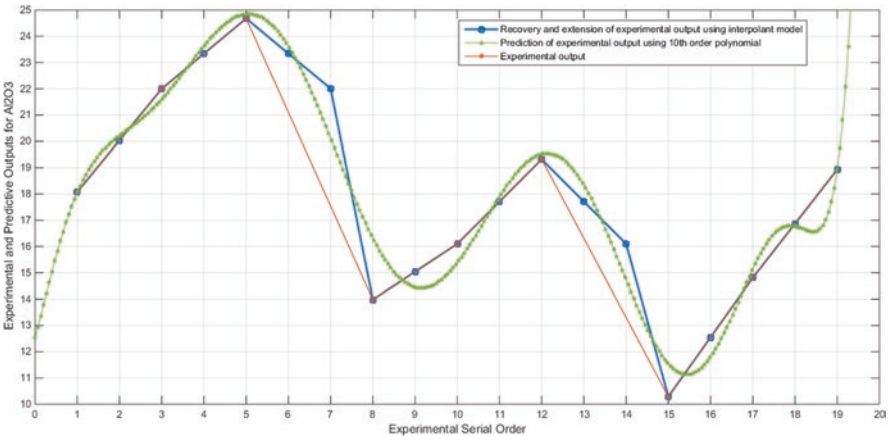

Fig. 4.7 Experimental and predictive output for Al_2O_3 [3]

margin in comparison with Fig. 4.8b except at the tenth serial number of the experimental sequence. This is an indication of the high effectiveness of the interpolant model over the polynomial curve fitting model.

The error graph plotted from the datasets generated by the interpolant and polynomial predictive models relative to the experimental dataset is as presented in Fig. 4.9a, b, respectively. Figure 4.9a presents a relatively consistently low error margin in comparison with Fig. 4.9b except at the fifth serial number of the experimental sequence.

The error margin for the iron compounds Fe_3O_4:Fe_2O_3 is presented in Fig. 4.10a, b, respectively. They showed the plotted errors for the interpolant and polynomial models. Unlike in the earlier scenarios as observed with CuO and $CuSO_4$, Fig. 4.10a, b presents seemingly equal error distribution margins.

Figure 4.11a, b, respectively, presents the plotted errors for the interpolant and polynomial models for CuO under DS pretreated WCD. Figure 4.11a presents a relatively consistent low error margin in comparison with Fig. 4.11b except at the 12th serial number of the experimental sequence. This is an indication of the high effectiveness of the interpolant model over the polynomial curve fitting model.

The Fe_2O_3 error graph plotted from the datasets generated by the interpolant and polynomial predictive models relative to the experimental dataset for DS pretreated WCD are presented in Fig. 4.12a, b, respectively. Figure 4.12a presents a relatively consistently low error margin in comparison with Fig. 4.12b except at the fifth serial number of the experimental sequence.

The SiO_2 error margin for DS pretreated WCD is presented in Fig. 4.13a, b, respectively, and the graphs show the plotted errors for the interpolant and polynomial models. Unlike in the previous scenarios as observed with CuO and Fe_2O_3, Fig. 4.13a, b presents significantly dissimilar error distribution margins. While Fig. 4.13a presents a relatively consistent low error margin in comparison with

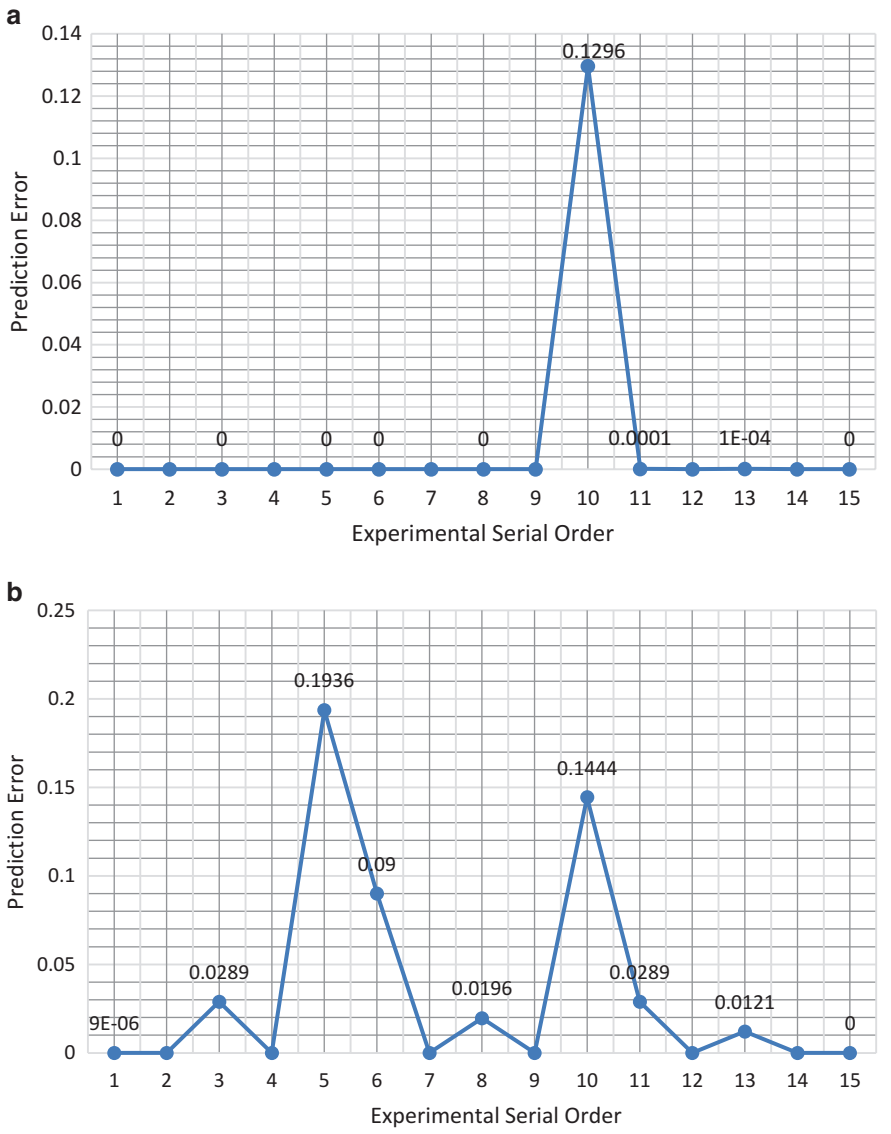

Fig. 4.8 (**a**) Interpolant model and experimental data error margin (CuO) for OR. (**b**) Polynomial curve fitting and experimental data error margin (CuO) for OR

Fig. 4.11b except at the 5th, 12th, 17th serial number of the experimental sequence, Fig. 4.13b presents dissimilar error margins with the highest error margin at eighth serial number of the experimental sequence. This is also an indication of the high effectiveness of the interpolant model over the polynomial curve fitting model.

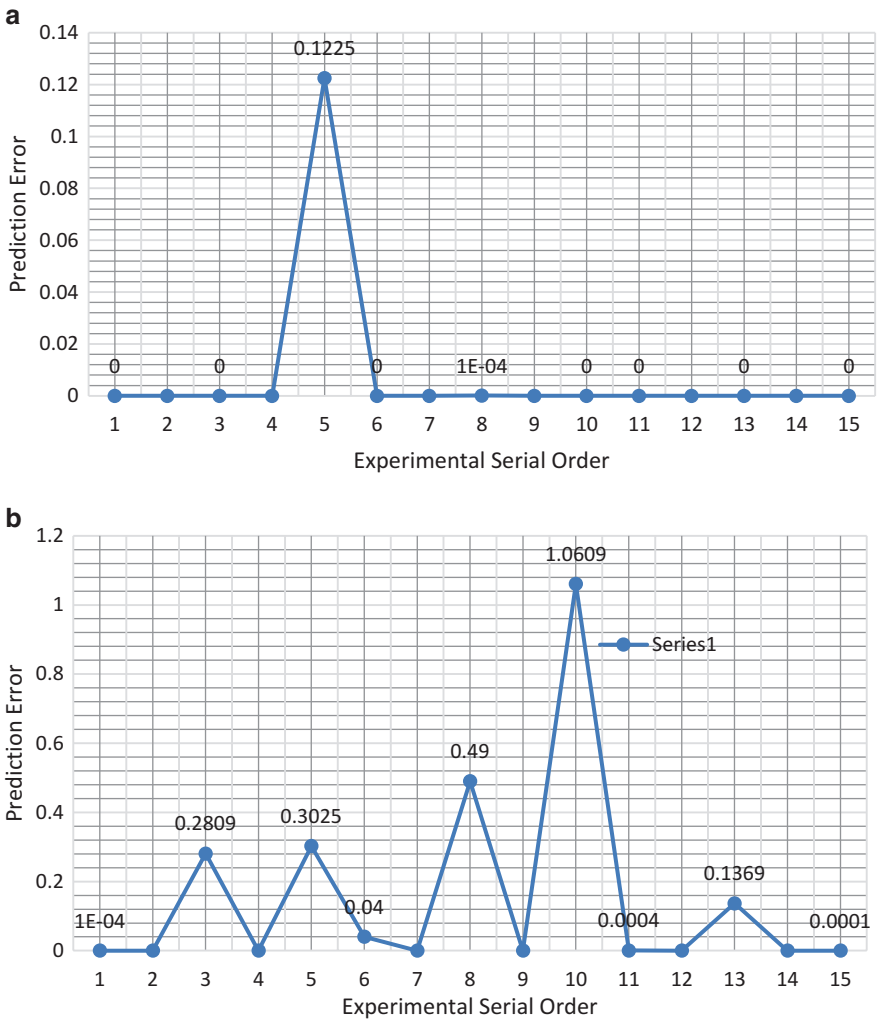

Fig. 4.9 (**a**) Interpolant model and experimental data error margin ($CuSO_4$) for OR. (**b**) Polynomial curve fitting and experimental data error margin ($CuSO_4$) for OR

The Al_2O_3 error margin for DS pretreated CSD is presented in Fig. 4.14a, b, respectively, while showing the plotted errors for the interpolant and polynomial models. Consistent with previous observations like FeO scenario, Fig. 4.14a presents a relatively consistently low error margin in comparison with Fig. 4.14b except at the fifth and tenth serial number of the experimental sequence.

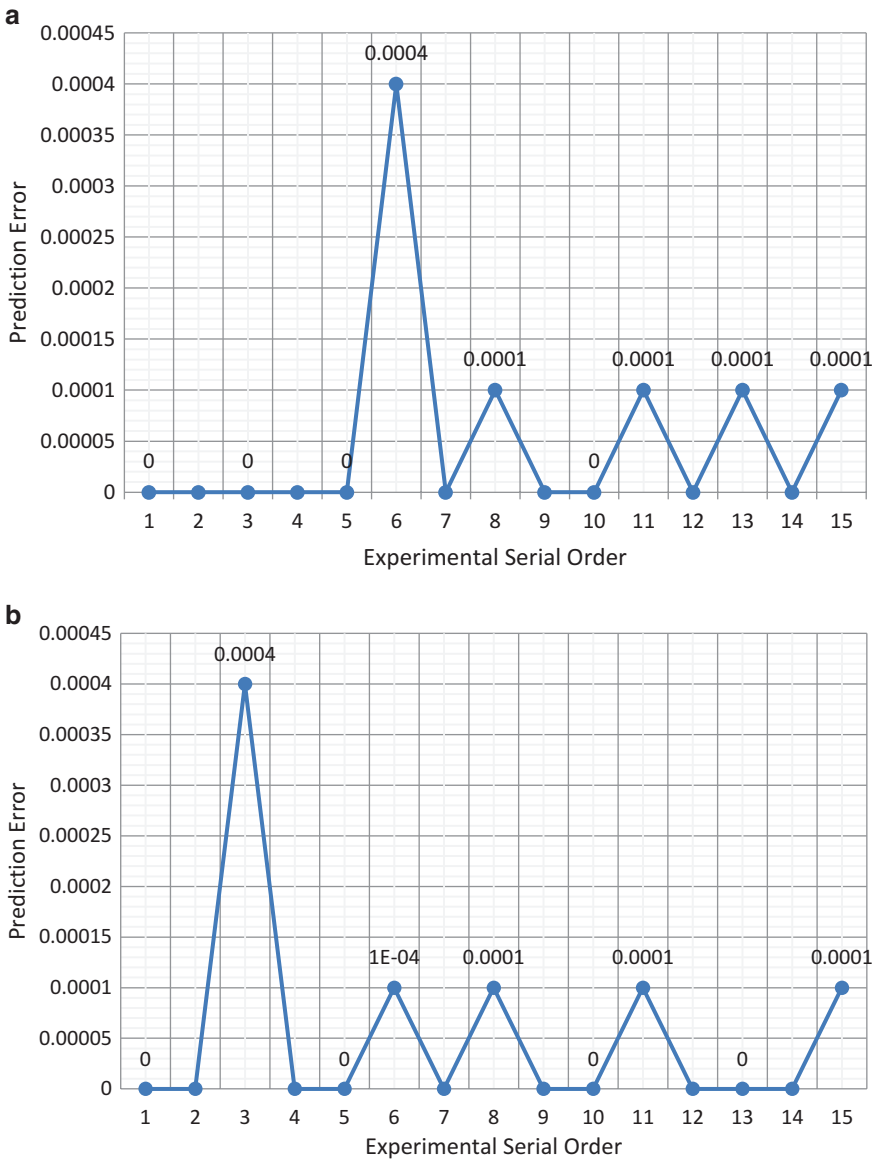

Fig. 4.10 (**a**) Interpolant model and experimental data error margin (Fe_3O_4:Fe_2O_3) for OR. (**b**) Polynomial curve fitting and experimental data error margin (Fe_3O_4:Fe_2O_3) for OR

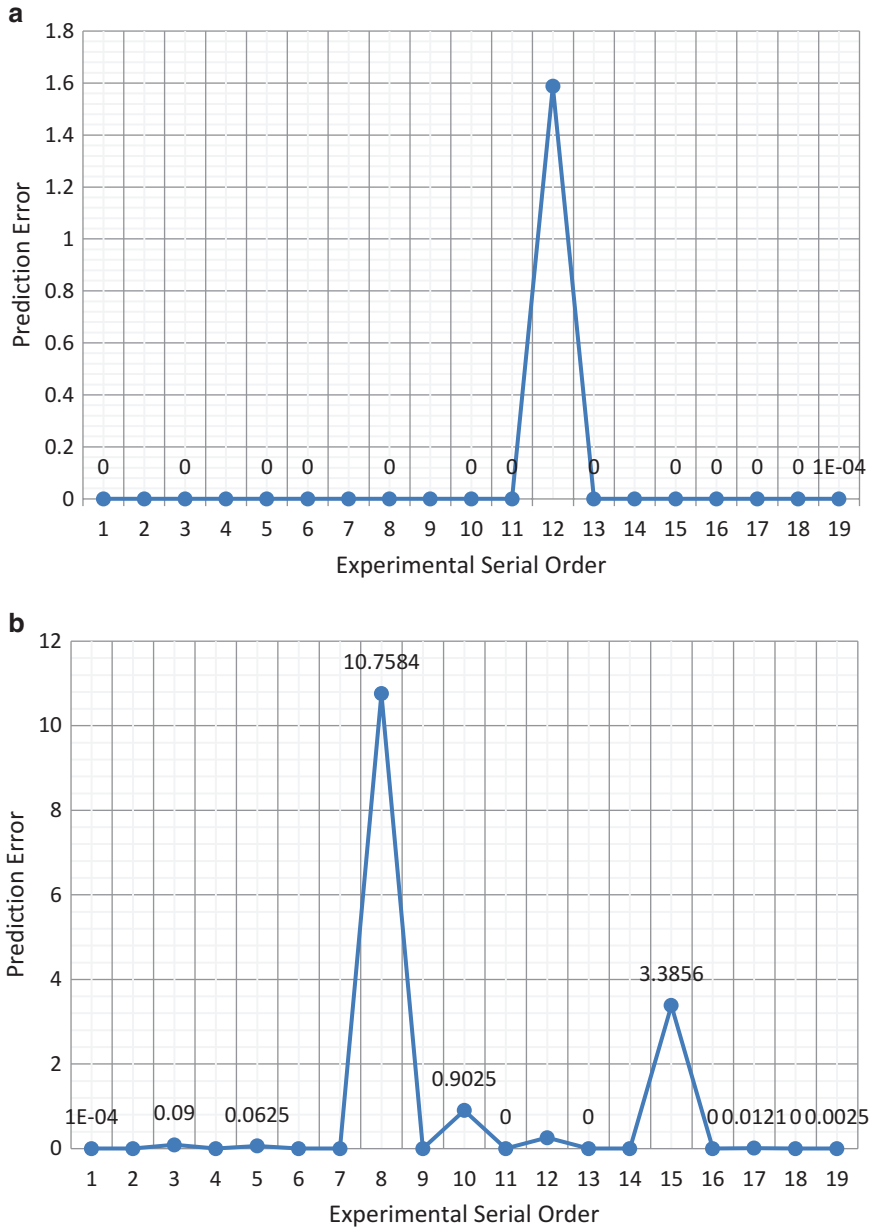

Fig. 4.11 (**a**) Interpolant model and experimental data error margin (CuO) for DS. (**b**) Polynomial curve fitting and experimental data error margin (CuO) for DS

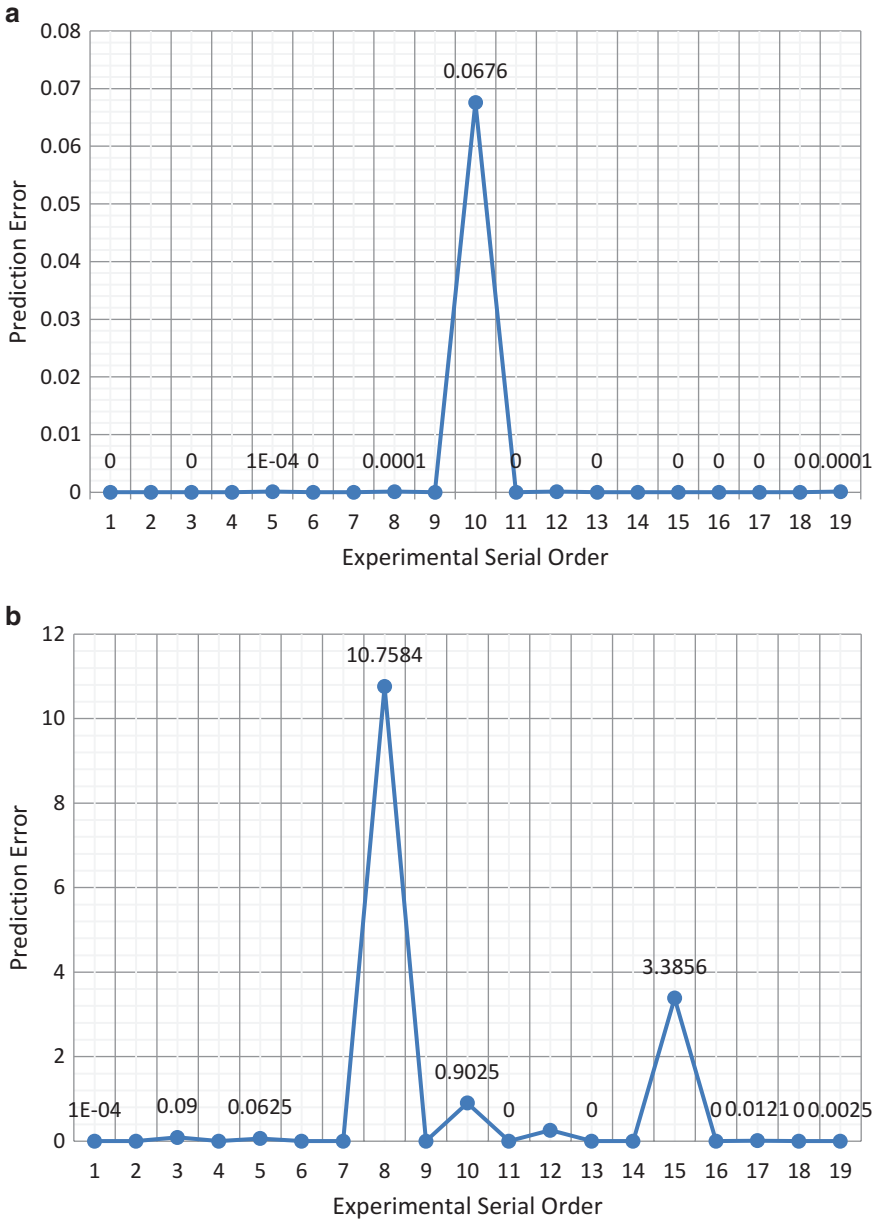

Fig. 4.12 (**a**) Interpolant model and experimental data error margin (Fe_2O_3) for DS. (**b**) Polynomial curve fitting and experimental data error margin (Fe_2O_3) for DS

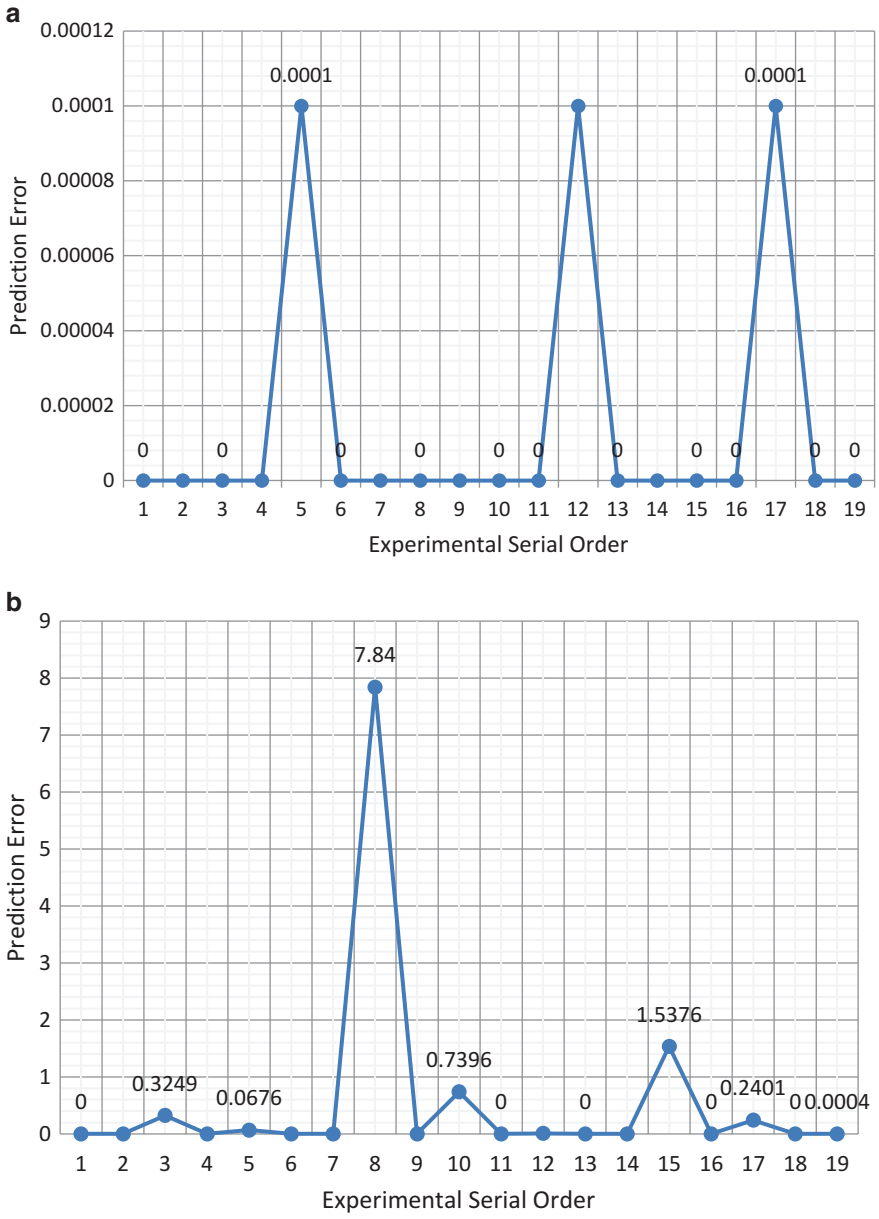

Fig. 4.13 (**a**) Interpolant model and experimental data error margin (SiO_2) for DS. (**b**) Polynomial curve fitting and experimental data error margin (SiO_2) for DS

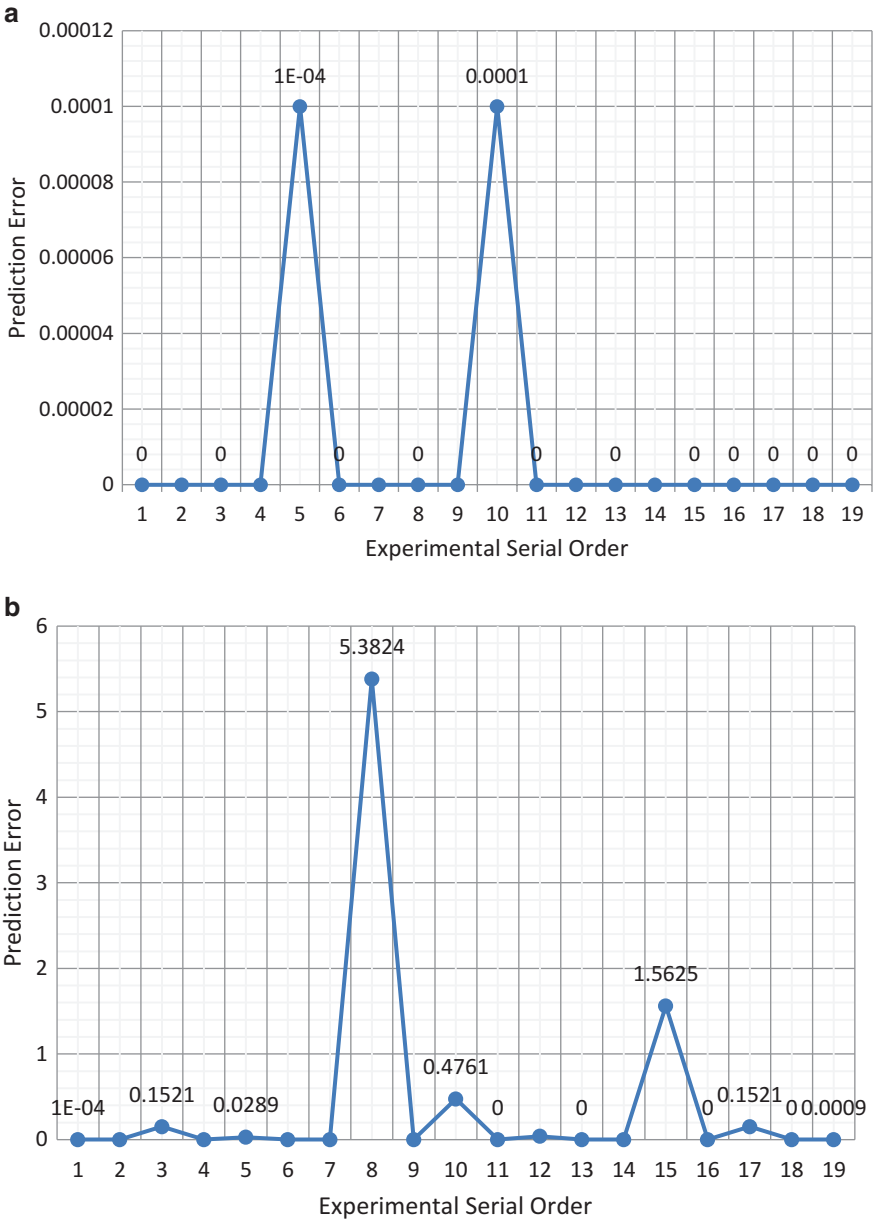

Fig. 4.14 (**a**) Interpolant model and experimental data error margin (Al_2O_3) for DS. (**b**) Polynomial curve fitting and experimental data error margin (Al_2O_3) for DS

4.4 Conclusions

The aim of this paper was to development of an optimum predictive model for pretreatment of a WCD. The deductions reached as a result of this study are as follows:

1. Time is the most influential factor than temperature, time-temperature during OR of WCD; additionally, an optimum time of 2 h is established as the time required for production of high-yield roast products [4].
2. The error margins obtained OR pretreated WCD process were between 0.00% and 0.07%. Based on the predictive model, further outputs can be generated prior to conducting laboratory experiments. Hence, the derived models can be further used to track experimental deviations from desired plans.
3. During the density separation of WCD, it was observed that both variables considered, i.e. FWFR and RBS had major influence on the experimentation process of the concentrates from the centrifugal concentrator.
4. The predicted values obtained using the models were in good agreement with the observed values with an error margin between 0.00% and 0.06%.

It can therefore be concluded that constraint interpolant model predicted both the known and unknown experimental outputs for oxidative roasting and density separation of WCD. Therefore, it can be recommended that this method be adopted, so as to predict outputs for un-experimented conditions beyond initial DOE. Hence, providing an authentication basis to predict the outputs of "intended experimental trials" before they are carried out or the provision of estimated output results in a situation where further experiments cannot be carried out due to fatigue, breakdown of facilities or extreme conditions of input parameters amongst others is quite relevant to this research.

Acknowledgements The authors would like to thank the following institutions for allowing access to their facilities:

1. Tshwane University of Technology (TUT), Pretoria, Republic of South Africa,
2. Vaal University of Technology (VUT), Vanderbijlpark, Republic of South Africa,
3. Gravity concentrator Africa (GCA), Johannesburg, Republic of South Africa.

References

1. L. Cao, Y. Wang, Q. Liu, X. Feng, Physical and mathematical modeling of multiphase flows in a converter. Isij Int., ISIJINT-2017, 1–12 (2018). https://doi.org/10.2355/isijinternational.ISIJINT-2017-680
2. J. Szekely, The mathematical modeling revolution in extractive metallurgy. Metall. Trans. B **19**(4), 525–540 (1988)
3. D. Okanigbe, P. Olawale, A. Popoola, A. Abraham, A. Michael, K. Andrei, Centrifugal separation experimentation and optimum predictive model development for copper recovery from waste copper smelter dust. Cogent Eng. **5**(1), 1551175 (2018)

4. D.O. Okanigbe, M.K. Ayomoh, O.M. Popoola, P.A. Popoola, V.S. Aigbodion, Oxidative roasting experimentation and optimum predictive model development for copper and iron recovery from a copper smelter dust. Results Eng. **7**, 100125 (2020)
5. G. Akar Sen, Application of full factorial experimental design and response surface methodology for chromite beneficiation by Knelson concentrator. Fortschr. Mineral. **6**(1), 5 (2016)
6. N. Aslan, Application of response surface methodology and central composite rotatable design for modeling and optimization of a multi-gravity separator for chromite concentration. Powder Technol. **185**(1), 80–86 (2008)
7. Z. Xiao, A. Vien, Experimental designs for precise parameter estimation for non-linear models. Miner. Eng. **17**(3), 431–436 (2004)

Part III
Extraction of Copper Oxide

Chapter 5
Extraction of Copper Oxide (I): Purified $CuSO_4$ Solution

Zenzele Magwanyana, Daniel Ogochukwu Okanigbe, Abimbola Patricia Popoola, and Abraham Adewale Adeleke

5.1 Introduction

Heating and melting are frequently used to extract copper (Cu) from its parent ores [1–4]. Roasting, smelting, and conversion are the three phases of the heating and melting process for primary copper ores [5–11]. Significant amounts of copper are lost as dust in the first and second phases; this dust is referred to as waste copper dust (WCD). According to the research done by Gorai, Jana, and Khan [12], for every 1000 tons of Cu concentrate treated, over 70–100 tons are lost as WCD.

According to reports on the mineralogy of WCD by Balladares et al. [13], Wang et al. [14], Jaroková et al. [15], and Okanigbe et al. [16], the considerable Cu content of WCD was deduced by Gorai et al. [12]. Additionally, according to these mineralogical investigations, WCD is a complex low-grade copper ore in which the copper content frequently occurs in conjunction with other metals including iron (Fe), zinc (Zn), lead (Pb), silicon (Si), aluminum (Al), and others. Lacking a reliable waste management method, disposing of WCD in landfills defies the purpose of protecting the planet's mineral resources [17].

Z. Magwanyana · A. P. Popoola
Department of Chemical, Metallurgical and Materials Engineering, Faculty of Engineering and the Built Environment, Tshwane University of Technology, Pretoria, South Africa

D. O. Okanigbe (✉)
Department of Chemical, Metallurgical and Materials Engineering, Faculty of Engineering and the Built Environment, Tshwane University of Technology, Pretoria, South Africa

Pantheon Virtual Engineering Solutions, Nigel, South Africa
e-mail: okanigbedo@tut.ac.za; okanigbeogochukwu@gmail.com

A. A. Adeleke
Department of Materials Science and Engineering, Faculty of Technology, Obafemi Awolowo University, Ile-ife, Osun state, Nigeria

D. O. Okanigbe, A. P. Popoola (eds.), *Resource Recovery and Recycling from Waste Metal Dust*, https://doi.org/10.1007/978-3-031-22492-8_5

According to Morales et al. [18], a hydrometallurgical process that operates at room temperature, atmospheric pressure, dilute reagent, few unit operations, and low energy cost should be the best waste management technique for the treatment of WCD. However, using hydrometallurgy alone presents difficulties due to an extremely small pH window, leading to the following:

1. Side reactions by contaminants that reduce leaching efficiency.
2. Contaminants co-exist in pregnant leach solution.
3. High chances of contaminants carry over to the extraction stage.
4. Increase in the number of cycles required to achieve 99.9% pure copper electrolyte.
5. Increase in the cost of recovery.
6. Increase in the use of toxic extractants deleterious to the environment.

Three steps make up hydrometallurgy: leaching, solvent extraction, and electrowinning. Sulfuric acid (H_2SO_4) is frequently utilized as the leaching agent during the leaching stage. In comparison to hydrochloric and nitric acid, Teir et al. [19] and Habashi [20] indicated that (H_2SO_4) is the most effective and often used acid for leaching oxides. H_2SO_4 is a low-cost leachant that is also frequently used to treat metallurgical wastes that contain copper [21]. The choice of H_2SO_4 as reagent for the hydrometallurgical treatment of WCD is established by its usage as a reagent for the conversion step, i.e., electrolysis to create copper cathode [22].

The inability of H_2SO_4 to prevent iron from dissolving from copper ore, however, poses a selectivity difficulty that reduces the likelihood of achieving pure Cu electrolyte at a low cost. As a result, the PLS's solvent extraction (SX) stage was added to decrease and eliminate iron [23, 24].

Emulsification problems exist for SX because they lead to extractant loss and electrolyte contamination. Additionally, iron impurity induces entrainment and crud development in the SX process, according to Chen et al. [25]. In addition, SX is extremely sensitive to low temperatures and low-grade solutions. Expensive organic reagents that are hazardous to the environment further complicate the process. Because iron is involved in a parasitic reaction that causes electricity to be diverted from plating of copper as it is oxidized from ferrous to ferric at the anode and reduced from ferric to ferrous at the cathode, a high concentration of iron in SX-treated PLS affects current efficiency during electrowinning [26].

Even though the dosage of H_2SO_4 is frequently the key economic component in the process of leaching copper in its oxide form from this ore, copper oxide ore dissolves in H_2SO_4 solution at room temperature. Researchers have also identified other factors, such as acid content, leaching period, temperature, pulp stirring, solid-to-solution ratio, etc., that can affect leach rates during recovery [27, 28]. Pulp stirring has been shown as a crucial process parameter for efficient leaching, according to Ghosh and Ray [29].

The results of comparing digital hotplate leaching with oven leaching will be presented in this chapter first, based on the discussion that has led up to this point. Second, it will be discussed how altering the compositional proportion of H_2SO_4: $FeSO_4.7H_2O$ can prevent iron from dissolving into pregnant leach solution (PLS).

5.2 Materials and Methods

5.2.1 Material

The study's primary source of material is the WCD from South Africa.

5.2.2 Methods

5.2.2.1 Sampling Using Rotary Splitter

Since it creates the least variance between samples and can produce a greater number of samples in one operation, the rotary splitter was employed to separate WCD into representative samples. A vibratory feeder was fed 4000 g of the WCD from a feed hopper (Fig. 5.1). As depicted in Fig. 5.1, the feeder evenly disperses the material into a succession of collectors on a spinning table.

Before the feed hopper is empty, the turntable speed was adjusted so that each sample collector would pass several times beneath the feeder. The revolving speed was made slow enough to prevent the edge of the sample collectors from touching the falling particles, which would cause them to leap into a different container or fling them out of the machine entirely. This was done in order to obtain consistent and dependable findings. To attain a WCD mass of 250 g in each sample collector, the speed was optimized, and the rotation switch was set at 17 rpm.

5.2.2.2 Sampling Using the Coning and Quartering Method

WCD was first poured over a level surface until it assumed a cone-like shape. The coned WCD was then flattened into a cake and cut into four equal pieces (A, B, C, and D), as shown in Fig. 5.2. The two pieces that are directly across from one

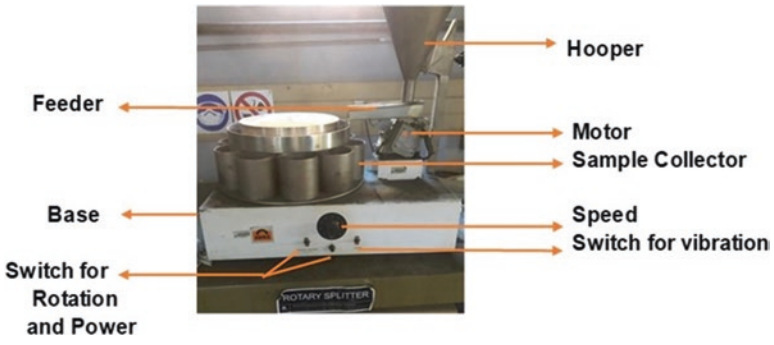

Fig. 5.1 Rotary splitter sampling

Fig. 5.2 WCD coning and quartering sampling

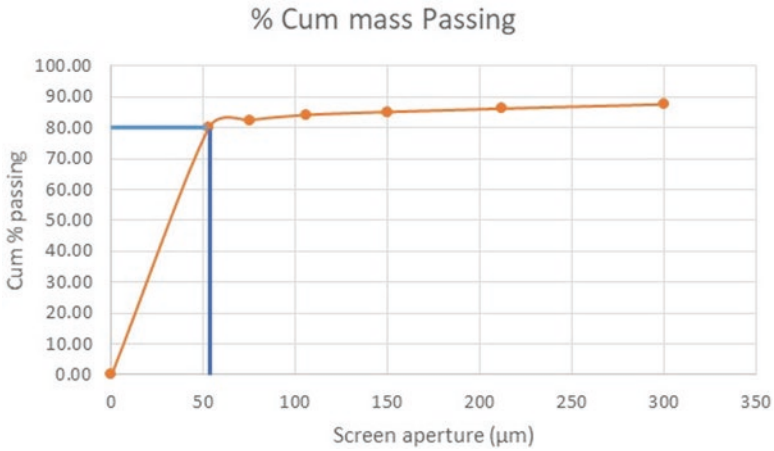

Fig. 5.3 Graphical representation of WCD's PSD

another are removed, for example, A and C (Fig. 5.2), while the remaining two (B and D) are joined to create the reduced sample. The same procedure was carried out four times until a suitable sample size of 4 g of 60 WCD remained.

These aliquot WCD samples of 4 g each were used for subsequent test works like characterization and leaching exercises.

5.2.2.3 Particle Size Distribution (PSD) of As-Received WCD

Following screening tests on the WCD sample, Fig. 5.3 displays the intended 80% mass passage of WCD at a −53 m screen size aperture.

5.2.2.4 Calculations for Preparing Sulfuric Acid Solution

The calculations were made using the following concentrations of 2 M, 4 M, 6 M, 8 M, and 10 M:

Molarity (M) = mol/L
Density (D) = 1.84 g/mL
Molar mass (MM) = 98.079 g/mol

For 2 M sulfuric solution Molarity was calculated using Eq. (5.1)

$$\begin{aligned} M &= D \times MM \\ &= \frac{1.84\text{g}}{\text{mL}} \times \frac{1000\text{mL}}{1\text{L}} \times \frac{1\text{mol}}{98.1\text{g}} \\ &= \frac{(1.84 \times 1000)\text{mol}}{98.1\text{L}} \\ &= \frac{1840\text{mol}}{98.1\text{L}} \\ &= 18.75\text{mol/L} \end{aligned} \tag{5.1}$$

We shall start with 2.5 L of roughly 18.8 M H_2SO_4 in this experiment to recover copper from the WCD; hence, the amount of water needed to make the 2 M diluted H_2SO_4 acid solution will be determined from the dilution factor in Eq. (5.2) as follows:

$$\begin{aligned} M1V1 &= M2V2 \\ 18.8\text{M} \times 2.5\text{L} &= 2\text{M} \times V2 \\ V2 &= \frac{18.8\text{M} \times 2.5\text{L}}{2\text{M}} \\ V2 &= \frac{47\text{L}}{2} \end{aligned} \tag{5.2}$$

This assumes that in order to prepare the 2 M diluted H_2SO_4 acid solution, we require 23.5 times as much water as 18.8 M. Therefore, we would apply the algebraic expression given below (Eq. 5.3) to generate a 40 mL, 2 M diluted H_2SO_4 solution:

$$x + 23.5x = 40\,\text{mL} \tag{5.3}$$

where $23.5x$ = volume of water.

From Eq. (5.3)

$$\begin{aligned} 24.5x &= 40\text{mL} \\ x &= 1.63\text{mL} \end{aligned}$$

As a result, 1.63 mL of concentrated acid is needed, whereas 40 mL of water is needed to dilute it.

$$\begin{aligned} &= 1.63 \times 23.5 \\ &= 38.37\text{mL} \end{aligned}$$

Total volume according to Eq. (5.3)

$$1.63 + 38.37 = 40\text{mL}.$$

These calculations were repeated for 4 M, 6 M, 8 M, and 10 M.

5.2.2.5 Leaching Parameters

The experiment was conducted under certain circumstances, with the following points being stressed:

- The temperature was kept constant at 45 °C.
- The leaching ratio of 1:10.
- Time: 30, 60, and 90 minutes.
- Speed: 300 Rev/min.

5.2.2.6 Experimental Procedures for Sulfuric Acid Leaching

The subsequent experimental procedures were broken down into two parts. The leaching of WCD from ovens is one topic, while the leaching of WCD from hotplates is another. The following steps are detailed.

Experimental Procedure for Leaching of WCD Using Hotplate with Stirrer

1. Fill a 250 mL conical flask with 4 g of WCD.
2. Prepare a 2 M diluted H_2SO_4 acid solution by adding 1.63 mL of H_2SO_4 acid to a beaker using a pipette.
3. Fill the beaker with concentrated H_2SO_4 acid solution with 38.37 mL of pure water (i.e., 2 M dilute H_2SO_4 solution).
4. Place a stirring bar inside the conical flask containing the 4 g of WCD and this 2 M diluted H_2SO_4 solution.
5. Place a piece of aluminum foil over the opening of the conical flask containing the acid and WCD.
6. Repeat steps 1, 2, 3, and 4 in reverse order.
7. Place the two conical flasks holding acid and WCD that have been coated in aluminum foil on the magnetic stirrer that has a heater set to 45 °C and an agitation speed of 340 rpm.
8. Wait 30 minutes after using the conical flask and its contents.
9. Repeat steps 1 through 7 for 30, 60, and 90 minutes.
10. After these leaching periods, take the conical flask and its contents out of the oven.
11. Use filter paper to separate the leach solution from the waste.

12. Fill a sample with the leach solution, and then label it for quick identification.
13. Keep the contents of the sample bottle at room temperature.

These steps were repeated for 4 M, 6 M, 8 M, and 10 M.

Experimental Procedures for Leaching of WCD Using a Laboratory Oven

1. Fill a 250 mL conical flask with 4 g of WCD.
2. Prepare a 2 M diluted sulfuric acid solution by adding 1.63 mL of sulfuric acid to a beaker using a pipette.
3. Fill the beaker with concentrated H_2SO_4 acid solution with 38.37 mL of pure water (i.e., 2 M dilute H_2SO_4 solution).
4. Fill the conical flask containing the 4 g WCD with this 2 M diluted H_2SO_4 solution.
5. Place a piece of aluminum foil over the opening of the conical flask containing the acid and WCD.
6. Repeat steps 1, 2, 3, 4, and 5 twice.
7. Preheat the oven to 45 °C, and place the two aluminum-foil-covered conical flasks containing acid and WCD inside.
8. Wait 30 minutes after using the conical flask and its contents.
9. Repeat Steps 1 through 7 for 30, 60, and 90 minutes.
10. After these leaching durations, remove the conical flask and its contents from the oven.
11. Using filter paper, separate the leach solution from the waste.
12. Fill a sample container with the leach solution, and then label it for quick identification.
13. Keep the contents of the sample bottle at room temperature.

These steps were for 4 M, 6 M, 8 M, and 10 M.

5.2.2.7 Sample Filtration

In this investigation, gravity-driven filtration was used. As seen in Fig. 5.4, the PLS was allowed to fall through gravity from the cylinder into the conical flask.

5.2.2.8 Proposed Process Flow Diagram

An outline of the hydrometallurgical group projects at Tshwane University of Technology in Pretoria, South Africa, can be found in Fig. 5.5. The topic of this study is sulfuric acid leaching, with red arrows indicating the process flow (Fig. 5.5).

Fig. 5.4 Gravity-driven filtration process of copper recovery from WCD

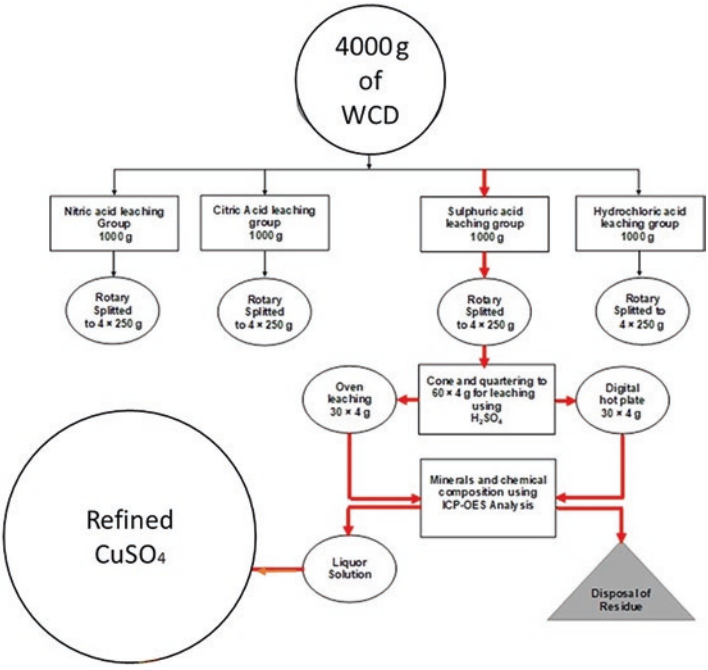

Fig. 5.5 Initial process flowsheet for Cu leaching from WCD

5.3 Results and Discussion

The recovery method for the copper value that was present in WCD was determined by its distinctive characteristics [16]. Consequently, hydrometallurgy was selected as an acceptable technique for its treatment. This investigation is restricted to the hydrometallurgical dissolution of copper from the WCD. The experiment will

contrast agitation leaching with oven leaching techniques. This report offers commentary on accomplishments accomplished during the B-Tech period, with a particular emphasis on project test work carried out at Tshwane University of Technology in Pretoria, South Africa. The findings and discussion related to the following sub-heading are reported in this chapter:

1. Visual observation of as-received WCD
2. Visual observation of residue after leaching
3. Visual analysis of digital hotplate leachate
4. Visual analysis of oven leachate
5. Results on mass balance

5.3.1 Visual Observation of As-Received WCD

Before the test work was done, the WCD by-product sample was scrutinized. As seen in Fig. 5.6, the WCD was discovered to be a dark gray color. According to the WCD by-product XRF data, the ore mostly comprises copper, iron, and gypsum as impurities, along with other minerals. These metals and the impurities significantly influenced the ore's color. The sample felt generally powdery; however, the feel was uneven and parts of the particle were not very fine, as shown in Fig. 5.6. The head assay examination for the WCD as received reveals that the ore contains very fine particle, mostly in the -53 μm size fraction.

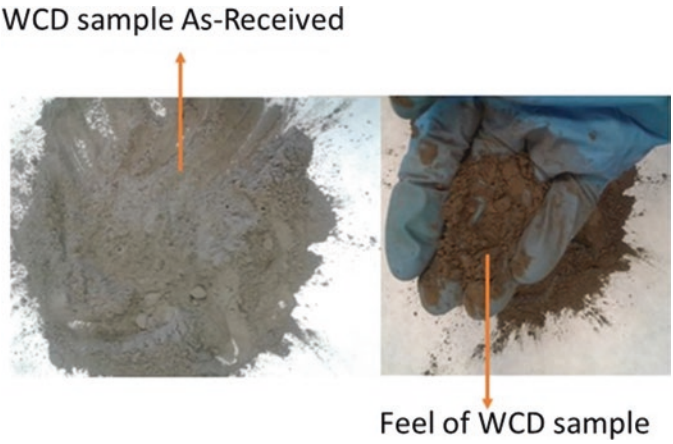

Fig. 5.6 Visual analysis for CSD by-product as received

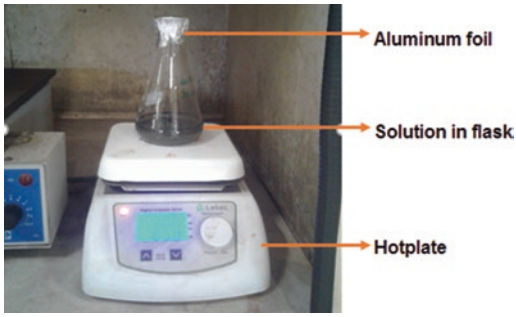

Fig. 5.7 Digital hotplate leaching process

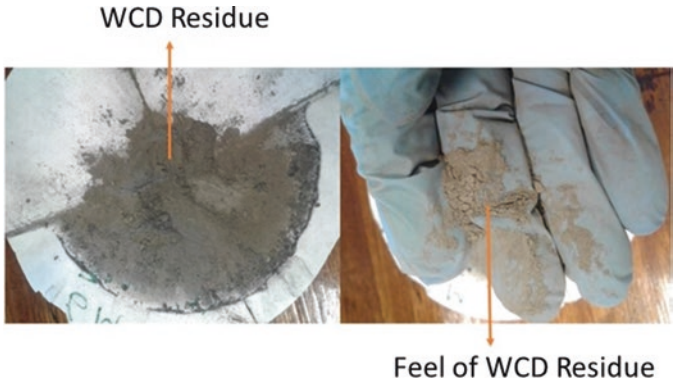

Fig. 5.8 Visual analysis of residue after leaching process

5.3.2 Digital Hotplate Leaching Process of WCD

The leaching process utilizing a digital hotplate is shown in Fig. 5.7. The leaching process may be impacted by the black mineral in the solution that was seen to be separating from and sticking to the conical flask above the solution.

5.3.3 Visual Analysis of Residue After Leaching Process

Following the leaching procedure, the solution was filtered to remove the solid particles from the liquid, and the leftovers were dried. The observation was successfully performed. The WCD residue had a more uniform texture and felt more powdery as depicted in Fig. 5.8. The light gray color of the WCD residue indicates that the majority of the metals responsible for the dark color of the WCD as received have been taken into the leach solution.

5.3.4 Visual Analysis Digital Hotplate Leachate

The difference in leachate color after the filtration process was clearly seen on digital hotplate leachate, as illustrated in Fig. 5.9. The solution was seen to be a dark blue color. Clearly, the majority of the copper metal was taken.

5.3.5 Visual Analysis on Oven Leachate

In addition, oven leachate was observed, as can be shown in the following Fig. 5.10. The leachate's pale blue color is evident in the results. The results almost certainly point to a sizeable number of copper metals that are still trapped in gangue particles.

5.3.6 Results on Mass Balance: Digital Hotplate

The comprehensive test work for digital hotplate leaching is detailed as follows.

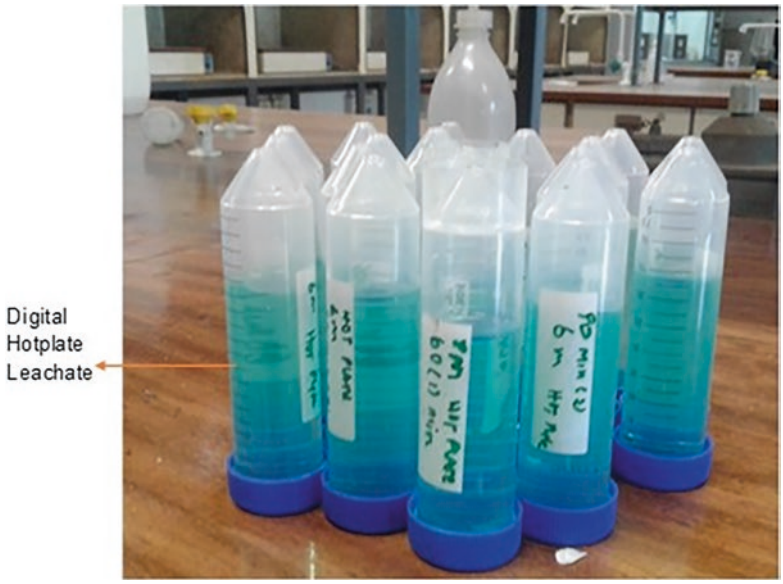

Fig. 5.9 Leachate from hotplate leaching

Fig. 5.10 Leachate from oven leaching

Table 5.1 Test 1 hotplate leaching results for 2 M H_2SO_4

Test no.	Time (minutes)	Initial mass (g)	Volume of H_2SO_4 (mL)	Mass of residue (g)	Volume of deionized water (mL)
1	30	4.0140	1.6347	3.0590	38.3700
	60	4.0230	1.6329	2.7890	
	90	4.0330	1.6317	2.9305	
Total		12.0700		8.7785	

5.3.6.1 Test 1 Hotplate Leaching Results for 2 M H_2SO_4

According to the data in Table 5.1, leaching that took place in 60 minutes produced the least amount of residue when compared to leaching that took place in 30 and 90 minutes, whereas leaching that took place in 30 minutes produced the most mass. The total mass percentage of residues was 73%.

5.3.6.2 Test 2 Hotplate Leaching Results for 2 M H_2SO_4

According to the data in Table 5.2, leaching that was completed in 60 minutes produced the least amount of residue when compared to when the solution was leached for 30 and 90 minutes, while leaching that was completed in 90 minutes produced the most mass.

Overall, a mass percentage of 90% residue was obtained.

Table 5.2 Test 2 hotplate leaching results for 2 M H_2SO_4

Test no.	Time (minutes)	Initial mass (g)	Volume of H_2SO_4 (mL)	Mass of residue (g)	Volume of deionized water (mL)
2	30	4.0080	1.6332	3.5279	38.3700
	60	4.0090	1.6320	3.4492	
	90	4.0010	1.6330	3.8754	
Total		12.0180		10.853	

Table 5.3 Test 1 hotplate leaching results for 4 M H_2SO_4

Test no.	Time (minutes)	Initial mass (g)	Volume of H_2SO_4 (mL)	Mass of residue (g)	Volume of deionized water (mL)
1	30	4.0100	3.1380	3.5600	36.8700
	60	4.0800	3.1400	3.7900	
	90	4.0600	3.1390	3.4500	
Total		12.1500		10.8000	

5.3.6.3 Test 1 Hotplate Leaching Results for 4 M H_2SO_4

According to the findings in Table 5.3, the leaching process that was carried out in 90 minutes produced the least quantity of residue as compared to when the solution was leached for 30 and 90 minutes. In comparison to 90 and 30 minutes, the leaching operation carried out in 60 minutes produced the highest mass. After leaching, residue was collected in an overall mass percentage of 89%.

5.3.6.4 Test 2 Hotplate Leaching Results for 4 M H_2SO_4

Compared to when the solution was leached for 30 and 90 minutes, the results in Table 5.4 demonstrate that the leaching process done in 30 minutes obtained the least quantity of residue after leaching. In comparison to 60 and 30 minutes, the leaching operation carried out in 90 minutes produced the highest mass. After leaching, residual mass percentage reached 90% overall.

5.3.6.5 Test 1 Hotplate Leaching Results for 6 M H_2SO_4

Compared to when the solution was leached for 30 and 60 minutes, the results in Table 5.5 demonstrate that the leaching process done in 90 minutes yielded the least quantity of residue after leaching. In comparison to 60 and 30 minutes, the leaching operation carried out in 60 minutes produced the highest mass. After leaching, a residual mass percentage of 91% was achieved.

Table 5.4 Test 2 hotplate leaching results for 4 M H_2SO_4

Test no.	Time (minutes)	Initial mass (g)	Volume of H_2SO_4 (mL)	Mass of residue (g)	Volume of deionized water (mL)
2	30	4.0200	3.1370	3.2900	36.8700
	60	4.0000	3.1400	3.6500	
	90	4.0100	3.1390	3.9200	
Total		12.0300		10.8600	

Table 5.5 Test 1 hotplate leaching results for 6 M H_2SO_4

Test no.	Time (minutes)	Initial mass (g)	Volume of H_2SO_4 (mL)	Mass of residue (g)	Volume of deionized water (mL)
1	30	4.0100	4.5360	3.6000	35.4700
	60	4.0100	4.5300	3.8100	
	90	4.0100	4.5400	3.5500	
Total		12.0300		10.9600	

5.3.6.6 Test 2 Hotplate Leaching Results for 6 M H_2SO_4

The results in Table 5.6 obtained show that leaching process executed in 30 minutes obtained the least amount of residue after leaching compared when the solution was leached for 30 and 60 minutes. The leaching process conducted in 90 minutes achieved the highest mass compared to 60 and 30 minutes. The overall 92% mass percentage was obtained of residue after leaching.

5.3.7 Results on Mass Balance: Oven

5.3.7.1 Test 1 Oven Leaching Results for 2 M H_2SO_4

According to the results in Table 5.7, the solution was leached for 30 and 60 minutes, and the 60-minute method yielded the least quantity of residue after oven leaching. In comparison to 60 and 30 minutes, the leaching operation carried out in 30 minutes produced the highest mass. After leaching, residue was collected in an overall mass percentage of 87%.

5.3.7.2 Test 2 Oven Leaching Results for 2 M H_2SO_4

In comparison to leaching the solution for 30 and 60 minutes, the results in Table 5.8 reveal that leaching processes completed in 30 minutes yielded the least amount of residue after oven leaching. In comparison to 60 and 30 minutes, the leaching operation carried out in 90 minutes produced the highest mass. After leaching, residue was collected in an overall mass percentage of 86%.

Table 5.6 Test 2 hotplate leaching results for 6 M H_2SO_4

Test no.	Time (minutes)	Initial mass (g)	Volume of H_2SO_4 (mL)	Mass of residue (g)	Volume of deionized water (mL)
2	30	4.0000	4.5320	3.4600	35.4700
	60	4.0000	4.5430	3.6500	
	90	4.0200	4.5320	3.9200	
Total		12.0200		11.0300	

Table 5.7 Test 1 oven leaching results for 2 M H_2SO_4

Test no.	Time (minutes)	Initial mass (g)	Volume of H_2SO_4 (mL)	Mass of residue (g)	Volume of deionized water (mL)
1	30	4.0061	1.6343	3.5649	38.3700
	60	4.0020	1.6305	3.3438	
	90	4.0041	1.6345	3.5164	
Total		12.0120		10.4250	

Table 5.8 Test 2 oven leaching results for 2 M H_2SO_4

Test no.	Time (minutes)	Initial mass (g)	Volume of H_2SO_4 (mL)	Mass of residue (g)	Volume of deionized water (mL)
2	30	4.0212	1.6308	3.2393	38.3700
	60	4.0027	1.6316	3.4590	
	90	4.0020	1.6349	3.6144	
Total		12.0260		10.3130	

5.3.7.3 Test 1 Oven Leaching Results for 4 M H_2SO_4

In comparison to leaching the solution for 30 and 60 minutes, the results in Table 5.9 reveal that leaching processes completed in 30 minutes yielded the least amount of residue after oven leaching. In comparison to 60 and 30 minutes, the leaching operation carried out in 90 minutes produced the highest mass. After leaching, residue was collected in an overall mass percentage of 89%.

5.3.7.4 Test 2 Oven Leaching Results for 4 M H_2SO_4

In comparison to leaching the solution for 30 and 60 minutes, the results in Table 5.10 reveal that leaching processes completed in 30 minutes yielded the least quantity of residue after oven leaching. In comparison to 60 and 30 minutes, the leaching operation carried out in 90 minutes produced the highest mass. After leaching, residue was collected in an overall mass percentage of 87%.

Table 5.9 Test 1 oven leaching results for 4 M H_2SO_4

Test no.	Time (minutes)	Initial mass (g)	Volume of H_2SO_4 (mL)	Mass of residue (g)	Volume of deionized water (mL)
1	30	4.0100	3.1380	3.1300	36.8600
	60	4.0000	3.1360	3.6200	
	90	4.0000	3.1380	3.9300	
Total		12.0100		10.6800	

Table 5.10 Test 2 oven leaching results for 4 M H_2SO_4

Test no.	Time (minutes)	Initial mass (g)	Volume of H_2SO_4 (mL)	Mass of residue (g)	Volume of deionized water (mL)
1	30	4.0000	3.3170	2.7500	36.8600
	60	4.0000	3.1380	3.7400	
	90	4.0000	3.1370	3.9600	
Total		12.0000		10.4500	

5.3.7.5 Test 1 Oven Leaching Results for 6 M H_2SO_4

According to the results in Table 5.11, the solution was leached for 30 and 60 minutes, and the 60-minute method yielded the least quantity of residue after oven leaching. In comparison to 60 and 30 minutes, the leaching operation carried out in 90 minutes produced the highest mass. After leaching, residue was collected in an overall mass percentage of 84%.

5.3.7.6 Test 2 Oven Leaching Results for 6 M H_2SO_4

The data shown in Table 5.12 indicate that when the solution was leached for 90 minutes as opposed to 30 or 60 minutes, there was the least quantity of residue left over.

In comparison to 60 and 30 minutes, the leaching operation carried out in 60 minutes produced the highest mass. After leaching, residue was collected in an overall mass percentage of 87%.

5.3.7.7 Test 1 Oven Leaching Results for 8 M H_2SO_4

The results in Table 5.13 demonstrate that, when compared to leaching the solution for 30 and 60 minutes, leaching the solution for 30 minutes yielded the least quantity of residue following oven leaching. In comparison to 60 and 30 minutes, the leaching operation carried out in 90 minutes produced the highest mass. After leaching, a residual mass percentage of 85% was achieved.

Table 5.11 Test 1 oven leaching results for 6 M H_2SO_4

Test no.	Time (minutes)	Initial mass (g)	Volume of H_2SO_4 (mL)	Mass of residue (g)	Volume of deionized water (mL)
1	30	4.0100	4.5320	3.4640	36.8600
	60	4.0100	4.5350	2.8200	
	90	4.0000	4.5320	3.8620	
Total		12.0200		10.1460	

Table 5.12 Test 2 oven leaching results for 6 M H_2SO_4

Test no.	Time (minutes)	Initial mass (g)	Volume of H_2SO_4 (mL)	Mass of residue (g)	Volume of deionized water (mL)
2	30	4.0000	4.5360	3.8500	35.0000
	60	4.0100	4.5340	3.4400	
	90	4.0100	4.5350	3.3400	
Total		12.0200		10.6300	

Table 5.13 Test 1 oven leaching results for 8 M H_2SO_4

Test no.	Time (minutes)	Initial mass (g)	Volume of H_2SO_4 (mL)	Mass of residue (g)	Volume of deionized water (mL)
1	30	4.010	5.8150	3.2900	34.1800
	60	4.000	5.8130	3.5500	
	90	4.010	5.8150	3.4100	
Total		12.0200		10.2500	

5.3.7.8 Test 2 Oven Leaching Results for 8 M H_2SO_4

When compared to leaching the solution for 30 and 60 minutes, the results in Table 5.14 reveal that a 90-minute leaching method yielded the least quantity of residue after oven leaching. In comparison to 60 and 30 minutes, the leaching operation carried out in 60 minutes produced the highest mass. After leaching, residue was collected in an overall mass percentage of 95%.

5.3.7.9 Test 1 Oven Leaching Results for 10 M H_2SO_4

According to the data in Table 5.15, the leaching process that was carried out in 90 minutes yielded the least quantity of residue following oven leaching as compared to when the solution was leached for 60 and 90 minutes. Comparing 60- and 30-minute leaching processes, the 60-minute method produced the highest mass. After leaching, residue had a mass percentage of 91% overall.

Table 5.14 Test 2 oven leaching results for 8 M H_2SO_4

Test no.	Time (minutes)	Initial mass (g)	Volume of H_2SO_4 (mL)	Mass of residue (g)	Volume of deionized water (mL)
2	30	4.0100	5.8130	3.9000	34.1800
	60	4.0000	5.8140	3.9100	
	90	4.0200	5.8130	3.6400	
Total		12.0300		11.4500	

Table 5.15 Test 1 oven leaching results for 10 M H_2SO_4

Test no.	Time (minutes)	Initial mass (g)	Volume of H_2SO_4 (mL)	Mass of residue (g)	Volume of deionized water (mL)
2	30	4.0100	7.0240	3.6000	32.9900
	60	4.0100	7.0510	3.8100	
	90	4.0100	7.0340	3.5500	
Total		12.0300		11.4500	

5.3.7.10 Test 2 Oven Leaching Results for 10 M H_2SO_4

Based on the data from Table 5.16, it can be seen that when the solution was leached for 90 minutes as opposed to 60 or 90 minutes, there was the least amount of residue left behind after leaching in the oven. Comparing 60 and 30 minutes, the leaching process conducted in 60 achieved the highest mass. Leaching produced residue with a mass percentage of 91% overall.

5.3.8 Graphical Leaching Results for Digital Hotplate

Cu was leached using a digital hotplate, and the findings were tabulated and graphically displayed.

5.3.8.1 Digital Hotplate Leaching for 2 M H_2SO_4 Test Work

The following may be seen from the results of the digital hotplate leaching for 2 M H_2SO_4 in Fig. 5.11:

(i) Test 1 residue leftovers' average mass was determined to have the least residue, with residue levels averaging 73% and metal recovery rates of 27% in 60 minutes for average mass ranging from 2.7 to 3.1 g.
(ii) Test 2 average residue weight ranged between 3.4 and 3.8 g, and after 60 minutes, 13% of the metals and 87% of the average residue were recovered.

Table 5.16 Test 2 oven leaching results for 10 M H_2SO_4

Test no.	Time (minutes)	Initial mass (g)	Volume of H_2SO_4 (mL)	Mass of residue (g)	Volume of deionized water (mL)
2	30	4.0100	7.0280	3.4600	32.9900
	60	4.0100	7.0250	3.6500	
	90	4.0200	7.0320	3.9200	
Total		12.0200		11.0300	

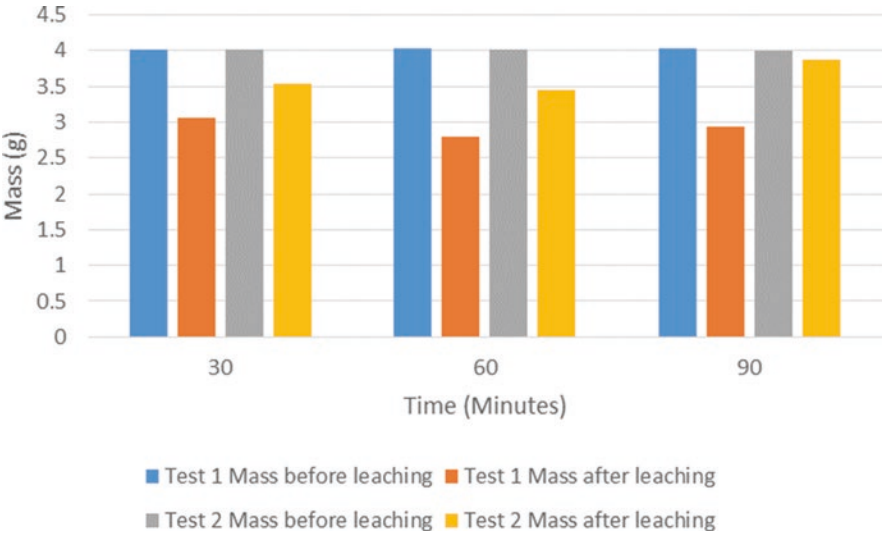

Fig. 5.11 Graphical results for 2 M H_2SO_4 hotplate leaching

5.3.8.2 Digital Hotplate Leaching for 4 M H_2SO_4 Test Work

The following may be seen from the results of the digital hotplate leaching for 4 M H_2SO_4 in Fig. 5.12:

(i) The residue of Test 1 average mass in the intervals of 30 and 60 minutes obtained the least quantity of residue.
(ii) The average mass of Test 1 varied between 3.4 and 3.5 g, with an average residue content of 86.03% and a 60-minute metal recovery rate of 13.97%.
(iii) Test 2 average residue weight ranged between 3.2 and 3.6 g, and after 60 minutes, 13% of the metals and 87% of the average residue were recovered.

5.3.8.3 Digital Hotplate Leaching for 6 M H_2SO_4 Test Work

The results of the digital hotplate leaching for 6 M H_2SO_4 are shown in Fig. 5.13.

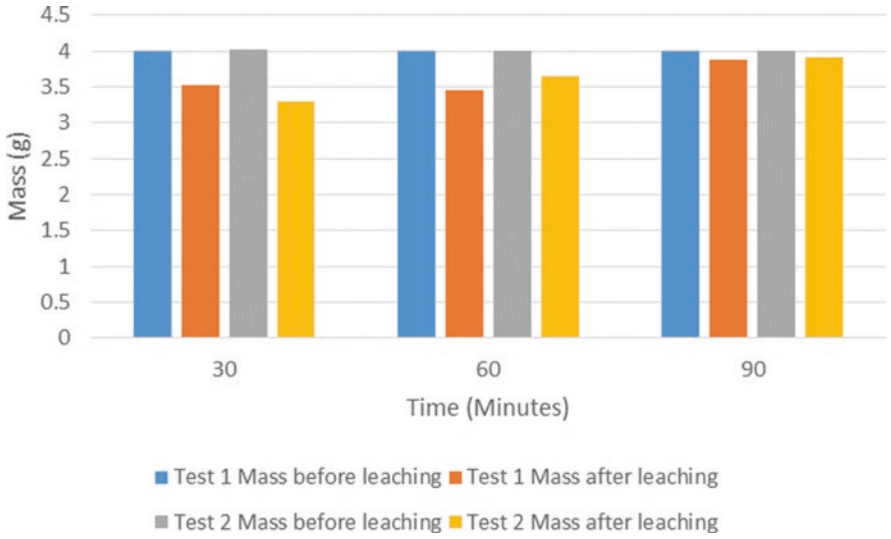

Fig. 5.12 Graphical results for 4 M H_2SO_4 hotplate leaching

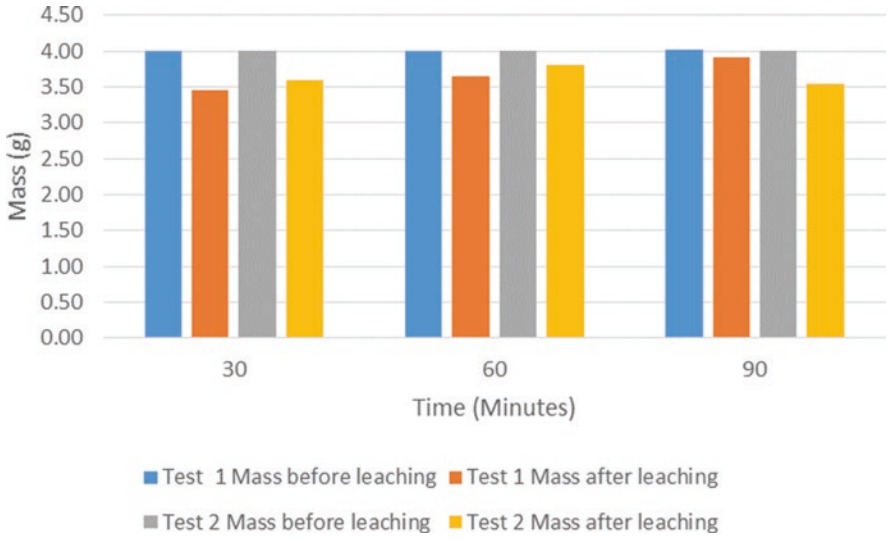

Fig. 5.13 Graphical results for 6 M H_2SO_4 hotplate leaching

(i) The residue of Test 1 average mass was produced with the least quantity of residue in the intervals of 30 and 60 minutes.
(ii) The average mass of Test 1 ranged between 3.46 and 3.65 g, with an average residue recovery rate of 86.5% and a metal recovery rate of 13.5% in just 30 minutes.

(iii) Test 2 average residue weight ranged between 3.5 and 3.8 g, and in 90 minutes, an average of 88.3% of the residue and 11.7% of the metals were recovered.
(iv) The process was found to be dormant after 90 minutes.

5.3.8.4 Oven Leaching for 2 M H_2SO_4 Test Work

The results obtained on oven leaching for 2 M H_2SO_4 in Fig. 5.14 show the following:

(i) The residue of Test 1 average mass in 60 and 90 minutes interval achieved least amount of residue.
(ii) The average mass of Test 1 varied from 3.34 to 3.56 g, and about 83.5% average of residue and 16.5% of metal were recovered in 90 minutes.
(iii) Test 2 average residue varied between 3.24–3.6 g , and about 80.8% average residue and 19.20% of metals were recovered in 90 minutes.

5.3.8.5 Results for Oven Leaching of 4 M H_2SO_4

The following can be seen from the oven leaching results for 4 M H_2SO_4 in Fig. 5.15:

(i) The residue of Test 1 average mass in the intervals of 60 and 90 minutes obtained the least quantity of residue.
(ii) The average mass of Test 1 ranged from 3.34 to 3.56 g, and in 90 minutes, an average of 83.5% residue and 16.5% metal were recovered.
(iii) Test 2average residue weight ranged between 3.24 and 3.6 g, and in 90 minutes, an average of 80.8% of the residue and 19.20% of the metals were recovered.

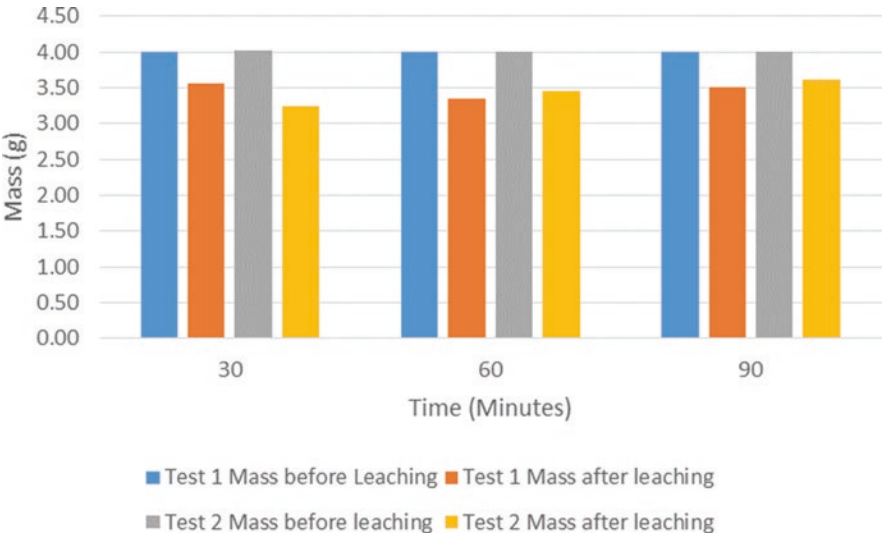

Fig. 5.14 Graphical results for oven leaching of 2 M H_2SO_4

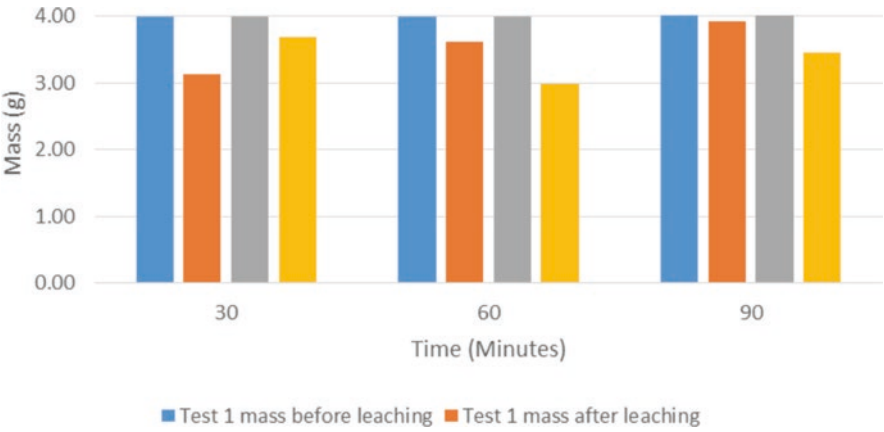

Fig. 5.15 Graphical results for oven leaching of 4 M H_2SO_4

5.3.8.6 Results for Oven Leaching of 6 M H_2SO_4

The following can be seen from the oven leaching findings for 6 M H_2SO_4 in Fig. 5.16:

(i) The residue of Test 1 average mass in the intervals of 30 and 60 minutes obtained the least quantity of residue.
(ii) The average mass of Test 1 ranged from 2.82 to 3.86 g, and in 60 minutes, an average of 70.5% residue and 25.5% metal were recovered.
(iii) Test 2 average residue weight ranged between 3.34 and 3.86 g, and in 90 minutes, an average of 83.5% of the residue and 16.5% of the metals were recovered.

5.3.8.7 Results for Oven Leaching of 8 M H_2SO_4

The following can be seen from the oven leaching findings for 8 M H_2SO_4 in Fig. 5.17:

(i) The residue of Test 1 average mass was produced with the least quantity of residue after 30, 60, and 90 minutes.
(ii) The average mass of Test 1 varied between 3.29 and 3.55 g, with an average residue content of 82.04% and a 30-minute metal recovery rate of 17.94%.
(iii) Test 2 average residue weight ranged from 3.64 to 3.91 g, and in 90 minutes, an average amount of 90.77% of the residue and 9.23% of the metals were recovered.

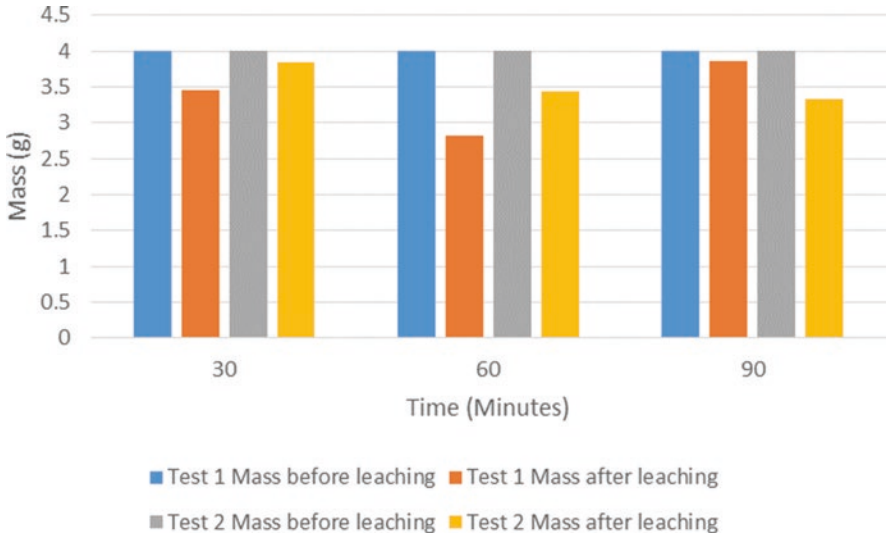

Fig. 5.16 Graphical results for oven leaching of 6 M H_2SO_4

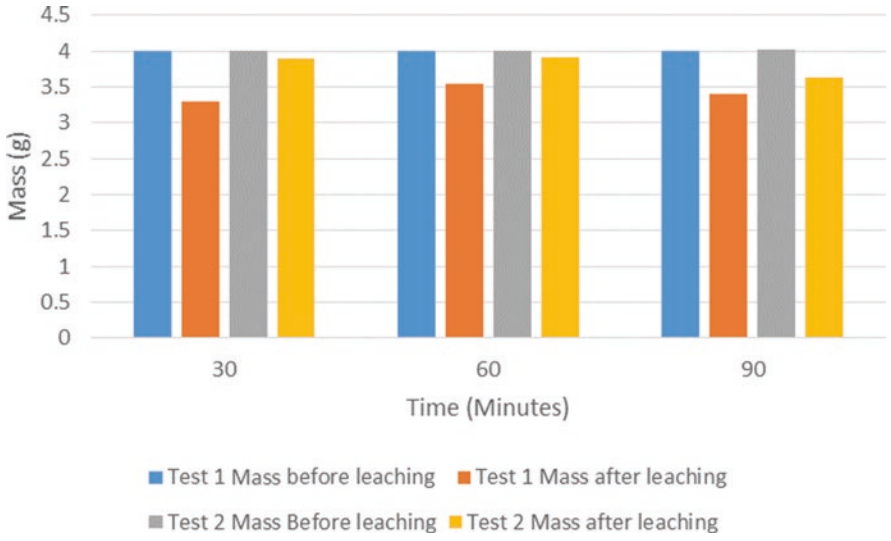

Fig. 5.17 Graphical results for oven leaching of 8 M H_2SO_4

5.3.8.8 Results for Oven Leaching of 10 M H_2SO_4

The following can be seen from the oven leaching findings for 10 M H_2SO_4 in

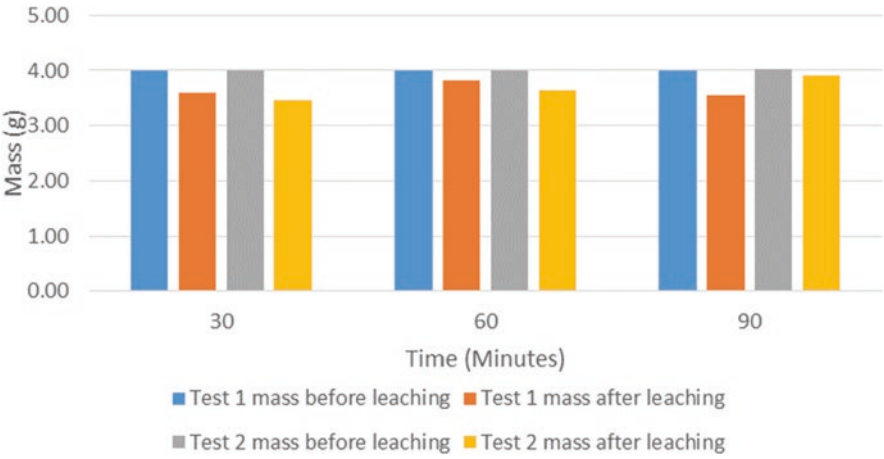

Fig. 5.18 Graphical results for oven leaching of 10 M H_2SO_4

Fig. 5.18:

(i) The residue of Test 1 average mass was produced with the least quantity of residue after 30, 60, and 90 minutes.
(ii) The average mass of Test 1 ranged from 3.55 to 3.81 g, and in 90 minutes, an average of 88.5% residue and 11.5% metal was recovered.
(iii) Test 2 average residue ranged between 3.46 and 3.92 g, and in 90 minutes, 13.72% of the average residue and 86.28% of the average residue were recovered.

5.3.9 Production of Purified Pregnant Leach Solution from Leachate

In the leach solution, the copper to iron ratio is typically 1 to 0.73. This proportion is rather high; hence, the following strategy is used.

By adding a little amount of $FeSO_4.7H_2O$ to the leaching system to slow down the dissolving of iron, the iron in the $CuSO_4$ solution was reduced. By doing this, iron was precipitated from the $CuSO_4$ solution by the hydrolysis of iron III (Fe^{3+}), which then produced complexed iron hydroxides and solid precipitates. Stumm and Lee [30], Lawson [31], and Dutrizac [32], respectively, explain the chemical reactions occurring in Eqs. (5.4), (5.5), and (5.6).

$$4Fe^{2+} + O_{2(aq)} + 4H^{+} \rightarrow 4Fe^{3+} + 2H_2O \tag{5.4}$$

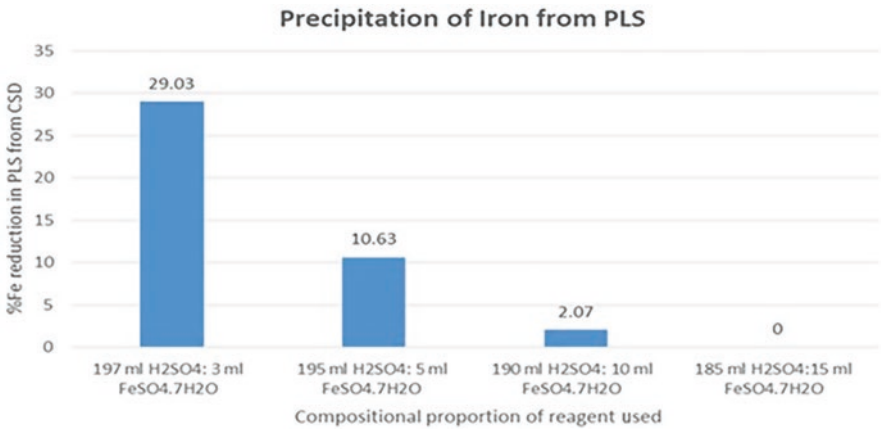

Fig. 5.19 Reduction of iron content in $CuSO_4$ solution

$$Fe\left(OH_2\right)_6^{3+} \rightarrow Fe\left(OH\right)n\left(OH_2\right)_{6-n}^{3-n} + n\mathrm{H}^+ \tag{5.5}$$

$$2Fe^{3+} + 2\mathrm{H_2O} \rightarrow Fe_2\left(OH\right)_2^{4+} + 2\mathrm{H}^+ \tag{5.6}$$

Iron was reduced by 29.03% using a mixture of 197 mL H_2SO_4: 3 mL $FeSO_4.7H_2O$ (Fig. 5.19). The enhanced reduction in dissolved iron is explained by the formation of insoluble but thermodynamically stable species such as goethite (α-FeOOH) and hematite (α-Fe_2O_3). As precipitation started at 75 °C, this reaction is percentage.

When the CSD was treated with 185 mL H_2SO_4: 15 mL $FeSO_4.7H_2O$, there was a noticeable decrease (0.5%) in the reduction of dissolved iron. This can be linked to the formation of soluble, thermodynamically stable iron sulfate precipitates like jarosite [33].

In ferrihydrite complexes, some of the sulfur may not be structurally combined but may instead be adsorbed to the surface of the iron species, according to Bigham et al. [34]. Sulfur is treated as an anionic contaminant in these situations. The iron sulfate complexes, as shown by Eqs. (5.7) and (5.8), have the potential to act as an intermediary in the formation of iron sulfate precipitates [35].

$$Fe^{3+} + \mathrm{SO_4}^{2-} \rightarrow Fe\left(\mathrm{SO_4}\right)^+ \tag{5.7}$$

$$Fe\left(\mathrm{SO_4}\right)^+ \mathrm{SO_4}^{3-} \rightarrow Fe\left(\mathrm{SO_4}\right)_2^- \tag{5.8}$$

5.4 Conclusion

The leaching of copper from WCD by H_2SO_4 acid is the goal of this study. The outcomes of the digital hotplate leaching test work demonstrate that the best outcomes were obtained between 30 and 60 minutes. This demonstrates how processes attain equilibrium after a specific amount of time. Hotplate leaching has been significantly impacted by stirring rate, concentration, and temperature.

The majority of the results from oven leaching indicate that leaching time and concentration play a significant role in achieving high recovery of important metals in WCD ore. The conclusion is that if the process is conducted for a long time, the best leaching results can be attained.

Under the situation of a compositional ratio of 197 mL H_2SO_4: 3 mL $FeSO_4.7H_2O$, the inhibition of iron dissolution resulted in a reduction of iron by 29.03%.

Acknowledgments We thank Pantheon Virtual Engineering Solutions, Nigel, South Africa, and Tshwane University of Technology, Pretoria, South Africa, for the support received.

References

1. C. Samuelsson, B. Björkman, Copper recycling, in *Handbook of Recycling*, (Elsevier, 2014), pp. 85–94
2. M.E. Schlesinger, K.C. Sole, W.G. Davenport, G.R. Alvear, *Extractive Metallurgy of Copper* (Elsevier, 2021)
3. W.E. Halter, C.A. Heinrich, T. Pettke, Magma evolution and the formation of porphyry Cu–Au ore fluids: Evidence from silicate and sulfide melt inclusions. Mineral. Deposita **39**(8), 845–863 (2005)
4. D. Killick, From ores to metals, in *Archaeometallurgy in Global Perspective*, (Springer, New York, 2014), pp. 11–45
5. M. Shamsuddin, Sulfide smelting, in *Physical Chemistry of Metallurgical Processes*, 2nd edn., (Springer, Cham, 2021), pp. 69–106
6. D. Gregurek, F. Melcher, V.A. Pavlov, C. Reimann, E.F. Stumpfl, Mineralogy and mineral chemistry of snow filter residues in the vicinity of the nickel-copper processing industry, Kola Peninsula, NW Russia. Mineral. Petrol. **65**(1), 87–111 (1999)
7. P.N. Prasad, H. Thomas, A. Lennartsson, C. Samuelsson, Redistribution of minor and trace elements during roasting of Cu-rich complex concentrate in inert atmosphere. Metall. Mater. Trans. B **53**(3), 1875–1893 (2022)
8. R. Ma, L. Zhang, J. Cui, A.A. Tishkin, S.P. Grushin, E.G. Vertman, D. Chang, D. Hu, Late Bronze Age metallurgy in Rudnyi Altai. Archaeol. Anthropol. Sci. **14**(8), 1–12 (2022)
9. F. Tesfaye, D. Lindberg, D. Sukhomlinov, P. Taskinen, L. Hupa, Thermal analysis and optimization of the phase diagram of the Cu-Ag sulfide system. *Energies* **15**(2), 593 (2022)
10. M. Pearce, S. Merkel, A. Hauptmann, F. Nicolis, The smelting of copper in the third millennium cal BC Trentino, north-eastern Italy. Archaeol. Anthropol. Sci. **14**(1), 1–21 (2022)
11. G. Atesoglu, İ. Atilgan, Effect of roasting temperature on the leaching of chalcopyrite concentrate in sulphuric acid. Min. Metall. Explor. **39**, 2199–2208 (2022)
12. B. Gorai, R.K. Jana, Z.H. Khan, Electrorefining electrolyte from copper plant dust. Mater. Trans. **43**(3), 532–536 (2002)

13. E. Balladares, U. Kelm, S. Helle, R. Parra, E. Araneda, Chemical-mineralogical characterization of copper smelting flue dust. Dyna **81**(186), 11–18 (2014)
14. F. Wang, Y. Zhao, T. Zhang, C. Duan, L. Wang, Mineralogical analysis of dust collected from typical recycling line of waste printed circuit boards. Waste Manag. **43**, 434–441 (2015)
15. A. Jarošíková, V. Ettler, M. Mihaljevič, P. Drahota, A. Culka, M. Racek, Characterization and pH-dependent environmental stability of arsenic trioxide-containing copper smelter flue dust. J. Environ. Manag. **209**, 71–80 (2018)
16. D.O. Okanigbe, A.P.I. Popoola, A.A. Adeleke, Characterization of copper smelter dust for copper recovery. Procedia Manuf. **7**, 121–126 (2017)
17. T. Henckens, Scarce mineral resources: Extraction, consumption and limits of sustainability. Resour. Conserv. Recycl. **169**, 105511 (2021)
18. A. Morales, M. Cruells, A. Roca, R. Bergó, Treatment of copper flash smelter flue dusts for copper and zinc extraction and arsenic stabilization. Hydrometallurgy **105**(1–2), 148–154 (2010)
19. S. Teir, H. Revitzer, S. Eloneva, C.J. Fogelholm, R. Zevenhoven, Dissolution of natural serpentinite in mineral and organic acids. Int. J. Miner. Process. **83**(1–2), 36–46 (2007)
20. F. Habashi, *A Textbook of Hydrometallurgy*, 2nd edn. (Métallurgie Extractive Québec, Québec City, 1999), 750 p
21. R.K.K. Mbaya, M.M. Ramakokovhu, C.K. Thubakgale, Atmospheric pressure leaching application for the recovery of copper and nickel from low-grade sources, in *The Southern African Institute of Mining and Metallurgy (Base Metals Conference 2013)*, (The Southern African Institute of Mining and Metallurgy, Johannesburg, 2013), pp. 255–268
22. J.Y. Wu, F.C. Chang, H.P. Wang, M.J. Tsai, C.H. Ko, C.C. Chen, Selective leaching process for the recovery of copper and zinc oxide from copper-containing dust. Environ. Technol. **36**(23), 2952–2958 (2015)
23. P. Littlejohn, D. Dreisinger, *Technical review–copper solvent extraction in hydrometallurgy*. Submitted to Dr. David Dreisinger, grudzień (2007)
24. N.B. Du Preez, J.J. Taute, Evaluation of copper solvent-extraction circuit data and performance, in *Proceedings of the 8th Southern African Base Metals Conference*, Livingstone, Zambia, July 2015, pp. 6–8
25. Y. Chen, T. Liao, G. Li, B. Chen, X. Shi, Recovery of bismuth and arsenic from copper smelter flue dusts after copper and zinc extraction. Miner. Eng. **39**, 23–28 (2012)
26. B. Lucheva, P. Iliev, D. Kolev, Hydro-pyrometallurgical treatment of copper converter flue dust. J. Chem. Technol. Metall. **52**(2), 320–325 (2017)
27. R.A. Shawabkeh, Hydrometallurgical extraction of zinc from Jordanian electric arc furnace dust. Hydrometallurgy **104**(1), 61–65 (2010)
28. P. Oustadakis, P.E. Tsakiridis, A. Katsiapi, S. Agatzini-Leonardou, Hydrometallurgical process for zinc recovery from electric arc furnace dust (EAFD): Part I: Characterization and leaching by diluted sulphuric acid. J. Hazard. Mater. **179**(1–3), 1–7 (2010)
29. A. Ghosh, H.S. Ray, *Principles of Extractive Metallurgy* (New Age International, 1991)
30. W. Stumm, G.F. Lee, Oxygenation of ferrous iron. Ind. Eng. Chem. **53**(2), 143–146 (1961)
31. D.R. Lawson, J.G. Wendt, Acid deposition in California. SAE Trans. **91**, 3949–3967 (1982)
32. J.E. Dutrizac, The Fe_{1-x} S–PbS–ZnS phase system. Can. J. Chem. **58**(7), 739–743 (1980)
33. H. Jiang, F. Lawson, Reaction mechanism for the formation of ammonium jarosite. Hydrometallurgy **82**(3–4), 195–198 (2006)
34. J.M. Bigham, U. Schwertmann, S.J. Traina, R.L. Winland, M. Wolf, Schwertmannite and the chemical modeling of iron in acid sulfate waters. Geochim. Cosmochim. Acta **60**(12), 2111–2121 (1996)
35. R.M. Cornell, U. Schwertmann, *The Iron Oxides: Structure, Properties, Reactions, Occurrences, and Uses*, vol 664 (Wiley-VCH, Weinheim, 2003)

Chapter 6
Extraction of Copper Oxide (II): Copper Oxide Nanoparticles

Daniel Ogochukwu Okanigbe

6.1 Introduction

The available resource recovery processes have capital and operating expenses that are higher than what the revenue from the recovered metal can support. In order to recover the copper value from metallurgical wastes such as copper anode slimes, copper slags, waste copper dust (WCD), the copper smelting industry is becoming more and more interested in inventing ways for doing so. It would be advantageous to have a processing technique that could eliminate impurities from the WCD while maintaining a suitable level of revenue metals in the resultant concentrate.

To facilitate the management of accumulated WCD, it would be desirable if this could be done economically. It is believed that recovering copper as oxides of nanoparticles (CuO-NPs) from purified pregnant leach solution (PPLS) is preferable to recovering it as cathode slabs [1]. This is because CuO-NPs outperform conventional copper oxide in many applications thanks to their exceptional physicochemical characteristics. Recently, there has been increased interest in producing CuO-NPs with p-type semiconductivity [2]. CuO-NPs are recognized as one of the best inorganic semiconductors with desirable properties [3].

Moreover, CuO-NPs can be used in a wide range of technological applications, such as gas sensors [4, 5], magnetic phase transmitters [6], heterogeneous catalysts [7–9], and optical switches [6, 10, 11], nanofluids [12, 13], solar energy transformer [4, 14], lithium ion electrode materials [8, 15], and field emitter [6, 11].

Due to the vast range of uses for metallic/metallic oxide nanoparticles, numerous methods for manufacturing them via chemical, physical, and biological processes

D. O. Okanigbe (✉)
Department of Chemical, Metallurgical and Materials Engineering, Faculty of Engineering and the Built Environment, Tshwane University of Technology, Pretoria, South Africa

Pantheon Virtual Engineering Solutions, Nigel, South Africa
e-mail: okanigbedo@tut.ac.za; okanigbeogochukwu@gmail.com

D. O. Okanigbe, A. P. Popoola (eds.), *Resource Recovery and Recycling from Waste Metal Dust*, https://doi.org/10.1007/978-3-031-22492-8_6

have also been documented (CuO-NPs). Sol-gel [16], wet chemical approaches [17, 18], thermal oxidation of Cu substrates [10], and solvothermal methods [4, 6], microwave irradiation [19], sonochemical [20], and microemulsion [21], electrochemical [22], hydrothermal [23, 24], solid-state reaction [25, 26], submerged arc [27], and precipitation methods [12, 28, 29] are a few examples of these techniques. Co-precipitation and the thermal degradation of precursors are additional methods for producing nanoparticles [28, 30–32].

A key consideration in selecting the best technique is how to generate copper or copper oxide nanoparticles with an acceptable level of purity [27]. In a closed vessel, such as an autoclave, solvents are heated significantly above their boiling temperatures in a solvothermal process that involves chemical interaction. When water is used as the solvent, the process is referred to as a hydrothermal one. A variety of literatures have discussed how this strategy is used [33, 34]. Byrappa and Yoshimura [35] described the hydrothermal process as a process involving a heterogeneous chemical reaction in a closed system, in the presence of an aqueous or non-aqueous solvent above room temperature, and at pressures more than 1 atm.

When water is 647.15 K and 221 bar above atmospheric pressure, it is referred to as a supercritical fluid. Water or other fluids that are supercritical behave both like liquids and like gases. Surface tension is decreased when a solid and a supercritical fluid come into contact, and chemical compounds that are extremely difficult to dissolve in ambient conditions are also dissolved. These techniques largely take use of the metal's higher solubility and reactivity [36]. There are many advantages to using supercritical conditions, including simplicity, very small grain size, the presence of a single phase, and the creation of high-purity nanocrystals with outstanding crystallinity and green properties [37].

The thermal reduction technique is an illustration of a solvothermal process. This technology exceeds older ones like the chemical reduction method in terms of cleanliness, speed, and cost despite being relatively new. It requires the appropriate precursor to be picked, as well as focused heating. Numerous studies have shown that this method can produce copper oxide nanoparticles. According to Zhang et al. [8], the thermal breakdown of the copper oxalate precursor produced CuO-NPs with an average diameter of 10 nm. CuO nanoparticles were also produced from the thermal breakdown of the precursors brochantite $Cu_4(SO_4)(OH)_6$ and posnjakite $Cu_4(SO_4)(OH)_6.H_2O$ [38]. Simpleness, a high possibility of single-phase, high-purity nanocrystals with high crystallinity, low particle size, and favourable environmental effects are all guaranteed by this method [27, 37].

A few studies have been done on the production of CuO-NPs by the thermal breakdown of copper precursors in a CSD's leach solution [27, 32, 38]. Additionally, the thermal decomposition method for creating CuO-NPs from CSD requires careful selection of a copper precursor, as was previously mentioned in the preceding paragraphs [27]. Therefore, it is essential to optimize the process parameters of agitation speed, temperature, flow rate, and concentration of both Na_2CO_3 and $CuSO_4$ in order to obtain the best copper precursor, which will support the production of CuO-NPs with enhanced grade and recovery during its thermal decomposition.

Thus, this chapter presents the results of the inquiry into the production of CuO-NPs from this low-grade waste metal dust (i.e. CSD).

6.2 Experimental Method

6.2.1 Material

6.2.1.1 Waste Metal Dust

The WCD from South Africa served as the waste metal dust in this investigation.

6.2.2 Methods

6.2.2.1 Production of Pregnant Leach Solution (PPLS)

In Okanigbe [39], the method for creating the PPLS employed in the synthesis of the CuO-NPs is described.

6.2.2.2 Design of Experiment and Procedure for Production of Copper Precursor

Starting with the manufacture of copper precursor from PPLS, CuO-NP manufacturing began. The 3-by-2 complete factorial experimental design approach was used to create the experiment design for the manufacture of copper precursor from PPLS, as illustrated in Tables 6.1 and 6.2.

The copper precursor was made by adding 2 M Na_2CO_3 solution dropwise to 0.2 M $CuSO_4$ solution in a 500-ml conical flask that was set on a hot plate while the mixture was stirred with a magnetic stirrer at various temperatures (Fig. 6.1). Filtration was used to separate the resultant green precipitate, which was then washed with distilled water and pure ethanol. Then, for 24 h, this green precipitate is dried in an oven at 105 °C.

Table 6.1 Parameters considered for the production of copper precursor

	Levels		
Parameters	Low	Medium	High
Temperature (°C)	25	55	85
Rotational speed (rpm)	340	740	1480

Table 6.2 Design of experiment for the production of copper precursor

Tests	Temperature (°C)	Rotational speed (rpm)	Treatment combinations (TC)
1	25	340	25 °C/340 rpm
2	25	740	25 °C/740 rpm
3	25	1480	25 °C/1480 rpm
4	55	340	55 °C/340 rpm
5	55	740	55 °C/740 rpm
6	55	1480	55 °C/1480 rpm
7	85	340	85 °C/340 rpm
8	85	740	85 °C/740 rpm
9	85	1480	85 °C/1480 rpm

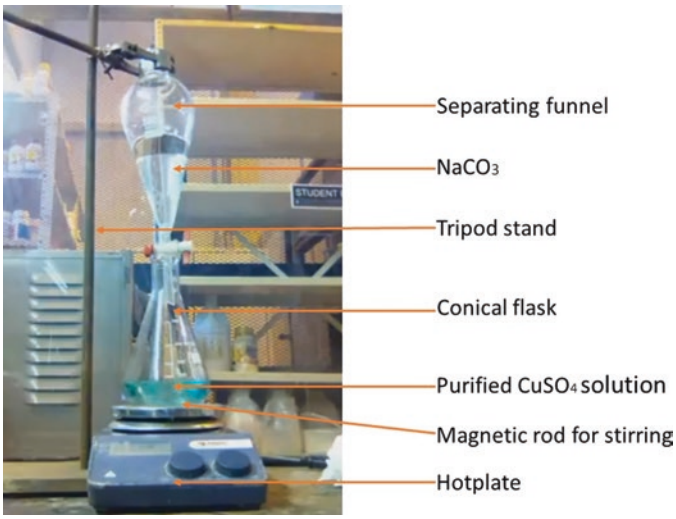

Fig. 6.1 Experimental setup for the production of copper precursor

6.2.2.3 Design of Experiment and Procedure for Production of CuO-NPs from Copper Precursor

Using a thermogravimetric analyser and an atmospheric flow, it was determined how the synthetized copper precursor behaved thermally. Thirty-five milligrams of samples was placed in a platinum crucible on the microbalance pan and heated between 25 and 1000 °C at rates of 5, 10, 15, and 20 °C/min.

The 3-by-2 complete factorial experimental design method was used to create the study (Tables 6.1 and 6.2). Soon after becoming familiar with the copper precursor's thermal behaviour, the experiment was planned using the data, as can be seen in Tables 6.3 and 6.4 for the production of CuO-NPs. Experimental procedure can be found in Okanigbe [39].

Table 6.3 Parameters considered for the production of CuO-NPs

Parameters	Levels		
	Low	Medium	High
Temperature (°C)	650	750	850
Time (h)	1	2	3

Table 6.4 Design of experiment for production of copper nanoparticles

Tests	Temperature (°C)	Time (h)	TC
1	650	1	650 °C/1 h
2	650	2	650 °C/2 h
3	650	3	650 °C/3 h
4	750	1	750 °C/1 h
5	750	2	750 °C/2 h
6	750	3	750 °C/3 h
7	850	1	850 °C/1 h
8	850	2	850 °C/2 h
9	850	3	850 °C/3 h

6.3 Results and Discussion

6.3.1 Mineralogy of Copper Precursor

This investigation into the synthesis of CuO-NPs from low-grade waste metal dust PPLS from South African CSD focuses on the synthesis and characterization of copper precursors before thermally decomposing the copper precursors to produce CuO-NPs. The many physical and chemical techniques used for material characterization are summarized in this section. Various physical characterization techniques, including powder X-ray diffraction, SEM, and TEM, were used to evaluate the copper precursor and CuO-NPs samples that were produced.

According to published literatures [27, 32, 40, 41], the thermal dehydration and desulpheration processes (Eqs. 6.1–6.3) are part of the reaction pathway that leads to copper (II) oxide. Equations 6.1–6.3 demonstrate that the three separate steps of the decomposition of $CuSO_4$ in solution were dehydration (Eq. 6.1), crystallization (Eq. 6.2), and desulphurization (Eq. 6.3) according to Koga et al. [41].

$$Cu_4\left(SO_4\right)\left(OH\right)_6.xH_2O \rightarrow^{170-180^{\circ}C} \rightarrow CuSO_4.3Cu\left(OH\right)_2 + xH_2O \tag{6.1}$$

$$CuSO_4.3Cu\left(OH\right)_2 \rightarrow^{170-180^{\circ}C} \rightarrow CuSO_4.2Cu\left(OH\right)_2 + CuO + xH_2O \tag{6.2}$$

$$CuSO_4.2Cu\left(OH\right)_2 \rightarrow^{170-180^{\circ}C} \rightarrow CuO + xH_2O + SO_2 + \frac{1}{2}H_2O \tag{6.3}$$

6.3.1.1 Mineralogy of Copper Precursor Produced Under TC 25 °C/340 rpm

The XRD machine was used to characterize the crystal structure and phase purity of the copper precursor generated under TC of 25 °C/340 rpm (Table 6.2). Figure 6.2 demonstrates that exactly 87.1% of all the diffraction peaks were indexed to hydrotalcite, while 4.8% of the peaks were indexed to aragonite, and the remaining 8.2% of the peaks were indexed to the copper-containing compounds 0.1% posnjakite and 8.1% cuprite.

6.3.1.2 Mineralogy of Copper Precursor Produced Under TC 25 °C/740 rpm

Figure 6.3 displays the crystal structure and phase purity of the copper precursor produced at TC of 25 °C/740 rpm (Table 6.2). The majority of the diffraction peaks, 82.9%, were attributed to hydrotalcite, while 5.0% is indexed to aragonite. The remaining 0.1% and 12.1% of the peaks were attributed to the copper-containing minerals posnjakite and cuprite, respectively.

6.3.1.3 Mineralogy of Copper Precursor Produced Under TC 25 °C/1480 rpm

XRD was used to characterize the crystal structure and phase purity of the copper precursor generated under TC of 25 °C/340 rpm (Table 6.2). As can be seen in Fig. 6.4, hydrotalcite accounted for exactly 86.5% of all the diffraction peaks, while

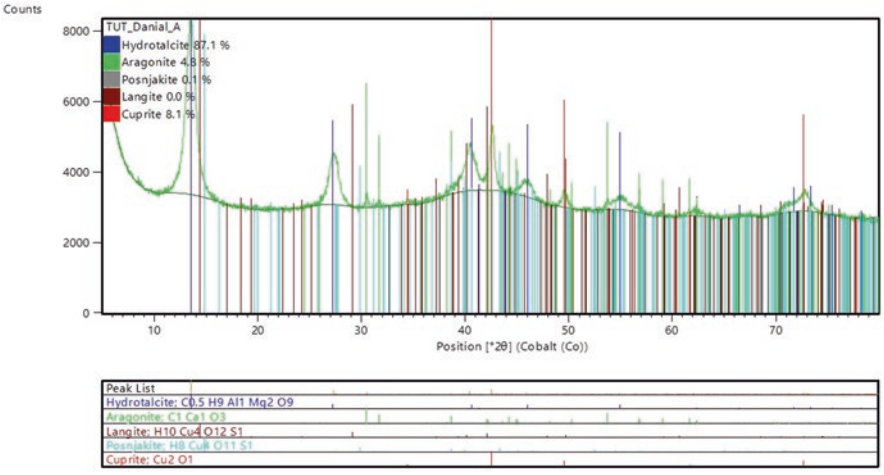

Fig. 6.2 XRD result of copper precursor obtained under 25 °C/340 rpm TC

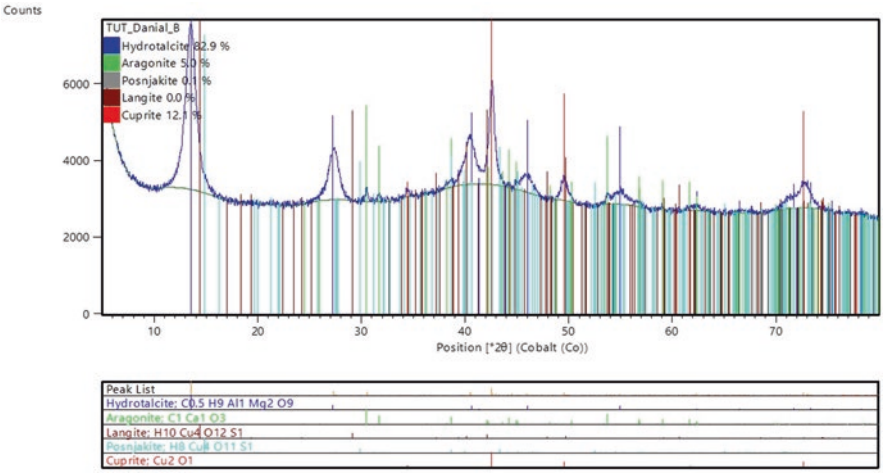

Fig. 6.3 XRD result of copper precursor obtained under 25 °C/740 rpm TC

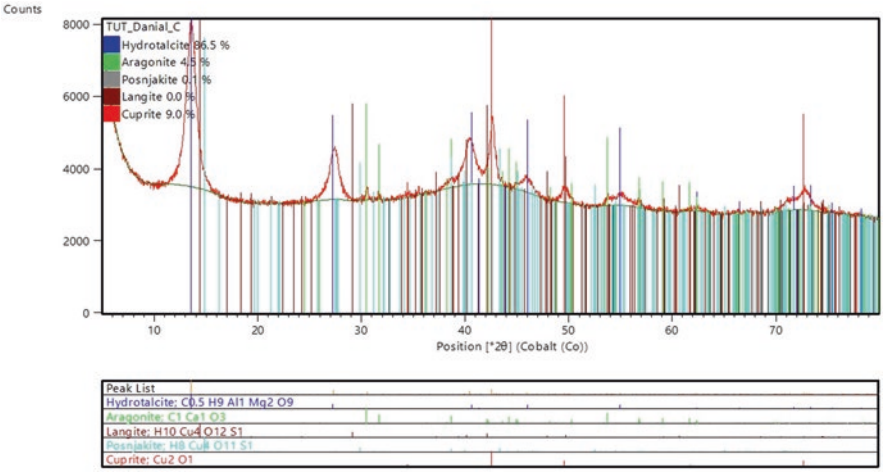

Fig. 6.4 XRD result of copper precursor obtained under 25 °C/1480 rpm

4.5% of them were indexed to aragonite, the other diffraction peaks were indexed to posnjakite (0.1%) and cuprite (9.0%).

6.3.1.4 Mineralogy of Copper Precursor Produced Under TC 55 °C/340 rpm

By using the XRD, the crystal structure and phase purity of the copper precursor produced at TC of 55 °C/340 rpm (Table 6.2) were identified. According to Fig. 6.5, the exact percentage of diffraction peaks indexed to hydrotalcite was 92.3%, the percentage indexed to aragonite was 2.7%, and the percentage indexed to cuprite was 5.1%.

6.3.1.5 Mineralogy of Copper Precursor Produced Under TC 55 °C/740 rpm

XRD was used to characterize the crystal structure and phase purity of the copper precursor generated under TC of 55 °C/740 rpm (Table 6.2). Figure 6.6 demonstrates that exactly 88.1% of all the diffraction peaks were indexed to hydrotalcite, while 3.0% of the peaks were indexed to aragonite, and the remaining 0.1% and 8.8% of the peaks were indexed to cuprite.

6.3.1.6 Mineralogy of Copper Precursor Produced Under TC 55 °C/1480 rpm

XRD was used to characterize the crystal structure and phase purity of the copper precursor generated under TC of 55 °C/1480 rpm (Table 6.2). As can be seen in Fig. 6.7, hydrotalcite accounted for exactly 89.5% of all the diffraction peaks, while 2.6% of them were indexed to aragonite, the other diffraction peaks were indexed to

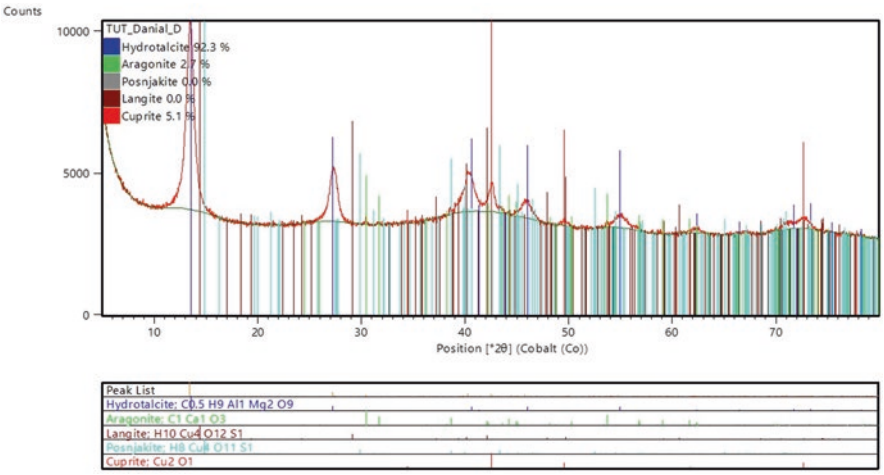

Fig. 6.5 XRD result of copper precursor obtained under 55 °C/340 rpm

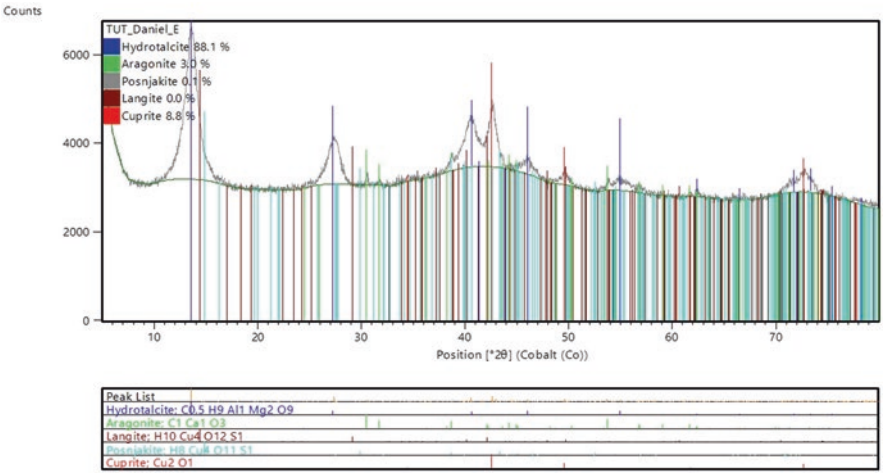

Fig. 6.6 XRD result of copper precursor obtained under 55 °C/740 rpm

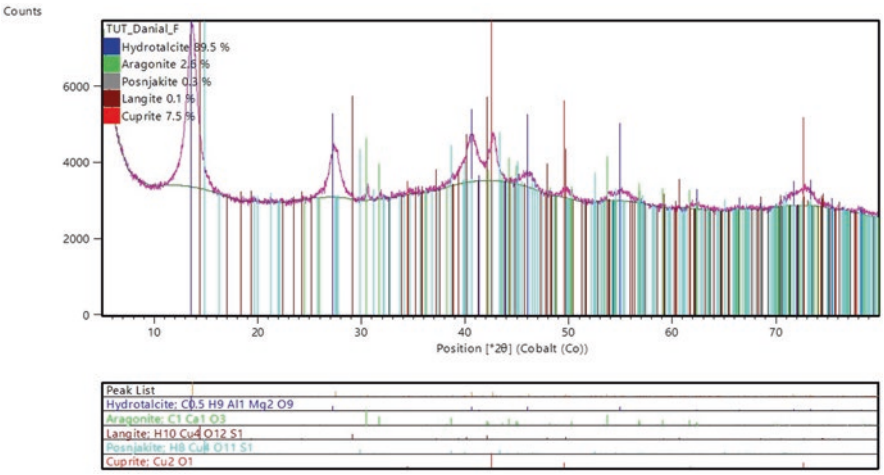

Fig. 6.7 XRD result of copper precursor obtained under 55 °C/1480 rpm

the copper-containing compounds posnjakite (0.3%), langite (0.1%), and cuprite (7.5%).

6.3.1.7 Mineralogy of Copper Precursor Produced Under TC 85 °C/340 rpm

The copper precursor produced at TC 85 °C/340 rpm (Table 6.2) was examined using the XRD apparatus for its crystal structure and phase purity. According to Fig. 6.8, precisely 68.3% of all the diffraction peaks were indexed to hydrotalcite, 11.0% to aragonite, and the remaining peaks were indexed to posnjakite (4.8%) and cuprite (15.9%).

6.3.1.8 Mineralogy of Copper Precursor Produced Under TC 85 °C/740 rpm

The XRD machine was used to characterize the crystal structure and phase purity of the copper precursor generated under TC of 85 °C/740 rpm (Table 6.2). Figure 6.9 reveals that exactly 83.2% of all the diffraction peaks were indexed to hydrotalcite, while 3.5% of the peaks were indexed to aragonite, and the remaining 13.3% of the peaks were indexed to posnjakite (0.1%) and cuprite (13.2%).

6.3.1.9 Mineralogy of Copper Precursor Produced Under TC 85 °C/1480 rpm

The crystal structure and phase purity of the copper precursor produced at TC of 85 °C/1480 rpm (Table 6.2) are shown in Fig. 6.10. 70.3% of the diffraction peaks were attributable to hydrotalcite, whereas aragonite was responsible for 10.6% of the peaks. Posnjakite, langite, and cuprite are the copper-containing minerals that are responsible for the remaining diffraction peaks, 5.8%, 1.6%, and 11.7%, respectively.

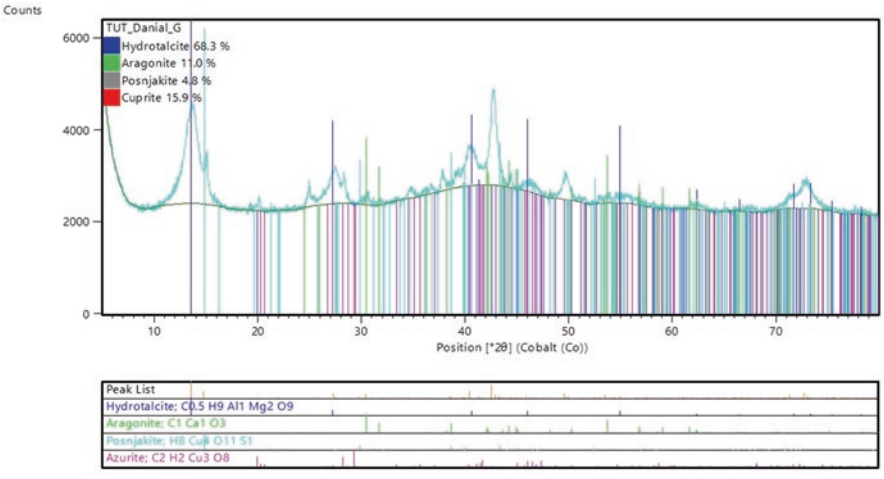

Fig. 6.8 XRD result of copper precursor obtained under 85 °C/340 rpm

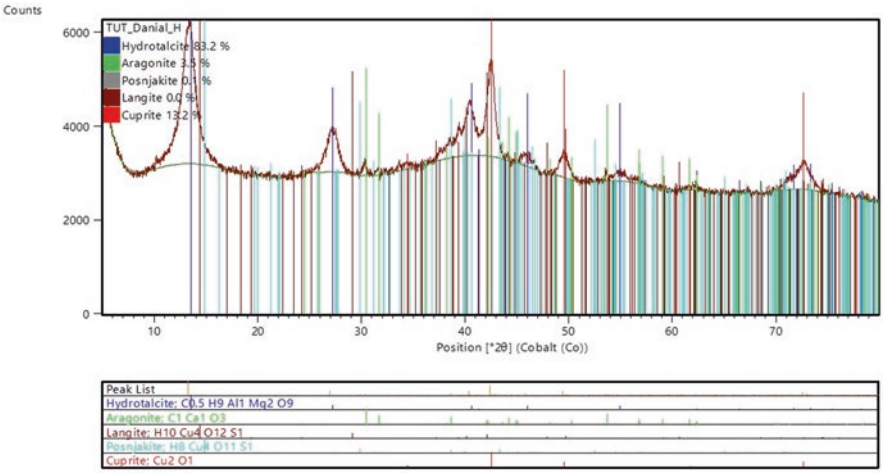

Fig. 6.9 XRD result of copper precursor obtained under 85 °C/740 rpm

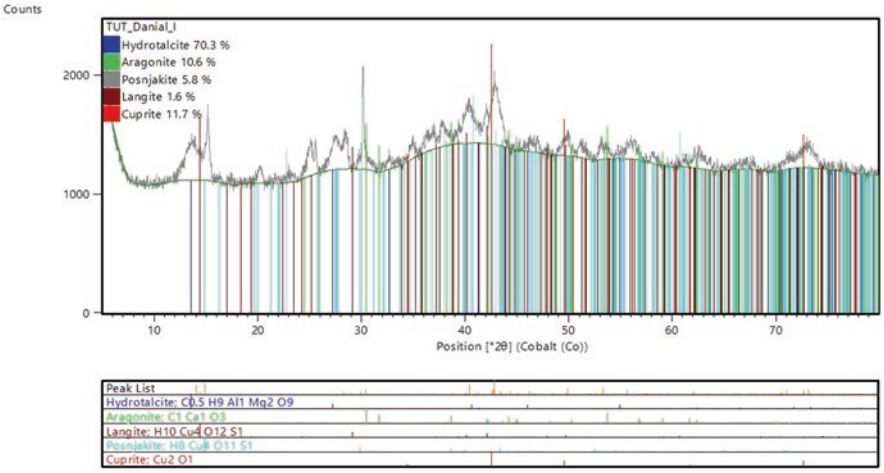

Fig. 6.10 XRD result of copper precursor obtained under 85 °C/480 rpm

6.3.1.10 Optimum TC for Production of Copper Precursor

It is shown that the amount of copper-containing compounds (CCC) in the copper precursor obtained from the PPLS of low-grade waste metal dust (i.e. CSD) can be measured accurately by using the TC of temperature and agitation speed (Table 6.2). Based on the results obtained (Table 6.5), the optimum TC that produced the highest CCC (20.7%) is 85 °C/340 rpm (Fig. 6.11).

The variation in percentage contents of hydrotalcite and aragonite in copper precursor can be seen in Table 6.5. Based on the results obtained in Table 7.5, the

highest combination of hydrotalcite (92.3%) and aragonite (2.7%) contents, none-copper-containing compounds is obtained under TC 55 °C/340 rpm (Fig. 6.12) while the least combination of hydrotalcite (68.3%) and aragonite (11.0%) contents is obtained under TC 85 °C/340 rpm (Fig. 6.12); this is consistent with the claim of optimum TC for production copper precursor is 85 °C/340 rpm (Table 6.5).

6.3.2 Mineralogy of Copper Oxide Nanoparticles

The copper precursor that was produced under optimum TC (Table 6.5) was used as the starting material for the production of the copper oxide nanoparticles (CuO-NPs). This copper precursor was subjected to the TC in Table 6.4. The results of the TC are reported in the subsequent part of this paper.

6.3.2.1 Mineralogy of CuO-NPs Produced under 650 °C/1 h

The XRD machine was used to characterize the crystal structure and phase purity of the CuO-NPs generated under TC of 650 °C/1 h (Table 6.4). Figure 6.13 demonstrates that exactly 47.2% of all the diffraction peaks were indexed to tenorite, while 12.5%, 15.4%, 16.0%, 5.4%, and 3.6% of the remaining peaks were indexed to the none-copper-containing compounds, which are magnetite, sodium aluminium phosphate, disodium calcium silicate, grossular ferrian, periclase, respectively.

Table 6.5 Percentage mineralogical composition of copper precursor

TC	Mineralogy of copper precursor					
	Hydrotalcite (%)	Aragonite (%)	Copper-containing compounds			TCCC (%)
			Posnjakite (%)	Langite (%)	Cuprite (%)	
25 °C/340 rpm	87.1	4.8	0.1	0.0	8.1	8.2
25 °C/740 rpm	82.9	5.0	0.1	0.0	12.1	12.2
25 °C/1480 rpm	86.5	4.5	0.1	0.0	9.0	9.1
55 °C/340 rpm	92.3	2.7	0.0	0.0	5.1	5.1
55 °C/740 rpm	88.1	3.0	0.1	0.0	8.8	8.9
55 °C/1480 rpm	89.5	2.6	0.3	0.1	7.5	7.9
85 °C/340 rpm	68.3	11.0	4.8	0.0	15.9	20.7
85 °C/740 rpm	83.2	3.5	0.1	0.0	13.2	13.2
85 °C/1480 rpm	70.3	10.6	5.8	1.6	11.7	19.1

Key: TCCC = Total copper-containing compounds

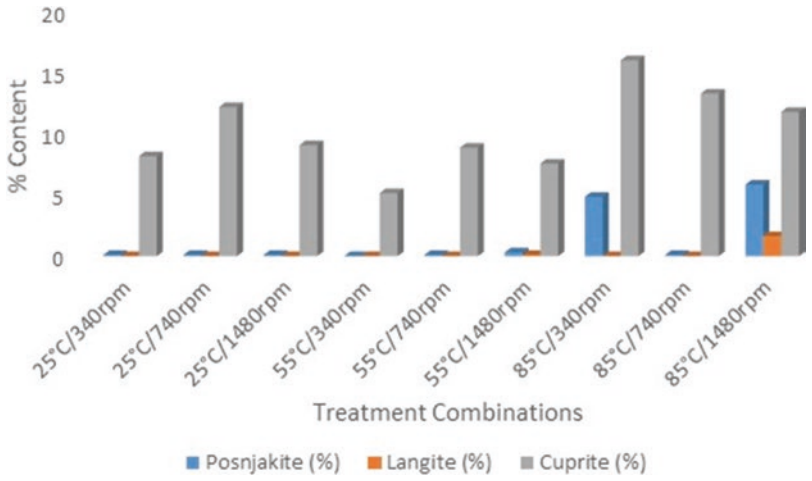

Fig. 6.11 Percentage content of copper-containing compounds in copper precursor at different TC

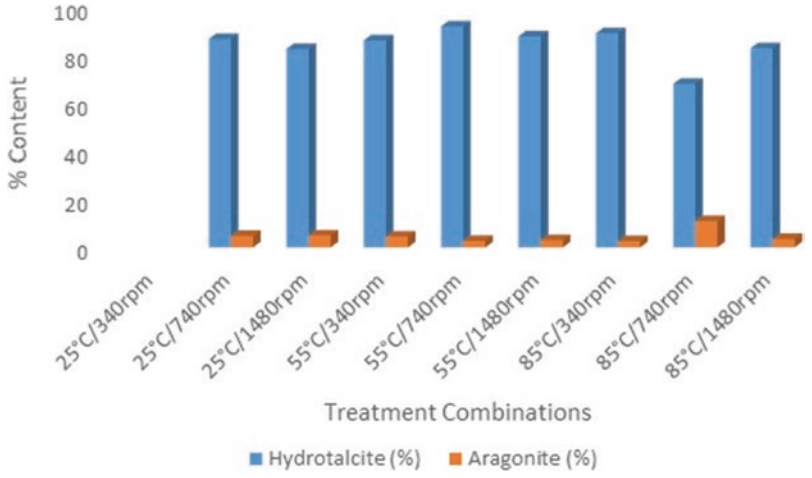

Fig. 6.12 Percentage content of hydrotalcite and aragonite in copper precursor at different TC

6.3.2.2 Mineralogy of CuO-NPs Produced under 650 °C/2 h

The CuO-NPs produced under TC of 650 °C/2 h (Table 6.4) were characterized in terms of their crystal structure and phase purity using an XRD machine. Figure 6.14 shows that exactly 46.7% of all the diffraction peaks were indexed to tenorite, while the remaining peaks were indexed to the non-copper-containing substances, such as magnetite, sodium aluminium phosphate, disodium calcium silicate, grossular ferrian, and periclase, at rates of 14.0%, 15.8%, 11.6%, 8.1%, and 3.8%, respectively.

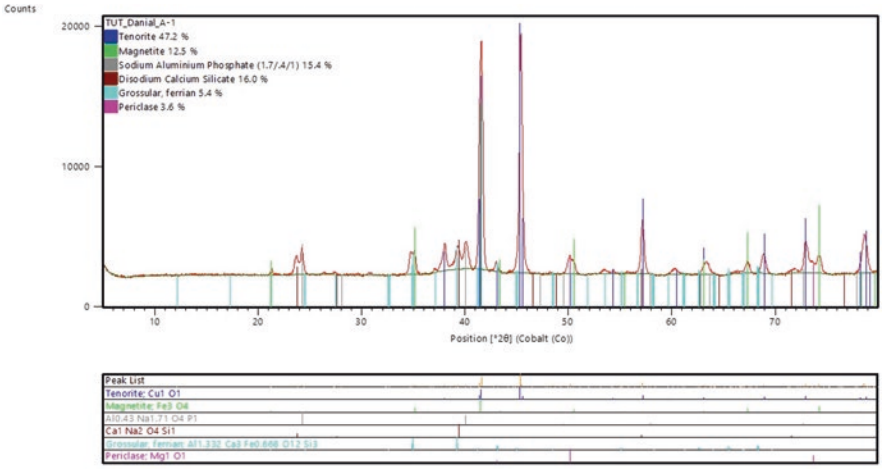

Fig. 6.13 XRD result of CuO-NPs obtained under 650 °C/1 h

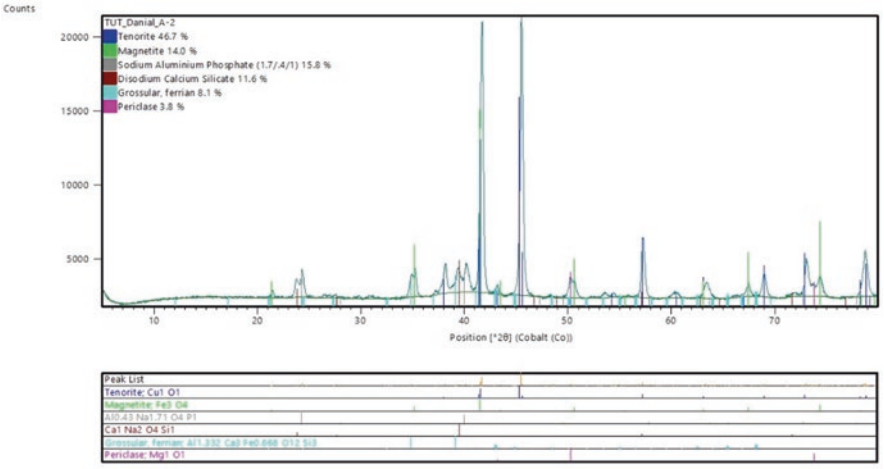

Fig. 6.14 XRD result of CuO-NPs obtained under 650 °C/2 h

6.3.2.3 Mineralogy of CuO-NPs Produced under 650 °C/3 h

Using the XRD machine, the CuO-NPs produced at TC of 650 °C/3 h (Table 7.4) were examined for their crystal structure and phase purity. Figure 6.15 demonstrates that exactly 50.1% of all the diffraction peaks were indexed to tenorite, while the remaining peaks were indexed, at percentages of 12.8%, 14.9%, 13.1%, 5.4%, and 3.8%, to the non-copper-containing materials, such as magnetite, sodium aluminium phosphate, disodium calcium silicate, grossular ferrian, and periclase, respectively.

6.3.2.4 Mineralogy of CuO-NPs Produced Under 750 °C/1 h

CuO-NPs generated at TC of 750 °C/1 h (Table 7.4) were subjected to XRD analysis to determine the crystal structure and phase purity. Figure 6.16 shows that exactly 48.7% of all the diffraction peaks were indexed to tenorite, while the remaining peaks were indexed to non-copper-containing compounds like magnetite, sodium aluminium phosphate, disodium calcium silicate, grossular ferrian, and periclase at percentages of 8.8%, 13.0%, 17.5%, 8.6%, and 3.4%, respectively.

6.3.2.5 Mineralogy of CuO-NPs Produced Under 750 °C/2 h

To ascertain the crystal structure and phase purity of CuO-NPs produced at TC of 750 °C/2 h (Table 6.4), XRD analysis was performed. Figure 6.17 demonstrates that exactly 51.3% of all diffraction peaks were assigned to tenorite, while the remaining peaks were assigned to non-copper-containing substances like magnetite, sodium aluminium phosphate, disodium calcium silicate, grossular ferrian, and periclase at percentages of 12.0%, 17.8%, 10.1%, 6.0%, and 2.7%, respectively.

6.3.2.6 Mineralogy of CuO-NPs Produced Under 750 °C/3 h

XRD examination was done to determine the crystal structure and phase purity of CuO-NPs produced at a TC of 750 °C/3 h (Table 6.4). According to Fig. 6.18, tenorite accounted for exactly 50.8% of all diffraction peaks, with the remaining peaks being assigned to non-copper-containing materials like magnetite, sodium aluminium phosphate, disodium calcium silicate, grossular ferrian, and periclase at percentages of 11.1%, 16.8%, 13.2%, 6.2%, and 1.9%, respectively.

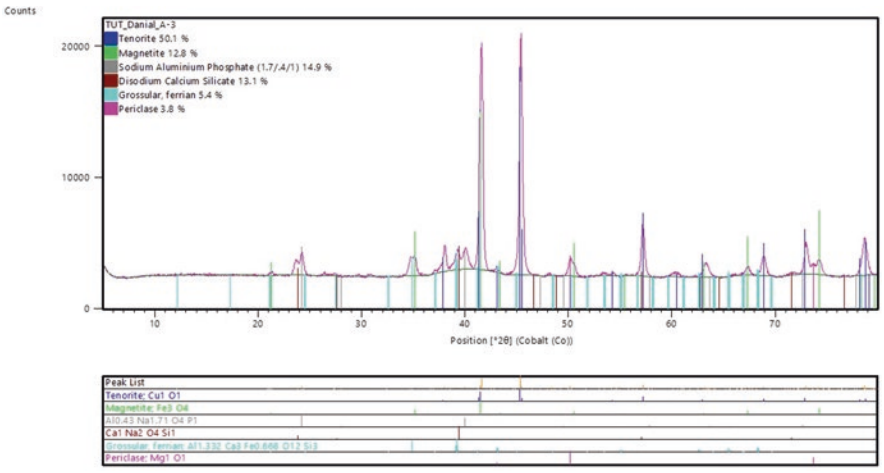

Fig. 6.15 XRD result of CuO-NPs obtained under 650 °C/3 h

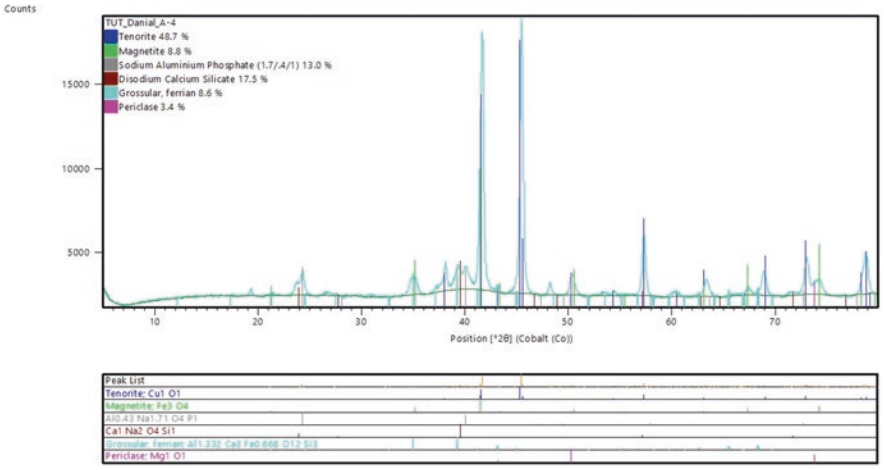

Fig. 6.16 XRD result of CuO-NPs obtained under 750 °C/1 h

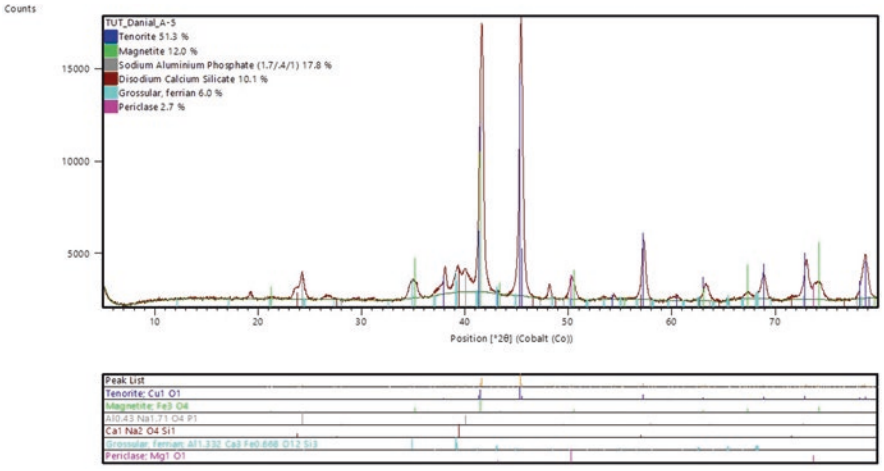

Fig. 6.17 XRD result of CuO-NPs obtained under 750 °C/2 h

6.3.2.7 Mineralogy of CuO-NPs Produced Under 850 °C/1 h

CuO-NPs generated at a TC of 850 °C/1 h (Table 6.4) were subjected to an XRD investigation to ascertain their crystal structure and phase purity. Tenorite accounted for exactly 51.3% of all diffraction peaks. The remaining peaks were ascribed to non-copper-containing substances such as magnetite, sodium aluminium phosphate, disodium calcium silicate, and grossular ferrian, at percentages of 14.4%, 17.7%, 11.4%, and 5.2%, respectively. These are all shown in Fig. 6.19.

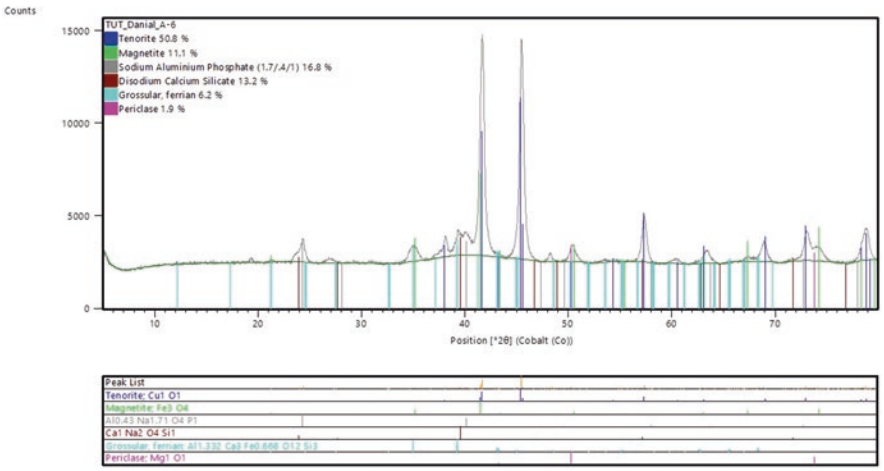

Fig. 6.18 XRD result of CuO-NPs obtained under 750 °C/3 h

6.3.2.8 Mineralogy of CuO-NPs Produced Under 850 °C/2 h

An XRD analysis was performed on CuO-NPs produced at a TC of 850 °C/2 h (Table 6.4) to determine their crystal structure and phase purity. Exactly 48.9% of all diffraction peaks were accounted for by tenorite. The remaining peaks, with percentages of 15.9%, 14.9%, 14.4%, and 5.9%, were attributed to non-copper-containing materials such as magnetite, sodium aluminium phosphate, disodium calcium silicate, and grossular ferrian. All of these are displayed in Fig. 6.20.

6.3.2.9 Mineralogy of CuO-NPs Produced Under 850 °C/3 h

CuO-NPs produced at a TC of 850 °C/3 h (Table 6.4) were subjected to an XRD investigation to ascertain their crystal structure and phase purity. Tenorite accounted for exactly 47.0% of all diffraction peaks. Non-copper-containing substances including magnetite, sodium aluminium phosphate, disodium calcium silicate, and grossular ferrian were blamed for the remaining peaks, which had percentages of 16.8%, 10.9%, 17.9%, and 7.5%. These are all shown in Fig. 6.21.

6.3.2.10 Optimum TC for Production of CuO-NPs

It is shown that the amount of copper compound (CC) in the CuO-NPs obtained from the copper precursor produced from the WCD can be measured accurately by using the TC of temperature and agitation speed (Table 6.4). Based on the results obtained (Table 6.6), the optimum TC that produced the highest CC (51.3%) is 750 °C/2 h (Fig. 6.22).

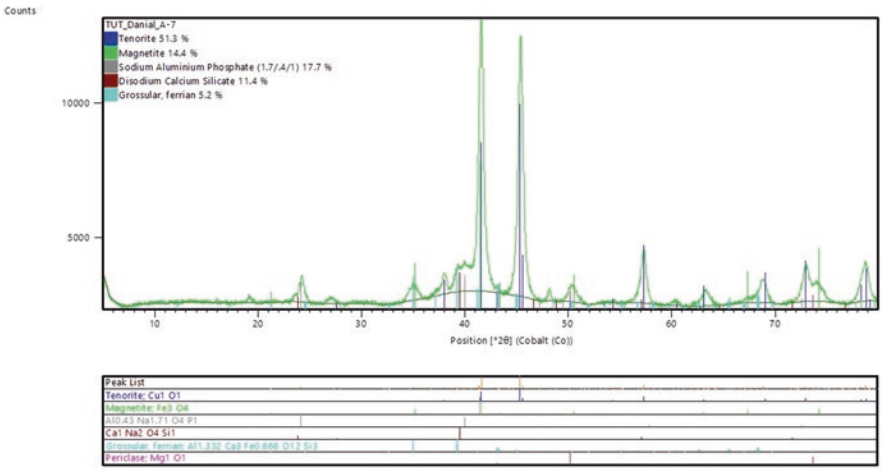

Fig. 6.19 XRD result of CuO-NPs obtained under 850 °C/1 h

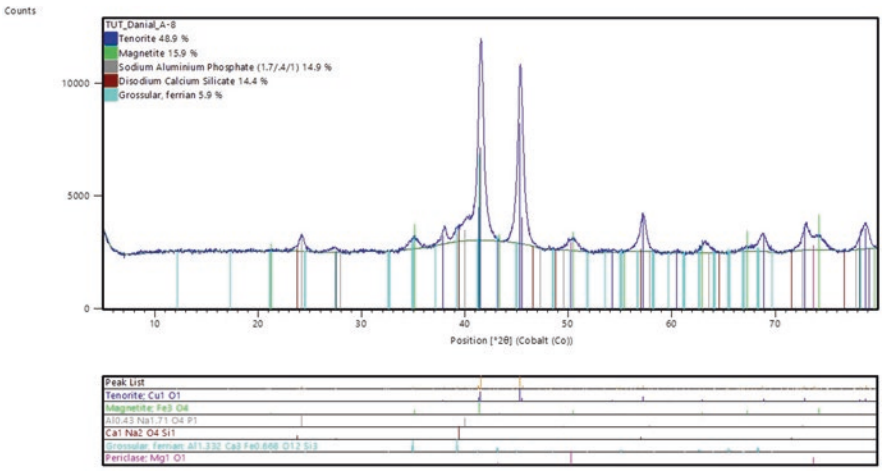

Fig. 6.20 XRD result of CuO-NPs obtained under 850 °C/2 h

The variation in percentage contents of magnetite, sodium aluminium phosphate, disodium calcium silicate, grossular ferrian, and periclase in CuO-NPs can be seen in Table 6.6. Based on the results obtained in Table 6.6, the highest combination of magnetite (14.0%), sodium aluminium phosphate (15.8%), disodium calcium silicate (11.6%), grossular ferrian (8.1%), and periclase (3.8%), none-copper-containing compounds (NCCC) is obtained under TC 650 °C/2 h (Fig. 6.23) while the least combination of magnetite (12.0%), sodium aluminium phosphate (17.8%), disodium calcium silicate (10.1%), grossular ferrian (6.0%), and periclase (2.7%) contents is obtained under TC 750 °C/2 h (Fig. 6.23); this is consistent with the claim of optimum TC for production Cu-NPs is 750 °C/2 h (Table 6.6).

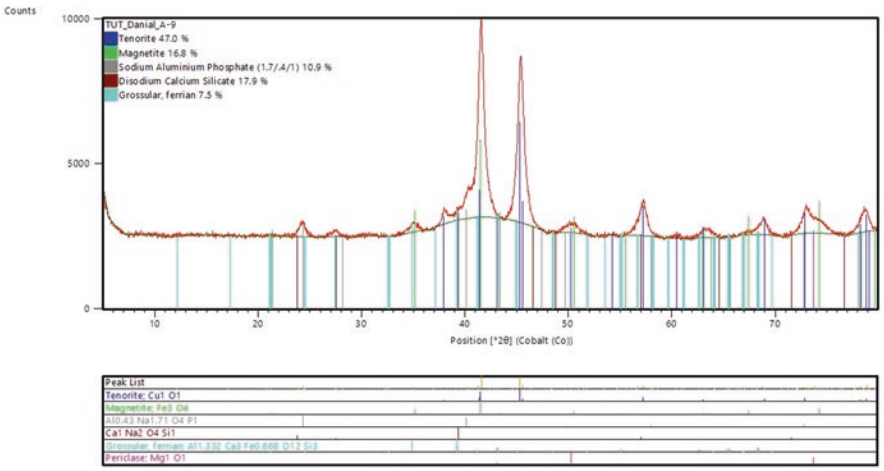

Fig. 6.21 XRD result of CuO-NPs obtained under 850 °C/3 h

Table 6.6 Summary of mineralogical composition of CuO-NPs at different TC

TC	Mineralogical composition of CuO-NPs						Total NCCC (%)
	Tenorite (%)	None-copper-containing compounds (NCCC)					
		Magnetite (%)	Sodium aluminium phosphate (%)	Disodium calcium silicate (%)	Grossular ferrian (%)	Periclase (%)	
650 °C/1 h	47.2	12.5	15.4	16.0	5.4	3.6	52.9
650 °C/2 h	46.7	14.0	15.8	11.6	8.1	3.8	53.3
650 °C/3 h	50.1	12.8	14.9	13.1	5.4	3.8	50.0
750 °C/1 h	48.7	8.8	13.0	17.5	8.6	3.4	51.3
750 °C/2 h	51.3	12.0	17.8	10.1	6.0	2.7	48.6
750 °C/3 h	50.8	11.1	16.8	13.2	6.2	1.9	48.2
850 °C/1 h	51.3	14.4	17.7	11.4	5.2	0.0	48.7
850 °C/2 h	48.9	15.9	14.9	14.4	5.9	0.0	51.1
850 °C/3 h	47.0	16.8	10.9	17.9	7.5	0.0	53.1

6.3.3 Characterization of CuO-NPs

6.3.3.1 SEM

The morphology of the CuO-NPs powder was examined using the SEM machine (Fig. 6.24). The SEM images indicate that the particles are flower like in shape. Temperature is observed to play an important part in the morphology of the developed CuO-NPs, presupposing that the shape of the CuO-NPs can be tuned by changing the temperature.

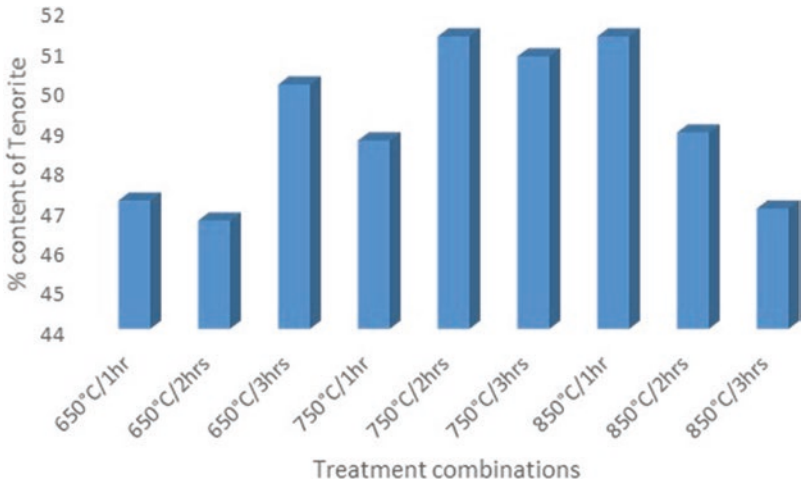

Fig. 6.22 Percentage content of CC in CuO-NPs at different TC

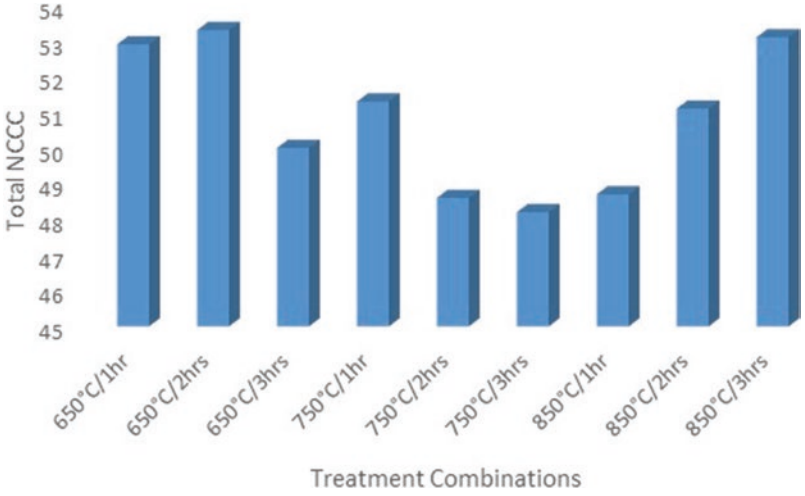

Fig. 6.23 Percentage content of NCCC in CuO-NPs at different TC

6.3.3.2 TEM

The TEM images in Fig. 6.25 show no specific defect and average crystallite size is estimated as 35 ± 5 nm. The TEM images indicate that the particles are cube like in shape.

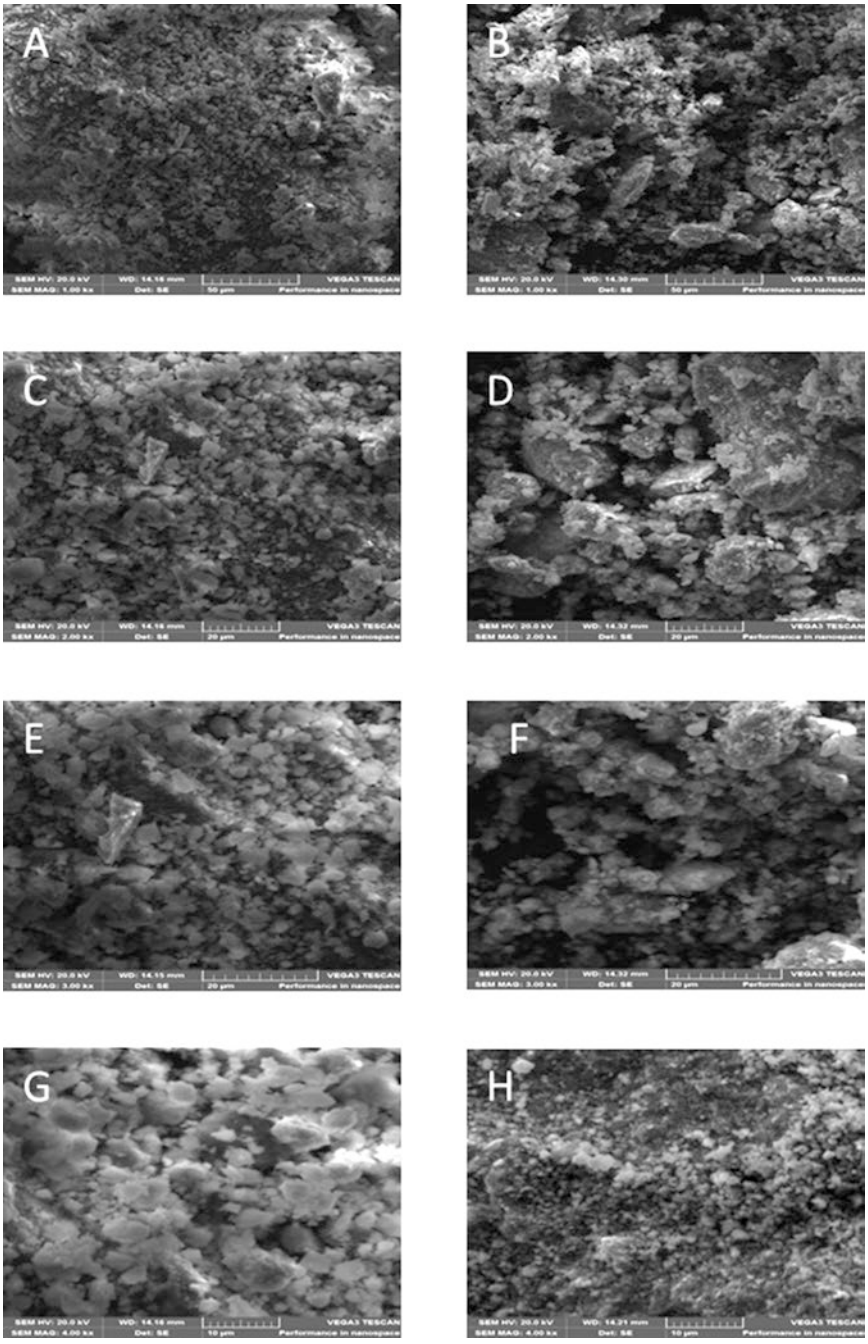

Fig. 6.24 SEM images showing the flower like shape of developed CuO-NPs observed under (**a** and **b**) 10, 000x, (**c** and **d**) 20,000×, (**e** and **f**) 30,000×, and (**g** and **h**) 40,000× magnifications

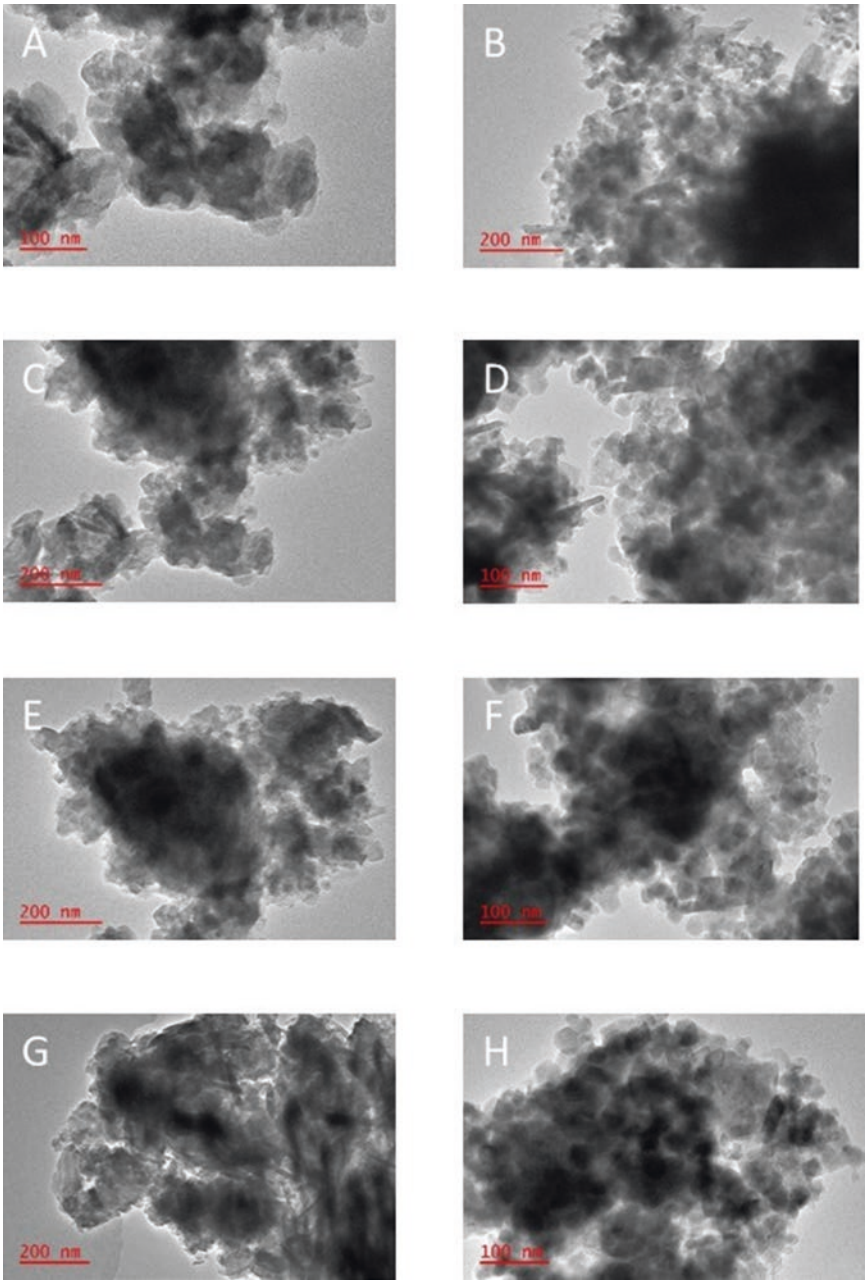

Fig. 6.25 TEM images of the CuO-NPs [A-H], produced from WCD

6.4 Conclusions

The aim of the study was to develop CuO-NPs from leach solution of low-grade WCD. Several deductions were reached in the course of this study. Amongst these deductions are the following:

1. The optimum TC that produced the highest copper-containing compounds in the copper precursor (20.7%) is 85 °C/340 rpm.
2. The optimum TC that produced the highest copper compound in the CuO-NPs (51.3%) is 750 °C/2 h.
3. Angulars to spherical CuO-NPs were successfully prepared by thermal decomposition method with mean diameter of 35 ± 5 nm.

These results represent a trend towards optimum experimental conditions aimed at maximizing CuO-NPs output and minimizing contaminants. It can be concluded that since this method does not require organic solvents, expensive raw materials, and complicated equipment, it is superior to the other methods for the synthesis of CuO-NPs from leach solution (i.e. $CuSO_4$ solution) of low-grade WCD.

Acknowledgements The author wishes to acknowledge the support received from Tshwane University of Technology, the Council for Scientific and Industrial Research, and National Research Foundation in Pretoria, South Africa.

References

1. D.O. Okanigbe, A.P.I. Popoola, A.A. Adeleke, Characterization of copper smelter dust for copper recovery. Procedia Manuf. **7**, 121–126 (2017)
2. X. Zhang, D. Zhang, X. Ni, J. Song, H. Zheng, Synthesis and electrochemical properties of different sizes of the CuO particles. J. Nanopart. Res. **10**(5), 839–844 (2008)
3. M.A. Rafea, N. Roushdy, Determination of the optical band gap for amorphous and nanocrystalline copper oxide thin films prepared by SILAR technique. J. Phys. D. Appl. Phys. **42**(1), 015413 (2008)
4. T. Kida, T. Oka, M. Nagano, Y. Ishiwata, X.G. Zheng, Synthesis and application of stable copper oxide nanoparticle suspensions for nanoparticulate film fabrication. J. Am. Ceram. Soc. **90**(1), 107–110 (2007)
5. N. Topnani, S. Kushwaha, T. Athar, Wet synthesis of copper oxide nanopowder. Int. J. Green Nanotechnol. Mater. Sci. Eng. **1**(2), M67–M73 (2010)
6. M.A. Dar, Y.S. Kim, W.B. Kim, J.M. Sohn, H.S. Shin, Structural and magnetic properties of CuO nanoneedles synthesized by hydrothermal method. Appl. Surf. Sci. **254**(22), 7477–7481 (2008)
7. J. Wang, S. He, Z. Li, X. Jing, M. Zhang, Synthesis of claw-like CuO and its catalytic activity in the thermal decomposition of ammonium perchlorate. Mater. Sci. Pol. **27**(2), 501–507 (2009)
8. X. Zhang, D. Zhang, X. Ni, H. Zheng, Optical and electrochemical properties of nanosized CuO via thermal decomposition of copper oxalate. Solid State Electron. **52**(2), 245–248 (2008)
9. C. Li, Y. Yin, H. Hou, N. Fan, F. Yuan, Y. Shi, Q. Meng, Preparation and characterization of Cu(OH)2 and CuO nanowires by the coupling route of microemulsion with homogenous precipitation. Solid State Commun. **150**(13–14), 585–589 (2010)

10. B.J. Hansen, N. Kouklin, G. Lu, I.K. Lin, J. Chen, X. Zhang, Transport, analyte detection, and opto-electronic response of p-type CuO nanowires. J. Phys. Chem. C **114**(6), 2440–2447 (2010)
11. C.T. Hsieh, J.M. Chen, H.H. Lin, H.C. Shih, Field emission from various CuO nanostructures. Appl. Phys. Lett. **83**(16), 3383–3385 (2003)
12. C.C. Li, M.H. Chang, Colloidal stability of CuO nanoparticles in alkanes via oleate modifications. Mater. Lett. **58**(30), 3903–3907 (2004)
13. M.H. Chang, H.S. Liu, C.Y. Tai, Preparation of copper oxide nanoparticles and its application in nanofluid. Powder Technol. **207**(1–3), 378–386 (2011)
14. S. Anandan, X. Wen, S. Yang, Room temperature growth of CuO nanorod arrays on copper and their application as a cathode in dye-sensitized solar cells. Mater. Chem. Phys. **93**(1), 35–40 (2005)
15. X.P. Gao, J.L. Bao, G.L. Pan, H.Y. Zhu, P.X. Huang, F. Wu, D.Y. Song, Preparation and electrochemical performance of polycrystalline and single crystalline CuO nanorods as anode materials for Li ion battery. J. Phys. Chem. B **108**(18), 5547–5551 (2004)
16. C.L. Carnes, K.J. Klabunde, The catalytic methanol synthesis over nanoparticle metal oxide catalysts. J. Mol. Catal. A Chem. **194**(1–2), 227–236 (2003)
17. Y. Kobayashi, T. Maeda, K. Watanabe, K. Ihara, Y. Yasuda, T. Morita, Preparation of CuO nanoparticles by metal salt-base reaction in aqueous solution and their metallic bonding property. J. Nanopart. Res. **13**(10), 5365–5372 (2011)
18. L. Sun, Z. Zhang, Z. Wang, Z. Wu, H. Dang, Synthesis and characterization of CuO nanoparticles from liquid ammonia. Mater. Res. Bull. **40**(6), 1024–1027 (2005)
19. P.J. Cai, M. Shi, Large scale synthesis of shuttle like CuO nanocrystals by microwave irradiation, in *Advanced Materials Research*, vol. 92, (Trans Tech Publications Ltd., 2010), pp. 117–123
20. D. Han, H. Yang, C. Zhu, F. Wang, Controlled synthesis of CuO nanoparticles using Triton X-100-based water-in-oil reverse micelles. Powder Technol. **185**(3), 286–290 (2008)
21. R. Ranjbar-Karimi, A. Bazmandegan-Shamili, A. Aslani, K. Kaviani, Sonochemical synthesis, characterization and thermal and optical analysis of CuO nanoparticles. Phys. B Condens. Matter **405**(15), 3096–3100 (2010)
22. N. Liu, D. Wu, H. Wu, C. Liu, F. Luo, A versatile and "green" electrochemical method for synthesis of copper and other transition metal oxide and hydroxide nanostructures. Mater. Chem. Phys. **107**(2–3), 511–517 (2008)
23. Q. Liu, H. Liu, Y. Liang, Z. Xu, G. Yin, Large-scale synthesis of single-crystalline CuO nanoplatelets by a hydrothermal process. Mater. Res. Bull. **41**(4), 697–702 (2006)
24. W. Jia, E. Reitz, P. Shimpi, E.G. Rodriguez, P.X. Gao, Y. Lei, Spherical CuO synthesized by a simple hydrothermal reaction: Concentration-dependent size and its electrocatalytic application. Mater. Res. Bull. **44**(8), 1681–1686 (2009)
25. W. Jisen, Y. Jinkai, S. Jinquan, B. Ying, Synthesis of copper oxide nanomaterials and the growth mechanism of copper oxide nanorods. Mater. Des. **25**(7), 625–629 (2004)
26. W. Wang, Y. Zhan, X. Wang, Y. Liu, C. Zheng, G. Wang, Synthesis and characterization of CuO nanowhiskers by a novel one-step, solid-state reaction in the presence of a nonionic surfactant. Mater. Res. Bull. **37**(6), 1093–1100 (2002)
27. F. Bakhtiari, Synthesis and characterization of tenorite (CuO) nanoparticles from smelting furnace dust (SFD). J. Min. Metall. B Metall. **49**(1), 21–21 (2013)
28. J. Zhu, D. Li, H. Chen, X. Yang, L. Lu, X. Wang, Highly dispersed CuO nanoparticles prepared by a novel quick-precipitation method. Mater. Lett. **58**(26), 3324–3327 (2004)
29. R. Wu, Z. Ma, Z. Gu, Y. Yang, Preparation and characterization of CuO nanoparticles with different morphology through a simple quick-precipitation method in DMAC–water mixed solvent. J. Alloys Compd. **504**(1), 45–49 (2010)
30. R. Ahmadi, M.H. Hosseini, A. Masoudi, Avrami behavior of magnetite nanoparticles formation in co-precipitation process. J. Min. Metall. B Metall. **47**(2), 211–218 (2011)
31. H. Fan, L. Yang, W. Hua, X. Wu, Z. Wu, S. Xie, B. Zou, Controlled synthesis of monodispersed CuO nanocrystals. Nanotechnology **15**(1), 37 (2003)

32. F. Bakhtiari, E. Darezereshki, One-step synthesis of tenorite (CuO) nano-particles from Cu4(SO4)(OH)6 by direct thermal-decomposition method. Mater. Lett. **65**(2), 171–174 (2011)
33. S. Thimmaiah, M. Rajamathi, N. Singh, P. Bera, F. Meldrum, N. Chandrasekhar, R. Seshadri, A solvothermal route to capped nanoparticles of γ-Fe2O3 and CoFe2O4. J. Mater. Chem. **11**(12), 3215–3221 (2001)
34. J. Yang, G.H. Cheng, J.H. Zeng, S.H. Yu, X.M. Liu, Y.T. Qian, Shape control and characterization of transition metal diselenides MSe2 (M=Ni, Co, Fe) prepared by a solvothermal-reduction process. Chem. Mater. **13**(3), 848–853 (2001)
35. K. Byrappa, M. Yoshimura, *Handbook of Hydrothermal Technology* (William Andrew, 2012)
36. A. Umer, S. Naveed, N. Ramzan, M.S. Rafique, Selection of a suitable method for the synthesis of copper nanoparticles. Nano **7**(05), 1230005 (2012)
37. K. Byrappa, Growth of quartz crystals, in *Bulk Crystal Growth of Electronic, Optical and Optoelectronic Materials*, (Wiley, 2005), pp. 387–406
38. E. Darezereshki, F. Bakhtiari, A novel technique to synthesis of tenorite (CuO) nanoparticles from low concentration CuSO4 solution. J. Min. Metall. B Metall. **47**(1), 73–78 (2011)
39. D.O. Okanigbe, Production of copper and copper oxide nano-particles from leach solution of low grade copper smelter dust. Thesis, Dissertation, 2019.
40. S. Makaka, M. Aziz, A. Nesbitt, Copper recovery in a bench-scale carrier facilitated tubular supported liquid membrane system. J. Min. Metall. B Metall. **46**, 67 (2010)
41. N. Koga, J.M. Criado, H. Tanaka, Reaction pathway and kinetics of the thermal decomposition of synthetic brochantite. J. Therm. Anal. Calorim. **49**(3), 1467–1475 (1997)

Part IV
Thermal and Mechanical Properties

Chapter 7
Thermal and Mechanical Properties (I): Optimum Predictive Thermal Conduction Model Development for Epoxy-Filled Copper Oxide Nanoparticles Composite Coatings on Spent Nuclear Fuel Steel Casks

Daniel Ogochukwu Okanigbe and Shade Rouxzeta Van Der Merwe

7.1 Introduction

Nuclear reactors use radioactive elements to generate power [1, 2]. While the by-product of generating energy from radioactive materials is known as spent nuclear fuels (SNF) [3, 4], it is anticipated that this waste will be safely stored and disposed of following conditioning and treatment [5–7]. Consequently, one of the biggest issues facing the nuclear industry is SNF management [8, 9]. All transportation casks are anticipated to be built to comply with radiation safety regulations as part of managing SNF [10–12].

Therefore, type B casks (Fig. 7.1) are used to transport SNF assemblies in order to comply with requirements that restrict radiation leaks and doses that represent a risk to the general public's health and safety as well as the environment [13–16]. The casks are made of steel (or a steel and lead alloy) and are shielded [17–19]. The steel is typically around 30 cm thick and protects the fuel element while shielding the casks from radiation.

It has been discovered that the deposition of radioactive salts during spent fuel transportation frequently results in high-radiation levels in casks. The technique of

D. O. Okanigbe (✉)
Department of Chemical, Metallurgical and Materials Engineering, Faculty of Engineering and the Built Environment, Tshwane University of Technology, Pretoria, South Africa

Pantheon Virtual Engineering Solutions, Nigel, South Africa
e-mail: okanigbedo@tut.ac.za; okanigbeogochukwu@gmail.com

S. R. Van Der Merwe
Department of Mechanical and Mechatronics Engineering, Faculty of Engineering and the Built Environment, Tshwane University of Technology, Pretoria, South Africa
e-mail: vandermerweR1@tut.ac.za

D. O. Okanigbe, A. P. Popoola (eds.), *Resource Recovery and Recycling from Waste Metal Dust*, https://doi.org/10.1007/978-3-031-22492-8_7

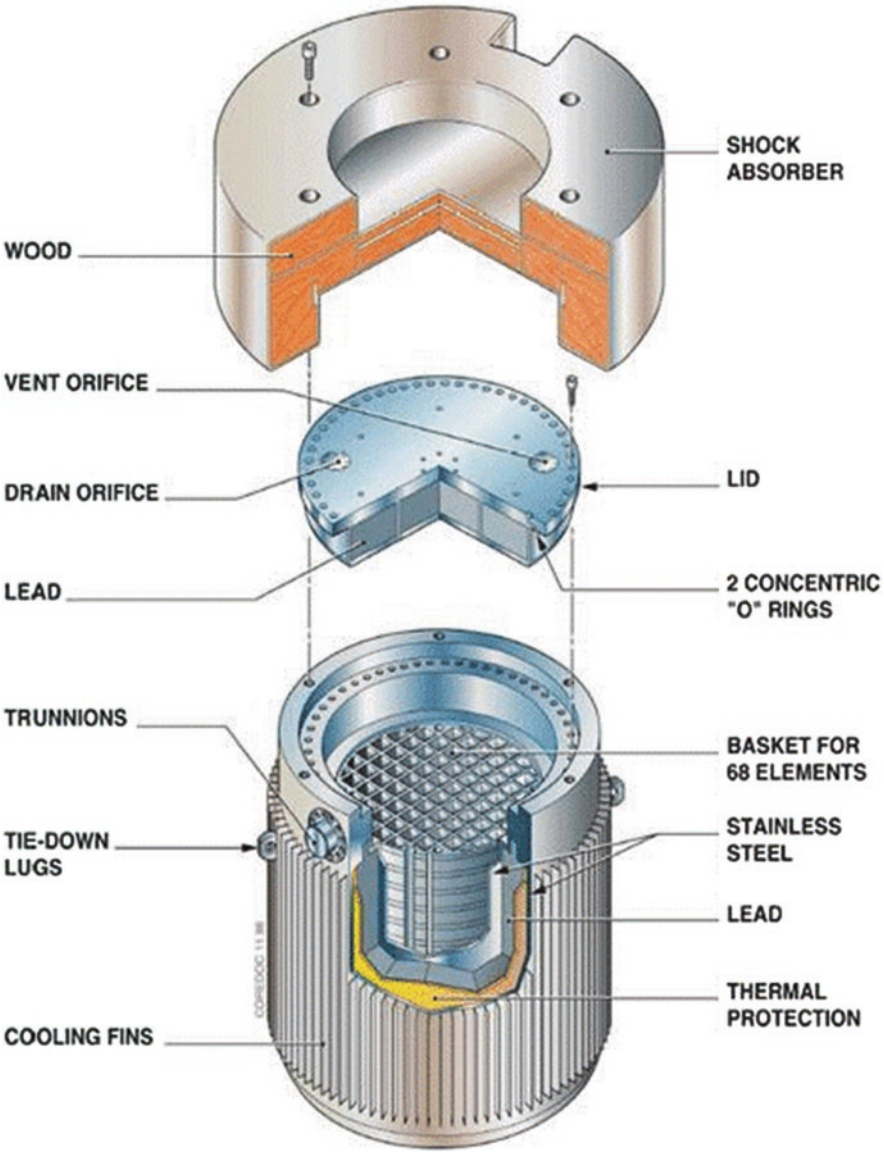

Fig. 7.1 A typical type B SNF transportation cask. (Source: Google image)

eliminating these salts involves sanding, which involves directing an airstream filled with sand toward areas where they have gathered and there is a lot of radiation since this causes mechanical corrosion in those areas [20].

In accordance with Shkoukani Al-Qous [21], steel is exposed to radiation both internally and externally. As a result, the cumulative gamma irradiation effect on steel corrosion behavior results in a rise in corrosion rate with increasing irradiation dose.

As was previously indicated, the corrosion of the steel used to protect the casks (Fig. 7.1) can cause significant economic losses as well as potential safety issues [22]. Surface coating has frequently been employed to protect the steel casks from mechanical and biological corrosion in order to alleviate these issues. However, surface coatings have a low resistance to electrolyte diffusion, which prevents them from offering long-term protection against corrosion [23]. As a result, numerous recent studies have been carried out to enhance these coatings' anticorrosion abilities [20, 24, 25].

Tensile stress, a corrosive environment, and a susceptible material are the three prerequisites for corrosion of steel casks, according to Ross et al. [26]. When assessing corrosion susceptibility, it is important to comprehend and take these circumstances into account. The three criteria will eventually be met in dry storage of SNF, according to previous studies [27–35].

Knight et al. [16] emphasized the significance of a material that is vulnerable to corrosion. The majority of SNF canisters is constructed of 304 stainless steel, which means that weld residual tensile stresses are adequate for corrosion to occur and that a corrosive environment has the potential to develop, according to the researchers. The presence of a chloride-rich brine on the surface of SNF canisters poses the greatest risk for corrosion [36–46].

By reducing or completely eliminating the interaction of a corrosive brine with the canister surface, the researchers continued to emphasize the significance of surface coating materials in the prevention, mitigation, and repair potential of corrosion. By separating the metal surface from the corrosive environment on the coated canister surface, an efficient coating would do away with the chance of corrosion. By acting as a physical barrier that restricts mass transfer to the metal substrate, the majority of coatings either isolate the metal surface from exposure to aggressive chemistry or prevent corrosion by using corrosion inhibitors, such as organic inhibitors (i.e., organic coatings). Organic inhibitors protect the metal by forming a hydrophobic film on the metal surface. The chemical make-up, molecular structure, and surface affinities of this class of inhibitors all affect how effective they are.

These anticorrosion coatings must, however, have excellent thermal conductivity properties as prescribed by the energy application (i.e., steel cask for transportation of SNF). A composite made of thermally conductive nano- or micro-sized particles spread in a polymer matrix is therefore one of the most efficient ways to create a thermally functional layer [47–51]. In terms of cost and mass production, copper oxide (CuO), which is dark and has a high emissivity of more than 0.9, stands out among these materials and is a potential option for altering the metal heat sink surface to enhance heat dissipation in passive cooling [52].

By creating nanocomposite coatings and adding inorganic nano-fillers to the coating composition, the characteristics of organic coatings can be further enhanced [53]. The most often utilized inorganic nano-sized reinforcing fillers include carbon nanotubes, copper, zinc, titanium, magnesium, and gold [54, 55]. In terms of thermal stability, mechanical, electrical, and catalytic capabilities, these hybrid coatings are discovered to be superior. The enhancement of these properties is due to the robust interfacial interaction between the polymer and the inorganic components,

which results from the substantial specific surface area of the nano-sized inorganic components [56]. However, to create hybrid materials with desired qualities, a homogenous dispersion of the inorganic fillers must be attained inside the polymer matrix [57].

Additionally, because the contact between the coating layer and the metal surface depends on mechanical interlocking, bonding that is not at the atomic or molecular level, showing high-interfacial thermal resistance, and as an example, polymer/ceramic composite coating significantly increases the interfacial thermal resistance on the metal surface [58–62].

Up until this point, numerous researchers have created a variety of thermally conductive polymers and their composites using filled type [63]. The thermal conductivity coefficient (λ) values of these polymers and their composites fall short of expectations, which has become the main bottleneck for their energy applications.

Due to this, several types of copper oxide nanoparticles (CuO-NPs) will be produced in the proposed study from concentrates acquired during the density separation of waste copper dust (WCD), depending on their copper oxide, aluminum oxide, and silicon oxide contents [64]. This class of organic–inorganic composite coating will be studied to better understand the phenomenon of interfacial thermal resistance, an understanding that should assist with improving the coating's performance when used as a surface coating on steel casks during the transportation of SNF [65, 66]. These various compositions of CuO-NPs will be used to create an epoxy/CuO-NPs composite coating.

7.2 Problem Statement

The following basic discussions pertain to steel containers used to transport SNF and its surface coating:

1. Despite the enormous research efforts, there are still problems with the current hydrophobic coating methods, including poor mechanical strength and limited durability [54].
2. Despite numerous attempts to prepare a variety of thermally conductive epoxy composites using filler type [67], these epoxy composites frequently struggle to meet expectations in terms of their thermal conductivity coefficient values, which restrict their use in energy applications [68].
3. Epoxy composites with a higher filler content display deposition and agglomeration in the polymer matrix, which leads to poor adhesion between the filler particles and epoxy resin and reduced mechanical strength and durability [69].

7.3 Research Objectives

7.3.1 Main Objective

Investigating the interfacial thermal resistance and anticorrosion performance of CuO-NPs-Epoxy composite coatings from WMD on SNF steel casks is the main objective of this study.

7.3.2 Sub-Objectives

By responding to the following research questions provided as sub-objectives, the main goal will be accomplished:

1. What is WCD's characteristics?
2. What makes up the concentrates and tailings produced by the WCD density separation?
3. What is the makeup of the leach solutions made from the various concentrate compositions?
4. What is the makeup of the copper precursor produced by the chemical reaction between reagents and leach solutions?
5. What makes up the CuO-NPs created by the thermal breakdown of various copper precursors?
6. What is the interfacial thermal resistance of the hybrid nanocomposite coatings made by adding different compositions of CuO-NPs to epoxy resin?
7. What is the anticorrosion behavior of hybrid nanocomposite coatings made by adding various compositions of CuO-NPs to epoxy resin?
8. What are the CuO-NPs/epoxy composite coatings' calculated and predicted thermal conductivity value (λ) for the given system?

7.4 Research Hypotheses

On the basis of the model proposed to overcome the challenges noted, the following can be hypothesized:

1. Decreased thermal resistance between surfaces.
2. Hybrid coatings' improved anticorrosion behavior.
3. Decreased cost of hybrid coating production.
4. Utilization of the earth's mineral resources sustainably.

7.5 Significance of Study

The positive outcome of this research will be advantageous to the following areas:

1. Creation of a hybrid coating that enables the economical design of superb thermally conductive steel containers for the transfer of SNF.
2. The earth's ability to support life despite other deteriorating environmental factors, while also providing WCD as a natural resource replacement for copper-based surface exploration.
3. Using an economical and effective approach of fabrication and processing to create hybrid coatings for steel barrel designs.

7.6 Literature Review

7.6.1 Background and Literature Survey

7.6.1.1 Background

Transportation of SNF

Every year, about 20 million transports of radioactive materials are made worldwide. However, shipping of materials used in the production of electricity make up a very minor portion of all radioactive material shipments made globally. The global transportation of used nuclear fuel has been done safely. No incident or mishap involving the transfer of SNF in the past 45 years has had a substantial radiological effect on either people or the environment. To date, used nuclear fuel has been shipped throughout the globe in excess of 80,000 tons.

Strong international transportation standards that have been approved and implemented by national regulatory programs are directly responsible for the industry's great safety record. According to the laws, radioactive material packages and casks must meet performance standards that are appropriate for the level of risk posed by the substances they are intended to hold. Extra-regulatory testing of radioactive material transportation packages and casks as well as investigations into serious, non-radioactive accident cases have shown that the current regulatory system is effective and that it is safe to transport radioactive materials, including SNF.

In some circumstances, such as transfer to another storage facility or transportation to a central storage location, a cask may need to be transported from one storage location to another storage location. This may be due to economic factors, such as enabling the full decommissioning of the facilities at a reactor site, or political factors such as the political consolidation of storage facilities in a given region or nation.

A cask could occasionally need to be moved from the storage location to the repository. The architecture of the disposal facility and the type of storage

technology to be employed both need to be taken into account. Some storage methods used in the US were based on sealed canisters enclosed in concrete storage casks, with the idea being that the canister would act as a containment boundary in the repository rather than requiring the fuel to be unloaded.

However, if the container design does not completely satisfy the standards for the repository or the geological environment in which the fuel will be stored, repackaging of containers may be necessary. Before being disposed of, the fuel is to be repackaged in multipurpose containers or casks, according to alternative repository designs. This idea will be applied in Germany where casks will be accepted at the Pilot Conditioning Plant. There, the spent fuel will be removed from the storage cask and consolidated before being repackaged into disposal casks for disposal in a subterranean repository.

Types of Casks for Transportation of SNF

To specify safety requirements that offer an adequate level of control over radiological dangers, regulations controlling the packaging of radioactive materials have been devised. The laws utilize a graduated approach to the packing requirements because not all radioactive dangers are equal (radiopharmaceuticals used in medicine do not present the same hazard as an SNF).

The packing of radioactive materials depends on the material's classification before it is transported. Excepted, industrial (Type IP), Type A, Type B, and Type C are the five package categories.

Excepted Packages
Materials exhibiting negligible radiological dangers, such as shipments of radiopharmaceuticals, are covered by excepted packages.

Industrial Packages
Industrial packages (Type IP-1, Type IP-2, and Type IP-3) are intended to hold radioactive materials with low-activity levels or radioactive materials with difficult-to-spread radioactivity. The regulatory specifications for the three types of industrial packages range from meeting the general specifications for all packages (Type IP-1), to being able to withstand conditions that might be anticipated during normal transport (Type IP-3), such as falling from a moving vehicle or being struck by a sharp object. Industrial packages are primarily used for the transportation of radioactive ores, low- and intermediate-level radioactive waste, and unirradiated nuclear fuel.

Type A packages
Type A packages are frequently used for the transportation of small but large amounts of radioactive materials. However, the laws include a cap on how much radionuclides they can have. A variety of tests imitating typical transit conditions are performed on Type A packages. For the purpose of reducing possible dispersal in the case of an accident, packages with liquid contents must meet additional

standards. Radioisotopes used for medical diagnosis and some low- and intermediate-level radioactive waste are typical examples of items delivered in Type A packaging.

Type B packages

Type B packaging is necessary for the transportation of highly radioactive materials, such as radioactive sources used in medical imaging equipment, parts taken from nuclear reactor cores, and SNF (Figs. 7.2 and 7.3). Packaging designated as Type B must be able to withstand extreme accident circumstances without leaking or spilling. The relevant authorities or regulators of each nation where the packages are utilized must certify Type B package designs.

Type C packages

The 1996 revision of the IAEA regulations saw the introduction of Type C packages [70]. They are designed for the air transportation of extremely radioactive materials. This kind of bundle has not yet been created. The packaging design can differ greatly among any of the categories for radioactive materials. For instance, Type B packaging intended for used nuclear fuel are frequently very big and heavy, yet Type B packages intended for radioactive sources utilized in different industrial devices may be tiny enough to fit in a car's trunk.

The standards for packing, with the exception of Type C packages, are essentially irrespective of the mode of transportation, whether it is by road, rail, water, or air.

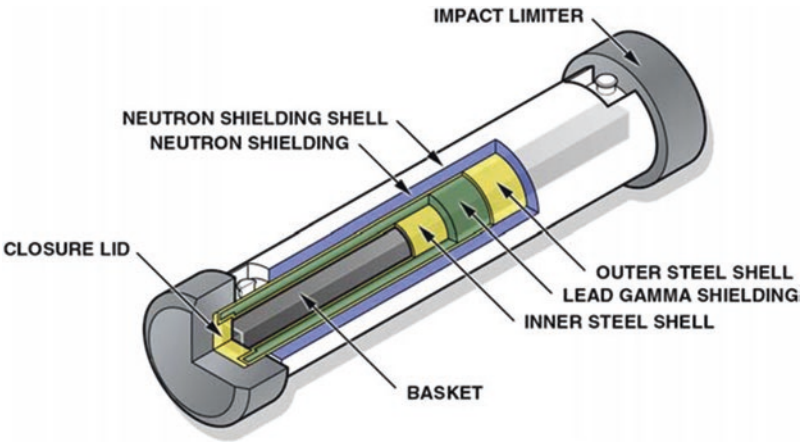

Fig. 7.2 A typical Type B Truck cask for transportation of spent nuclear fuel. (Source: Google image)

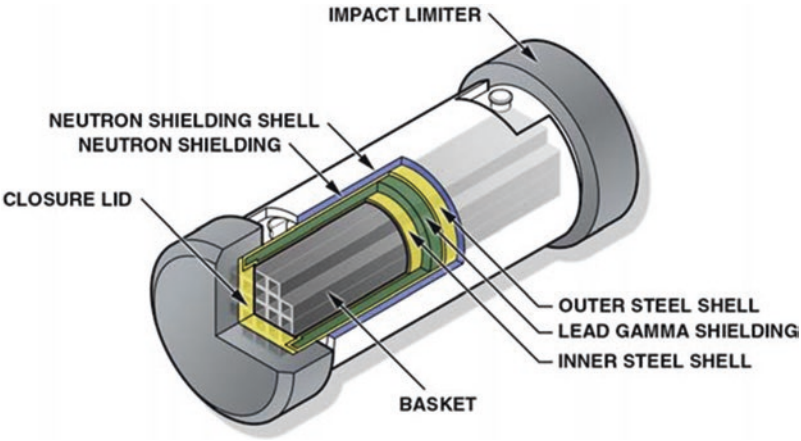

Fig. 7.3 A typical Type B rail cask for transportation of spent nuclear fuel. (Source: Google image)

Steel

In order to increase its strength and fracture resistance compared to other forms of iron, steel used in the production of casks is an alloy composed of iron with typically a few tenths of a percent of carbon. Many additional components could be included or added.

Modern steels are created using various alloy metal combinations to serve a variety of functions. 90% of steel is produced as carbon steel, which is only iron and carbon. To increase the hardenability of thick sections, low-alloy steel is alloyed with additional elements, typically molybdenum, manganese, chromium, or nickel, in amounts up to 10% by weight. In order to boost strength while only slightly raising price, high-strength low-alloy steel incorporates tiny additions (generally 2% by weight) of other elements, often 1.5% manganese.

Steel is susceptible to corrosion, which is caused by electrolysis, in which the metallic surface releases electrons into an electrolyte, such as a layer of moisture in the presence of oxygen. Because metals have a propensity to revert to their original states, this electrochemical reaction takes place.

Therefore, the following techniques are used to prevent corrosion in steel:

1. Store items properly. To considerably slow down rust, store metal products or parts in a low-moisture region or inside a temperature- and humidity-controlled environment.
2. Desiccant drying agents are also useful in this storage.
3. Surface coating, such as galvanizing, which involves dipping metals like iron or steel into a molten Zn metal bath to coat the metal surfaces.

Surface Coatings

Any mixture of film-forming components combined with pigments, solvents, and other additives is referred to as a surface coating. When applied to a surface, this mixture cures or dries to produce a thin film that is both useful and frequently beautiful. Paints, varnishes, enamels, oils, greases, waxes, concrete, lacquers, powder coatings, metal coatings, and fire-retardant formulas are all examples of surface coatings.

According to the composition of their binder, surface coatings are classified as organic or inorganic. Coatings with an organic binder are known as organic coatings. Coatings classified as inorganic contain an inorganic binder, such as a silicate. Surface coating is a method of surface engineering in which the surface of a material is covered with a different material, such as powder, film, or bulk, depending on the desired applications and the coating material.

The following are examples of common coating materials:

1. Pure metals, including Molybdenum (Mo), Copper (Cu), and Aluminum (Al).
2. Alloys like aluminum bronze (CuAl), nickel chrome (NiCr), nickel aluminum (NiAl), etc.
3. Ceramic (Oxide), such as Zirconium Oxide (ZrO_2), Titanium Oxide (TiO_2), Aluminum Oxide (Al_2O_3), etc.
4. Polymers like urethane, silicone, acrylic, phenolic resins, nitrocellulose, and epoxy, as well as natural and synthetic rubber.

Epoxy Coatings

Steel will rust and corrode if it is not protected from the elements. One of the most popular steel coatings in the industrial and marine sectors is epoxy. Epoxy coating is used to add an additional layer of protection to steel. A polyamine hardener and an epoxy resin are the two different components that make up an epoxy coating (also known as a catalyst). When combined, the resin and hardener undergo a chemical reaction that causes the components to cross-link as the mixture dries.

Epoxies are known for having excellent adhesion to steel and provide good chemical resistance. They are also often sold as “surface tolerant”, which means they will adhere well to surfaces with minimal surface preparation.

However, the following qualities should be stated and considered when choosing a coating for steel casks (both interior and external):

1. Reliability,
2. Cleanliness,
3. Emission and Absorption,
4. Capability of touch-up and repairs on the loaded (warm) casks.

7.6.2 Literature Survey

7.6.2.1 Introduction

Because of their low cost, high-specific strength/modulus, easy processing, great chemical stability, and light weight, polymers like epoxy-resin are frequently employed as coating materials in the energy sector [71]. Epoxy has good anticorrosion properties, but its λ values, 0.18–0.44 W m^{-1} K^{-1}, are frequently low and cannot meet the demands of highly efficient and quick thermal conduction/dissipation from components like the steel casks used in storage and transportation of SNF [72].

Therefore, the study and development of epoxy and their composites with high-thermal conduction/dissipation capabilities and excellent mechanical properties have urgent theoretical relevance and real-world application values for the development of materials in the energy domains. According to the method of preparation, thermally conductive polymer coatings can be split into two categories: intrinsic type and filled type [67].

Intrinsically Thermally Conductive Epoxy (ITCE) Coatings

In order to increase the intrinsic thermal conductivities of the polymers, ITCE are obtained through special physical structures (such as orientation, liquid crystalline, and crystalline structure) by altering the structures of polymer chain units during the polymer synthesis and processing processes.

Filled-Type Thermally Conductive Epoxy (FTCE) Composites Coatings

FTCE are created by incorporating highly thermally conductive fillers into the polymer matrix and then physically blending the polymers to give them exceptional thermal conductivities.

7.6.2.2 Review of Publications on Anticorrosion Properties and Interfacial Thermal Resistance of Epoxy Composite Coatings

Anticorrosion Property of Epoxy Composites Coatings

Coatings are a frequent, practical, and preferred technique of preventing corrosion in metals [73]. Epoxy composite coatings with fillers have been widely employed as anticorrosion materials, claimed by Zhang et al. [74]. The Metal–Organic Frameworks (MOFs) are useful for a variety of industrial applications due to their unique and varied building units and customizable features [75]. Because of this,

organic polymer coatings based on graphene are used often nowadays as corrosion-prevention techniques.

Graphene and graphene oxide offer a wide range of potential uses in the field of metal protection due to their superior dispersion, chemical activity, and physical barrier capabilities [68], while their barrier features make them suitable for protecting materials [76]. The substantial potential of advanced nanomaterials like graphene oxide as smart containers for the controlled desorption of inhibitors and their performance as dual active/passive anti-corrosive agents in the polymeric composites have been recognized in recent studies by Keshmiri et al. [75]. The effectiveness of graphene and graphene oxide/polymer composite coatings as protective materials is significantly influenced by the interface design in the resin matrix [47].

Despite the extensive research efforts, the existing hydrophobic coating options still have issues, such as weak mechanical strength and limited endurance [54].

The homogenous, 50-m thick epoxy coatings and composite epoxy coatings with 2 wt% of 130-nm silica particles were successfully manufactured in earlier papers on MOF, according to the report by Conradi et al. [77] on austenitic stainless steel of the type AISI 316L. As shown by the increased hardness, increased surface roughness, and induced hydrophobicity, the silica particles were found to significantly improve the microstructure of the coating matrix. In a chloride-ion-rich environment, the silica/epoxy coating was also demonstrated to have excellent anticorrosive performance. This was shown by the fact that the zigzagging of the diffusion path open to the ionic species resulted in a lower rate of corrosion and a higher coating resistance.

Direct mixed oxidation was employed to produce polyaniline (PANI) nanofibers utilizing four various inorganic acids [78]. The findings showed that the Q235 steel is protected to varying degrees by the various composite coatings of PANI doped by various inorganic acids. In conclusion, both the morphology and counter-anion would have an impact on the anticorrosion effect of the doped PANI.

Ghahremani et al. [79] developed a special nano-carrier by modifying the MWCNT surface with polydopamine (PDA), chitosan (CH), and zinc cations. The epoxy coating was improved with the inclusion of the OMWCNT-PDA-CH-Zn nanocomposite, yielding remarkable barrier performance and stable corrosion retardation for nearly 9 weeks.

Motamedi et al.'s [80] innovative nano-pigment, which combines performance epoxy and a nanoceria-decorated cerium (III)-imidazole network (NC/CIN), is similar to a MOF. After 7 weeks of exposure of the intact coating to saline solution, the results showed that the epoxy composite containing NC/CIN offered exceptional barrier-inhibitive protection for mild steel in corrosive environments as well as self-repairing protective properties in the artificially defective nanocomposite (log |*Z*|10 mHz = 9.91 cm^2).

Titanium dioxide was used to make an epoxy composite (DGPMDAP/MDA/TiO2) in the work by Hsissou et al. [81] in order to examine its rheological and anticorrosion properties. The results showed that adding more TiO_2 improved the rheological properties of DGPMDAP/MDA/TiO2. The epoxy polymer with anticorrosion capabilities decaglycidyl pentamethylene dianiline of phosphorus

(DGPMDAP) displayed mixed-type inhibitor activity and had a maximum corrosive inhibition efficacy of 92% at 103 M (when stationary electrochemical method was used). However, the transient electrochemical method showed that, at 103 M of DGPMDAP, it was a 91% effective carbon steel inhibitor in 1 M HCl solution. The Langmuir isotherm was also used to predict how DGPMDAP adhered to the surface of carbon steel.

In a ground-breaking study by Lashgari et al. [82], ZIF-67 nanoparticles were developed and used as a corrosion inhibitor container to enhance the barrier/active corrosion protection capabilities of the epoxy coating. The protective performance of the ZIF-67 and ZIF-67@APS NPs filled epoxy composites was evaluated utilizing EIS, salt-fog, and cathodic delamination experiments. The coating resistance values of the ZIF-67 and ZIF-67@APS NPs loaded epoxy coatings fell from $3.49 \times 10^{10}\Omega.\ cm^2$ to $2.47 \times 10^{9}\Omega.\ cm^2$ and from $8.16 \times 10^{10}\Omega.\ cm^2$ to $5.78 \times 10^{9}\Omega.\ cm^2$, respectively, after 50 days of immersion. The active corrosion inhibition effect of the epoxy/ZIF-67@APS NPs was demonstrated using electrochemical results.

Chhetri et al. [83] presented an intercalation modification technique to improve the anticorrosion properties of polymeric coatings. The layered double hydroxide (LDH) reservoir was functionalized to increase LDH's interfacial adhesion with the polymer matrix and steel surfaces, and an inhibitor, molybdate, was intercalated to impart inhibitive characteristics. The electrochemical results showed that the addition of functionalized double hydroxide significantly increased the protective efficiency of the epoxy coating. The corrosion protection efficiency of the composite coating was raised by more than 98% and the corrosion rate was decreased by around 98% with the addition of 1 wt% of functionalized LDH.

Cao et al. [84] developed a nano-structured hybrid molecule with strong corrosion inhibitor encapsulating capability and the ability of controlled distribution of benzotriazole in order to simultaneously increase the hydrophobic property and corrosion resistance of epoxy coatings (BTA). Additionally, a film covering the Ce-metal organic frameworks (Ce-MOF), which were developed and used as nanocontainers, was made using tetraethyl orthosilicate (TEOS). The addition of benzotriazole to nanocontainers gave the coating system exceptional anti-corrosion performance. The breakthrough is that the tetraethyl orthosilicate membrane would split and produce pores in an acidic environment, uniformly releasing benzotriazole. This self-healing system used polymer coatings to effectively release a corrosion inhibitor under the control of pH. The results showed that the epoxy coatings with organic frameworks containing 3 wt% Ce-metal had the best anti-corrosion capabilities.

In a 3.5-wt% sodium chloride solution, Wu et al. [85] produced h-BN/SZP aqueous epoxy composite coatings and examined their corrosion protection efficacy. They achieved this by fusing the corrosion-inhibiting ability of strontium zinc phosphate (SZP) with the impermeability of hexagonal boron nitride (h-BN) nanosheets. The anti-corrosion performance of the coatings was evaluated using potential and impedance tests, fitting pore (pinhole) resistance, salt spray, and waterborne epoxy composite coatings applied to mild steels. The analysis of the synthesized (Fh-BN, SZP)/EP coating's localized electrochemical impedance spectroscopy (LEIS) and

corrosion byproducts suggested that the combined effects of h-physical BN's barrier function and SZP's inhibition were responsible for the coated mild steel's superior corrosion resistance. Our method offers a new protection mechanism in coatings for metallic substrates while advancing the fundamental research and industrial uses of h-BN nanosheets.

Interfacial Thermal Resistance of Epoxy Composite Coatings

In thermally conductive polymer composites, interfaces are crucial and significantly affect [86]. The vibration harmonic, acoustic, and modulus mismatch that occurs for phonons at the interfaces during the thermal conduction process leads to severe scattering and a sharp decrease in the phonon's mean free path [87]. According to corresponding macroscopic evidence, the heat flow is frequently partially blocked at the interface, leading to significant heat loss and decreasing the effectiveness of polymer composites [88]. Therefore, in order to further increase the of polymer composites, it will be crucial to enhance the interfaces in thermally conductive polymer composites and minimize interfacial thermal resistance (ITR).

Researchers found that fabricating thermally conductive fillers with hetero-structures can significantly reduce the ITR between filler to filler [89, 90].

In order to create hetero-structured Al_2O_3-BNNS thermally conductive fillers, Zou et al. [91] covered the surface of alumina (Al_2O_3) with boron nitride nanosheets (BNNS) before creating thermally conductive Al_2O_3-BNNS/epoxy composites. The value of thermally conductive Al_2O_3-BNNS/epoxy composites reached 2.43 W m^{-1} K^{-1}, higher than pure epoxy-resin (0.21 W m^{-1} K^{-1}), single Al_2O_3/epoxy (1.39 W m^{-1} K^{-1}), and simply blended (Al_2O_3/BNNS)/epoxy (1.94 W m^{-1} K^{-1}) composites under the same fillers amount. This was true when the volume ratio of BNNS to Al_2O_3 was 1:7 and the amount of Al_2O_3/BNNS was 65 vol%.

Further work by Han et al. [92], on the use hetero-structured silicon carbide-BNNS (SiC-BNNS) thermally conductive fillers, proved that fabrication of thermally conductive fillers with hetero-structures corroborated can improve the interfaces between different types of fillers, reduce the phonon scattering at the interfaces and decrease ITR filler to filler.

The thermal characteristics of epoxy-based composites with large loading fractions of electrically conductive graphene fillers and electrically insulating boron nitride fillers randomly orientated were studied by Kargar et al. [93]. It was discovered that at the loading fraction fT > 20 vol%, both types of composites showed a unique thermal percolation threshold. The loading of graphene needed to achieve thermal percolation, fT, was significantly higher than the loading needed to achieve electrical percolation, fE. In terms of improving heat conductivity, graphene fillers fared better than boron nitride fillers. It was determined that heat conduction through the network of percolating fillers dominates thermal transport in composites with large filler loadings, f ≥ fT. Unexpectedly, it was discovered that the

quasi-two-dimensional fillers' cross-plane thermal conductivity had a significant impact on the high-loading composites' thermal transport parameters. The results acquired provide insight into the highly contested mechanism of thermal percolation and aid in the creation of the next generation of effective thermal interface materials for electronic applications.

7.6.2.3 Review of Publications on Neutron Shielding, Anticorrosion Properties and interfacial Thermal Resistance of CuO-NPs-Epoxy Composite Coatings

Neutron Shielding Capacity of Epoxy-CuO-NPs Coatings

The work by Künzel and Okuno [94] examines how particle size, material concentration, and radiation energy affect X-ray absorption. Separately, 5%, 10%, and 30% of the resin mass of a polymeric resin were treated with CuO nanoparticles and microparticles. We investigated the X-ray absorption of these materials using a CdTe detector. The nanostructured material displays more X-ray absorption than the microstructured one for all CuO concentrations.

In the study by Mahmud et al. [95], doping recycled high-density polyethylene (R-HDPE) with phosphotungstic acid (PTA) and CuO-NPs resulted in the creation of an unique (R-HDPE/CuO-NP-PTA) nanocomposite (CuO-NPs). Because the constructed nanocomposites had high-density components including CuO-NPs and phosphotungstic acid, they were discovered to be extremely resistant against rays. When phototungstic acid (PTA) and CuO-NPs were added to R-HDPE, it was discovered that PTA raised the composites' electron density (Nel), mass attenuation coefficient (mm), and effective atomic number (Zeff) more than CuO-NPs did.

According to Abd El-Lateef and Gouda [96], hydrothermal fabrication was successfully used to create new metal oxide–organic frameworks, including cellulose nanocrystals (CNCs), copper oxide/melamine/cellulose nanocrystals (CuO/MEL/CNCs), and nickel oxide/melamine/cellulose nanocrystals (NiO/MEL/CNCs). At 300 mg L^{-1}, the ability to prevent corrosion was determined to be in the following order: NiO/MEL/CNCs (98.3%), CuO/MEL/CNCs (96.8%), and CNCs (85.3%). According to the current study, CNCs and metal oxide-melamine frameworks at CNCs may be viable candidates to prevent AISI360-steel corrosion in the petroleum industry as low-cost, environmentally benign inhibitors.

Hassan and Hashim [97] researched the high-quality and low-cost synthesis of (polystyrene-copper oxide) nanocomposites and studied their structural and optical properties for biological application. The outcomes demonstrated that the nanocomposites have a high-UV region absorption. As the concentration of CuO nanoparticles rises, the attenuation coefficients for the gamma radiation source (Cs-137) do as well.

Thermal Conductivity of Epoxy-CuO-NPs Coatings

Copper oxide nanoparticles (CuO-NPs) with an octahedral morphology that were created using a hydrazine reduction reaction were used to create a new epoxy-based nanocomposite by Sunny et al. [98]. By putting forth a mechanism based on the distribution of nCOP domains in the epoxy matrix and the current volume of restricted epoxy chains, the behavior of epoxy-nCOP nanocomposites has been explained in this study.

A novel epoxy-based nanocomposite material was created using nanosized copper (I) oxide particles (nCOP) created through a chemical reduction reaction, according to Sunny et al. [99]. The shape and microstructure development in the nanocomposites have been associated with the tuning of the epoxy resin's hydrophilicity in the presence of variable nCOP content.

Rajendren and Subramani [100] claim that making epoxy materials into good conducting materials for extremely complex applications can make them more appealing. Cu/CNT composite powder increases the thermal stability of epoxy composites while lowering onset temperature as CNT concentration in Cu is increased. Epoxy composites with the highest thermal conductivity and shore hardness were found to have values of 0.253 W/mK and 83.3 ± 0.4, respectively, with corresponding improvements of 24.3 and 10% over pure epoxy. Regardless of the Cu-CNT concentration, the maximum value of epoxy-based composites is attained at 1.0 Epoxy/Comp25 composites and is then reduced.

According to Jasim et al. [101], polymeric composites are among the most isolated materials, yet they also offer a high degree of mechanical flexibility. The findings indicate that at 65% EP + 35% Cu the highest glass transition temperature (T_g) of (EP/Cu) composites was 58.949 °C. Hardness increases as copper concentration rises, reaching a maximum of 83.9 for (55%EP + 45%Cu). To match the warm summer temperatures in our country, this composite can be used to coat surfaces and floors.

Anticorrosion and Mechanical Properties of Epoxy-CuO-NPs Coatings

According to Nazari et al. [102], a number of techniques have been used to shield metal assets against corrosion damage, one of which is the use of very effective and affordable organic coatings. It has been found that the most promising nanofillers for enhancing the barrier performance of organic coatings are those that are carbon- and bio-based. As they could be controlled to release mending or protective compounds, primarily to corrosion faults or damaged parts of the coating once triggered by external stimuli, smart nanocomposite organic coatings were then investigated. Then, superior and long-lasting corrosion protection offered by high-performance nanocomposite organic coatings was looked at. Then, sophisticated characterization techniques for researching organic nanocomposite coatings were briefly covered. We wrapped up by summarizing the major discoveries and the unmet research requirements.

Zhang et al. [103], by using electrochemical impedance spectroscopy (EIS), Fourier transform infrared spectroscopy (FTIR), and scanning electron microscope (SEM/EDS) methods, the degradation processes of two self-polishing antifouling coatings containing copper-based agents (CuSCN and Cu_2O) in 3.5% NaCl solution as well as the protection effect of the coating systems were investigated. The findings show that the two coating systems still have extremely good protective properties for the 5083 Al alloy substrate after immersion for 1525 days at room temperature, as seen by the high value of the low-frequency impedance. The antifouling topcoat suffers severe damage from the alternate high- and low-temperature immersion test (45 °C for 12 h + 25 °C for 12 h), and the failure is primarily characterized by numerous micro-pores and micro-cracks. The micro-pores created after the agents were dissolved and released during the hydrolysis process of the antifouling coating are relatively larger, because the CuSCN antifouling agent particle has a larger diameter and a slightly higher solubility than the Cu_2O agent. This causes a greater decrease in impedance and a worse protective property of the coating system for the substrate.

In order to demonstrate the benefits of incorporating CuO nanofillers into the epoxy resin polymer, a comparison study (structural, thermal, mechanical, and electrical) between the neat-epoxy resin polymer matrix and the epoxy resin polymer decorated with (Ag-CuO) nanoparticles (NPs) and (Mg-CuO) nanosheets has been conducted by El-Masry and Imam [104]. It was shown that the interaction of (Ag-CuO) nanoparticles or (Mg-CuO) nanosheets with epoxy networks enhanced the physical/chemical properties of neat-epoxy by providing it a new, captivating performance that satisfies the requirements of advanced applications. Epoxy plastic's behavior was altered by Mg-CuO nanofillers to exhibit the ductile feature. Epoxy's thermal stability, electrical conductivity, dielectric constant, and lowest activation energy were all increased by (Ag-CuO) NPs. A low-cost option for usage in numerous electrical applications is the Ag-CuO/Epoxy nanocomposite. On the stress–strain curve, Mg-CuO/Epoxy has a broader elasticity region. In comparison to the individual constituent phases and the matrix, the hybrid nanocomposite between neat-epoxy and (Ag/Mg-CuO) NPs presents the solution for more functional applications.

7.6.2.4 Thermal Conduction Models and Inner Mechanisms of Thermally Conductive Epoxy Composite

The following are some of the most successful thermal conduction models that have been proposed by researchers.

For filled polymers with particles, Agari and Uno [105] suggested a new thermal conduction model, and projected values from the new model are compared with experimental results. The model is basically based on a generalization of composite parallel and series conduction models, which has been further refined to account for the isotropy of heat conduction in a random dispersion system. The new model yields the following equation: $\log\lambda = V \cdot C_2 \cdot \log\lambda_2 + (1 - V) \cdot \log(C_1 \cdot \lambda_1)$. As a result,

the equation may be used to estimate the thermal conductivity of the filled polymer (λ) with any volume content (V) of particles when the thermal conductivities of the polymer and particles (λ_1, λ_2) are known. Experimental results for polyethylene, polystyrene, and polyamide are filled with graphite, copper, or Al_2O_3.

This study by Agrawal and Satapathy [106] investigates ways to improve the ability of aluminum nitride-loaded epoxy composites to conduct heat. In order to build a theoretical model for one-dimensional heat conduction through such a composite, the laws of least thermal resistance and specific equivalent thermal conductivity were combined. The values obtained using the suggested mathematical correlation were compared with experimental findings that were measured as well as with values that were estimated using other well-known correlations such the Rule-of-Mixture, Maxwell's model, Bruggeman model, and Nielson-Lewis model. This comparison shows that although none of the aforementioned models are capable of accurately forecasting the composites' effective thermal conductivity, the outcomes of the proposed model that incorporates a correction factor are in decent accordance with the experimental results.

Conclusion on Literature Review

There are always some discrepancies between the predicted values by models and the experimental values because the current thermal conduction models only have a limited application range and do not account for ITR, shape, amount, and surface properties of thermally conductive fillers, among other factors. Future research on thermal conduction models must fully take into account additional practical influencing factors, quantify them, and incorporate them into the models in order to increase the degree of agreement between the models and the experimental data.

This will result in the establishment of general mathematical models on interfacial thermal resistance for novel shapes and properties of thermally conductive epoxy composites.

7.7 Methodology

7.7.1 Materials and Methods

7.7.1.1 Materials

WCD

The WCD from SA will serve as the raw material for the creation of CuO-NPs with various compositions.

Epoxy-Resin

The two major elements of the ultraviolet curable coatings will be epoxy acrylate and tripropylene glycol diacrylate, while vinyltrimethoxysilane and castor oil will function as plasticizers and coupling agents, respectively.

Steel

The substrate for this study will be mild steel sheets (7 × 3.5 × 0.1 cm).

7.7.1.2 Methods

The WCD will first go through gravity separation to create concentrates with varied copper oxide, aluminum oxide, and silicon oxide contents as explained in the following sub-sections.

Density Separation of WCD

To separate the WCD based on densities, the rotational bowl speed and fluidized water flow rate will be altered at three levels (Table 7.1). Table 7.2 details the test process for the density separation of the WCD. After five passes through the separator, 45 test samples will be generated (Table 7.3). These concentrates will be used as the basic ingredient in the production of copper precursors. The calculations that will be performed before creating the slurry that will be used for the density separation experimentation are described in detail in Okanigbe's thesis [107].

Design of Experiment and Procedure for Production of Copper Precursor from Concentrates

Manufacturing of CuO-NPs started with the production of copper precursor from leached concentrates. The experiment design for the production of copper precursor from leached concentrates was developed using the 3 × 2 complete factorial experimental design approach, as shown in Tables 7.4 and 7.5.

The copper precursor will be created by adding dropwise 2 M Na_2CO_3 solution to 0.2 M $CuSO_4$ solution in a 500-ml conical flask positioned on a hot plate while

Table 7.1 Parameters measured for density separation experiment

S.N	Parameters	Low (0)	Medium (1)	High (2)
X_1	RBS (m/s^2)	60	90	120
X_2	FWFR (l/min)	3.0	4.5	6.0

Table 7.2 Test protocol for density separation of CSD

Tests	RBS (G)	FWFR (l/min)	Treatment combination (TC)
1	A	A	AA
2	A	B	AB
3	A	C	AC
4	B	A	BA
5	B	B	BB
6	B	C	BC
7	C	A	CA
8	C	B	CB
9	C	C	CC

Table 7.3 Test protocol for production of concentrates with different copper oxide, aluminum oxide, and silicon oxide contents

	Tests and tailings								
Passes	(1)	(2)	(3)	(4)	(5)	(6)	(7)	(8)	(9)
1	1(1)	1(2)	1(3)	1(4)	1(5)	1(6)	1(7)	1(8)	1(9)
2	2(1)	2(2)	2(3)	2(4)	2(5)	2(6)	2(7)	2(8)	2(9)
3	3(1)	3(2)	3(3)	3(4)	3(5)	3(6)	3(7)	3(8)	3(9)
4	4(1)	4(2)	4(3)	4(4)	4(5)	4(6)	4(7)	4(8)	4(9)
5	5(1)	5(2)	5(3)	5(4)	5(5)	5(6)	5(7)	5(8)	5(9)

stirring the mixture with a magnetic stirrer at various temperatures (Fig. 7.4). The resulting green precipitate will be separated by filtration and then washed with distilled water and pure ethanol. The green precipitate will then be dried in a 105 °C oven for 24 h.

Design of Experiment and Procedure for Production of CuO-NPs from Copper Precursor

On the basis of an air flow and a thermogravimetric analyzer, the thermal behavior of the synthesized copper precursor will be measured. A platinum crucible containing 35 mg of samples will be placed on the microbalance pan and heated at rates of 5, 10, 15, and 20 °C/min between 25 and 1000 °C.

The investigation will be conducted using a 3 × 2 complete factorial experimental design method (Tables 7.4 and 7.5). After familiarizing oneself with the thermal behavior of the copper precursor, Tables 7.6 and 7.7 show how the experiment will be planned based on the data for the generation of CuO-NPs. An experimental approach can be found in Okanigbe [107].

Table 7.4 Parameters considered for the production of copper precursor

Parameters	Levels		
	Low	Medium	High
Temperature (°C)	25	55	85
Rotational speed (rpm)	340	740	1480

Table 7.5 The design of experiment for the production of copper precursor

Tests	Temperature (°C)	Rotational speed (rpm)	Treatment combinations (TC) (°C/rpm)
1	25	340	25/340
2	25	740	25/740
3	25	1480	25/1480
4	55	340	55/340
5	55	740	55/740
6	55	1480	55/1480
7	85	340	85/340
8	85	740	85/740
9	85	1480	85/1480

Preparation and Polymerization of Hybrid Nanocomposite Coatings by Electron Beam Radiation

Six solvent-free coating formulations (blank L_0) will be created using epoxy acrylate (EA) oligomer as the binder, TPGDA as the thinner, CO as the plasticizer, and VTMS as the coupling agent. Developed coating formulations (hybrid) will be measured against blank L_0 to determine performance enhancement. Different CuO-NP compositions (CuO, and other trace oxides wt%) will be added to the formulations L-1(1) to L-5(9) as shown in Table 7.8. These different compositions will be used to create hybrid organic–inorganic composite coatings. These hybrid formulations will then be homogenized using a homogenizer at room temperature after being sonicated for 20 min and lightly blended for a further 15 min at 10.000 revolutions per minute (rpm). Using a film applicator (Elcometer 3540, USA), all hybrid formulations will then be applied as thin films with a thickness of 100 mm onto steel panels and subsequently polymerized with a dose of 10 kGy of electron beam irradiation.

Development of Predictive Models

Modeling Technique for Predictive Output

The fundamental processes used in the modelling approach described in this research are presented in this subsection:

Step 1: Analyze the trends in the experimental samples.

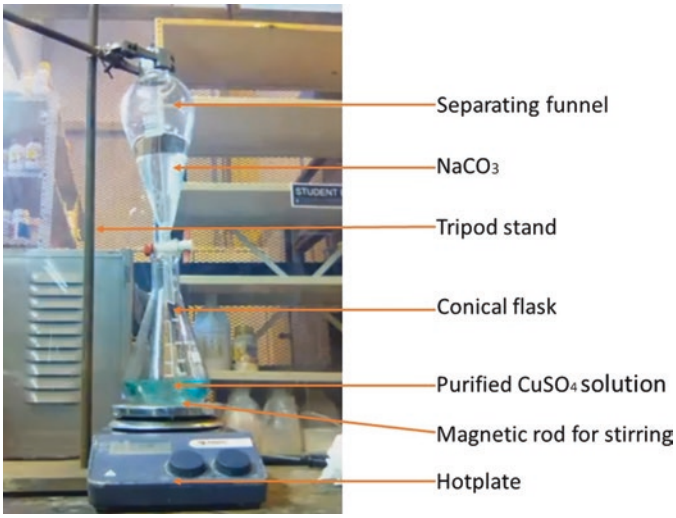

Fig. 7.4 Experimental set-up for the production of copper precursor

Table 7.6 Parameters considered for the production of CuO-NPs

	Levels		
Parameters	Low	Medium	High
Temperature (°C)	650	750	850
Time (h)	1	2	3

Step 2: Establish constraint models to classify and divide samples into sub-classes in accordance with Step 1.
Step 3: Calculate the absolute difference between input and output samples belonging to the same class as those classified in Step 2.
Step 4: Determine various experimental levels for the classes.
Step 5: Predict output using an interpolant model.
Step 6: Finish.

Table 7.9 contains a generalized form of the modeling variables. The possible effects of the various mineral constituents observed in the experimental concentrations were calculated using a model that took these variables into account. The modeling strategy discussed here is based on the constrained interpolation of findings from any three sequential experimental samples. Two of these outputs are frequently known by experience, and predictive modeling is used to identify the third unknown output. First and second columns of Table 7.9 display the ordered experimental trials that are used for interpolation. The (%) proportions of the inputs (p_{i_1} , p_{i_2} , and p_{i_3}) and outputs (p_{o_1} , p_{o_2} , and p_{o_3}) for the investigated mineral constituents are shown in the third and fourth columns, respectively. Additionally, for each of the three experimental samples under examination, column six shows the

Table 7.7 The design of experiment for production of copper nanoparticles

Tests	Temperature (°C)	Time (h)	TC (°C/h)
1	650	1	650/1
2	650	2	650/2
3	650	3	650/3
4	750	1	750/1
5	750	2	750/2
6	750	3	750/3
7	850	1	850/1
8	850	2	850/2
9	850	3	850/3

absolute difference between the input and output values stated in terms of, and column five shows the experimental levels.

The following under listed are modelling notations as presented in this research:

$$\text{Output} = f\left(\text{speed}, \text{flow rate}, \text{input}, \text{feed rate}, \text{liquid solid ratio}\right)$$

Let: serial number for inputs: $s_{\text{i}} = \{1, \ldots, n-1, n\}$ and serial number for outputs $s_{\text{o}} = \{1, \ldots, n-1, n\}$ for $\forall n \in R$.

Where:

$\exp_{(\text{i})i,j}$ = Experimental inputs,
$\exp_{(\text{o})i,j}$ = Experimental outputs,
$\text{Pre}_{(\text{o})i,j}$ = Predictive outputs,
p_{i_j} = % input proportion of selected samples,
p_{o_j} = % output proportion of selected samples,
$\Delta p_j = \left| p_{\text{i}_j} - p_{\text{o}_j} \right|$ absolute difference between p_{i_j} and p_{o_j}

Where $j = \{1, \ldots, k-1, k\}$ represents experimental levels.

The "absolute difference" models defined in terms of the experimental levels are shown in Eqs. (7.1) through (7.3), and the final computational models for projecting the unknown outputs are shown in Eqs. (7.4) through (7.6) with respect to Table 7.9.

$$\Phi_1 = \left[\frac{\Phi_3(\mu - \xi) - \Phi_2(\mu - \xi) - \Phi_2(\sigma - \mu)}{(\mu - \sigma)} \right] \tag{7.1}$$

$$\Phi_2 = \left[\frac{\Phi_3(\mu - \xi) + \Phi_1(\sigma - \mu)}{(\sigma - \mu) + (\mu - \xi)} \right] \tag{7.2}$$

$$\Phi_3 = \left[\frac{\Phi_1(\mu - \sigma) + \Phi_2(\sigma - \mu) + \Phi_2(\mu - \xi)}{(\mu - \xi)} \right] \tag{7.3}$$

Table 7.8 Compositional formulations of different epoxy-CuO-NPs coatings

	Compositional formulations						
Coating	EA (wt%)	TPGDA (wt%)	CO (wt%)	Total	VTMS (wt%)	CuO-NPs (wt%)	Irradiation dose (kGy)
Blank (L_0)	70	20	10	100	1	0.5	10
L-1(1)	70	20	10	100	1	0.5	10
L-1(2)	70	20	10	100	1	0.5	10
L-1(3)	70	20	10	100	1	0.5	10
L-1(4)	70	20	10	100	1	0.5	10
L-1(5)	70	20	10	100	1	0.5	10
L-1(6)	70	20	10	100	1	0.5	10
L-1(7)	70	20	10	100	1	0.5	10
L-1(8)	70	20	10	100	1	0.5	10
L-1(9)	70	20	10	100	1	0.5	10
L-2(1)	70	20	10	100	1	0.5	10
L-2(2)	70	20	10	100	1	0.5	10
L-2(3)	70	20	10	100	1	0.5	10
L-2(4)	70	20	10	100	1	0.5	10
L-2(5)	70	20	10	100	1	0.5	10
L-2(6)	70	20	10	100	1	0.5	10
L-2(7)	70	20	10	100	1	0.5	10
L-2(8)	70	20	10	100	1	0.5	10
L-2(9)	70	20	10	100	1	0.5	10
L-3(1)	70	20	10	100	1	0.5	10
L-3(2)	70	20	10	100	1	0.5	10
L-3(3)	70	20	10	100	1	0.5	10
L-3(4)	70	20	10	100	1	0.5	10
L-3(5)	70	20	10	100	1	0.5	10
L-3(6)	70	20	10	100	1	0.5	10
L-3(7)	70	20	10	100	1	0.5	10
L-3(8)	70	20	10	100	1	0.5	10
L-3(9)	70	20	10	100	1	0.5	10
L-4(1)	70	20	10	100	1	0.5	10
L-4(2)	70	20	10	100	1	0.5	10
L-4(3)	70	20	10	100	1	0.5	10
L-4(4)	70	20	10	100	1	0.5	10
L-4(5)	70	20	10	100	1	0.5	10
L-4(6)	70	20	10	100	1	0.5	10
L-4(7)	70	20	10	100	1	0.5	10
L-4(8)	70	20	10	100	1	0.5	10
L-4(9)	70	20	10	100	1	0.5	10
L-5(1)	70	20	10	100	1	0.5	10
L-5(2)	70	20	10	100	1	0.5	10

(continued)

Table 7.8 (continued)

Coating	Compositional formulations						
	EA (wt%)	TPGDA (wt%)	CO (wt%)	Total	VTMS (wt%)	CuO-NPs (wt%)	Irradiation dose (kGy)
L-5(3)	70	20	10	100	1	0.5	10
L-5(4)	70	20	10	100	1	0.5	10
L-5(5)	70	20	10	100	1	0.5	10
L-5(6)	70	20	10	100	1	0.5	10
L-5(7)	70	20	10	100	1	0.5	10
L-5(8)	70	20	10	100	1	0.5	10
L-5(9)	70	20	10	100	1	0.5	10

Table 7.9 Generalized representation of model variables

Level	Data acquisition procedure	Input value for variant factor p_{i_j}	Output value for variant factor p_{o_j}	Expt. levels	Absolute difference between p_{i_j} and p_{o_j}
1-First	Prediction	p_{i_1}	p_{o_1}	ξ	$\lvert p_{i_1} - p_{o_1} \rvert = \Phi_1$
2-Second	Experiment	p_{i_2}	p_{o_2}	μ	$\lvert p_{i_2} - p_{o_2} \rvert = \Phi_2$
3-Third	Experiment	p_{i_3}	p_{o_3}	σ	$\lvert p_{i_3} - p_{o_3} \rvert = \Phi_3$

$$\left| p_{i_1} - p_{o_1} \right| = \Phi_1 \tag{7.4}$$

$$\left| p_{i_2} - p_{o_2} \right| = \Phi_2 \tag{7.5}$$

$$\left| p_{i_3} - p_{o_3} \right| = \Phi_3 \tag{7.6}$$

Hence, $\Delta p_j = \Phi_j$.

Experimental Validation and Simulation

The epoxy-CuO-NPs composite coatings thermal conductivity, anticorrosion, and mechanical properties will be experimentally determined in order to validate the expected ideal composition of the organic–inorganic composite coating.

Characterization of the Developed Epoxy-CuO-NPs Composite Coatings

All coated films will be characterized using the following:

1. Fourier transform infrared spectroscopy,
2. Transmission electron microscopy,

3. Thermogravimetric analyzer,
4. X-ray diffraction,
5. Scanning electron microscopy,
6. UV–Vis–NIR spectroscopy,
7. Atomic force microscope,
8. Contact angle meter.

Measurement of the Basic Properties of the Developed Epoxy-CuO-NPs Composite Coatings

For each of the following listed measurements, the average of five readings will be calculated:

1. Hardness measurement
2. Bending measurement
3. Adhesion measurement
4. Glossiness measurement
5. Coating steel scratch measurement
6. Acid/alkali resistance measurement

Corrosion Tests

According to ASTM, corrosion tests for hybrid coating films were estimated as follows: the degree of rust under the coated film was determined according to ASTM D 610–01; the degree of blistering under the coated film was performed according to ASTM D 714–7 (2000), and the degree of adhesion failure of the X-cut was made according to ASTM D 1654–92 (2000).

Weight Loss Measurements

Mild steel sheets measuring 3 × 3 × 0.1 cm were used. The steel sheets have been thoroughly cleaned and weighed. The following Eq. (7.7) will be used to get the average weight reduction for coated steel:

$$W = \left(W_1 - W_2\right) / S, \tag{7.7}$$

where W is the average weight loss (mg/cm^2), W_1 is the average weight loss of the coated steel before immersion, W_2 is the average weight loss of the coated steel after immersion, and S is the total area of the mild steel panel.

The plates in the current investigation will be removed from sodium chloride (NaCl) solution at the intervals of 10, 20, 30, and 60 days in accordance with ASTM D 2688-94 (1999). Analyses of the electrochemical kind Galvanic charge/discharge measurements will be carried out using a Biologic SP300 and three electrodes. After 30 days of exposure to a 3.5% NaCl solution, the hybrid-coated steel plates will be removed, and the open circuit potential will be measured over the frequency range of 0.1–103 Hz with an amplitude of 10 mV.

Thermal Conductivity Measurements

Using a test rig apparatus, the epoxy coating's thermal conductivity will be determined at various concentrations of copper nanoparticles. A thermocouple, a uniform plate heater with a resistance, a voltage control, a switch, and a temperature reader will be included in this test apparatus.

7.8 Contribution to Knowledge

At the end of the investigation, the following details will be made public:

1. The creation of a brand-new epoxy/CuO-NPs composite coating.
2. For improved heat conductivity and anticorrosion of mild steel, hence this composite coating has not yet been used in the design of cask for transportation of SNF.
3. As a result, the composition is brand-new.
4. The availability of WCD, a fresh secondary supply of CuO-NPs, enabling the creation of organic–inorganic coatings.
5. WCD is a secondary resource that has not been utilized as an inorganic material to improve the thermal conductivity and anticorrosion of mild steel.
6. The CuO-NPs substance is therefore brand-new.

7.9 Ethical Considerations

This project has no unethical components.

7.10 Dissemination

The Department of Higher Education and Training (DHET) recognized journals listed below are just a few that will publish the findings of the study:

1. Nano-micro Letter, Publisher: Springer
2. Journal of Metals, Publisher: Springer

Additionally, the findings will be presented at national and international conferences in addition to being published in full in the conference proceedings.

7.11 Budget and Time Frame

7.11.1 Budget

The estimated budget for this proposed study can be seen in Table 7.10.

7.11.2 Time Frame

The estimated time for the completion of this proposed study can be seen in Table 7.11.

Table 7.10 Estimated budget of the project

Items	Cost (R)	Source
Literature sourcing and stationaries	To be estimated	X
Materials and supplies	To be estimated	X
Analytical equipment	To be estimated	X
Travelling expenses	To be estimated	X
Miscellaneous expenses	To be estimated	X
Total		X

Key: TUT = Tshwane University of Technology; R = Rand

Table 7.11 Estimated time frame of the project

S.N	Task name	Year	
1	Proposal (compilation and presentation)	WIP	WIP
2	Literature review	WIP	WIP
3	Material sourcing	WIP	WIP
4	Sample preparation (sampling)	WIP	WIP
5	Fabrication of test samples optimization process	WIP	WIP
6	Fabrication of test samples	WIP	WIP
7	Thermal conductivity and wear resistance tests	WIP	WIP
8	Results, data, and analysis	WIP	WIP
9	Optimum predictive model development	WIP	WIP
10	3D print of brake rotor and validation of optimum prediction	WIP	WIP
11	Compilation and presentation of final report	WIP	WIP

Key: WIP = Work in progress

References

1. M.K. Nematchoua, J.A. Orosa, Life cycle assessment of radioactive materials from a residential neighbourhood. Sustain. Mater. Technol. **33**, e00468 (2022)
2. G. Vaidyanathan, R.D. Kale, India's nuclear power program: A critical review. Sādhanā **47**(3), 1–18 (2022)
3. T.A. Kurniawan, M.H.D. Othman, D. Singh, R. Avtar, G.H. Hwang, T. Setiadi, W.H. Lo, Technological solutions for long-term storage of partially used nuclear waste: A critical review. Ann. Nucl. Energy **166**, 108736 (2022)
4. T. Sakuragi, T. Okamura, R. Hamada, H. Asano, E. Minari, M. Nakase, K. Takeshita, T. Oniki, M. Uchiyama, Optimal waste loading in high-level nuclear waste glass from high-burnup spent fuel for waste volume and geological disposal footprint reduction. MRS Adv. **7**(7), 150–154 (2022)
5. M.S. Yim, Characteristics of spent fuel and its storage and transportation, in *Nuclear Waste Management*, (Springer, Dordrecht, 2022), pp. 257–339
6. M.S. Yim, Spent fuel reprocessing and nuclear waste transmutation, in *Nuclear Waste Management*, (Springer, Dordrecht, 2022), pp. 341–384
7. M.S. Yim, Management of low and intermediate level waste, in *Nuclear Waste Management*, (Springer, Dordrecht, 2022), pp. 635–685
8. M. Alwaeli, V. Mannheim, Investigation into the current state of nuclear energy and nuclear waste management—A state-of-the-art review. Energies **15**(12), 4275 (2022)
9. A. Yadav, A. Singh, A. Shukla, Nuclear energy and conventional clean fuel, in *Status and Future Challenges for Non-conventional Energy Sources*, vol. 1, (Springer, Singapore, 2022), pp. 23–44
10. Safety Series No. 6, *Regulations for the Safe Transport of Radioactive Materials* (International Atomic Energy Agency, Vienna, 1985)
11. Standard Safety Series No. TS-R-1, *Regulations for the Safe Transport of Radioactive Materials* (International Atomic Energy Agency, Vienna, 2003)
12. Standard Safety Series, *Transportation of Spent Research Reactor Fuel to USA* (Phoenix, 2011)
13. S. Kang, D.H. Kim, Y.S. Chang, S. Lee, Integrity assessment of spent fuel assembly in vertically and obliquely dropping cask. J. Mech. Sci. Technol. **35**(9), 3821–3827 (2021)
14. D. Grgić, M. Matijević, P. Dučkić, R. Ječmenica, Analysis of the HI-TRAC VW transfer cask dose rates for spent fuel assemblies loaded in nuclear power plant Krsko storage campaign one. J. Nucl. Eng. Radiat. Sci. **8**(4), 041902 (2022)
15. Y. Liu, B. Craig, Z. Han, J. Li, K. Byrne, H. Takeda, T. Saegusa, RAMM-TM for detection of gas leakage from canisters containing spent nuclear fuel. Nucl. Eng. Des. **385**, 111534 (2021)
16. A. Knight, B. Nation, C. Bryan, R. Schaller, *FY21 Status Report: SNF Canister Coatings for Corrosion Prevention and Mitigation*. (No. SAND2021-10810R) (Sandia National Lab (SNL-NM), Albuquerque, 2021)
17. P. Goyal, V. Verma, A. Dutta, J. Chattopadhyay, Quantification of lead melting in a radioactive transport cask using CFD. *BARC Newsletter* (2021)
18. L. Vergari, M. Fratoni, Spent fuel management strategies for fluoride-cooled pebble bed reactors. Nucl. Eng. Des. **378**, 111189 (2021)
19. M.G. El-Samrah, A.F. Tawfic, S.E. Chidiac, Spent nuclear fuel interim dry storage; design requirements, most common methods, and evolution: A review. Ann. Nucl. Energy **160**, 108408 (2021)
20. I.M. Mousaa, N.A. Abdelreheim, S.A. Elnaggar, R.M. Fathy, Green synthesis and use of copper oxide nanoparticles to prepare a highly thermal, antimicrobial, and anticorrosion hybrid coating for mild steel under electron beam irradiation. Anti-Corros. Methods Mater. **69**(2), 160–170 (2022)
21. G.Y. Shkoukani Al-Qous, *Shielding and Corrosion Behavior of Materials in Nuclear Applications* (North Carolina State University ProQuest Dissertations Publishing, 2021)

22. D. Asefi, M. Arami, N.M. Mahmoodi, Electrochemical effect of cationic gemini surfactant and halide salts on corrosion inhibition of low carbon steel in acid medium. Corros. Sci. **52**(3), 794–800 (2010)
23. I.M. Mousaa, N.M. Ali, M.K. Attia, Preparation of high performance coating films based on urethane acrylate oligomer and liquid silicone rubber for corrosion protection of mild steel using electron beam radiation. Prog. Org. Coat. **155**, 106222 (2021)
24. T. Wang, Q. Guo, T.C. Zhang, Y.X. Zhang, S. Yuan, Large-scale prepared superhydrophobic HDTMS-modified diatomite/epoxy resin composite coatings for high-performance corrosion protection of magnesium alloys. Prog. Org. Coat. **170**, 106999 (2022)
25. O. Mazzantini, F. D'Auria, J.R. Riznic, Atucha II plant description, in *Pressurized Heavy Water Reactors*, (Elsevier, 2022), pp. 1–49
26. K.A. Ross, M. Pole, B. Gwalani, T.J. Montoya, R. Schaller, E. Karasz, *Cold Spray for Mitigation and Repair of Spent Nuclear Fuel Dry Storage Canisters*. (No. PNNL-32917) (Pacific Northwest National Lab (PNNL), Richland, 2022)
27. S.G. Acharyya, A. Khandelwal, V. Kain, A. Kumar, I. Samajdar, Surface working of 304L stainless steel: Impact on microstructure, electrochemical behavior and SCC resistance. Mater. Charact. **72**, 68–76 (2012)
28. ASTM Standard, *Standard Test Methods for Determining Area Percentage Porosity in Thermal Sprayed Coatings* (ASTM International, West Conshohocken, 2014), pp. 2–8
29. J. Fiebig, E. Bakan, T. Kalfhaus, G. Mauer, O. Guillon, R. Vaßen, Thermal spray processes for the repair of gas turbine components. Adv. Eng. Mater. **22**(6), 1901237 (2020)
30. S. Ghosh, V. Kain, Effect of surface machining and cold working on the ambient temperature chloride stress corrosion cracking susceptibility of AISI 304L stainless steel. Mater. Sci. Eng. A **527**(3), 679–683 (2010)
31. S.W. Glass, M.R. Larche, M.S. Prowant, J.D. Suter, J.P. Lareau, X. Jiang, K.A. Ross, Cold spray NDE for porosity and other process anomalies, in *AIP Conference Proceedings*, vol. 1949, no. 1, (AIP Publishing LLC, 2018), p. 020010
32. M.R. Rokni, C.A. Widener, O.C. Ozdemir, G.A. Crawford, Microstructure and mechanical properties of cold sprayed 6061 Al in As-sprayed and heat treated condition. Surf. Coat. Technol. **309**, 641–650 (2017)
33. B. Hanson, H. Alsaed, C. Stockman, D. Enos, R. Meyer, K. Sorenson, *Gap Analysis to Support Extended Storage of Used Nuclear Fuel*. (No. PNNL-20509) (2012)
34. R. Hosler, J. Hall, *Outside Diameter Initiated Stress Corrosion Cracking*. (No. PA-MSC-0474) (2010)
35. J.P. Lareau, *Operating Experience with Chloride Induced Stress Corrosion Cracking*. (EPRI ESCP) (2014)
36. A.W. Knight, R. Schaller, C.R. Bryan, T.J. Montoya, A.M. Parey, J. Carpenter, M. Maguire, K. Ross, *Corrosion-Resistant Coatings for Mitigation and Repair of Spent Nuclear Fuel Dry Storage Canisters*. (No. SAND-2020-7916R) (Sandia National Lab (SNL-NM), Albuquerque, 2020)
37. S.J. Saltzstein, B. Hanson, G.A. Freeze, *Spent Fuel and Waste Science and Technology Storage and Transportation R&D Strategic Plan*. (No. SAND2020-11667C) (Sandia National Lab (SNL-NM), Albuquerque, 2020)
38. C.R. Bryan, D.G. Enos, *Analysis of Dust Samples Collected from Spent Nuclear Fuel Interim Storage Containers at Hope Creek, Delaware, and Diablo Canyon, California*. (No. SAND2014-16383) (Sandia National Lab (SNL-NM), Albuquerque, 2014)
39. C.R. Bryan, D. Enos, *Analysis of Dust Samples Collected from an Unused Spent Nuclear Fuel Interim Storage Container at Hope Creek, Delaware*. (No. SAND-2015-1746) (Sandia National Lab (SNL-NM), Albuquerque, 2015)
40. C.R. Bryan, A.W. Knight, *Analysis of Dust Samples Collected from an Inland ISFSI Site (Site A)*. (No. SAND-2020-13674) (Sandia National Lab (SNL-NM), Albuquerque, 2020)

41. C.R. Bryan, E.J. Schindelholz, *Analysis of Samples Collected from the Surface of Interim Storage Canisters at Calvert Cliffs in June 2017: Revision 01*. (No. SAND2017-12429) (Sandia National Lab (SNL-NM), Albuquerque, 2017)
42. C.R. Bryan, E.J. Schindelholz, *FY18 Status Report: SNL Research into Stress Corrosion Cracking of SNF Interim Storage Canisters*. (No. SAND-2018-12595R) (Sandia National Lab (SNL-NM), Albuquerque, 2018)
43. R.F. Schaller, A.W. Knight, C. Bryan, B. Nation, T.J. Montoya, R.M. Katona, *FY20 Status Report: SNF Interim Storage Canister Corrosion and Surface Environment Investigations*. (No. M2SF-21SN010207055) (US Department of Energy. Sandia National Laboratories, Albuquerque, 2020)
44. E.J. Schindelholz, C.R. Bryan, C.L. Alexander, *FY17 Status Report: Research on Stress Corrosion Cracking of SNF Interim Storage Canisters*. (No. SAND-2017-10338R) (Sandia National Lab (SNL-NM), Albuquerque, 2017)
45. A. Knight, C. Bryan, *Analysis of Dust Samples Collected from an Inland ISFSI Site ("Site B")*. (No. SAND2020-14144) (Sandia National Lab (SNL-NM), Albuquerque, 2020)
46. C.R. Bryan, D.G. Enos, *Interim Storage Environment: Considerations for Corrosion Testing of SNF Dry Storage Containers*. (No. SAND2013-3519C) (Sandia National Lab (SNL-NM), Albuquerque, 2013)
47. H. Wu, L. Cheng, C. Liu, X. Lan, H. Zhao, Engineering the interface in graphene oxide/epoxy composites using bio-based epoxy-graphene oxide nanomaterial to achieve superior anticorrosion performance. J. Colloid Interface Sci. **587**, 755–766 (2021)
48. Y. Hu, L. Zeng, A.J. Minnich, M.S. Dresselhaus, G. Chen, Spectral mapping of thermal conductivity through nanoscale ballistic transport. Nat. Nanotechnol. **10**(8), 701–706 (2015)
49. Y. Lin, Y. Jia, G. Alva, G. Fang, Review on thermal conductivity enhancement, thermal properties and applications of phase change materials in thermal energy storage. Renew. Sust. Energ. Rev. **82**, 2730–2742 (2018)
50. M.K. Hassanzadeh-Aghdam, R. Ansari, H.M. Deylami, Influence of graphene nano-platelets on thermal transport performance of carbon fiber-polymer hybrid composites: Overall assessment of microstructural aspects. Int. J. Therm. Sci. **171**, 107209 (2022)
51. M.K. Hassanzadeh-Aghdam, R. Ansari, A micromechanics-based hierarchical analysis of thermal conductivity of metallic nanocomposites with agglomerated ceramic nanoparticles. Arab. J. Sci. Eng. **46**(8), 7143–7151 (2021)
52. J. Park, D. Kim, H. Kim, J. Lee, W. Chung, Thermal radiative copper oxide layer for enhancing heat dissipation of metal surface. Nanomaterials **11**(11), 2819 (2021)
53. M. Ramezanzadeh, B. Ramezanzadeh, Thermomechanical and anticorrosion characteristics of metal-organic frameworks, in *Metal-Organic Frameworks for Chemical Reactions*, (Elsevier, 2021), pp. 295–330
54. X. Wang, Z. Lin, Robust, hydrophobic anti-corrosion coating prepared by PDMS modified epoxy composite with graphite nanoplatelets/nano-silica hybrid nanofillers. Surf. Coat. Technol. **421**, 127440 (2021)
55. G.M. Nair, T. Sajini, B. Mathew, Advanced green approaches for metal and metal oxide nanoparticles synthesis and their environmental applications. Talanta Open **5**, 100080 (2021)
56. S. Kango, S. Kalia, A. Celli, J. Njuguna, Y. Habibi, R. Kumar, Surface modification of inorganic nanoparticles for development of organic–inorganic nanocomposites—A review. Prog. Polym. Sci. **38**(8), 1232–1261 (2013)
57. A.M. El Saeed, M. Abd El-Fattah, A.M. Azzam, Synthesis of ZnO nanoparticles and studying its influence on the antimicrobial, anticorrosion and mechanical behavior of polyurethane composite for surface coating. Dyes Pigments **121**, 282–289 (2015)
58. X. Xiao, L. Miao, G. Xu, L. Lu, Z. Su, N. Wang, S. Tanemura, A facile process to prepare copper oxide thin films as solar selective absorbers. Appl. Surf. Sci. **257**(24), 10729–10736 (2011)
59. R. Albatici, F. Passerini, A.M. Tonelli, S. Gialanella, Assessment of the thermal emissivity value of building materials using an infrared thermovision technique emissometer. Energ. Buildings **66**, 33–40 (2013)

60. A.H. Jayatissa, K. Guo, A.C. Jayasuriya, Fabrication of cuprous and cupric oxide thin films by heat treatment. Appl. Surf. Sci. **255**(23), 9474–9479 (2009)
61. J. Karthikeyan, The advantages and disadvantages of the cold spray coating process, in *The Cold Spray Materials Deposition Process*, (Woodhead Publishing, 2007), pp. 62–71
62. W.J. Stepniowski, W.Z. Misiolek, Review of fabrication methods, physical properties, and applications of nanostructured copper oxides formed via electrochemical oxidation. Nanomaterials **8**(6), 379 (2018)
63. F. Jiang, W. Zhao, Y. Wu, J. Dong, K. Zhou, G. Lu, J. Pu, Anti-corrosion behaviors of epoxy composite coatings enhanced via graphene oxide with different aspect ratios. Prog. Org. Coat. **127**, 70–79 (2019)
64. D. Okanigbe, P. Olawale, A. Popoola, A. Abraham, A. Michael, K. Andrei, Centrifugal separation experimentation and optimum predictive model development for copper recovery from waste copper smelter dust. Cogent Eng. **5**(1), 1551175 (2018)
65. S. Saha, J. Khan, T. Knight, T. Farouk, A global model for predicting vacuum drying of used nuclear fuel assemblies. Nucl. Technol. **208**(3), 414–427 (2022)
66. A. Pasha, S. Khasim, A.A.A. Darwish, T.A. Hamdalla, S.A. Al-Ghamdi, High performance organic coatings of polypyrrole embedded with manganese iron oxide nanoparticles for corrosion protection of conductive copper surface. J. Inorg. Organomet. Polym. Mater. **32**(2), 499–512 (2022)
67. C. Huang, X. Qian, R. Yang, Thermal conductivity of polymers and polymer nanocomposites. Mater. Sci. Eng. R Rep. **132**, 1–22 (2018)
68. F. Jiang, S. Cui, C. Rungnim, N. Song, L. Shi, P. Ding, Control of a dual-cross-linked boron nitride framework and the optimized design of the thermal conductive network for its thermo-responsive polymeric composites. Chem. Mater. **31**(18), 7686–7695 (2019)
69. X. Fu, Z. Ji, W. Lin, Y. Yu, T. Wu, The advancement of neutron shielding materials for the storage of spent nuclear fuel. Sci. Technol. Nucl. Install. **2021**, 5541047 (2021)
70. C.K. Wilson, The 1996 IAEA regulations for the safe transport of radioactive materials—The transport of fissile material. Int. J. Radioact. Mater. Transp. **8**(2), 127–132 (1997)
71. Y. Song, F. Jiang, N. Song, L. Shi, P. Ding, Multilayered structural design of flexible films for smart thermal management. Compos. A: Appl. Sci. Manuf. **141**, 106222 (2021)
72. Z. Zhu, C. Li, E. Songfeng, L. Xie, R. Geng, C.T. Lin, L. Li, Y. Yao, Enhanced thermal conductivity of polyurethane composites via engineering small/large sizes interconnected boron nitride nanosheets. Compos. Sci. Technol. **170**, 93–100 (2019)
73. J.S. George, J.K. Paduvilan, N. Salim, J. Sunarso, N. Kalarikkal, N. Hameed, S. Thomas, Advances and future outlook in epoxy/graphene composites for anticorrosive applications. Prog. Org. Coat. **162**, 106571 (2022)
74. J. Zhang, W. Zhang, L. Wei, L. Pu, J. Liu, H. Liu, Y. Li, J. Fan, T. Ding, Z. Guo, Alternating multilayer structural epoxy composite coating for corrosion protection of steel. Macromol. Mater. Eng. **304**(12), 1900374 (2019)
75. N. Keshmiri, P. Najmi, M. Ramezanzadeh, B. Ramezanzadeh, Designing an eco-friendly lanthanide-based metal organic framework (MOF) assembled graphene-oxide with superior active anti-corrosion performance in epoxy composite. J. Clean. Prod. **319**, 128732 (2021)
76. Z. Yu, L. Lv, Y. Ma, H. Di, Y. He, Covalent modification of graphene oxide by metronidazole for reinforced anti-corrosion properties of epoxy coatings. RSC Adv. **6**(22), 18217–18226 (2016)
77. M. Conradi, A. Kocijan, D. Kek-Merl, M. Zorko, I. Verpoest, Mechanical and anticorrosion properties of nanosilica-filled epoxy-resin composite coatings. Appl. Surf. Sci. **292**, 432–437 (2014)
78. C.Y. Ge, X.G. Yang, B.R. Hou, Synthesis of polyaniline nanofiber and anticorrosion property of polyaniline–epoxy composite coating for Q235 steel. J. Coat. Technol. Res. **9**(1), 59–69 (2012)
79. P. Ghahremani, A.H. Mostafatabar, G. Bahlakeh, B. Ramezanzadeh, Rational design of a novel multi-functional carbon-based nano-carrier based on multi-walled-CNT-oxide/polydo-

pamine/chitosan for epoxy composite with robust pH-sensitive active anti-corrosion properties. Carbon **189**, 113–141 (2022)
80. M. Motamedi, M. Ramezanzadeh, B. Ramezanzadeh, M. Mahdavian, One-pot synthesis and construction of a high performance metal–organic structured nano pigment based on nanoceria decorated cerium (III)-imidazole network (NC/CIN) for effective epoxy composite coating anti-corrosion and thermo-mechanical properties improvement. Chem. Eng. J. **382**, 122820 (2020)
81. R. Hsissou, O. Dagdag, M. Berradi, M. El Bouchti, M. Assouag, A. Elharfi, Development rheological and anti-corrosion property of epoxy polymer and its composite. Heliyon **5**(11), e02789 (2019)
82. S.M. Lashgari, H. Yari, M. Mahdavian, B. Ramezanzadeh, G. Bahlakeh, M. Ramezanzadeh, Application of nanoporous cobalt-based ZIF-67 metal-organic framework (MOF) for construction of an epoxy-composite coating with superior anti-corrosion properties. Corros. Sci. **178**, 109099 (2021)
83. S. Chhetri, P. Samanta, N.C. Murmu, T. Kuila, Anticorrosion properties of epoxy composite coating reinforced by molybdate-intercalated functionalized layered double hydroxide. J. Compos. Sci. **3**(1), 11 (2019)
84. K. Cao, Z. Yu, D. Yin, Preparation of Ce-MOF@ TEOS to enhance the anti-corrosion properties of epoxy coatings. Prog. Org. Coat. **135**, 613–621 (2019)
85. Y. Wu, J. Yu, W. Zhao, C. Wang, B. Wu, G. Lu, Investigating the anti-corrosion behaviors of the waterborne epoxy composite coatings with barrier and inhibition roles on mild steel. Prog. Org. Coat. **133**, 8–18 (2019)
86. C. Yu, J. Zhang, Z. Li, W. Tian, L. Wang, J. Luo, Q. Li, X. Fan, Y. Yao, Enhanced through-plane thermal conductivity of boron nitride/epoxy composites. Compos. A: Appl. Sci. Manuf. **98**, 25–31 (2017)
87. F. Jiang, S. Cui, N. Song, L. Shi, P. Ding, Hydrogen bond-regulated boron nitride network structures for improved thermal conductive property of polyamide-imide composites. ACS Appl. Mater. Interfaces **10**(19), 16812–16821 (2018)
88. X.J. Zha, J. Yang, J.H. Pu, C.P. Feng, L. Bai, R.Y. Bao, Z.Y. Liu, M.B. Yang, W. Yang, Enhanced thermal conductivity and balanced mechanical performance of PP/BN composites with 1 vol% finely dispersed MWCNTs assisted by OBC. Adv. Mater. Interfaces **6**(9), 1900081 (2019)
89. J. Gu, K. Ruan, Breaking through bottlenecks for thermally conductive polymer composites: A perspective for intrinsic thermal conductivity, interfacial thermal resistance and theoretics. Nanomicro Lett. **13**(1), 1–9 (2021)
90. A. Aparna, A.S. Sethulekshmi, J.S. Jayan, A. Saritha, K. Joseph, Recent advances in boron nitride based hybrid polymer nanocomposites. Macromol. Mater. Eng. **306**(11), 2100429 (2021)
91. D. Zou, X. Huang, Y. Zhu, J. Chen, P. Jiang, Boron nitride nanosheets endow the traditional dielectric polymer composites with advanced thermal management capability. Compos. Sci. Technol. **177**, 88–95 (2019)
92. Y. Han, X. Shi, X. Yang, Y. Guo, J. Zhang, J. Kong, J. Gu, Enhanced thermal conductivities of epoxy nanocomposites via incorporating in-situ fabricated hetero-structured SiC-BNNS fillers. Compos. Sci. Technol. **187**, 107944 (2020)
93. F. Kargar, Z. Barani, R. Salgado, B. Debnath, J.S. Lewis, E. Aytan, R.K. Lake, A.A. Balandin, Thermal percolation threshold and thermal properties of composites with high loading of graphene and boron nitride fillers. ACS Appl. Mater. Interfaces **10**(43), 37555–37565 (2018)
94. R. Künzel, E. Okuno, Effects of the particle sizes and concentrations on the X-ray absorption by CuO compounds. Appl. Radiat. Isot. **70**(4), 781–784 (2012)
95. M.E. Mahmoud, R.M. El-Sharkawy, E.A. Allam, R. Elsaman, A. El-Taher, Fabrication and characterization of phosphotungstic acid-copper oxide nanoparticles-plastic waste nanocomposites for enhanced radiation-shielding. J. Alloys Compd. **803**, 768–777 (2019)

96. H.M. Abd El-Lateef, M. Gouda, Novel nanocomposites of nickel and copper oxide nanoparticles embedded in a melamine framework containing cellulose nanocrystals: Material features and corrosion protection applications. J. Mol. Liq. **342**, 116960 (2021)
97. D. Hassan, A. Hashim, Structural and optical properties of (polystyrene–copper oxide) nanocomposites for biological applications. J. Bionanosci. **12**(3), 341–345 (2018)
98. A.T. Sunny, M. Mozetic, G. Primc, S. Mathew, S. Thomas, Tunable morphology and hydrophilicity to epoxy resin from copper oxide nanoparticles. Compos. Sci. Technol. **146**, 34–41 (2017)
99. A.T. Sunny, R. Adhikari, S. Mathew, S. Thomas, Copper oxide nanoparticles in an epoxy network: Microstructure, chain confinement and mechanical behaviour. Phys. Chem. Chem. Phys. **18**(29), 19655–19667 (2016)
100. V.B. Rajendren, K. Subramani, *Studies on Thermal Conductivity and Thermal Stability of Cu-CNT Composite Powder Filled Epoxy Composites Using a Novel Approach for Sophisticated Thermal Management Applications* (2021)
101. K.A. Jasim, R.N. Fadhil, A.H. Shaban, H.I. Jaafar, B.K. Maiyaly, S.H. Aleabi, E.M. Salman, The effects of copper additives on the glass transition temperature and hardness for epoxy resin. Prog. Ind. Ecol. Int. J. **13**(2), 163–172 (2019)
102. M.H. Nazari, Y. Zhang, A. Mahmoodi, G. Xu, J. Yu, J. Wu, X. Shi, Nanocomposite organic coatings for corrosion protection of metals: A review of recent advances. Prog. Org. Coat. **162**, 106573 (2022)
103. H. Zhang, J. Cao, L. Sun, F. Kong, J. Tang, X. Zhao, Y. Tang, Y. Zuo, Comparative study on the degradation of two self-polishing antifouling coating systems with copper-based antifouling agents. Coatings **12**(8), 1156 (2022)
104. M.M. El-Masry, N.G. Imam, A comparative study between Ag-CuO/epoxy and Mg-CuO/epoxy hybrid nanocomposites: Impressive electrical, mechanical and thermal properties. J. Mater. Res. Technol. **18**, 1784–1801 (2022)
105. Y. Agari, T. Uno, Estimation on thermal conductivities of filled polymers. J. Appl. Polym. Sci. **32**(7), 5705–5712 (1986)
106. A. Agrawal, A. Satapathy, Development of a heat conduction model and investigation on thermal conductivity enhancement of AlN/epoxy composites. Procedia Eng. **51**, 573–578 (2013)
107. D.O. Okanigbe, Production of copper and copper oxide nano-particles from leach solution of low grade copper smelter dust. Dissertation, Tshwane University of Technology, 2019

Chapter 8
Thermal and Mechanical Properties (II): Spark Plasma Sintered Ti–6Al–4V Alloy Reinforced with Mullite-Rich Tailings for Production of Energy Efficient Brake Rotor

Daniel Ogochukwu Okanigbe, Shade Rouxzeta Van Der Merwe, Abimbola Patricia Popoola, Olawale Moshood Popoola, and Pretty Lindiwe Linda

8.1 Introduction

The method to increase the energy efficiency of automobiles can be implemented in a variety of ways [1–9]. For instance, it can be accomplished by lowering parasitic frictional losses in the engine and drive-train, as well as by lowering rolling resistance of the tires, while designing the shape of the vehicle to enhance lower aerodynamic drag [10–18]. The disadvantage of these methods for reducing drag is that they make cars more difficult to stop [18, 20, 21].

Brakes are used to help stop vehicles. A brake, then, is a mechanical device that prevents motion by soaking up energy from a moving system. It is used to slow

D. O. Okanigbe (✉)
Department of Chemical, Metallurgical and Materials Engineering, Faculty of Engineering and the Built Environment, Tshwane University of Technology, Pretoria, South Africa

Pantheon Virtual Engineering Solutions, Nigel, South Africa
e-mail: okanigbedo@tut.ac.za; okanigbeogochukwu@gmail.com

S. R. Van Der Merwe (✉)
Department of Mechanical and Mechatronics Engineering, Faculty of Engineering and the Built environment, Tshwane University of Technology, Pretoria, South Africa
e-mail: vandermerweR1@tut.ac.za

A. P. Popoola · P. L. Linda
Department of Chemical, Metallurgical and Materials Engineering, Faculty of Engineering and the Built Environment, Tshwane University of Technology, Pretoria, South Africa

O. M. Popoola
Centre for Energy and Electric Power, Tshwane University of Technology, Pretoria, South Africa

D. O. Okanigbe, A. P. Popoola (eds.), *Resource Recovery and Recycling from Waste Metal Dust*, https://doi.org/10.1007/978-3-031-22492-8_8

down, halt, or prevent motion in a moving vehicle, wheel, or axle, and is most frequently performed using friction [22]. The brakes are a crucial component of a car because they provide all necessary stopping purposes [23]. There are two main categories of brake configurations:

1. Drum brakes, in which flat pads are pressed against a circle rotor that is attached to the wheel hub, and
2. Disc brakes, in which curved contact surfaces (or "shoes") are forced outward against a circular drum's inner diameter.

Disc brakes are typically a standard part of cars, as well as some types of lorries and buses [24–27]. Compared to drum/shoe type brakes, the rotor/pad configuration of disc brakes often exhibits superior resistance to fade (i.e., reduction in friction as a function of rise in brake temperature) [28]. To prevent thermal cracking and rotor distortion, compositional changes and heat treatments are also adjusted [29, 30].

Most disc brake rotors are commonly constructed of gray cast iron (GCI), which is typically 3.5% carbon- and additive-free [31–33]. Because to its high-melting point, excellent heat storage, castability, and machinability, damping capacity, and cost-effectiveness [34]. Due to its durable performance, GCI is still the material of choice for braking discs and rotors [35]. With GCI, brake emissions in the form of dust (a non-exhaust emission) and particulate matter that are harmful to human health are produced [36–41], but poor corrosion resistance and excessive wear of the brake disc material during service remain issues of concern [34]. In an effort to reduce weight, a number of lightweight alloys have been investigated as replacements; nevertheless, due to their low-melting point and high-intrinsic costs, their widespread application has been constrained [34].

To evaluate lightweight materials for new energy-efficient brakes, however, there is a requirement to look into a number of research initiatives [42–44]. Ceramic composites [44], graphite materials [45], composites based on aluminum [46–48], and composites based on titanium [49, 50] are a few possible materials that could be used for this purpose.

Numerous titanium-based materials' tribological properties have been studied and described in literature [50–53]. This interest was partly sparked by recent studies that promise to lower the price of titanium's raw materials and so make more applications economically viable [54]. Furthermore, titanium alloys have not seen much commercial use in brake rotors outside of specialized racing applications [53, 55]. However, due to their low density (7.4 g/cm^3), good stiffness, relatively high strength, and resistance to corrosive attack by ice-melting salts, they have been given some consideration for use in automotive braking systems [56].

The metallurgy and processing of titanium alloys are well understood as a result of previous and current research and development activities [57–60]. Their tribological properties, however, are less well recognized. While there has been a lot of research on the fretting properties of titanium alloys, there have been relatively few studies that discuss the thermal stress, sliding wear, and friction of titanium alloys [61, 62]. According to the reports based on published works, titanium alloys are unlikely to be suitable rotor materials in the absence of surface modification,

particle additions, or coating [20, 54]. While titanium-based alloys have many benefits for brakes, they also have three significant drawbacks.

1. Titanium has a low-thermal conductivity compared to cast iron,
2. The material is unfamiliar to the automotive sector, and
3. Titanium parts are expensive.

In terms of braking function, pad material selection, and rotor design, thermal behavior is especially important [63–65]. Raw materials, processing, fabrication, surface treatment (if any), and machining are some of the cost-related factors. By including reinforcements [20, 54] to create a composite [66], it is possible to address some of these flaws in Ti–6Al–4V alloy.

In order to retain the matrix-reinforcement system in the compact form and to guarantee the desired shape and dimensions of products made of such materials, a composite matrix material is composed of a material that is the continuous phase and fills the gap between the reinforcement. In addition to distributing loads to the reinforcement and shielding it from harm or adverse environmental effects, a matrix is frequently essential for the chemical and thermal properties of a composite material.

Any metal, including ferroalloys, magnesium alloys, aluminum alloys, zinc alloys, silver alloys, nickel alloys, copper alloys, and titanium alloys, can be used as a matrix material.

In addition, it can be made of non-metal, a ceramic matrix (such as aluminum oxide, silicon carbide, aluminum nitride, graphite, cement, and chamotte), and an organic matrix made of polymeric materials (such as polypropylene, polycarbonate, polyesters, epoxide, and polyamide), or carbon [67–71]. A component with superior attributes—usually strength properties—than the matrix properties is added to a matrix (that is a reinforcement).

The role of a reinforcement in a composite is typically to ensure, among other things, the required rigidity, increased yield strength and strength at room temperature, to prevent the propagation of cracks and to alter matrix susceptibility to plastic deformations [67–71]. A reinforcement can be either in the form of fibers, particles, or elements with complex geometric characteristics and even such ordered spatially.

However, because reinforcement is a generic phrase, its function for some composite materials may not only enhance mechanical or tribological capabilities but also enhance certain physiochemical properties, such as electric, thermal, or magnetic properties. As a result, the reinforcement of Ti–6Al–4V alloy with aluminosilicates like mullite, which has improved thermal shock and thermal stress resistance due to low-thermal expansion, good strength, and interlocking grain structure properties, can reduce the effects of poor thermal and wear resistance when used as brake rotors [72–74].

Mullite, a key ingredient in aluminosilicate ceramics, has been used in pottery and refractories for thousands of years [75]. Mullite is an old material that is finding new applications in electronics, optics, high-temperature structural products, and more as our understanding of it advances [76]. Compared to the majority of other metal oxide compounds, including alumina, several of its high-temperature properties are superior [75–78]. The use of Ti–6Al–4V + 3Al2O32SiO2 composite in the

production of brake rotors will undoubtedly be prevented by the high cost of raw materials, including metal powders like mullite that can act as reinforcement for Ti–6Al–4V alloy [54]. This is because Ti–6Al–4V is significantly more expensive than alternatives like steel and aluminum (Table 8.1).

As a result, it becomes necessary to get mullite from secondary resources like slags, slimes, or mullite-rich tailings (MRT) from density separation of waste copper dust (WCD) [79], not only promotes environmental sustainability but also reduces environmental pollution caused by non-biodegradable solid wastes, such as metallic solid wastes, and powdery materials, among others [79]. Additionally, the high cost associated with using Ti–6Al–4V alloy will be significantly reduced by using tailings rich in mullite to create Ti–6Al–4V + 3Al2O32SiO2 composite [54].

The manufacturing of Ti–6Al–4V-based composites, such as Ti–6Al–4V + 3Al2O32SiO2, is not without its challenges. These issues stem from the processing of Ti–6Al–4V composites' high affinities for nitrogen and oxygen, which impairs the ductility of the resulting Ti–6Al–4V products [80]. The processing of Ti–6Al–4V products must therefore be done in regulated, high-temperature, and vacuum environments if the bulk material's characteristics are to be protected and unaffected by interstitial components [81]. Due to this method, Ti–6Al–4V products are exceedingly expensive and have a small range of applications. Researchers have typically found spark plasma sintering (SPS) to be affordable and cost-effective, giving great energy conservation and efficiency over the traditional sintering methods [82–84]. SPS is a new, emerging, and advanced powder consolidation technology.

The method has continued to draw a lot of interest from researchers since it offers the option of high heating vs. fast cooling rates while sintering powders to full densification in a little period of time, under a low-vacuum atmosphere, and at significantly lower temperatures [85, 86]. The most common ultra-rapid sintering method used to create nanostructured materials, carbon nanotube-based composites, intermetallic compounds, amorphous materials, metal/ceramic matrix composites, highly porous and refractory metals/ceramics, functionally graded materials, and other advanced materials is the SPS technique [87, 88].

The Ti–6Al–4V alloy can therefore clearly play a more substantial role in the design of brake rotors with superior heat conductivity and mechanical qualities in light of the aforementioned. To achieve this, the price must be brought down. Investigating the thermal conductivity and mechanical characteristics of SPS Ti–6Al–4V+ 3Al2O32SiO2 composite, for the manufacturing of brake rotors, is one suggested strategy for reaching this goal; nevertheless, this study.

Table 8.1 Cost of titanium compared to competing automobile materials [54]

	Material ($ per pound contained)			
Item	Steel	Aluminum	Magnesium	Titanium
Ore	0.02	0.10	0.01	0.30
Metal	0.10	0.68	0.54	2.00
Ingot	0.15	0.70	0.60	4.50
Sheet	0.30–0.06	1.00–5.00	4.00–9.00	8.00-

Key: Magnesium sheet is not commonly used. Castings are $2.50–$10.00 per pound

8.2 Problem Statement

The following are general discussions of brakes rotors as it pertains to challenges faced with the integrity and durability of structural materials used in its design:

1. Developing the design of cars to improve reduce aerodynamic drag has the consequence of making the vehicles more difficult to stop [19–21].
2. Due to its durable performance, GC) is still the material of choice for braking discs/rotors [35]. Weight, low-corrosion resistance, and excessive brake disc material wear throughout service remain topics of concern, but [34].
3. Using GCI as a brake disc or rotor material causes brake emissions in the form of dust and particulate matter, which are harmful to human health [36–41].
4. Due to the limitations of GCI as a material for brake rotor/disc design, new, energy-efficient brakes must be made of lightweight materials [42–44].

Although titanium alloy (Ti–6Al–4V) is used to create brake rotors that are lightweight, it also offers potential benefits in terms of its high strength, low density, high-fracture toughness, and great corrosion resistance. For effective operation while in service, there are still several limits that must be addressed. These restrictions include the following:

5. The use of titanium alloy (Ti–6Al–4V) as a lightweight material to construct brake rotors is constrained by its high fabrication and processing costs, limited heat conductivity, and poor wear resistance [20].
6. Because of their strong affinities for nitrogen and oxygen during processing, Ti–6Al–4V composites exhibit reduced ductility [80].

8.3 Research Objectives

8.3.1 Main Objective

This project's primary goal is to analyze the thermal conductivity and mechanical property of a composite made from SPS Ti–6Al–4V and MRT that will be used to make brake rotors.

8.3.2 Sub-Objectives

1. The four sub-objectives of ore sampling, ore preparation, characterization of MRT and determination of the true density of MRT are to be completed in order to meet the aim.
2. Ti–6Al–4V+MRT composites SPS process optimization.

3. Determine how compositional variation in the SPS Ti–6Al–4V+MRT composites affects thermal conductivity.
4. Analyze the impact of compositional change on the wear resistance of composites made from SPS Ti–6Al–4V and MRT.
5. For the thermal conductivity and wear resistance of SPS Ti–6Al–4V+MRT tailings composites, create the best predictive model possible.
6. As a suitable structural material for production brake rotors, SPS Ti–6Al–4V+MRT composites will be validated experimentally and by simulation of its thermal conductivity and wear resistance.

8.4 Research Hypotheses

The following can be hypothesized based on the model suggested to address the difficulties identified:

1. Reduced aerodynamic drag.
2. Improved brake rotor material resistance to corrosion and wear in use.
3. Improved thermal conductivity of the material used to make brake rotors.
4. Removal of non-exhaust emissions.
5. Lowered cost of manufactured material for brake rotors.
6. Improved material ductility of brake rotors.

8.5 Significance of Study

These areas will benefit from this research's successful conclusion:

1. Production of a brake rotor that supports the low-cost development of an energy-efficient car.
2. The sustainability of the earth, in spite of other deteriorating environmental variables, while offering mullite as a substitute natural resource for MRT-based surface exploration.
3. The creation of material for brake rotor design using a method of fabrication and processing that is both affordable and efficient.

8.6 Literature Review

8.6.1 Introduction

With the help of a brake—a mechanical device that prevents motion by collecting energy from a moving system—rolling resistance of tires can be reduced. The brakes are a crucial component of a car because they provide all necessary stopping purposes [23]. According to Dizdar et al. [90], GCI has traditionally been used to

make brake rotors because it has strong wear resistance and good thermal conductivity properties. However, a GCI brake rotor is hefty since GCI is thick in comparison to other materials. At least three factors make a hefty brake rotor undesirable:

1. A vehicle's overall weight is increased by a hefty brake rotor, which decreases fuel efficiency and raises emissions.
2. The vehicle weight below the springs, or the unsprung vehicle weight, includes brake rotors. Unsprung weight increases the "NVH" (also referred to as "noise, vibration, and harshness") associated with vehicle operation. NVH often gets better when unsprung weight is lowered.
3. A vehicle component that needs to be rotated while in use is a brake rotor. As a result, a heavier brake rotor needs more energy to change its rotational speed.

Hence, researching for an alternative lightweight material that can be used to design energy efficient brake rotors is very important.

8.6.2 Theoretical Background

8.6.2.1 Titanium and Ti–6Al–4V Alloy

Lightweight materials titanium (Ti) and its alloys (Ti–6Al–4V alloy) are known for their superior mechanical qualities. Their high price relative to other lightweight materials like aluminum (Al), however, restricts their use for a variety of engineering applications; a notable illustration of this limitation is their use as a structural material for the construction of automobile brake rotors.

8.6.2.2 Mullite

Due to its high-temperature stability [91] and suitable properties like high-melting point, thermal shock resistance, excellent dielectric strength, and good creep resistance, and corrosion stability, mullite is an important ceramic material for both conventional and advanced structural applications.

Neveling [92] provided a breakdown of WCD deposition rate during copper pyrometallurgy at South Africa's copper mine. The chemical composition of WCD is detailed in Table 8.2 [93, 94] (Fig. 8.1).

8.6.2.3 Design of Brake Rotors

The brake assembly should be built with high strength, good corrosion resistance, low noise, light weight, good thermal conductivity, long durability, strong wear resistance, consistent friction, and an acceptable cost-to-benefit ratio in mind. The numerous kinds of braking rotors are depicted in Fig. 8.2. Drum brakes have curved contact surfaces that are forced against the internal diameter of a drum, while uniform pads in disc brakes press against a circular disc that is mounted to the wheel [95].

Table 8.2 Mineralogical composition of PC's WCD [93, 94]

S/N	Minerals	Chemical formulae	Weight (%)
1	Cuprospinel	$Cu_{6.88}Fe_{17.12}O_{32.00}$	24.34
2	Chalcopyrite	$Cu_{6.88}Fe_{4.00}S_{8.00}$	7.95
3	Mullite	$Al(Al_{0.69}Si_{1.22}O_{4.85})$	42.97
4	Gypsum	$Ca(SO_{4.00})(H_{2.00}O)_{2.00}$	11.69
5	Quartz	$SiO_{2.00}$	11.45
6	Magnetite	$Mg_{0.04}Fe_{2.96}O_{4.00}$	1.60

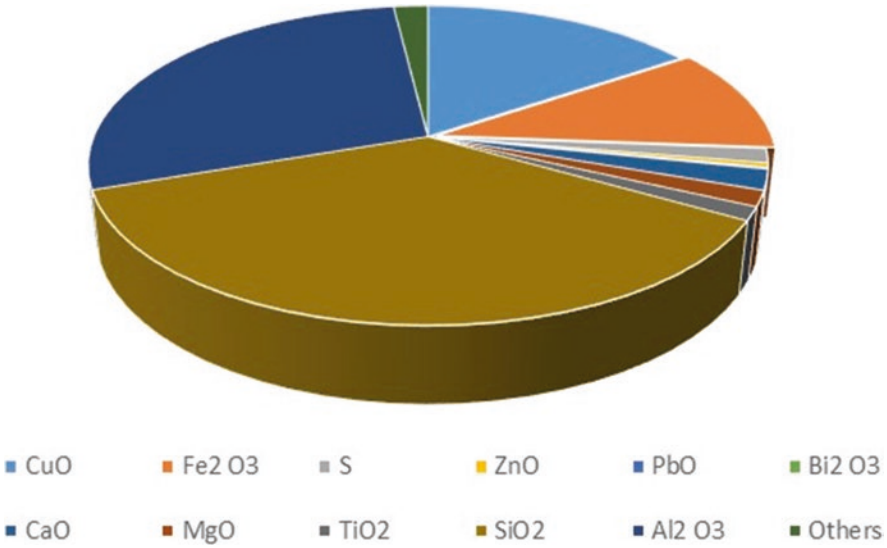

Fig. 8.1 Chemical composition of MRT as determined by X-ray fluorescence [123]

8.6.3 Review: Use of TI–6Al–4V Alloy to Design Brake Rotors

Ti–6Al–4V alloy works, notably as a structural material for engineering applications in the automotive industry, as shown by the performance advantages that have been identified and extensively published in vehicle applications over many years [56]. The Ti–6Al–4V alloy has a high strength-to-density ratio and extraordinarily good corrosion resistance, according to the reports in the open literature [96–101].

Due to Ti and its alloys' remarkable corrosion resistance, they are used as brake pad guide pins and sealing rings in brake line connection flanges. As Ti has a limited thermal conductivity, the brake fluid is safeguarded [56].

In the conclusion section of their research, Froes et al. [56] stressed that Ti can unquestionably play a role in the development of fuel-efficient lightweight cars. The authors concede that there are methods that can be used to modify Ti–6Al–4V alloy in order to accomplish this goal (the creation of lightweight, fuel-efficient automobiles), but they caution that the method chosen must be economical.

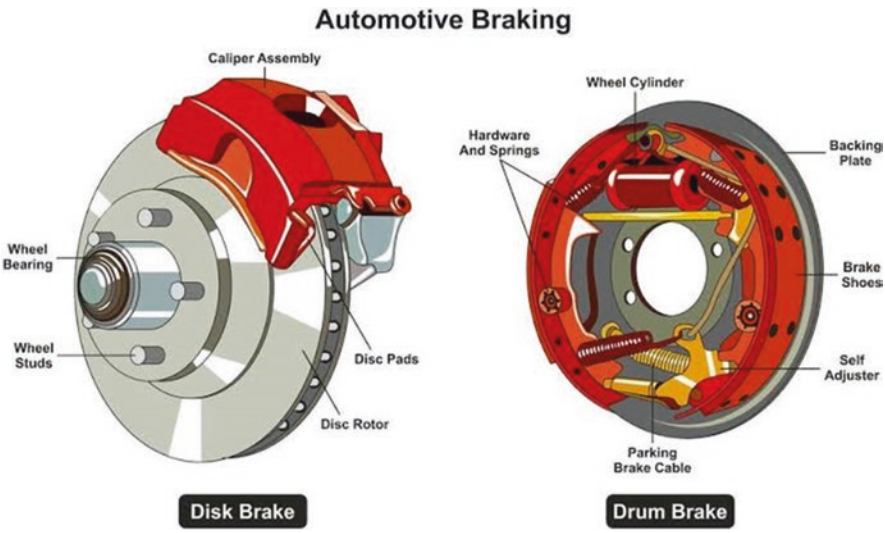

Fig. 8.2 Disc rake and drum brake (source: google image)

The authors concluded their report by stating that, given that 50 million cars and light trucks are produced around the world annually and that the current global titanium market is estimated to be worth 50,000 metric tons, even a small increase in titanium consumption per vehicle would have a significant impact.

However, it is vital to pinpoint the knowledge gap in order to develop a better Ti–6Al–4V matrix composite and construct resilient, energy-efficient automotive brake rotors. As a result, the parts that follow give a concentrated literature overview.

8.6.3.1 Problem Definition and Solution Formulation of Ti–6Al–4V Alloy for Design of Vehicle Brake Rotors

Problem Definition

The lifespan and performance of a vehicle's brake rotor are significantly influenced by the quality of the metal used in its construction. The brake rotor will function better on the car if a better material was chosen for its design. Ti–6Al–4V components that are lightweight can lighten the load on the vehicle, improving fuel efficiency [89]. However, Ti–6Al–4V alloy has a lower Young's modulus than steel and machining challenges in addition to other drawbacks like poor wear resistance and poor thermal conductivity [102, 103], an essential physical property that helps in the transfer of heat quickly and prevents thermo-mechanical fatigue, deformation, and hot cracking, thus prospering the applications of Ti–6Al–4V alloy in more complex or harsh conditions and improving the service life of engineering components desired.

Ti–6Al–4V alloy has only been used in a few high-end road vehicles and racing automobiles due to the high cost of metal alloy powders [56]. Ti–6Al–4V alloy is therefore unlikely to be a suitable structural material, especially in applications that emphasize weight-to-cost savings.

Solution Formulation

The automobile industry has previously set high financial and life cycle expectations, and the titanium sector has worked to accomplish these goals by concentrating on three key areas:

1. Enhanced wear resistance via Ti–6Al–4V alloy surface modification or coating.
2. Improved thermal conductivity achieved by using less expensive composite materials.
3. Investigating low-cost manufacturing techniques.

8.6.3.2 Additive Manufacturing of Ti–6Al–4V Alloy and Effect on Its Wear and Thermal Conductivity Properties as Material for Design of Brake Rotors

Because additive manufacturing is a low-cost production method, a recent trend in additive manufacturing of the Ti–6Al–4V alloy is to change the process parameters or add alloying elements to change the microstructure in order to get the desired performance.

Microstructural Modification of Ti–6Al–4V Alloy

Two-phase (α+β) alloys with high strength are typically used in structural applications. These alloys' mechanical characteristics are highly dependent on their microstructure (geometrical arrangement of the two phases). Ti–6Al–4V is the most widely used of all α+β Ti alloys with Al as α phase (Fig. 8.3a) stabilizer and vanadium as a β phase (Fig. 8.3b) stabilizer [104].

As a result, the strong demand for new Ti–6Al–4V materials that perform well in severe settings has been sparked by developments in microstructural modification of Ti–6Al–4V alloy (such as the one brake rotors operate in). However, novel low-cost Ti–6Al–4V materials with improved wear resistance and thermal conductivity are in high demand, especially in the automotive sector, as a material to design brake rotors.

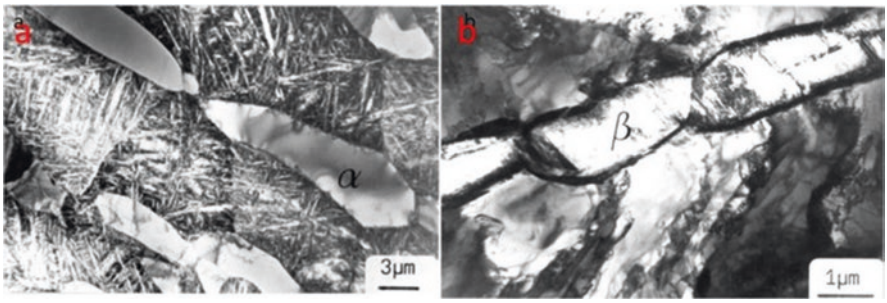

Fig. 8.3 TEM image of Ti–6Al–4V recrystallization to (**a**) bi-modal structure (950 °C) and (**b**) a globular structure [105]

Coating of Ti–6Al–4V Alloy

The low scratch and wear resistance of Ti–6Al–4V alloy, according to Yazdi et al. [106], can be improved by a diffusion treatment. Thermal oxidation at 850 °C for 3 and 6 h led to the formation of an oxygen diffusion layer (ODL) on Ti–6Al–4V. In comparison to Ti–6Al–4V alloy, the ODL Ti–6Al–4V samples shown greater hardness and less plastic deformation. When the ODL Ti–6Al–4V samples were subjected to normal loads of 40 N and 50 N, their brittle nature caused the development of cracks and substantial acoustic signals during scratching. The obtained results also indicated that ODL Ti–6Al–4V samples had stronger scratch and wear resistance than Ti–6Al–4V samples. However, oxygen enrichment would have a negative impact on the fatigue characteristics and consequently would not be appropriate for revolving brake rotors [107].

A vehicle brake rotor component was manufactured in the study by Martino [108] using a Ti base powder alloy that had been 3D printed to the correct shape before coating. On this 3D printed part, the wear surface coating was either plasma sprayed on or integrated into the body after the main component was created. Therefore, bond coat and topcoat are present on each braking surface. Typically, the topcoat is a ceramic layer made of zirconium oxide (65 to 75 parts by weight) and chromium carbide (25 to 35 parts by weight), with Al as an additional component in the bond coat. Less nickel and aluminum can be present in the topcoat and intermediate coat than in the bond coat.

After that, the combined product was subjected to sintering, machining, and double disc grinding. The enhanced rotor was made of two outer layers of Ti metal mixed with other metals, sandwiching a center layer made of Ti metal and metal alloy. This technology also offered a better way to create a vehicle brake rotor using 3D printing techniques.

Chromium and zirconium ($10 per 100 g and $15 per 100 g, respectively) are used in both case situations (i.e., [108, 109]), which defeats the purpose of a cost-effective strategy as suggested by Froes et al. [56]. As temperature decreases, the likelihood of the oxide layer detaching from the surface increases. This is due to the

significant mismatch between the lattices of titanium and metal oxide [110], the large ratio of the oxide to titanium specific volume [111], and the significant difference in the coefficients of thermal expansion between titanium and metal oxide [112].

In another study, Blau [20] tested a full-scale Ti rotor on a dynamometer to examine the potential of Ti-based materials as truck disc brake rotors. The designs for a commercial hydraulic truck rotor were used to create four full-sized, investment-cast Ti alloy rotors, which served the intended purpose. After that, a proprietary, ceramic-containing coating that was about 1–2 mm thick was thermally sprayed onto the rotors (Fig. 8.4a). They were put through standard industry tests to determine how well the Ti brake rotors performed.

According to the results, the Ti rotor ran hundreds of degrees Celsius hotter than the GCI under comparable circumstances. Figure 8.4b depicts the rotor's thermal picture. Due to previous laboratory testing and Ti's lower heat conductivity compared to Fe, maximum temperatures for thermally sprayed Ti rotor surfaces were higher than those for GCI. There was a time during the hot performance test portion when the pad ran the hottest and the rotor ran the coldest. The maximum lining temperature to maximum rotor temperature ratio for the series of sliding pairs reflects this. Then it was suggested that brake hardware made of Ti should not just be replaced with GCI using the same designs, but rather should be constructed to take these features into account. Better brake lining materials that are tailored for Ti-based rotors also need to be created and put to the test. In order to help transmit heat away, this will need to have a higher metallic content. It also needs to have acceptable wear lifetimes for both the pads and the rotors.

Reinforcement

According to Falodun et al. [104], the use of Ti–6Al–4V alloy is limited to temperatures about 400 °C because it loses effectiveness as wear resistance as temperature increases. The authors claim that the influence of reinforcing phases is responsible

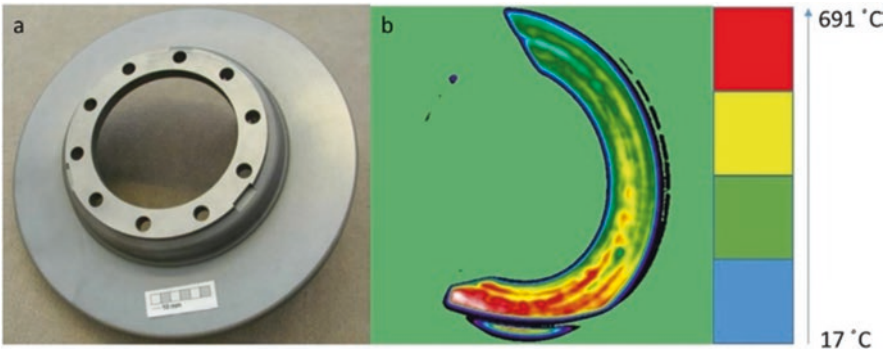

Fig. 8.4 (**a**) Ti alloy truck brake rotor with a protective thermally sprayed coating applied to the friction surfaces and (**b**) infrared image of a Ti-based brake rotor [20]

for the improved attributes of metal matrix composites (MMCs), including wear resistance and thermal conductivity, among others.

In the study by Patil et al. [113], optical microscopy, scanning electron microscopy (SEM), X-ray diffraction (XRD), electron back scattered diffraction, and pin-on-disk tribometry were used to examine the impact of adding TiB2 to Ti–6Al–4V on the wear performance. The results demonstrated that the microstructure altered from martensite laths to a refined bi-modular structure with the addition of TiB2. As a result, wear performance was improved. It is suggested that a slower cooling rate be used to create the bi-modal structure (Fig. 8.5) rather than the martensite structure that is typically seen in Ti–6Al–4V alloy treated with DMLS.

Thermal conductivity tests were made on unreinforced Ti and Ti–6Al–4V alloy, reinforced Ti with short fiber SiC, particulate SiC and particulate TiB2, and reinforced Ti–6Al–4V alloy with long fiber SiC in the study done by Gordon et al. [115]. Instead of both forms of particle, the data obtained indicated an improvement in thermal conductivity with the TiB2 reinforcement. The significant heat resistance of the SiC/Ti interface was cited as the cause of the anomaly and was linked to the type of reaction layer that was produced at the interface during processing. The high-thermal resistance of the interface also reduced the transverse conductivity of the Ti–6Al–4V reinforced with long SiC fibers, though in this instance the effect was less noticeable due to the reinforcement's larger diameter, which lowers the frequency at which heat must be transported across an interface. Finally, the short SiC fiber/Ti composite had comparable traits, with the exception that the axial

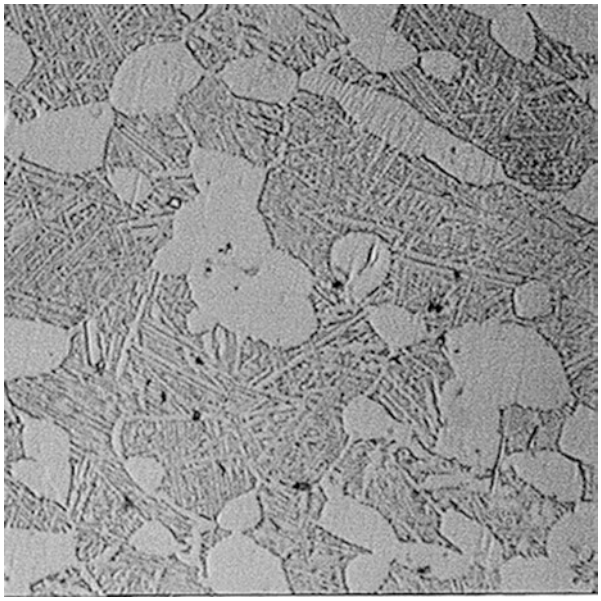

Fig. 8.5 The bi-modal microstructure when the globular α is surrounded by the Widmanstätten platelets [114]

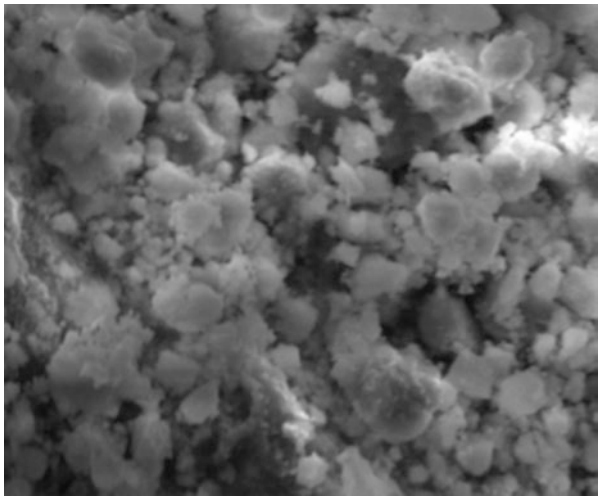

Fig. 8.6 Image of secondary resource of mullite from Palabora copper (PTY) company, Limpopo, South Africa. (Image taken by scanning electron microscopy)

conductivity was somewhat less than anticipated. This result was attributed to localized matrix porosity at the ends of the fibers.

The work of Kushch [116], which concentrated on the numerical algorithm of the multipole expansion approach for conductivity of ellipsoidal particle composite, is in accordance with Gordon et al. [115] and their study. The algorithm-based method, according to the authors, offers a quick and accurate analysis of the local potential fields and the effective conductivity of composites with a sufficient account for the arrangement and direction of inhomogeneities. According to the authors' findings, the volume content of inhomogeneities, their organization, size, and form (Fig. 8.6), inhomogeneity-matrix conductivity ratio, and normalized interface conductivity all affect an elliptic fiber composite's effective transverse conductivity [116]. The original cell shape was established as a perfect (square or hexagonal) fiber packing, imposing the porosity, or, alternatively, the number of fibers, mean fiber radius, and fiber volume fraction [117].

Secondary Resource of Mullite as Reinforcement to Ti–6Al–4V Alloy

Halloysite transforms to mullite (i.e., an aluminum silicate 3Al2O32SiO2) during thermal processes, while in service as engine blocks, pistons, cylinders, and brake discs, according to Dobrzaski et al. [68]. This is why halloysite was chosen to develop aluminum porous skeletons (and, by extension, Ti porous skeletons), they reported. A sintered porous skeleton of Al or Ti alloy matrix composite materials created by gas-pressure infiltration processes will use the mullite as reinforcement.

However, it is anticipated that using inexpensive secondary resources, such as MRTs from density-separated copper smelter dust (Fig. 8.6), as reinforcement

material to either of these lightweight alloys will result in similar enhanced thermal conductivity properties without the need for phase transformation as in the case of the halloysite.

Ti and Ti–6Al–4V alloys have good physical and mechanical characteristics, with the exception of thermal conductivity and wear resistance, as was previously mentioned. Thus, low-cost processing equipment and raw materials such regular kaolinite or other clay minerals are required. The cost-effective method suggested by Froes et al. [56] can be achieved by using materials with high-thermal conductivity, such as mullite particles from secondary resources, such as MRT from density separated copper smelter dust, to manufacture Ti–6Al–4V-matrix composites.

Manufacturing Method

In the study by Tabrizi et al. [118], Ti alloy matrix composite reinforced by in-situ TiB whiskers (TiBw) and TiC particles were created by SPS fabrication of a powder combination consisting of Ti–6Al–4V and B4C at a temperature of 1100 °C (TiCp). For TiBw and TiCp, the reinforcement content in vol% ranged from 0.12 to 0.5 and from 0.5 to 2, respectively. The outcomes demonstrated the alignment of TiBw in the rolling direction of the rolled samples and the refining of alternative/lamellae. The Ti–6Al–4V—0.5 vol%, TiBw—0.12 vol% TiCp sample exhibited the maximum flexural yield strength, according to the findings of three-point bending tests (1850 MPa). It was discovered that the greatest flexural strength achieved by the Ti–6Al–4V-1 vol% TiBw-0.23 vol% TiCp composite was 2100 MPa after samples were subjected to a 66% reduction during hot rolling. Fractography analysis of the composite samples made using the SPS approach revealed that clustering of whiskers decreased flexural strength at greater reinforcing amounts.

Ti–6Al–4V foams were created by SPS employing a mixture of Ti–6Al–4V and NaCl powders in the works of Quan et al. [119]. The manufactured composite was unable to reach high-relative densities due to flaws (pores), which were present. The SPS was used to post-heat treat these sintered foams at 1100 °C for 5 min. While densifying the foam walls, these heat treatments were successful in reducing the micro porosity. The foams' Young' s moduli ranged from 33.0 to 9.5 GPa, while their yield strengths ranged from 110.2 to 43.0 MPa and their porosity values ranged from 44.7 to 70.0%, all of which obeyed the Gibson–Ashby models. The post-heat treatment in a pressureless mode of the SPS at the stated 1100 °C for 5 min can be used to reduce the amount of porosity in pore-filled SPS-fabricated Ti–6Al–4V reinforced MRTs, even though these mechanical qualities appear unsatisfactory for brake rotor applications (TRMRT).

In the study by Adegbenjo et al. [120], which examined the densification, hardness, and tribological properties of Ti–6Al–4V reinforced by multi-walled carbon nanotubes (MWCNTs) compacts solidified by SPS. According to the authors, 1, 2, and 3 wt% MWCNTs were distributed in Ti–6Al–4V using high-intensity ball milling, and the powders from the milling process were then solidified using SPS at temperatures between 850 and 1000 °C. Ti–6Al–4V, MWCNTs, ground powders,

and the consolidated compacts were all characterized using SEM, transmission electron microscopy, and XRD as they were being received. On the Ti–6Al–4V and the Ti–6Al–4V/MWCNTs compacts sintered at 1000 °C, dry sliding wear tests were carried out at three load levels of 5, 15, and 25 N utilizing the ball-on-flat tribometer configuration with tungsten carbide (WC) as the counter face material. According to the findings, the relative density of compact Ti–6Al–4V/MWCNTs increased with higher sintering temperatures but decreased as more MWCNTs were added to the Ti–6Al–4V (Table 8.3). Vickers microhardness was improved by raising the sintering temperature and MWCNTs concentration. In comparison to unreinforced Ti–6Al–4V alloy, the wear volume loss and coefficient of friction for the compacts containing MWCNTs were improved [121].

Ti–6Al–4V alloy combines useful technical features, making it an intriguing material for the construction of vehicle brake rotors, according to Abe et al. [122]. The goal of the authors was to examine the effects of different refractory nitrides on the microstructure, mechanical, chemical, and high-temperature oxidation properties of Ti–6Al–4V. These nitrides included titanium nitride (TiN), hexagonal boron nitride (h-BN), and aluminum nitride (AlN). The three refractory nitrides as well as the Ti–6Al–4V powder were effectively combined using the SPS approach (AlN, TiN, and h-BN). SEM, optical microscopy, and XRD were used to analyze the SPS Ti–6Al–4V-based composites' microstructure and phase composition. According to the Archimedes principle and the Vickers microhardness tests, densification and microhardness of the test samples were measured.

The findings demonstrated that due to sufficient diffusional mass movement in strongly bonded particles at the matrix-reinforcement interfaces, the binary composites achieved close to full theoretical relative densification (i.e., 98.23%–99.54%). The relative densification (99.54%) and microhardness (7030 MPa) of the Ti–6Al–4V-3h-BN composite were ideal, exceeding those of the monolithic alloy by 200% and the Ti–6Al–4V alloy reinforced with AlN and TiN by roughly 48%, respectively. With AlN and TiN nanoparticle reinforcement, the matrix's yield and ultimate tensile strengths increased by about 47%, and with nano-h-BN reinforcement, they increased by 116%. In the high-temperature oxidizing environment, Ti–6Al–4V-3TiN demonstrated the highest resistance to oxidation with the least normalized weight gain of 0.85 mg/cm^2.

Table 8.3 Density and microhardness properties of Ti-6Al-4V and Ti-6Al-4V/MWCNTs compacts sintered at 1000 °C [120]

S/N	MWCNT content (wt%)	Theoretical density[a] (g/cm^3)	Measured density[b] (g/cm^3)	Relative density (%)	Microhardness (GPa)
1	0	4.43	4.41 ± 0.01	99.60 ± 0.03	3.55 ± 0.13
2	1	4.41	4.37 ± 0.01	99.10 ± 0.02	3.71 ± 0.09
3	2	4.38	4.31 ± 0.02	98.40 ± 0.04	3.88 ± 0.07
3	3	4.36	4.27 ± 0.01	97.90 ± 0.02	3.90 ± 0.05

Key: [a]Rule of mixture (ρ Ti6Al4V ¼ 4.43 g/cm^3 and r MWCNT ¼ 2.1 g/cm^3)
[b]Archimedes principle

Conclusion on Literature Review
The authors have determined from the studied literature that developing a vehicle's shape to reduce aerodynamic drag has the disadvantage of making the vehicle more difficult to stop. Additionally, authors concur that due to its durable performance, GCI is still the best material for brake rotors. However, the usage of GCI as a brake rotor material produces particulate matter that is harmful to human health and non-exhaust emissions. Due to the GCI's limitations as a material for brake rotor design, new, lightweight materials for energy-efficient brake rotors are required. The Ti–6Al–4V alloy is generally acknowledged by authors to be a deserving lightweight material for the design of energy-efficient brake rotors, despite its high cost, subpar thermal conductivity, and subpar wear resistance. However, in order to address the final two issues, numerous researchers have suggested that Ti–6Al–4V alloy be reinforced with ceramic elements like mullite (i.e., poor thermal conductivity and poor wear resistance). However, scholars concur that the price of metal powders, such as mullite and Ti–6Al–4V alloy, is too high to support the economics of the proposed composite (TRMRT). Although it has not been documented in the open literature, obtaining mullite from trash (i.e., a secondary supply of mullite) to accomplish this goal has the potential to be a cost-effective strategy. As a result, a knowledge gap has been found in the field of TRMRT for the manufacture of energy-efficient brake rotors. Therefore, it is suggested that future research efforts concentrate on examining the mechanical and thermal conductivity characteristics of SPS-TRMRT in order to produce brake rotors that are energy efficient.

8.7 Methodology

Due to its efficiency in terms of cost, it is possible to produce energy-efficient brake rotors by using secondary resources of mullite as reinforcement to Ti–6Al–4V. Therefore, the proposed methodology is described in this section.

8.7.1 Materials

8.7.1.1 Matrix Material

Titanium alloy will be the matrix material in this study (i.e., Ti–6Al–4V).

8.7.1.2 Reinforcement Materials

The MRT from the density separated WCD must be used as the reinforcing material. On Fig. 8.1, you can see the planned MRT's chemical compositions.

8.7.1.3 Equipment and Tools

The equipment/machine on Table 8.4 will be used for ample preparation or characterization during this proposed study.

8.7.1.4 Methods

Powder Weighing

The proposed Ti–6Al–4V + 3Al2O32SiO2 composite is made of the selected powders, which are 10, 20, and 30% by weight accordingly and are made of Ti–6Al–4V and tailings from the density separated copper smelting dust. Use an electronic scale to determine the weight of the amount.

Powder Mixing

A tube mixer will be used to properly combine the measured particles.

The mixed sample will be put into an SPS graphite die for a predetermined amount of time and at a predetermined temperature and pressure.

Density Measurement

Following sintering, the electronic densimeter will be used to measure density. We shall use Archimedes' principle to examine the effects of sintered composites.

Process Optimization

The percentage of Ti–6Al–4V alloy and MRT in the composite will be chosen as the two key parameters to be researched based on prior research and the literature. Three levels were selected for each parameter using the full factorial method (FFM),

Table 8.4 Equipment/machine for proposed study

S/N	Equipment/Machine	Purpose	Equipment/Machine	Purpose
1	Container mixer	SP	X-ray Diffractometer	CH
2	Rotating die splitter	SP	Scanning electron microscope	CH
3	SPS machine	SP	Energy dispersive spectroscope	CH
4	Grinding-polishing	SP	Electronic densimeter	CH
5	Stopwatch-tachometer	SP	Optical magnifying glass	CH
6	Electronic scale	SP	Hardness tester	CH

Key: *SP* Sample preparation, *CH* Characterization

Table 8.5 Experimental parameters and their relative levels

S/N	Parameters	Low (L)	Medium (M)	High (H)
1	Ti-6Al-4V	70	80	90
2	MRT	30	20	10

Table 8.6 Full factorial experimental design method for influencing factors and their levels coded with values in parenthesis

Tests	Percentage content of Ti-6Al-4V (%)	Percentage content of tailings (%)
1	L(70)	L(30)
2	L(70)	M(20)
3	L(70)	H(10)
4	M(80)	L(30)
5	M(80)	M(20)
6	M(80)	H(10)
7	H(90)	L(30)
8	H(90)	M(20)
9	H(90)	H(10)

as shown in Table 8.5. To carry out the experiment, an FFM was constructed taking into account the two factors (Table 8.5) and their pertinent three levels. Therefore, nine experiments will be carried out as given in Table 8.6. The relative levels of the parameters listed in Table 8.6 range from one (1) to three (3) levels. Interactions between parameters are not to be considered in this experiment.

Spark Plasma Sintering

The Ti–6Al–4V + 3Al2O3.2SiO2 composite will be made using SPS technology.

For this, a predetermined volume of raw powder materials (Ti–6Al–4V, 3Al2O32SiO2) must be placed into a conductive graphite die. Then, under pulsed, low-voltage electric current flowing through the die assembly, mechanical pressure must be applied to the graphite die along the vertical axis. To track the sintering temperature while processing the powder, an optical pyrometer or thermocouple must be focused on the die outside wall.

Development of Predictive Models

Modeling Technique for Predictive Output

This sub-section presents the basic steps utilized in the modelling process as contained in this paper:

Step #1: Study trend of experimental samples.
Step #2: Set-up constraint models to categorize and group samples into sub-classes based on #1.

Step #3: Compute absolute difference between input and output samples in same class as grouped in #2.
Step #4: Identify different experimental levels for selected classes.
Step #5: Apply interpolant model to predict output.
Step #6: End.

Table 8.7 contains a generalized representation of the modelling variables. These variables were built into a model and used for the determination of the predictive outputs of the different mineral constituents as contained in the experimental concentrates. The modelling procedure herein is premised on constrained interpolation of outputs from any three sequenced experimental samples. Usually, two of these outputs are known via experimentation, while the third unknown output is obtained via predictive modelling. In Table 8.7, the first and second columns represent the sequenced experimental trials under consideration for interpolation. The third and fourth columns, respectively, represent the (%) proportions of the inputs (p_{i1}, $p_{i2,}$ and p_{i3}) and outputs (p_{o1}, $p_{o2,}$ and p_{o3}) for the mineral constituents under investigation. Furthermore, column five represents the experimental levels, while column six represents the absolute difference between the input and output values expressed in terms of Φ_1, Φ_2, and Φ_3 for each of the three experimental samples under consideration.

The following under listed are modelling notations as presented in this research:

$$\text{Output} = f\left(\text{speed, flow rate, input, feed rate, liquid solid ratio}\right)$$

Let: serial number for inputs:$s_i = \{1, \ldots., n-1, n\}$ and serial number for outputs$s_o = \{1, \ldots., n-1, n\}$ for $\forall n \in R$

where:

$$\exp_{(i)i,j} = \text{Experimental inputs}$$

$$\exp_{(o)i,j} = \text{Experimental outputs}$$

$$\text{Pre}_{(o)i,j} = \text{Predictive outputs}$$

$$p_{ij} = \%\text{input proportion of selected samples}$$

Table 8.7 Generalized representation of model variables

Level	Data acquisition procedure	Input value for variant factor p_{ij}	Output value for variant factor p_{oj}	Expt. levels	Absolute difference between $p_{ij}$and p_{oj}
1-First	Prediction	p_{i1}	p_{o1}	ξ	$\lvert p_{i1} - p_{o1}\rvert = \Phi_1$
2-second	Experiment	p_{i2}	p_{o2}	μ	$\lvert p_{i2} - p_{o2}\rvert = \Phi_2$
3-Third	Experiment	p_{i3}	p_{o3}	σ	$\lvert p_{i3} - p_{o3}\rvert = \Phi_3$

$$p_{oj} = \%\text{output proportion of selected samples}$$

$$\Delta p_j = \left| p_{ij} - p_{oj} \right| \text{absolute difference between } \; p_{ij} \text{ and } p_{oj}$$

where $j = \{1, \ldots, k-1, k\}$ represents the experimental levels.

The "absolute difference" models defined in terms of the experimental levels are shown in Eqs. (8.1), (8.2), and (8.3), and the final computational models for projecting the unknown outputs are shown in Eqs. (8.4), (8.5), and (8.6) with respect to Table 8.8.

$$\Phi_1 = \left[\frac{\Phi_3(\mu - \xi) - \Phi_2(\mu - \xi) - \Phi_2(\sigma - \mu)}{(\mu - \sigma)} \right] \tag{8.1}$$

$$\Phi_2 = \left[\frac{\Phi_3(\mu - \xi) + \Phi_1(\sigma - \mu)}{(\sigma - \mu) + (\mu - \xi)} \right] \tag{8.2}$$

$$\Phi_3 = \left[\frac{\Phi_1(\mu - \sigma) + \Phi_2(\sigma - \mu) + \Phi_2(\mu - \xi)}{(\mu - \xi)} \right] \tag{8.3}$$

$$\left| p_{i1} - p_{o1} \right| = \Phi_1 \tag{8.4}$$

$$\left| p_{i2} - p_{o2} \right| = \Phi_2 \tag{8.5}$$

$$\left| p_{i3} - p_{o3} \right| = \Phi_3 \tag{8.6}$$

Hence, $\Delta p_j = \Phi j$.

Experimental Validation and Simulation

The metal matrix composite's thermal conductivity and wear resistance will be experimentally determined in order to validate the expected ideal composition of Ti–6Al–4V + 3Al2O32SiO2.

Characterization and Tribological Measurement

Characterization

1. Scanning Electron Microscope (SEM) with Energy Dispersive Spectroscopy (EDS)

To ascertain the phase composition of the produced sample, the SEM/EDS shall be employed.

2. X-Ray Diffractogram (XRD)

To ascertain the phase composition of the produced sample, an X-ray diffractometer with monochromatic Cu K radiation must be used.

3. Microstructural Analysis

The microstructure of the produced composites will be assessed using an optical microscope and an electron microscope.

Tribological Measurement

The DUCOM TR 20-M-106 pin-on-disk sliding tribometer will be used to test the wear and frictional characteristics of the SPSed TARMRT in accordance with ASTM G99-05 standard (ASTM Standard, 2010). The disk samples will be loaded against the brake rotor material that has been cut into the shape of a square-headed pin while rotating at a predetermined revolution per minute (RPM). The tests will be run at various speeds of 2 and 3 m/s with a 65-N load over a 2000-m sliding distance. The pin will also be heated during the testing to a temperature of 2001 °C in order to mimic the effect of friction-induced heating during braking. The disk surface temperature will be gauged on-site using an infrared pyrometer (Omega OS550). The associated software will be used to continuously track changes in frictional force and depth of wear. Using an electronic balance with 0.1 mg precision, the weight loss of both the pin and the disk will be determined at the conclusion of each experiment. The coefficient of friction (Eq. 8.7), wear volume loss (Eq. 8.8), and wear rate (Eq. 8.9) will be calculated using the following equations based on the weight loss (Eq. 8.10) measurements and frictional force:

$$\text{Coefficient of friction CoF}(\mu) = \frac{F}{N} \tag{8.7}$$

$$\text{Wear volume loss} V_{\text{L}}\left(\text{mm}^3\right) = \frac{WL}{\rho} \tag{8.8}$$

$$\text{Wear rate} R\left(\text{mm}^3 / \text{Nm}\right) = \frac{VL}{N \times D} \tag{8.9}$$

$$\text{Wight loss} W_{\text{L}}(\text{g}) = W_{\text{I}} - W_{\text{F}} \tag{8.10}$$

where F is the frictional force (N), ρ the density of disk material (g/cm^3), N the normal load (N), D the sliding distance (m), W_{I} initial weight of the disk (g), and W_{F} = the final weight of the disk (g).

8.8 Contribution to Knowledge

The following information will be disclosed at the study's conclusion:

1. A new Ti–4Al–6V+ CSD tailings composite compositional blend is made available.

2. For improved heat conductivity and wear resistance of Ti–4Al–6V alloy, this compositional blend has not yet been used in the construction of braking rotors.
3. Consequently, the composition is brand-new.
4. The provision of mullite, a brand-new secondary resource.
5. Mullite is a secondary resource that has not been utilized as a ceramic material to improve the mechanical and thermal conductivity of Ti–4Al–6V alloy.
7. Consequently, the reinforcement material is fresh.

8.9 Ethical Considerations

This project has no unethical components.

8.10 Dissemination

The findings of this study will be published in publications recognized by the Department of Higher Education and Training (DHET), such as the ones listed below:

1. Reports in the Journal of Materials Science and Engineering, Publishers at Elsevier
2. Additive Manufacturing Journal, Publishers at Elsevier
3. Journal of Compounds and Alloy, Publishers at Elsevier, Materials Science Journal.
4. Publishers by Springer, Journal of OM, Publishers by Springer

The full article will be published in the conference proceedings, and the results will also be presented at regional and worldwide conferences.

8.11 Budget and Time Frame

8.11.1 Budget

Table 8.8 Estimated budget of the project

Items	Cost (R)	Source
Literature sourcing and stationaries	To be estimated	X
Materials and supplies	To be estimated	X
Analytical equipment	To be estimated	X
Travelling expenses	To be estimated	X
Miscellaneous expenses	To be estimated	X
Total		X

Key: *TUT* Tshwane University of Technology; *R* Rand

8.11.2 Time Frame (Table 8.9)

Table 8.9 Estimated time frame of the project

S/N	Task name	Year	
1	Proposal (compilation and presentation)	WIP	WIP
2	Literature review	WIP	WIP
3	Material sourcing	WIP	WIP
4	Sample preparation (sampling)	WIP	WIP
5	Fabrication of test samples optimization process	WIP	WIP
6	Fabrication of test samples	WIP	WIP
7	Thermal conductivity and wear resistance tests	WIP	WIP
8	Results, data, and analysis	WIP	WIP
9	Optimum predictive model development	WIP	WIP
10	3D print of brake rotor and validation of optimum prediction	WIP	WIP
11	Compilation and presentation of final report	WIP	WIP

Key: *WIP* work in progress

References

1. Y. Miao, P. Hynan, A. Von Jouanne, A. Yokochi, Current Li-ion battery technologies in electric vehicles and opportunities for advancements. Energies **12**(6), 1074 (2019)
2. D.X. Yang, L.S. Qiu, J.J. Yan, Z.Y. Chen, M. Jiang, The government regulation and market behavior of the new energy automotive industry. J. Clean. Prod. **210**, 1281–1288 (2019)
3. B. Tanç, H.T. Arat, E. Baltacıoğlu, K. Aydın, Overview of the next quarter century vision of hydrogen fuel cell electric vehicles. Int. J. Hydrog. Energy **44**(20), 10120–10128 (2019)
4. Y. Chen, J. Gonder, S. Young, E. Wood, Quantifying autonomous vehicles national fuel consumption impacts: A data-rich approach. Transp. Res. A Policy Pract. **122**, 134–145 (2019)
5. L.X. Hesselink, E.J. Chappin, Adoption of energy efficient technologies by households–barriers, policies and agent-based modelling studies. Renew. Sust. Energ. Rev. **99**, 29–41 (2019)
6. L. Zhou, Q. Fu, C. Huo, M. Tong, X. Liu, D. Hu, Mullite whisker-mullite/yttrium aluminosilicate oxidation protective coatings for SiC coated C/C composites. Ceram. Int. **45**(18), 24022–24030 (2019)
7. X. Qu, Y. Yu, M. Zhou, C.T. Lin, X. Wang, Jointly dampening traffic oscillations and improving energy consumption with electric, connected and automated vehicles: A reinforcement learning based approach. Appl. Energy **257**, 114030 (2020)
8. D. Phan, A. Bab-Hadiashar, C.Y. Lai, B. Crawford, R. Hoseinnezhad, R.N. Jazar, H. Khayyam, Intelligent energy management system for conventional autonomous vehicles. Energy **191**, 116476 (2020)
9. S. Thomas, J. Rosenow, Drivers of increasing energy consumption in Europe and policy implications. Energy Policy **137**, 111108 (2020)
10. D. Colavincenzo, F.V. Diaz, J. Geither, Bendix commercial vehicle systems LLC, 2020. Front end motor-generator system and hybrid electric vehicle operating method. U.S. Patent Application 16/689,343, 2020
11. D. Smith, B. Ozpineci, R.L. Graves, P.T. Jones, J. Lustbader, K. Kelly, K. Walkowicz, A. Birky, G. Payne, C. Sigler, J. Mosbacher, Medium-and heavy-duty vehicle electrification: An assessment of technology and knowledge gaps (No. ORNL/SPR-2020/7). Oak Ridge National Lab.(ORNL), Oak Ridge, TN (United States), 2020

12. Y.T. Shah, *Modular Systems for Energy Usage Management*. Boca Raton, Florida: CRC Press Taylor & Francis Ltd, 2020.
13. Y.Y. Wang, V.P. Atluri, D. Li, C.J. Lee, GM Global Technology Operations LLC, Coordinated torque and speed control systems and logic for hybrid electric vehicles. U.S. Patent 10,597,022, 2020
14. N. Bizon, *Optimization of the Fuel Cell Renewable Hybrid Power Systems* (Springer, Cham, 2020)
15. A. Mohanadass, Making the Most of the Energy We Have: Vehicle Efficiency. In: Quang Dinh T, ed. Intelligent and Efficient Transport Systems - Design, Modelling, Control and Simulation [Internet]. IntechOpen, 2020
16. J. Lee, K.P. Ha, J. Lee, K. Nam, A study on the design and development of an integrated 48V motor with motorized internal combustion engine (No. 2020-01-0446). SAE Technical Paper, 2020
17. A.M. Dudar, K. Miller, T.G. Leone, Ford Global Technologies LLC. Engine oil warm up using inductive heating. U.S. Patent 10,704,433, 2020
18. J.T. Dalum, Power technology holdings LLC. Hybrd vehicle drive system and method and idle reduction system and method. U.S. Patent Application 16/808,067, 2020
19. S.W. Baek, S.W. Lee, Aerodynamic drag reduction on a realistic vehicle using continuous blowing. Microsyst. Technol. **26**(1), 11–23 (2020)
20. P.J. Blau, Prospects for titanium-based materials as truck disc brake rotors. ORNL Tech Report, ORNL TM-2007-111, 2007
21. J.M.L. Jeyan, K.S. Nair, G. Vincent, CFD analysis on various commercial vehicles to evaluate the aerodynamic characteristics-a comparative study. J. Adv. Res **6**, 59 (2020)
22. A.P. Borse, Design and analysis of brake rotor (DISC), 2019
23. A. Kruczek, A. Stribrsky, A full-car model for active suspension-some practical aspects, in *Proceedings of the IEEE International Conference on Mechatronics, 2004. ICM'04*, (IEEE, 2004), pp. 41–45
24. L.F. da Cruz, C. Rudek, R.Z. Freire, Different approaches on how to improve braking performance in M3 vehicles to meet secondary brake requirements from ECE R13 regulation through low cost solutions (No. 2019-36-0011). SAE Technical Paper, 2020
25. N.V. Vetter, A.C. De Oliveira, E.H.S. Fontes, F. Nogueira, G.H. Fonseca, L.F.N. De Souza, R.D.O. Dos Reis, V.C. Manenti, Development challenges of hydraulic brakes for commercial vehicles (No. 2019-36-0013). SAE Technical Paper, 2020
26. G. Gopinath, P. Murali, Analysis of redesigned brake shoe. Mater. Today Proc **22**, 507–513 (2020)
27. A.Y. Tripariyanto, L.D. Indrasari, S.V. Widodo, A. Komari, Disc brake type of braking system on rear shaft of Go-kart Daiho 7.5 HP. J. Phys. Conf. Ser. **1569**(3), 032049 IOP Publishing (2020)
28. P.J. Blau, J.C. Mclaughlin, Effects of water films and sliding speed on the frictional behavior of truck disc brake materials. Tribol. Int. **36**(10), 709–715 (2003)
29. P.J. Blau, B.C. Jolly, J. Qu, W.H. Peter, C.A. Blue, Tribological investigation of titanium-based materials for brakes. Wear **263**(7–12), 1202–1211 (2007)
30. W. Li, X. Yang, S. Wang, J. Xiao, Q. Hou, Comprehensive analysis on the performance and material of automobile brake discs. Metals **10**(3), 377 (2020)
31. A. Polak, J. Grzybek, The mechanism of changes in the surface layer of grey cast iron automotive brake disc. Mater. Res. **8**(4), 475–479 (2005)
32. R. Srivastava, B. Singh, K.K. Saxena, Influence of S and Mn on mechanical properties and microstructure of grey cast iron: An overview. Mater. Today Proc **26**, 2770 (2020)
33. I. Mutlu, O. Eldogan, F. Findik, Tribological properties of some phenolic composites suggested for automotive brakes. Tribol. Int. **39**(4), 317–325 (2006)
34. O. Aranke, W. Algenaid, S. Awe, S. Joshi, Coatings for automotive gray cast iron brake discs: A review. Coatings **9**(9), 552 (2019)
35. D.B. Miracle, Metal matrix composites–from science to technological significance. Compos. Sci. Technol. **65**(15–16), 2526–2540 (2005)

36. A. Thorpe, R.M. Harrison, Sources and properties of non-exhaust particulate matter from road traffic: A review. Sci. Total Environ. **400**(1–3), 270–282 (2008)
37. T. Grigoratos, G. Martini, Brake wear particle emissions: A review. Environ. Sci. Pollut. Res. **22**(4), 2491–2504 (2015)
38. J. Kukutschová, V. Roubíček, M. Mašláň, D. Jančík, V. Slovák, K. Malachová, Z. Pavlíčková, P. Filip, Wear performance and wear debris of semi metallic automotive brake materials. Wear **268**(1–2), 86–93 (2010)
39. T.A. Cahill, D.E. Barnes, N.J. Spada, J.A. Lawton, T.M. Cahill, Very fine and ultrafine metals and ischemic heart disease in the California Central Valley 1: 2003–2007. Aerosol Sci. Technol. **45**(9), 1123–1134 (2011)
40. L. Ntziachristos, P. Boulter, Road vehicle tyre and brake wear road surface wear. In: Joint EMEP/CORINAIR emission inventory guidebook, 3rd ed., european environment, agency, copenhagen, pp. B770-1–B770-25 (2003)
41. M. Penkała, P. Ogrodnik, W. Rogula-Kozłowska, Particulate matter from the road surface abrasion as a problem of non-exhaust emission control. Environments **5**(1), 9 (2018)
42. A. Mohan, S. Sripad, P. Vaishnav, V. Viswanathan, Trade-offs between automation and light vehicle electrification. Nat. Energy **5**, 1–7 (2020)
43. D.O. Ayogwu, I.S. Sintali, M.A. Bawa, A review on brake pad materials and methods of production. Compos. Mater **4**(1), 8 (2020)
44. M.A. Ts, M. Kt, Study and comparison of mechanical properties of brake rotors made of steel based hybrid metal matrix composite and grey cast iron, 2020
45. Y. Lyu, U. Olofsson, On black carbon emission from automotive disc brakes. J. Aerosol Sci. **148**, 105610 (2020)
46. A.A. Agbeleye, D.E. Esezobor, S.A. Balogun, J.O. Agunsoye, J. Solis, A. Neville, Tribological properties of aluminium- clay composites for brake disc rotor applications. J. King Saud Univ. Sci **32**(1), 21–28 (2020)
47. S.A. Paul, Honda Motor Co Ltd. Aluminum Ceramic Composite Brake Assembly. U.S. Patent Application 16/264,352, 2020
48. F.M. Firouz, E. Mohamed, A. Lotfy, A. Daoud, M.T. Abou El-Khair, Thermal expansion and fatigue properties of automotive brake rotor made of AlSi–SiC composites. Mater. Res. Exp. **6**(12), 1265d2 (2020)
49. N.K. Konada, K.N.S. Suman, Brake friction materials-a review. I-Manager's J. Mater. Sci **7**(4), 51 (2020)
50. B. Zheng, F. Dong, X. Yuan, Y. Zhang, H. Huang, X. Zuo, L. Luo, L. Wang, Y. Su, X. Wang, K. Shi, Evaluation on Tribological characteristics of (TiC+ TiB)/Ti–6Al–4V composite in the range from 25°C to 600°C. Wear **450–451**, 203256 (2020)
51. S. Gheorghe, C.I. Pascu, C. Nicolicescu, Titanium-based sintered alloy with improved wear resistance, in *Applied Mechanics and Materials*, vol. 896, (Trans Tech Publications Ltd., 2020), pp. 270–275
52. R. Yamanoglu, Network distribution of molybdenum among pure titanium powders for enhanced wear properties. Metal Powder Report, 2020
53. M.J. Donachie, *Titanium: a Technical Guide* 2nd ed. (ASM International: Materials Park, OH, 2000).
54. H. Friedrich, J. Kiese, H.G. Haldenwanger, A. Stich, Titanium in automotive applications–nightmare, vision or reality, in *Proceedings 10th World Conference on Titanium*, ed. by G. Lutjering, (Wiley–VCH, Weinheim, 2003)
55. V.A. Joshi, *Titanium Alloys: An Atlas of Structures and Fracture Features* CRC Taylor & Francis Group, Boca Raton, p 1–2, 2006.
56. F.H. Froes, H. Friedrich, J. Kiese, D. Bergoint, Titanium in the family automobile: The cost challenge. JOM **56**(2), 40–44 (2004)
57. M. Jackson, K. Dring, A review of advances. In processing and metallurgy of titanium alloys. Mater. Sci. Technol. **22**(8), 881–887 (2006)
58. L. Bolzoni, E.M. Ruiz-Navas, E. Gordo, Quantifying the properties of low-cost powder metallurgy titanium alloys. Mater. Sci. Eng. A **687**, 47–53 (2017)

59. I. Chang, Y.E.D.S. Zhao, *Advances in Powder Metallurgy: Properties, Processing and Applications* Vol 60 Woodhead Publishing, Oxford, 2013.
60. S. Bahl, S. Suwas, K. Chatterjee, Comprehensive review on alloy design, processing, and performance of β titanium alloys as biomedical materials. Int. Mater. Rev., **66**, 114–139 (2020)
61. J.E. Allison, G.S. Cole, Metal-matrix composites in the automotive industry: Opportunities and challenges. JOM **45**(1), 19–24 (1993)
62. A.M. Sherman, C.J. Sommer, F.H. Froes, The use of titanium in production automobiles: Potential and challenges. JOM **49**(5), 38–41 (1997)
63. H.J. Cho, C.D. Cho, A study of thermal and mechanical behavior for the optimal design of automotive disc brakes. Proc. Instit. Mech. Eng. Part D J. Automob. Eng **222**(6), 895–915 (2008)
64. A. Belhocine, O.I. Abdullah, Thermomechanical model for the analysis of disc brake using the finite element method in frictional contact. Multiscale Sci. Eng **2**, 1–15 (2020)
65. A. Belhocine, A. Afzal, Computational finite element analysis of brake disc rotors employing different materials. Aust. J. Mech. Eng. **20**, 1–14 (2020)
66. A. Celotto, In situ tensile tests of additively manufactured and wrought Ti-6Al-4V alloys, 2020
67. A.K. Kaw, *Mechanics of Composite Materials* 2nd edition, CRC Press, Boca Raton, FL, USA, 2005.
68. L.A. Dobrzański, G. Matula, A.D. Dobrzańska-Danikiewicz, P. Malara, M. Kremzer, B. Tomiczek, M. Kujawa, E. Hajduczek, A. Achtelik-Franczak, L.B. Dobrzański, J. Krzysteczko, Composite materials infiltrated by aluminium alloys based on porous skeletons from alumina, mullite and titanium produced by powder metallurgy techniques, in *Powder Metallurgy-Fundamentals and Case Studies*, (2017)
69. K.K. Chawla, Carbon fiber/carbon matrix composites, in *Composite Materials*, (Springer, Cham, 2019), pp. 297–311
70. B.O. Baba, S. Thoppul, R.F. Gibson, Experimental and numerical investigation of free vibrations of composite Sandwich beams with curvature and debonds. Exp. Mech. **51**(6), 857–868 (2011)
71. P.K. Hg, A. Xavior, Processing of graphene/CNT-metal powder, in *Powder Technology*, Intechopen, (2018), p. 45
72. L. Zhuang, Q.G. Fu, X. Yu, Improved thermal shock resistance of SiCnw/PyC Core-Shell structure-toughened CVD-SiC coating. J. Eur. Ceram. Soc. **38**(7), 2808–2814 (2018)
73. J.P. Zhang, Q.G. Fu, J.L. Qu, L. Zhuang, P.P. Wang, H.J. Li, An inlaid interface of carbon/carbon composites to enhance the thermal shock resistance of Sic coating in combustion environment. Surf. Coat. Technol. **294**, 95–101 (2016)
74. Y. Zhou, A. Ravey, M.C. Péra, A survey on driving prediction techniques for predictive energy management of plug-in hybrid electric vehicles. J. Power Sources **412**, 480–495 (2019)
75. D.J. Duval, S.H. Risbud, J.F. Shackelford, Mullite, in *Ceramic and Glass Materials*, (Springer, Boston, MA, 2008), pp. 27–39
76. J.F. Shackelford, R.H. Doremus, in *Ceramic and Glass Materials*: Structure, Properties and Processing. New York: Springer, (2008)
77. H. Schneider, J. Schreuer, B. Hildmann, Structure and properties of Mullite—A review. J. Eur. Ceram. Soc. **28**(2), 329–344 (2008)
78. C. Sadik, I.E. El Amrani, A. Albizane, Recent advances in silica-alumina refractory: A review. J. Asian Ceramic Soc. **2**(2), 83–96 (2014)
79. D. Okanigbe, P. Olawale, A. Popoola, A. Abraham, A. Michael, K. Andrei, Centrifugal separation experimentation and optimum predictive model development for copper recovery from waste copper smelter dust. Cogent Eng **5**(1), 1551175 (2018)
80. A.O. Adegbenjo, P.A. Olubambi, J.H. Potgieter, E. Nsiah-Baafi, M.B. Shongwe, Interfacial reaction during high energy ball milling dispersion of carbon nanotubes into Ti6Al4V. J. Mater. Eng. Perform. **26**(12), 6047–6056 (2017)
81. M. Yan, W. Xu, M.S. Dargusch, H.P. Tang, M. Brandt, M. Qian, Review of effect of oxygen on room temperature ductility of titanium and titanium alloys. Powder Metall. **57**(4), 251–257 (2014)

82. N.S. Weston, F. Derguti, A. Tudball, M. Jackson, Spark plasma sintering of commercial and development titanium alloy powders. J. Mater. Sci. **50**(14), 4860–4878 (2015)
83. F. Zhang, M. Reich, O. Kessler, E. Burkel, The potential of rapid cooling spark plasma sintering for metallic materials. Mater. Today **16**(5), 192–197 (2013)
84. A. Azarniya, S. Sovizi, A. Azarniya, M.R.R.T. Boyuk, T. Varol, P. Nithyadharseni, H.R.M. Hosseini, S. Ramakrishna, M.V. Reddy, Physicomechanical properties of spark plasma sintered carbon nanotube-containing ceramic matrix nanocomposites. Nanoscale **9**(35), 12779–12820 (2017)
85. V.N. Chuvildeev, D.V. Panov, M.S. Boldin, A.V. Nokhrin, Y.V. Blagoveshchensky, N.V. Sakharov, S.V. Shotin, D.N. Kotkov, Structure and properties of advanced materials obtained by spark plasma sintering. Acta Astronaut. **109**, 172–176 (2015)
86. Z.H. Zhang, Z.F. Liu, J.F. Lu, X.B. Shen, F.C. Wang, Y.D. Wang, The sintering mechanism in spark plasma sintering–proof of the occurrence of spark discharge. Scr. Mater. **81**, 56–59 (2014)
87. H.C. Oh, S.H. Lee, S.C. Choi, The reaction mechanism for the low temperature synthesis of Cr_2AlC under electronic field. J. Alloys Compd. **587**, 296–302 (2014)
88. M. Tokita, The potential of spark plasma sintering (SPS) method for the fabrication on an industrial scale of functionally graded materials, in *Advances in Science and Technology*, vol. 63, (Trans Tech Publications Ltd., 2010), pp. 322–331
89. P. Wang, J. Song, M.L.S. Nai, J. Wei, Experimental analysis of additively manufactured component and design guidelines for lightweight structures: A case study using electron beam melting. Addit. Manuf. **33**, 101088 (2020)
90. S. Dizdar, Y. Lyu, C. Lampa, U. Olofsson, Grey cast iron brake discs laser cladded with nickel-tungsten carbide—Friction, wear and airborne wear particle emission. Atmos. **11**(6), 621 (2020)
91. G.H. Wang, Y.X. Li, Thermal conductivity of cast iron--A review. China Found **17**(2), 85 (2020)
92. U. Neveling, Palabora mining company annual report on ambient air quality monitoring, 2011
93. D.O. Okanigbe, Production of copper and copper oxide nano-particles from leach solution of low grade copper smelter dust, 2019
94. D.O. Okanigbe, A.P.I. Popoola, A.A. Adeleke, Characterization of copper smelter dust for copper recovery. Proc. Manuf **7**, 121–126 (2017)
95. J.E. Duffy, *Modern Automotive Technology* (The Goodheart-Willcox Company. INC, Tinley Park, 2004)
96. H. Attar, M.J. Bermingham, S. Ehtemam-Haghighi, A. Dehghan-Manshadi, D. Kent, M.S. Dargusch, Evaluation of the mechanical and wear properties of titanium produced by three different additive manufacturing methods for biomedical application. Mater. Sci. Eng. A **760**, 339–345 (2019)
97. A. Woźniak, M. Adamiak, G. Chladek, M. Bonek, W. Walke, O. Bialas, The influence of hybrid surface modification on the selected properties of CP titanium grade II manufactured by selective laser melting. Materials **13**(12), 2829 (2020)
98. V. Vaithiyanathan, V. Balasubramanian, S. Malarvizhi, V. Petley, S. Verma, Establishing relationship between fusion zone hardness and grain size of gas tungsten constricted arc welded thin sheets of titanium alloy. SN Appl. Sci **2**(1), 1–12 (2020)
99. D.P. Yan, X. Jin, Characterization of shear band formation and microstructure evolution during orthogonal cutting of Ti-5553: Part I—Shear angle, strain and strain rate. J. Mater. Eng. Perform. **29**, 1–12 (2020)
100. A. Hadadian, R. Sedaghati, Analysis and design optimization of double-sided deep cold rolling process of a Ti-6Al-4V blade. Int. J. Adv. Manuf. Technol. **108**, 2103–2120 (2020)
101. G. Lütjering, J.C. Williams, Alpha + Beta alloys, in *Titanium*, (Springer, 2003) https://doi.org/10.1007/978-3-540-71398-2_5
102. P. Fonda, Z. Wang, K. Yamazaki, Y. Akutsu, A fundamental study on Ti–6Al–4V's thermal and electrical properties and their relation to EDM productivity. J. Mater. Process. Technol. **202**(1–3), 583–589 (2008)

103. F. Borgioli, E. Galvanetto, F. Iozzelli, G. Pradelli, Improvement of wear resistance of Ti–6Al–4V alloy by means of thermal oxidation. Mater. Lett. **59**(17), 2159–2162 (2005)
104. O.E. Falodun, B.A. Obadele, S.R. Oke, O.O. Ige, P.A. Olubambi, M.L. Lethabane, S.W. Bhero, Influence of spark plasma sintering on microstructure and wear behaviour of Ti-6Al-4V reinforced with nanosized TiN. Trans. Nonferrous Metals Soc. China **28**(1), 47–54 (2018)
105. G.E.R.D. Lütjering, Influence of processing on microstructure and mechanical properties of (α+ β) titanium alloys. Mater. Sci. Eng. A **243**(1–2), 32–45 (1998)
106. R. Yazdi, H.M. Ghasemi, M. Abedini, C. Wang, A. Neville, Oxygen diffusion layer on Ti–6Al–4V alloy: Scratch and dry wear resistance. Tribol. Lett. **67**(4), 1–15 (2019)
107. Y.R. Choi, S.D. Sun, Q. Liu, M. Brandt, M. Qian, Influence of deposition strategy on the microstructure and fatigue properties of laser metal deposited Ti-6Al-4V powder on Ti-6Al-4V substrate. Int. J. Fatigue **130**, 105236 (2020)
108. G. Martino, U.S. Patent Application No. 16/104,659, 2019
109. J. Qu, P.J. Blau, B.C. Jolly, Oxygen-diffused titanium as a candidate brake rotor material. Wear **267**(5–8), 818–822 (2009)
110. G.P. Burns, Titanium dioxide dielectric films formed by rapid thermal oxidation. J. Appl. Phys. **65**(5), 2095–2097 (1989)
111. C. Boettcher, First prize deep case hardening of titanium alloys with oxygen. Surf. Eng. **16**(2), 148–152 (2000)
112. H. Dong, A. Bloyce, P.H. Morton, T. Bell, Surface engineering to improve tribological performance of Ti–6Al–4V. Surf. Eng. **13**(5), 402–406 (1997)
113. A.S. Patil, V.D. Hiwarkar, P.K. Verma, R.K. Khatirkar, Effect of TiB2 addition on the microstructure and wear resistance of Ti-6Al-4V alloy fabricated through direct metal laser sintering (DMLS). J. Alloys Compd. **777**, 165–173 (2019)
114. N. Saunders, Modelling of phase equilibria in Ti-alloys, in *Titanium'95- Science and Technology*, Vol. 3, pp. 2167–2176 (1996)
115. F.H. Gordon, S.P. Turner, R. Taylor, T.W. Clyne, The effect of the interface on the thermal conductivity of titanium-based composites. Composites **25**(7), 583–592 (1994)
116. V.I. Kushch, Numerical algorithm of multipole expansion method for conductivity of ellipsoidal particle composite. J. Comput. Phys. **418**, 109642 (2020)
117. B.M. Kim, Y.K. Cho, S.Y. Yoon, R. Stevens, H.C. Park, Mullite whiskers derived from kaolin. Ceram. Int. **35**(2), 579–583 (2009)
118. S.G. Tabrizi, S.A. Sajjadi, A. Babakhani, W. Lu, Influence of spark plasma sintering and subsequent hot rolling on microstructure and flexural behavior of in-situ TiB and TiC reinforced Ti-6Al-4V composite. Mater. Sci. Eng. A **624**, 271–278 (2015)
119. Y. Quan, F. Zhang, H. Rebl, B. Nebe, O. Kebler, E. Burkel, Ti-6Al-4V foams fabricated by spark plasma sintering with post-heat treatment. Mater. Sci. Eng. A **565**, 118–125 (2013)
120. A.O. Adegbenjo, B.A. Obadele, P.A. Olubambi, Densification, hardness and tribological characteristics of MWCNTs reinforced Ti6Al4V compacts consolidated by spark plasma sintering. J. Alloys Compd. **749**, 818–833 (2018)
121. G.D. Revankar, R. Shetty, S.S. Rao, V.N. Gaitonde, Wear resistance enhancement of titanium alloy (Ti–6Al–4V) by ball burnishing process. J. Mater. Res. Technol. **6**(1), 13–32 (2017)
122. J.O. Abe, A.P.I. Popoola, O.M. Popoola, Consolidation of Ti-6Al-4V alloy and refractory nitride nanoparticles by spark plasma sintering method: Microstructure, mechanical, corrosion and oxidation characteristics. Mater. Sci. Eng. A **774**, 138920 (2020)
123. P.L. Linda, D.O. Okanigbe, A.P.I. Popoola, O.M. Popoola, Characterization of density separated mullite rich tailings from a secondary copper resource, a potential reinforcement material for development of an enhanced thermally conductive and wear resistant TI-6Al-4V matrix composite, in *The Proceedings of the 60th International Conference of Metallurgist. Canada*, (2021)

Part V
Other Engineering Applications

Chapter 9
Wave Energy Converter Design: Seawater Integrity and Durability of Epoxy Resin-Filled Corrosive Microorganism Surface-Modified Waste Copper Dust

Daniel Ogochukwu Okanigbe and Shade Rouxzeta Van Der Merwe

9.1 Introduction

Engineering depends critically on the properties of materials [1]. They are crucial in the selection of components for various machines and constructions [2]. These parts should be extremely resilient to fatigue for example and resistant to the many environments they will be utilized in [3]. Before introducing something wholly new, researchers in the field of material science and engineering consider all potential solutions (including material selection) to achieve structural integrity and durability during the design stage of engineering projects [4].

In light of the aforementioned, epoxy resins are materials used not only for making parts but also for attaching them [5]. Epoxy resins have good mechanical properties in terms of strength and stiffness [6]. Epoxy has several advantages, including being fireproof and having a strong resilience to high temperatures [7]. Epoxy resins are largely employed in the maritime and aviation industries, while they are used in many different industrial sectors [8].

Epoxy resins are used in the maritime sector for a range of tasks, such as coating and laminating wooden boat frames to stop seawater corrosion [9]. When liquid, epoxy resins can be utilized to attach components made of diverse materials [10]. When epoxy resins are cured, they become strong, resilient structures with

D. O. Okanigbe (✉)
Department of Chemical, Metallurgical and Materials Engineering, Faculty of Engineering and the Built Envirinment, Tshwane University of Technology, Pretoria, South Africa

Pantheon Virtual Engineering Solutions, Nigel, South Africa
e-mail: okanigbedo@tut.ac.za; okanigbeogochukwu@gmail.com

S. R. Van Der Merwe
Department of Mechanical and Mechatronics Engineering, Faculty of Engineering and the Built environment, Tshwane University of Technology, Pretoria, South Africa
e-mail: vandermerweR1@tut.ac.za

D. O. Okanigbe, A. P. Popoola (eds.), *Resource Recovery and Recycling from Waste Metal Dust*, https://doi.org/10.1007/978-3-031-22492-8_9

low-specific weight and a variety of capabilities in a variety of environments, including water [11–13], moisture [14], humid conditions [15], hydrothermal conditions [16, 17] or seawater conditions [18–20].

Epoxy resins used in the maritime industry are frequently subjected to the impacts of seawater, which is one of the most harmful environments for the service life of engineering structures, as was already mentioned [5]. Epoxy resins contribute to assembly weight reduction, which improves performance, simplifies and, in most cases, greatly lowers the cost of assembly, and provides acceptable load-bearing strength without compromising quality. Epoxy resins used in the maritime industry are regularly subjected to the impacts of seawater, which has already been identified as one of the conditions that is most damaging to the service life of engineering constructions [5]. Epoxy resins aid in the weight reduction of the assembly, which improves performance, makes assembly easier and, in most cases, much less expensive, and provides enough load-bearing strength without compromising quality.

Epoxy resins are therefore a real part of their assemblages. They are designed to function in accordance with specifications unique to the assembly [21, 22]. An important factor in bonding that is frequently essential to ensuring that structural integrity and durability are not compromised [23–25].

The need for economically feasible, environmentally friendly alternatives is increasing exponentially in response to the global desire for alternative energy sources. Thus, using epoxy resins for applications involving renewable energy has the following advantages: lower installation costs, lower maintenance costs, higher power production efficiency, longer equipment lifespan, fewer stress points, simpler labor operations, and more space on the floor.

The potential for ocean wave renewable energy is enormous [26–28]. Since they are still in their infancy, wave energy converters (WEC) are conceivably the least advanced ocean energy generation technology [29–31]. South Africa (SA) may benefit greatly from wave energy given its extensive coastline and high wave energy potential [32–36]. According to Joubert [37], South Africa's 2800 km of coastline has a significant potential for wave energy [38] as shown in Table 9.1.

Additionally, SA's coastline has a production capacity of 25–50 MW/km, according to Banks and Schäffler [38]. There is an estimated total power supply of 56,800 MW throughout the entire coast [39]. Fourie and Johnson [40] estimate that this resource might increase SA's electricity supply by 8–10 GW, made possible by the Electricity Supply Commission (Eskom).

In SA, Eskom is a vertically integrated company that produces, transmits, and distributes power. Eskom generates 95 percent (95%) of the power used in SA. The wave power resources off the east and west coastlines of SA are now being researched by Eskom. Wave data must be recorded and then adjusted in order to conduct the feasibility study that will determine whether it is likely to be worthwhile to invest in a new generation of technology. Depending on the outcome of the resource assessment, Eskom will test several ocean energy conversion technologies in a laboratory. These experiments will assist Eskom's feasibility assessment, which will take place over several years, in selecting the best technology for use on SA's beaches.

Table 9.1 Relevant information of wave recording stations [39]

Rec. Station	Lat./long. Coord.	D.O. (km)	W.D. (m)	Description of data	Recording period	% coverage	Wave recorder
Port Nolloth	29° 46.8′S/16° 46′E	30	100	3 Hourly H_{m0} and T_p	1987/04/08 to 1996/08/31	63	Waverider
Slangkop	34° 7.6′S/18° 10.6′E	13	170	6 Hourly H_{m0} and T_p	1978/10/03 to 1993/06/12	72	Waverider
Cape point	34° 12.2′S/18° 17.2′E	7	70	3 Hourly H_{m0} and T_p	2000/07/01 to 2006/06/30	92	Waverider
FA platform	34° 58.2′S/22° 10.2′E	72.5	113	1 Hourly H_{m0}, T_z, and H_{max}	1998/01/01 to 2003/12/31	97	Radar
Durban	29° 59.2′S/30° 59.9′E	2.3	42	3 Hourly H_{m0} and T_p	1992/08/11 to 2001/10/31	69	Waverider

Key: *Rec. station* Recording Station; *Lat./long. Coord.* Latitude and longitude coordinates; *D.O.* Distance offshore; *W.D.* Water depth

The majority of feasibility studies to date have focused on evaluating various and unique device technologies, on which several review papers have been written [30, 41–44]. The cost of WEC is currently high compared to other mature technologies, such as wind energy conversion systems [45], making it essential for the development of this technology to lower operating and maintenance (O & M) costs. Due to access limits for O&M, which are already a concern for the offshore wind industry, wave farm developments in offshore wave climates may encounter difficulties [46]. Therefore, maintenance activities should be as brief and rare as possible. Material choice may be important in this context [47, 48].

Recent studies and publications have emphasized the need for deeper research into more specialized design areas, typically emphasizing the need for the creation of "new" material solutions.

Traditional welded steel construction has been replaced by the use of marine composite materials, glass fiber-reinforced polymers (GFRP), and carbon fiber-reinforced polymers (CFRP) [49–54]. Numerous advantages of GFRP and CFRP include their low weight (for transportation, installation, and use), durability (against fatigue and corrosion), ease of maintenance, and capacity to produce intricate, seamless structures [55–57].

The importance of composite materials in the development of WEC cannot be overstated, even though there is still a lack of knowledge regarding the mechanical strength of adhesively bonded polymer composite materials under combined factors of internal pressure (i.e., water pressure) and external pressure (i.e., wave loads). In order to do this, investigations into the following material properties are often carried out in order to gauge their potential for the production of WEC: Matrix resins, laminated plates with a range of fiber orientations and thicknesses, sandwich panels with a range of core materials, and material fibers (such as E-glass and S-glass).

Numerous publications in the literature have addressed the effect of water on the integrity and toughness of resin matrices used in maritime applications. In the works of Fernades et al. [58], authors described the fracture envelope of an epoxy resin utilized in the automotive sector as a function of the epoxy-water resin's content. Specimens of the Double Cantilever Beam (DCB) and Open-DCB (ODCB) were matured in distilled and salt water conditions. Bordes et al. [59] looked studied the long-term behavior of epoxy resins-bonded double lap shear steel joints aged in seawater as well as the degradation of an epoxy-mechanical resin's properties.

Bulk epoxy resin was aged in deionized water, salt water, and seawater at 20 °C, 40 °C, and 60 °C. Heshmati et al. [60] investigated the effects of aging the epoxy resins and bonded joints (fiber-reinforced polymer/steel joints) in five demanding conditions, including salt water solution at various temperatures (20 °C and 45 °C). The three-dimensional (3D) moisture diffusion capabilities of various fiber-reinforced polymer/steel (FRP) and epoxy-resin materials under varied aging conditions were investigated.

In a different study, Heshmati, Haghani, and Al-Emrani [61] discussed the effects of cyclic wet-dry, freeze-thaw, and combined wet and freeze-thaw conditions (i.e., distilled water and salt water, when combined with freeze-thaw for 125 and 250 cycles) on the mechanical behavior of bonded FRP/steel joints. The research has shown that drying epoxy resins from a wet state decreases their ductility, among other things. The material properties of these polymer matrix composite constructions decrease when exposed to seawater, which lowers their dependability. Understanding seawater aging and how it affects epoxy resins used in marine applications is crucial.

Therefore, the mechanical strength of epoxy resins can be altered by the powder addition of metallic or nonmetallic components. It was mentioned that one such method involved mixing cured, single-part epoxy resins with copper and aluminum powders to improve thermal conductivity for uses such as metal cutting tools. According to this study, heat conductivity can be greatly increased by including modest amounts of copper and aluminum powder. It should go without saying that any advantages of higher thermal conductivity should not be outweighed by a reduction in mechanical strength. The main subject of this study was how metal particles alter an adhesive's mechanical properties. Results and characteristics are contrasted with those of the adhesive without the inclusion of powder.

Although it is expected that modifying epoxy resins by adding fillers (i.e., metal powders) like copper and aluminum may impact the mechanical integrity and longevity of structural components, it is utilized to develop; however, the prohibitive cost of these metal powders will limit their use [62]. Metal powders that have been purified are too expensive to be commercially useful as fillers. Therefore, it becomes important to obtain metal powders from secondary resources such as slags, slimes, tailings, or waste copper dust in order to mitigate the effects of the high cost of metal powders required for this purpose (WCD). When WCD is used for this reason, environmental contamination from nonbiodegradable solid wastes such metallic solid wastes and powdered materials, among other things, would be reduced. This will not only help the world remain sustainable [63].

Therefore, the proposed study analyzes a few mechanical properties of cured epoxy resin that has aged in seawater conditions, both unmodified and modified. Additionally, the performance of the proposed epoxy-filled WCD composite will be examined in relation to the impact of surface modification of WCD utilizing corrosive microorganisms. The ambient tensile fatigue strength of the aged and cured epoxy resins being tested will be assessed and compared during the testing.

9.2 Problem Statement

Epoxy resin provides a wide range of maritime applications and good strength and stiffness characteristics [6], and it has a wide range of marine applications [64]. The following are actual difficulties with epoxy resins and use to produce WEC for renewable energy harvesting along the South African coastline:

1. One of the circumstances that is most destructive to the service life of engineering structures in this environment is the combination of fatigue and seawater, which frequently affects epoxy resin used in the maritime industry [5].
2. According to Joubert [37], wave energy conversion has a lot of potential along SA's 2800 km of coastline [65, 66], but the technology to harness this natural resource is still under development.
3. By choosing the right materials, the issue of WEC's high O&M expenses [45] can be reduced to a minimum.
4. WCD cannot be used as epoxy fillers because, although being quick and simple, physical and chemical techniques of surface preparation greatly increase the cost of filler [67].
5. Due to a lack of information on joint performance, particularly in regards to how they behave in harsh environments and under cyclic loads, building structural adhesive joints continues to be a significant problem. They are still unable to provide a useful design basis after conducting a significant number of trials to compare the outcomes. Future study in this area will continue to focus on physical testing as a primary goal [68].

9.3 Research Objectives

9.3.1 Main Objective

Studying the integrity and durability of epoxy resin-filled, corrosive microorganism surface-modified WCD for WEC design is the main objective of this project.

9.3.2 Sub-Objectives

The main objective will be achieved by the following sub-objectives:

9.3.2.1 To Determine the Following Mechanical Properties of Unmodified Epoxy Resin

(a) Tensile strength
(b) Fatigue strength

9.3.2.2 To Optimize the Following Mechanical Properties of Epoxy Resin-Filled Synthetic Copper Powder Without Surface Modification

(c) Tensile strength
(d) Fatigue strength

9.3.2.3 To Optimize the Following Mechanical Properties of Epoxy Resin-Filled Synthetic Copper Powder with Surface Modification

(e) Tensile strength
(f) Fatigue strength

9.3.2.4 To Optimize the Following Mechanical Properties of Epoxy Resin-Filled Synthetic Aluminum Powder Without Surface Modification

(g) Tensile strength
(h) Fatigue tensile strength

9.3.2.5 To Optimize the Following Mechanical Properties of Epoxy Rresin-Filled Synthetic Aluminum Powder with Surface Modification

(i) Tensile strength
(j) Fatigue tensile strength

9.3.2.6 To Optimize the Following Mechanical Properties of Epoxy Resin-Filled WCD Without Surface Modification

(k) Tensile strength
(l) Fatigue tensile strength

9.3.2.7 To Optimize the Following Mechanical Properties of Epoxy Resin-Filled WCD with Surface Modification

(m) Tensile strength
(n) Fatigue tensile strength

9.3.2.8 To Determine the Effect of Seawater Aging on Tensile Strength and Fatigue Strength of the Following Composites Chosen at Optimum Test Conditions

1. Stand-alone epoxy resin.
2. Optimum proportion of epoxy resin to copper powder.
3. Optimum proportion of epoxy resin to aluminum powder.
4. Optimum proportion of epoxy resin to WCD.

9.3.2.9 Development of Optimum Predictive Models for the Different Epoxy Resin Composites and the Experimental Validation of Optimum Predictive Models

9.4 Research Hypotheses

The following presumptions can be made based on the model suggested to address the difficulties identified:

1. Epoxy resin with filled WCD will enable wave energy device development at a lower cost.
2. When subjected to internal pressure from seawater, the epoxy resin won't degrade if you utilize epoxy resin that is filled with WCD.
3. When exposed to external pressure from wave stresses, the use of epoxy resin-filled WCD will improve the mechanical properties of epoxy composite.
4. As a result, the durability of WEC created utilizing epoxy resin-filled WCD will be increased.
5. Using a corrosive microbe will help bring down the cost of the filler and hence encourage the usage of WCD as an epoxy-resin filler.

9.5 Significance of Study

The following areas will benefit if this research is completed successfully:

1. Development of a WEC that supports the objective of developing a renewable energy technology, that is energy efficient in order to combat the effect of the ozone layer's depletion due to gas emissions from the combustion of fossil fuels.
2. The sustainability of the planet in the face of other environmental problems while offering a different way to use of natural resources like WCD.

9.6 Background and Literature Survey

9.6.1 Background

Due to the First and Second World Wars, there were significant advancements in the research and production of new plastics and resins during the 1920s, 1930s, and 1940s [69]. By enabling the use of newly discovered materials with a variety of qualities, these developments significantly boosted the development of adhesives [70, 71]. New synthetic adhesives are still being developed today to meet changing needs and advance technologically [72, 73].

In the works of Gleich [74], the usage of adhesive bonds as an alternative to conventional jointing techniques like bolting and welding was compared. There have been more attempts than ever before to use it as a composite material (i.e., a polymer composite material) in new construction projects since it compares favorably to these other conventional techniques of jointing [75, 76] as presenting in Table 9.1. As a result, increasing amounts of research is being done to enhance their strength characteristics [77, 78].

In addition to enhancing the strength features of adhesive bonding, current research efforts attempt to better understand its performance characteristics [79–81], like the necessity of surface preparation [82, 83], such as the need for surface preparation [84, 85], as additional structural weight [86, 87] fatigue resistance [88, 89], corrosion resistance [90, 91], the simplicity of assembly [92], production costs [93], and environmental resistance [94, 95] as shown in Table 9.2.

Yemm et al. [96] believe that despite the progress being made in this field of study, there is still a knowledge gap regarding the behavior of Adhesively Bonded joints (ABJ) as the primary structural element in the hostile maritime environments, especially as it relates to the design of WEC.

WEC operates in a marine environment that causes material degradation because of the following factors: salinity, surface temperature, wave heights, and wind speed [97]. Mehta [98] divided these causes of material degradation into two categories: physical degradation (such as cracking due to cyclic loading and surface wear due

Table 9.2 Comparison of various jointing techniques [74]

S/N	Jointing method	Bonded	Bolted	Welded	Bonded and bolted
1	Surface preparation required	Extensive	Little	Little	Extensive
2	Joining of dissimilar materials	Good	Limited	Poor	Good
3	Added weight to structure	Low	High	Moderate	Moderate
4	Fatigue resistance	High	Poor	Moderate	Moderate
5	Corrosion resistance	High	Poor	Moderate	Moderate
6	Ease of disassembly	Difficult	Easy	Difficult	Difficult
7	Production cost	Medium	Low	Low	High
8	Environmental resistance	Poor	Poor	Moderate	Moderate

to abrasion) and chemical degradation (i.e., physicochemistry, which refers to exchange reactions between aggressive fluid and adhesive bond).

9.6.1.1 Physicochemistry

Over time, research on ABJ, which was made possible by the advancement of the scientific discipline known as surface physicochemistry [99–101] has led to a definition of adhesion that is more consistent but also multidirectional [102, 103].

The range of phenomena that may occur at the touch of surfaces of related materials was specified by Dutkiewicz [99], Pizzi and Mittal [100], Baldan [102], and Szewczak [104]. However, such a broad description only partially explains this phenomenon. Due to the fact that adhesion depends on numerous elements, efforts to describe it in a precise manner are particularly difficult [100, 105].

One of the first definitions was developed by McBain and Hopkins [106]. It was based on an adhesion model that illustrated how two surfaces interlocked with one another. This idea was expanded as a result of additional research, the creation of fresh research techniques, and a deeper comprehension of adhesion. As a result, various models of adhesion are used in literature along with the key variables affecting them. Figure 9.2 presents the division that appears the most frequently in the literature.

9.6.1.2 Adhesion

Mechanical Adhesion

As observed in Fig. 9.1, there are additional parameters that affect adhesion in addition to the first mechanical model, which is a function of the interlocking rough surfaces present in the materials to be joined [100].

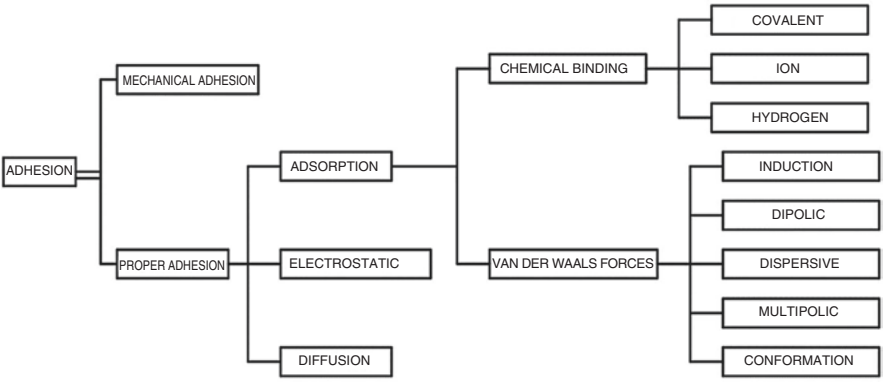

Fig. 9.1 Adhesion types and models [104]

Proper Adhesion

While proper adhesion is essentially dependent on physicomechanical interactions, particularly the potential for chemical bonds to form between atoms on adjacent surfaces (Fig. 9.2). The following adhesion mechanisms are some of those that are described as proper adhesion:

Adsorption Mechanism
Chemical bonds are considered in the so-called adsorption theory, although depending on the circumstances and technique used to attach materials as well as their chemical makeup, different forms of chemical bonds may not necessarily exist at the same moment [107]. Both the more permanent van der Waals interactions required for adhesion and the traditional chemical bonds produced by chemical reactions are significant [104].

However, it is thought that the adhesion brought on by intermolecular interactions is best described by the adsorption theory [99, 108, 109].

Electrostatic Mechanism
The result of charge interactions at the contact is this adhesion process [110].

Diffusion Mechanism
This adhesion mechanism is demonstrated in joining materials due to the reciprocal passage and permeation of charges between surface layers [100, 111, 112], the theory of weak boundary layers accounting for the possibility of the occurrence of factors weakening adhesion on the joined surfaces, i.e., surface pores, impurities, and voids [100, 108, 113, 114].

9.6.1.3 Adhesive

According to ASTM D 907 [115], an adhesive is a substance that can hold things together by surface attachment. Adherends are the two surfaces. The forces of attraction hold the materials to one another at the contact between the adhesive and

adherents. Mechanical interlocking or chemical bonding resulting from physical interactions can be these forces of attraction. As a result, it is critical that the bond strength depends on more than just the bulk properties of the adhesive and adherents.

A structural adhesive is any glue that can unite two stiff materials, withstand or transfer loads, and be reliable over an extended length of time. Chemical categories for structural adhesives include phenolic, acrylic, cyanoacrylate, urethane, and epoxy [68].

Phenolic

One of the main types of phenolic compounds found in plants is phenolic or phenolcarboxylic acid, which is a form of phytochemical referred to as a polyphenol. They can be found in a wide range of plant-based meals, with the largest concentrations being in seeds, fruit and vegetable skins, and leafy greens [116, 117].

Acrylic

A translucent plastic with exceptional strength, rigidity, and optical clarity is acrylic. Acrylic sheet is simple to manufacture, adheres well to solvents and adhesives, and is simple to thermoform. Compared to many other transparent plastics, it offers better weathering characteristics [118].

Cyanoacrylate

Strong, quick-drying adhesives in the cyanoacrylate family are used in industry, healthcare, and everyday life. They come from esters related to ethyl cyanoacrylate. In the presence of water, the cyanoacrylate group in the monomer quickly polymerizes to create lengthy, durable chains [119, 120]. They are slightly harmful in various ways.

Urethane

The chemical formula for ethyl carbamate is CH3CH2OCNH2. It is a whitish solid that is an ester of carbamic acid. It is not a part of polyurethanes, despite its name [121, 122]. Although it is rarely utilized due to its carcinogenic nature, it naturally appears in small amounts in a variety of fermented foods and beverages.

Epoxy Resins

The focus of this study is on epoxy resins as the structural glue because they are employed in segmental construction and have been one of the most popular adhesives since the 1940s.

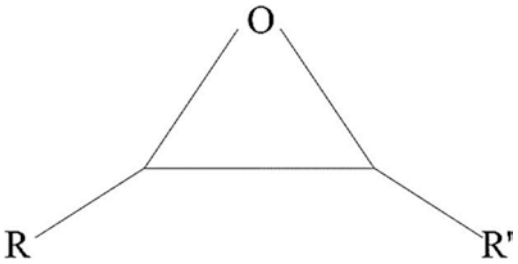

Fig. 9.2 Basic structure of epoxy resin, R refers to any group of molecule with attached carbon atom [123]

One oxygen and two carbon atoms form the fundamental molecular structure of epoxy resin, a thermosetting reactive polymer (Fig. 9.2). Epicholorohydrin is a key basic material found in the majority of commercially available epoxy resins. This molecular foundation is highly malleable and gives rise to a variety of epoxies. Epoxy resins can interact with a wide range of therapeutic agents or hardeners, including amines and anhydrides. There could be an endless number of epoxies with varying properties given the different curative combinations [123]. Glass transition temperature (Tg), mechanical performance, stability, viscosity at room temperature, curing time, chemical resistance, and substrate type are the typical attributes used to describe epoxy resins. These attributes all depend on the formulation of the epoxy resin.

Due to their high fatigue resistance, low production cost, sealing, and thermal or electrical insulation features, epoxy resins have several advantages over bolted or welded joints, but they also have significant drawbacks. They should not, for instance, be intended to withstand peel and cleavage stress. Additionally, they require extensive surface preparation and are vulnerable to deterioration in harsh conditions or at high temperatures.

According to Hartshorn [68], creating structural adhesive joints remains a significant issue because there is a dearth of knowledge regarding the performance of joints, particularly their behavior in harsh environments and when subjected to cyclic loads. Despite a sizable number of experiments to compare the results, they are still unable to offer a practical foundation for design. Physical testing is still a key objective for this kind of research in the future.

It should be reiterated that one of the most widely utilized matrices for creating adhesive compositions, which are then used as structural adhesives in the maritime industry, is epoxy resin [124, 125]. This is a result of a number of factors, such as very good adhesion to a wide variety of materials, reasonably high cure strength (both static and fatigue), minimal cure shrinkage, and resistance to a variety of exploitation forces [126–128].

Epoxy resins can fail to meet a product's performance requirements despite these remarkable qualities. Therefore, it is frequently necessary to change the properties of epoxy resins with various additives to create epoxy-resin composites in order to achieve these performance expectations [129–133]. Diluents, providing agents,

pigments, colors, softening agents, antioxidants, stabilizers, and fillers are a few examples of modifying compounds [129, 131, 134].

9.6.2 Literature Survey

The research on epoxy resin is currently focused on two methods of modification.

9.6.2.1 Modification of Epoxy Resin with Fiber Reinforcement

The first direction entails creating new epoxy composites by adding fiber reinforcements.

Effect of External Pressure (i.e., Cyclic Loads) on Epoxy Resin-Bonded Polymer Composite Performance

Due to the water ballast used to lower the buoy's inherent frequency so that it is not in resonance with waves, the buoys of WEC are sensitive to external pressure from waves. The creation of novel materials that can function under such external pressure has thus been the subject of numerous research papers. As a result, epoxy resin is included, as the following literature reports confirm:

Capela, Oliveira, and Ferreira [135] used short carbon fibers mixed with epoxy resin to help researchers better understand how low stiffness and resistance efficiency values affect failure mechanisms of short fiber composites with large fiber volume fractions. The authors noted that the composites' static mechanical characteristics at low volume fractions are nearly proportional to their fiber content. Low efficiency was found for both tensile stiffness and strength at high volume fraction, though. As anticipated, as the fiber content increases, the strain at failure lowers.

Similar to static strength, fatigue strength rises until the volume of fibers reaches 17.5%, after which it essentially stays constant. The key factors affecting fatigue life are fiber dispersion and porosity.

According to Xu et al. [136], the tensile strength and modulus of an epoxy resin-based composite film were significantly boosted by 300% and 612% as compared to those of pure resin with just 1 weight percent of silk fiber. The material also demonstrated exceptional tear resistance, remaining intact after over 30,000 tensile cycles.

As an alternative to epoxy resin-based FRP plates for the reinforcing of concrete structures, carbon fiber-reinforced polymer (CFRP) and grid-reinforced engineered cementitious composites (ECC) were created in the work by Zhu et al. [137]. The findings demonstrated that every CFRP-ECC plate failed, with the internal CFRP grid rupturing and a dominant crack appearing in the ECC matrix. Regardless of the cyclic loading strategy used, the envelopes of the cyclic tensile stress-strain curves followed the static stress-stain curves. The unloading and reloading trajectories of

CFRP-ECC plates under cyclic uniaxial tensile loads were proposed to be modeled using a nonlinear stress-strain model.

Basalt fiber-reinforced thermoplastic epoxy polymer composites were the subject of a study by Wang et al. [138] to determine their static, fatigue, and damage mechanisms.

Under long-term cyclic loading, the stress-life curves and stiffness deterioration were examined. The findings demonstrated that the basalt fiber-reinforced thermoplastic epoxy polymer has favorable interface properties between the fiber and new thermoplastic epoxy, leading to high tensile strength and ductility. The basalt fiber-reinforced thermoplastic epoxy polymer composites show different degradation rates for low- and high-cycle fatigue loads, and they are as follows:

1. High levels of fatigue stress led to a high rate of fatigue life degradation, which was related to fiber fractures.
2. Matrix cracking and interface debonding dominate the damage pattern at low and medium fatigue stress levels, which has a low impact on the pace at which the fatigue life degrades.
3. At a stress ratio of 0.8, stiffness degradations of 80–90% were seen before to failure for all stress levels.
4. Basalt fiber-reinforced thermoplastic epoxy polymer has a similar static strength and fatigue life at high stress levels to thermosetting epoxy-based thermoplastic epoxy polymer. The fatigue life of the polymer, however, is significantly longer than that of the thermosetting one at low stress levels.

Gonabadi et al. [139] reported that the stiffness degradation of the regions at the fiber/matrix interface regions was strongly correlated with the results of nanoindentation testing on the polymer composite microstructure of environmentally fatigued composite test coupons. This finding validated the degradation of composite constituents.

The mechanical properties of 40 volume percent ramie fiber and 1.5 volume percent organo-montmorillonite (OMMT) nanoclay are found to be improved, according to Sivaperumal and Jancirani [140]. According to wear testing, a composite of 40% fiber and 1% OMMT nanoclay achieved high abrasion resistance. Similar to this, 44,218 cycles of fatigue life are shown in composites containing 1.0vol% OMMT nanoclay. Because of silane-treated ramie fiber and OMMT nanoclay in epoxy composite, water absorption resistance is balanced. When compared to bare resin, the hydrophobicity has not significantly decreased. The SEM images demonstrate improved Ramie fiber adherence to the matrix as well as exfoliation of OMMT nanoclay in the matrix.

According to da Silva Batista et al. [141], after 100,000 cycles of a fatigue test, the tensile strength of epoxy composites supplemented with sisal fibers was 1.4 times that of neat epoxy resin. The composite is also thought to withstand loads of 20% of its maximum tensile strength for 200,000 h before cracking due to creep. In conclusion, the effective adhesion between sisal fibers and epoxy obtained through NaOH treatment allowed the epoxy composite to have good mechanical behavior.

Yan et al. [142] reported that an epoxy resin called PEI-ER was created as a new cathode binder for lithium-sulfur (Li-S) batteries by in situ cross-linking between an epoxide compound and polyethylenimine. With this novel binder, Li-S batteries demonstrated impressive cycling stability and high initial specific capacity.

Effect of Internal Pressure (i.e., Water) on Epoxy Resin-Bonded Polymer Composite Performance

Interlinear shear strength tests on all three carbon/epoxy composites, according to Tual et al. [143], showed that seawater aging had an impact on interfacial adhesion. The combination of electrochemical oxidation and sizing treatments effectively increased the long-term interlaminar shear strength retention for carbon fiber-reinforced polymer in hydrothermal environment from 0.24–0.38 to 0.74–0.86, thus aligning with the specified environmental reduction factor C_E (0.85) given in ACI 440.2R-08. This was reported in the work done by Wang et al. [144]. Scanning electron microscopy and moisture absorption and desorption tests further demonstrated the enhanced toughness of the fiber/epoxy interface (SEM).

Wang and Ploehn [145] found a substantial correlation between water absorption and interfacial adhesion and the degree of an additional relaxation mechanism, known as -relaxation. The tests undertaken were more likely to have difficulties because of water loss, the authors stated. In dry and wet composites, respectively, apparent activation energies of the – and -relaxation processes were statistically significant markers of interfacial adhesion.

The interface debonding during the uptake of hot (100 °C) water was studied by Xu and Ashbee [146]. The differences in the durability of interfacial bonding and the fiber failure modes for variously coated fibers have been determined by studying the formation of stress birefringence during resin swelling in the resin next to individual fibers. The findings demonstrate that the condition of self-stress in model composites, which consist of a single carbon fiber in a coating of epoxy resin, can be increased to the point where the axial tension in the fiber can be sufficient to cause fiber fracture by submersion in hot distilled water.

Additionally, in the study carried out by Pérez-Pacheco et al. [147], carbon fiber/epoxy unidirectional laminated composite was subjected to three levels of humidity—25%, 55%, and 95%—while maintaining a constant temperature of 25 °C. The outcomes demonstrated that each fiber surface treatment has a significant impact on the mechanical properties. Failure mode for the silane-treated carbon fiber-reinforced epoxy laminate was attributed to matrix yielding followed by fiber failure with no indication of fiber-matrix interface failure for moisture contents up to 1.89%, while failure mode for the untreated carbon fiber was attributed to fiber-matrix interfacial failure.

In order to determine the impacts of seawater and temperature on the structural properties of produced composites, Mourad et al. [148] investigated the durability of fiber-reinforced polymer in warm environments and seawater. According to the findings, seawater absorption rose with both immersion time and temperature.

However, moisture causes a dual mechanism of stress relaxation—swelling—mechanical adhesion, and breakdown of chemical connections between fiber and matrix at the interface. The matrix in both composites was effective at protecting the fibers from corrosive substances in saltwater. High temperatures are believed to hasten the breakdown process in composites. The glass/polyurethane composite's tensile strength fell by 19% and 31%, respectively, after one year of exposure to seawater at ambient temperature and 65 °C. The matrix fails ductilely as a result of plasticization brought on by moisture absorption.

In order to assess the kinetics of water diffusion and the impacts of wet aging on the mechanical quasi-static properties at various aging periods, Boisseau et al. [149] tested three types of GRP epoxy laminates. The type of glass fiber used did not significantly change the diffusion behavior, according to the authors.

Utilizing four-point bending tests of three injected composites across various aging times at 60 °C, the mechanical behavior was also assessed. The quasi-static composite flexural strength was reduced by 40–56%, which indicates that saltwater aging has a significant impact on the flexural failure stress. Long aging durations resulted in a failure mode transition from compressive to tensile.

Combined Effect of External and Internal Pressures on Epoxy Resin-Bonded Polymer Composite Performance

According to what was previously mentioned, Dawson et al. [150] investigated the impact of the test environment variables, including temperature, conditioning medium (natural seawater or deionized water), and pressure, on the seawater aging of prepreg and infused glass/epoxy composites in terms of laminate weight gain and mechanical properties. This study was carried out to acquire a thorough grasp of how to design for a short service life.

The infused laminate, created with a final cure at 80 °C, also underwent a fatigue test. The following were the key findings:

- The temperature accelerated the weight gain of all specimens after two years of immersion at various temperatures (4 °C, 25 °C, 40 °C, 60 °C, and 80 °C), and prepreg laminates took longer to saturate than the injected ones.
- Proper temperature control is essential to avoiding severe degradation effects.
- Deionized water-conditioned specimens gained weight more quickly than seawater-conditioned specimens did.
- The weight growth of either type of laminate did not differ appreciably when subjected to conditioning at high pressure (500 bar).
- Aging in deionized water and natural saltwater significantly decreased the interlaminar shear strength as well as the tensile strength. The effect was stronger for deionized water.

9.6.2.2 Modification of Epoxy Resin with Powder Fillers

The findings of experiments conducted Kilik and Davies [151], to ascertain the mechanical characteristics of an adhesive containing metallic particles are reported. The glue was a hardened, one-part epoxy with admixed copper and aluminum powders in varying proportions, each with a variety of grain sizes. Tensile strength, shear strength, peel force, impact strength, and fatigue strength results were obtained. All findings were contrasted with those found in the glue without the addition of powder.

Based on this, the second trend in polymer chemistry involves adding additives, like powder fillers, to adjust the properties of polymers like epoxy resins [152, 153]. The functional, mechanical, physicochemical, and rheological characteristics of the adhesive may be greatly impacted by its application. Additionally, by using them, it is feasible to reduce the quantity of adhesive that is often produced during the processing and refining of crude oil or through the expensive process of synthesizing other mers.

Epoxy Composite

According to Shojaei and Khasraghi [154], an epoxy composite is a polymeric substance made up of at least two phases: an epoxy matrix and a continuous or noncontinuous filler or reinforcement like fibers, whiskers, or particles. The exploration of epoxy composites is a result of epoxy materials' inability to meet a product's performance standards, as was hinted at in the paragraph preceding.

According to research, a little amount of filler can be added to the epoxy to improve its qualities [155]. Today's market offers a wide variety of fillers for commercial use. However, mineral-based fillers are still a suitable choice because they are affordable and widespread in nature [156].

The matrix material can be made from a variety of polymeric materials, such as polyester, epoxy, and phenolic, as shown in Fig. 9.3. Copper, aluminum, corundum, aluminum silicate, chalk, silica, glass, graphite, quartz, metal fibers, carbon nanotubes, and carbon black are among the fillers that are frequently employed [124, 157, 158]. Filler additions to adhesive compositions increase the strength and durability of adhesive connections by 25–30% [159, 160].

Powder Fillers

Ground Limestone and Dolomite

The ideal reinforcement materials for polymeric materials are dolomite and limestone since they are readily available, inexpensive, have a high degree of stiffness and hardness, and even have customizable surface chemistry [156]. In recent years, dolomite and limestone have drawn more attention as fillers in polymer composite systems [104, 161, 162], as studies have successfully demonstrated their

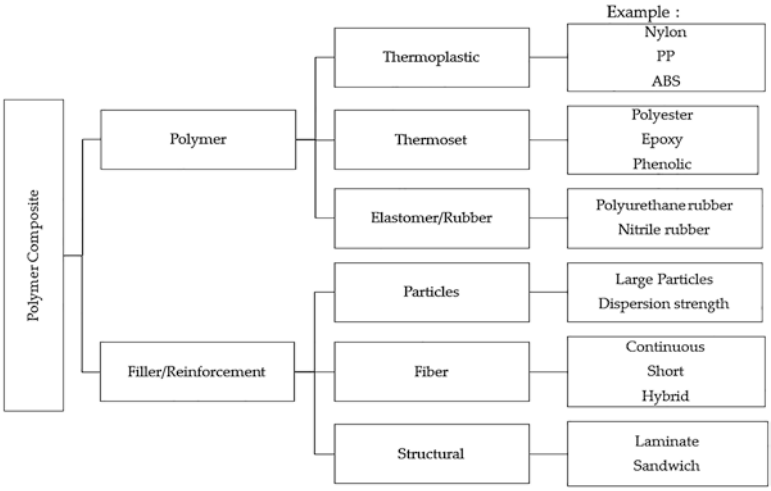

Fig. 9.3 Polymer composite: matrices and fillers [156]

ability to enhance the mechanical, physical, and thermal properties of various polymeric materials. However, in order to make raw dolomite an effective reinforcing filler, it must be treated or modified chemically or physically. This was supported by the research done by Pahlevani and Sahajwalla [163], who stated that all treated panels had attributes that were on par with, or even superior to, those of natural stone (Quartz off-cut, sand, waste seashell, dolomite, limestone aggregates, concrete waste, and limestone dust).

Furthermore, according to Pahlevani and Sahajwalla [163], variables including the smooth particle morphology of glass, dolomite, and limestone as well as concrete's porous structure and clumps of ultra-fine powder in limestone dust reduce the strength of final panels.

Chalk

The results of using chemically precipitated chalk as an active, highly distributed filler in compositions based on epoxy oligomers are presented by Galeev et al. [164]. Used chemically precipitated chalk (both original and hydrophobized) is produced by precipitating, drying, dehydrating, and classifying sludge from a chemical water treatment facility. Two techniques of preparing the reaction mixture for curing are taken into consideration in order to achieve the homogeneity of composites: the initial injection of the filler into the epoxy oligomer and the introduction of the filler into the amine hardener. The discovered formulations can be used for producing adhesives and coatings as well as structural composites, depending on the manner of filler introduction and its concentration in the binder (0.5–10.0% of the mass of the epoxy oligomer). The method of measuring microhardness was used to the research of mechanical properties, allowing evaluation of the impact of filler particle size and comparison of their efficacy with modest concentrations of carbon-containing nanofillers (0.005–0.5%).

The article by Miturska et al. [165], offers the preliminary test findings analyzing fundamental technological parameters that affect the qualities of adhesive epoxide compositions, such as the type of modifying agent and seasoning time. The purpose of the study was to develop adhesive formulations including 2% of the chosen natural fillers (activated carbon powder C, powdered chalk (powder)—$CaCO_3$, and montmorillonite NanoBent ZR-2), and to evaluate their strength characteristics. The epoxide resins utilized in industry—Epidian 5 and Epidian 53—cured by the addition of an aminomethyl group, where curing occurs through the Mannich reaction, made up the polymeric matrix needed to make an adhesive composition. As a benchmark, an epoxide resin mixture with a curing agent but no modifying agents was utilized. The tests reported in this article attempted to demonstrate the importance of the effect of the fillers used on the strength properties of the compositions under investigation. Using a scanning electron microscope, the fracture surface of epoxide adhesive compositions modified with the chosen fillers was examined.

Clay from Ground Brick and Other Ceramic Materials

According to Zhao et al. [166], scrap brick powder can be used to partially or entirely swap out limestone filler for self-compacting mortar.

The article by Pati and Satpathy [167], discusses a new class of epoxy composites that contain microsized red brick dust (RBD) particles and details its characterization and erosion wear performance. Its potential as a filler material in polymeric matrices has not yet been investigated, despite the fact that a number of uses for it have been proposed in the past. In this work, composites with various RBD contents are created using a straightforward hand layup approach. The density, porosity, microhardness, and strength characteristics of the composites are described. A well-planned experimental schedule based on Taguchi design-of-experiments is followed for conducting solid particle erosion trials. Following that, scanning electron microscopy is used to analyze the morphology of composite surfaces. Additionally, an unique ant lion optimizer (ALO) algorithm inspired by nature is suggested in this work to obtain the lowest possible erosion wear rate. This algorithm imitates the actions of antlions in the wild. Due to its traits like enhanced exploration, avoiding local optimum, rapid convergence, and fewer tuning parameters, it outperforms other evolutionary algorithms in terms of performance. Comparing the traditional Taguchi result to the wear rate value acquired by ALO, it shows the lowest value [167].

Mostovoi and Kurbatova [168]. The physicomechanical characteristics of the epoxy composite are improved by covering the filler surface with silane, ensuring chemical contact at the filler-binder interface, and treating the mixture with ultrasound: A factor of 2–3 is added to the elastic modulus of bending and the failure stress. It is important to notice that even at 50% filling, there is a significant (2.5-fold) increase in impact resilience.

The use of modified brick dust improves the epoxy composite's heat resistance and thermal conductivity.

Microsilica, Quartz Flour, Granite

Szewczak and Szelg [169] conducted a research by adding microsilica to epoxy resin alters its viscosity and free surface energy, which are also factors that affect the polymer's ability to adhere to concrete surfaces.

According to Pahlevani and Sahajwalla [163], their research showed that silica-based panels, such as quartz, sand, and glass, which contain silica particles of great strength and hardness, perform better than panels made of calcium carbonate.

Their dosage is solely based on the final qualities of the resulting adhesive that must be met. It may be feasible to activate the filler molecules in the bulk of the glue and form new chemical bonds depending on the filler molecules' chemical makeup [170, 171].

The orientation of the functional groups during cross-linking and attachment of the adhesive to the substrate can also be impacted by the electrons in the filler atoms. This fact is especially significant when considering how the polymer layer ages over time as a result of structural modifications to its interior that primarily involve the movement of electrons and the weakening of chemical bonds between molecules [101, 172, 173].

9.6.2.3 Physical Parameters of Powder Fillers

The following physical characteristics are among them:

Specific Surface

Filler surface area has a significant impact on dispersion; the bigger the surface area, the less dispersion there will be [174]. This outcome is probably the result of smaller aggregates, which are more likely to interact with one another in a dry condition and are typically seen in high surface area aggregates.

Shape

Ahmad et al. [175] studied the effects of silica mineral particle shape on the characteristics of epoxy composites at filler loadings of 15% and 45%. Shared observations included the following:

1. The angular silica mineral composites showed the lowest trend, while the elongated silica mineral composites displayed the maximum tensile strength and modulus.
2. Spherical particles had the lowest aspect ratio of the three particle shapes examined, while high aspect ratio particles (elongated particles) acquired the maximum tensile strength and modulus (Table 9.3). Aspect ratios, or large surface areas per volume, may result in higher levels of stress transferability, according to Ahmad et al. [175].

Table 9.3 Aspect ratio of various shape of silica [175]

S/N	Sample	Aspect ratio
1	Angular (silica mineral)	0.824
2	Cubical (silica mineral)	1.122
3	Elongated (silica mineral)	2.954

3. The aspect ratio factor and the results of the tensile test can be connected. Although numerous parameters, including filler particle size, filler particle distribution in the matrix polymer, and strong adhesion at the interface surface, may have an impact on the tensile capabilities of a particulate filler filled system instead of the aspect ratio component [175].

These physical characteristics enable the adhesive to adhere to the target surface with greater force [176, 177].

9.6.2.4 Surface Modification Methods

In order to enhance this interaction between the polymer and the filler and to enable new composite technologies, filler surface treatment is a widespread process in the polymer industry [178]. This is because filler and polymers are not always compatible, necessitating surface modification of the particles to achieve desired performance. There are numerous surface modification techniques that can be used to improve reinforcement to polymers when fly ash (FA), a finely split byproduct produced by the combustion of pulverized coal and transferred from the combustion chamber, is used as a filler [67].

Among these are chemical modifications using acidic or basic solutions, coupling agents, and microbial modification.

Acidic or Basic Solutions

Increased particle roughness and total surface area are produced when FA particles are treated with a strong acid or basic solution. FA that had been exposed to NaOH or HCl exhibited greater surface area and roughness (FA 146 m^2/g), which was equivalent to precipitated silica (179 m^2/g). Despite having a larger surface area, rubber composites formed with the treated FA exhibited lower tensile strength and bound rubber than silica composites [179].

The interfacial area between the particle and the polymer is increased as a result of this treatment, according to the results, but the compatibility between the FA and the polymer is not improved. Additionally, some research contend that subjecting FA to acid and/or alkali treatment may increase or expose the FA's more chemically active amorphous component [179]. Therefore, this treatment by itself might not improve FA's capacity for reinforcement. By altering the alkalinity or acidity of the particles, acidic or basic treatment of FA may also be employed to influence the curing behavior [180].

Coupling Agents

The most popular technique for increasing compatibility, fortifying the interface between polymer and filler, and for preventing the adsorption of cures on the filler surface is coupling agents. These chemical elements serve as molecular connectors between the filler and rubber [67].

Although compatibility has improved with various coupling agents, treated FA reinforcement is still inferior than treated silica reinforcement [67].

This may be because silica's complex structure develops from primary particle aggregation and FA's larger particle size, which suggests that, similar to acid-base treatment, coupling agents alone can enhance FA's reinforcing efficiency but fall short of matching the reinforcement of treated commercial silica. Using coupling agents in addition to mechanical size reduction and/or acid-based therapy may be the best option.

Microorganisms

Although straightforward and effective, physical and chemical surface treatment methods raise the filler's cost, which may prevent the use of FA and other metallurgical wastes like the waste copper dust [181, 182], as fillers for polymers like epoxy. As an alternative and affordable method of FA surface modification, corrosive microorganisms, such as dissimilatory iron-reducing bacteria and sulfate-reducing bacteria, have been investigated [67]. These specific bacteria can easily adhere to the particles and change the structure and composition of the FA since they need many of the nutrients found in FA to develop.

While bacterial growth and metabolites produced by the bacteria make the surface chemistry of the particles lipophilic, corrosive bacteria can decrease sulfur and iron oxides to create a porous structure in the particles. Additionally, ferrosulfide nanoparticles can be created when reduced iron and sulfur combine.

As a result of the collapse of particles following severe corrosion, microbial treatment of FA led to increased pore volume, smaller particle size, and a reduced lipophilic contact angle compared to untreated FA.

Conclusion

One of the most common types of resins used as structural adhesives is epoxy resins (ERs). Despite this, ERs have several weaknesses, most of which are caused by the heavily cross-linked network that remains after the curing process. Building structural epoxy joints continues to be a major challenge since there is a dearth of knowledge on joint performance, particularly in respect to how they react in harsh environments and under cyclic loads. After running a sizable number of trials to compare the results, they are still unable to offer a helpful design basis. Physical testing will continue to be the main objective of any further research in this field.

Epoxy resins can also have fillers added to them as enhancers to improve their strength and durability when used in maritime situations. However, the utilization is

restricted since metal powders are so expensive. In order to reduce the high cost of metal powders and improve the integrity and dependability of epoxy resins in marine environments, it has been proposed to employ WCD. Before using this enhancer, WCD must first have its surface modified. Physical and chemical methods of surface preparation, while rapid and easy, significantly raise the cost of filler. A practical method for changing the surface of WCD is to use corrosive microorganisms.

Due to the observed knowledge gaps, wave energy converter design is the suggested area of research: Epoxy resin packed with corrosive microorganism surface-modified waste copper dust has good seawater integrity and durability.

9.7 Methodology

9.7.1 Materials and Methods

9.7.1.1 Materials

The unmodified epoxy resin and the modified epoxy resin are the two variations of an epoxy resin that will be examined.

Unmodified Epoxy Resin

The curing agent and epoxy resin-based adhesive compound will be used to create this variation of epoxy resin. We will ascertain the cured epoxy's mechanical characteristics and use those results to fill out Table 9.4.

Curing Agent

The curing agent that will be employed in this investigation is one that was produced especially for curing low-molecule resin compounds, such as the epoxy resin that will be used as the study's main material.

Table 9.4 Mechanical properties of cured epoxy resin

S/N	Properties	Value (MPa)
1	Bending strength	X
2	Compressive strength (MPa)	X
3	Shear strength for 16 h at 20–25 °C, 6 h at 80 ± 2 °C, not lower than	X
4	Shear strength for 7 days at 20–25 °C, not lower than	X

Filler

1. One type of copper powder has spherical particles and a purity of 99.0%.
2. 99.7% pure aluminum powder with agglomerated, sporadic-shaped particles.
3. WCD: Figure 9.4 provides more information on the chemical makeup of the WCD as determined by the x-ray efflorescence (XRF) method.
4. MRT: Figure 9.5 describes the chemical makeup of the MRT as determined by the x-ray efflorescence (XRF) method.

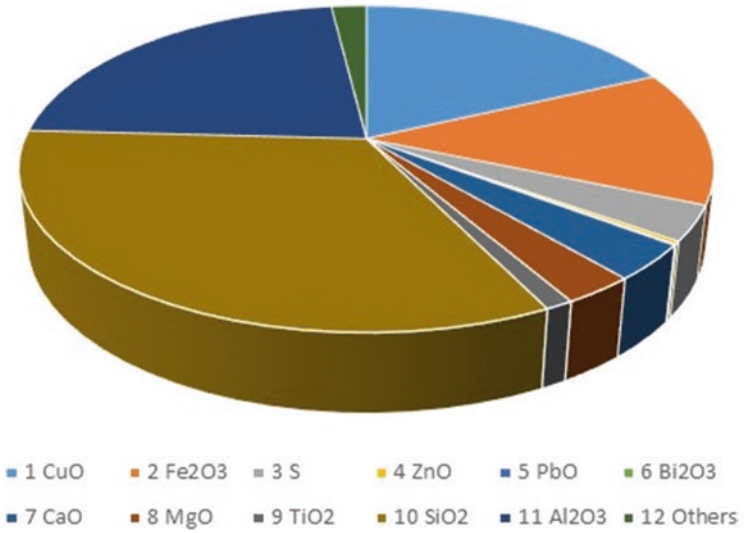

Fig. 9.4 Chemical composition of WCD

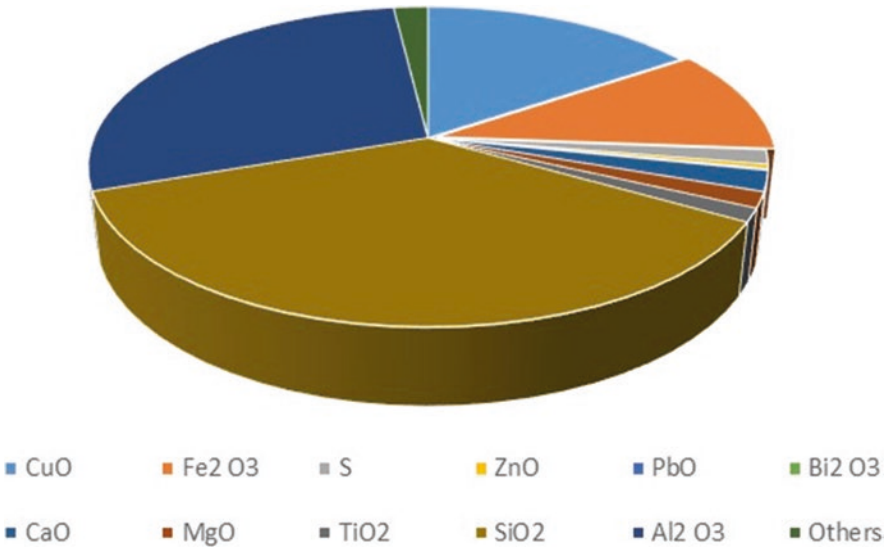

Fig. 9.5 Chemical composition of MRT

Surface Modifying Agent

We will investigate alternate and affordable WCD surface modification agents, such as corrosive microorganisms such as iron-reducing bacteria and sulfate-reducing bacteria.

9.7.1.2 Methods

Preparation of Unmodified and Modified Epoxy Resin

The components of the two types of epoxy resin (i.e., modified and unmodified) that will be examined in this investigation are described in Table 9.5.

Starting out, both unmodified and modified epoxy resin will be combined in a stoichiometric ratio of 100:80 with the curing agent. In addition to the materials indicated, modified epoxy resins will also comprise 80 g of a curing agent, 2 g each of WCD, MRT, copper powder, and aluminum powder per 100 g of epoxy resin. Table 9.5 provides a thorough description of the composites (i.e., modified epoxy resin) that will be created during the course of this investigation.

The following is the technique for making unmodified epoxy resin: Using a balance that can read to four decimal spaces, the proper amounts of epoxy resin components will be weighed (0.0000). A homogenous mass will be produced after the components are mechanically combined for 90 seconds at a shear rate of 128 m/min in a polymer container. A vacuum pump will be used to remove gas bubbles that were created during the mixing process from the compound. Weighing and combining the epoxy resin components will take place at a temperature of 23 °C ± 3 °C and a relative humidity of 23% ± 6%.

The following is the technique for making modified epoxy resin: weigh (Table 9.6) the required amounts of epoxy resin and metal fillers (such as copper powder, aluminum powder, WCD, and MRT) and combine them. The compound will then receive the curing agent. For both modified and unmodified epoxy resin, the preparation procedure parameters will remain the same.

Table 9.5 Characteristic description of epoxy resin components

S/N	ERBAC components	Variants of epoxy resin				
		Unmodified	Cu-powder	Al-powder	CSD	MRT
1	Resin type	Epoxy resin	Synthetic	Synthetic	Natural	Natural
2	Amount (g)	100	100	100	100	100
3	Curing agent	AA	AA	AA	AA	AA
4	Amount (g)	80	80	80	80	80
5	Filler type	–	Cu	Al	Cu-Al^{others}	Cu-Al^{others}
7	Designation	U-1	U-2	U-3	U-4	U-5

Table 9.6 Description of developed composites from epoxy resin

Designation	Constituents of modified epoxy resin			
U-2	Epoxy resin	Cu-powder	Epoxy resin + Cu	Composite
U-3	Epoxy resin	Al-powder	Epoxy resin + Al	Composite
U-4	Epoxy resin	WCD	Epoxy resin + Cu-Al^{others}	Composite
U-5	Epoxy resin	MRT	Epoxy resin + Cu-Al^{others}	Composite

Optimization of Mechanical Properties of Adhesive with Filler

According to Table 9.7, the following process variables will be taken into account in order to optimize the mechanical properties of epoxy resin that has been filled with synthetic and natural fillers. While Table 9.8 shows the design of experiment (DOE) design for process optimization.

Tables 9.9, 9.10, and 9.11 show experimental situations with unknown % output proportions in addition to the whole DOE sample space that is shown here in Table 9.8. The original experimental conditions from the DOE are described using numeric serial order, whereas these novel inputs are represented using alphabetic serial order (Tables 9.9, 9.10, and 9.11).

MATLAB Code Used for Model Development

- Modeling procedure for output prediction

This sub-section presents the basic steps utilized in the modeling process as contained in this paper:

Step #1: Study trend of experimental samples.
Step #2: Set-up constraint models to categorize and group samples into sub-classes based on #1.
Step #3: Compute absolute difference between input and output samples in same class as grouped in #2.
Step #4: Identify different experimental levels for selected classes.
Step #5: Apply interpolant model to predict output.
Step #6: End4.

A generalized representation of the modeling variables can be found in Table 9.12. These factors were incorporated into a model and utilized to calculate the predictive results of the various unmodified and modified epoxy-resin compositions.

Modeling notations as they are shown in this research are as follows:

$$\text{Output} = f\left(\text{speed,flowrate,input,feedrate,liquidssolidratio}\right)$$

Let: serial number for inputs: $s_i = \{1, \ldots, n-1, n\}$ and serial number for outputs $s_o = \{1, \ldots, n-1, n\}$ for $\forall n \in R$

Where:

Table 9.7 Process parameters to consider for the development of filled adhesive bond

S/N	Parameters	Level 1	Level 2	Level 3
1	Amount of synthetic and natural fillers (g)	1.5	2	2.5
2	Curing temperature (°C)	40	50	70

Table 9.8 Design of experiment using the 2 by 3 full factorial experimental method

S/N	Fillers (g)	Curing temperature (°C)	Treatment combination (TC)
1	1.5	40	(1.5)(40)
2	2.0	50	(2.0)(50)
3	2.5	60	(2.5)(60)
4	1.5	50	(1.5)(50)
5	2.0	60	(2.0)(60)
6	2.5	40	(2.5)(40)
7	1.5	60	(1.5)(60)
8	2.0	40	(2.0)(40)
9	2.5	50	(2.5)(50)

$$\exp_{(i)i,j} = \text{Experimental inputs}$$

$$\exp_{(o)i,j} = \text{Experimental outputs}$$

$$\text{Pre}_{(o)i,j} = \text{Predictive outputs}$$

$$p_{ij} = \%\ \text{inputproportionofselectedsamples}$$

$$p_{oj} = \%\ \text{inputproportionofselectedsamples}$$

$$\Delta p_j = \left|p_{ij} - p_{oj}\right| \text{absolutedifferencebetween} p_{ij} \text{and} p_{oj}$$

Where: $j = \{1, \ldots, \quad k-1, k\}$ represents experimental levels.

The "absolute difference" models expressed in terms of the experimental levels are as presented in Eqs. 9.1, 9.2, and 9.3 while 9.4, 9.5 and 9.6 with respect to Table 9.12 represent the final computational models for predicting the unknown outputs.

$$\Phi_1 = \left[\frac{\Phi_3(\mu-\xi) - \Phi_2(\mu-\xi) - \Phi_2(\sigma-\mu)}{(\mu-\sigma)}\right] \tag{9.1}$$

$$\Phi_2 = \left[\frac{\Phi_3(\mu-\xi) + \Phi_1(\sigma-\mu)}{(\sigma-\mu)+(\mu-\xi)}\right] \tag{9.2}$$

Table 9.9 DOE for epoxy resin-filled synthetic fillers

Filling – Curing Temp	Inputs		Process Parameters					Outputs	
	T.S	F.S	S.M.P	L.D.C	S.S*	W.T.B.	T.T.B	M.S.T.S.	M.S. F.S
No filling	T.D	T.D	22.0	15.0	64.0	77.0	90.0	T.D	T.D
10F-40T	T.D	T.D	22.0	15.0	64.0	77.0	90.0	T.D	T.D
A	T.D	T.D	22.0	15.0	64.0	77.0	90.0	T.D	T.D
20F-50T	T.D	T.D	22.0	15.0	64.0	77.0	90.0	T.D	T.D
B	T.D	T.D	22.0	15.0	64.0	77.0	90.0	T.D	T.D
30F-60T	T.D	T.D	22.0	15.0	64.0	77.0	90.0	T.D	T.D
C	T.D	T.D	22.0	15.0	64.0	77.0	90.0	T.D	T.D
10F-50T	T.D	T.D	22.0	15.0	64.0	77.0	90.0	T.D	T.D
D	T.D	T.D	22.0	15.0	64.0	77.0	90.0	T.D	T.D
20F-60T	T.D	T.D	22.0	15.0	64.0	77.0	90.0	T.D	T.D
E	T.D	T.D	22.0	15.0	64.0	77.0	90.0	T.D	T.D
30F-40T	T.D	T.D	22.0	15.0	64.0	77.0	90.0	T.D	T.D
F	T.D	T.D	22.0	15.0	64.0	77.0	90.0	T.D	T.D
10F-60T	T.D	T.D	22.0	15.0	64.0	77.0	90.0	T.D	T.D
G	T.D	T.D	22.0	15.0	64.0	77.0	90.0	T.D	T.D
20F-40T	T.D	T.D	22.0	15.0	64.0	77.0	90.0	T.D	T.D
H	T.D	T.D	22.0	15.0	64.0	77.0	90.0	T.D	T.D
30F-50T	T.D	T.D	22.0	15.0	64.0	77.0	90.0	T.D	T.D
I	T.D	T.D	22.0	15.0	64.0	77.0	90.0	T.D	T.D

Key: *Wt* **weight;** *T. S.* **tensile strength,** *F.S.* **fatigue strength,** *M.S.T.S.* **modified surface tensile strength,** *M.S. F.S.* **modified surface fatigue strength,** *S.M.P* **stress in mid-point,** *L.D.C* **loads given at deflection curve,** *S.S** **support span,** *W.T.B.* **width of the test beam,** *T.T.B.* **thickness of the test beam**

$$\Phi_3 = \left[\frac{\Phi_1(\mu - \sigma) + \Phi_2(\sigma - \mu) + \Phi_2(\mu - \xi)}{(\mu - \xi)} \right] \tag{9.3}$$

$$\left| p_{i1} - p_{o1} \right| = \Phi_1 \tag{9.4}$$

$$\left| p_{i2} - p_{o2} \right| = \Phi_2 \tag{9.5}$$

Table 9.10 DOE for epoxy resin-filled natural fillers

Filling – Curing Temp	Inputs		Process Parameters					Outputs	
	T.S	F.S	S.M.P	L.D.C	S.S*	W.T.B.	T.T.B	M.S.T.S.	M.S. F.S
No filling	T.D	T.D	22.0	15.0	64.0	77.0	90.0	T.D	T.D
10F-40T	T.D	T.D	22.0	15.0	64.0	77.0	90.0	T.D	T.D
A	T.D	T.D	22.0	15.0	64.0	77.0	90.0	T.D	T.D
20F-50T	T.D	T.D	22.0	15.0	64.0	77.0	90.0	T.D	T.D
B	T.D	T.D	22.0	15.0	64.0	77.0	90.0	T.D	T.D
30F-60T	T.D	T.D	22.0	15.0	64.0	77.0	90.0	T.D	T.D
C	T.D	T.D	22.0	15.0	64.0	77.0	90.0	T.D	T.D
10F-50T	T.D	T.D	22.0	15.0	64.0	77.0	90.0	T.D	T.D
D	T.D	T.D	22.0	15.0	64.0	77.0	90.0	T.D	T.D
20F-60T	T.D	T.D	22.0	15.0	64.0	77.0	90.0	T.D	T.D
E	T.D	T.D	22.0	15.0	64.0	77.0	90.0	T.D	T.D
30F-40T	T.D	T.D	22.0	15.0	64.0	77.0	90.0	T.D	T.D
F	T.D	T.D	22.0	15.0	64.0	77.0	90.0	T.D	T.D
10F-60T	T.D	T.D	22.0	15.0	64.0	77.0	90.0	T.D	T.D
G	T.D	T.D	22.0	15.0	64.0	77.0	90.0	T.D	T.D
20F-40T	T.D	T.D	22.0	15.0	64.0	77.0	90.0	T.D	T.D
H	T.D	T.D	22.0	15.0	64.0	77.0	90.0	T.D	T.D
30F-50T	T.D	T.D	22.0	15.0	64.0	77.0	90.0	T.D	T.D
I	T.D	T.D	22.0	15.0	64.0	77.0	90.0	T.D	T.D

Key: *T. S.* **tensile strength;** *F.S.* **fatigue strength,** *M.S.T.S.* **modified surface tensile strength,** *M.S. F.S.* **modified surface fatigue strength,** *S.M.P* **stress in mid-point,** *L.D.C* **loads given at deflection curve,** *S.S** **support span,** *W.T.B.* **width of the test beam,** *T.T.B.* **thickness of the test beam**

$$\left|p_{i3} - p_{o3}\right| = \Phi_3 \tag{9.6}$$

Hence, $\Delta p_j = \Phi_j$

Experimental Validation and Simulation

The strongest filled adhesives will be simulated using finite element analysis after being empirically confirmed for their weight, tensile strength, and consistency during environmental fatigue.

Table 9.11 DOE of epoxy resin-filled synthetic and natural fillers at optimum processing conditions under cyclic loading and seawater aging

Filling – Curing Temp	Inputs			FPB Process Parameters					Outputs		
	Wt	M.S.T.S	M.S. F.S	S.M.P	L.D.C	S.S*	W.T.B.	T.T.B	Wt	M.S.E. T.S.	M.S.E. F.S.
CSD filling @30°C	T.D	T.D	T.D	22.0	15.0	64.0	77.0	90.0	T.D	T.D	T.D
A	T.D	T.D	T.D	22.0	15.0	64.0	77.0	90.0	T.D	T.D	T.D
CSD filling @50°C	T.D	T.D	T.D	22.0	15.0	64.0	77.0	90.0	T.D	T.D	T.D
B	T.D	T.D	T.D	22.0	15.0	64.0	77.0	90.0	T.D	T.D	T.D
CSD filling @70°C	T.D	T.D	T.D	22.0	15.0	64.0	77.0	90.0	T.D	T.D	T.D
C	T.D	T.D	T.D	22.0	15.0	64.0	77.0	90.0	T.D	T.D	T.D
MRT filling @30°C	T.D	T.D	T.D	22.0	15.0	64.0	77.0	90.0	T.D	T.D	T.D
D	T.D	T.D	T.D	22.0	15.0	64.0	77.0	90.0	T.D	T.D	T.D
MRT filling @50°C	T.D	T.D	T.D	22.0	15.0	64.0	77.0	90.0	T.D	T.D	T.D
E	T.D	T.D	T.D	22.0	15.0	64.0	77.0	90.0	T.D	T.D	T.D
MRT filling @70°C	T.D	T.D	T.D	22.0	15.0	64.0	77.0	90.0	T.D	T.D	T.D
F	T.D	T.D	T.D	22.0	15.0	64.0	77.0	90.0	T.D	T.D	T.D
Cu filling @ 30°C	T.D	T.D	T.D	22.0	15.0	64.0	77.0	90.0	T.D	T.D	T.D
G	T.D	T.D	T.D	22.0	15.0	64.0	77.0	90.0	T.D	T.D	T.D
Cu filling @ 50°C	T.D	T.D	T.D	22.0	15.0	64.0	77.0	90.0	T.D	T.D	T.D
H	T.D	T.D	T.D	22.0	15.0	64.0	77.0	90.0	T.D	T.D	T.D
Cu filling @ 70°C	T.D	T.D	T.D	22.0	15.0	64.0	77.0	90.0	T.D	T.D	T.D
I	T.D	T.D	T.D	22.0	15.0	64.0	77.0	90.0	T.D	T.D	T.D
Al filling @ 30°C	T.D	T.D	T.D	22.0	15.0	64.0	77.0	90.0	T.D	T.D	T.D
J	T.D	T.D	T.D	22.0	15.0	64.0	77.0	90.0	T.D	T.D	T.D
Al filling @ 50°C	T.D	T.D	T.D	22.0	15.0	64.0	77.0	90.0	T.D	T.D	T.D
K	T.D	T.D	T.D	22.0	15.0	64.0	77.0	90.0	T.D	T.D	T.D
Al filling @ 70°C	T.D	T.D	T.D	22.0	15.0	64.0	77.0	90.0	T.D	T.D	T.D
L	T.D	T.D	T.D	22.0	15.0	64.0	77.0	90.0	T.D	T.D	T.D

Key: *Wt* **weight,** *M.S.T.S.* **modified surface tensile strength,** *M.S. F.S.* **modified surface fatigue strength,** *M.S.E.T.S.* **modified surface environmental tensile strength,** *M.S.E.F.S.* **modified surface environment fatigue strength,** *S.M.P* **stress in mid-point,** *L.D.C* **loads given at deflection curve,** *S.S** **support span,** *W.T.B.* **width of the test beam,** *T.T.B.* **thickness of the test beam**

Table 9.12 Generalized representation of model variables

Level	Data acquisition procedure	Input value for variant factor p_{ij}	Output value for variant factor p_{oj}	Expt. levels	Absolute difference between p_{ij} and p_{oj}
1-First	Prediction	p_{i1}	p_{o1}	ξ	$\lvert p_{i1} - p_{o1} \rvert = \Phi_1$
2-Second	Experiment	p_{i2}	p_{o2}	μ	$\lvert p_{i2} - p_{o2} \rvert = \Phi_2$
3-Third	Experiment	p_{i3}	p_{o3}	σ	$\lvert p_{i3} - p_{o3} \rvert = \Phi_3$

Shape, Dimension, and Fabrication of the Unmodified and Modified Samples

Strength test samples (Fig. 9.6a) and microscopic test samples are the two types of cylinder samples that will be utilized in the tests (Fig. 9.6b).

The original and modified epoxy-resin test samples will be made by casting them in 10 mL and 20 mL cylindrical molds. Unmodified and modified epoxy resin will be prepared, and then it will be poured into molds that will have silicon spray inside of them to make it easier to separate the cast from the mold. The samples will be allowed to cure for 7 days at 24 °C ± 3 °C and 23% ± 6% humidity.

In order to make the epoxy-resin test samples uniform in length and surface smoothness, they will be machined using grinding and milling. The finished samples will be 40 ± 0.3 mm in length and 15 ± 0.1 mm in diameter on average.

The samples will be taken out of the molds after the curing process and condition for 24 h at a constant temperature of 22.1 °C and a relative humidity of 25% ± 1%. After that, the samples will be put in a marine environment (Fig. 9.7).

Combined Cyclic Loading and Seawater Aging

The combined effect of cyclic loading and saltwater aging on the integrity and durability of the unmodified epoxy resin and produced epoxy-resin composites will be tested utilizing a four-point bending in a water bath since water has the potential to cause separation of epoxy resin and metal fillers (Fig. 9.7).

The manufactured epoxy-resin test samples will be aged in a seawater environment under cyclic stresses as part of the investigations. The proper amounts of tap water and sea salt (NaCl) will be measured out to create the seawater environment. The salinity of 35%, which represents the average salinity of the world's saltwater, will serve as the study's reference point. The testing will make use of tap water that is at room temperature.

Microstructural Analysis of Deformed Samples

Using a digital microscope, scheduled microscopic examinations will be carried out to examine the microstructure of the adhesive compounds and the effects of the studied aqueous environments on their appearance and properties. The timing of these tests will rely on the aging period. About 200 items will make up the entire batch of epoxy-resin samples being analyzed (for each type of epoxy-resin variants:

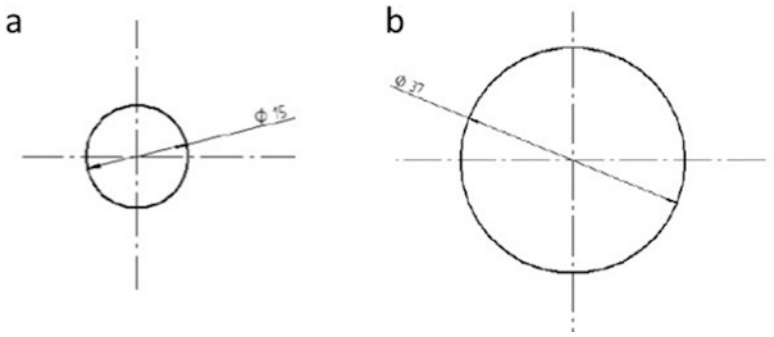

Fig. 9.6 Shape and dimensions of epoxy-resin samples: (**a**) strength test samples (**b**) microscopic test samples

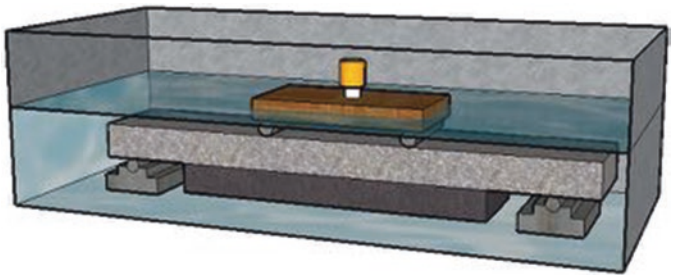

Fig. 9.7 Four-point bending + seawater aging experimental setup; mimicking WEC environmental condition

unmodified and modified: 5 batches of environment types × 3 variants of aging time × 6 samples and 6 standard samples). The results' fundamental statistics will be taken into account. In order to evaluate the mean and standard deviation, data that represent obvious errors in the findings will be excluded.

The strength test results for the unmodified and modified epoxy-resin samples will be contrasted.

9.8 Contribution to Knowledge

The following information will be revealed at the conclusion of this study:

- This study will offer an innovative secondary copper resource at a low cost. One that can affordably act as a metal filler for epoxy resin. This secondary resource, which includes copper and aluminum, is unusual because it has never been employed as a metal filler for epoxy resin.

- Additionally, a brand-new compositional ratio of adhesive to waste metal dust will be made available. In the design of wave energy converters, this compositional percentage has not been used as a structural material. However, the ideal filler to adhesive ratio is a new discovery.
- The combined waste metal dust and epoxy-resin composite's seawater degrading behavior have not before been documented in the literature; consequently, its novelty.

9.9 Ethical Considerations

This project has no unethical components.

9.10 Dissemination

The full paper will also be published in the related conference proceedings. The results will be presented at regional and worldwide conferences. The following journals, recognized by the Department of Higher Education and Training, will publish more findings:

- Journal of Materials Science. Springer publishers.
- JOM Journal. Springer publishers.

9.11 Budget (Table 9.13)

Table 9.13 Estimated budget of the project

Items	Cost	Source
Literature sourcing and stationaries	XXX	XXX
Materials and supplies	XXX	XXX
Analytical equipment	XXX	XXX
Traveling expenses	XXX	XXX
Miscellaneous expenses	XXX	XXX
Total	XXXXX	

Key: *TUT* Tshwane University of Technology, *R* Rand

9.12 Time Frame (Table 9.14)

Table 9.14 Estimated time frame of the project

S/N	Task name	Year	
		2020	2021
1	Proposal (compilation and presentation)	WIP	WIP
2	Literature review	WIP	WIP
3	Material sourcing	WIP	WIP
4	Sample preparation (sampling)	WIP	WIP
6	Fabrication of test samples	WIP	WIP
7	Mechanical tests on filled and unfilled samples in air	WIP	WIP
8	Mechanical tests on filled and unfilled samples in seawater	WIP	WIP
9	Results, data and analysis	WIP	WIP
10	Optimum predictive model development	WIP	WIP
11	Finite element simulation	WIP	WIP
12	Compilation and presentation of final report	WIP	WIP

References

1. E. Karana, P. Hekkert, P. Kandachar, Material considerations in product design: A survey on crucial material aspects used by product designers. Mater. Des. ***29***(6), 1081–1089 (2008)
2. M. Sipper, Fifty years of research on self-replication: An overview. Artif. Life ***4***(3), 237–257 (1998)
3. K.L. Murty, I. Charit, Structural materials for Gen-IV nuclear reactors: Challenges and opportunities. J. Nucl. Mater. ***383***(1-2), 189–195 (2008)
4. M.L. Patten, M. Newhart, *Understanding Research Methods: An Overview of the Essentials* (Routledge, New York, 2017)
5. A. Rudawska, The effect of the salt water aging on the mechanical properties of epoxy adhesives compounds. Polymers ***12***(4), 843 (2020)
6. Y. Sliozberg, J. Andzelm, C.B. Hatter, B. Anasori, Y. Gogotsi, A. Hall, Interface binding and mechanical properties of MXene-epoxy nanocomposites. Compos. Sci. Technol. ***192***, 108124 (2020)
7. L. Cheng, J. Feng, Flexible and fire-resistant all-inorganic composite film with high in-plane thermal conductivity. Chem. Eng. J. ***398***, 125633 (2020)
8. F.A. Gonçalves, M. Santos, T. Cernadas, P. Alves, P. Ferreira, Influence of fillers on epoxy resins properties: A review. J. Mater. Sci. ***57***, 15183–15212 (2022)
9. J.H. Mallinson, *Corrosion-Resistant Plastic Composites in Chemical Plant Design* (CRC Press, Boca Raton, 2020)
10. J. Powell, S. Green, The challenges of bonding composite materials and some innovative solutions. Reinf. Plast. ***65***(1), 36–39 (2021)
11. R. Léger, A. Roy, J.C. Grandidier, A study of the impact of humid aging on the strength of industrial adhesive joints. Int. J. Adhes. Adhes. ***44***, 66–77 (2013)
12. G.U.I.L.H.E.R.M.E. Viana, M.A.R.C.E.L.O. Costa, M.D. Banea, L.F. da Silva, Water diffusion in double cantilever beam adhesive joints. Lat. Am. J. Solids Struct. ***14***(2), 188–201 (2017)

13. B. De Neve, M.E.R. Shanahan, Physical and chemical effects in an epoxy resin exposed to water vapour. J. Adhes. ***49***(3-4), 165–176 (1995)
14. M. Lai, J. Botsis, J. Cugnoni, D. Coric, An experimental–numerical study of moisture absorption in an epoxy. Compos. Part A Appl. Sci. Manuf. ***43***(7), 1053–1060 (2012)
15. D.R. Lefebvre, K.M. Takahashi, A.J. Muller, V.R. Raju, Degradation of epoxy coatings in humid environments: The critical relative humidity for adhesion loss. J. Adhes. Sci. Technol. ***5***(3), 201–227 (1991)
16. R.A. Pethrick, Design and ageing of adhesives for structural adhesive bonding–A review. Proc. Inst. Mech. Eng. Part L: J. Mater. Des. Appl. ***229***(5), 349–379 (2015)
17. A. Rudawska, V. Brunella, The effect of ageing in water solution containing iron sulfate on the mechanical properties of epoxy adhesives. Polymers ***12***(1), 218 (2020)
18. A. Hassan, R. Khan, N. Khan, M. Aamir, D.Y. Pimenov, K. Giasin, Effect of seawater ageing on fracture toughness of stitched glass fiber/epoxy laminates for marine applications. J. Mar. Sci. Eng. ***9***(2), 196 (2021)
19. C. Rubio-González, M. Hernández-Santos, E. José-Trujillo, J.A. Rodríguez-González, Effect of seawater aging on impact behavior of glass fiber/epoxy laminates with drilled holes. J. Compos. Mater. ***56***(10), 1481–1493 (2022)
20. H. Ulus, H.B. Kaybal, V. Eskizeybek, A. Avcı, Significantly improved shear, dynamic-mechanical, and mode II fracture performance of seawater aged basalt/epoxy composites: The impact of halloysite nanotube reinforcement. Eng. Sci. Technol. Int. J. ***24***(4), 1005–1014 (2021)
21. R.J. Hussey, J. Wilson, *Structural Adhesives: Directory and Databook* (Springer Science & Business Media, London, 1996)
22. J. Bishopp, Aerospace: A pioneer in structural adhesive bonding, in *Handbook of Adhesives and Sealants*, vol. 1, (Elsevier Science Ltd., Amsterdam, 2005), pp. 215–347
23. J.G. Broughton, A.R. Hutchinson, Adhesive systems for structural connections in timber. Int. J. Adhes. Adhes. ***21***(3), 177–186 (2001)
24. P. Kumar, A. Patnaik, S. Chaudhary, A review on application of structural adhesives in concrete and steel–concrete composite and factors influencing the performance of composite connections. Int. J. Adhes. Adhes. ***77***, 1–14 (2017)
25. C.R. Frihart, C.G. Hunt, Adhesives with wood materials: Bond formation and performance, in *Wood Handbook: Wood as an Engineering Material: Chapter 10. Centennial Ed. General Technical Report FPL; GTR-190*, (US Dept. of Agriculture, Forest Service, Forest Products Laboratory, Madison, 2010), pp. 10.1–10.24, 190
26. R. Pelc, R.M. Fujita, Renewable energy from the ocean. Mar. Policy ***26***(6), 471–479 (2002)
27. B. Drew, A.R. Plummer, M.N. Sahinkaya, A review of wave energy converter technology. Proc. Inst. Mech. Eng. A: J. Power Energy ***223***(8), 887–902 (2009)
28. P.A. Owusu, S. Asumadu-Sarkodie, A review of renewable energy sources, sustainability issues and climate change mitigation. Cogent Eng. ***3***(1), 1167990 (2016)
29. A. Babarit, J. Hals, M.J. Muliawan, A. Kurniawan, T. Moan, J. Krokstad, Numerical benchmarking study of a selection of wave energy converters. Renew. Energy ***41***, 44–63 (2012)
30. O. Langhamer, K. Haikonen, J. Sundberg, Wave power—Sustainable energy or environmentally costly? A review with special emphasis on linear wave energy converters. Renew. Sustain. Energy Rev. ***14***(4), 1329–1335 (2010)
31. S. Doyle, G.A. Aggidis, Development of multi-oscillating water columns as wave energy converters. Renew. Sustain. Energy Rev. ***107***, 75–86 (2019)
32. J. Frick, *Implementation Plan for the Stellenbosch Wave Energy Converter on the South-West Coast of South Africa* (Master's thesis, University of Cape Town, 2014)
33. S. Manju, N. Sagar, Renewable energy integrated desalination: A sustainable solution to overcome future fresh-water scarcity in India. Renew. Sustain. Energy Rev. ***73***, 594–609 (2017)
34. M. Melikoglu, Current status and future of ocean energy sources: A global review. Ocean Eng. ***148***, 563–573 (2018)

35. C. Rautenbach, T. Daniels, M. de Vos, M.A. Barnes, A coupled wave, tide and storm surge operational forecasting system for South Africa: Validation and physical description. Nat. Hazards ***103***, 1407–1439 (2020)
36. E. Belletti, M. McBride, Against the tide: Potential for marine renewable energy in Eastern and Southern Africa. Consilience: The Journal of Sustainable Development. ***23***, 1–14, (2021)
37. J.R. Joubert, *Design and Development of a Novel Wave Energy Converter* (Stellenbosch University, Faculty of Engineering, Doctor of Engineering Thesis, 2013)
38. D. Banks, J. Schäffler, *The Potential Contribution of Renewable Energy in South Africa* (Sustainable Energy & Climate Change Project (SECCP), Johannesburg, 2005)
39. O.R. Energy, *White Paper on Renewable Energy*. Department of minerals and energy, Republic of south Africa (2003)
40. C.J.S. Fourie, D. Johnson, *The Wave Power Potential of South Africa*. Power-Gen Africa, Johannesburg, South Africa, (18–20 July 2007)
41. R. Ahamed, K. McKee, I. Howard, Advancements of wave energy converters based on power take off (PTO) systems: A review. Ocean Eng. ***204***, 107248 (2020)
42. M. Penalba, G. Giorgi, J.V. Ringwood, Mathematical modelling of wave energy converters: A review of nonlinear approaches. Renew. Sustain. Energy Rev. ***78***, 1188–1207 (2017)
43. J. Falnes, A review of wave-energy extraction. Mar. Struct. ***20***(4), 185–201 (2007)
44. J. Hals, J. Falnes, T. Moan, A comparison of selected strategies for adaptive control of wave energy converters. J. Offshore Mech. Arct. Eng. ***133***(3), 031101 (2011)
45. C. Pérez-Collazo, D. Greaves, G. Iglesias, A review of combined wave and offshore wind energy. Renew. Sustain. Energy Rev. ***42***, 141–153 (2015)
46. S. Astariz, J. Abanades, C. Perez-Collazo, G. Iglesias, Improving wind farm accessibility for operation & maintenance through a co-located wave farm: Influence of layout and wave climate. Energy Convers. Manage. ***95***, 229–241 (2015)
47. R. Tiron, F. Mallon, F. Dias, E.G. Reynaud, The challenging life of wave energy devices at sea: A few points to consider. Renew. Sustain. Energy Rev. ***43***, 1263–1272 (2015)
48. J.A. Hudson, D.C. Phillips, N.J.M. Wilkins, Materials aspects of wave energy converters. J. Mater. Sci. ***15***(6), 1337–1363 (1980)
49. R.P.M. Parker, G.P. Harrison, J.P. Chick, Energy and carbon audit of an offshore wave energy converter. Proc. Inst. Mech. Eng. A: J. Power Energy ***221***(8), 1119–1130 (2007)
50. T.W. Thorpe, M.J. Picken, Wave energy devices and the marine environment. IEE Proc. A Sci. Measur. Technol. ***140***(1), 63–70 (1993)
51. Z. Wang, X.L. Zhao, G. Xian, G. Wu, R.S. Raman, S. Al-Saadi, Durability study on interlaminar shear behaviour of basalt-, glass-and carbon-fibre-reinforced polymer (B/G/CFRP) bars in seawater sea sand concrete environment. Construct. Build Mater. ***156***, 985–1004 (2017)
52. P. Alam, D. Mamalis, C. Robert, C. Floreani, C.M.Ó. Brádaigh, The fatigue of carbon fibre-reinforced plastics-A review. Compos. Part B Eng. ***166***, 555–579 (2019)
53. M. Calvário, L.S. Sutherland, C. Guedes Soares, A review of the applications composite materials in wave and tidal energy devices, in *Natural and Artificial Fiber-Reinforced Composites as Renewable Sources. Developments in Maritime Transportation and Harvesting of Sea Resources: Proceedings of the 17th International Congress of the International Maritime Association of the Mediterranean (IMAM 2017)* (2017)
54. W. Zhishen, W. Xin, W. Gang, Advancement of structural safety and sustainability with basalt fiber-reinforced polymers, in *CICE2012*, vol 13 (Rome, 2012), pp. 15–29
55. M.N. Gururaja, A.H. Rao, A review on recent applications and future prospectus of hybrid composites. Int. J. Soft Comput. Eng. ***1***(6), 352–355 (2012)
56. V. Mara, R. Haghani, P. Harryson, Bridge decks of fibre-reinforced polymer (FRP): A sustainable solution. Construct. Build Mater. ***50***, 190–199 (2014)
57. L.C. Hollaway, The evolution of and the way forward for advanced polymer composites in the civil infrastructure. Construct. Build Mater. ***17***(6-7), 365–378 (2003)

58. P. Fernandes, G. Viana, R.J.C. Carbas, M. Costa, L.F.M. da Silva, M.D. Banea, The influence of water on the fracture envelope of an adhesive joint. Theor. Appl. Fract. Mech. ***89***, 1–15 (2017)
59. M. Bordes, P. Davies, J.Y. Cognard, L. Sohier, V. Sauvant-Moynot, J. Galy, Prediction of long-term strength of adhesively bonded steel/epoxy joints in sea water. Int. J. Adhes. Adhes. ***29***(6), 595–608 (2009)
60. M. Heshmati, R. Haghani, M. Al-Emrani, Effects of moisture on the long-term performance of adhesively bonded FRP/steel joints used in bridges. Compos. Part B Eng. ***92***, 447–462 (2016)
61. M. Heshmati, R. Haghani, M. Al-Emrani, Durability of CFRP/steel joints under cyclic wet-dry and freeze-thaw conditions. Compos. Part B Eng. ***126***, 211–226 (2017)
62. S. Owuamanam, D. Cree, Progress of bio-calcium carbonate waste eggshell and seashell fillers in polymer composites: A review. J. Compos. Sci. ***4***(2), 70 (2020)
63. D. Okanigbe, P. Olawale, A. Popoola, A. Abraham, A. Michael, K. Andrei, Centrifugal separation experimentation and optimum predictive model development for copper recovery from waste copper smelter dust. Cogent Eng. ***5***(1), 1551175 (2018)
64. B. Barsotti, M. Gaiotti, C.M. Rizzo, Recent industrial developments of marine composites limit states and design approaches on strength. J. Mar. Sci. Appl. ***19***(4), 553–566 (2020)
65. M.L. Martínez, G. Vázquez, O. Pérez-Maqueo, R. Silva, P. Moreno-Casasola, G. Mendoza-González, J. López-Portillo, I. MacGregor-Fors, G. Heckel, J.R. Hernández-Santana, J.G. García-Franco, A systemic view of potential environmental impacts of ocean energy production. Renew. Sustain. Energy Rev. ***149***, 111332 (2021)
66. A. Adesanya, S. Misra, R. Maskeliunas, R. Damasevicius, Prospects of ocean-based renewable energy for West Africa's sustainable energy future. Smart Sustain. Built Environ. ***10***(1), 37–50 (2020)
67. C.S. Barrera, K. Cornish, Fly ash as a potential filler for the rubber industry. J. Handb. Fly Ash, ***1***, 763–792 (2022)
68. S.R. Hartshorn (ed.), *Structural Adhesives: Chemistry and Technology* (Springer Science & Business Media, New York, 2012)
69. F.A. Keimel, Historical development of adhesives and adhesive bonding. In *Handbook of Adhesive Technology*, Revised and Expanded; Marcel Dekker, Inc.: New York, NY, USA, 1–12 (2003)
70. T.M. Carole, J. Pellegrino, M.D. Paster, Opportunities in the industrial biobased products industry, in *Proceedings of the Twenty-Fifth Symposium on Biotechnology for Fuels and Chemicals Held May 4–7, 2003, in Breckenridge, CO*, (Humana Press, Totowa, 2004), pp. 871–885
71. K. Hirano, M. Asami, Phenolic resins—100 years of progress and their future. React. Funct. Polym. ***73***(2), 256–269 (2013)
72. R. Vendamme, N. Schüwer, W. Eevers, Recent synthetic approaches and emerging bio-inspired strategies for the development of sustainable pressure-sensitive adhesives derived from renewable building blocks. J. Appl. Polym. Sci. ***131***(17) (2014)
73. H. Wang, X. Gong, J. Gong, Current and future challenges of bio-based adhesives for wood composite industries, in *Eco-Friendly Adhesives for Wood and Natural Fiber Composites*, (Springer, Singapore, 2021), pp. 147–164
74. D.M. Gleich, *Stress Analysis of Structural Bonded Joints*. TU Delft, Delft University of Technology, (2002)
75. A.A. Baker, L.F. Rose, R. Jones (eds.), *Advances in the Bonded Composite Repair of Metallic Aircraft Structure* (Elsevier, Burlington, 2003)
76. S.M.R. Khalili, M.H. Jafarkarimi, M.A. Abdollahi, Creep analysis of fibre- reinforced adhesives in single lap joints—Experimental study. Int. J. Adhes. Adhes. ***29***(6), 656–661 (2009)
77. A. Skorulska, P. Piszko, Z. Rybak, M. Szymonowicz, M. Dobrzyński, Review on polymer, ceramic and composite materials for cad/cam indirect restorations in dentistry—Application, mechanical characteristics and comparison. *Materials* ***14***(7), 1592 (2021)

78. J. Zhu, Z. Zhang, S. Zhao, A.S. Westover, I. Belharouak, P.F. Cao, Single-ion conducting polymer electrolytes for solid-state lithium–metal batteries: Design, performance, and challenges. Adv. Energy Mater. ***11***(14), 2003836 (2021)
79. S.V. Levchik, E.D. Weil, Flame retardancy of thermoplastic polyesters—A review of the recent literature. Polym. Int. ***54***(1), 11–35 (2005)
80. C. T'Joen, Y. Park, Q. Wang, A. Sommers, X. Han, A. Jacobi, A review on polymer heat exchangers for HVAC&R applications. Int. J. Refrig. ***32***(5), 763–779 (2009)
81. I.A. Kinloch, J. Suhr, J. Lou, R.J. Young, P.M. Ajayan, Composites with carbon nanotubes and graphene: An outlook. *Science* ***362***(6414), 547–553 (2018)
82. S. De Barros, P.P. Kenedi, S.M. Ferreira, S. Budhe, A.J. Bernardino, L.F.G. Souza, Influence of mechanical surface treatment on fatigue life of bonded joints. J. Adhes. ***93***(8), 599–612 (2017)
83. Y. Xie, B. Yang, L. Lu, Z. Wan, X. Liu, Shear strength of bonded joints of carbon fiber-reinforced plastic (CFRP) laminates enhanced by a two-step laser surface treatment. Compos. Struct. ***232***, 111559 (2020)
84. M. Afendi, M.A. Majid, R. Daud, A.A. Rahman, T. Teramoto, Strength prediction and reliability of brittle epoxy adhesively bonded dissimilar joint. Int. J. Adhes. Adhes. ***45***, 21–31 (2013)
85. M.V. Cakir, D. Kinay, MWCNT, nano-silica, and nano-clay additives effects on adhesion performance of dissimilar materials bonded joints. Polym. Compos. ***42***(11), 5880–5892 (2021)
86. G. Marami, S.A. Nazari, S.A. Faghidian, F. Vakili-Tahami, S. Etemadi, Improving the mechanical behavior of the adhesively bonded joints using RGO additive. Int. J. Adhes. Adhes. ***70***, 277–286 (2016)
87. Y. Korkmaz, K. Gültekin, Improvement of structural, thermal and mechanical properties of epoxy composites and bonded joints exposed to water environment by incorporating boron nanoparticles. Int. J. Adhes. Adhes. ***116***, 103141 (2022)
88. İ. Saraç, H. Adin, Ş. Temiz, Experimental determination of the static and fatigue strength of the adhesive joints bonded by epoxy adhesive including different particles. Compos. Part B Eng. ***155***, 92–103 (2018)
89. R.B. Ladani, S. Wu, A.J. Kinloch, K. Ghorbani, A.P. Mouritz, C.H. Wang, Enhancing fatigue resistance and damage characterisation in adhesively-bonded composite joints by carbon nanofibres. Compos. Sci. Technol. ***149***, 116–126 (2017)
90. S.Y. Park, W.J. Choi, B.C. Yoon, Analysis of effects of process factors on corrosion resistance of adhesive bonded joints for aluminum alloys. J. Mater. Process. Technol. ***276***, 116412 (2020)
91. H. Wan, J. Lin, J. Min, Effect of laser ablation treatment on corrosion resistance of adhesive-bonded Al alloy joints. Surf. Coat. Technol. ***345***, 13–21 (2018)
92. C. Sato, R.J. Carbas, E.A. Marques, A. Akhavan-Safar, L.F. da Silva, Effect of disassembly on environmental and recycling issues in bonded joints, in *Adhesive Bonding*, (Woodhead Publishing, Oxford, 2021), pp. 407–436
93. P. Chalkley, A. Rider, Toughening boron/epoxy-bonded joints using the resin film infusion technique. Compos. Part A Appl. Sci. Manuf. ***34***(4), 341–348 (2003)
94. N. Brack, A.N. Rider, The influence of mechanical and chemical treatments on the environmental resistance of epoxy adhesive bonds to titanium. Int. J. Adhes. Adhes. ***48***, 20–27 (2014)
95. C.E. Yue, S. Dong, L. Weng, Y. Wang, L. Zhao, Environmental resistance and fatigue behaviors of epoxy/nano-boron nitride thermally conductive structural film adhesive toughened by polyphenoxy. *Polymers* ***13***(19), 3253 (2021)
96. R. Yemm, D. Pizer, C. Retzler, R. Henderson, Pelamis: Experience from concept to connection. Philos. Trans. R. Soc. A Math. Phys. Eng. Sci. ***370***(1959), 365–380 (2012)
97. S. Helland, R. Aarstein, M. Maage, In-field performance of North Sea offshore platforms with regard to chloride resistance. Struct. Concr. ***11***(1), 15–24 (2010)
98. P.K. Mehta, Greening of the concrete industry for sustainable development. Concr. Int. ***24***(7), 23–28 (2002)

99. E. Dutkiewicz, *Fizykochemia powierzchni* (Wydawnictwa Naukowo-Techniczne, Warszawa, 1998)
100. A. Pizzi, K.L. Mittal (eds.), *Handbook of Adhesive Technology* (CRC Press, Boca Raton, 2017)
101. K. Kelar, D. Ciesielska, *Fizykochemia polimerÁłw: wybrane zagadnienia* (Wydawnictwo Politechniki PoznaĹ, skiej, 1997)
102. A. Baldan, Adhesion phenomena in bonded joints. Int. J. Adhes. Adhes. ***38***, 95–116 (2012)
103. K.L. DeVries, D.O. Adams, Mechanical testing of adhesive joints, in *Adhesion Science and Engineering*, (Elsevier Pub., The Netherlands, 2002), pp. 193–234
104. A. Szewczak, Influence of epoxy glue modification on the adhesion of CFRP tapes to concrete surface. *Materials* ***14***(21), 6339 (2021)
105. M. Żenkiewicz, *Adhezja i modyfikowanie warstwy wierzchniej tworzyw wielkocząsteczkowych* (Wydawnictwa Naukowo-Techniczne, Warszawa, 2000)
106. J.W. McBain, D.G. Hopkins, On adhesives and adhesive action. J. Phys. Chem. ***29***(2), 188–204 (2002)
107. A. Clark, *The Theory of Adsorption and Catalysis* (Academic, New York, 2018)
108. L.H. Lee (ed.), *Fundamentals of Adhesion* (Springer Science & Business Media, Berlin, 2013)
109. A.V. Pocius, D. Dillard, *Adhesion Science and Engineering: Surfaces, Chemistry and Applications* (Elsevier, Amsterdam, 2002)
110. D. Ruffatto III, A. Parness, M. Spenko, Improving controllable adhesion on both rough and smooth surfaces with a hybrid electrostatic/gecko-like adhesive. J. R. Soc. Interface ***11***(93), 20131089 (2014)
111. S.S. Voyutskii, V.L. Vakula, The role of diffusion phenomena in polymer-to-polymer adhesion. J. Appl. Polym. Sci. ***7***(2), 475–491 (1963)
112. V.Y. Popov, A.S. Yanyushkin, Adhesion-diffusion interaction of contact surfaces with the treatment diamond grinding wheels. East. Eur. Sci. J. **2**, 301–310 (2014)
113. J.J. Bikerman, *The Science of Adhesive Joints* (Acad. Press, New York, 1968)
114. F.M. Fowkes, Role of acid-base interfacial bonding in adhesion. J. Adhes. Sci. Technol. ***1***(1), 7–27 (1987)
115. I. Astm, ASTM52900-15 standard terminology for additive manufacturing—general principles—terminology. ASTM Int., West Conshohocken, PA ***3***(4), 5 (2015)
116. L.P. Devendra, R.K. Sukumaran, Comparative evaluation of lignin derived from different sugarcane bagasse pretreatments in the synthesis of wood adhesive. *BioEnergy Res.*, ***15*** 1–12 (2022)
117. S. Zhou, F. Wang, J. Chen, D. Alhashmialameer, S. Wang, M.H.H. Mahmoud, G.A. Mersal, J. Huang, Q. Zhang, G. Zhao, Y. Liu, Enhanced mechanical, thermal, and tribological performance of 2D-laminated molybdenum disulfide/RGO nanohybrid filling phenolic resin composites. Adv. Compos. Hybrid Mater. ***5***(2), 1206–1220 (2022)
118. W. Zhou, H. Zhao, Z. Li, X. Huang, Autopolymerizing acrylic repair resin containing low concentration of dimethylaminohexadecyl methacrylate to combat saliva-derived bacteria. J. Mater. Sci.: Mater. Med. ***33***(6), 1–13 (2022)
119. N. Sukprasert, C. Harnirattisai, P. Senawongse, H. Sano, P. Saikaew, Delayed light activation of resin composite affects the bond strength of adhesives under dynamic simulated pulpal pressure. Clin. Oral Investig., ***26***(11), 6743–6752 (2022)
120. E.L.D.A. de Cianoacrilato, Longitudinal evaluation of ethyl cyanoacrylate adhesives on Candida albicans biofilm. Int. J. Odontostomat. ***16***(1), 68–72 (2022)
121. P. Sonkusare, P. Agarwal, S.K. Dhakad, R.S. Rana, A review paper: Study of various renewable resources polymer and different types of nanocomposite materials, in *Technology Innovation in Mechanical Engineering*, (Springer, Singapore, 2022), pp. 63–73
122. M. Bilal, S.A. Qamar, M. Qamar, V. Yadav, M.J. Taherzadeh, S.S. Lam, H. Iqbal, Bioprospecting lignin biomass into environmentally friendly polymers—Applied perspective to reconcile sustainable circular bioeconomy. Biomass Convers. Biorefin. ***12***, 1–27 (2022)
123. M.A. Boyle, C.J. Martin, J.D. Neuner, Epoxy resins. ASM Handb ***21***, 78–89 (2001)

124. E. Ciecierska, A. Boczkowska, M. Kubis, P. Chabera, T. Wisniewski, Epoxy composites with carbon fillers. Structure and properties. Przem. Chem. ***94***(11), 2033–2037 (2015)
125. K. Wang, L. Chen, J. Wu, M.L. Toh, C. He, A.F. Yee, Epoxy nanocomposites with highly exfoliated clay: Mechanical properties and fracture mechanisms. *Macromolecules* ***38***(3), 788–800 (2005)
126. S. Ebnesajjad, A.H. Landrock, *Adhesives Technology Handbook* (William Andrew, Amsterdam, 2014)
127. G.C. Mays, A.R. Hutchinson, *Adhesives in Civil Engineering*, vol 32 (Cambridge University Press, Cambridge, 1992)
128. K.K. Chawla, Metal matrix composites, in *Composite Materials*, (Springer, New York, 2012), pp. 197–248
129. B. Ellis (ed.), *Chemistry and Technology of Epoxy Resins*, 1st edn. (Blackie Academic & Professional, London, 1993), pp. 212–213
130. J.H. Koo, *Polymer Nanocomposites: Processing, Characterization, and Applications* (McGraw-Hill Education, New York, 2019)
131. A.B. Strong, *Plastics: Materials and Processing* (Prentice Hall, Upper Saddle River, 2006)
132. Q. Wang, Z. Yang, Y. Yang, C. Long, H. Li, A bibliometric analysis of research on the risk of engineering nanomaterials during 1999–2012. Sci. Total Environ. ***473***, 483–489 (2014)
133. I.N. Yoon, Y. Lee, D. Kang, J. Min, J. Won, M. Kim, Y.S. Kang, S.H. Kim, J.J. Kim, Modification of hydrogenated Bisphenol A epoxy adhesives using nanomaterials. Int. J. Adhes. Adhes. ***31***(2), 119–125 (2011)
134. A. Rudawska, M. Czarnota, Selected aspects of epoxy adhesive compositions curing process. J. Adhes. Sci. Technol. ***27***(17), 1933–1950 (2013)
135. C. Capela, S.E. Oliveira, J.A.M. Ferreira, Fatigue behavior of short carbon fiber-reinforced epoxy composites. Compos. Part B Eng. ***164***, 191–197 (2019)
136. Z. Xu, M. Wu, W. Gao, H. Bai, A transparent, skin-inspired composite film with outstanding tear resistance based on flat silk cocoon. Adv. Mater. ***32***(34), 2002695 (2020)
137. Z.F. Zhu, W.W. Wang, K.A. Harries, Y.Z. Zheng, Uniaxial tensile stress-strain behavior of carbon-fiber grid-reinforced engineered cementitious composites. J. Compos. Constr. ***22***(6), 04018057 (2018)
138. X. Wang, X. Zhao, S. Chen, Z. Wu, Static and fatigue behavior of basalt fiber-reinforced thermoplastic epoxy composites. J. Compos. Mater. ***54***(18), 2389–2398 (2020)
139. H. Gonabadi, A. Oila, A. Yadav, S. Bull, Investigation of the effects of environmental fatigue on the mechanical properties of GFRP composite constituents using nanoindentation. Exp. Mech. ***62***(4), 585–602 (2022)
140. R. Sivaperumal, J. Jancirani, Characterization of amino silane modified ramie fibre, OMMT nanoclay-reinforced epoxy resin composite. *Silicon*, ***14***(12), 7193–7202 (2022)
141. M. da Silva Batista, L.A. Teixeira, A. de Souza Louly, S.O. Silva, S.M. da Luz, Fatigue damage propagation and creep behavior on sisal/epoxy composites. *Polímeros: Ciência e Tecnologia* ***32***(1), 0 (2022)
142. L. Yan, X. Gao, F. Wahid-Pedro, J.T.E. Quinn, Y. Meng, Y. Li, A novel epoxy resin-based cathode binder for low cost, long cycling life, and high-energy lithium–sulfur batteries. J. Mater. Chem. A ***6***(29), 14315–14323 (2018)
143. N. Tual, N. Carrere, P. Davies, T. Bonnemains, E. Lolive, Characterization of sea water ageing effects on mechanical properties of carbon/epoxy composites for tidal turbine blades. Compos. Part A Appl. Sci. Manuf. ***78***, 380–389 (2015)
144. Z. Wang, G. Xian, X.L. Zhao, Effects of hydrothermal aging on carbon fibre/epoxy composites with different interfacial bonding strength. Construct. Build Mater. ***161***, 634–648 (2018)
145. J.Y. Wang, H.J. Ploehn, Dynamic mechanical analysis of the effect of water on glass bead–epoxy composites. J. Appl. Polym. Sci. ***59***(2), 345–357 (1996)
146. Z.R. Xu, K.H.G. Ashbee, Photoelastic study of the durability of interfacial bonding of carbon fibre-epoxy resin composites. J. Mater. Sci. ***29***(2), 394–403 (1994)

147. E. Pérez-Pacheco, J.I. Cauich-Cupul, A. Valadez-González, P.J. Herrera-Franco, Effect of moisture absorption on the mechanical behavior of carbon fiber/epoxy matrix composites. J. Mater. Sci. ***48***(5), 1873–1882 (2013)
148. A.H.I. Mourad, B.M. Abdel-Magid, T. El-Maaddawy, M.E. Grami, Effect of seawater and warm environment on glass/epoxy and glass/polyurethane composites. Appl. Compos. Mater. ***17***(5), 557–573 (2010)
149. A. Boisseau, P. Davies, F. Thiebaud, Sea water ageing of composites for ocean energy conversion systems: Influence of glass fibre type on static behaviour. Appl. Compos. Mater. ***19***(3), 459–473 (2012)
150. M. Dawson, P. Davies, P. Harper, S. Wilkinson, Effects of conditioning parameters and test environment on composite materials for marine applications, in *SAMPE Europe Conference*, (2016)
151. R. Kilik, R. Davies, Mechanical properties of adhesive filled with metal powders. Int. J. Adhes. Adhes. ***9***(4), 224–228 (1989)
152. J. Murphy (ed.), *Additives for Plastics Handbook* (Elsevier, Oxford, 2001)
153. N. Tarannum, K.M. Pooja, R. Khan, Preparation and applications of hydrophobic multicomponent based redispersible polymer powder: A review. Construct. Build Mater. ***247***, 118579 (2020)
154. A. Shojaei, S.S. Khasraghi, Self-healing and self-sensing smart polymer composites, in *Composite Materials*; Low, I.-M., Yu, D., Eds.; Elsevier: Amsterdam, The Netherlands, pp. 307–357 (2021)
155. K.M. Nambiraj, K. Rajkumar, P. Sabarinathan, A novel approach on reusing silicon wafer kerf particle as potential filler material in polymer composite. *Silicon* ***14***(4), 1537–1548 (2022)
156. A.A. Ahmad Fauzi, A.F. Osman, A.A. Alrashdi, Z. Mustafa, K.A. Abdul Halim, On the use of dolomite as a mineral filler and co-filler in the field of polymer composites: A review. *Polymers* ***14***(14), 2843 (2022)
157. U.A. Khashaba, A.A. Aljinaidi, M.A. Hamed, Fatigue and reliability analysis of nano-modified scarf adhesive joints in carbon fiber composites. Compos. Part B Eng. ***120***, 103–117 (2017)
158. M.H. Wichmann, J. Sumfleth, F.H. Gojny, M. Quaresimin, B. Fiedler, K. Schulte, Glass-fibre-reinforced composites with enhanced mechanical and electrical properties–benefits and limitations of a nanoparticle modified matrix. Eng. Fract. Mech. ***73***(16), 2346–2359 (2006)
159. A. Rudawska, D. Stančeková, N. Cubonova, T. Vitenko, M. Müller, P. Valášek, Adhesive properties and adhesive joints strength of graphite/epoxy composites. J. Phys.: Conf. Ser. **842**(1), 012073 (2017). IOP Publishing
160. T. Yokoyama, K. Nakai, Determination of the impact tensile strength of structural adhesive butt joints with a modified split Hopkinson pressure bar. Int. J. Adhes. Adhes. ***56***, 13–23 (2015)
161. A. Girge, V. Goel, G. Gupta, D. Fuloria, P.R. Pati, A. Sharma, V.K. Mishra, Industrial waste filled polymer composites–A review. Mater. Today Proc. ***47***, 2852–2863 (2021)
162. R. Kumar, A review on epoxy and polyester-based polymer concrete and exploration of polyfurfuryl alcohol as polymer concrete. J. Polym. ***2016***, 7249743 (2016)
163. F. Pahlevani, V. Sahajwalla, Effect of different waste filler and silane coupling agent on the mechanical properties of powder-resin composite. J. Clean. Prod. ***224***, 940–956 (2019)
164. R.R. Galeev, R.K. Nizamov, L.A. Abdrakhmanova, January. Filling of epoxy polymers with chemically precipitated chalk from chemical water treatment sludge, in *International Conference Industrial and Civil Construction*, (Springer, Cham, 2021), pp. 93–97
165. I. Miturska, A. Rudawska, M. Müller, P. Valášek, The influence of modification with natural fillers on the mechanical properties of epoxy adhesive compositions after storage time. *Materials* ***13***(2), 291 (2020)
166. Z. Zhao, A. Grellier, M.E.K. Bouarroudj, F. Michel, D. Bulteel, L. Courard, Substitution of limestone filler by waste brick powder in self-compacting mortars: Properties and durability. J. Build. Eng. ***43***, 102898 (2021)

167. P.R. Pati, M.P. Satpathy, Investigation on red brick dust filled epoxy composites using ant lion optimization approach. Polym. Compos. ***40***(10), 3877–3885 (2019)
168. A.S. Mostovoi, E.A. Kurbatova, Controlling the properties of epoxy composites filled with brick dust. Russ. J. Appl. Chem. ***90***(2), 267–276 (2017)
169. A. Szewczak, M. Szeląg, Physico-mechanical and rheological properties of epoxy adhesives modified by microsilica and sonication process. *Materials* ***13***(23), 5310 (2020)
170. J.M. González-Domínguez, Y. Martínez-Rubí, A.M. Díez-Pascual, A. Ansón-Casaos, M. Gómez-Fatou, B. Simard, M.T. Martínez, Reactive fillers based on SWCNTs functionalized with matrix-based moieties for the production of epoxy composites with superior and tunable properties. *Nanotechnology* ***23***(28), 285702 (2012)
171. G. Wypych, Plasticizers use and selection for specific polymers. In *Handbook of Plasticizers*; Wypych, G., Ed.; ChemTec Publishing: Toronto, Canada,; Chapter 11; pp. 273–379 (2004)
172. J.F. Rabek, *Współczesna wiedza o polimerach: wybrane zagadnienia* (Wydawnictwo Naukowe PWN, Warszawa, 2008)
173. W.W. Gerberich, M.J. Cordill, Physics of adhesion. Rep. Prog. Phys. ***69***(7), 2157 (2006)
174. L. Karasek, M. Sumita, Characterization of dispersion state of filler and polymer-filler Interactions in rubber-carbon black composites. J. Mater. Sci. ***31***(2), 281–289 (1996)
175. F.N. Ahmad, M. Jaafar, S. Palaniandy, K.A.M. Azizli, Effect of particle shape of silica mineral on the properties of epoxy composites. Compos. Sci. Technol. ***68***(2), 346–353 (2008)
176. C. Creton, Pressure-sensitive adhesives: An introductory course. MRS Bull. ***28***(6), 434–439 (2003)
177. K. von der Mark, J. Park, S. Bauer, P. Schmuki, Nanoscale engineering of biomimetic surfaces: Cues from the extracellular matrix. Cell Tissue Res. ***339***(1), 131–153 (2010)
178. A. Hejna, M. Przybysz-Romatowska, P. Kosmela, Ł. Zedler, J. Korol, K. Formela, Recent advances in compatibilization strategies of wood-polymer composites by isocyanates. Wood Sci. Technol. ***54***(5), 1091–1119 (2020)
179. S. Yang, J. Tian, X. Bian, Y. Wu, High performance NBR/fly ash composites prepared by an environment-friendly method. Combust. Sci. Technol. ***186***, 107909 (2020)
180. A. Kaleni, S.I. Magagula, M.T. Motloung, M.J. Mochane, T.C. Mokhena, Preparation and characterization of coal fly ash-reinforced polymer composites: An overview. Express Polym. Lett. ***16***(7), 735–759 (2022)
181. D.O. Okanigbe, A.P.I. Popoola, A.A. Adeleke, Characterization of copper smelter dust for copper recovery. Procedia Manuf. ***7***, 121–126 (2017)
182. D.O. Okanigbe, A.P.I. Popoola, A.A. Adeleke, Hydrometallurgical processing of copper smelter dust for copper recovery as nano-particles: A review. Energy Technol. ***2017***, 205–226 (2017)

Chapter 10
Aircraft Engine Fan Blade Design: Impact Tolerance Prediction of Partially Filled 3D Printed Aluminum, Titanium, and PEEK-Filled Waste Metal Dusts

Shade Rouxzeta Van Der Merwe, Daniel Ogochukwu Okanigbe, Dawood Ahmed Desai, and Glen Campbell Snedden

10.1 Introduction

The gross domestic product (GDP) contribution of the air transport sector in South Africa (SA), comprising airlines and its supply chain, is estimated at US $5.2 billion (GDP). An additional US $4.3 billion, or US $9.4 billion, of the nation's GDP is supported by international visitor spending [1]. In order to maintain competitiveness in the global tourism industry, further technological developments in aircraft operation are motivated by this support, which helps to increase SA's GDP growth. And as a result of this need for further technological development in operational aircraft, opportunities are formed for the discovery of new materials, unique design concepts, and the production of engineering components [2, 3].

Cheap structural ceramics, such as the Mullite Rich Tailings (MRT) from density separation of copper smelter dust [4, 5], will undoubtedly find a position to play a significant part in the consequent technological developments in the aerospace industry [6] by taking use of these prospects. The use of ceramic matrix composites in the hot section of engines has recently gained increased support from aircraft

S. R. Van Der Merwe · D. A. Desai
Department of Mechanical and Mechatronics Engineering, Faculty of Engineering and the Built environment, Tshwane University of Technology, Pretoria, South Africa
e-mail: vandermerweR1@tut.ac.za

D. O. Okanigbe (✉)
Department of Chemical, Metallurgical and Materials Engineering, Faculty of Engineering, Tshwane University of Technology, Pretoria, South Africa

Pantheon Virtual Engineering Solutions, Nigel, South Africa
e-mail: okanigbedo@tut.ac.za; okanigbeogochukwu@gmail.com

G. C. Snedden
Department of Mechanical Engineering, Aerospace Systems Research Group Gate, University of KwaZulu-Natal, Durban, South Africa

D. O. Okanigbe, A. P. Popoola (eds.), *Resource Recovery and Recycling from Waste Metal Dust*, https://doi.org/10.1007/978-3-031-22492-8_10

engine manufacturers, in line with this school of thought [7, 8]. Mullite ceramics are capable of operating at temperatures of up to 1600 °C and have a high thermal shock, claim Zhao et al. [9], Lee, Zhu and Lima [10], and Suleimanov et al. [11]. These characteristics make this structural material more appealing for aerospace applications than standard materials; in particular, because it reduces weight, needs less cooling air, and as a result helps to lower fuel consumption and increase aircraft performance [10, 12].

However, Padture [13] asserts that it is doubtful to fully utilize the capabilities of MRT to simply replace metallic or polymer components in existing propulsion systems, such as the aircraft engine fan blade (Fig. 10.1), with mullite ceramics (e.g., MRT). The processing and production of components using these novel composites [14] will also continue to be difficult [15], but they offer a fertile ground for innovation, thus they must be included in the endeavor [16]. For example, using impact tolerance of partially filled 3D printed turbine component as a function of varied infill densities, will need to be developed in order to account for the excessive cost of extensive component-level testing under realistic engine conditions [17–19]. Additionally, reliable physics [20–22] and mechanisms-based models [23] that describe the behavior of the constituent MRT [13, 24, 25], the composites [26–28], and the component at temporal scales [29].

In order to coordinate the operations of the composites, i.e., of reinforcement (MRT) and matrix (metal or polymer), while embracing and utilizing the growing complexity at temporal scales, it will be necessary to design aircraft components with distributed systems. Noting that achieving necessary qualities inside composites that cannot be satisfied by existing materials will be necessary for the expedited development of new MRT reinforcing.

Fig. 10.1 Picture of the Boeing 747's engine with its fan blades. (Source: Google image)

The process must be put through an integrated design-modeling-experiment-manufacturing strategy, which should span composites-3D printed components-system hierarchy, in order to test these desired qualities. A strategy that, for accelerated development, should embrace integrated computational materials engineering and the materials genome initiative principles. By doing this, the MRT's full potential can be realized.

Furthermore, a thorough understanding of material cost savings associated with 3Dprinting aircraft components is necessary to fully realize MRT's potential for creating composites for aerospace applications. During the manufacturing of aircraft components using composite materials, materials' cost savings can be realized by optimizing 3D process parameters (especially infill density) to get the best percentage material content [30–32].

There is no need to fill the interior of 3D printed components, according to Moradi, Meiabadi, and Kaplan [33], because the optimized specimen has better mechanical properties, a lighter part weight, a faster build time, and lower production costs than the filled specimen. Consequently, fuel consumption was decreased as a result of the lighter components made under these circumstances.

It is crucial to research the possibilities of using MRT as reinforcement in the development of aerospace materials for the production of 3D printed engineering components. More specifically, how this waste can further improve material cost savings and produce higher mechanical qualities like impact tolerance. This idea is supported by the proposed study, which tries to optimize the infill density of 3D printed turbine blades and choose the best construction capable of withstanding the highest expected loads with the least amount of material and production time.

10.2 The Problem Statement

The degree to which specific process parameters like time and material are managed can determine whether the impact tolerance of 3D printed components is acceptable or unwanted. The best conditions, approach, and/or requirements have not yet been discovered to produce the best impact tolerance of partially filled 3D printed components from a combination of all the characteristics. The goal of maximizing profit in the aerospace industry is defeated since, in order to obtain optimum tensile strength of a 3Dprinted turbopump component, an infill is frequently 100% filled. This implies greater expenses (i.e., in terms of time and material) and heavier components.

Sub-problem 1 What are the main factors affecting the 3D printing process?

This will specify the components of the 3D printing procedure necessary to generate results of material advantages to be assessed for optimization. When changed, these components, also known as influential parameters, have a significant impact on the output and define the functionality and output of the 3D print process.

Sub-problem 2 What are the optimization objectives?

This forces the researcher to establish design goals in the form of objectives, the anticipated outcomes of the 3D printing process, and which elements of these outputs should be maximized and which elements should be minimized. In order to achieve the overall goal of increasing the impact tolerance of partially filled 3D print components, this will help determine what outcomes need to be traded off in exchange for gains on other sides, what properties should increase and what properties must decrease, what beneficial aspects need to be strengthened and what harmful aspects need to be weakened.

Sub-problem 3 What strategy will be used to model the problem and improve the model simulation's outcomes?

Sub-problem 4 Which set of ideal parameters best addresses the research problem's numerous objectives?

This study's optimization deliverable is a multiobjective problem with multiple potential solutions rather than a single ideal one. In order to achieve the optimal combination or sets of combinations, we must now solve the problem of defining the amount of weights and impact coefficients to be assigned to the various sub-objectives, designating them in order of importance while limiting those with unclear possibilities.

10.3 Research Hypotheses

For this study, the following tentative assumptions have been implemented to serve as the foundation for addressing the key questions which this research presents.

Hypothesis 1 The following elements comprise the parameters for this optimization problem that affect the anticipated result of the 3D print:

(a) 3D print attributes

- Speed
- Size
- Accuracy
- Durability
- Material

(b) Factors defining material behavior

- Temperature
- Pressure
- Strain rate
- Material content (% infill)

(c) Mechanical component tolerance

- Size
- Shape
- Volume

Hypothesis 2 The results of an impact tolerance test on a partially filled 3D component are induced tensional residual stresses, material hardening, and uniaxial yield stress as a result of brittle deformation, therefore optimization goals must be specified for all three results. These consist of:

- Tensional residual stress maximization
- Reduced material hardening
- Reduced uniaxial yield stress as a result of brittle deformation

Hypothesis 3 Impact tolerance of a 3D print can be modeled as short, intense pressure pulses from an outside item that collide and transmit energy to the material. The primary factors governing the transfer of energy can be quantitatively modeled and evaluated using finite element material modeling. In addition to ABAQUS, the parametric optimization software tool Isight can find the best combinations that will cause the 3D printing process to deliver the desired response(s).

Hypothesis 4 It is anticipated that the optimization process will produce more than one feasible solution. In this scenario, the designated sub-objectives can be iterated with respect to the various responses they produce, with weights and scaling factors arranged in order of importance and impact. Using a decision-making matrix, a set or sets of multiple combinations of the best solutions can then be obtained.

10.4 Research Objectives

10.4.1 Main Objectives

The main objectives of the proposed research study are to predict the impact tolerance of a 3D printed turbine component that is partially filled and to identify the subsequent best infill.

10.4.2 Sub-Objectives

The primary goal of this study will be accomplished by simulation and experimental model validation. The following set of supporting goals will help to attain this main goal:

1. The creation of a numerical turbine model using finite element analysis (FEA).
2. Examine the impact tolerance of the turbine developed at various infill levels (i.e., 20%, 25%, 30%, 35%, 40%, 45%, 50%, 55%, 60%, 70%, 75%, 80%, 85%), as well as the impact on the deformation pattern (Plastic or brittle).
3. To experimentally check the consistency of the FEA model as well as to validate it analytically using the moment of inertia methodology.
4. Last but not least, suggest the ideal infill for a 3D printed turbine component that will conserve both time and material.

10.5 The Assumptions

To optimize the infill density of the 3D printed turbine blade and choose the best structure able to handle the highest expected loads with the least amount of material and manufacturing time, finite element analysis will be used. The study and resolution of the issue will be conducted under the following set of presumptions in order to do this:

1. The foreign object strikes the turbine blade at an angle that is normal to its surface.
2. The entire procedure conserves energy.
3. Each disk's blades are permanently fastened to the disk and have the same characteristics.
4. Radial displacement and torsion are disregarded because it is presumed that the blade angle motion is minimal.
5. The ith fan blade's motion consists of out-of-plane motion in the axial direction of the rotor and in-plane motion along the circumferential direction of the disk.
6. Homogeneous and isotropic mechanical characteristics of unmixed material, metal matrix composites, and polymer matrix composites will be assumed.
7. Unmixed materials, metal matrix composites, and polymer matrix composites are assumed to act linearly ideal elastically, which means that the law of linear elasticity is applied to each individual layer.
8. The apparent-level compressive modulus (E_c) measured experimentally and combinations of infill densities will be used to represent the unmixed material, metal matrix composites, and polymer matrix composites as a continuum (20%, 25%, 30%, 35%, 40%, 45%, 50%, 55%, 60%, 65%, 70%, 75%, 80%, 85%).
9. The hypothesis excludes flaws like fractures and air bubbles.
10. It is assumed that the layers formed by the particle and matrix composition are orthotropic and properly adhered to one another.
11. Because the particles are not evaluated separately from the matrix or the binder layer, interface effects are disregarded.
12. The various layers are perfectly connected to one another. When loads are applied, it is presumed that relative slip won't happen.

10.6 The Project Deliverables

When this research study is finished, it should produce the following results:

1. A flexible, finite element-based model that has been experimentally verified can be used to forecast the impact tolerance of a partially filled 3D printed turbine component.
2. A process that can be used to increase the impact tolerance of a 3D printed, partially filled turbine component.
3. Identification of the optimal process parameter combinations that influence the outcomes of 3D printing methods.

10.7 Importance of Study

This study's importance rests on:

10.7.1 Benefits to the Academia, Research, and Development

1. In order to maximize benefits and reduce manifestation of side effects of the surface treatment process, the research aims to examine and provide answers regarding how, where, when, and which ways laser peening should be employed in the surface treatment of LP steam turbine blades.
2. It offers methods for methodically and nondestructively enhancing the mechanical characteristics of turbomachinery components in an effort to increase reliability, cut downtime, lower the likelihood of in-service failure, and extend the useful life of steam turbine blades.
3. The results of this study will be helpful for improving material tensional residual stress in a variety of production and manufacturing applications, including the power, energy, production, oil and gas, aviation, and automotive industries, where turbopump machinery is a crucial component of operations and production.
4. Finally, the research's uniqueness may lead to a patent, which would add to the body of knowledge by encouraging other studies into asset integrity management and additive manufacturing. When this research is finished, journal articles in reputable, high impact journals and presentations at national and/or worldwide peer review conferences are also promised results.

10.7.2 Benefits to the Industry

The results of this research will provide the industry with the following advantages in addition to the other two listed above:

1. The creation of best practice recommendations for 3D printing parts in industry to remain compatible with the systems of the fourth industrial revolution.
2. Designs can be strengthened where they are weak without necessarily adding weight or substance.
3. Decrease in equipment downtime, inspection time, and maintenance expenses as a result of replacing faulty components while they were still operating.
4. A significant decrease in the amount of time needed to complete 3D printing tasks on plant and equipment parts during maintenance sessions. Prolonging the equipment's overall usable life.
5. Enhanced industrial and power plant operation and maintenance efficiency.
6. Increased guarantee of the components used in industry's safety and quality.

10.7.3 Benefits to South Africa

The national development goals of energy security and innovation to commercialization are perfectly aligned with this research. Therefore, the research output will contribute to a greater South African society in addition to benefiting academics and business, and it will be highly appealing to the goals of the government of the republic of South Africa in the following areas:

1. Decrease in the price of producing electricity
2. Improved industrial and power plant operation and maintenance efficiency
3. Reduction in the likelihood that components of operating industrial or power plants would collapse catastrophically
4. Increased assurance of the components' quality used in industry

Creation of test models and protocols to certify and accredit replacement component suppliers for industrial application.

10.8 Overview of the Study

Chapter 1 Acts as the study's introduction. It gives the study background, the problem statement, the hypotheses, the research technique, the assumptions, the delimitations, the project planning, and the research project's financial budget. Additionally, the dissertation's whole chapter-by-chapter research project outline is provided.

Chapter 2 Consists of a study of the literature done on blade containment difficulties.

This covers relevant literature found in the standards as well as earlier studies, books, conference reports, and more. This chapter will also include further studies on the actual experimental setup, tools, and equipment.

Chapter 3 Introduces mathematical modeling of phenomena pertinent to the study's goals.

Chapters 4 and 5 Focus on developing material models and a numerical model to predict impact tolerance using ABAQUS FEA software.

Chapters 6 and 7 ABAQUS's complementary parametric optimization software tool Isight will be used to optimize the impact tolerance simulation's key parameters in order to find the best combinations that will lead to the impact tolerance process's desired response or responses.

Chapter 8 Includes a description of the experimental characterization, which will cover the actual setup, analysis, and results tabulation. The experiments will be carried out when the physical testing specimen has been prepared.

Chapter 9 Presents the research's overall findings and results, along with any comparisons and explanations of the findings.

Chapter 10 Broad conclusions about the work, acknowledges unresolved issues, and makes suggestions for future work that can be done. This chapter will also include advice on how to deal with the underlying issue.

Chapter Summary
The reader is introduced to the research study in this chapter, which also emphasizes the key reasons why it should be pursued. This part of the research project also includes the problem statement, project objectives, research methodology, and study scope. The background and literature review of this study effort are presented in the following chapter. It comprises the theoretical information required to comprehend this research endeavor and its relevance by making use of prior research.

10.9 Literature Review

10.9.1 Introduction

Short lead times for product development without sacrificing the quality of the developed part are required by modern production processes. Rapid prototyping (RP) is one of the unique manufacturing techniques and materials that have been developed as a result of this [34–38]. Additive manufacturing, often known as 3D

printing, refers to procedures that manufacture objects by depositing material layer by layer without the need for finishing, as with traditional manufacturing processes.

Using only the fabrication machine, additive manufacturing enables the direct production of intricately structured items from their computer-aided design (CAD) models. Low maintenance costs, easy material swapping, a cool working environment, supervision-free operation, and small size are some of this technique's primary benefits [39]. The typical method for product development among manufacturers is now 3D printing [40, 41]. Production in a computer-integrated industrial environment is facilitated by 3D printing.

Manufacturing processes can be significantly improved by integrating 3D printing and concurrent engineering [42]. Fused Deposition Modeling, or 3D printing, is the most popular method (FDM). This method involves layer-by-layer application of melted filament, often made of Acrylonitrile Butadiene Styrene (ABS) or polylactic acid (PLA), which finally cools to create the solid object. The plastic filament is melted by an extruder that may move in the x-y plane and is then deposited on a bed that moves in the z direction to create the final 3D item.

FDM models reduce waste and make the process environmentally benign because they can be recycled [43]. The unique feature of the FDM method is its capacity to locally regulate the mechanical, density, and porosity characteristics of the created object [44]. FDM is a technique that can be used to create functioning items in addition to prototypes. The FDM needs to be improved in several ways in order to be used as a manufacturing tool. These include improved surface polish, tighter tolerances, and better dimensional control. Additionally, a wider variety of polymers should be available for usage, and prototyped parts' mechanical qualities should be improved to preserve their integrity while in use [45].

Contrary to the majority of manufacturing processes, the values of process parameters in additive manufacturing techniques can often be more important than the characteristics of the part material. Different sets of process settings will result in completely different attributes for parts with the same shape, such as strength [46, 47] or precision [48]. Each set of process variables, including bed temperature, layer thickness, infill pattern, and infill density, will result in a unique component structure, which will in turn provide unique mechanical property values.

Consequently, the papers under the following subheadings will be evaluated in this review section:

1. A review of publications on the impact of raster orientation and air gap on mechanical properties of 3D printed components.
2. A review of articles on how the mechanical qualities of 3D printed components are affected by printing speed, binder characteristics, infill rate, and layer thickness.
3. An analysis of papers examining the impact of PEEK use against ABS on the mechanical characteristics of 3D printed components.
4. An analysis of research on the impact of the infill pattern and density on the mechanical characteristics of 3D printed components.

10.9.2 Review of Publications: Present and Past

10.9.2.1 Review of Articles on the Impact of Infill Density on the Mechanical Characteristics of 3D Printed Components

Using the Taguchi approach, Abbas et al. [49] assessed the tensile, compressive, and bending strength of polylactic acid (PLA) samples by adjusting the infill density and other process variables. With increasing infill density, a rise in strength was seen. While cutting back on the infill density, printing time was significantly reduced.

The same scenario played out as an increase in infill density led to an increase in tensile strength in a related study by Srinivasan et al. [50]. According to the authors, an infill density that yielded a tensile strength of 17.38 MPa at 100% infill produced a tensile strength of 32.12 MPa.

By adjusting the infill density and pattern, Ebel and Sinnemann [51] created PLA and ABS samples. It was determined that PLA samples had greater tensile strength than ABS samples. Additionally, samples that were fully filled were stronger than those that were partially filled.

This line of reasoning was documented in the study by Tanveer, Haleem, and Suhaib [52], not only for the impact strength but also for the tensile strength of 3D printed PLA parts. In their research, all of the FDM process parameters were held constant while the infill density was changed (A = 100%, B = 75%, C = 50%). According to the combinations listed in Table 10.1, a total of nine kinds of specimens were claimed to have been created. Following are the results of this study's findings:

1. That substantially less raw material can be used by stacking layers with various infill densities.
2. That by keeping the infill density of inner layers dense and the infill density of outer layers less dense, the tensile strength of the 3D printed PLA part can be improved. These arrangements, according to the authors, give resistance to crack development while fostering flexibility in the interior structure.

Table 10.1 The way the infill density is organized

S/N	Classification (C)	Infill density		
		Outer layer	Inner layer	Outer layer
1	A	100	100	100
2	B	75	75	75
3	C	50	50	50
4	ABA	100	75	100
5	BAB	75	100	75
6	ACA	100	50	100
7	CAC	50	100	50
8	BCB	75	50	75
9	CBC	50	75	50

Table 10.2 The specimen's weight and impact resistance

C	Izod strength (KJ/m^2)	Weight (g)	Charpy strength (KJ/m^2)	Weight (g)
A	4.2	24.23	4.75	12.12
B	2.9	20.02	3.45	9.87
C	2.42	17.42	2.75	8.80
ABA	1.7	19.14	3.00	10.84
BAB	1.85	18.57	3.75	10.12
ACA	2.58	19.82	2.90	9.88
CAC	3.15	17.50	3.50	9.11
BCB	2.75	22.70	1.90	9.84
CBC	3.54	21.35	2.10	9.27

3. For the impact test, the infill density and impact strength have a linear relationship, as shown in Table 10.2. Impact strength was found to decrease when different infill densities were mixed.
4. Unlike in the case of tensile strength, impact strength rises when the inner layer has a higher infill density and a lower density outer shell.

The observations made by Abbas et al. [49], Srinivasan et al. [50], and Ebel and Sinnemann [51] were also made in a different study by Gunasekaran et al. [53]. According to the authors, the mechanical characteristics of PLA printed specimens improved as infill density rose from 25% to 100%. The hardness, tensile strength, impact strength, and flexural strength values for the PLA specimen printed with a 100% infill density were 97 HRC, 53 MPa, 70 J/m^2, and 53 MPa, respectively. The authors suggested using PLA specimens produced with a 100% infill density to create components for a variety of applications in light of their findings.

But according to the research by Moradi, Meiabadi, and Kaplan [33], there is no need to fill the interior of 3D printed parts because the optimized specimen has better mechanical properties, a lighter part weight, requires less time to build, and costs less to produce overall than the filled specimen.

10.9.2.2 A Review of Publications on Selective Laser Melted Aluminum Alloys for Development of Aerospace Components

Aluminum is frequently combined with Zn, Cu, Mg, Mn, and Si to create age-hardening alloys, casting alloys, and work-hardening alloys, as indicated in Fig. 10.2 [54–57] according to AtiK et al. [54]. In this review, the emphasis is on the mechanical properties of aluminum-silicon (Al-Si) alloys produced using the metal additive manufacturing technology of selective laser melting (SLM).

Due to their castability and weldability, Al-Si alloys are frequently suited for SLM processing. According to findings in the literature [59–63], AlSi10Mg and AlSi12 are the most often used SLM aluminum alloys. These publications describe

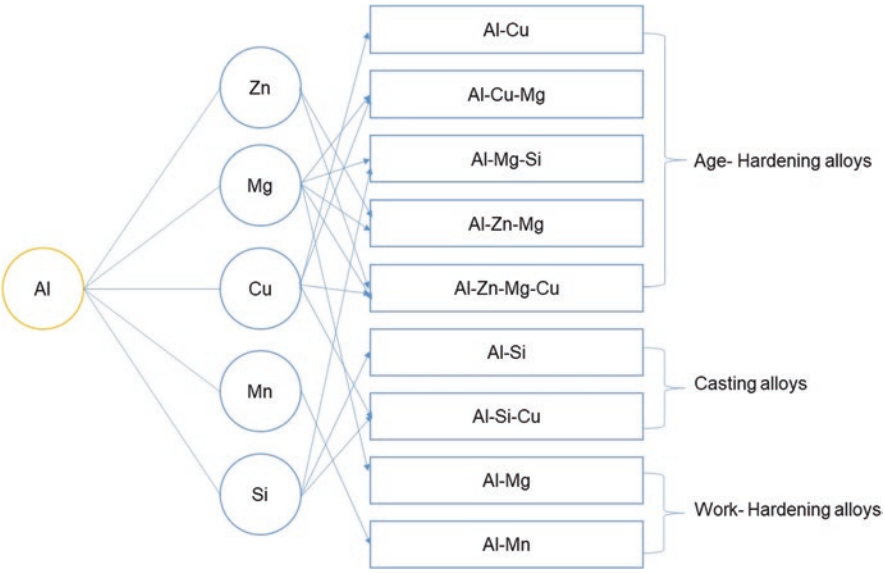

Fig. 10.2 Important aluminum alloys. (Adapted from Altenpohl [58])

the four basic types of Al-Si aluminum alloys and the classification of SLM-processed aluminum alloys in terms of process optimization.

These publications provided an orderly criticism of several types of investigations into the mechanical characteristics of SLM aluminum parts. It is noted that the majority of these papers have focused on the tensile mechanical characteristics of SLM aluminum alloys. A relative few research have been done on the dynamic behavior of 3D printed components in tension and compression [59–61, 64, 65], fatigue [66, 67], impact tolerance [62, 68], wear [69, 70], and flexural response [63, 71].

10.9.2.3 An Analysis of Articles on the Use of Selective Laser Melting to Create PEEK for Aerospace Components

Polyetheretherketone (PEEK) is increasingly being employed in selective laser sintering (SLS), as indicated by Patel et al. [72], due to its good mechanical and thermal properties as well as biocompatibility. It is known that SLS powder's qualities control how well components can be processed and produced. However, there is still more research needed to understand how this thermal history affects part quality. As a result, Patel et al. [72] used spectroscopic, morphological, and rheological characterizations to assess changes in thermally treated PEEK powder. Although the particle size and form of the melted PEEK powder were significantly raised in viscosity, with somewhat improved flowability, the authors observed that crystallinity rose only slightly within the first 2 h.

Wang et al. [73] reaffirmed that PEEK is an engineering thermoplastic with outstanding biocompatibility and strong mechanical qualities, confirming the claim stated by Patel et al. [72]. They agree that PEEK's high viscosity and high melting temperature pose difficulties for FDM. For the best surface quality and enhanced mechanical qualities, authors employed finite element analysis (FEA) to simulate the melting conditions and fluidity of PEEK in a flow channel. For consistency in the outcomes for the mechanical characteristics, microstructure, and surface quality of printed PEEK parts, models were experimentally validated. Based on the results, the authors concluded that layer thickness of 0.1 mm, printing at a speed of 20 mm/s, and a higher heating temperature of 440 °C [74] can increase the density of PEEK parts while reducing internal defects, binding layers, and infill filaments, and surface roughness to the absolute minimum.

SLS is one of the cutting-edge additive manufacturing techniques that can construct the geometrically complicated structure from a three-dimensional CAD model, according to Wang et al. [75]. PEEK is one of the materials that can be used for SLS and has drawn considerable interest because of its great characteristics [72]. Thermally induced phase separation (TIPS), a new methodology was used by the authors to manufacture pristine PEEK and PEEK/CNT composite powders with nearly spherical shapes, desirable particle sizes, and size distributions for SLS applications. It was discovered that the powders created with TIPS had good flowability and processability. According to the results, PEEK's storage and loss modulus were both increased with the addition of 0.1% CNT.

10.9.2.4 A Review of Works on Selective Laser Melting of Ti–6Al–4V for Use in Aerospace Parts

The authors of Knowles, Becker, and Tait's studies [76] stated that SLM of Ti–6Al–4V has enormous promise in the aerospace and biotechnology sectors. The utilization of a concentrated laser beam using SLM to melt successive layers of metallic powder into intricate components was also disclosed by the authors. The authors claim that this method has the potential to generate significant residual strains caused by heat. They believe that at relatively modest cyclic stresses, these residual stresses, along with microflaws/pores from the underlying fabrication process, have the potential to produce premature fatigue fracture initiation and propagation. In order to ascertain residual stresses within SLM Ti–6Al–4V specimens and comprehend the underlying mechanisms for SLM Ti–6Al–4V's effective industrial application, the hole-drilling strain gauge method was used.

Beta Ti-alloys are most suited for applications requiring high fracture toughness and ductility, such as the aerospace and biomedical industries, as indicated by Madikizela, et al. [77]. The authors also said that the aerospace sector has looked into SLM of the alpha + beta Ti–6Al–4V alloy in great detail. Despite the success in fabricating small parts, it is difficult to build big parts with an acicular microstructure. Ti–6Al–4V has an acicular microstructure, which reduces its ductility and fracture toughness (10% elongation), causing components to distort and delaminate

from the base plate even before they are finished because of stress buildup. This led the authors to investigate the microstructure and mechanical characteristics of two-phase Ti–6Al–4V and beta titanium alloy Ti-38,644 in their as-built state. The findings demonstrated that Ti-38,644 had a complete microstructure and lower strength than Ti–6Al–4V, which had a fine martensitic structure inside columnar grains. Ti-38,644 had three times the percentage elongation of Ti–6Al–4V, indicating the possibility of fabricating massive parts from it.

Yang et al. [78] studied the SLM-produced Ti–6Al–4V crystallographic pattern at various laser energy densities. The outcomes demonstrated that the mechanical anisotropy of SLMed Ti–6Al–4V samples is significantly influenced by the crystallographic orientation dependent on laser energy density (LED). The SLMed Ti–6Al–4V samples have a completely martensite microstructure. With laser LED, the content of prismatic orientations rises from 101 to 269 J/mm^3, while the proportion of basal orientations falls in martensites. The tensile properties of samples that were created horizontally and vertically differ, according to the authors, and this anisotropy is visible with LED. Higher Schmid factor values of grains in vertically built tensile samples than in horizontally built tensile samples are thought to be the cause of anisotropy.

Conclusion on Literature Review

In order to identify the knowledge gap and research priorities from the perspective of aerospace applications, these review section analyzed various types of investigations on the mechanical properties of SLM aluminum, PEEK, and Ti–6Al–4V parts.

Conclusion: Although 3D printed airplane parts are frequently strong and lightweight, there is still a significant knowledge gap when parameters like infill density are set to 100% for maximum tensile strength of printed components. This knowledge gap is evident from the literature review.

Thus, the prediction of impact tolerance for a partially filled 3D printed turbine component became the study's main focus.

10.10 Research Methodology

In order to address the highlighted problems, numerical and experimental methods will be employed.

10.10.1 Material Study and Selection

10.10.1.1 Material Study

Aluminum alloys, titanium alloys, thermoplastics, high-strength steels, nickel metal alloys, magnesium alloy, and composites are the most often utilized structural materials in commercial aerospace, and together they make up more than 90% of the weight of airframes.

10.10.1.2 Material Selection

Unmixed Material

Out of the aforementioned materials, three were identified and chosen for this investigation. Table 10.3 lists these three materials along with their mechanical material characteristics.

Composite Materials

As particulate reinforcements to the pure materials (i.e., Aluminum 6082-T651 alloy, PEEK 1000, Ti–6Al–4V alloy), waste copper dust (WCD) and mullite-rich tailings (MRT) from density-separated WCD will be used.

These combinations of matrix and reinforcements will result in the following categories of composites (aluminum composites, PEEK composites, Ti–6Al–4V composites), which are depicted in Figs. 10.3, 10.4, and 10.5, respectively:

Table 10.3 The mechanical material properties (MMP) of the aluminum 6082-T651 alloy, PEEK 1000

MMP	Units	Materials		
		Aluminum 6082-T651 alloy	PEEK 1000	Ti–6Al–4V alloy
Elastic modulus (E)	GPa	70 [79, 80]	3.6 [79]	107 [77]
Density (ρ)	kg/m^3	2700 [79, 80]	1304 [79]	2560 [81]
Poisson's ratio (ν)		0.33 [79, 80]	0.4 [79]	0.33 [82]
Coefficient of Kinetic friction (μ)		1.4 [79, 80]	1.0 [79]	0.25 [83]

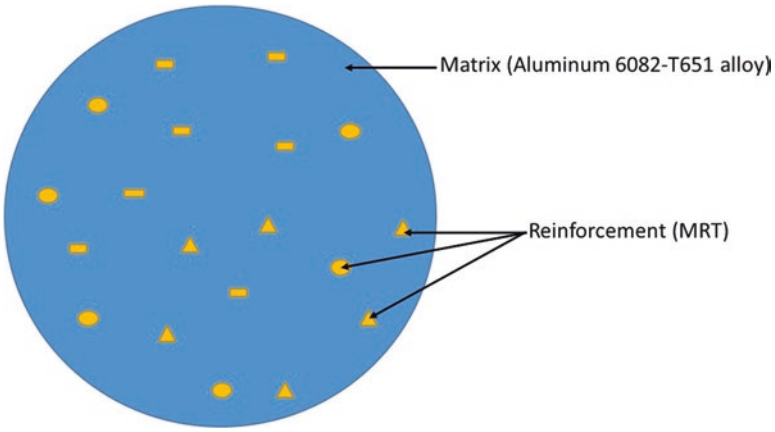

Fig. 10.3 Image of Aluminum 6082-T651-composites

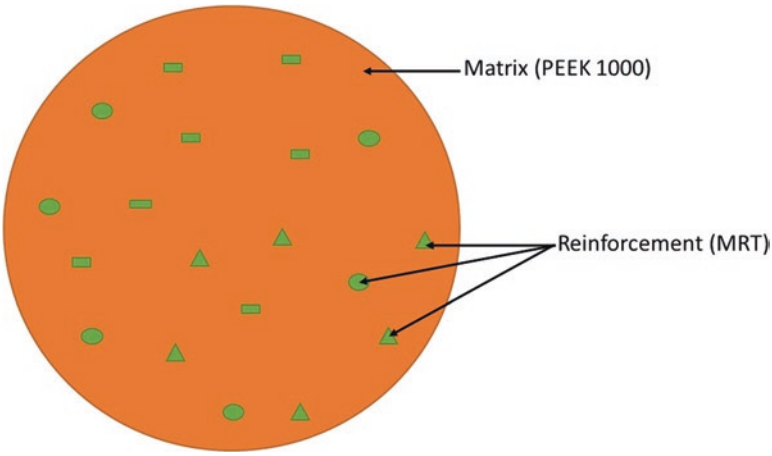

Fig. 10.4 Image of PEEK 1000-composites

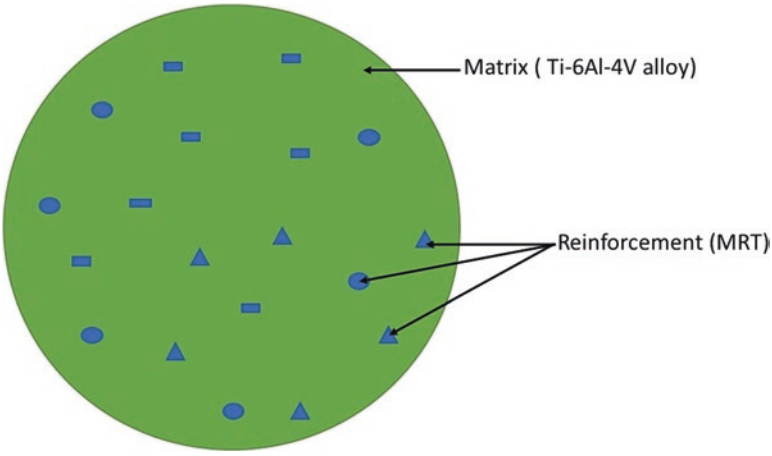

Fig. 10.5 Image of Ti–6Al–4V-composites

Aluminum 6082-T651-CSD and Aluminum 6082-T651-MRT composites, PEEK 1000-CSD and PEEK 1000-MRT composites, and Ti–6Al–4V-CSD and Ti–6Al–4V-MRT composites.

It will be decided what the MMP of the generated composites is, and that information will be utilized to fill out Table 10.4 with data that will be used to simulate models for these various composites.

Table 10.4 The mechanical material properties (MMP) of the aluminum 6082-T651-MRT, PEEK 1000-MRT, and Ti–6Al–4V-MRT composites

MMP	Units	Materials					
		1	2	3	4	5	6
Elastic modulus (E)	GPa	YTBD	YTBD	YTBD	YTBD	YTBD	YTBD
Density (ρ)	kg/m^3	YTBD	YTBD	YTBD	YTBD	YTBD	YTBD
Poisson's ratio (ν)		YTBD	YTBD	YTBD	YTBD	YTBD	YTBD
Coefficient of Kinetic friction (μ)		YTBD	YTBD	YTBD	YTBD	YTBD	YTBD

Key: Aluminum 6082-T651-CSD composite = 1; Aluminum 6082-T651-MRT composite = 2; PEEK 1000-CSD composite = 3; PEEK 1000-MRT composite = 4; Ti–6Al–4V-CSD composite = 5; Ti–6Al–4V-MRT composite = 6; YTBD = Yet to be determined

10.10.2 Methods

10.10.2.1 Scaling and Similitude of Turbine Blade

Utilizing engineering concepts, the simpler turbine blade will be scaled. An SGL-formatted CAD turbine blade model will be created in order to accomplish this. The scaled turbine blade model and the real turbine blade will both have the same geometric similarity, kinematic similarity, and dynamic similarity as a result of the scaling and similitude operations. This is done in an effort to get the printer to manufacture a model of a turbine blade that resembles a real turbine blade. The following phase of the investigation will make use of this scaled model.

10.10.2.2 Optimization in the Abaqus Environment Using TOSCA

It is standard procedure to discover the ideal parameter (in this case, infill density) that satisfies the functional impact tolerance requirements after scaling and simulating the engineering structure (i.e., turbine blade). In this study, sizing optimization tools like SIMULIA Tosca Structure, which integrates optimization technologies in real-world engineering environments as an add-on module easily integrated into the existing Abaqus workflows as shown in Fig. 10.6, will be used instead of trial and error, which is a time-consuming and slow process.

The scaled turbine model from the earlier part will go through an optimization job where the objective function, or infill density, will be chosen and defined for minimization or maximization, and the corresponding restrictions and elements will be defined as design elements. Abaqus will be used for all setups and definitions, with computer-aided engineering (CAE) used for preprocessing (Fig. 10.6).

The model is then automatically updated and adjusted using a robust nonlinear constrained optimizer based on sensitivities obtained using the semi-analytical adjoint method, and the optimization work is then finished by an iterative process. The Abaqus solver will be used to resolve the adjoint equations as well as the finite element equilibrium equations. The final model with optimum infill densities will

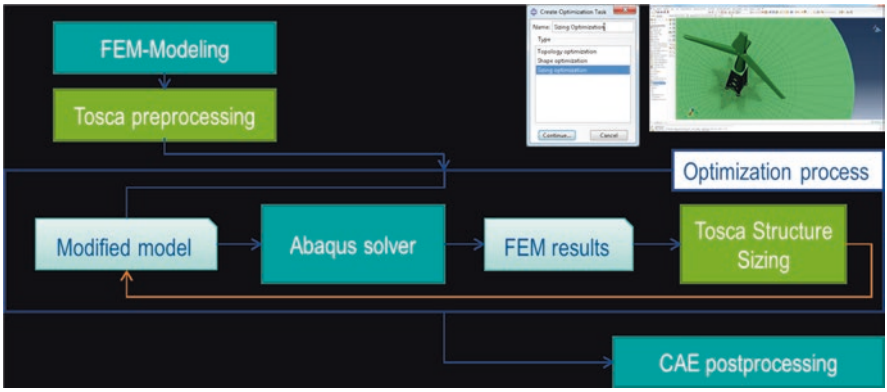

Fig. 10.6 Tosca sizing process workflow [84]

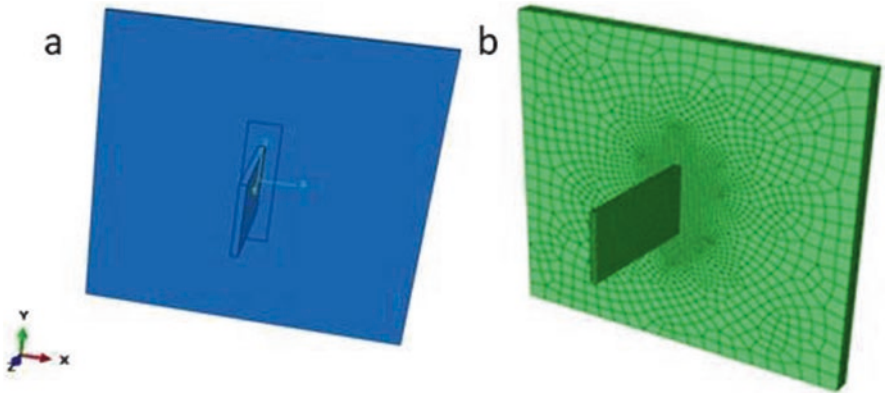

Fig. 10.7 (**a**) The Blade model and interactions, (**b**) Mesh refinement on the whole model: i.e., the turbine blade and the casing

be made available for the CAE postprocessing at the conclusion of the optimization operation.

10.10.2.3 Impact Analysis in Abaqus Based on Tosca's Optimal Solutions

Figure 10.7a depicts a simplified blade model with dimensions of 22 mm in width, 37 mm in length, and 2 mm in thickness. The thickness can range from 2 to 5 mm. In this study, nine different blade materials—aluminum 6082-T651, PEEK 1000, Ti–6Al–4V, aluminum 6082-T651-CSD composite, PEEK 1000-CSD composite, Ti–6Al–4V-CSD composite, aluminum 6082-T651-MRT composite, PEEK 1000-MRT composite, and Ti–6Al–4V-MRT composite—will be impact tested on an aluminum 6082-T651 casing.

Since a clearance distance of 1 mm is permitted between the blade and the casing in the design of an actual aircraft turbine blade, the interactions and predetermined loading will rely on the assembly. As shown in Fig. 10.7a, the analysis of the casing will be fixed for this study, and the blade will be translated to the casing's center with a design clearance of 1 mm.

The actual design of the air engine will have a permissible clearance of 1 mm, whereas the clearance between the blade and casing will be 1 mm. With a time of 0.002 s, the analysis will be done in a dynamically explicit manner. This should provide researchers enough time to monitor the extent of damage the blade causes before it bounces off the casing and causes less damage. Due to the assumption that the blade is a freely detachable blade moving at 255 m/s, there won't be any boundary conditions for it.

It is anticipated that the impact zone of the casing will experience considerable deformation and subsequent elementary distortion as a result of the blade's ballistic impact. So, to obtain a particular mesh and performance, adaptive meshing will be applied (Fig. 10.7b). The stability of the nodes will be examined during a mesh quality check. By making the seeds smaller, a finer mesh will be created to increase the density of the elements. As a result, the partition's mesh size is 1 mm. As illustrated in Fig. 10.8, the mesh refinement will take place at the partitioned section. While the model's nodes and elements will have the following numbers at different

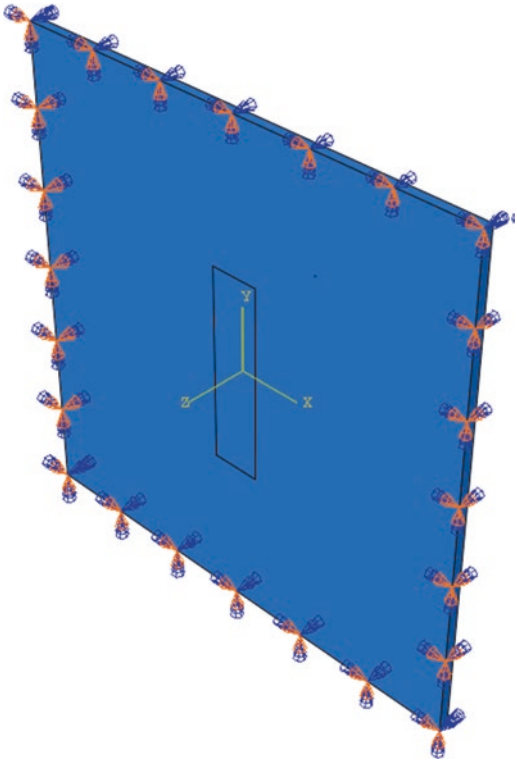

Fig. 10.8 Boundary conditions for Aluminum 6082-T651 alloy casing

case thicknesses (2, 3, 4, and 5): Elements are 5406, 7668, 13,576, and 10,506 respectively, while nodes are 5442, 7612, 10,584, and 13,781 correspondingly.

As demonstrated in Fig. 10.8, the bottom and top of the casing will be prevented from shifting and rotating in the x and y directions while being free to deform. Due to the assumption that the blade is detached from the hub, as was previously mentioned, the blade has free boundary conditions.

10.10.2.4 3D Printing of the Turbine Blade

The simplified turbine blade model that has been optimized and thoroughly examined will be divided into layers that overlap by 35–50 μm to create the turbine blade components. The size of the material's particles will range from 20 to 55 μm. In this study, the turbine blades will be printed using the powder bed additive CSIR Selective Laser Melting (SLM) apparatus for further analysis.

10.10.2.5 Experimental Validation

In order to verify the consistency of the Abaqus results, an experimental impact study will be performed utilizing the Charpy impact tester on the printed optimized/analyzed simplified turbine blade model.

10.10.2.6 Measurements and Microstructural Analysis of Damaged Samples

Scanning Electron Microscopy (SEM)

With the help of scanning electron microscopy (SEM) in the FEI model Inspect F-50 operating in both secondary (SE) and backscattered (BSE) electron modes, it will be possible to determine the spatial distribution of the CSD and MRT in the matrices (Aluminum, PEEK, Ti–6Al–4V alloy), as well as the degree of damage to both unreinforced and reinforced materials. It will be furnished with a Link Analytical ISIS system for elemental analysis, both qualitative and quantitative (EDX). To supplement SEM characterization, a RayScan model 250E computed x-ray microtomography investigation was performed.

Electron Backscatter Diffraction (EBSD)

To evaluate the deformation caused in the unreinforced and reinforced materials in terms of potential phase change, recrystallization, strain hardening, and deformation texture, EBSD will be carried out using a Zeiss model Ultra 55 microscope fitted with an Oxford detector.

X-Ray Diffraction (XRD)

X-ray diffraction (XRD) analysis will be performed in addition using Panalytical's X Pert PRO equipment. Since creating the reinforced composites depends on creating the samples, rigorous procedures will be taken into account at this point.

10.11 Project Plan and Financial Budget

10.11.1 Project Plan

The layout and timeline for the proposed study can be seen in Table 10.5.

10.11.2 Financial Budget

Detailed in Table 10.6 is the estimated budget for the proposed study.

Table 10.5 Layout and timeline for the proposed study

		Year	
S/N	Task name	XXXX	XXXX
1	Registration	WIP	WIP
2	Development of research topic	WIP	WIP
3	Development of research proposal and approval	WIP	WIP
4	Chapter 1	WIP	WIP
6	Chapter 2	WIP	WIP
7	Chapter 3	WIP	WIP
8	Chapter 4	WIP	WIP
9	Chapter 5	WIP	WIP
10	Chapter 6	WIP	WIP
11	Chapter 7	WIP	WIP
12	Chapter 8	WIP	WIP
13	Chapter 9	WIP	WIP
14	Chapter 10	WIP	WIP
15	Colloquium	WIP	WIP
16	Thesis defence	WIP	WIP
17	Production of final dissertation	WIP	WIP
18	Submission	WIP	WIP

Table 10.6 Estimated budget for the proposed study

S/N	General items	Description	Cost (ZAR)
1	Tuition fees	Registration (DEng)	X
		Deng fees	X
2	Study materials	Journals	X
3	Experimentation and model manufacture	Component from Aluminum, PEEK, and Ti–6Al–4V materials and FEA software	X
4	Instrumentation	Data recording instruments, turbine blade parts for impact tolerance measurement	X
	Submission cost	Report binding for at least four copies	X
Grand total			X

References

1. O.A. Akinboade, L.A. Braimoh, International tourism and economic development in South Africa: A Granger causality test. Int. J. Tour. Res. **12**(2), 149–163 (2010)
2. A. Gisario, M. Kazarian, F. Martina, M. Mehrpouya, Metal additive manufacturing in the commercial aviation industry: A review. J. Manuf. Syst. **53**, 124–149 (2019)
3. S. Ford, M. Despeisse, Additive manufacturing and sustainability: An exploratory study of the advantages and challenges. J. Clean. Prod. **137**, 1573–1587 (2016)
4. D.O. Okanigbe, A.P.I. Popoola, T.N. Makua, Determination of physico-chemical and hardness properties of mullite-rich tailings from density separated copper smelter dust for ceramic application, in *TMS 2021 150th Annual Meeting & Exhibition Supplemental Proceedings*, (Springer, Cham, 2021), pp. 1026–1035
5. P.L. Linda, D.O. Okanigbe, A.P.I. Popoola, O.M. Popoola, Characterization of density separated mullite-rich tailings from a secondary copper resource, a potential reinforcement material for development of an enhanced thermally conductive and wear resistant Ti-6Al-4V matrix composite, in *The Proceedings of the 60th International Conference of Metallurgist*. Canada, (2021)
6. M.K. Niaki, F. Nonino, *The Management of Additive Manufacturing*, vol 10 (Springer, 2018), pp. 978–973
7. J.A. Castillo-Robles, A.P. Dimas-Muñoz, J.A. Rodríguez-García, C.A. Calles-Arriaga, E.N. Armendáriz-Mireles, W.J. Pech-Rodríguez, E. Rocha-Rangel, Mechanical and microstructural response of aluminum composites reinforced with ceramic micro-particles. J. Compos. Sci. ***5***(9), 228 (2021)
8. N. Kota, M.S. Charan, T. Laha, S. Roy, Review on development of metal/ceramic interpenetrating phase composites and critical analysis of their properties. Ceram. Int. **48**(2), 1451–1483 (2022)
9. D. Zhao, D. Wu, J. Shi, F. Niu, G. Ma, Microstructure and mechanical properties of melt-grown alumina-mullite/glass composites fabricated by directed laser deposition. J. Adv. Ceram. **11**(1), 75–93 (2022)
10. K.N. Lee, D. Zhu, R.S. Lima, Perspectives on environmental barrier coatings (EBCs) manufactured via air plasma spray (APS) on ceramic matrix composites (CMCs): A tutorial paper. J. Therm. Spray Technol. **30**, 1–19 (2021)
11. S.K. Suleimanov, V.G. Babashov, M.U. Dzhanklich, V.G. Dyskin, M.I. Daskovskii, S.Y. Skripachev, N.A. Kulagina, G.M. Arushanov, Behavior of a heat-protective material based on Al 2 O 3 and SiO 2 fibers under exposure to concentrated solar energy flux. Refract. Ind. Ceram. **61**(6), 675–679 (2021)

12. O. Zaporozhets, V. Isaienko, K. Synylo, PARE preliminary analysis of ACARE FlightPath 2050 environmental impact goals. CEAS Aeronaut. J. **12**(3), 653–667 (2021)
13. N.P. Padture, Advanced structural ceramics in aerospace propulsion. Nat. Mater. **15**(8), 804–809 (2016)
14. J. King, P. Greaves, H. Low, Composite materials in aero gas turbines: Performance potential versus commercial constraint. Aircr. Eng. Aerosp. Technol **70**, 3 (1998)
15. J. Cheung, J. Scanlan, J. Wong, J. Forrester, H. Eres, P. Collopy, P. Hollingsworth, S. Wiseall, S. Briceno, Application of value-driven design to commercial aeroengine systems. J. Aircr. **49**(3), 688–702 (2012)
16. T.D. Ngo, A. Kashani, G. Imbalzano, K.T. Nguyen, D. Hui, Additive manufacturing (3D printing): A review of materials, methods, applications and challenges. Compos. Part B **143**, 172–196 (2018)
17. J. Kraft, S. Kuntzagk, Engine fleet-management: The use of digital twins from a MRO perspective, in *Turbo expo: Power for Land, Sea, and Air*, vol. 50770, (American Society of Mechanical Engineers, 2017), p. V001T01A007
18. G.M. Laskowski, J. Kopriva, V. Michelassi, S. Shankaran, U. Paliath, R. Bhaskaran, Q. Wang, C. Talnikar, Z.J. Wang, F. Jia, Future directions of high fidelity CFD for aerothermal turbomachinery analysis and design, in *46th AIAA Fluid Dynamics Conference*, (AIAA, 2016), p. 3322
19. R. Jansen, C. Bowman, A. Jankovsky, R. Dyson, J. Felder, Overview of NASA electrified aircraft propulsion (EAP) research for large subsonic transports, in *53rd AIAA/SAE/ASEE Joint Propulsion Conference*, (AIAA, 2017), p. 4701
20. S.K. Sinha, S. Dorbala, Dynamic loads in the fan containment structure of a turbofan engine. J. Aerosp. Eng. **22**(3), 260–269 (2009)
21. J. Carter, Simulation software to assess how, why, where and when components will fail, in *2018 Annual Reliability and Maintainability Symposium (RAMS)*, (IEEE, 2018), pp. 1–5
22. B. Strack, V. Nagpal, S. Pai, A software tool subjecting component designs to system-level reliability constraints, in *48th AIAA/ASME/ASCE/AHS/ASC Structures, Structural Dynamics, and Materials Conference*, (AIAA, 2007), p. 2292
23. R. Saltoğlu, *Opportunities of cost reduction and risks of budget overrun in maintenance spending of an airline in the current market conditions*. Doctoral dissertation, Fen Bilimleri Enstitüsü, 2019
24. N. Kedir, C. Gong, L. Sanchez, M.J. Presby, S. Kane, D.C. Faucett, S.R. Choi, Erosion in gas-turbine grade ceramic matrix composites. J. Eng. Gas Turbines Power **141**(1), 011019 (2019). https://doi.org/10.1115/1.4040848
25. A.K. Misra, L.A. Greenbauer-Seng, Aerospace propulsion and power materials and structures research at NASA Glenn Research Center. J. Aerosp. Eng. **26**(2), 459–490 (2013)
26. P.W. Beaumont, On the problems of cracking and the question of structural integrity of engineering composite materials. Appl. Compos. Mater. **21**(1), 5–43 (2014)
27. M. Schwab, H.E. Pettermann, Modelling and simulation of damage and failure in large composite components subjected to impact loads. Compos. Struct. **158**, 208–216 (2016)
28. K. Raju, T.E. Tay, V.B.C. Tan, A review of the FE 2 method for composites. Multiscale Multidiscip. Model. Exp. Des **4**, 1–24 (2021)
29. Y. Sun, Y. Zhang, Y. Zhou, H. Zhang, H. Zeng, K. Yang, Evaluating impact damage of flat composite plate for surrogate bird-strike testing of Aeroengine fan blade. J. Compos. Sci. ***5***(7), 171 (2021)
30. S.W. Ahmed, G. Hussain, K. Altaf, S. Ali, M. Alkahtani, M.H. Abidi, A. Alzabidi, On the effects of process parameters and optimization of interlaminate bond strength in 3D printed ABS/CF-PLA composite. Polymers **12**(9), 2155 (2020)
31. G.D. Goh, Y.L. Yap, H.K.J. Tan, S.L. Sing, G.L. Goh, W.Y. Yeong, Process–structure–properties in polymer additive manufacturing via material extrusion: A review. Crit. Rev. Solid State Mater. Sci. **45**(2), 113–133 (2020)
32. N. Mohan, P. Senthil, S. Vinodh, N. Jayanth, A review on composite materials and process parameters optimisation for the fused deposition modelling process. Virtual Phys. Prototyp. **12**(1), 47–59 (2017)

33. M. Moradi, S. Meiabadi, A. Kaplan, 3D printed parts with honeycomb internal pattern by fused deposition modelling; experimental characterization and production optimization. Met. Mater. Int. **25**(5), 1312–1325 (2019)
34. T. Muthuramalingam, B. Mohan, Application of Taguchi-grey multi responses optimization on process parameters in electro erosion. Measurement **58**, 495–502 (2014)
35. T. Geethapriyan, K. Kalaichelvan, T. Muthuramalingam, Multi performance optimization of electrochemical micro-machining process surface related parameters on machining Inconel 718 using Taguchi-grey relational analysis. La Metallurgia Italiana **4**, 13–19 (2016)
36. İ. Istif, K. Feratoğlu, A. Acar, Investigation of mechanical behaviours of PLA parts manufactured by fused deposition modeling, in *56th ISC of the University of Ruse'17, Ruse, Bulgaristan*, (2017), pp. 26–29
37. N. Singh, I.U.H. Mir, A. Raina, A. Anand, V. Kumar, S.M. Sharma, Synthesis and tribological investigation of Al-SiC based nano hybrid composite. Alex. Eng. J. **57**(3), 1323–1330 (2018)
38. M.I.U. Haq, A. Anand, Dry sliding friction and wear behavior of AA7075-Si 3 N 4 composite. SILICON **10**(5), 1819–1829 (2018)
39. A. Bernard, A. Fischer, New trends in rapid product development. CIRP Ann. **51**(2), 635–652 (2002)
40. M.I.H.C. Abdullah, M.F.B. Abdollah, H. Amiruddin, N. Tamaldin, N.R.M. Nuri, Optimization of tribological performance of hBN/AL2O3Nanoparticles as engine oil additives. Procedia Eng. **68**, 313–319 (2013)
41. C.K. Chua, K.F. Leong, C.S. Lim, *Rapid Prototyping: Principles and Applications (with Companion CD-ROM)* (World Scientific Publishing Company, 2010)
42. M. Vaezi, C.K. Chua, Effects of layer thickness and binder saturation level parameters on 3D printing process. Int. J. Adv. Manuf. Technol. **53**(1), 275–284 (2011)
43. F. Górski, R. Wichniarek, W. Kuczko, P. Zawadzki, P. Buń, Strength of ABS parts produced by fused deposition modelling technology–a critical orientation problem. Adv. Sci. Tecnol. Res. J. **9**(26), 12–19 (2015)
44. L. Li, Q. Sun, C. Bellehumeur, P. Gu, Composite modeling and analysis for fabrication of FDM prototypes with locally controlled properties. J. Manuf. Process. **4**(2), 129–141 (2002)
45. I. Gajdoš, J. Slota, Influence of printing conditions on structure in FDM prototypes. Tehnički Vjesnik **20**(2), 231–236 (2013)
46. A. Bellini, S. Güçeri, Mechanical characterization of parts fabricated using fused deposition modeling. Rapid Prototyp. J. **9**, 252 (2003)
47. S.H. Ahn, C. Baek, S. Lee, I.S. Ahn, Anisotropic tensile failure model of rapid prototyping parts-fused deposition modeling (FDM). Int. J. Mod. Phys. B ***17***(08n09), 1510–1516 (2003)
48. F. Górski, W. Kuczko, R. Wichniarek, Influence of process parameters on dimensional accuracy of parts manufactured using fused deposition modelling technology. Adv. Sci. Tecnol. Res. J. **7**(19), 27–35 (2013)
49. T.F. Abbas, F.M. Othman, H.B. Ali, Influence of layer thickness on impact property of 3D-printed PLA. Int. Res. J. Eng. Technol. (IRJET) **5**, 1–4 (2018)
50. R. Srinivasan, W. Ruban, A. Deepanraj, R. Bhuvanesh, T. Bhuvanesh, Effect on infill density on mechanical properties of PETG part fabricated by fused deposition modelling. Mater. Today: Proc. **27**, 1838–1842 (2020)
51. E. Ebel, T. Sinnemann, Fabrication of FDM 3D objects with ABS and PLA and determination of their mechanical properties. Rapid Technol **2014**(1), 4–22 (2014)
52. M.Q. Tanveer, A. Haleem, M. Suhaib, Effect of variable infill density on mechanical behaviour of 3-D printed PLA specimen: An experimental investigation. SN Appl. Sci. **1**(12), 1–12 (2019)
53. K.N. Gunasekaran, V. Aravinth, C.M. Kumaran, K. Madhankumar, S.P. Kumar, Investigation of mechanical properties of PLA printed materials under varying infill density. Mater. Today: Proc. **45**, 1849–1856 (2021)
54. E. AtiK, C. Meriç, B. Karlik, Determination of yield strength of 2014 Aluminium alloy under aging conditions by means of Artifical neural networks method. Math. Comput. Appl. **1**(2), 16–20 (1996)

55. P.P.N.K.V. Rambabu, N.E. Prasad, V.V. Kutumbarao, R.J.H. Wanhill, Aluminium alloys for aerospace applications, in *Aerospace Materials and Material Technologies*, (Springer, 2017), pp. 29–52
56. P. Mukhopadhyay, Alloy designation, processing, and use of AA6XXX series aluminium alloys. Int. Sch. Res. Not. **2012**, 165082 (2012)
57. C. Kammer, Aluminum and aluminum alloys, in *Springer Handbook of Materials Data*, (Springer, Cham, 2018), pp. 161–197
58. D. Altenpohl, *Aluminum Viewed from Within: An Introduction into the Metallurgy of Aluminum Fabrication* (Aluminium-Verlag GmbH, Konigsallee, 1982), p. 223
59. S.R. Ch, A. Raja, P. Nadig, R. Jayaganthan, N.J. Vasa, Influence of working environment and built orientation on the tensile properties of selective laser melted $AlSi_{10}Mg$ alloy. Mater. Sci. Eng. A **750**, 141–151 (2019)
60. K.G. Prashanth, S. Scudino, J. Eckert, Defining the tensile properties of Al-12Si parts produced by selective laser melting. Acta Mater. **126**, 25–35 (2017)
61. Y. Ou, Q. Zhang, Y. Wei, Y. Hu, S. Sui, J. Chen, X. Wang, W. Li, Evolution of heterogeneous microstructure and its effects on tensile properties of selective laser melted AlSi10Mg alloy. J. Mater. Eng. Perform. **30**(6), 4341–4355 (2021)
62. M.S. Kumar, H.R. Javidrad, R. Shanmugam, M. Ramoni, A.A. Adediran, C.I. Pruncu, Impact of print orientation on morphological and mechanical properties of L-PBF based AlSi7Mg parts for aerospace applications. Silicon **14**, 1–15 (2021)
63. M. Gowda, M. Karthick, S.K. Niketh, M. Kanagil, V. Guptha, A. Bharatish, R. Sharma, Effect of laser parameters on the vibrational characteristics of $AlSi_{10}Mg$ parts produced using selective laser melting (SLM). Lasers Eng. (Old City Publishing) **51**(1–5), p187–203. 17p, (2021)
64. D. Dai, D. Gu, H. Zhang, J. Xiong, C. Ma, C. Hong, R. Poprawe, Influence of scan strategy and molten pool configuration on microstructures and tensile properties of selective laser melting additive manufactured aluminum-based parts. Opt. Laser Technol. **99**, 91–100 (2018)
65. J. Bi, Y.B. Chen, X. Chen, M.D. Starostenkov, G.J. Dong, Densification, microstructural features and tensile properties of selective laser melted AlMgSiScZr alloy from single track to block specimen. J. Cent. South Univ. **28**(4), 1129–1143 (2021)
66. P. Ponnusamy, S.H. Masood, D. Ruan, S. Palanisamy, R.R. Rashid, R. Mukhlis, N.J. Edwards, Dynamic compressive behaviour of selective laser melted $AlSi_{12}$ alloy: Effect of elevated temperature and heat treatment. Addit. Manuf. **36**, 101614 (2020)
67. M. Awd, S. Siddique, F. Walther, Microstructural damage and fracture mechanisms of selective laser melted Al-Si alloys under fatigue loading. Theor. Appl. Fract. Mech. **106**, 102483 (2020)
68. A. Mishra, R. Agarwal, N. Kumar, A. Rana, A.K. Pandey, S.P. Dwivedi, A critical review on the additive manufacturing of aluminium alloys. Mater. Today: Proc. **47**, 4074 (2021)
69. K.C. Bae, K.S. Ha, Y.H. Kim, J.J. Oak, W. Lee, Y.H. Park, Building direction dependence of wear resistance of selective laser melted AISI 316L stainless steel under high-speed tribological environment. Int. J. Adv. Manuf. Technol. **108**, 2385–2396 (2020)
70. P. Wang, S. Yu, J. Shergill, A. Chaubey, J. Eckert, K.G. Prashanth, S. Scudino, Selective laser melting of Al-7Si-0.5 mg-0.5 cu: Effect of heat treatment on microstructure evolution, mechanical properties and Wear resistance. Acta Metall. Sin. (English Letters) **35**, 1–8 (2021)
71. T. Maconachie, M. Leary, P. Tran, J. Harris, Q. Liu, G. Lu, D. Ruan, O. Faruque, M. Brandt, The effect of topology on the quasi-static and dynamic behaviour of SLM $AlSi_{10}Mg$ lattice structures. Int. J. Adv. Manuf. Technol. **118**, 1–20 (2021)
72. A. Patel, V. Venoor, F. Yang, X. Chen, M.J. Sobkowicz, Evaluating poly (ether ether ketone) powder recyclability for selective laser sintering applications. Polym. Degrad. Stab. **185**, 109502 (2021)
73. P. Wang, B. Zou, H. Xiao, S. Ding, C. Huang, Effects of printing parameters of fused deposition modeling on mechanical properties, surface quality, and microstructure of PEEK. J. Mater. Process. Technol. **271**, 62–74 (2019)
74. T. Niino, T. Uehara, Low temperature selective laser melting of high tempertaure plastic powder, in *Proceedings Solid Freeform Fabrication Symposium*, (2015), pp. 866–877

75. Y. Wang, J. Shen, M. Yan, X. Tian, Poly ether ether ketone and its composite powder prepared by thermally induced phase separation for high temperature selective laser sintering. Mater. Des. **201**, 109510 (2021)
76. C.R. Knowles, T.H. Becker, R.B. Tait, Residual stress measurements and structural integrity implications for selective laser melted Ti-6Al-4V: General article. S. Afr. J. Ind. Eng. **23**(3), 119–129 (2012)
77. C. Madikizela, L.A. Cornish, L.H. Chown, H. Möller, Microstructure and mechanical properties of selective laser melted Ti-3Al-8V-6Cr-4Zr-4Mo compared to Ti-6Al-4V. Mater. Sci. Eng. A **747**, 225–231 (2019)
78. J. Yang, H. Yu, Z. Wang, X. Zeng, Effect of crystallographic orientation on mechanical anisotropy of selective laser melted Ti-6Al-4V alloy. Mater. Charact. **127**, 137–145 (2017)
79. D. García-González, M. Rodríguez-Millán, A. Vaz-Romero, A. Arias, High impact velocity on multi-layered composite of polyether ether ketone and aluminium. Compos. Interfaces **22**(8), 705–715 (2015)
80. I.S. Boldyrev, I.A. Shchurov, A.V. Nikonov, Numerical simulation of the aluminum 6061-T6 cutting and the effect of the constitutive material model and failure criteria on cutting forces' prediction. Procedia Eng. **150**, 866–870 (2016)
81. J. Ran, F. Jiang, X. Sun, Z. Chen, C. Tian, H. Zhao, Microstructure and mechanical properties of Ti-6Al-4V fabricated by electron beam melting. Crystals **10**(11), 972 (2020)
82. C. Charles, *Microstructure model for Ti-6Al-4V used in simulation of additive manufacturing*. Doctoral dissertation, Luleå Tekniska Universitet, 2016
83. M. Fellah, M. Labaïz, O. Assala, L. Dekhil, A. Taleb, H. Rezag, A. Iost, Tribological behavior of Ti-6Al-4V and Ti-6Al-7Nb alloys for total hip prosthesis. Adv Tribol. **2014**, 1 (2014)
84. A.A.S. Miguel, P.M. Matos, B.W. Claus, Sizing optimization for industrial applications, in *Proceeding of 11th World Congress on Structural and Multidisciplinary Optimization*, (ACM, 2015), pp. 1–6

Part VI
Preparation and Characterization of Hydrotalcite-Derived Material from Mullite-Rich Tailings

Chapter 11
Preparation and Characterization of Hydrotalcite-Derived Material from Mullite-Rich Tailings (I): Transesterification of Used Cooking Oil to Biodiesel

Daniel Ogochukwu Okanigbe and Shade Rouxzeta Van Der Merwe

11.1 Introduction

The interest in renewable fuels for internal combustion engines has significantly expanded due to environmental worries about climate change and global warming. Furthermore, finding alternative fuels is necessary to meet the current global energy demand because fossil fuels are running out day by day. As a result, biodiesel has emerged as a very desirable alternative fuel for diesel engines since it has less negative environmental consequences and has a smaller impact on acid rain and greenhouse gas emissions.

The usage of biodiesel is regarded as favorable in comparison with that of diesel fuel because of these features, as well as its biodegradability, largely sulfur-free nature, and aromatic nature [1]. In order to produce the necessary fatty acid methyl esters (FAME) and glycerol as a by-product, vegetable oils are transesterified with methanol in the presence of a catalyst to produce biodiesel, which is the most popular biofuel in Europe [2].

D. O. Okanigbe (✉)
Department of Chemical, Metallurgical and Materials Engineering, Faculty of Engineering and the Built Environment, Tshwane University of Technology, Pretoria, South Africa

Pantheon Virtual Engineering Solutions, Nigel, South Africa
e-mail: okanigbedo@tut.ac.za; okanigbeogochukwu@gmail.com

S. R. Van Der Merwe
Department of Mechanical and Mechatronics Engineering, Faculty of Engineering and the Built Environment, Tshwane University of Technology, Pretoria, South Africa
e-mail: vandermerweR1@tut.ac.za

D. O. Okanigbe, A. P. Popoola (eds.), *Resource Recovery and Recycling from Waste Metal Dust*, https://doi.org/10.1007/978-3-031-22492-8_11

The most widely used technology favors the employment of homogenous basic catalysts that have been dissolved in methanol, primarily NaOH or KOH [1]. Although a homogeneously catalyzed biodiesel synthesis can achieve high conversion rates and is reasonably quick, there are some significant limitations when the starting material has a high acidity [3]. At the conclusion of the reaction in this instance, the catalyst must be neutralized and removed from the methyl ester phase, resulting in the production of a sizable amount of waste water [4].

The formation of soaps as well as the separation and purification of biodiesel may be minimized by the use of heterogeneous catalysts [5, 6]. Furthermore, the application of heterogeneous catalysts could significantly lower the price of biodiesel while dramatically simplifying the process of product post-treatment. Different approaches have been suggested, including the use of solid catalysts for biodiesel generation, such as basic zeolites, alkaline earth metal oxides, and hydrotalcites (HT) among others [7–9], provided that the higher the raw material acidity, the lower the conversion efficiency [3]. Zeolites are superior to other heterogeneous catalysts in many ways; however, their catalytic activity in transesterification reactions using a pure mixture of fatty acids only reached 92% conversion, which is less than expected [10]. Owing to its promising performance, HT has been employed as a catalyst precursor [11].

Hydrotalcites (HT) are brucite-like octahedral-layered anionic materials with di and trivalent metal ions commonly referred to as layered double hydroxide (LDH) [12, 13]. Recently, HT are being investigated in the process of transesterification as catalyst in the production of biodiesel [14–16], although there is the existence of other types of catalyst, HT, as mentioned earlier has gained popularity because of their ease of separation, requirement of mild condition, ease of regeneration, reusability, hence affordable [17].

The most effective method for producing HT is co-precipitation, which involves mixing sodium carbonate solution with a mixed-metal solution that has been dissolved in deionized water. Sodium hydroxide solution is used to maintain a consistent pH. Nevertheless, it costs a lot of money to make HT from pure chemicals. A situation that has prompted research into developing cost-effective approaches for producing HT [13, 18], particularly from waste materials [19]. An example was presented in the work of Gil et al. [19], when they produced HT from saline slag wastes. Using a reflux system over a 2-hour period, saline slags were chemically treated with 2 mol/dm^3 aqueous solutions of NaOH. With the help of cobalt, magnesium, and nickel nitrates, as well as Na_2CO_3, aluminum aqueous solutions were employed as precursors to create HT materials with two different mole M^{2+}/Al^{3+} ratios, 2:1 and 4:1.

Despite efforts like the one mentioned in the paragraph before, costs associated with producing biodiesel are still being driven by raw materials [20]. The availability and price of the raw material have a major role in the choosing. Using edible oil to make biodiesel could potentially reduce the amount of oil available as food for both people and farm animals [2]. Hence, another laudable approach to minimizing the cost of biodiesel production will be the use of waste cooking oil/fat (which typically shows high acidity) which has been examined as a feedstock for biodiesel production [21].

To the best of my knowledge, not much research has described the usage of HT from metallurgical wastes to enhance the transesterification of WCO to biodiesel. In one similar study, Brito et al. [22] converted WCO into biodiesel using as-received HT and heat-treated HT. After, following an 8-hour reaction period, Hernandez et al. added up to 10% salt to heat-treated HT and observed a favorable response from the catalyst [23].

Premised on introduction leading to this point, the following subsequent aspects of this proposal report: problem statement, research objectives, research hypothesis, significance of study, literature review, and methodology, will elucidate the essence of this proposed research.

11.2 Problem Statement

Despite the potential of employing other sources, such as producing biodiesel from waste and biological sources [24–26], South Africa is still dealing with issues that prevent the biodiesel business from taking off. These include the following:

1. A lack of innovative activities that could assist in bringing down the cost of biodiesel to a reasonable level.
2. Choosing feedstocks that might potentially greatly reduce the overall cost of biodiesel manufacturing in South Africa is a difficult task.
3. It costs a lot of money to make HT from pure chemicals.

11.3 Research Objectives

11.3.1 Main Objective

Preparing and characterizing a hydrotalcite-derived material from mullite-rich tailings for the transesterification of waste cooking oil into biodiesel will be the main objective of this study.

11.3.2 Sub-objectives

The following sub-objectives will help to achieve the main objectives:

1. Preparation of edible cooking oil and WCO for transesterification
2. Characterization of edible cooking oil and WCO
3. Preparation and characterization of the waste copper dust (WCD)
4. Thermodynamic modeling of WCD oxidative roasting
5. Experimental oxidative roasting of the WCD
6. Density separation of WCD for production of MRT

7. Optimization of hydrotalcite production from MRT for the following:
   (i) Catalyst loading on catalyst activity.
   (ii) Molar ratio of methanol to oil on catalyst activity.
   (iii) Reaction time on the catalyst activity will be investigated to optimize transesterification conditions.
8. Characterization of the produced biodiesel for the following:
   (i) Thermal stability
   (ii) Physical properties
   (iii) Isoconversional models

11.4 Research Hypotheses

Premised on the proposed scientific idea, the following can be hypothesized:

1. That the use of WCO as feedstock will assist with the lowering of overall cost of biodiesel production in South Africa.
2. The use of WCO as feedstock for biodiesel production will eliminate the high cost of its disposal and associated environmental threats it poses.
3. Using WCO instead of edible cooking oil to make biodiesel will potentially increase the amount of edible cooking oil available as food for both people and farm animals.
4. Preparation and characterization of hydrotalcite-derived material from waste metal dust (i.e., MRT) for transesterification of WCO to biodiesel will assist with the cost reduction of biodiesel production in SA.
5. Since high basicity is one of the desired characteristics of heterogeneous catalyst used for transesterification, exploring the basicity of MRT to prepare and characterize a hydrotalcite-like material for transesterification will result in a much fast process than the existing one with existent catalysts.
6. The application of HT from MRT for the industrial production of biodiesel will contribute to addressing ecological and global stresses associated with environment.

11.5 Significance of Study

The information in this study will contribute to bridging the gap of knowledge that exist in the following studies:

1. The catalytic application of hydrotalcite-like materials:
   Among numerous applications of hydrotalcite-like material, its catalytical application as a heterogeneous catalyst in the process of transesterification at the industrial level of the production of biodiesel.

2. The catalytic effect of MRT elements in a HT:
   The choice of MRT and its availability, the role and contribution of the MRT element constituent for a HT structural feature, and their role in transesterification, leading to further feasibility studies on the preparation of a HDM from another material containing MRT-like elements.
3. Optimization of the preparation of a HDM from MRT:
   Paving ways on an optimal route of preparation of a HDM from MRT for future application and crystal structure studies.
4. Contribution of the HDM in the transesterification:
   Based on the results obtained, there will be clarity about the contribution of the HDM in the transesterification process.
5. Impact of the application of HDM as a catalyst on an industrial scale:
   Evaluate the economic possibility of using HDM from MRT as a catalyst in the transesterification process on an industrial scale.

11.6 Literature Review

11.6.1 Introduction

Interest in biofuels for transportation has been sparked by high energy prices, rising energy imports, supply concerns, and growing environmental awareness of the effects of fossil fuels [27]. As a result, the development of biofuels has multiplied enormously in response to the need for affordable, viable energy sources that do not harm the environment [28, 29]. Reiterating this, the pressure on petroleum-based fuels in the transportation sector has resulted in the development of vegetable oil-based fuels as the primary alternative fuel to non-renewable fossil fuel types [30, 31]. When using alternative sources, researchers can get the best outcomes by converting wastes and biological energy sources into goods, in this case, biodiesel [24–26].

11.6.2 Biodiesel Production in South Africa

Many nations are promoting the use and production of biodiesel because it reduces the need for foreign oil, increases domestic energy security, is safe for the environment by lowering greenhouse gas emissions, is renewable, and is both affordable and practical [31–34]. As at year 2010, it was estimated that 10% replacement of South Africa's diesel usage will result in a 1 billion liters increase South Africa's biodiesel market.

Table 11.1 Manufacturing costs of biodiesel for various feedstocks in SA [35]

SEBP plant		COBP plant	
Local feedstock	Manufacturing cost	Imported feedstock	Manufacturing cost
Canola	R4.81/liter	Palm oil	R6.62/liter
Sunflower seeds	R6.67/liter	Soybean oil	R6.89/liter
Soybeans	R6.70/liter	Sunflower oil	R7.48/liter
		Rapeseed oil	R9.28/liter

11.6.3 Manufacturing Cost of Biodiesel in South Africa

The ideal size of a biodiesel plant in South Africa (SA), according to Nolte [35], is between 1500 and 3000 kg/h [35]. A seed extraction biodiesel production plant (SEBP) uses locally produced oilseeds as feedstock, and a crude oil biodiesel production plant (COBP) uses imported crude vegetable oil as feedstock, according to the author's study. A COBP plant would require a capital expenditure of roughly R45 to R50 million (amounts inclusive of working capital of approximately R35), while a SEBP plant would require a capital investment of between R110 and R145 million. The calculated biodiesel manufacturing costs of the two types of plants for various feedstocks were computed on August 30, 2006, at the current prices, and this can be seen in Table 11.1.

11.6.4 The Choice of Feedstock and Its Impact on Biodiesel Production

The decision to use biodiesel as an alternative engine fuel is based on its characteristics, which are somewhat different from regular diesel and are frequently determined by the oil feedstock and alcohol utilized, although being otherwise extremely similar to diesel fuel [2, 36, 37]. According to Pratas et al. [38], Cao et al. [39], and Sajjadi et al. [40], it is made up of a lengthy organic chain of fatty acid methyl ester (FAME), also known as plant oil-based.

Plant oil-based (POB) fuels have long been successfully tested in diesel engines as an alternative engine fuel [32, 41, 42]. Short-chain alcohols, which are now combined with gasoline, and biodiesels, which are typically made from seed oils, are examples of POB fuels. Soybeans have established a reputation as the main source of biomass-derived diesel in the United States and Brazil because they produce the greatest oil by weight among the POB fuel feedstocks, up to 20% [43–45].

11.6.5 Soybean in South Africa

As a good substitute for biodiesel made from fossil fuels, soybean-derived biodiesel can be used to generate electricity [44]. According to the amount of land cultivated and the amount produced, soybeans are one of the most important grain crops in South Africa [38–40]. Since soybean has such a high socioeconomic value in South Africa, it is grown in all nine of the provinces there [46, 47]. The issue of waste management is a result of this, though.

11.6.6 Waste from Soybean Production

Tofu, soymilk, soymilk powder, beansprouts, dried tofu, soy sauce, soy flour, and soybean oil are only a few of the delicacies made from soybean in Asian nations. Every year, Japan disposes of around 800,000 tons of waste products from the manufacture of soybean oil. The annual disposal cost is roughly 2.1 million rand [48]. Currently, the garbage from this source is burned to create CO_2, disposed of in landfills, and other waste management techniques [49]. The environmental issues brought on by this source's large waste production have received a lot of attention [50]. According to Redondo-Cuenca, Villanueva-Suárez, and Mateos-Aparicio [51], waste from soybean oil is frequently high in moisture content (70–80%), making it difficult to manage and expensive to dry by conventional methods.

11.6.7 Proactive Measures for South Africa's Biodiesel Industry

While preparing for government assistance to help South Africa's biodiesel industry get off the ground, proactive steps are needed, especially in the field of creative initiatives that can help lower the price of biodiesel down to a respectable level. The selection of feedstock like those in Table 11.2 is an innovative strategy that has the potential to significantly lower the overall cost of biodiesel production in South Africa. Waste cooking oil (WCO) is an illustration of a plant-based oil waste product. WCO is a synthetic oil that has lost its ability to be used for cooking due to the presence of a significant number of contaminants and the loss of its original qualities. WCO is produced by a variety of sources, including residential, commercial, and industrial food manufacturers, which have an impact on the environment. One of the best methods to use the material effectively and affordably is to produce biodiesel from WCO.

WCO biodiesel has been regarded as a promising option, claims Demirbas [31]. For the production of biodiesel, WCO is inexpensive when compared to the price of fresh vegetable oil and, consequently, commercial diesel fuel (Table 11.3). Detailed

Table 11.2 Feedstock categories of biodiesel production [41]

Category	Classes		Feedstock	References
Oilseeds	Edible	C:	Soybean, rapeseed/canola, sunflower, palm, coconut, olive	[31, 52, 53]
		A:	False fax, safflower, sesame, marula, pumpkin, African peer seed, Sclerocarya birrea, Terminalia catappa L., yellow nut-sedge tuber, rice bran	[52, 54–60]
	Inedible	A:	Jatropha, karanja, mahua, linseed, rubber seed, cottonseed, neem, camelina, putranjiva, tobacco, polanga, cardoon, deccan hemp, castor, jojoba, moringa, poon, koroch seed, desert date, eruca sativa gars, see mango, pilu, crambe, syringa, milkweed, field pennycress, stillingia, radish Ethiopian mustard, tomato seed, kusum, cuphea, camellia, paradise, cuphea, terminalia, michelia champaca, garcinia indica, zanthoxylum bungeanum	[52, 61–70]
Animal fats		C:	Beef tallow, pork lard	[54]
		A:	Waste salmon, melon bug, sorghum bug, chicken fat	[54]
Waste materials		C:	Cooking oil, frying oil	[71, 72]
		A:	Vegetable oil soap stocks, acid oils, tall oil, dried distiller's grains (DDG), pomace oil	[73, 74]
Algae			Botryococcus braunii, Chlorella sp., Chlorella vulgaris, Crypthecodinium cohnii, Cylindrotheca sp., Dunaliella primolecta, Dunaliella salina, Isochrysis sp., Haematococcus pluvialis, Monallanthus salina, Muriellopsis sp. Nannochloris sp., Neochloris oleoabundans, Nitzschia sp., Phaeodactylum tricornutum, Porphyridium cruentum Schizochytrium sp., Spirulina, Arthrospira platensis, Tetraselmis suecica	[75–77]

Key: *A* alternative, *C* conventional

Table 11.3 Comparison of the qualities of commercial diesel fuel, waste cooking oil, and biodiesel from waste cooking oil [31]

Fuel property	WCO	Biodiesel (WCO)	Commercial diesel
Kinematic viscosity (mm^2/s, at 313 K)	36.4	5.3	1.9–4.1
Density (kg/L, at 288 K)	0.924	0.897	0.075–0.840
Flash point (K)	485	469	340–358
Pour point (K)	284	262	254–260
Cetane number	49	54	40–46
Ash content (%)	0.006	0.004	0.008–0.010
Sulfur content (%)	0.09	0.06	0.35–0.55
Carbon residue (%)	0.46	0.33	0.35–0.40
Water content (%)	0.42	0.04	0.02–0.05
Higher heating value (MJ/kg)	41.40	42.65	45.62–46.48
Free fatty acid (mg KOH/g oil)	1.32	0.10	–
Saponification value	188.2	–	–
Iodine value	141.5	–	–

analysis in Table 11.3 demonstrates that there are numerous similarities between the properties of biodiesel and diesel fuels in general. As a result, biodiesel is viewed as a suitable diesel substitute. The methyl esters made by transesterification of old cooking oil have a molecular weight that is nearly one-third lower, a viscosity that is about one-seventh lower, a flash point that is a little lower, a volatility that is a little higher, and a pour point that is a lot lower.

11.6.8 Transesterification of WCO to Biodiesel

Straight vegetable oil can be used as a fuel for diesel engines; however, there are a number of drawbacks, including high viscosity, injector coking, and engine deposits. By transforming the vegetable oils into their methyl esters, these issues can be somewhat resolved. This is accomplished by utilizing heterogeneous catalysts in the transesterification reaction. Fatty acid methyl ester (FAME), the end outcome, is also referred to as biodiesel.

Heterogeneous catalysts have been offering a sustainable and workable answer to issues occurring in various techno-economic limits of catalysis in recent years. The methods and technologies used to create these systems should serve as inspiration for addressing ecological and global environmental concerns. In recent years, intensive research has been conducted to produce these catalysts, and their prospective applications in a wide range of fields have been investigated. As previously mentioned, transesterification is one process where the use of these catalysts could soon have a significant impact on the manufacture of biodiesel at an industrial scale [14–16].

Although there are many different kinds of catalysts, including NaOH, KOH, HCl, and H_2SO_4 [78], heterogeneous catalysis has grown in popularity since it is simple to separate, only needs mild conditions, can be recycled, and can lower production costs [17]. Given their high surface area, basicity, and low production costs, zeolites made from bagasse and fly ash [79, 80], calcined cement waste [81], Li-modified rice husk [82], and CaO obtained from natural waste shells have all been investigated for their potential as heterogeneous catalysts like hydrotalcite in the production of biodiesel.

In the recent year, hydrotalcite has gained popularity in several fields and have been the topic of different studies due to their structural features and several applications [83]. Hydrotalcites are double-layered double showing a variety of stoichiometry due to the different arrangement of the stacking of the layers, ordering of the metal cations, as well as the arrangement of anions and water molecules, in the interlayer galleries, they are synthetic or natural occurring crystalline materials consisting of positively charged two-dimensional sheets with water and exchangeable charge compensating anions in the interlayer region as shown in Fig. 11.1.

The compounds of the hydrotalcite group show a wide range of the possible applications due to their specific properties, such as their large surface area, ion exchange ability, the insolubility in water and most of the organic sorbents, and others. Hydrotalcite-like compounds also referred to as anionic clays or layered double hydroxides (LDHs) are a valuable and commonly reported group of materials with a complex structure that is composed of positively charged brucite-like layers [M^{2+} or M^{3+} $(OH)_2]^{x+}$. In which an isomorphous substitution of the divalent M^{2+} and the trivalent cation M^{3+} are distributed among octahedral positions, alternating with disordered and negatively charged interlayers $[A_{x/n}]^{n-}$ formed for instance by inorganic ions, heteropoly acids, organic acids, and others, which is represent by the formula of type $[M_{1-x2} + M_{x3} + (OH)_2]_x + [A_{x/n}]^{n-} \cdot mH_2O$.

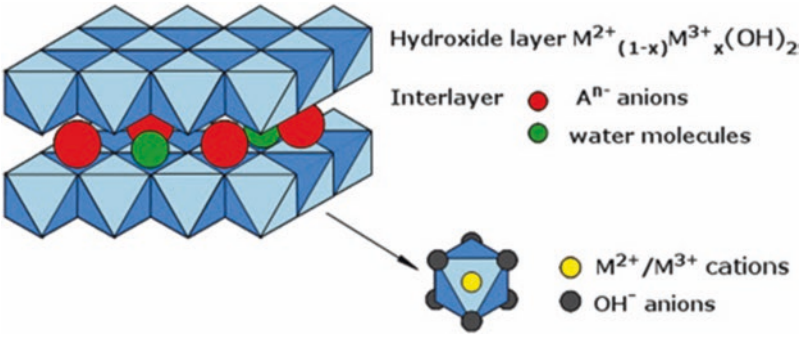

Fig. 11.1 Hydrotalcite structural representation. (Source: Google Image)

11.6.9 Production of Hydrotalcite from Natural Resources

11.6.9.1 Natural Dolomite

Dolomite is a naturally occurring double carbonate and a source of calcium and magnesium ions, according to Hosni and Srasra [84]. In their research, a straightforward process was used to create Mg-Al-CO_3 layered double hydroxide from dolomite feedstock. On their structure and textural qualities, the influence of synthesis parameters, including the M^{2+}/Al^{3+} ratio, reaction temperature, and pH, was investigated. X-ray diffraction, Fourier transform infrared spectroscopy, thermogravimetric analysis (TGA), and Brunauer, Emmett, and Teller (BET) measurements were used to determine the structural characteristics of the materials.

The authors came to the conclusion that dolomite can be processed into pure and well-crystalline phases of Mg-Al-CO3 LDH in an aqueous Na_2CO_3 solution. That a key consideration was the preparation's pH. Pure LDH was generated at a pH of 9.5. The LDH's crystallinity dropped below this threshold. Conditions that are quite alkaline do not seem to be favorable for the synthesis. The ideal dolomite/Al molar ratio was approximately 1. Above this ratio, brucite was generated. Low dolomite/Al ratios resulted in products with poor crystallinity. A factor that was thought to be crucial for regulating crystallinity and particle size was aging temperature. According to experimental research, hydrotalcite must be at a high temperature to form a well-crystalline phase.

11.6.9.2 Bittern

An assessment of the viability of employing Class C fly ash for the synthesis of faujasite (Type X) and tschernichite (Type A) type zeolite materials is shown in the study by Kunecki et al. [85]. Syntheses were performed to produce the well-formed zeolites. The variables were as follows: water, the filtrate (post-reaction solutions obtained during the hydrothermal synthesis of zeolites rich in Si), the ratio of fly ash to NaOH, and the quantity of aluminum foil added.

According to the analysis, three of the most efficient reactions (from which Samples 21–23 were formed) took place in the following circumstances: the amounts of H_2O, filtrate, and aluminum foil added were 100, 100, and 50 ml for each of the three reactions, respectively. The ratio of NaOH to fly ash was 1.6, 2.0, and 1.25, with fusion temperatures of 550 °C for each of the three reactions, fusion times of 1 hour, and reaction times of 4 hours. The reaction temperature was 80 °C for each of the three reactions (for each of the three reactions).

The three best zeolite materials (Samples 21–23) were submitted to mineralogical, chemical, and textural analytical characterization using X-ray powder diffraction (XRD), scanning electron microscopy-energy-dispersive X-ray spectroscopy (SEM-EDS), and X-ray fluorescence (XRF), Brunauer–Emmett–Teller (BET), to determine specific surface area and pore volume and size). The produced zeolites,

according to studies, have a Type A (Samples 21–22) and Type X (Sample 23) structure, as well as well-formed grains with isometric and cubic properties. The obtained zeolites' computed unit cell characteristics point to a cubic crystal system and are quite similar to the reference values for the structures of X- and A-type zeolites.

The ratio of SiO_2/Al_2O_3 in each of the three tested zeolite materials was as follows: 2.16, 1.98, and 2.41. For samples 21–23, the specific surface area was 106, 104, and 256 m^2/g, respectively. The outcomes were comparable to the zeolite structures discovered in Class F fly ash. As a result, we can draw the conclusion that the Class C fly ash under analysis may also be a useful substrate for the synthesis of Type X and Type A zeolite materials.

11.6.9.3 Blast Furnace Steel Slag

The authors of this study by Kunecki et al. [86] reported the effect of time on the creation of the mineral structure of GIS Na-P1 zeolite. Aluminum and silica were obtained from thin microspheres. The material used in this project was created utilizing a prototype installation at a quarter-technical scale. X-ray diffraction (XRD), X-ray fluorescence (XRF), scanning electron microscopy equipped with a system of chemical composition analysis based on energy dispersive X-ray (SEM-EDS), volumetric adsorption analyzer, Fourier transform infrared spectroscopy (FTIR), and particle size analyzer were used to determine the chemical, mineralogical, and textural properties of the material (PSA).

The interesting and in some cases remarkable phenomena of the lattice parameters ripening as a function of time is demonstrated by experimental calculations based on Miller indices. With longer synthesis times, both the number of zeolites present and the unit cell characteristics (a, b, c, and volume) rise. With the use of the XRD and FTIR techniques, this process may be seen clearly. The finished product's structural, morphological, and textural characteristics suggest that it might be beneficial as an adsorbent for several kinds of environmental pollution.

Muriithi et al. [87] reported the production of hydrotalcites (HT) from mineral waste (e.g., blast furnace slag), an area of research attracting growing attention. This paper describes a unique method for producing HT from fly ash, a common waste product of coal-fired power plants in South Africa. The optimization procedure, which highlights the boundary conditions for this mineral phase's crystallization, is the second area of originality.

The HCl content, aging duration and temperature, pH during the aging process, and crystallization time and temperature were the variables examined for the optimization of HT synthesis from fly ash. The best synthesis conditions were as follows: 3 M HCl concentration, 30 minutes of aging, 65 °C of aging, 11.5 pH during aging, 12 hours of crystallization, and 70 °C of crystallization temperature. The exterior surface area and microporosity of HT were both quite high.

The majority of the morphological components of synthesized HT were submicron, plate-like particles. Except for the presence of calcite, the structural features of HT made from fly ash were comparable to those of HT obtained from

analytical grade chemicals. The waste Class F fly ash from SA was used in an innovative way to create high-quality HT under optimal processing conditions that reduced the production of secondary undesirable mineral phases like calcite or hydrogarnet.

11.6.9.4 Aluminum Slag

In this study by Wajima [88], hydrotalcite was created from bittern solution by adding $AlCl_3$ (the solution's Mg/Al molar ratio was 3), and its capacity to remove phosphate and nitrate from water was tested. Both bittern and seawater can be used to make hydrotalcite, although the product made from bittern has a higher hydrotalcite content than the one made from seawater. Higher than commercial hydrotalcite, the bittern product has phosphate and nitrate removal capabilities.

The experimental data are found to better fit the Langmuir than the Freundlich isotherm models when calculating the equilibrium adsorption capacity of the product for phosphate and nitrate ions. Because of the ion exchange process between chlorine and sulfate in the product, phosphate adsorption on the product reached saturation in 30 minutes and was essentially steady after that. Nitrate adsorption on the product increased in 15 minutes and then gradually decreased.

The main constituents of blast furnace slag (BFS) are CaO, SiO_2, Al_2O_3, MgO, and trace amounts of transition metals like Fe, Ti, and Mn, according to Kuwahara et al. [89] in their study titled "A novel conversion process for waste slag: synthesis of a hydrotalcite-like compound and zeolite from blast furnace slag and evaluation of adsorption capacities." We successfully used the chemical method of acid-leaching and precipitation to create a hydrotalcite-like molecule from BFS.

After undergoing HCl acid-leaching, BFS was separated into hydrated silica with 92 wt.% SiO_2 and leaching solution containing other components, which provided a hydrotalcite-like product after further NaOH addition in a high yield. The result generated at 100 °C was determined to be a Ca-Al hydrocalumite complex by XRD and chemical analysis. Its stoichiometric molar ratios are Ca: Al: Cl = 2: 1: 1, and it contains other metal cations in its structure.

The hydrotalcite-like compound had an elevated phosphate adsorption capacity of about 40 mg P/g, which was more than three times more than that of typical Mg-Al-based hydrotalcite. The phosphate adsorption capacity of the raw slag was 1.5 mg P/g. In addition, utilizing the remaining silica and a hydrothermal treatment lasting 6 hours at 100 °C, single-phase A- and X-type zeolites with high crystallinities and outstanding water adsorption capacities (247 and 333 mg g^{-1}, respectively) were effectively created. From the perspective of making efficient use of BFS, this conversion procedure, which enables us to create two distinct types of valuable materials from BFS at a cheap cost and with simple preparatory stages, is unquestionably advantageous.

According to Galindo et al. [90], due to environmental concerns, the powdered solid strapped in filter sleeves in the aluminum tertiary industry is currently disposed of in secure landfills. They are categorized as hazardous waste because they

contain a lot of aluminum, either in the form of metallic aluminum or in compounds like aluminum nitride.

These substances have the ability to react with extremely little moisture, releasing toxic or dangerous gases like hydrogen and ammonia.

In three steps, the low-cost method described in this study allows for the complete recovery of this hazardous waste and the creation of two different added-value components. The trash is subjected to mild acid hydrolysis in the first step in order to produce an inert cake and a concentrated solution of aluminum. The subsequent steps involve synthesizing hydrotalcite from the resultant solution and using the cake to create transparent glasses based on the CaO-Al_2O_3-SiO_2 system. The products' characteristics show that the hydrotalcites can easily absorb anionic contaminants (molybdates), while the glasses offer better optical properties than those made by directly vitrifying the trash.

11.6.9.5 Oil Shale Ash

With the aid of ammonia and triethanolamine at pH 10, Galindo et al. [91] reported that hydrotalcite-like compounds were co-precipitated with dilute sodium hydroxide from an unconventional aluminum source: the aluminum waste produced by the tertiary aluminum industry. To compare results, these compounds were characterized using a variety of techniques (XRD, FT-IR, UV-vis-NIR, SEM, DTA-TG, and BET procedures).

Characterization of the products revealed considerable variations based on the choice of basic reagent. Products that co-precipitated with ammonia exhibited less crystal development, a higher internal surface area, and a structure that contained significantly more iron. Triethanolamine-derived products demonstrated how organic molecules entered the multilayer framework. These results were crucial for the development of waste treatment techniques that turned hazardous wastes made of aluminum into stacked double hydroxides, a product with additional value.

11.6.9.6 Coal Fly Ash

In the study conducted by Muriithi et al. [87], South African Class F coal fly ash, a generally available and inexpensive chemical feedstock, was used to successfully produce HT under optimal conditions. With the exception of the presence of calcite, the produced HT exhibited structural traits that were comparable to those of that made using analytical-grade chemicals. In the context of carbon capture and storage in South Africa, the production process might thus serve as a dual strategy for the re-exploitation of coal fly ash from power plants and for the reduction of CO_2. Additionally, authors recommend that future research should focus on stopping the co-precipitation of calcite, while showing how these HT may be suitable for both short- and long-term CO_2 collection. On the possibility for wet or dry ash dams to naturally collect carbon, very little information is currently known. This study

compared a naturally occurring occurrence with accelerated ex-situ mineral carbonation of fresh fly ash to determine the degree of carbon capture in a wet-dumped ash dam and the mineralogical changes supporting CO_2 capture (FA). Sr, Ba, and Zr trace metals at significant concentrations were found in both fresh ash and weathered ash. However, it was discovered that weathered ash had more Nb, Y, Sr, Th, and Ba than fresh ash did.

Fresh ash is composed of quartz, mullite, hematite, magnetite, and lime from a mineral perspective; however, weathered and carbonated ashes also contained other phases like calcite and aragonite. The fresh FA was able to trap up to 6.5 wt% CO_2, and accelerated carbonation (done at 2 hours, 4 MPa, 90 °C, bulk ash, and a S/L ratio of 1) resulted in a 60% conversion of calcium to $CaCO_3$. On the other hand, it was discovered that over the course of 20 years of moist disposal of ash, 6.8 wt percent CO_2 was naturally carbonated.

Thus, the ash dumps' spontaneous carbonation is considerable and may be useful in extracting CO_2.

In their study, Gil et al. [19] described the co-precipitation method's use of aluminum recovered from saline slag wastes to synthesize hydrotalcite-like materials. Using a reflux system over a 2-hour period, saline slags were chemically treated with 2 mol/dm^3 aqueous solutions of NaOH. With the help of cobalt, magnesium, and nickel nitrates, as well as Na_2CO_3, aluminum aqueous solutions were employed as precursors to create hydrotalcite-like materials with two different mole M^{2+}/Al^{3+} ratios, 2:1 and 4:1.

X-ray diffraction, thermogravimetric studies, nitrogen adsorption at 196 °C, and scanning electron microscopy were used to analyze the resultant solids. The CO_2 adsorption at 50, 100, and 200 °C was assessed under dry conditions after thermal treatment at 200 °C. The Mg: Al-2: 1 sample had a remarkable sorption capacity of 5.26 mmol/g at 80 kPa and 50 °C, which was significantly greater than the sorption capacities previously reported in the literature for hydrotalcites under comparable conditions.

The values of the Henry's law constants, which range from 0.01 to 4.20 mmol/kPag, were directly deduced from the adsorption isotherms at low pressures. Using the Clausius-Clapeyron equation, the isosteric heats of CO_2 adsorption were discovered to be between 5.2 and 16.8 kJ/mol.

11.6.9.7 Mullite-Rich Tailings from Density-Separated Waste Copper Dust (WCD)

According to Linda et al. [92], the mullite-rich tailings (MRT) from WCD can serve as a secondary resource of mullite, because it contains 67.15% of aluminosilicates. It is therefore recommended that MRT be used to lower the cost of mullite refined powders in later engineering applications due to its size, potential, and possibilities, after several other studies.

Conclusion

The manufacture of biodiesel is acknowledged to lessen the demand for imported oil, boost domestic energy security, and be safe for the environment by reducing greenhouse gas emissions because it is a renewable resource. However, the effectiveness of biodiesel as an alternative engine fuel depends on its properties, which are usually influenced by the type of alcohol and oil used as feedstock. Diesel engines have long been successfully tested with plant oil base (POB) fuels as an alternative engine fuel. Among the POB fuel feedstocks, soybeans yield the most oil by weight, up to 20%, and have earned a reputation as the primary source of biomass-derived diesel in the United States and Brazil.

Despite initiatives like the one stated in the preceding paragraph, the cost of generating biodiesel is still largely determined by the cost of raw ingredients. The choice is heavily influenced by the raw material's availability and cost. Making biodiesel from edible oil can result in less oil being accessible for human and farm animal use. Therefore, the use of used cooking oil or fat, which normally exhibits high acidity, has been investigated as a feedstock for biodiesel synthesis, is another admirable strategy for reducing the cost of biodiesel manufacturing.

The second type of waste conversion to product will use the transesterification method to convert WCO to biodiesel using mullite-rich tailings (MRT) from density-separated waste copper dust.

To my knowledge, very little study has discussed the use of HT derived from metallurgical wastes to speed up the conversion of WCO to biodiesel. Therefore, the development of an affordable biodiesel production process in South Africa may be aided by research into an effective catalyst to convert a WCO into biodiesel.

11.7 Methodology

11.7.1 Introduction

The investigation on the preparation and characterization of hydrotalcites derived material from waste metal dust for transesterification of waste cooking oil to biodiesel will be carried out according to the methodology detailed as follows:

11.7.1.1 Materials

Waste Cooking Oil

The raw material that will be used for the production of biodiesel in this proposed study is a waste cooking oil.

Waste Metal Dusts

Two waste metal dust will serve as primary (i.e., mullite-rich tailings) and secondary (copper smelter dust) materials for synthesis of the heterogeneous catalyst (i.e., hydrotalcites derived material) that will be used to enhance the transesterification process of the waste cooking oil to biodiesel.

11.7.1.2 Methods

Preparation of WCO Feedstock for Transesterification

The contamination in the WCO will be filtered using a 5-μm filter cloth in a vacuum filtration unit. Seven WCO samples of 1000 ml each will be filtered in the machine.

The edible cooking oil (ECO) will be characterized for free fatty acid (FFA) content, relative density (RA), acid value (AV), saponification number (SN), and ester value (EV). These values will be compared with the properties evaluated from seven purified WCO samples as illustrated in Table 11.4. The best among these six samples will be used as feedstock for this study.

Density Separation of WCD

The WCD will be subjected to physical separation into using a centrifugal gravity separator. The parameters that will be optimized for the centrifugal gravity separation (CGS) will be the rotational bowl speed (RBS) and the fluidized water flow rate (FWFR) as detailed in Table 11.5.

The protocol for the CGS is detailed in Table 11.6, and it will involve 9 tests in total. These nine tests will be repeated 5 times as passes. The starting material for each new pass will be the tailings from the previous test. Based on this experimental plan, 45 test samples will be generated as shown in Table 11.7. These outputs from the CGS of WCD will be used as raw material for the production of the hydrotalcite-derived material (HDM).

Table 11.4 Characteristics of FSO and WCO

Characteristics	FSO	WCO1	WCO2	WCO3	WCO4	WCO5	WCO6	WCO7
FFA	YTBD	YTBD	YTBD	YTBD	YTBD	YTBD	YTBD	YTBD
RA	YTBD	YTBD	YTBD	YTBD	YTBD	YTBD	YTBD	YTBD
AV	YTBD	YTBD	YTBD	YTBD	YTBD	YTBD	YTBD	YTBD
SN	YTBD	YTBD	YTBD	YTBD	YTBD	YTBD	YTBD	YTBD
EV	YTBD	YTBD	YTBD	YTBD	YTBD	YTBD	YTBD	YTBD

Key: *YTBD* yet to be determined

Table 11.5 Parameters measured for density separation experiment

S/N	Parameters	Low (0)	Medium (1)	High (2)
X_1	RBS (m/s^2)	60	90	120
X_2	FWFR (l/min)	3.0	4.5	6.0

Table 11.6 Test protocol for density separation of WCD

Tests	RBS (G)	FWFR (l/min)	Treatment combination (TC)
1	A	A	AA
2	A	B	AB
3	A	C	AC
4	B	A	BA
5	B	B	BB
6	B	C	BC
7	C	A	CA
8	C	B	CB
9	C	C	CC

Table 11.7 Outputs from CGS of WCD

	MRT								
Passes	(1)	(2)	(3)	(4)	(5)	(6)	(7)	(8)	(9)
1	1(1)	1(2)	1(3)	1(4)	1(5)	1(6)	1(7)	1(8)	1(9)
2	2(1)	2(2)	2(3)	2(4)	2(5)	2(6)	2(7)	2(8)	2(9)
3	3(1)	3(2)	3(3)	3(4)	3(5)	3(6)	3(7)	3(8)	3(9)
4	4(1)	4(2)	4(3)	4(4)	4(5)	4(6)	4(7)	4(8)	4(9)
5	5(1)	5(2)	5(3)	5(4)	5(5)	5(6)	5(7)	5(8)	5(9)

Optimization of Hydrotalcite Production from MRT

Pregnant leach solutions (PLS) will be obtained from the 45 MRT samples following the procedure that has been reported in by Okanigbe [93] and Baktiari [94]. The different grades of PLS will be subjected to co-precipitation (Fig. 11.2). The parameters for the co-precipitation process will be optimized following Tables 11.8 and 11.9

Optimization of Catalytic Activity

The transesterification of filtered WCO will be carried out in a 500-ml three-necked round-bottom flask equipped with reflux condenser and a magnetic stirrer. Varied ratios of WCO: Alcohol (Table 11.10) will be mixed with varied concentrations of HT_{MRT} (Table 11.10) and stirred at a fixed temperature of 65.5 °C. This process will be optimized following the test protocol in Table 11.11. After carrying out the reaction, the mixture was cooled to room temperature, centrifuged at 6000 rpm for

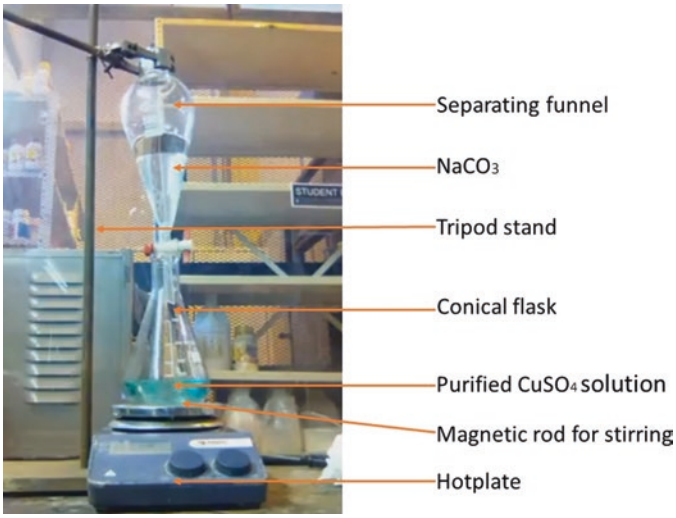

Fig. 11.2 Proposed experimental setup for production of HDM from waste copper dust

Table 11.8 Parameters considered for the production of hydrotalcite

	Levels		
Parameters	Low	Medium	High
Temperature (°C)	25	55	85
Rotational speed (rpm)	340	740	1480

Table 11.9 Design of experiment for the production of hydrotalcite

Tests	Temperature (°C)	Rotational speed (rpm)	Treatment Combination
1	25	340	25 °C–340 rpm
2	25	740	25 °C–740 rpm
3	25	1480	25 °C–1480 rpm
4	55	340	55 °C–340 rpm
5	55	740	55 °C–740 rpm
6	55	1480	55 °C–1480 rpm
7	85	340	85 °C–340 rpm
8	85	740	85 °C–740 rpm
9	85	1480	85 °C–1480 rpm

Table 11.10 Parameters measured for density separation experiment

S/N	Parameters	Low (0)	Medium (1)	High (2)
X_1	WCO: Alcohol	1:5	1:6	1:7
X_2	Catalyst concentration (wt %)	0.5	1.0	1.5

Table 11.11 Test protocol for optimization of HT_{MRT} activity

Tests	WCO: alcohol	Catalyst conc. (wt %)	Treatment combination (TC)
1	1:5	0.5	(1:5)(0.5)
2	1:5	1.0	(1:5)(1.0)
3	1:5	1.5	(1:5)(1.5)
4	1:6	0.5	(1:6)(0.5)
5	1:6	1.0	(1:6)(1.0)
6	1:6	1.5	(1:6)(1.5)
7	1:7	0.5	(1:7)(0.5)
8	1:7	1.0	(1:7)(1.0)
9	1:7	1.5	(1:7)(1.5)

10 minutes for catalyst separation, and the unreacted methanol was removed using rotary evaporator.

The biodiesel yield will be estimated using Eq. (11.1)

$$\text{yield}\% = \frac{\text{weight of methyl ester}(\text{g})}{\text{weight of oil}(\text{g})} \times 100 \tag{11.1}$$

Characterization of Biodiesel

The biodiesel produced will be characterized for physical and chemical properties. Specific gravities of all the samples will be measured using specific gravity bottle as per American society for testing and materials (ASTM) D 1298-85. The viscosities of the samples will be measured at 40 °C using rheometer (Rheostress RS 1) from Thermo Electron, according to ASTM D 445. Acidic value will be determined as per ASTM D664-89. Calorific values of the samples will be measured using bomb calorimeter according to ASTM D 240-92. 1H-NMR analysis will be performed at 25 °C.

11.7.2 Contribution to Knowledge

The information in this study will contribute to bridging the gap of knowledge that exist in the following studies:

- The catalytic application of hydrotalcite-like materials
- The catalytic effect of copper smelter dust in a hydrotalcite

- Optimization of the Preparation of a hydrotalcite-like material from copper smelter dust
- Contribution of the hydrotalcite-like materials in the transesterification
- Impact of the application of hydrotalcite-like materials as a catalyst on an industrial scale

11.7.3 Ethical Considerations

There are no ethical issues in this project.

11.7.4 Dissemination

The results will be presented at local and international conferences, while the full paper will be published in the corresponding conference proceedings. Other results will be published in Department of Higher Education and Training (DHET)-accredited journals like the following:

- Material Cycles and Waste Management—Journal —Springer
- Materials for Renewable and Sustainable Energy—Journal—Springer

11.7.5 Budget (Table 11.12)

Table 11.12 Estimated budget of the project

Items	Cost	Source
Literature sourcing and stationaries	X	TUT
Materials and supplies	X	TUT
Analytical equipment	X	TUT
Travelling expenses	X	TUT
Miscellaneous expenses	X	TUT
Total	X	TUT

Key: *TUT* **Tshwane University of Technology,** *R* **Rand**

11.7.6 Time Frame (Table 11.13)

Table 11.13 Estimated time frame of the project

S/N	Task name	Year	
		2020	2021
1	Proposal (compilation and presentation)	X	X
2	Literature review	X	X
3	Material sourcing	X	X
4	Sample preparation (sampling)	X	X
5	Fabrication of test samples optimization process	X	X
6	Fabrication of test samples	X	X
7	Thermal conductivity and wear resistance tests	X	X
8	Results, data, and analysis	X	X
9	Optimum predictive model development	X	X
10	3D print of brake rotor and validation of optimum prediction	X	X
11	Compilation and presentation of final report	X	X

References

1. M. Corral Bobadilla, R. Lostado Lorza, R. Escribano García, F. Somovilla Gómez, E.P. Vergara González, An improvement in biodiesel production from waste cooking oil by applying thought multi-response surface methodology using desirability functions. Energies **10**(1), 130 (2017)
2. S.G.I.L. Pinzi, I.L. Garcia, F.J. Lopez-Gimenez, M.D. Luque de Castro, G. Dorado, M.P. Dorado, The ideal vegetable oil-based biodiesel composition: A review of social, economical and technical implications. Energy Fuel **23**(5), 2325–2341 (2009)
3. M.P. Dorado, E. Ballesteros, J.A. De Almeida, C. Schellert, H.P. Löhrlein, R. Krause, An alkali–catalyzed transesterification process for high free fatty acid waste oils. Trans. ASAE **45**(3), 525 (2002)
4. M.P. Dorado, E. Ballesteros, F.J. López, M. Mittelbach, Optimization of alkali-catalyzed transesterification of Brassica Carinata oil for biodiesel production. Energy Fuel **18**(1), 77–83 (2004)
5. Y.C. Sharma, B. Singh, J. Korstad, Latest developments on application of heterogenous basic catalysts for an efficient and eco-friendly synthesis of biodiesel: A review. Fuel **90**(4), 1309–1324 (2011)
6. H.V. Lee, J.C. Juan, T.Y. Yun Hin, H.C. Ong, Environment-friendly heterogeneous alkaline-based mixed metal oxide catalysts for biodiesel production. Energies **9**(8), 611 (2016)
7. G. Arzamendi, I. Campo, E. Arguinarena, M. Sánchez, M. Montes, L.M. Gandia, Synthesis of biodiesel with heterogeneous NaOH/alumina catalysts: Comparison with homogeneous NaOH. Chem. Eng. J. **134**(1–3), 123–130 (2007)
8. I. Reyero, G. Arzamendi, L.M. Gandía, Heterogenization of the biodiesel synthesis catalysis: CaO and novel calcium compounds as transesterification catalysts. Chem. Eng. Res. Des. **92**(8), 1519–1530 (2014)
9. E. Santacesaria, G.M. Vicente, M. Di Serio, R. Tesser, Main technologies in biodiesel production: State of the art and future challenges. Catal. Today **195**(1), 2–13 (2012)
10. E.J.M. de Paiva, S. Sterchele, M.L. Corazza, D.Y. Murzin, F. Wypych, T. Salmi, Esterification of fatty acids with ethanol over layered zinc laurate and zinc stearate–kinetic modeling. Fuel **153**, 445–454 (2015)

11. A. Navajas, I. Campo, A. Moral, J. Echave, O. Sanz, M. Montes, J.A. Odriozola, G. Arzamendi, L.M. Gandía, Outstanding performance of rehydrated Mg-Al hydrotalcites as heterogeneous methanolysis catalysts for the synthesis of biodiesel. Fuel **211**, 173–181 (2018)
12. J.C. Villegas, Part I. Manganese oxide containing layered double hydroxides materials: Synthesis and characterization. Part II. Manganese oxide octahedral molecular sieves (OMS-2): Synthesis, particle size control, characterization, and catalytic applications, University of Connecticut, 2006
13. V. Volli, M.K. Purkait, Preparation and characterization of hydrotalcite-like materials from flyash for transesterification. Clean Techn. Environ. Policy **18**(2), 529–540 (2016)
14. L.L. Myint, M.M. El-Halwagi, Process analysis and optimization of biodiesel production from soybean oil. Clean Techn. Environ. Policy **11**(3), 263–276 (2009)
15. J.H. Ng, H.K. Ng, S. Gan, Advances in biodiesel fuel for application in compression ignition engines. Clean Techn. Environ. Policy **12**(5), 459–493 (2010)
16. J.H. Ng, H.K. Ng, S. Gan, Recent trends in policies, socioeconomy and future directions of the biodiesel industry. Clean Techn. Environ. Policy **12**(3), 213–238 (2010)
17. M.K. Lam, K.T. Lee, A.R. Mohamed, Homogeneous, heterogeneous and enzymatic catalysis for transesterification of high free fatty acid oil (waste cooking oil) to biodiesel: A review. Biotechnol. Adv. **28**(4), 500–518 (2010)
18. S.H. Wang, Y.B. Wang, Y.M. Dai, J.M. Jehng, Preparation and characterization of hydrotalcite-like compounds containing transition metal as a solid base catalyst for the transesterification. Appl. Catal. A Gen. **439**, 135–141 (2012)
19. A. Gil, E. Arrieta, M.A. Vicente, S.A. Korili, Synthesis and CO_2 adsorption properties of hydrotalcite-like compounds prepared from aluminum saline slag wastes. Chem. Eng. J. **334**, 1341–1350 (2018)
20. M.P. Dorado, F. Cruz, J.M. Palomar, F.J. Lopez, An approach to the economics of two vegetable oil-based biofuels in Spain. Renew. Energy **31**(8), 1231–1237 (2006)
21. A.B. Chhetri, K.C. Watts, M.R. Islam, Waste cooking oil as an alternate feedstock for biodiesel production. Energies **1**(1), 3–18 (2008)
22. A. Brito, M.E. Borges, M. Garín, A. Hernández, Biodiesel production from waste oil using Mg− Al layered double hydroxide catalysts. Energy Fuel **23**(6), 2952–2958 (2009)
23. M. del Remedio Hernandez, J.A. Reyes-Labarta, F.J. Valdes, New heterogeneous catalytic transesterification of vegetable and used frying oil. Ind. Eng. Chem. Res. **49**(19), 9068–9076 (2010)
24. A. Demirbas, Use of algae as biofuel sources. Energy Convers. Manag. **51**(12), 2738–2749 (2010)
25. L. Brennan, P. Owende, Biofuels from microalgae—A review of technologies for production, processing, and extractions of biofuels and co-products. Renew. Sust. Energ. Rev. **14**(2), 557–577 (2010)
26. T.K. Hari, Z. Yaakob, N.N. Binitha, Aviation biofuel from renewable resources: Routes, opportunities and challenges. Renew. Sust. Energ. Rev. **42**, 1234–1244 (2015)
27. J. Hill, E. Nelson, D. Tilman, S. Polasky, D. Tiffany, Environmental, economic, and energetic costs and benefits of biodiesel and ethanol biofuels. Proc. Natl. Acad. Sci. **103**(30), 11206–11210 (2006)
28. A.L. Ahmad, N.M. Yasin, C.J.C. Derek, J.K. Lim, Microalgae as a sustainable energy source for biodiesel production: A review. Renew. Sust. Energ. Rev. **15**(1), 584–593 (2011)
29. M. Ayoub, A.Z. Abdullah, Critical review on the current scenario and significance of crude glycerol resulting from biodiesel industry towards more sustainable renewable energy industry. Renew. Sust. Energ. Rev. **16**(5), 2671–2686 (2012)
30. Y.Y. Tye, K.T. Lee, W.N.W. Abdullah, C.P. Leh, Second-generation bioethanol as a sustainable energy source in Malaysia transportation sector: Status, potential and future prospects. Renew. Sust. Energ. Rev. **15**(9), 4521–4536 (2011)
31. A. Demirbas, Progress and recent trends in biodiesel fuels. Energy Convers. Manag. **50**(1), 14–34 (2009)

32. J.M. Ogden, R.H. Williams, E.D. Larson, Societal lifecycle costs of cars with alternative fuels/engines. Energy Policy **32**(1), 7–27 (2004)
33. P.A. Owusu, S. Asumadu-Sarkodie, A review of renewable energy sources, sustainability issues and climate change mitigation. Cogent Eng. **3**(1), 1167990 (2016)
34. S. Mekhilef, S. Siga, R. Saidur, A review on palm oil biodiesel as a source of renewable fuel. Renew. Sust. Energ. Rev. **15**(4), 1937–1949 (2011)
35. M. Nolte, Commercial biodiesel production in South Africa: A preliminary economic feasibility study, Doctoral dissertation, University of Stellenbosch, Stellenbosch, 2007
36. A.K. Agarwal, Biofuels (alcohols and biodiesel) applications as fuels for internal combustion engines. Prog. Energy Combust. Sci. **33**(3), 233–271 (2007)
37. M.K. Yesilyurt, C. Cesur, V. Aslan, Z. Yilbasi, The production of biodiesel from safflower (Carthamus tinctorius L.) oil as a potential feedstock and its usage in compression ignition engine: A comprehensive review. Renew. Sustain. Energy Rev. **119**, 109574 (2020)
38. M.J. Pratas, S. Freitas, M.B. Oliveira, S.C. Monteiro, Á.S. Lima, J.A. Coutinho, Densities and viscosities of minority fatty acid methyl and ethyl esters present in biodiesel. J. Chem. Eng. Data **56**(5), 2175–2180 (2011)
39. P. Cao, M.A. Dubé, A.Y. Tremblay, High-purity fatty acid methyl ester production from canola, soybean, palm, and yellow grease lipids by means of a membrane reactor. Biomass Bioenergy **32**(11), 1028–1036 (2008)
40. B. Sajjadi, A.A.A. Raman, H. Arandiyan, A comprehensive review on properties of edible and non-edible vegetable oil-based biodiesel: Composition, specifications and prediction models. Renew. Sust. Energ. Rev. **63**, 62–92 (2016)
41. S.Y. No, Inedible vegetable oils and their derivatives for alternative diesel fuels in CI engines: A review. Renew. Sust. Energ. Rev. **15**(1), 131–149 (2011)
42. A.Z. Abdullah, B. Salamatinia, H. Mootabadi, S. Bhatia, Current status and policies on biodiesel industry in Malaysia as the world's leading producer of palm oil. Energy Policy **37**(12), 5440–5448 (2009)
43. A.S. Carlsson, Plant oils as feedstock alternatives to petroleum–a short survey of potential oil crop platforms. Biochimie **91**(6), 665–670 (2009)
44. H. Huo, M. Wang, C. Bloyd, V. Putsche, Life-cycle assessment of energy use and greenhouse gas emissions of soybean-derived biodiesel and renewable fuels. Environ. Sci. Technol. **43**(3), 750–756 (2009)
45. B.D. Solomon, Biofuels and sustainability. Ann. N. Y. Acad. Sci. **1185**(1), 119–134 (2010)
46. C.H. Foyer, K.H. Siddique, A.P. Tai, S. Anders, N. Fodor, F.L. Wong, N. Ludidi, M.A. Chapman, B.J. Ferguson, M.J. Considine, F. Zabel, Modelling predicts that soybean is poised to dominate crop production across Africa. Plant Cell Environ. **42**(1), 373–385 (2019)
47. G. Engelbrecht, S. Claassens, C. Mienie, H. Fourie, South Africa: An important soybean producer in sub-Saharan Africa and the quest for managing nematode pests of the crop. Agriculture **10**(6), 242 (2020)
48. K. Muroyama, R. Atsumi, A. Andoh, Effect of pretreatment on lactic acid fermentation of bean curd refuse with simultaneous saccharification, in *Studies in Surface Science and Catalysis*, (Elsevier, Amsterdam, 2006), pp. 133–136
49. K. Muroyama, T. Mochizuki, T. Wakamura, Methane fermentation of bean curd refuse. J. Biosci. Bioeng. **91**(2), 208–212 (2001)
50. F. Cuadros, F. López-Rodríguez, A. Ruiz-Celma, F. Rubiales, A. González-González, Recycling, reuse and energetic valuation of meat industry wastes in Extremadura (Spain). Resour. Conserv. Recycl. **55**(4), 393–399 (2011)
51. A. Redondo-Cuenca, M.J. Villanueva-Suárez, I. Mateos-Aparicio, Soybean seeds and its by-product okara as sources of dietary fibre. Measurement by AOAC and Englyst methods. Food Chem. **108**(3), 1099–1105 (2008)
52. S.P. Singh, D. Singh, Biodiesel production through the use of different sources and characterization of oils and their esters as the substitute of diesel: A review. Renew. Sust. Energ. Rev. **14**(1), 200–216 (2010)

53. M. Balat, Fuel characteristics and the use of biodiesel as a transportation fuel. Energy Sources, Part A **28**(9), 855–864 (2006)
54. B.R. Moser, Biodiesel production, properties, and feedstocks, in *Biofuels*, (Springer, New York, 2011), pp. 285–347
55. U. Rashid, F. Anwar, Production of biodiesel through base-catalyzed transesterification of safflower oil using an optimized protocol. Energy Fuel **22**(2), 1306–1312 (2008)
56. V.I.E. Ajiwe, A.E. Obika, African pear seed oil: Potential alternative source to diesel oil. Energy Fuel **14**(1), 112–116 (2000)
57. H.Y. Zhang, M.A. Hanna, Y. Ali, L. Nan, Yellow nut-sedge (Cyperus esculentus L.) tuber oil as a fuel. Ind. Crop. Prod. **5**(3), 177–181 (1996)
58. P. Schinas, G. Karavalakis, C. Davaris, G. Anastopoulos, D. Karonis, F. Zannikos, S. Stournas, E. Lois, Pumpkin (Cucurbita pepo L.) seed oil as an alternative feedstock for the production of biodiesel in Greece. Biomass Bioenergy **33**(1), 44–49 (2009)
59. I.C.F. Dos Santos, S.H.V. De Carvalho, J.I. Solleti, W.F. de La Salles, K.T.D.S. de La, S.M.P. Meneghetti, Studies of Terminalia catappa L. oil: Characterization and biodiesel production. Bioresour. Technol. **99**(14), 6545–6549 (2008)
60. A. Mariod, S. Klupsch, I.H. Hussein, B. Ondruschka, Synthesis of alkyl esters from three unconventional Sudanese oils for their use as biodiesel. Energy Fuel **20**(5), 2249–2252 (2006)
61. M. Balat, H. Balat, Progress in biodiesel processing. Appl. Energy **87**(6), 1815–1835 (2010)
62. O.D. Hebbal, K.V. Reddy, K. Rajagopal, Performance characteristics of a diesel engine with deccan hemp oil. Fuel **85**(14–15), 2187–2194 (2006)
63. H. Shao, L. Chu, Resource evaluation of typical energy plants and possible functional zone planning in China. Biomass Bioenergy **32**(4), 283–288 (2008)
64. U. Rashid, F. Anwar, B.R. Moser, G. Knothe, Moringa oleifera oil: A possible source of biodiesel. Bioresour. Technol. **99**(17), 8175–8179 (2008)
65. J. Kansedo, K.T. Lee, S. Bhatia, Cerbera odollam (sea mango) oil as a promising non-edible feedstock for biodiesel production. Fuel **88**(6), 1148–1150 (2009)
66. Y.C. Sharma, B. Singh, An ideal feedstock, kusum (Schleichera trijuga) for preparation of biodiesel: Optimization of parameters. Fuel **89**(7), 1470–1474 (2010)
67. P.K. Devan, N.V. Mahalakshmi, Performance, emission and combustion characteristics of poon oil and its diesel blends in a DI diesel engine. Fuel **88**(5), 861–867 (2009)
68. G. Knothe, S.C. Cermak, R.L. Evangelista, Cuphea oil as source of biodiesel with improved fuel properties caused by high content of methyl decanoate. Energy Fuel **23**(3), 1743–1747 (2009)
69. B.P. Chapagain, Y. Yehoshua, Z. Wiesman, Desert date (Balanites aegyptiaca) as an arid lands sustainable bioresource for biodiesel. Bioresour. Technol. **100**(3), 1221–1226 (2009)
70. P.N. Giannelos, S. Sxizas, E. Lois, F. Zannikos, G. Anastopoulos, Physical, chemical and fuel related properties of tomato seed oil for evaluating its direct use in diesel engines. Ind. Crop. Prod. **22**(3), 193–199 (2005)
71. M.G. Kulkarni, A.K. Dalai, Waste cooking oil an economical source for biodiesel: A review. Ind. Eng. Chem. Res. **45**(9), 2901–2913 (2006)
72. C.C. Enweremadu, M.M. Mbarawa, Technical aspects of production and analysis of biodiesel from used cooking oil—A review. Renew. Sust. Energ. Rev. **13**(9), 2205–2224 (2009)
73. M.J. Haas, Improving the economics of biodiesel production through the use of low value lipids as feedstocks: Vegetable oil soapstock. Fuel Process. Technol. **86**(10), 1087–1096 (2005)
74. S. Çaynak, M. Gürü, A. Biçer, A. Keskin, Y. Içingür, Biodiesel production from pomace oil and improvement of its properties with synthetic manganese additive. Fuel **88**(3), 534–538 (2009)
75. Y. Chisti, Biodiesel from microalgae. Biotechnol. Adv. **25**(3), 294–306 (2007)
76. R. Harun, M. Singh, G.M. Forde, M.K. Danquah, Bioprocess engineering of microalgae to produce a variety of consumer products. Renew. Sust. Energ. Rev. **14**(3), 1037–1047 (2010)
77. G. Huang, F. Chen, D. Wei, X. Zhang, G. Chen, Biodiesel production by microalgal biotechnology. Appl. Energy **87**(1), 38–46 (2010)
78. F. Ma, M.A. Hanna, Biodiesel production: A review. Bioresour. Technol. **70**(1), 1–15 (1999)

79. C.W. Purnomo, C. Salim, H. Hinode, Synthesis of pure Na–X and Na–A zeolite from bagasse fly ash. Microporous Mesoporous Mater. **162**, 6 (2012)
80. M. Wdowin, M. Franus, R. Panek, L. Badura, W. Franus, The conversion technology of fly ash into zeolites. Clean Techn. Environ. Policy **16**(6), 1217–1223 (2014)
81. Q. Wang, D. O'Hare, Recent advances in the synthesis and application of layered double hydroxide (LDH) nanosheets. Chem. Rev. **112**(7), 4124–4155 (2012)
82. K.T. Chen, J.X. Wang, Y.M. Dai, P.H. Wang, C.Y. Liou, C.W. Nien, J.S. Wu, C.C. Chen, Rice husk ash as a catalyst precursor for biodiesel production. J. Taiwan Inst. Chem. Eng. **44**(4), 622–629 (2013)
83. K. Yan, X. Xie, J. Li, X. Wang, Z. Wang, Preparation, characterization, and catalytical application of Mg coal hydrotalcite-like compounds. J. Nat. Gas Chem. **16**(4), 371–376 (2007)
84. K. Hosni, E. Srasra, Simplified synthesis of layered double hydroxide using a natural source of magnesium. Appl. Clay Sci. **43**(3–4), 415–419 (2009)
85. P. Kunecki, R. Panek, M. Wdowin, W. Franus, Synthesis of faujasite (FAU) and tschernichite (LTA) type zeolites as a potential direction of the development of lime Class C fly ash. Int. J. Miner. Process. **166**, 69–78 (2017)
86. P. Kunecki, R. Panek, A. Koteja, W. Franus, Influence of the reaction time on the crystal structure of Na-P1 zeolite obtained from coal fly ash microspheres. Microporous Mesoporous Mater. **266**, 102–108 (2018)
87. G.N. Muriithi, L.F. Petrik, W.M. Gitari, F.J. Doucet, Synthesis and characterization of hydrotalcite from South African Coal fly ash. Powder Technol. **312**, 299–309 (2017)
88. T. Wajima, Synthesis of hydrotalcite from bittern, and its removal abilities of phosphate and nitrate. Int. J. Chem. Eng. Appl. **6**(4), 228 (2015)
89. Y. Kuwahara, T. Ohmichi, T. Kamegawa, K. Mori, H. Yamashita, A novel conversion process for waste slag: Synthesis of a hydrotalcite-like compound and zeolite from blast furnace slag and evaluation of adsorption capacities. J. Mater. Chem. **20**(24), 5052–5062 (2010)
90. R. Galindo, A. López-Delgado, I. Padilla, M. Yates, Synthesis and characterisation of hydrotalcites produced by an aluminium hazardous waste: A comparison between the use of ammonia and the use of triethanolamine. Appl. Clay Sci. **115**, 115–123 (2015)
91. R. Galindo, I. Padilla, R. Sánchez-Hernández, J.I. Robla, G. Monrós, A. López-Delgado, Production of added-value materials from a hazardous waste in the aluminium tertiary industry: Synergistic effect between hydrotalcites and glasses. J. Environ. Chem. Eng. **3**(4), 2552–2559 (2015)
92. P.L. Linda, D.O. Okanigbe, A.P.I. Popoola, O.M. Popoola, Characterization of density separated mullite rich tailings from a secondary copper resource, a potential reinforcement material for development of an enhanced thermally conductive and wear resistant ti-6al-4v matrix composite, in *The proceedings of the 60th International Conference of Metallurgist*, Canada, 2021
93. D.O. Okanigbe, Production of copper and copper oxide nano-particles from leach solution of low grade copper smelter dust, 2019
94. F. Bakhtiari, Synthesis and characterization of tenorite (CuO) nanoparticles from smelting furnace dust (SFD). J. Min. Metall. Sect. B. **49**(1), 21–21 (2013)

Chapter 12
Preparation and Characterization of Hydrotalcite-Derived Material from Mullite-Rich Tailings (II): CO_2 Capture from Coal-Fired Thermal Power Plants

Daniel Ogochukwu Okanigbe and Shade Rouxzeta Van Der Merwe

12.1 Introduction

With an increase of about 2.7%, or 60% greater than that of the late twentieth century, CO_2 is thought to be the main greenhouse gas causing global warming [1]. Therefore, there is now a global consensus on the control and decrease of CO_2. For instance, South Africa (SA) is one of the nations that is severely impacted by carbon emissions; the nation is the top emitter of CO_2 in Africa and is included among the top twelve emitters globally [2], as depicted in Fig. 12.1a–c.

The energy and manufacturing industries, which emit significant volumes of CO_2 into the atmosphere, boost the nation's emissions. For instance, it was estimated that SA released 367.6 million tons of CO_2 in 2011, and this number increased by almost 30% in 2015. As seen in Fig. 12.2, coal combustion produces the majority of SA's CO_2 emissions [4]. Future projections indicate that CO_2 emissions will progressively rise unless steps are taken to counteract this trend, such as developing carbon-neutral technologies that can mitigate this issue or incorporating CO_2 capture technologies into major sources of anthropogenic CO_2 emission, like coal-fired thermal power plants [5].

D. O. Okanigbe (✉)
Department of Chemical, Metallurgical and Materials Engineering, Faculty of Engineering and the Built Environment, Tshwane University of Technology, Pretoria, South Africa

Pantheon Virtual Engineering Solutions, Nigel, South Africa
e-mail: okanigbedo@tut.ac.za; okanigbeogochukwu@gmail.com

S. R. Van Der Merwe
Department of Mechanical and Mechatronics Engineering, Faculty of Engineering and the Built Environment, Tshwane University of Technology, Pretoria, South Africa
e-mail: vandermerweR1@tut.ac.za

D. O. Okanigbe, A. P. Popoola (eds.), *Resource Recovery and Recycling from Waste Metal Dust*, https://doi.org/10.1007/978-3-031-22492-8_12

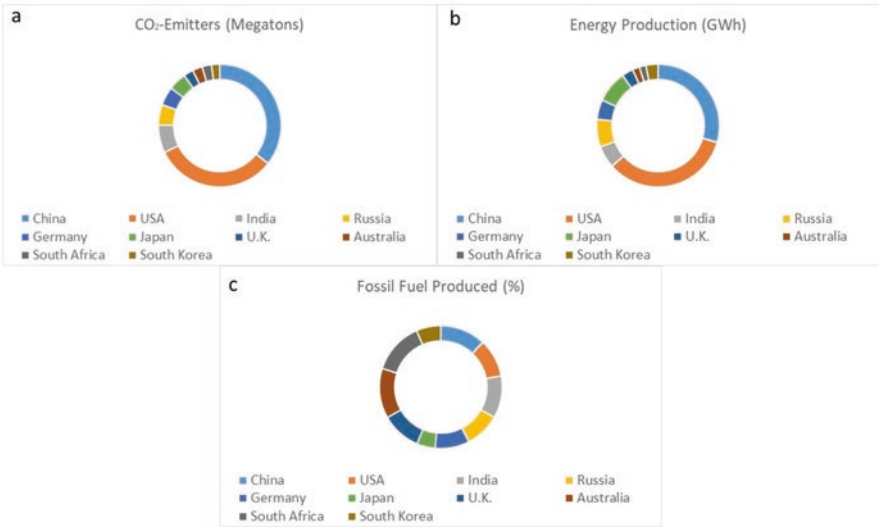

Fig. 12.1 (**a**) World's largest CO_2-emitting coal-fired power plants, (**b**) energy production, (**c**) fossil fuel produced by country as adapted from Yoro and Sekoai [3]

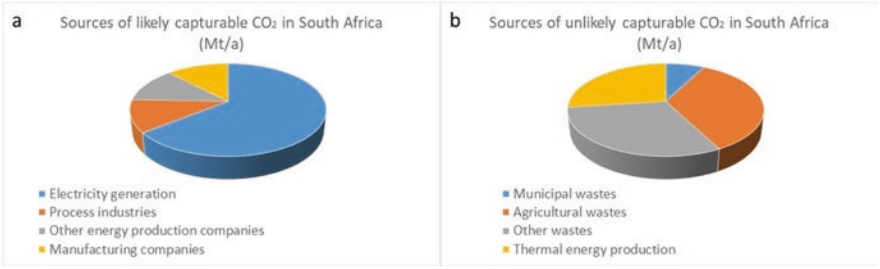

Fig. 12.2 Sources of CO_2 emissions in SA [3, 6, 7]

Therefore, wet absorption, membrane separation, and cryogenic fractionation are only a few of the CO_2 capture techniques that researchers around the globe are interested in for coal-fired power plants [8–11]. These technologies do have certain drawbacks, though, including high cost, high energy usage, and the emission of toxic by-products [12, 13]. It follows that there is a clear demand for more affordable and energy-efficient separation and capture methods. As a result, new methods for post-combustion capture, like adsorption, are constantly being investigated [14].

A particularly interesting alternative approach for trapping CO_2 is adsorption on solid sorbents [15]. There are currently several promising solid sorbents in development. According to Lee and Park [16] and Creamer and Gao [17], they can be broadly divided into carbonaceous materials (such as activated carbons, ordered porous carbons, activated carbon fibers, and graphene) and non-carbonaceous materials (such as zeolites, hydrotalcite, silica, metal-organic frameworks and porous polymers, alkali metals, and metal oxide carbonates). The ability of coal fly ash (CFA), an

abundantly produced incombustible aluminosilicate waste during the burning of pulverized coal in thermoelectric power plants, to capture CO_2 has also been documented [18–20]. CFA is not thought as a substantial sorbent in and of itself.

However, by employing it as a widely accessible, inexpensive feedstock to create a variety of solid porous materials for CO_2 capture, its CO_2 collecting capability can be increased [20]. For example, potassium-based sorbents [21], activated carbon [22], sodium silicate sorbents [23], and mesoporous silica materials (such as MCM-41 [24]) have all been created using CFA for high-temperature CO_2 capture. A developing area of research involves creating CO_2 aluminosilicate sorbents such as zeolites [25] and hydrotalcites (HT) [26] from CFA waste [27]. This method may also represent a superior process choice that does not endanger life or health and has the potential to improve waste management procedures.

The layered crystal structure of HT, which are magnesium-aluminum hydroxycarbonates, exists in a variety of isostructural and polytype forms [28] and is created by the periodic stacking of positively charged $(M^{2+}, M^{3+})(OH)_6$ octahedral layers similar to the structure of brucite $(Mg(OH)_2)$ and negatively charged interlayers made up of anions and water molecules. Although utilizing pure chemicals raises their production costs, HT are easily made in the laboratory using analytical-grade chemicals. This eliminates the challenges brought on by many anions in the structural matrix and makes it easier to identify trends and characteristics. This drawback has led to investigations in the synthesis of HT from alternative sources of starting materials. The alternative raw materials for synthesizing HT include natural dolomite [29] and bittern [30], but also industrial wastes such as blast furnace steel slag [31], aluminum slag [32–34], oil shale ash [35], and more recently CFA [26, 36].

The difficulty in synthesizing aluminosilicate sorbents like zeolites and/or HT from coal fly ash is that it is unclear how metal oxides from the raw CFA will affect these materials' structural properties. The presence of iron oxides is also anticipated to be crucial for the use of waste copper dust (WCD) as CO_2 adsorbents, while it is unclear how much the iron concentration affects the hydrotalcites'ability to adsorb. In this view, further research is still needed to fully grasp the issue of how to classify CFA in terms of the primary chemical constituents that affect their capacity to trap CO_2.

Neveling [37], provided a breakdown of the rate of WCD deposition during copper pyrometallurgy, near a smelter and it's environ in South Africa. According to the author WCD deposition is significant constituting a nuisance to the environment; a situation that provoked study on the pre-treatment of WCD with the gravity separation technique [38, 39]. This pre-treatment study produced tailings rich in mullite, herewith referred to as mullite-rich tailings (MRT). The potential of using this MRT to produce a solid sorbent for CO_2 capture is yet to be reported in literature.

Hence, the proposed study will aim at preparing and characterizing HT from MRT to capture CO_2 from coal-fired thermal power plants. The proposed study will also make efforts to clarify how properties of the produced HT and their capacity to capture CO_2 are influenced by macro-component composition of MRT from the density separated WCD. These properties and behavior of the produced HT for CO_2 capture under equilibrium and dynamic settings will be compared.

12.2 Problem Statement

With regard to cost effectiveness and energy efficiency, research into the production of solid sorbents from waste materials to absorb CO_2 has recently experienced expansion in the coal-fired thermal power plants industry. But the following problems still demand attention:

12.2.1 Economic Problems

Financial limitations have been the biggest obstacle to the adoption of carbon capture and storage technology (CCS). Depending on the CO_2 collection technique employed, the cost of integrating CCS in power systems varies between 30% and 70% [40, 41]. Maver [42] shown that the main obstacles to CCS adoption internationally are economic, social, and legal in nature. Economic hurdles arise from the fact that CCS is expensive and cannot be adopted by the majority of poor nations.

Nevertheless, SA is one of the quickly emerging countries with strong economic structures and regulations that will allow it to successfully adopt CCS in its coal-fired power stations. The deployment of CCS technology in SA has also been met with some skepticism; it has been argued that doing so will jeopardize the nation's efforts to create renewable and sustainable energy sources because they also call for significant financial incentives from the government [42]. However, the CO_2 produced by the nation's coal-fired thermal power plants is posing a number of problems in terms of environmental pollution and health risks.

In order to regulate this technology in SA, regulatory frameworks must be put in place [43]. A lack of funding for enforcement, a low priority for enforcement, an ineffective administrative structure, issues with the complaint-driven system used to enforce the law, and the minimal deterrent effect of sanctioning penalties are some other issues encountered when establishing regulatory frameworks that will oversee this technology.

So, one method to save costs is to look at the unit processes that make up key components of these technologies. For example, when HT is synthesized in the lab with analytical-grade chemicals, this removes the challenges brought on by many anions in the structural matrix and makes it easier to identify trends and features. However, using pure chemicals drives up the cost of manufacture [44].

12.2.2 Environmental Problems

There are a number of environmental issues with CCS, including the potential for CO_2 leaks to contaminate groundwater and the possibility that the sequestered CO_2 could trigger earthquakes owing to pressure buildup [45]. If the sequestered CO_2 is

kept in subsurface rocks, it may seep into the atmosphere, worsening the effects of climate change. Additionally, if stored underground, leaking could have a severe impact on the quality of the soil, trees, and other vegetation [46]. This problem could be solved in SA because, in addition to being stored in subsurface rocks, the captured CO_2 can also be put into the basins that are available, as stated in the earlier chapters of this study. There are numerous geological formations and unmineable coal resources in SA where captured CO_2 can be stored safely for the environment [47].

12.2.3 Social Problems

Because of the need for significant research and the fact that CCS is a relatively new technology in SA, its introduction may rekindle public debate. It is not fully understood how it will affect the environment and people in the long run. To highlight its benefits, such as the reduction of CO_2 emissions and environmental degradation, public awareness is necessary. This might then pique the interest of numerous parties, which might help it become a reality in SA [48].

12.3 Research Objectives

12.3.1 Main Objective

The preparation and characterization of hydrotalcite-derived material from mullite-rich tailings for CO_2 capture from coal-fired thermal power plants will be the main objective of this project.

12.3.2 Sub-Objectives

The main objective will be achieved by the following sub-objectives:

1. Characterization of the waste copper dust (WCD)
2. Thermodynamic modeling of the heat-treated WCD
3. Oxidative roasting of WCD
4. Density separation of WCD
5. Optimization of HT_{MRT} preparation
6. Characterization of HT_{MRT}
7. Comparative study of structural properties of synthesized HT_{MRT} versus commercial HT
8. CO_2 capture studies of HT_{MRT}

A. Determine effect of molar ratio
B. Determine effect of temperature
C. Determine effect of calcination
D. Determine effect of diluted CO_2 and moisture on sorption/desorption
E. Determine regeneration of developed sorbents

12.4 Research Hypotheses

The following can be hypothesized based on the scientific hypothesis (model) created to address the difficulties identified:

A good understanding of the macro-component composition of MRT from WCD and how it influences the produced HT will assist with optimizing its CO_2 capturing capacity.

The use of it for the commercial manufacture of solid adsorbent will assist to alleviate ecological and worldwide environmental concerns.

12.5 Significance of Study

The significance of this study are detailed as follows:

Application of hydrotalcite-like material from WCD (HT_{MRT}) for CO_2 capture:

One of the many uses for hydrotalcite-like material is the industrial-level CO_2 capture capabilities at coal-fired thermal power plants.

The HT_{MRT} components' ability to capture CO_2

The selection of MRT and its accessibility, the function and contribution of the MRT element constituent for an HT structural feature, and their role in CO_2 capture led to additional feasibility studies on the creation of an HT-like material from another material-containing MRT-like elements.

Improving the process for creating an HT-like material from MRT:

Laying the groundwork for the best method of creating an HT-like material from MRT for next applications and crystal structure research.

The use of materials similar to HT in CO_2 capture:

There will be clarity regarding the role of the HT_{MRT} in the CO_2-capturing process based on the results that will be collected.

Industrial-scale effects of the use of HT-like materials as solid adsorbents:

Analyze the viability of employing HT-like materials from MRT as a solid adsorbent in an industrial-scale CO_2 capture process.

12.6 Literature Review

12.6.1 Introduction

It is clear that SA, a rapidly developing nation with a heavily coal-dependent energy budget, has the capacity to implement CCS in the power industry. The largest emitting sources, including coal-fired power plants that produce electricity, which are a major emitting source, have the ability to capture CO_2. The potential for using this technology in SA's electricity sector is illustrated by the establishment of the South African Center for Carbon Capture and Storage (SACCCS). The global adoption of CCS faces a number of challenges. However, it is clear that SA, a member to the Kyoto Protocol, is a nation with a strong commitment to sustainable and renewable energy.

SA is focusing on important sources of CO_2 emission, such as the nation's coal-fired thermal power plants, in an effort to reduce its carbon footprint. Furthermore, it has mandated SACCCS to oversee the implementation of CCS rules and has incorporated them into its legislation. The immense potential for deploying CCS in the nation's coal-fired thermal power facilities is made abundantly obvious by this. In fact, the urgent needs for reducing CO_2 emissions need research in SA on clean and sustainable energy technologies like CCS.

For the installation of CCS in SA's coal-fired power stations, the following suggestions were made:

1. Due to budgetary constraints, a lack of frameworks, and a lack of technical skills, the installation of CCS has stalled in South African coal-fired power stations. However, this obstacle can be solved by utilizing solid, affordable composite adsorbents, which have recently been demonstrated to be commercially viable, to enhance CCS operations.
2. CO_2 capture heavily relies on chemical absorbents like monoethanolamine. A chemical absorbent with a higher loading capacity, such as amine 2-amino-2-methyl-1-propanol (AMP). It should be utilized if the absorption technique is required for the post-combustion CO_2 capture from these South African power plants due to some restrictions on the solvent capacity of those systems.
3. Given the widespread adoption of post-combustion CO_2 capture technology, its overall system performance with reference to SA's coal-fired power plants should be evaluated using experimental data from pilot plants at these power plants, and these data should be checked for accuracy.

Therefore, the goal of this literature review is to identify the knowledge gaps in this field of study and, using the knowledge gained, to define a research focus for developing a practical and energy-efficient method for CO_2 capture in SA. The following sub-sections will be taken into account in order to accomplish this objective:

1. A review of publications on the formulation of problems and solutions.
2. A review of articles on the South African topic of preparation and characterization of hydrotalcite-derived material from waste metal dust for CO_2 capture from coal-fired thermal power plants.
3. A review of international papers on the preparation and characterization of hydrotalcite-derived material from waste metal dust for the capture of CO_2 from coal-fired thermal power plants.
4. An analysis of articles on technological CO_2 capture routes.

12.6.2 Review: Past and Current Publications

12.6.2.1 A Review of Works on the Definition of Problems and Formulation of Solutions

Problem definition

The majority of hydrogen is produced via the steam methane reforming (SMR) process with a catalyst made of Ni/Al_2O_3 at temperatures between 750 and 900 °C, pressures between 50 and 600 psig. The sorption-enhanced reaction process (SERP), which employs a combination of CO_2 adsorbent and SMR catalyst, can increase the production of hydrogen [49]. The creation of an adsorbent with a high CO_2 working capacity at a fairly high temperature of 300–500 °C is a crucial need for the commercial application of the SERP. At room temperature, zeolite A, zeolite X, and activated carbon are extensively utilized as CO_2 adsorbents; however, at high temperatures (>500 °C), these materials perform poorly as CO_2 adsorbents. These adsorbents are therefore insufficient for the applications.

For CO_2 adsorption at high temperatures, the adsorbent should have a number of distinctive characteristics [50]. Significant volumes of CO_2 must be adsorbed by the adsorbent at high temperatures with desired adsorption/desorption kinetics. Additionally, regular adsorption/desorption cycles are necessary to maintain the CO_2's adsorption capacity. Most high-temperature CO_2 adsorbents are made of alkali metal oxides, which use their basic characteristics to absorb acidic CO_2.

The basic properties of alkali metal oxides like CaO, MgO, and Al_2O_3 make them ideal for adsorbing CO_2 at high temperatures. Recent reports suggest that hydrotalcite-like compounds are effective adsorbents for CO_2 adsorption at high temperatures [49, 51]. Particularly, the family of solid super bases known as layered double hydroxides (LDH) that contain magnesium and aluminum is effective catalyst for aldol condensations, epoxidations, and alkene isomerizations [52–56]. Additionally, the Mg/Al ratio affects the surface basicity of the calcined hydrotalcites, and the ratio also affects the number of basic sites [57].

Solution Formulation

Hydrotalcite is a double-layered substance made up of a layer that is positively charged and brucite-like and a layer that is negatively charged. Trivalent cations replace divalent cations in the brucite structure, generating a positive charge that is balanced by an anion already present in the interlayer. Its usual molecular formula is $[M(II)_{1-x}M(III)_x(OH)_2]^{n+}A_{x/n}^{n-}$ yH_2O wherein M(II) = Mg, Cu, Ni, Co, Mn, Zn; M(III) = Al, Fe, Cr, V; An− is any interlayer anion such as CO_3^{2-}, Cl^-, NO^{3-}, SO_4^{2-}, and $x = 0.1–0.33$ [58].

The type of cation, M^{2+}/M^{3+} ratio, type of anion present in the interlayer, and activation circumstances all affect the hydrotalcite's basicity. For instance, mixed metal oxides with strong basicity and high surface area are produced when the hydrotalcite is calcined at temperatures exceeding 450 °C. As a base catalyst or catalyst support, it is therefore versatile [59].

In order to employ them as adsorbents for CO_2 adsorption at high temperatures, a variety of Mg/Al-based hydrotalcites should be created utilizing different manufacturing methods, Mg/Al ratios, and K_2CO_3 amounts. It is therefore important to investigate the link between preparation techniques and CO_2 adsorption capacity at high temperatures in order to produce the best hydrotalcite with a high CO_2 adsorption capacity suitable for the adsorbent in the sorption-enhanced reaction process.

12.6.2.2 Review of Publications on Technological Routes for CO_2 Capture

Absorption Technology

Chemical solvents are employed in the absorption technology to absorb CO_2.

It is a thoroughly studied, reliable, and established technology that sees extensive industrial use. There are two types of absorption: chemical and physical. The absorption of CO_2 from the flue gas happens at high pressure and low temperature in the former, which is dependent on temperature and pressure. In contrast, the latter relies on an acid-base neutralization reaction employing basic solvents to absorb CO_2 from the flue gas [60–63]. The three main types of solvents that are most frequently employed for CO_2 absorption from flue gases are amines [64], cooled methanol [65], and ammonia solution [66]. Despite being a proven technology for CO_2 capture, absorption technique uses solvents, which makes it expensive, corrosive, and energy-intensive due to high energy needs during solvent regeneration.

Additionally, because this method uses liquid absorbents in power plants, it is not well suited for usage in the coal-fired power plants in SA [67]. Liquids, like monoethanolamine, react with CO_2 easily. While the method can be used to remove CO_2 from the resulting liquid, it is not financially feasible for use in power plants. The method may cost 30% of the country's annual increase in gross domestic product if it were implemented at every power plant in SA [68]. It is necessary to look into less expensive techniques for capturing CO_2 and hydrocarbon emissions with low energy costs.

Membrane Separation Technology

The authors of the study [69] looked into CO_2 capture using membranes and came to the conclusion that the use of membranes to capture CO_2 from flue gases can only be competitive if the flue gas's CO_2 concentration is greater than 10%. The idea behind CO_2 capture utilizing membranes is that the physical or chemical interactions between the CO_2 gas and the membrane might differ, allowing one gas to move through the membrane more quickly than the other. The membrane modules can be utilized as a typical membrane separation unit or as a gas absorption column [70–74].

It is well known for its low selectivity, high energy requirements during separation, and relative youth of the membrane technology [75–81]. This presents a significant drawback for membrane-based CO_2 capture [82–84]. Furthermore, this method [85, 86] employs either organic polymeric membranes or inorganic ceramic membranes. Ceramic membranes are relatively pricey, but it is highly challenging to pass CO_2 in the flue gas through a single-stage ceramic or polymeric membrane with a high degree of separation and a high purity of CO_2 at the same time. This is yet another significant drawback of this CO_2 collecting method.

Due to the high cost of using ceramic membranes or fouling in the case of polymeric membranes, post-combustion CO_2 capture technology is not viable for adoption in South African coal-fired power plants. The polymeric membranes may plasticize under the impact of CO_2 in the membrane while having great selectivity and permeability for CO_2 capture due to their extremely low heat stability. As a result, the use of membrane technology for post-combustion CO_2 capture in power plants like the coal-fired thermal power plants in SA is limited. As an alternative to the use of membranes for post-combustion CO_2 capture, effective CO_2 capture methods with cheap cost and high CO_2 capture potential, as well as selectivity, need to be further researched [87].

Cryogenic Separation Technology

The condensation and chilling principle form the foundation of the cryogenic separation method for CO_2 capture [88–92]. It is mostly utilized in CO_2 capture systems where there is a high concentration of CO_2 in the gas streams. Because the CO_2 stream from power plants is more diluted, cryogenic separation cannot be employed to capture CO_2 from those facilities [93, 94].

The fact that this technique is energy-intensive, or that it uses a lot of energy to separate CO_2, is another drawback. This CO_2 separation technology is challenging to apply in SA due to the low CO_2 concentration from the country's coal-fired power facilities. The ideal conditions for cryogenic separation are also those with extremely low temperatures [95–101].

However, coal-fired power stations find it challenging to reach the extremely low temperatures required for this method of CO_2 collection. The majority of cryogenic separation methods involve a succession of compression, chilling, and separation

phases to separate different components in gas mixtures [102]. In cryogenic separation operations, impurities cause the phase transition temperature of CO_2 to drop as low as −80 °C. In this situation, the energy cost of refrigeration rises significantly, and there is a high likelihood of CO_2 frost production, which endangers the safety of the equipment [102–105].

It is necessary to look into another technique that is both commercially and environmentally feasible.

Adsorption Technology

Chemical and environmental processes make substantial use of the adsorption technology. For the purpose of CO_2 capture, it makes use of a variety of adsorbents, including zeolites, activated carbon, polyaspartamide, metal oxides, porous silicates, metal-organic frameworks, and chitosan [106]. However, when employed in power plants, CO_2 capture by adsorption employing activated carbon fibers and a carbon fiber component is thought to be an effective method [107].

Adsorption technology is gaining popularity as a result of its attributes, which include low energy consumption, simple operation, inexpensive maintenance, and adaptability [108].

Temperature swing adsorption (TSA), one of the adsorption methods described in the literature, is a good method since it costs little and consumes little thermal energy. Incorporating it into coal-fired plants can therefore save operating costs [109]. For CO_2 capture, however, longer cooling and heating durations are necessary [110].

However, it has several disadvantages of its own, such as its sensitivity to input gas temperature. The flue gas may require further heat treatment to condition it before being injected into the VSA plant; this has an impact on the process's economics and separation efficiency. Since PSA uses a wide range of temperatures and pressures and uses little energy, it has emerged as a promising technology in recent years. Its minimal investment costs are an additional benefit [111].

Although the adsorption process has some drawbacks, such as slow kinetics and poor heat transfer, particularly in tightly packed beds, these drawbacks are significantly outweighed by its benefits [112]. This method has potential since it makes it simple to regenerate the adsorbent using pressure modulation while using less energy in the coal-fired power plants in SA.

Solid adsorbents can be utilized to collect CO_2 emissions from coal-fired power stations.

Although less developed than the absorption process, it is less expensive, requires little energy, and employs non-corrosive materials. Different solid support systems, including activated carbon, zeolites, carbon molecular sieves, and polymeric adsorbents such amine-grafted polyaspartamide, can be used to produce CO_2 adsorption [113]. In the studies mentioned by Chaffee et al. [114], solid adsorbents are used physically absorb CO_2 with less energy than other CO_2 capture devices.

With equivalent pressure in the feed and product streams, physical CO_2 adsorption only needs around 0.09 KWh/kg CO_2, which is significantly less energy than chemical CO_2 adsorption, which needs about 0.34 KWh/kg CO_2. Yang et al's [115]. investigation into pressure swing adsorption methods for CO_2 capture using activated carbon and zeolite 13X and modeling the physical adsorption of CO_2 using solid physical adsorbents led to the conclusion that the adsorption technology is less expensive and less energy-intensive for CO_2 capture.

When employing molecular sieves and activated carbon materials, Othman et al. [116] corroborated similar findings. Rivas et al. [113] indicated that solid adsorbents are more efficient than liquid systems. For instance, solid adsorbents function better when the partial pressure of CO_2 is higher than 50 KPa [117–120]. However, when combined with chemical absorbents, liquid absorbents stabilize. Since CO_2 capture from these power plants must be done at high pressures and since the adsorption of gases is encouraged by higher pressures and lower temperatures, adsorption technology will be perfect for efficient CO_2 capture.

Physical adsorbents, which have a strong affinity for CO_2, have also been shown to capture CO2. However, the downstream procedure causes the gas's purity to decline [121]. The best physical adsorbents to use for CO_2 capture, according to the research, are those based on polymers and activated carbon. They generate a stream of CO_2 that is between 75% and 80% pure and recover 90% [122]. Adsorption systems do not require a lot of energy, and their recovery is far lower than that of chemical absorption techniques [123].

The previous paragraphs made reference to how expensive and energy-intensive these technologies are [124]. Consequently, a cost- and energy-efficient strategy is required.

12.6.2.3 Review of Papers on Various Fly Ash-Based Sorbent Types That Have Been Prepared and Characterized

Potassium-Based Sorbents

The potential of potassium-fly ash (K-FA) sorbents for high-temperature CO_2 sorption was examined in the work of Sanna and Maroto-Valer [21]. Coal fly ash was used as a source of silica and aluminum for the production of K-FA. To test the synthesized materials' ability to trap CO_2, Li_2CO_3 and $Ca(OH)_2$ were also added.

The findings demonstrated that temperature had a significant impact on the K-FA sorbents' ability to absorb CO_2, with a CO_2 uptake of 1.45 mmol CO_2/g sorbent for K-FA 1:1 at 700 °C. Li_2CO_3 (10 wt%) improved the CO_2 sorption, allowing the K-FA 1:1 to absorb 2.38 mmol CO_2/g sorbent at 700 °C for 5 minutes. In comparison with previously created Li-Na-FA (2.54 mmol/g) and Li-FA (2.4 mmol/g) sorbents, this sorption was determined to be similar. Additionally, sorption and desorption were enhanced by the addition of 10% Li_2CO_3.

The findings suggested that the creation of the K-Li eutectic phase, which favors the diffusion of potassium and CO_2 in the material matrix, is responsible for the

higher uptake of CO_2 and faster reaction rates in the presence of K-FA. The cyclic testing revealed that throughout the course of 10 cycles, the CO_2 uptake and reaction rates were stable for the K-FA materials.

Activated Carbon

In the research conducted by Alhamed et al. [22], activated carbon (AC) treated with KOH at a higher temperature and assessed for CO_2 capture effectiveness were made from fly ash (FA), which was produced in desalination and power plants. The N_2 adsorption isotherm was used to measure the morphological properties of FA, including BET-specific surface area (SSA), pore volume, pore diameter, and pore size distribution (PSD). Thermogravimetric analysis was used to determine the CO_2 adsorption capacity and isotherms of CO_2 over AC at various temperatures.

By activating at a KOH/FA ratio of 5 at 700 °C and activating for 2 hours, it is possible to get a BET SSA of 161 m^2g^{-1} and an adsorption capacity of 26 mg CO_2/g AC. Therefore, there is a lot of potential for making AC from FA, which will help to lessen the problem of landfills and global warming.

Sodium Silicate Sorbents

Na-silicates have been suggested as effective sorbents at room temperature; however, Sanna and Maroto-Valer [23] claim that their potential as high-temperature CO_2 sorbents has not yet been investigated. In this study, the CO_2 sorption of sodium silicates made from fly ash was assessed at 500, 600, and 700 °C. On CO_2 sorption, the effects of 2–12 vol% moisture, 12.5–100 vol% CO_2, and CO_2 sorption boosters were also assessed.

The findings show that the CO_2 sorption capacity and regeneration temperature were considerably influenced by the carbonate: silica ratio utilized in the sorbent synthesis. The production of metastable sodium silicate phases, which led to greater CO_2 uptake, made calcination at 800 °C preferable. Na-FA 0.5:1 was chosen as the preferable developed sorbent because it was able to sustain CO_2 sorption/desorption capability after five cycles (compared to 1:1 and 1.5:1). At post-combustion conditions (12.5 percent CO2, 12% H_2O, and 700 °C), NA-FA 0.5:1 had an excellent capacity. The 20% CO_2 sorption was improved by the addition of 20% Li_2CO_3.

Overall, the CO_2 collection capacity and recyclability of the Na-FA 0.5:1 sorbent were equivalent to those of other high-temperature sorbents.

Mesoporous Silica Materials

In the study by Panek et al. [24], the researchers used silicate filtrate, a by-product of hydrothermal zeolite manufacturing, to create mesoporous silicate molecular sieve, MCM-41, from pulverized coal fly ash (PFA). In this study, rice husk ash was

likewise employed as a comparator, but sodium hydroxide was fused with it in a manner reminiscent of other findings that used PFA as a precursor for the synthesis of MCM-41 to create the silicate filtrate.

The MCM-41 samples have greater pore volumes dominated by mesopores (0.92–1.13 cf. 0.88 cm^3g^{-1}) but are otherwise chemically and mineralogically comparable to a commercially available sample. The ash-derived MCM-41 samples displayed higher uptakes than the commercial sample after polyethyleneimine (PEI) impregnation for CO_2 capture, with the maximum achievable PEI loading of 60 wt.% PEI (dry basis) before particle agglomeration occurs, corresponding to approximately 13 compared to 11 wt.%, the latter being comparable to earlier reports in the literature.

The PFA sample that exhibits the quickest absorption kinetics to reach 90% of equilibrium had the biggest mesopore volume, measuring 1.13 cm^3g^{-1}. Production costs for MCM-41 derived from PFA are predicted to be significantly lower than for MCM-41 derived from RHA because PFA-derived MCM-41 uses a waste silicate solution for hydrothermal preparation and no prior preparation is required. This is true even if ash is used, as it is for the RHA-derived MCM-41 used here.

12.6.2.4 CO_2 Aluminosilicate Sorbents

Zeolites

In the works of Liu et al. [25], the authors used an alkali fusion technique to create Zeolite A and A + X mixes from coal fly ash imported from China. Both of the materials were crystalline and repeatable, according to X-ray diffraction. Pure zeolite A particles have a cubic morphology, according to scanning microscopy, but the combination exhibits intergrowth of cubic and pyramidal crystals.

A + X combination had a surface area of around 330 m^2/g, which is greater than zeolite A but less than ordinary X zeolite. Adsorption isotherms for CO_2 and N_2 were measured, and the dual-site Langmuir equation was used to fit the data. Then, in a nine-step cycle, these zeolites were evaluated for CO_2 absorption at various temperatures. Both the zeolite A + X mixture and the zeolite A made from fly ash performed better in CO_2 capture from flue gas when compared to 13X zeolites at higher temperatures (90 °C) because they have stronger selectivity of CO_2 over N_2.

Hydrotalcites (HT)

According to Muriithi et al. [26], the authors noted that there is growing interest in the production of adsorbents such hydrotalcites (HT) from mineral waste, such as blast furnace slag. This paper describes a unique method for producing HT from fly ash, a common waste product of coal-fired power plants in SA.

The optimization procedure, which highlights the boundary conditions for this mineral phase's crystallization, is the second area of originality. The HCl content,

aging duration and temperature, pH during the aging process, and crystallization time and temperature were the variables examined for the optimization of HT synthesis from fly ash. The best synthesis conditions were as follows: 3 M HCl concentration, 30 minutes of aging, 65 °C of aging, 11.5 pH during aging, 12 hours of crystallization, and 70 °C of crystallization temperature. The exterior surface area and microporosity of HT were both quite high.

The majority of the morphological components of synthesized HT were submicron, plate-like particles. Except for the presence of calcite, the structural features of HT made from fly ash were comparable to those of HT obtained from analytical-grade chemicals. Under optimal process conditions that reduced the development of secondary undesirable mineral phases like calcite or hydrogarnet, a novel usage of waste South African Class F fly ash was as a suitable feedstock for the synthesis of high-quality HT.

12.6.2.5 Preparation and Characterization of Hydrotalcite-Derived Material from Various Feedstocks

Natural Dolomite

Dolomite is a naturally occurring double carbonate and a source of calcium and magnesium ions, according to Hosni and Srasra [29]. In their research, a straightforward process was used to create Mg-Al-CO_3 layered double hydroxide from dolomite feedstock. On their structure and textural qualities, the influence of synthesis parameters including the M^{2+}/Al^{3+} ratio, reaction temperature, and pH was investigated. X-ray diffraction, Fourier transform infrared spectroscopy, thermogravimetric analysis (TGA), and Brunauer, Emmett, and Teller (BET) measurements were used to determine the structural characteristics of the materials.

The authors came to the conclusion that dolomite can be processed into pure and well-crystalline phases of Mg-Al-CO3 LDH in an aqueous Na_2CO_3 solution. That a key consideration was the preparation's pH. Pure LDH was generated at a pH of 9.5. The LDH's crystallinity dropped below this threshold. Conditions that are quite alkaline do not seem to be favorable for the synthesis. The ideal dolomite/Al molar ratio was approximately 1. Above this ratio, brucite was generated. Low dolomite/Al ratios resulted in products with poor crystallinity. A factor that was thought to be crucial for regulating crystallinity and particle size was aging temperature. According to experimental research, hydrotalcite must be at a high temperature to form a well-crystalline phase.

Bittern

An assessment of the viability of employing Class C fly ash for the synthesis of Faujasite (Type X) and Tschernichite (Type A) type zeolite materials is shown in the study by Kunecki et al. [30]. Syntheses were performed to produce the well-formed

zeolites. The variables were as follows: water, the filtrate (post-reaction solutions obtained during the hydrothermal synthesis of zeolites rich in Si), the ratio of fly ash to NaOH, and the quantity of aluminum foil added.

According to the analysis, three of the most efficient reactions (from which samples 21–23 were formed) took place in the following circumstances: the amounts of H_2O, filtrate, and aluminum foil added were 100, 100, and 50 ml for each of the three reactions, respectively. The ratio of NaOH to fly ash was 1.6, 2.0, and 1.25, with fusion temperatures of 550 °C for each of the three reactions, fusion times of 1 hour, and reaction times of 4 hours. The reaction temperature was 80 °C for each of the three reactions (for each of the three reactions).

"The three best zeolite materials (Samples 21–23) were submitted to mineralogical, chemical, and textural analytical characterization using X-ray powder diffraction (XRD), scanning electron microscopy–energy-dispersive X-ray spectroscopy (SEM-EDS), and X-ray fluorescence (XRF), Brunauer–Emmett–Teller (BET), to determine specific surface area and pore volume and size)." The produced zeolites, according to studies, have a Type A (Samples 21–22) and Type X (Sample 23) structure, as well as well-formed grains with isometric and cubic properties. The obtained zeolites' computed unit cell characteristics point to a cubic crystal system and are quite similar to the reference values for the structures of X and A type zeolites.

The ratio of SiO_2/Al_2O_3 in each of the three tested zeolite materials was as follows: 2.16, 1.98 and 2.41. For Samples 21–23, the specific surface area was 106, 104, and 256 m^2/g, respectively. The outcomes were comparable to the zeolite structures discovered in Class F fly ash. As a result, we can draw the conclusion that the Class C fly ash under analysis may also be a useful substrate for the synthesis of Type X and Type A zeolite materials.

Blast Furnace Steel Slag

The authors of this study by Kunecki et al. [31] reported the effect of time on the creation of the mineral structure of GIS Na-P1 zeolite. Aluminum and silica were obtained from thin microspheres. The material used in this project was created utilizing a prototype installation at a quarter-technical scale. X-ray diffraction (XRD), X-ray fluorescence (XRF), scanning electron microscopy equipped with a system of chemical composition analysis based on energy dispersive X-ray (SEM-EDS), volumetric adsorption analyzer, Fourier transform infrared spectroscopy (FTIR), and particle size analyzer were used to determine the chemical, mineralogical, and textural properties of the material (PSA).

The interesting and in some cases remarkable phenomena of the lattice parameters ripening as a function of time is demonstrated by experimental calculations based on Miller indices. With longer synthesis times, both the number of zeolites present and the unit cell characteristics (a, b, c, and volume) rise. With the use of the XRD and FTIR techniques, this process may be seen clearly. The finished product's structural, morphological, and textural characteristics suggest that it might be beneficial as an adsorbent for several kinds of environmental pollution.

Muriithi et al. [26] the synthesis of adsorbents such as hydrotalcites (HT) from mineral waste (e.g., blast furnace slag) is attracting growing attention. This paper describes an unique method for producing HT from fly ash, a common waste product of coal-fired power plants in South Africa. The optimization procedure, which highlights the boundary conditions for this mineral phase's crystallization, is the second area of originality.

The HCl content, aging duration and temperature, pH during the aging process, and crystallization time and temperature were the variables examined for the optimization of HT synthesis from fly ash. The best synthesis conditions were: 3 M HCl concentration, 30 minutes of aging, 65 °C of aging, 11.5 pH during aging, 12 hours of crystallization, and 70 °C of crystallization temperature. The exterior surface area and microporosity of HT were both quite high.

The majority of the morphological components of synthesized HT were submicron, plate-like particles. Except for the presence of calcite, the structural features of HT made from fly ash were comparable to those of HT obtained from analytical-grade chemicals. The waste Class F fly ash from SA was used in an innovative way to create high-quality HT under optimal processing conditions that reduced the production of secondary undesirable mineral phases like calcite or hydrogarnet.

Aluminum Slag

In this study by Wajima [32], hydrotalcite was created from bittern solution by adding $AlCl_3$ (the solution's Mg/Al molar ratio was 3), and its capacity to remove phosphate and nitrate from water was tested. Both bittern and seawater can be used to make hydrotalcite, although the product made from bittern has a higher hydrotalcite content than the one made from seawater. Higher than commercial hydrotalcite, the bittern product has phosphate and nitrate removal capabilities.

The experimental data are found to better fit the Langmuir than the Freundlich isotherm models when calculating the equilibrium adsorption capacity of the product for phosphate and nitrate ions. Because of the ion exchange process between chlorine and sulfate in the product, phosphate adsorption on the product reached saturation in 30 minutes and was essentially steady after that. Nitrate adsorption on the product increased in 15 minutes and then gradually decreased.

The main constituents of blast furnace slag (BFS) are CaO, SiO_2, Al_2O_3, MgO, and trace amounts of transition metals like Fe, Ti, and Mn, according to Kuwahara et al. in their study titled "A novel conversion process for waste slag: synthesis of a hydrotalcite-like compound and zeolite from blast furnace slag and evaluation of adsorption capacities" [33]. We successfully used the chemical method of acid-leaching and precipitation to create a hydrotalcite-like molecule from BFS.

After undergoing HCl acid-leaching, BFS was separated into hydrated silica with 92 wt.% SiO_2 and leaching solution containing other components, which provided a hydrotalcite-like product after further NaOH addition in a high yield. The result generated at 100 °C was determined to be a Ca-Al hydrocalumite complex by

XRD and chemical analysis. Its stoichiometric molar ratios are Ca: Al: Cl = 2: 1: 1, and it contains other metal cations in its structure.

The hydrotalcite-like compound had an elevated phosphate adsorption capacity of about 40 mg P/g, which was more than three times more than that of typical Mg-Al-based hydrotalcite. The phosphate adsorption capacity of the raw slag was 1.5 mg P/g. In addition, utilizing the remaining silica and a hydrothermal treatment lasting 6 hours at 100 °C, single-phase A- and X-type zeolites with high crystallinities and outstanding water adsorption capacities (247 and 333 mg g^{-1}, respectively) were effectively created. From the perspective of making efficient use of BFS, this conversion procedure, which enables us to create two distinct types of valuable materials from BFS at a cheap cost and with simple preparatory stages, is unquestionably advantageous.

According to Galindo et al. [34], due to environmental concerns, the powdered solid strapped in filter sleeves in the aluminum tertiary industry is currently disposed of in secure landfills. They are categorized as hazardous waste because they contain a lot of aluminum, either in the form of metallic aluminum or in compounds like aluminum nitride.

These substances have the ability to react with extremely little moisture, releasing toxic or dangerous gases like hydrogen and ammonia.

In three steps, the low-cost method described in this study allows for the complete recovery of this hazardous waste and the creation of two different added-value components. The trash is subjected to mild acid hydrolysis in the first step in order to produce an inert cake and a concentrated solution of aluminum. The subsequent steps involve synthesizing hydrotalcite from the resultant solution and using the cake to create transparent glasses based on the $CaO\text{-}Al_2O_3\text{-}SiO_2$ system. The products' characteristics show that the hydrotalcites can easily absorb anionic contaminants (molybdates), while the glasses offer better optical properties than those made by directly vitrifying the trash.

Oil Shale Ash

With the aid of ammonia and triethanolamine at pH 10, Galindo et al. [35] reported that hydrotalcite-like compounds were co-precipitated with dilute sodium hydroxide from an unconventional aluminum source: the aluminum waste produced by the tertiary aluminum industry. To compare results, these compounds were characterized using a variety of techniques (XRD, FT-IR, UV-vis-NIR, SEM, DTA-TG, and BET procedures).

Characterization of the products revealed considerable variations based on the choice of basic reagent. Products that co-precipitated with ammonia exhibited less crystal development, a higher internal surface area, and a structure that contained significantly more iron. Triethanolamine-derived products demonstrated how organic molecules entered the multilayer framework. These results were crucial for the development of waste treatment techniques that turned hazardous wastes made of aluminum into stacked double hydroxides, a product with additional value.

Coal Fly Ash

Muriithi et al. [26], by means of procedures including carbonation, dissolution, co-precipitation, and fluid transport mechanisms, natural weathering at coal power plants' ash dams results in the long-term chemical, physical, and geochemical changes in the ash. On the possibility for wet or dry ash dams to naturally collect carbon, very little information is currently known. This study compared a naturally occurring occurrence with accelerated ex-situ mineral carbonation of fresh fly ash to determine the degree of carbon capture in a wet-dumped ash dam and the mineralogical changes supporting CO_2 capture (FA). Sr, Ba, and Zr trace metals at significant concentrations were found in both fresh ash and weathered ash. However, it was discovered that weathered ash had more Nb, Y, Sr, Th, and Ba than fresh ash did.

Fresh ash is composed of quartz, mullite, hematite, magnetite, and lime from a mineral perspective; however, weathered and carbonated ashes also contained other phases like calcite and aragonite. The fresh FA was able to trap up to 6.5 wt% CO_2, and accelerated carbonation (done at 2 hours, 4 MPa, 90 °C, bulk ash, and a S/L ratio of 1) resulted in a 60% conversion of calcium to $CaCO_3$. On the other hand, it was discovered that over the course of 20 years of moist disposal of ash, 6.8 wt percent CO_2 was naturally carbonated.

Thus, the ash dumps' spontaneous carbonation is considerable and may be useful in extracting CO_2.

In their study, Gil et al. [36] described the co-precipitation method's use of aluminum recovered from saline slag wastes to synthesize hydrotalcite-like materials. Using a reflux system over a two-hour period, saline slags were chemically treated with 2 mol/dm^3 aqueous solutions of NaOH. With the help of cobalt, magnesium, and nickel nitrates, as well as Na_2CO_3, aluminum aqueous solutions were employed as precursors to create hydrotalcite-like materials with two different mole M^{2+}/Al^{3+} ratios, 2:1 and 4:1.

X-ray diffraction, thermogravimetric studies, nitrogen adsorption at 196 °C, and scanning electron microscopy were used to analyze the resultant solids. The CO_2 adsorption at 50, 100, and 200 °C was assessed under dry conditions after thermal treatment at 200 °C. The Mg: Al-2: 1 sample had a remarkable sorption capacity of 5.26 mmol/g at 80 kPa and 50 °C, which was significantly greater than the sorption capacities previously reported in the literature for hydrotalcites under comparable conditions.

The values of the Henry's law constants, which range from 0.01 to 4.20 mmol/kPag, were directly deduced from the adsorption isotherms at low pressures. Using the Clausius–Clapeyron equation, the isosteric heats of CO_2 adsorption were discovered to be between 5.2 and 16.8 kJ/mol.

Mullite-Rich Tailings

The WCD from SA was studied for particle size distribution, chemical, and morphological investigations in the work of Okanigbe, Popoola, and Adeleke [125]. The outcomes indicated that the majority of the dust's particles fall within the −53 μm size fraction.

Linda et al. [126] acknowledged that the high cost of metal powders like mullite will make it impractical to employ mullite for some engineering applications. As a result, they suggested obtaining mullite from WCD or its by-product (i.e., MRT).

Conclusion

Researchers concur that major emitting sources, such as coal-fired power plants that produce electricity, hold the key to the possibility for CO_2 collection. Researchers also concur that post-combustion CO_2 capture is the best method for capturing CO_2 for South African coal-fired power plants. The suitability is based on the simplicity of retrofitting capture equipment in the existing coal-fired power plants, according to the research reports. In support of this assertion, authors also concur that solid adsorbent adsorption technology will be more practical and cost-effective for CO_2 collection in South African coal-fired power stations.

According to reports on research into the use of solid adsorbents in the adsorption process, hydrotalcites has shown potential as a solid adsorbent for CO_2 capture, even at an industrial scale. The use of pure chemicals raises their production costs, despite the fact that it is simple to synthesize HT in the lab using analytical-grade chemicals, which remove the challenges brought on by many anions in the structural matrix and make it easier to identify trends and characteristics.

According to authors, producing HT from other sources of beginning materials can reduce the high production cost of HT to the bare minimum. The authors concurred that natural dolomite and bittern, as well as industrial wastes such blast furnace steel slag, aluminum slag, oil shale ash, and more recently coal fly ash, can be used as substitute raw materials for the synthesis of HTs.

According to authors, there are three key benefits of using waste materials like those listed in the previous paragraph to create CO_2 adsorbents like hydrotalcite. The first option is for copper smelting facilities to recycle their waste and sell the finished goods to power plants in order to store or release CO_2 emissions at a later time through changes in pressure or temperature. Second, recycling scrap metal dust would lessen the harm caused by disposing of it. Thirdly, employing the waste metal dust instead of coal fly ash will allow you to avoid spending money on dust management and disposal site restoration.

The influence of metal oxides conveyed from the raw coal fly ash has not been fully understood, according to scientists, which makes it difficult to synthesis aluminosilicate sorbents like HT and their structural features. The presence of iron oxides is predicted to be crucial for the use of coal fly ash as a CO_2 adsorbent, according to the scientists; however, it is unclear to what extent the iron concentration has a major impact on HT's adsorption ability. In this view, further research is still needed to fully grasp the issue of how to classify coal fly ash in terms of the primary chemical constituents that affect their capacity to trap CO_2.

Researchers from TUT produced HT by accident from the leach solution of copper WCD. Therefore, the authors concur that South African WCD was an appropriate feedstock for making high-purity HT, which should have good adsorption characteristics for CO_2 capture. The researchers did note, however, that metal oxides were transferred during the creation of HT from WCD. According to reports, as the heavy metal oxides reported to the concentrate during the density separation of WCD, the amount of heavy metal oxides in the tailings was reduced. Thus, there is a knowledge gap in the domain of making hydrotalcite from tailings rich in mullite from SA.

Consequently, the suggested research topic, "Preparation and Characterization of Hydrotalcite-Derived Material from Waste Metal Dust for CO_2 Capture from Coal-Fired Thermal Power Plants: South African WCD," came to be.

12.7 Methodology

12.7.1 Materials and Methods

12.7.1.1 Materials Description and Preparation

The elemental and mineralogical compositions of previously acquired WCD samples have been discussed in the literature (Okanigbe et al. [125]). This WCD from SA will be used as a starting material for the production of different HT_{MRT} grades.

12.7.1.2 Methods and Processes

As described in the next sub-sections, the WCD will first undergo gravity separation to produce tailings with different mullite contents.

Density Separation of WCD

The rotational bowl speed and fluidized water flow rate will be varied at three levels in order to separate the WCD on the basis of densities (Table 12.1). The test procedure for the density separation of the WCD is described in Table 12.2. Forty-five test samples will be produced after five passes of the separation (Table 12.3). These MRTs will serve as the raw material for making HT_{MRT}. The thesis by Okanigbe [38]

Table 12.1 Parameters measured for density separation experiment

S/N	Parameters	Low (0)	Medium (1)	High (2)
X_1	RBS (m/s^2)	60	90	120
X_2	FWFR (l/min)	3.0	4.5	6.0

Table 12.2 Test protocol for density separation of CSD

Tests	RBS (G)	FWFR (l/min)	Treatment combination (TC)
1	A	A	AA
2	A	B	AB
3	A	C	AC
4	B	A	BA
5	B	B	BB
6	B	C	BC
7	C	A	CA
8	C	B	CB
9	C	C	CC

Table 12.3 Test protocol for production of Mullite-Rich Tailings (MRT)

	Tests and tailings								
Passes	(1)	(2)	(3)	(4)	(5)	(6)	(7)	(8)	(9)
1	1(1)	1(2)	1(3)	1(4)	1(5)	1(6)	1(7)	1(8)	1(9)
2	2(1)	2(2)	2(3)	2(4)	2(5)	2(6)	2(7)	2(8)	2(9)
3	3(1)	3(2)	3(3)	3(4)	3(5)	3(6)	3(7)	3(8)	3(9)
4	4(1)	4(2)	4(3)	4(4)	4(5)	4(6)	4(7)	4(8)	4(9)
5	5(1)	5(2)	5(3)	5(4)	5(5)	5(6)	5(7)	5(8)	5(9)

includes specifics about the calculations that will be done prior to preparing the slurry that will be utilized for the density separation experimentation.

Synthesis of Hydrotalcite HT_{MRT}

During the optimization process for the production of HT, the details on Tables 12.4 and 12.5 will be adhered to. Under optimal leach conditions, the MRTs mentioned in Table 12.3 will be leached to produce pregnant leach solutions (PLS). To produce HTs with different grades, PLS will be treated to precipitation procedure (Fig. 12.3).

Characterization and Measurement

X-Ray Diffraction (XRD)
Utilizing XRD, mineralogical compositions will be examined (Bruker D8 Advance X-ray diffractometer).

Scanning Electron Microscopy (SEM)
A Hitachi X-650 scanning electron microanalyzer will be used for the morphological analysis.

Table 12.4 Parameters considered for the production of hydrotalcite

Parameters	Levels		
	Low	Medium	High
Temperature (°C)	25	55	85
Rotational speed (rpm)	340	740	1480

Table 12.5 Design of experiment for the production of hydrotalcite

Tests	Temperature (°C)	Rotational Speed (rpm)	Treatment Combination
1	25	340	25 °C–340 rpm
2	25	740	25 °C–740 rpm
3	25	1480	25 °C–1480 rpm
4	55	340	55 °C–340 rpm
5	55	740	55 °C–740 rpm
6	55	1480	55 °C–1480 rpm
7	85	340	85 °C–340 rpm
8	85	740	85 °C–740 rpm
9	85	1480	85 °C–1480 rpm

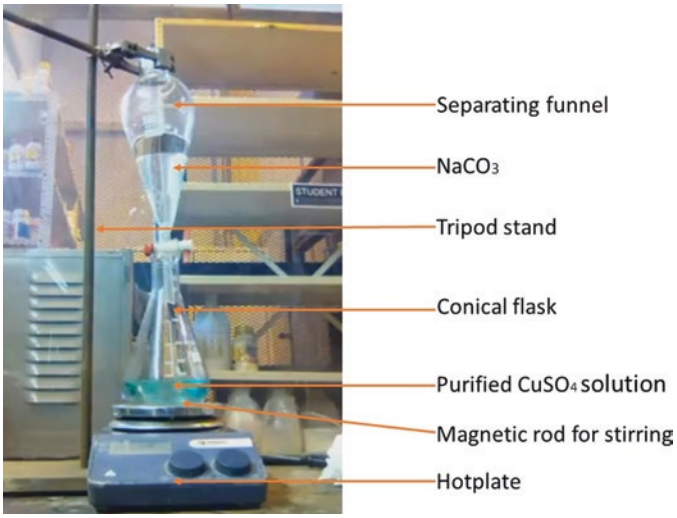

Fig. 12.3 Experimental setup for the production of hydrotalcites

Transmission Electron Microscopy (SEM)
HR-TEM will be used to further characterize the HT's surface morphology (Tecnai, G2 F20 X-Twin MAT).

Thermo-Graphical Analyzer (TGA)
Using a Mettler Toledo TGA/SDTA 851e with sample robot and a TSO800 GC gas control unit, thermal gravimetric analysis will be performed.

FTIR

A Micrometrics Tri Star 3000 Analyzer will be used to measure the surface area of the prepared hydrotalcite using a PerkinElmer Universal (ATR) mounted with a diamond crystal.

XRF

In order to show the benefit of including a density separation stage to the proposed methodology and to highlight the extent to which metal in the MRT will not be incorporated in the structure of the HT_{MRT}, aside from the divalent and trivalent cations, XRF analysis will be performed on the prepared hydrotalcite.

Brunauer–Emmett–Teller (BET)

Using the Brunauer–Emmett–Teller (BET) method, the porosity and surface area measurements of the starting materials and manufactured HT will be calculated using the N_2 adsorption/desorption isotherms at a temperature of 196 °C. The "classic theory model" of Barrett, Joyner, and Halenda will be used as a guide to compute the pore size distributions from the N_2 adsorption isotherms.

In order to confirm the applicability of the preparation procedures in producing hydrotalcite with the needed qualities from MOT, the results of these analyses' structural properties of the prepared hydrotalcite will be compared to those of commercial materials.

CO_2 Sorption on Synthesized HT_{MRT}

All generated HTMRT and commercial HTs adsorbents will be subjected to temperature-controlled desorption studies (CO_2-TPD) utilizing a micrometrics auto Chem (model 2950 HP). As the temperature is ramped up from 20 to 200 °C at a rate of 2 °C/min, each adsorbent will be degassed by having helium flow over its surface at a rate of 20 ml/min.

The HT samples will be cooled to ambient temperature with a flow of helium after the temperature is maintained at 200 °C for 1 hour.

The sample will be exposed to 4 hours of 99.99% instrument grade CO_2 for adsorption onto the basic sites of the sample at room temperature. After 4 hours of isothermal helium blowing over the adsorbent to remove extra CO_2, the TCD detector will be turned on, allowed to stabilize, and zeroed. The sample will be heated from ambient temperature to 900 °C at a ramping rate of 2 °C/min during the desorption of CO_2 in a helium environment at a flow rate of 20 ml/min. The amount of CO_2 evolved in relation to the temperature will then be detected by a TCD detector to produce the TPD profiles.

Experimentation to Determine the Effect of Molar Ratio on HT_{MRT} CO_2 Capture Capacity

The ability of various Na-HT_{MRT} sorbents to absorb CO_2 at temperatures typical of industrial CO_2 emitters, such as coal-fired thermal power plants, will be evaluated. We will look into how varied Na_2CO_3: HT_{MRT} molar ratios affect CO_2 sorption and desorption at 700 °C.

Experimentation to Determine the Effect of Temperature on HT_{MRT} CO_2 Capture Capacity
To ascertain the temperature corresponding to the highest CO_2 sorption capacity and the CO_2 sorption activation temperature, a non-isothermal CO_2 absorption test will be performed.

Experimentation to Determine Effect of Calcination on HT_{MRT} CO_2 Capture Capacity
By raising the calcination temperature, which can facilitate Na diffusion, the distribution of sodium (Na) in the calcination products can be altered. We will look into the CO_2 uptake characteristics of Na-HT_{MRT} sorbents that were calcined at 600, 800, and 900 °C.

Experimentation to Determine Effect of Diluted CO_2 and Moisture on Sorption/Desorption on HT_{CSD} CO_2 Capture Capacity
To assess their impact on the CO_2 sorption capacity, the CO_2 absorption capacity of the HTCSD sorbents will be investigated in the presence of diluted CO_2 (12.5%) and moisture (212%).

Experimentation to Determine Regeneration of Developed HT_{MRT} Sorbents after CO_2 Capture
With Na_2CO_3:SiO_2 molar ratios of 0.5:1, 1:1, and 1.5:1, five CO_2 sorption/desorption cycles for the Na-HT_{MRT} sorbent will be studied.

12.8 Contribution to Knowledge

The following information will be revealed at the conclusion of this study:

1. This project will offer an innovative, low-cost secondary supply of mullite. One which will act as a solid adsorbent for the CO_2 capture.
2. This secondary resource of mullite is new since it has never been used as a solid adsorbent for the extraction of CO_2.
3. Offering a novel HT_{MRT} with structural characteristics that have not been mentioned in the literature.
4. The ability of HT_{MRT} to absorb CO_2 will be revealed.
5. To ensure compatibility, the results of HT_{MRT}'s structural characteristics and CO_2 adsorption potential will be compared to those of commercial materials.

12.9 Ethical Considerations

There are no ethical issues in this project.

12.10 Dissemination

The results will be presented at local and international conferences, while and the full paper will be published in the corresponding conference proceedings. Other results will be published in Department of Higher Education and Training (DHET) accredited journals like the following:

- Korean Journal of Chemical Engineering by springer publisher.
- Journal of Materials Science by springer publisher.

12.11 Budget (Table 12.6)

Table 12.6 Estimated budget of the projectKey: *TUT* Tshwane University of Technology, *R* Rand

Items	Cost	Source
Literature sourcing and stationaries	X	TUT
Materials and supplies	X	TUT
Analytical equipment	X	TUT
Travelling expenses	X	TUT
Miscellaneous expenses	X	TUT
Total	X	TUT

12.12 Time Frame (Table 12.7)

Table 12.7 Estimated time frame of the project

S/N	Task name	Year	
		2020	2021
1	Proposal (compilation and presentation)	WIP	WIP
2	Literature review	WIP	WIP
3	Material sourcing	WIP	WIP
4	Sample preparation (sampling)	WIP	WIP
5	Fabrication of test sample optimization process	WIP	WIP
6	Fabrication of test samples	WIP	WIP
7	Thermal conductivity and wear resistance tests	WIP	WIP
8	Results, data, and analysis	WIP	WIP
9	Optimum predictive model development	WIP	WIP
10	3D print of brake rotor and validation of optimum prediction	WIP	WIP
11	Compilation and presentation of final report	WIP	WIP

Key*: WIP* Work in Progress

References

1. Y. Lim, J. Kim, J. Jung, C.S. Lee, C. Han, Modeling and simulation of CO_2 capture process for coal-based power plant using amine solvent in South Korea. Energy Procedia **37**, 1855–1862 (2013)
2. P.T. Sekoai, M.O. Daramola, Biohydrogen production as a potential energy fuel in South Africa. Biofuel Res. J. **2**(2), 223–226 (2015)
3. K.O. Yoro, P.T. Sekoai, The potential of CO_2 capture and storage technology in South Africa's coal-fired thermal power plants. Environments **3**(3), 24 (2016)
4. P.T. Sekoai, K.O. Yoro, Biofuel development initiatives in sub-Saharan Africa: Opportunities and challenges. Climate **4**(2), 33 (2016)
5. D.J. Wuebbles, A.K. Jain, Concerns about climate change and the role of fossil fuel use. Fuel Process. Technol. **71**(1–3), 99–119 (2001)
6. A. Engelbrecht, A. Golding, S. Hietkamp, S. Scholes, The potential for sequestration of carbon dioxide in South Africa. Report for the Department of Minerals & Energy. Pretoria, Council for Scientific and Industrial Research, 2004
7. P.J.D. Lloyd, *Carbon Capture and Storage in South Africa: Development and Climate Change* (University of Cape Town, Cape Town, 2014)
8. T.F. Wall, Combustion processes for carbon capture. Proc. Combust. Inst. **31**(1), 31–47 (2007)
9. R.S. Middleton, J.K. Eccles, The complex future of CO_2 capture and storage: Variable electricity generation and fossil fuel power. Appl. Energy **108**, 66–73 (2013)
10. K.J. Fricker, A.H.A. Park, Investigation of the different carbonate phases and their formation kinetics during Mg (OH) 2 slurry carbonation. Ind. Eng. Chem. Res. **53**(47), 18170–18179 (2014)
11. B. Li, Y. Duan, D. Luebke, B. Morreale, Advances in CO_2 capture technology: A patent review. Appl. Energy **102**, 1439–1447 (2013)
12. D.M. D'Alessandro, B. Smit, J.R. Long, Carbon dioxide capture: Prospects for new materials. Angew. Chem. Int. Ed. **49**(35), 6058–6082 (2010)
13. A.J. Reynolds, T.V. Verheyen, S.B. Adeloju, A.L. Chaffee, E. Meuleman, Monoethanolamine degradation during pilot-scale post-combustion capture of CO_2 from a brown coal-fired power station. Energy Fuel **29**(11), 7441–7455 (2015)
14. A.S. Bhown, B.C. Freeman, Analysis and status of post-combustion carbon dioxide capture technologies. Environ. Sci. Technol. **45**(20), 8624–8632 (2011)
15. J. Wang, L. Huang, R. Yang, Z. Zhang, J. Wu, Y. Gao, Q. Wang, D. O'Hare, Z. Zhong, Recent advances in solid sorbents for CO_2 capture and new development trends. Energy Environ. Sci. **7**(11), 3478–3518 (2014)
16. S.Y. Lee, S.J. Park, A review on solid adsorbents for carbon dioxide capture. J. Ind. Eng. Chem. **23**, 1–11 (2015)
17. A.E. Creamer, B. Gao, Carbon-based adsorbents for postcombustion CO_2 capture: A critical review. Environ. Sci. Technol. **50**(14), 7276–7289 (2016)
18. G.N. Muriithi, L.F. Petrik, O. Fatoba, W.M. Gitari, F.J. Doucet, J. Nel, S.M. Nyale, P.E. Chuks, Comparison of CO_2 capture by ex-situ accelerated carbonation and in in-situ naturally weathered coal fly ash. J. Environ. Manag. **127**, 212–220 (2013)
19. A. Dindi, D.V. Quang, L.F. Vega, E. Nashef, M.R. Abu-Zahra, Applications of fly ash for CO2 capture, utilization, and storage. J. CO2 Util. **29**, 82–102 (2019)
20. S.M.H. Asl, H. Javadian, M. Khavarpour, C. Belviso, M. Taghavi, M. Maghsudi, Porous adsorbents derived from coal fly ash as cost-effective and environmentally-friendly sources of aluminosilicate for sequestration of aqueous and gaseous pollutants: A review. J. Clean. Prod. **208**, 1131–1147 (2019)
21. A. Sanna, M.M. Maroto-Valer, Potassium-based sorbents from fly ash for high-temperature CO_2 capture. Environ. Sci. Pollut. Res. **23**(22), 22242–22252 (2016)

22. Y.A. Alhamed, S.U. Rather, A.H. El-Shazly, S.F. Zaman, M.A. Daous, A.A. Al-Zahrani, Preparation of activated carbon from fly ash and its application for CO_2 capture. Korean J. Chem. Eng. **32**(4), 723–730 (2015)
23. A. Sanna, M.M. Maroto-Valer, CO_2 capture at high temperature using fly ash-derived sodium silicates. Ind. Eng. Chem. Res. **55**(14), 4080–4088 (2016)
24. R. Panek, M. Wdowin, W. Franus, D. Czarna, L.A. Stevens, H. Deng, J. Liu, C. Sun, H. Liu, C.E. Snape, Fly ash-derived MCM-41 as a low-cost silica support for polyethyleneimine in post-combustion CO_2 capture. J. CO2 Util. **22**, 81–90 (2017)
25. L. Liu, R. Singh, P. Xiao, P.A. Webley, Y. Zhai, Zeolite synthesis from waste fly ash and its application in CO_2 capture from flue gas streams. Adsorption **17**(5), 795–800 (2011)
26. G.N. Muriithi, L.F. Petrik, W.M. Gitari, F.J. Doucet, Synthesis and characterization of hydrotalcite from South African Coal fly ash. Powder Technol. **312**, 299–309 (2017)
27. P.W. Du Plessis, T.V. Ojumu, O.O. Fatoba, R.O. Akinyeye, L.F. Petrik, Distributional fate of elements during the synthesis of zeolites from South African coal fly ash. Materials **7**(4), 3305–3318 (2014)
28. M. Ivanov, K. Klemkaite, A. Khinsky, A. Kareiva, J. Banys, Dielectric and conductive properties of hydrotalcite. Ferroelectrics **417**(1), 136–142 (2011)
29. K. Hosni, E. Srasra, Simplified synthesis of layered double hydroxide using a natural source of magnesium. Appl. Clay Sci. **43**(3–4), 415–419 (2009)
30. P. Kunecki, R. Panek, M. Wdowin, W. Franus, Synthesis of faujasite (FAU) and tschernichite (LTA) type zeolites as a potential direction of the development of lime Class C fly ash. Int. J. Miner. Process. **166**, 69–78 (2017)
31. P. Kunecki, R. Panek, A. Koteja, W. Franus, Influence of the reaction time on the crystal structure of Na-P1 zeolite obtained from coal fly ash microspheres. Microporous Mesoporous Mater. **266**, 102–108 (2018)
32. T. Wajima, Synthesis of hydrotalcite from bittern, and its removal abilities of phosphate and nitrate. Int. J. Chem. Eng. Appl. **6**(4), 228 (2015)
33. Y. Kuwahara, T. Ohmichi, T. Kamegawa, K. Mori, H. Yamashita, A novel conversion process for waste slag: Synthesis of a hydrotalcite-like compound and zeolite from blast furnace slag and evaluation of adsorption capacities. J. Mater. Chem. **20**(24), 5052–5062 (2010)
34. R. Galindo, A. López-Delgado, I. Padilla, M. Yates, Synthesis and characterisation of hydrotalcites produced by an aluminium hazardous waste: A comparison between the use of ammonia and the use of triethanolamine. Appl. Clay Sci. **115**, 115–123 (2015)
35. R. Galindo, I. Padilla, R. Sánchez-Hernández, J.I. Robla, G. Monrós, A. López-Delgado, Production of added-value materials from a hazardous waste in the aluminium tertiary industry: Synergistic effect between hydrotalcites and glasses. J. Environ. Chem. Eng. **3**(4), 2552–2559 (2015)
36. A. Gil, E. Arrieta, M.A. Vicente, S.A. Korili, Synthesis and CO_2 adsorption properties of hydrotalcite-like compounds prepared from aluminum saline slag wastes. Chem. Eng. J. **334**, 1341–1350 (2018)
37. U. Neveling, Palabora mining company annual report on ambient air quality monitoring, 2011
38. D.O. Okanigbe, Production of copper and copper oxide nano-particles from leach solution of low grade copper smelter dust, 2019
39. D. Okanigbe, P. Olawale, A. Popoola, A. Abraham, A. Michael, K. Andrei, Centrifugal separation experimentation and optimum predictive model development for copper recovery from waste copper smelter dust. Cogent Eng. **5**(1), 1551175 (2018)
40. U. Schacht, C. Jenkins, Soil gas monitoring of the Otway Project demonstration site in SE Victoria, Australia. Int. J. Greenhouse Gas Control **24**, 14–29 (2014)
41. S.E. Beaubien, D.G. Jones, F. Gal, A.K.A.P. Barkwith, G. Braibant, J.C. Baubron, G. Ciotoli, S. Graziani, T.R. Lister, S. Lombardi, K. Michel, Monitoring of near-surface gas geochemistry at the Weyburn, Canada, CO_2-EOR site, 2001–2011. Int. J. Greenhouse Gas Control **16**, S236–S262 (2013)

42. M. Maver, Barriers to carbon capture and storage. Available online: http://ehsjournal.org/marko-maver/barriers-to-carbon-capture-and-storage-ccs/2012/. Accessed on 5 June 2016
43. A. Voleno, M.C. Romano, D.M. Turi, P. Chiesa, M.T. Ho, D.E. Wiley, Post-combustion CO_2 capture from natural gas combined cycles by solvent supported membranes. Energy Procedia **63**, 7389–7397 (2014)
44. C. Zhang, D. Zhou, P. Li, F. Li, Y. Zhang, Z. Sun, Z. Zhao, CO_2 storage potential of the Qiongdongnan Basin, northwestern South China Sea. Greenhouse Gases Sci. Technol. **4**(6), 691–706 (2014)
45. M.Y. Lee, H. Hashim, Modelling and optimization of CO_2 abatement strategies. J. Clean. Prod. **71**, 40–47 (2014)
46. H. Leion, E. Jerndal, B.M. Steenari, S. Hermansson, M. Israelsson, E. Jansson, M. Johnsson, R. Thunberg, A. Vadenbo, T. Mattisson, A. Lyngfelt, Solid fuels in chemical-looping combustion using oxide scale and unprocessed iron ore as oxygen carriers. Fuel **88**(10), 1945–1954 (2009)
47. Y. Man, S. Yang, D. Xiang, X. Li, Y. Qian, Environmental impact and techno-economic analysis of the coal gasification process with/without CO_2 capture. J. Clean. Prod. **71**, 59–66 (2014)
48. P. Mores, N. Rodríguez, N. Scenna, S. Mussati, CO_2 capture in power plants: Minimization of the investment and operating cost of the post-combustion process using MEA aqueous solution. Int. J. Greenhouse Gas Control **10**, 148–163 (2012)
49. J.R. Hufton, S. Mayorga, S. Sircar, Sorption-enhanced reaction process for hydrogen production. AICHE J. **45**(2), 248–256 (1999)
50. Z. Yong, V. Mata, A.E. Rodrigues, Adsorption of carbon dioxide onto hydrotalcite-like compounds (HTlcs) at high temperatures. Ind. Eng. Chem. Res. **40**(1), 204–209 (2001)
51. J. Hufton, S. Mayorga, T. Gaffhey, S. Nataraj, Sorption enhanced reaction process (SERP) for the production of hydrogen, in *Hydrogen Program Review*, 21–23 May 1997
52. J. Santhanalakshmi, T. Raja, Selective N-methylation of aniline by calcined MgIIAlIII layered double hydroxides. Appl. Catal. A Gen. **147**(1), 69–80 (1996)
53. W.T. Reichle, Pulse microreactor examination of the vapor-phase aldol condensation of acetone. J. Catal. **63**(2), 295–306 (1980)
54. A. Corma, S. Iborra, J. Primo, F. Rey, One-step synthesis of citronitrile on hydrotalcite derived base catalysts. Appl. Catal. A Gen. **114**(2), 215–225 (1994)
55. C. Cativiela, F. Figueras, J. Fraile, J. García, J. Mayoral, Hydrotalcite-promoted epoxidation of electron-deficient alkenes with hydrogen peroxide. Tetrahedron Lett. **36**(23), 4125–4128 (1995)
56. H. Schaper, J.J. Berg-Slot, W.H.J. Stork, Stabilized magnesia: A novel catalyst (support) material. Appl. Catal. **54**(1), 79–90 (1989)
57. K. Parida, J. Das, Mg/Al hydrotalcites: Preparation, characterisation and ketonisation of acetic acid. J. Mol. Catal. A Chem. **151**(1–2), 185–192 (2000)
58. S. Velu, C.S. Swamy, Selective C-alkylation of phenol with methanol over catalysts derived from copper-aluminium hydrotalcite-like compounds. Appl. Catal. A Gen. **145**(1–2), 141–153 (1996)
59. A.L. McKenzie, C.T. Fishel, R.J. Davis, Investigation of the surface structure and basic properties of calcined hydrotalcites. J. Catal. **138**(2), 547–561 (1992)
60. M. Corsten, A. Ramírez, L. Shen, J. Koornneef, A. Faaij, Environmental impact assessment of CCS chains–lessons learned and limitations from LCA literature. Int. J. Greenhouse Gas Control **13**, 59–71 (2013)
61. B. Nykvist, Ten times more difficult: Quantifying the carbon capture and storage challenge. Energy Policy **55**, 683–689 (2013)
62. B.K. Sovacool, B. Brossmann, Symbolic convergence and the hydrogen economy. Energy Policy **38**(4), 1999–2012 (2010)
63. B.K. Sovacool, M.V. Ramana, Back to the future: Small modular reactors, nuclear fantasies, and symbolic convergence. Sci. Technol. Hum. Values **40**(1), 96–125 (2015)

64. J.P. Verdon, Significance for secure CO_2 storage of earthquakes induced by fluid injection. Environ. Res. Lett. **9**(6), 064022 (2014)
65. L. Vesnic-Alujevic, M. Breitegger, A.G. Pereira, What smart grids tell about innovation narratives in the European Union: Hopes, imaginaries and policy. Energy Res. Soc. Sci. **12**, 16–26 (2016)
66. M. Lisjak, A.Y. Lee, W.L. Gardner, When a threat to the brand is a threat to the self: The importance of brand identification and implicit self-esteem in predicting defensiveness. Personal. Soc. Psychol. Bull. **38**(9), 1120–1132 (2012)
67. M.G. Little, R.B. Jackson, Potential impacts of leakage from deep CO_2 geosequestration on overlying freshwater aquifers. Environ. Sci. Technol. **44**(23), 9225–9232 (2010)
68. P. Hoggett, Government and the perverse social defence. Br. J. Psychother. **26**(2), 202–212 (2010)
69. A. Corti, L. Lombardi, Reduction of carbon dioxide emissions from a SCGT/CC by ammonia solution absorption–preliminary results. Int. J. Thermodyn. **7**(4), 173–181 (2004)
70. B. Seoane, J. Coronas, I. Gascon, M.E. Benavides, O. Karvan, J. Caro, F. Kapteijn, J. Gascon, Metal–organic framework based mixed matrix membranes: A solution for highly efficient CO_2 capture? Chem. Soc. Rev. **44**(8), 2421–2454 (2015)
71. H. Feng, S. Wu, S. Huang, Y. Wu, J. Gao, Regenerable magnesium-based sorbent for high-pressure and moderate-temperature CO_2 capture: Physicochemical structures and capture performances. Fuel **159**, 559–569 (2015)
72. A. Alaswad, M. Dassisti, T. Prescott, A.G. Olabi, Technologies and developments of third generation biofuel production. Renew. Sust. Energ. Rev. **51**, 1446–1460 (2015)
73. A.S. Alshehry, M. Belloumi, Energy consumption, carbon dioxide emissions and economic growth: The case of Saudi Arabia. Renew. Sust. Energ. Rev. **41**, 237–247 (2015)
74. C. Ampelli, S. Perathoner, G. Centi, CO_2 utilization: An enabling element to move to a resource-and energy-efficient chemical and fuel production. Philos. Trans. R. Soc. A Math. Phys. Eng. Sci. **373**(2037), 20140177 (2015)
75. R.R. Ang, L.T. Sin, S.T. Bee, T.T. Tee, A.A.H. Kadhum, A.R. Rahmat, B.A. Wasmi, A review of copolymerization of greenhouse gas carbon dioxide and oxiranes to produce polycarbonate. J. Clean. Prod. **102**, 1–17 (2015)
76. M. Anjos, B.D. Fernandes, A.A. Vicente, J.A. Teixeira, G. Dragone, Optimization of CO_2 bio-mitigation by Chlorella vulgaris. Bioresour. Technol. **139**, 149–154 (2013)
77. P. Babu, P. Linga, R. Kumar, P. Englezos, A review of the hydrate based gas separation (HBGS) process for carbon dioxide pre-combustion capture. Energy **85**, 261–279 (2015)
78. D.B. Bacik, W. Yuan, C.B. Roberts, M.R. Eden, Systems analysis of benign hydrogen peroxide synthesis in supercritical CO_2, in *Computer Aided Chemical Engineering*, vol. 29, (Elsevier, 2011), pp. 392–396
79. I.A. Berg, Ecological aspects of the distribution of different autotrophic CO_2 fixation pathways. Appl. Environ. Microbiol. **77**(6), 1925–1936 (2011)
80. G. Centi, S. Perathoner, Opportunities and prospects in the chemical recycling of carbon dioxide to fuels. Catal. Today **148**(3–4), 191–205 (2009)
81. W.Y. Cheah, P.L. Show, J.S. Chang, T.C. Ling, J.C. Juan, Biosequestration of atmospheric CO_2 and flue gas-containing CO_2 by microalgae. Bioresour. Technol. **184**, 190–201 (2015)
82. C.Y. Chen, X.Q. Zhao, H.W. Yen, S.H. Ho, C.L. Cheng, D.J. Lee, F.W. Bai, J.S. Chang, Microalgae-based carbohydrates for biofuel production. Biochem. Eng. J. **78**, 1–10 (2013)
83. J. Cheng, Y. Huang, J. Feng, J. Sun, J. Zhou, K. Cen, Improving CO_2 fixation efficiency by optimizing Chlorella PY-ZU1 culture conditions in sequential bioreactors. Bioresour. Technol. **144**, 321–327 (2013)
84. J. Cheng, Y. Huang, J. Feng, J. Sun, J. Zhou, K. Cen, Mutate chlorella sp. by nuclear irradiation to fix high concentrations of CO_2. Bioresour. Technol. **136**, 496–501 (2013)
85. H.H. Cheng, L.M. Whang, K.C. Chan, M.C. Chung, S.H. Wu, C.P. Liu, S.Y. Tien, S.Y. Chen, J.S. Chang, W.J. Lee, Biological butanol production from microalgae-based biodiesel residues by Clostridium acetobutylicum. Bioresour. Technol. **184**, 379–385 (2015)

86. C.L. Chiang, C.M. Lee, P.C. Chen, Utilization of the cyanobacteria anabaena sp. CH1 in biological carbon dioxide mitigation processes. Bioresour. Technol. **102**(9), 5400–5405 (2011)
87. A.B. Fulke, K. Krishnamurthi, M.D. Giripunje, S.S. Devi, T. Chakrabarti, Biosequestration of carbon dioxide, biomass, calorific value and biodiesel precursors production using a novel flask culture photobioreactor. Biomass Bioenergy **72**, 136–142 (2015)
88. Y. Tan, W. Nookuea, H. Li, E. Thorin, J. Yan, Property impacts on Carbon Capture and Storage (CCS) processes: A review. Energy Convers. Manag. **118**, 204–222 (2016)
89. A. Raza, R. Rezaee, C.H. Bing, R. Gholami, M.A. Hamid, R. Nagarajan, Carbon dioxide storage in subsurface geologic medium: A review on capillary trapping mechanism. Egypt. J. Pet. **25**(3), 367–373 (2016)
90. J.A. Lake, I. Johnson, D.D. Cameron, Carbon Capture and Storage (CCS) pipeline operating temperature effects on UK soils: The first empirical data. Int. J. Greenhouse Gas Control **53**, 11–17 (2016)
91. D.Y. Leung, G. Caramanna, M.M. Maroto-Valer, An overview of current status of carbon dioxide capture and storage technologies. Renew. Sust. Energ. Rev. **39**, 426–443 (2014)
92. F. Chu, C. Jon, L. Yang, X. Du, Y. Yang, CO_2 absorption characteristics in ammonia solution inside the structured packed column. Ind. Eng. Chem. Res. **55**(12), 3696–3709 (2016)
93. G. Hu, N.J. Nicholas, K.H. Smith, K.A. Mumford, S.E. Kentish, G.W. Stevens, Carbon dioxide absorption into promoted potassium carbonate solutions: A review. Int. J. Greenhouse Gas Control **53**, 28–40 (2016)
94. K.O. Kwak, S.J. Jung, S.Y. Chung, C.M. Kang, Y.I. Huh, S.O. Bae, Optimization of culture conditions for CO_2 fixation by a chemoautotrophic microorganism, strain YN-1 using factorial design. Biochem. Eng. J. **31**(1), 1–7 (2006)
95. G.T. Rochelle, Amine scrubbing for CO_2 capture. Science **325**(5948), 1652–1654 (2009)
96. S. Kim, C.B. Park, Bio-inspired synthesis of minerals for energy, environment, and medicinal applications. Adv. Funct. Mater. **23**(1), 10–25 (2013)
97. S. Wang, K. Liu, X. Yao, L. Jiang, Bioinspired surfaces with superwettability: New insight on theory, design, and applications. Chem. Rev. **115**(16), 8230–8293 (2015)
98. S. Quan, S. Li, Z. Wang, X. Yan, Z. Guo, L. Shao, A bio-inspired CO_2-philic network membrane for enhanced sustainable gas separation. J. Mater. Chem. A **3**(26), 13758–13766 (2015)
99. U.G. Wegst, H. Bai, E. Saiz, A.P. Tomsia, R.O. Ritchie, Bioinspired structural materials. Nat. Mater. **14**(1), 23–36 (2015)
100. C.H. Lau, P. Li, F. Li, T.S. Chung, D.R. Paul, Reverse-selective polymeric membranes for gas separations. Prog. Polym. Sci. **38**(5), 740–766 (2013)
101. J. Su, R.C. Ong, P. Wang, T.S. Chung, B.J. Helmer, J.S. De Wit, Advanced FO membranes from newly synthesized CAP polymer for wastewater reclamation through an integrated FO-MD hybrid system. AICHE J. **59**(4), 1245–1254 (2013)
102. D.W. Mangindaan, N.M. Woon, G.M. Shi, T.S. Chung, P84 polyimide membranes modified by a tripodal amine for enhanced pervaporation dehydration of acetone. Chem. Eng. Sci. **122**, 14–23 (2015)
103. A.W. Xu, Y. Ma, H. Cölfen, Biomimetic mineralization. J. Mater. Chem. **17**(5), 415–449 (2007)
104. Y. Cai, J. Yao, Effect of proteins on the synthesis and assembly of calcium phosphate nanomaterials. Nanoscale **2**(10), 1842–1848 (2010)
105. B. Mondal, J. Song, F. Neese, S. Ye, Bio-inspired mechanistic insights into CO_2 reduction. Curr. Opin. Chem. Biol. **25**, 103–109 (2015)
106. M.K. Mondal, H.K. Balsora, P. Varshney, Progress and trends in CO_2 capture/separation technologies: A review. Energy **46**(1), 431–441 (2012)
107. E.S. Rubin, C. Chen, A.B. Rao, Cost and performance of fossil fuel power plants with CO_2 capture and storage. Energy Policy **35**(9), 4444–4454 (2007)
108. G. Cau, V. Tola, P. Deiana, Comparative performance assessment of USC and IGCC power plants integrated with CO_2 capture systems. Fuel **116**, 820–833 (2014)
109. M. Wang, A. Lawal, P. Stephenson, J. Sidders, C. Ramshaw, Post-combustion CO_2 capture with chemical absorption: A state-of-the-art review. Chem. Eng. Res. Des. **89**(9), 1609–1624 (2011)

110. G. Scheffknecht, L. Al-Makhadmeh, U. Schnell, J. Maier, Oxy-fuel coal combustion—A review of the current state-of-the-art. Int. J. Greenhouse Gas Control **5**, S16–S35 (2011)
111. S. Rehfeldt, C. Kuhr, F.P. Schiffer, P. Weckes, C. Bergins, First test results of Oxyfuel combustion with Hitachi's DST-burner at Vattenfall's 30 MWth Pilot Plant at Schwarze Pumpe. Energy Procedia **4**, 1002–1009 (2011)
112. C.C. Cormos, K. Vatopoulos, E. Tzimas, Assessment of the consumption of water and construction materials in state-of-the-art fossil fuel power generation technologies involving CO_2 capture. Energy **51**, 37–49 (2013)
113. O.R. Rivas, J.M. Prausnitz, Sweetening of sour natural gases by mixed-solvent absorption: Solubilities of ethane, carbon dioxide, and hydrogen sulfide in mixtures of physical and chemical solvents. AICHE J. **25**(6), 975–984 (1979)
114. A.L. Chaffee, G.P. Knowles, Z. Liang, J. Zhang, P. Xiao, P.A. Webley, CO_2 capture by adsorption: Materials and process development. Int. J. Greenhouse Gas Control **1**(1), 11–18 (2007)
115. H. Yang, Z. Xu, M. Fan, R. Gupta, R.B. Slimane, A.E. Bland, I. Wright, Progress in carbon dioxide separation and capture: A review. J. Environ. Sci. **20**(1), 14–27 (2008)
116. M.R. Othman, R. Zakaria, W.J.N. Fernando, Strategic planning on carbon capture from coal fired plants in Malaysia and Indonesia: A review. Energy Policy **37**(5), 1718–1735 (2009)
117. L. Álvarez, C. Yin, J. Riaza, C. Pevida, J.J. Pis, F. Rubiera, Biomass co-firing under oxy-fuel conditions: A computational fluid dynamics modelling study and experimental validation. Fuel Process. Technol. **120**, 22–33 (2014)
118. C.C. Cormos, Evaluation of energy integration aspects for IGCC-based hydrogen and electricity co-production with carbon capture and storage. Int. J. Hydrog. Energy **35**(14), 7485–7497 (2010)
119. M.H. Bade, S. Bandyopadhyay, Analysis of gas turbine integrated cogeneration plant: Process integration approach. Appl. Therm. Eng. **78**, 118–128 (2015)
120. C. Dinca, A. Badea, The parameters optimization for a CFBC pilot plant experimental study of post-combustion CO_2 capture by reactive absorption with MEA. Int. J. Greenhouse Gas Control **12**, 269–279 (2013)
121. R. Domenichini, S. Arienti, P. Cotone, S. Santos, Evaluation and analysis of water usage and loss of power in plants with CO_2 capture. Energy Procedia **4**, 1925–1932 (2011)
122. V. Tola, A. Pettinau, Power generation plants with carbon capture and storage: A techno-economic comparison between coal combustion and gasification technologies. Appl. Energy **113**, 1461–1474 (2014)
123. A.M. Oehlert, K.A. Lamb-Wozniak, Q.B. Devlin, G.J. Mackenzie, J.J. Reijmer, P.K. Swart, The stable carbon isotopic composition of organic material in platform derived sediments: Implications for reconstructing the global carbon cycle. Sedimentology **59**(1), 319–335 (2012)
124. M. Zhao, A.I. Minett, A.T. Harris, A review of techno-economic models for the retrofitting of conventional pulverised-coal power plants for post-combustion capture (PCC) of CO_2. Energy Environ. Sci. **6**(1), 25–40 (2013)
125. D.O. Okanigbe, A.P.I. Popoola, A.A. Adeleke, Characterization of copper smelter dust for copper recovery. Procedia Manuf. **7**, 121–126 (2017)
126. P.L. Linda, D.O. Okanigbe, A.P.I. Popoola, O.M. Popoola, Characterization of density separated mullite-rich tailings from a secondary copper resource, a potential reinforcement material for development of an enhanced thermally conductive and wear resistant ti-6al-4v matrix composite, in *The Proceedings of the 60th International Conference of Metallurgist*, (Canada, 2021)

Index

D. O. Okanigbe, A. P. Popoola (eds.), *Resource Recovery and Recycling from Waste Metal Dust*, https://doi.org/10.1007/978-3-031-22492-8